

Cumhuriyet Science Journal  
Faculty of Science, Cumhuriyet University  
58140 - Sivas - Türkiye  
Phone: +90(346) 487 13 72  
Fax: +90(346) 219 11 86  
e-mail: [csj@cumhuriyet.edu.tr](mailto:csj@cumhuriyet.edu.tr)  
<http://csj.cumhuriyet.edu.tr/en>  
<http://dergipark.org.tr/en/pub/csj>

Cumhuriyet Science Journal Vol: 46 No: 2 Year 2025



**Sivas Cumhuriyet University**

**ISSN : 2680-2587**

**e-ISSN : 246-2587X**

[dergipark.org.tr/tr/pub/csj](http://dergipark.org.tr/tr/pub/csj)  
e-mail: [csj@cumhuriyet.edu.tr](mailto:csj@cumhuriyet.edu.tr)



Cumhuriyet Science Journal (CSJ) is an official publication of Sivas Cumhuriyet University, Science Faculty. The high quality research papers related to the natural sciences are published as online four times a year. CSJ is an open access, free of charge journal and all articles in CSJ have undergone peer review and upon acceptance are immediately and permanently free for everyone to read and download.

**Volume: 46**

**Number: 2**

**Year: 2025**

# Cumhuriyet Science Journal (CSJ)



<b>ISSN:</b>	2587-2680
<b>e-ISSN:</b>	2587-246X
<b>Period:</b>	Quarterly
<b>Founded:</b>	2002
<b>Publisher:</b>	Sivas Cumhuriyet University
<b>Journal Previous Name:</b>	Cumhuriyet Üniversitesi Fen-Edebiyat Fakültesi Fen Bilimleri Dergisi
<b>Old ISSN:</b>	1300-1949

## Editor in Chief

Prof. Dr. Fatih UNGAN (Sivas Cumhuriyet University)

## Managing Editors

Prof. Dr. Baki KESKİN (Sivas Cumhuriyet University)

Prof. Dr. Halil İbrahim ULUSOY (Sivas Cumhuriyet University)

Editors	Subjects	Institution
Prof. Dr. Baki KESKİN bkeskin@cumhuriyet.edu.tr	Mathematics and Statistics	Sivas Cumhuriyet University
Prof. Dr. Halil İbrahim ULUSOY hiulusoy@cumhuriyet.edu.tr	Chemistry, Analytical Chemistry, Drug Analysis, Pharmacy	Sivas Cumhuriyet University
Prof. Dr. Ertan Mahir KORKMAZ ekorkmaz@cumhuriyet.edu.tr	Genomics and Transcriptomics, Computational Ecology, Phylogenetics	Sivas Cumhuriyet University
Prof. Dr. Hasret YAZARLI hyazarli@cumhuriyet.edu.tr	Algebra and Number Theory, Mathematical Logic, Set Theory	Sivas Cumhuriyet University
Prof. Dr. Nail ALTUNAY naltunay@cumhuriyet.edu.tr	Analytical Chemistry, Analytical Spectrometry, Instrumental Methods	Sivas Cumhuriyet University
Prof. Dr. Nilüfer TOPSAKAL ntopsakal@cumhuriyet.edu.tr	Numerical Analysis, Applied Mathematics, Biological Mathematics	Sivas Cumhuriyet University
Prof. Dr. Serkan AKKOYUN sakkoyun@cumhuriyet.edu.tr	Physical Sciences, Nuclear Physics	Sivas Cumhuriyet University
Prof. Dr. Serpil ŞAKİROĞLU serpil.sakiroglu@deu.edu.tr	Electronic and Magnetic Properties of Condensed Matter, Superconductivity	Dokuz Eylül University
Assoc. Prof. Dr. Sultan ERKAN sultanerkan@cumhuriyet.edu.tr	Chemical Sciences, Bioinorganic Chemistry, Organometallic Chemistry	Sivas Cumhuriyet University
Asst. Prof. Dr. Yener ÜNAL uyener@cumhuriyet.edu.tr	Statistics, Statistical Analysis, Probability Theory	Sivas Cumhuriyet University

Associate Editors	Subjects	Institution
Prof. Dr. Nuh DURNA ndurna@cumhuriyet.edu.tr	Operator Algebras, Functional Analysis	Sivas Cumhuriyet University
Assoc. Prof. Dr. Emre Bahadır AL ebahadir@cumhuriyet.edu.tr	Quantum Mechanics, Electronic and Magnetic Properties of Condensed Matter, Superconductivity	Sivas Cumhuriyet University
Asst. Prof. Dr. Didem MİMİROĞLU dmimiroglu@cumhuriyet.edu.tr	Cellular Interactions, Biochemistry and Cell Biology, Nanomedicine,	Sivas Cumhuriyet University
Asst. Prof. Dr. Ergün KASAKA ekasaka@cumhuriyet.edu.tr	Algology, Ecology, Limnology	Sivas Cumhuriyet University
Asst. Prof. Dr. Nil ÖZBİLÜM ŞAHİN nozibilum@cumhuriyet.edu.tr	Epigenetics, Gene Expression, Neurogenetics, Molecular Genetics, Medical Genetics	Sivas Cumhuriyet University

Editorial Board	Subjects	Institution
Prof. Dr. Adil ELİK	Chemistry and Chemical Engineering, Environmental Sciences, Basic Sciences	Sivas Cumhuriyet University
Prof. Dr. Abuzar KABİR	Analytical Biochemistry, Medical Biochemistry - Amino Acids and Metabolites, Instrumental Methods, Separation Science	Florida International University
Prof. Dr. Burhan ATEŞ	Enzymes, Chemical Sciences, Medicinal and Biomolecular Chemistry, Biomaterial , Nanomaterials	Inonu University
Prof. Dr. Debasis KUNDU	Statistical Analysis, Applied Statistics	Indian Institute of Technology
Prof. Dr. Duri Şehvar ÜNAL	Pharmacy Management, Clinical Chemistry, Analytical Spectrometry, Instrumental Methods, Separation Science	Istanbul University
Prof. Dr. Emirhan NEMUTLU	Pharmaceutical Analytical Chemistry, Analytical Chemistry, Instrumental Methods.	Hacettepe University
Prof. Dr. Hüseyin MERDAN	Applied Mathematics, Biological Mathematics	Tobb University of Economics and Technology
Prof. Dr. İdris ZORLUTUNA	Topology	Sivas Cumhuriyet University
Dr. Juan Carlos MARTÍNEZ OROZCO	Nonlinear Optics and Spectroscopy, Atomic, Molecular and Optical Physics	Universidad Autónoma de Zacatecas
Prof. Dr. Marcello LOCATELLI	Clinical Pharmacy and Pharmacy Practice, Clinical Chemistry, Analytical Chemistry	G. d'Annunzio
Prof. Dr. Margarita VALERO JUAN	Pharmaceutical Delivery Technologies, Inorganic Materials, Physical Organic Chemistry	Universidad de Salamanca
Prof. Dr. Mustafa TÜZEN	Structure and Dynamics of Materials	
Prof. Dr. Ramzi MAALEJ	Nuclear Physics, Nuclear and Plasma Physics (Other), Sensor Technology, Nanomaterials	Sfax University
Prof. Dr. Savaş KAYA	Inorganic Chemistry (Other), Theoretical and Computational Chemistry	Sivas Cumhuriyet University
Prof. Dr. Tuncay BAYRAM	Nuclear Medicine, Nuclear Physics, Nuclear Energy Systems, Detector Technology	Karadeniz Technical University

Layout Editors	Subjects	Institution
Asst. Prof. Dr. Yener ÜNAL	Statistics, Statistical Analysis, Probability Theory	Sivas Cumhuriyet University
Lecturer Aykut HASBEK	Machine Learning	Sivas Cumhuriyet University

Language Editors	Subjects	Institution
Lecturer İlke TALAK	Early English Languages	Sivas Cumhuriyet University
Instructor Mustafa Recep OKTAY	Translation and Interpretation Studies, Early English Languages	Sivas Cumhuriyet University
Instructor Rıza ÖZUTKU	Curriculum and Instruction	Sivas Cumhuriyet University

Proof Reader	Subjects	Institution
Lecturer Aykut HASBEK	Machine Learning	Sivas Cumhuriyet University

### Abstracted&Indexed

  
ULAKBİM TR-Dizin

  
Clarivate Analytics

  
Crossref

  
WorldCat

  
Arastirmax Bilimsel  
Yayın İndeksi

  
Bielefeld Academic Search  
Engine (BASE)

  
Google Scholar

  
Research Gate

  
Idealonline

### Publication Type

Peer Reviewed Journal

### Cite Type

Cumhuriyet Sci. J.

### Contact Information

Faculty of Science Cumhuriyet University 58140 Sivas- Türkiye

Phone: +90 (346) 487 13 72

Fax: +90 (346) 219 11 86

e-mail: [csj@cumhuriyet.edu.tr](mailto:csj@cumhuriyet.edu.tr)

<http://csj.cumhuriyet.edu.tr/en/>



	<b>CONTENTS</b>		<b>PAGES</b>
<b>1</b>	Chronic Otitis Media: Evaluations of Recent Approaches and Effects On Biological Systems by Means of Bibliometric Analyses Mansur Doğan	<i>Review Article</i>	185-194
<b>2</b>	Isolation and Molecular Identification of Yeast Strains Causing Spoilage in Labneh Cheese Özgür Kebapçı	<i>Research Article</i>	195-200
<b>3</b>	Effect of Bortezomib, Daptomycin and Their Combination on Antiproliferation in U266 Multiple Myeloma Cell Line Kübra Yılmaz , Ahmet Ozan Kaleci	<i>Research Article</i>	201-205
<b>4</b>	Determination of Irbesartan in Pharmaceutical Preparations by HPLC Bilal Yılmaz	<i>Research Article</i>	206-211
<b>5</b>	Precise Demonstration of Salt-Stress Induced Antifungal Activity of Origanum onites Essential Oil and Taraxacum officinale Extract Against Drug Resistant Isolates of Candida albicans and Aspergillus fumigatus Using Micro-Colony Method Esra Seyran	<i>Research Article</i>	212-224
<b>6</b>	Theoretical Investigation about Inhibition Performance of Acyclovir (ACV) Molecule on Corrosion of Fe (1 1 0) Surface in Acidic Medium: DFT, MC, Toxicity and Solubility Analyses Dilara Özbakır Işın , Savaş Kaya	<i>Research Article</i>	225-232
<b>7</b>	Molecular pKa Prediction with Deep Learning and Chemical Fingerprints Fatih Mehmet Avcu	<i>Research Article</i>	233-239
<b>8</b>	Detection of Biochemical, Cytotoxic, and Genotoxic Damage Caused by Glufosinate-Ammonium on the Zebrafish Cell Line Harika Eylül Esmer Duruel , Figen Esin Kayhan	<i>Research Article</i>	240-249
<b>9</b>	Temperature-Dependent Biochemical Alterations in Oreochromis niloticus exposed to Pendimethalin and Fluometuron Derya Kocamaz , Mine Beyazaslan , Aşkın Barış Kaya	<i>Research Article</i>	250-256
<b>10</b>	Morphological, Transcriptional, and Epigenetics Alterations due to L-arginine and L-methionine Treatment in Fusarium culmorum Fatma Berra Yücesan , Özlem Sefer , Emre Yörük	<i>Research Article</i>	257-263
<b>11</b>	Non-Competitive Inhibition of Xanthine Oxidase by N-Nitrosomorpholine: An In Vitro Study Deniz Bakır , Serkan Kapancı	<i>Research Article</i>	264-267
<b>12</b>	The Effect of NKCC1 Inhibitor Azosemide on Emotional Behaviors and Hippocampal GABA Levels in a Rat Model of Post-traumatic Stress Disorder Sebahattin Karabulut , Sümeyra Koç , Ayşegül Öztürk	<i>Research Article</i>	268-273
<b>13</b>	Investigation of a Stable Interaction of Levothyroxine with AFP Through Molecular Modelling Emel Akbaba , Deniz Karataş , Ataman Gönel , Ezgi Soylu , Beste Kiraz , Yusur Ammar Almahdi	<i>Research Article</i>	274-285
<b>14</b>	Biogenic Synthesis and Characterization of Silver Nanoparticles Using Hoya Carnosa Flower Extract Halil İbrahim Çetintaş	<i>Research Article</i>	286-291
<b>15</b>	Determination of Total Phenolic Amounts of Chloroform, Acetone and Methanol Extracts of Sargassum sp., Ulva sp. and Schizochytrium sp. Mehmet Naz	<i>Research Article</i>	292-297
<b>16</b>	The Role of Systemic Inflammation and Haematological Parameters in Autism Elif Abanoz , Merve Soyhan , Ayla Uzun Cicek , Ali Güven Say , Serkan Bolat	<i>Research Article</i>	298-303
<b>17</b>	Comparative Analysis of Sciatic Nerve Ligation and Oxaliplatin-Induced Neuropathic Pain Models: Thermal Nociception and Inflammatory Mechanisms Emre Gedikli , Ayşegül Öztürk , Şahin Yıldırım	<i>Research Article</i>	304-309
<b>18</b>	Eco-Friendly and Durable Sponge with In Situ Formed Silver Nanoparticles for Antimicrobial Filtration Furkan Şahin	<i>Research Article</i>	310-318
<b>19</b>	Potential Application of Al Doped Carbon Nanotubes for Tretinoin: a Theoretical Study Fatma Genç , Serap Senturk Dalgıç , Fatma Kandemirli	<i>Research Article</i>	319-328

20	Natural Remedies for Type 2 Diabetes: Evaluation of Phytochemicals with Bioinformatics and Molecular Approaches/ ADME/T Analysis Adem Necip	Research Article	329-337
21	Investigation of the Activity of Benzenesulfonamide Derivative Molecules Against Gastric Cancer Proteins with Gaussian Calculations and Docking Analysis Burak Tüzün	Research Article	338-347
22	Network Pharmacology-Based Approach to Unveil the Therapeutic Mechanism of Viburnum opulus L. on Glomerulonephritis Şeyda Kaya , Sevgi Durna Daştan	Research Article	348-359
23	Modeling The Physicochemical Characteristics of Benzene Compounds Through the Application of Zagreb Omicron Indices İdris Çiftçi	Research Article	360-368
24	Enhanced Breast Cancer Risk Classification Through Genetic Algorithm-Based Feature Selection and Machine Learning Techniques Aynur Yonar , Harun Yonar , Öznur Özaltın	Research Article	369-376
25	Genetic and Morphological Diversity of Tenthredopsis (Tenthredinidae: Symphyta: Hymenoptera) Species: A Case Study in Anatolia Sevda Hastaoğlu Örgen , Hasan Hüseyin Başıbüyük	Research Article	377-383
26	Superlattice Structure of Quantum Cascade Lasers: Structural and Morphological Effects of AsH <sub>3</sub> Flow Merve Nur Koçak , İlkey Demir	Research Article	384-389
27	MOVPE Growth and Doping Optimization of n-AlGaAs Layers for Laser Diode Applications Gamze Yolcu , İlkey Demir	Research Article	390-395
28	Optical Polarization Response of Hybrid Gratings Made of Metals and Polymers Based on Bruggeman Theory Talha Erdem , Emirhan Taze	Research Article	396-404
29	Recursive Polynomial Sets and Their Some Algebraic Applications Hacı Aktaş	Research Article	405-409
30	Digraph Groups Without Leaf Having An Arc Count One Greater Than Their Vertex Mehmet Sefa Cihan	Research Article	410-423

## Chronic Otitis Media: Evaluations of Recent Approaches and Effects On Biological Systems by Means of Bibliometric Analyses

Mansur Doğan<sup>1,a,\*</sup>

<sup>1</sup> Department of Otorhinolaryngology, Faculty of Medicine, Sivas Cumhuriyet University, Sivas, 58140 Türkiye

\*Corresponding author

### Review Article

#### History

Received: 30/04/2025

Accepted: XX/XX/XXXX



This article is licensed under a Creative Commons Attribution-NonCommercial 4.0 International License (CC BY-NC 4.0)

### ABSTRACT

Chronic Otitis Media (COM) is a health condition characterized by long-term infection and inflammation in the middle ear. Commonly seen in children, this condition can lead to severe hearing loss and intracranial complications (such as brain abscess, meningitis, etc.). Antibiotics form the first line of treatment, while surgical intervention may be required in resistant cases. Surgical treatment is effective in clearing infected foci and preventing complications. Recent bibliometric analyses indicate an increase in academic publications related to COM, particularly since the 2000s, with research from various disciplines broadening the perspective on the topic. The annual distribution of publications has gained further momentum since 2020, likely due to increased interest during the pandemic. In bibliometric analysis, the most cited studies focus on pediatric surgery and treatment outcomes, examining the reliability of surgical interventions and pathological processes. Keyword co-occurrence analysis plays a crucial role in identifying thematic structures within the research field. In conclusion, COM research requires more multidisciplinary collaboration, and public awareness on this issue should be increased. Bibliometric analyses provide valuable contributions to advancing knowledge in this field and guiding clinical practices. These analyses will help pave the way for new developments in understanding the causes, effects, and treatments of chronic otitis media.

**Keywords:** Chronic otitis media, Bibliometric analysis, Keyword co-occurrence, Thematic clustering, Auditory complications.

<sup>a</sup>  [mansurdogan@hotmail.com](mailto:mansurdogan@hotmail.com)  <https://orcid.org/0000-0002-3964-9363>

## Introduction

Chronic otitis media (COM) is a significant and persistent otologic health issue, characterized by long-standing infection and inflammation in the middle ear, often leading to progressive and irreversible hearing impairment, as well as potentially life-threatening intracranial and extracranial complications. This condition, frequently observed in pediatric populations, poses a substantial burden on public health systems, particularly in low- and middle-income countries where early diagnosis and effective treatment may be limited [1-3].

In recent years, bibliometric analyses of scientific studies focusing on the complications and treatment strategies of COM have provided valuable insights into the evolution of research trends, the diversity of therapeutic approaches, and the recurring clinical challenges encountered in managing the disease. These analyses not only map the intellectual structure of the field but also identify emerging research hotspots and collaboration networks among scholars and institutions [4,5].

COM is especially common in children and can cause serious intracranial and extracranial complications such as hearing loss, brain abscess, meningitis, perisinus abscess, and epidural abscess [6–10]. These complications arise primarily in cases where diagnosis and treatment are delayed, where infections are caused by multidrug-resistant (MDR) organisms, or where patients present

with immunocompromised states [4,8,11]. Notably, pediatric patients with untreated or poorly managed COM are at higher risk for neurological sequelae, including cognitive delays related to prolonged hearing loss [12,13].

The most frequently isolated pathogens in COM cases are *Pseudomonas aeruginosa* and *Staphylococcus aureus*. The increasing prevalence of antibiotic resistance among these microorganisms poses a substantial obstacle to effective medical treatment and underscores the urgent need for antimicrobial stewardship in otolaryngological practice [7,9,11,14]. Inadequate antibiotic response often necessitates a transition from conservative to invasive interventions [15].

Antibiotics constitute the first-line treatment for COM, particularly in cases that present without severe complications. However, in situations involving antibiotic-resistant bacteria or anatomical damage, surgical procedures such as mastoidectomy or tympanoplasty become indispensable therapeutic options [11,14,16]. These surgeries aim to eradicate infection foci, reconstruct middle ear structures, and preserve or restore auditory function [17,18]. Among patients with intracranial involvement, emergency surgical management in conjunction with targeted antibiotic therapy is regarded as the standard of care to reduce morbidity and mortality [4,6,10,16].

Microbiological analyses, including bacterial culture and antibiotic susceptibility testing, play a critical role in tailoring individualized treatment protocols, thereby enhancing therapeutic efficacy. Moreover, increasing public awareness about the signs and risks of COM is essential for promoting early diagnosis, timely referral to specialists, and adherence to treatment regimens, particularly in vulnerable pediatric and rural populations. Recent literature not only reaffirms the importance of accurate diagnosis and evidence-based treatment selection but also calls attention to the pressing need for innovative solutions to manage antibiotic resistance, reduce postoperative complications, and optimize long-term patient outcomes [19]. Advances in molecular diagnostics and biofilm-targeted therapies have shown promise in improving prognosis in recalcitrant cases. Bibliometric analyses further highlight the global disease burden of COM, with disproportionately high prevalence rates reported in developing regions, where health inequalities and infrastructure gaps often hinder early intervention strategies [7,9-11]. These analyses provide a macroscopic view of the research landscape and reinforce the necessity of international collaboration and policy-level interventions to improve clinical care.

In conclusion, studies focusing on the complications and therapeutic modalities of chronic otitis media consistently demonstrate that early diagnosis, rational antibiotic use, and surgical management, when indicated, are critical components in mitigating the adverse consequences of this disease. Furthermore, bibliometric research significantly contributes to the consolidation of knowledge, the identification of research priorities, and the refinement of clinical practices in the field of otology.

## Methodology

Bibliometric analysis is a systematic research method designed to quantitatively investigate the structural properties, developmental trends, and patterns of knowledge production and dissemination within scientific literature [20-22]. In this study, a comprehensive bibliometric analysis was conducted to evaluate the current state of academic research on *Chronic Otitis Media* (COM), with the aim of identifying leading authors, influential publication sources, and emerging thematic trends within the field.

The analytical process was structured in accordance with standard protocols commonly adopted in bibliometric research. The core research question guiding the study was defined as follows: "What is the quantitative distribution, thematic clustering, and structural interrelationship of scholarly publications on *Chronic Otitis Media*?" In line with this objective, the literature was systematically reviewed.

The *Web of Science* (WoS) database was selected as the primary data source due to its comprehensive indexing of high-impact journals in the health sciences,

particularly in otolaryngology and clinical research domains [23]. The data collection strategy involved a search of the WoS Core Collection using the keyword phrase "Chronic Otitis Media," restricted to the title field. The search excluded publications from the year 2025, included only records classified as "articles," and was limited to English-language publications. As a result, a total of 1,039 articles were included in the analysis.

The retrieved bibliographic records were exported to a reference management system for data organization. Duplicate records were removed, and essential variables such as author names, publication years, journal titles, citation counts, keywords, and institutional affiliations were extracted for analysis.

For data visualization and network mapping, the software tool VOSviewer was employed. This tool facilitated the creation of visual maps representing co-authorship networks, keyword co-occurrence relationships, and inter-publication citation linkages, thereby enabling a detailed exploration of the structural and thematic composition of the COM research field [24].

In the final stage of the analysis, the findings were interpreted to reveal prevailing research trends, thematic gaps, and potential areas for future inquiry. Accordingly, this bibliometric study not only provides a quantitative cartography of the *Chronic Otitis Media* literature but also offers strategic insights that may guide subsequent scientific endeavors in the field.

## Results

This section presents the findings of the bibliometric analysis conducted on the literature concerning *Chronic Otitis Media* (COM). The primary objective of the study is to investigate the quantitative dimensions of academic production in this clinical domain, reveal trends and structural characteristics within the literature, identify thematic clusters, and highlight research priorities. The results are systematically evaluated under subheadings such as publication trends by year, most highly cited articles, keyword analyses, and network visualizations.

Data collection was carried out through the Web of Science (WoS) database using the keyword "Chronic Otitis Media," limited to the title field. The search excluded records from the year 2025, focused solely on publications categorized as articles, and included only those written in English. Within this scope, a total of 1,039 articles were included for analysis. This dataset provides a valuable basis for examining the temporal evolution of academic research on COM.

The distribution of publications across years is critical for understanding the dynamics of scholarly interest in COM and evaluating the developmental trajectory of the literature. According to the data illustrated in Figure 1, the publication output between 1970 and 2024 was examined.

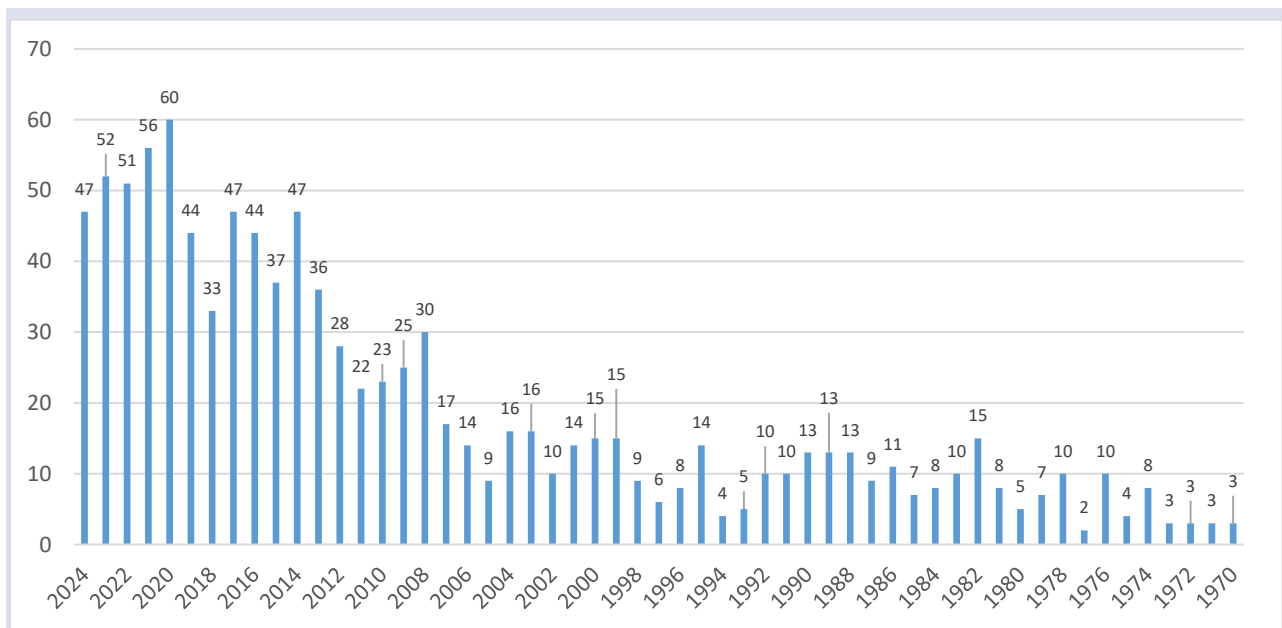


Figure 1. Annual distribution of publications on Chronic Otitis Media (1970–2024)

The earliest publications in the dataset appeared during the 1970s, a period characterized by limited academic attention to the topic. During the 1970s and 1980s, the annual number of publications ranged from approximately 2 to 10 articles per year. This modest volume suggests that COM research in its early stages was largely based on clinical observations and preliminary diagnostic frameworks.

A slight increase in publication frequency was observed in the 1990s, though the growth remained relatively moderate. The early 2000s, however, marked a turning point, with noticeable expansion in the literature—particularly in areas such as imaging technologies, surgical interventions, and antibiotic treatment strategies. From 2008 onwards, the number of publications began to follow a more consistent upward trajectory.

By the 2010s, COM began to be addressed not only as a clinical condition but also as a multidimensional issue encompassing public health, pediatric infections, and hearing loss. During this period, annual publication numbers consistently exceeded 30. A significant increase in scholarly output was recorded after 2020, with 60, 56, and 52 articles published in 2020, 2021, and 2023 respectively. This surge likely reflects the broader scientific interest in infectious diseases catalyzed by the COVID-19 pandemic. With 47 publications recorded in 2024, the momentum of academic production has been largely sustained.

The time-series data confirm the historical trajectory of scholarly interest in COM. The consistent rise in publications over the past 15 years demonstrates that COM remains a growing area of scientific inquiry, likely to attract further multidisciplinary attention in the future.

Subsequently, the analysis identified the ten most highly cited publications on COM indexed in the Web of Science database. These articles are presented in Table 1.

In the bibliometric analysis, the most highly cited publication was the study conducted by Hall-Stoodley et al. [25], which provided direct evidence of bacterial biofilms on the middle-ear mucosa of pediatric patients with chronic otitis media. Published in *JAMA*, this study has received 698 citations and has had a substantial impact on the field by underscoring the clinical relevance of biofilm formation in the pathogenesis of COM. The findings have contributed significantly to the evolving understanding of microbial persistence and antibiotic resistance in chronic middle-ear infections.

The second most cited article, by Gates et al. [26], is a randomized controlled trial evaluating the effectiveness of adenoidectomy and tympanostomy tube insertion in the treatment of chronic otitis media with effusion. Published in the *New England Journal of Medicine*, this study has garnered 261 citations and established the role of pediatric surgical interventions as a cornerstone in the management of COM with effusion.

Ranked third is the retrospective study by Osma et al. [27], which analyzed 93 cases of COM-related complications in Turkey. With 163 citations, this study is particularly notable for highlighting the morbidity and mortality risks associated with advanced-stage COM, offering critical insights into the consequences of delayed or inadequate treatment.

Subsequent highly cited works include those by Maw [28] and Zinkus et al. [29]. Maw's [28] research focuses on the long-term outcomes of surgical interventions such as adenotonsillectomy, while Zinkus [29] and colleagues examine the developmental and psychoeducational sequelae of chronic otitis media in children. Both studies are foundational contributions that underscore the intersection between clinical outcomes and pediatric development, emphasizing the long-term implications of recurrent middle-ear infections in early childhood.



Table 1. Top 10 Most Cited Publications in the Chronic Otitis Media Literature

Rank	Author(s)	Publication Title	Journal	Citations
1	Hall-Stoodley, L. et al. (2006)	Direct detection of bacterial biofilms on the middle-ear mucosa of children with chronic otitis media	<i>JAMA</i>	698
2	Gates, G. A. et al. (1987)	Effectiveness of adenoidectomy and tympanostomy tubes in the treatment of chronic otitis media with effusion	<i>New England Journal of Medicine</i>	261
3	Osma, U. et al. (2000)	The complications of chronic otitis media: report of 93 cases	<i>Journal of Laryngology and Otology</i>	163
4	Maw, A. R. (1983)	Chronic otitis media with effusion and adenotonsillectomy: prospective randomized controlled study	<i>BMJ</i>	134
5	Zinkus, P. W. et al. (1978)	Developmental and psychoeducational sequelae of chronic otitis media	<i>American Journal of Diseases of Children</i>	111
6	Nadol, J. B. et al. (2000)	Outcomes assessment for chronic otitis media: The Chronic Ear Survey	<i>Laryngoscope</i>	105
7	Mandel, E. M. et al. (1992)	Efficacy of myringotomy with and without tympanostomy tubes for chronic otitis media with effusion	<i>Pediatric Infectious Disease Journal</i>	103
8	Brook, I. & Finegold, S. M. (1979)	Bacteriology of chronic otitis media	<i>JAMA</i>	103
9	Riding, K. H. et al. (1978)	Microbiology of recurrent and chronic otitis media with effusion	<i>Journal of Pediatrics</i>	102
10	DeMaria, T. F. et al. (1984)	Endotoxin in middle-ear effusions from patients with chronic otitis media with effusion	<i>Journal of Clinical Microbiology</i>	100
11	Meyerhoff, W. L., Kim, C. S., & Paparella, M. M. (1978)	Pathology of chronic otitis media	<i>Annals of Otology, Rhinology &amp; Laryngology</i>	97
12	Mandel, E. M., Rockette, H. E., Bluestone, C. D., Paradise, J. L., & Nozza, R. J. (1989)	Myringotomy with and without tympanostomy tubes for chronic otitis media with effusion	<i>Archives of Otolaryngology-Head &amp; Neck Surgery</i>	96
13	Zinkus, P. W., & Gottlieb, M. I. (1980)	Patterns of perceptual and academic deficits related to early chronic otitis media	<i>Pediatrics</i>	90
14	Brook, I. (2008)	The role of anaerobic bacteria in chronic suppurative otitis media in children: Implications for medical therapy	<i>Anaerobe</i>	90
15	English, G. M., Northern, J. L., & Fria, T. J. (1988)	Chronic otitis media as a cause of sensorineural hearing loss	<i>Archives of otolaryngology</i>	89
16	Gates, G. A., Avery, C. A., & Prihoda, T. J. (1988)	Effect of adenoidectomy upon children with chronic otitis media with effusion	<i>The laryngoscope</i>	88
17	Smith, J. A., & Danner, C. J. (2006)	Complications of chronic otitis media and cholesteatoma	<i>Otolaryngologic Clinics of North America</i>	86
18	Costa, S. S. D., Rosito, L. P. S., & Dornelles, C. (2009)	Sensorineural hearing loss in patients with chronic otitis media	<i>European Archives of Oto-Rhino-Laryngology</i>	84
19	Alles, R., Parikh, A., Hawk, L., Darby, Y., Romero, J. N., & Scadding, G. (2001)	The prevalence of atopic disorders in children with chronic otitis media with effusion	<i>Pediatric allergy and immunology</i>	79
20	Phillips, J. S., Haggard, M., & Yung, M. (2014)	A new health-related quality of life measure for active chronic otitis media (COMQ-12): development and initial validation.	<i>Otology &amp; Neurotology</i>	77

Other top-cited articles in the list cover a broad range of topics, from diagnostic and therapeutic approaches to microbiological assessments. Among these, the work by Nadol et al. [30] stands out with the development of the

*Chronic Ear Survey*, a validated patient-reported outcome measure designed to assess ear-specific health status in individuals with COM. This tool has become integral to

evaluating treatment efficacy from the patient's perspective.

Overall, the most cited studies are predominantly focused on pediatric populations and often reflect multidisciplinary approaches combining surgical, microbiological, and developmental perspectives. This trend suggests that chronic otitis media is not only a concern within otolaryngology but also a significant topic of inquiry in pediatrics, microbiology, and public health policy. The sustained academic interest in these areas

reinforces the complex, multifactorial nature of COM and the need for integrated research strategies.

To further explore the conceptual structure of the literature, a keyword co-occurrence analysis was conducted. The resulting visualization highlights the prominent thematic relationships within the COM research domain. Such analyses are instrumental in identifying underlying research subfields, classifying focal areas, and structurally mapping the flow of scientific knowledge in the field.

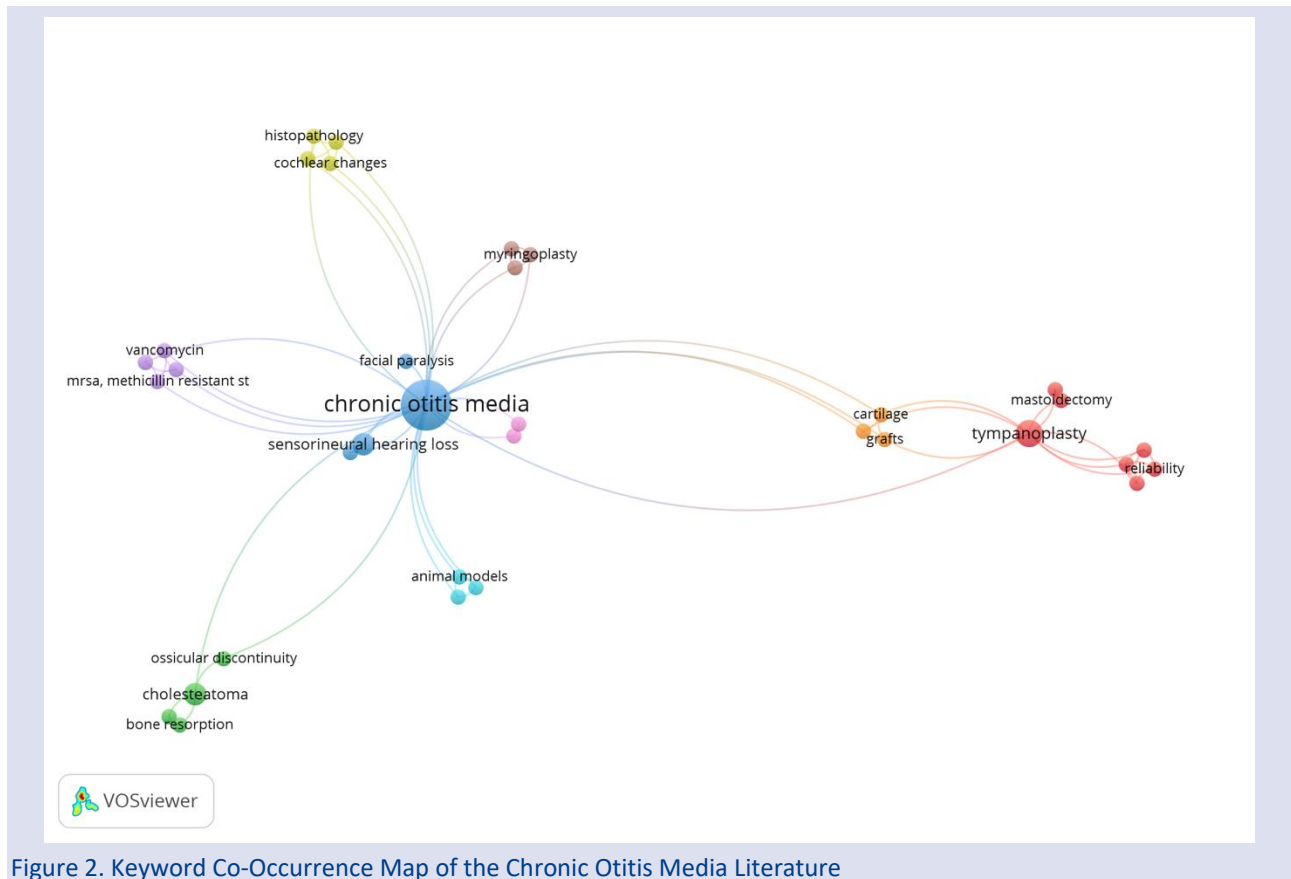


Figure 2. Keyword Co-Occurrence Map of the Chronic Otitis Media Literature

The visual map derived from the keyword co-occurrence analysis illustrates the conceptual diversity and thematic concentrations within the literature on *Chronic Otitis Media* (COM). At the center of the map lies the core keyword “chronic otitis media,” from which various thematic clusters radiate in multiple directions. These clusters are color-coded to represent distinct subtopics that have emerged as dominant areas of research focus in the literature.

On the right side of the visualization, the red-colored cluster comprises keywords such as “tympanoplasty,” “mastoidectomy,” and “reliability,” signifying a thematic concentration on surgical interventions and the assessment of their clinical effectiveness. This cluster occupies a central position in the network due to its relevance to treatment outcomes and procedural reliability in COM management. Adjacent to this, a smaller, orange-toned cluster featuring the terms “cartilage” and “grafts” reflects literature addressing

reconstructive surgical techniques and graft materials used in otologic procedures.

On the left side of the map, a green cluster emerges, which is primarily composed of keywords such as “cholesteatoma,” “ossicular discontinuity,” and “bone resorption.” These terms indicate a focus on the advanced pathological stages of COM, particularly the structural damage associated with ossicular chain disruption and bone erosion. These complications are critical considerations in surgical decision-making and treatment planning.

In the upper section of the map, a yellow-colored cluster is defined by terms such as “histopathology” and “cochlear changes,” representing studies that investigate microscopic alterations in the middle and inner ear tissues. Closer to the center, a blue cluster includes terms like “sensorineural hearing loss” and “facial paralysis,” emphasizing auditory and neurological complications of COM. These keywords highlight the disease’s potential to

affect adjacent anatomical structures, thus broadening the scope of investigation beyond the middle ear.

Additionally, a light blue cluster focused on “animal models” indicates the presence of experimental research employing *in vivo* models to elucidate the pathophysiological mechanisms of COM under laboratory conditions. A smaller, purple-toned cluster centers on pharmacological approaches, particularly antimicrobial resistance, as represented by keywords such as “vancomycin” and “methicillin-resistant *Staphylococcus* (MRSA).” Finally, a brown-colored cluster surrounding the keyword “myringoplasty” denotes alternative surgical techniques distinct from tympanoplasty, often used in specific clinical contexts or pediatric populations.

Overall, the keyword co-occurrence map demonstrates that COM research is structured across

multiple dimensions, including surgical treatment, complication management, pathological progression, and therapeutic strategies. The conceptual clustering within the visualization clearly reflects the interdisciplinary nature of the field and the continued intensity of both clinical and experimental research efforts.

Following the insights drawn from the keyword co-occurrence map, the thematic clusters identified in the literature have been systematically categorized. Each cluster represents a distinct research focus. The table below provides a comprehensive summary of these clusters, organized by thematic domain and highlighting prominent keywords associated with each.

Table 2. Thematic Clustering and Keyword Representation in Chronic Otitis Media Literature

Thematic Cluster	Prominent Keywords	Description
Surgical Interventions and Clinical Reliability	Tympanoplasty, Mastoidectomy, Reliability	This cluster comprises studies focusing on the surgical management of chronic otitis media, particularly evaluating the effectiveness and outcome reliability of procedures such as tympanoplasty and mastoidectomy.
Grafts and Reconstructive Surgical Techniques	Cartilage, Grafts	This group highlights research on graft materials used in otologic surgery—especially cartilage—and assesses the anatomical success and auditory outcomes of various reconstructive techniques.
Pathological Processes and Structural Degeneration	Cholesteatoma, Ossicular Discontinuity, Bone Resorption	Studies in this cluster address destructive anatomical changes observed in advanced stages of the disease, including ossicular chain disruption and bone erosion, with a focus on their underlying pathophysiology.
Histopathology and Cochlear Effects	Histopathology, Cochlear Changes	This theme centers on microscopic alterations in the middle ear and secondary effects in cochlear structures, with histopathological findings used to evaluate the systemic consequences of COM.
Auditory and Neurological Complications	Sensorineural Hearing Loss, Facial Paralysis	This cluster includes research addressing late-stage complications such as nerve damage and hearing loss, highlighting neurological sequelae and functional impairments associated with COM.
Experimental Research and Animal Models	Animal Models	This group consists of experimental studies employing animal models to explore the pathophysiological mechanisms of COM, particularly in preclinical laboratory settings.
Antibiotic Resistance and Microbiology	Vancomycin, MRSA ( <i>Methicillin-Resistant Staphylococcus aureus</i> )	This cluster encompasses literature focused on antimicrobial resistance, microbial strains, and treatment responses, offering detailed insight into the microbiological dimensions of chronic infections.
Alternative Surgical Techniques	Myringoplasty	This theme represents research evaluating less invasive surgical procedures beyond tympanoplasty, often applied in pediatric populations, and discusses their clinical effectiveness.

The keyword co-occurrence clusters presented in Table 2 reveal the thematically concentrated areas of research within the *Chronic Otitis Media* (COM) literature. These clusters, identified through VOSviewer software, categorize the principal research focuses in the field into eight thematic groups. The first cluster encompasses studies related to surgical interventions and the reliability of these procedures. Centered around keywords such as “tympanoplasty,” “mastoidectomy,” and “reliability,” this cluster reflects the body of literature that evaluates the success and outcome reliability of commonly employed surgical techniques in the treatment of COM.

The second cluster focuses on graft materials used in otologic surgery. Defined by keywords such as “cartilage” and “grafts,” this group represents literature that

examines the role of various tissue types in surgical success. Closely related to the first cluster, it reflects a sub-specialized focus on reconstructive techniques within surgical practice.

The third thematic cluster addresses the pathological changes observed in the advanced stages of COM. Terms such as “cholesteatoma,” “ossicular discontinuity,” and “bone resorption” point to structural damage in the middle ear and disruptions in auditory transmission. This group highlights the pathophysiological processes underlying destructive anatomical changes in the disease’s progression.

The fourth cluster encompasses studies investigating tissue-level changes in the middle and inner ear. Keywords such as “histopathology” and “cochlear changes”

characterize this group, which addresses the histological dimensions of COM and assesses its systemic effects based on microscopic alterations.

The fifth cluster focuses on the auditory and neurological complications of COM. Keywords like “sensorineural hearing loss” and “facial paralysis” signal interdisciplinary investigations into the disease’s secondary effects, including nerve damage and functional impairments that arise during later stages.

The sixth thematic cluster represents experimental studies involving animal models. Denoted by the term “animal models,” this group includes laboratory-based research aimed at elucidating the pathophysiological mechanisms underlying COM, especially through preclinical approaches.

The seventh cluster deals with antibiotic resistance and microbial pathogens. Defined by keywords such as “vancomycin” and “methicillin-resistant *Staphylococcus aureus* (MRSA),” this group addresses the challenges of resistant infections and explores antimicrobial treatment strategies.

Finally, the eighth cluster focuses on alternative surgical interventions, centered around the keyword “myringoplasty.” This group covers literature examining less invasive surgical techniques beyond tympanoplasty, particularly those applied in pediatric populations.

## Discussion

The findings of this bibliometric analysis provide a detailed picture of the evolving nature of scientific production in the field of *Chronic Otitis Media* (COM). The data reveal a marked increase in academic output on COM beginning in the early 2000s, with a pronounced acceleration after 2010. This trend underscores the shift in COM research from being a narrowly defined clinical issue in otolaryngology to a broad and interdisciplinary domain integrating contributions from microbiology, pediatrics, neurology, pathology, and public health.

While there were relatively few publications on COM in the 1970s and 1980s, a gradual increase began in the 1990s. However, this growth remained modest until the early 2000s, when advances in diagnostic imaging, surgical innovation, and emerging concerns around antibiotic resistance spurred a noticeable expansion in the literature. During this period, particular attention was paid to pediatric populations, with applied topics such as treatment efficacy and complication management gaining prominence.

The post-2020 surge in COM-related publications likely reflects the heightened global interest in infectious diseases during the COVID-19 pandemic. Given the infectious nature of COM, the pandemic-era increase in publications may also indicate growing concern for the broader implications of ear infections within the context of public health. This expansion points to a diversification of research interests beyond clinical management, extending into patient behavior, education, and healthcare systems.

Thus, the temporal distribution of publications reflects not only quantitative growth but also thematic diversification and enhanced interdisciplinary integration. The structural transformation of COM-related academic output suggests a continued trajectory of expansion in future research.

Examining the most cited publications provides insight into the dominant thematic currents and high-impact studies shaping the field. Most of these publications focus on practical, clinically relevant areas such as surgical treatment, microbiological agents, and complication management. This indicates that both scholars and clinicians are primarily drawn to research with direct implications for patient outcomes and therapeutic success.

One of the most cited works, the biofilm study by Hall-Stoodley et al. [25], introduced a novel perspective on COM pathogenesis by highlighting the clinical importance of biofilm formation—shifting attention beyond conventional microbial cultures. The study serves as a key reference for understanding and managing antibiotic-resistant infections.

Similarly, the randomized controlled trial by Gates et al. [26], which evaluated the effectiveness of adenoidectomy and tympanostomy tubes in pediatric patients, has been widely influential in shaping surgical treatment strategies. Maw’s [28] prospective study also examined the long-term outcomes of adenotonsillectomy procedures. Both studies underscore the central role of surgical intervention in pediatric otolaryngology for COM.

Other high-impact studies focus on complication frequency, microbiological profiling, and auditory outcomes. For instance, Osma et al. [27] conducted a retrospective study in Turkey that highlighted the prevalence and severity of COM-related complications. Nadol et al. [30], on the other hand, developed the Chronic Ear Survey—a patient-reported outcome tool that systematically assesses the daily-life impact of COM.

Collectively, the most frequently cited articles are predominantly practice-oriented, targeting treatment protocols and complication management, and are often centered on pediatric populations. This indicates that the clinical importance of COM extends beyond anatomical and pathophysiological concerns, encompassing quality of life and healthcare system implications. The pediatric dominance in the literature aligns with the epidemiological reality that COM is most prevalent in children, illustrating a strong relationship between research orientation and patient demographics.

Keyword co-occurrence analyses offer powerful tools for identifying the conceptual structures underlying scientific literature. The co-occurrence analysis conducted in this study identified eight key thematic clusters in COM research. These clusters highlight how knowledge production in the field is organized around distinct focal points. They reflect the dual emphasis on clinical applications and basic scientific inquiry, offering a comprehensive view of the literature’s multidimensional character.

Surgical interventions—represented by keywords like “tympanoplasty” and “mastoidectomy”—remain central to COM research, indicating that surgery continues to be a principal treatment modality. Similarly, keywords such as “cartilage” and “grafts” signify ongoing efforts to refine reconstructive techniques and enhance surgical outcomes.

Clusters encompassing terms like “cholesteatoma,” “bone resorption,” and “ossicular discontinuity” represent literature on structural deterioration in advanced disease stages, while others focus on more specialized topics including antimicrobial resistance (“vancomycin,” “MRSA”), animal models, neurological complications, and histopathological findings. These areas demonstrate that COM research extends well beyond treatment protocols, delving into pathogenesis, systemic impact, and molecular mechanisms.

In sum, the keyword co-occurrence map highlights the heterogeneity of knowledge production in COM and underscores its value as a rich field for both clinical practice and basic research. The thematic diversity identified is also of strategic importance for guiding future research directions.

The bibliometric findings of this study clearly demonstrate that COM research is not confined to otolaryngology. On the contrary, it is characterized by a robust interdisciplinary framework that draws from a variety of scientific fields. The thematic clusters identified via keyword mapping reveal that COM is examined in relation to microbiological pathogens, neurological complications, pediatric infections, and pathological progression.

Research on COM pathogenesis frequently overlaps with microbiology, especially concerning biofilm formation, antibiotic resistance, and microbial diversity. These themes require analytical tools beyond traditional ENT approaches and point to an increasing role for molecular biology and genetics in future studies.

Pediatrics remains one of the most prominent disciplines contributing to the COM literature. Given the high prevalence of COM in childhood, and its potential developmental, linguistic, and educational consequences, it is essential that researchers in child development and educational policy remain engaged in this area.

Complications in advanced COM cases—such as sensorineural hearing loss, facial nerve paralysis, and intracranial involvement—are closely related to neurology and pathology. These complications necessitate neurological evaluations and advanced imaging, reinforcing the importance of multidisciplinary collaboration in clinical settings.

Finally, from a public health perspective, COM should be recognized as a common infectious disease in developing countries that significantly affects quality of life and, if untreated, can lead to severe outcomes. Epidemiological research, health policy analysis, and economic burden assessments are critical for designing preventive healthcare services and improving access to treatment.

In conclusion, successful diagnosis, treatment, and management of COM require the coordinated efforts of professionals in otolaryngology, pediatrics, microbiology, neurology, pathology, and public health. Encouraging interdisciplinary research is essential for reducing the disease burden and developing more effective and integrated treatment strategies.

## Conclusion

This study examined the academic literature on *Chronic Otitis Media* (COM) using bibliometric methods, offering a multidimensional perspective on the historical development, thematic concentrations, and structural dynamics of the field. Based on the analysis of 1,039 articles retrieved from the Web of Science (WoS) database—limited to those written in English and containing the phrase “Chronic Otitis Media” in the title—the study not only quantitatively assessed the volume of academic production but also provided a detailed account of how scholarly interests have evolved over time.

The temporal distribution of publications demonstrates that COM has attracted increasing attention as a research area, particularly after the early 2000s. This surge reflects a period in which both clinical needs and technological advancements accelerated scientific inquiry. The sustained level of publication following the COVID-19 pandemic further suggests that COM continues to be a clinically significant issue within global health systems.

One of the study’s original contributions lies in its detailed mapping of thematic clusters within the literature. Research clustered around topics such as surgical interventions, grafting techniques, microbiological approaches, complication management, and experimental models reflects the multidimensional nature of COM. Moreover, the fact that the most frequently cited publications are predominantly clinically oriented reveals a strong alignment between academic inquiry and practical healthcare concerns.

Overall, the literature on COM is characterized by both expansion and diversification, demonstrating a rich research potential spanning both basic sciences and clinical practice. In this context, the bibliometric analysis provides a strategic framework that can guide researchers and policymakers by charting the landscape of knowledge production in the field.

The findings from this study clearly reveal not only a quantitative growth in the scientific literature on COM but also significant thematic transformations. The steady increase in publication output over the years underscores the growing global relevance of COM as a healthcare concern. Especially over the past fifteen years, research on COM has increasingly been regarded as a comprehensive field encompassing clinical management, healthcare policy, and the economic burden of disease.

The most highly cited publications primarily focus on therapeutic approaches, surgical techniques, complication management, and microbiological



foundations—areas that directly translate into clinical practice. Studies on surgical success rates, strategies targeting biofilm formation, and management of auditory sequelae demonstrate that the insights gained through research have tangible implications for clinical decision-making.

The thematic mapping based on keyword co-occurrence analysis highlights the interdisciplinary nature of COM research. Contributions from microbiology, histopathology, and neurology—alongside otolaryngology—reveal the need to consider COM as a complex clinical condition requiring holistic approaches. Notably, clusters surrounding terms such as “sensorineural hearing loss,” “facial paralysis,” and “cochlear changes” emphasize the long-term consequences and systemic implications of the disease.

Collectively, the findings of this study illustrate that COM is a multifaceted healthcare issue and that progress in research has a direct impact on clinical practice. The mapping of research trends enables a reassessment of existing knowledge and the identification of new areas of inquiry. In this regard, bibliometric findings reflect not only the intensity of academic interest but also the real-world relevance of scientific output.

This study offers a strategic roadmap for researchers by identifying dominant themes and emerging areas of opportunity within the field of COM. Topics such as antibiotic resistance, long-term outcomes of complications, and experimental studies using preclinical models present high potential for future investigation. Furthermore, patient-centered outcome measures can be integrated with broader datasets and evaluated within the context of healthcare policy.

It is important to acknowledge the study’s limitations. This analysis was based solely on the WoS database and therefore does not include publications indexed in other databases such as PubMed, Scopus, or Embase. Moreover, the dataset was restricted to articles containing “Chronic Otitis Media” in the title, which may have excluded relevant studies addressing the topic under alternative headings. Future research should consider broader database combinations and full-text content analyses to yield more comprehensive bibliometric insights.

### Conflict of interests

The author declare that has no conflicts of interest.

### Acknowledgments

I would like to thank Selçuk Yasin Yıldız, Assistant Professor at Cumhuriyet Social Sciences Vocational School, for her contributions to the article.

### References

- [1] Lewis A.T., Backous D., Choi B.Y., Jaramillo R., Kong K., Lenarz T., Hol M.K. Healthcare consumption among subjects with otitis media undergoing middle ear surgery—analysis of cost drivers, *European Archives of Oto-Rhino-Laryngology*, 280(1) (2023) 175-181.
- [2] Yang Y.Y., Guo L.R. Misdiagnosis of a fungus ball in the middle ear as chronic suppurative otitis media, *The Journal of Infection in Developing Countries*, 18(11) (2024) 1793-1797.
- [3] Bazzout A., Lachkar A., Benfadil D., Tsen A.A., Ghailan R. An chronic otitis media with effusion complicated with paravertebral abscess: Case report and review of the literature, *International Journal of Surgery Case Reports*, 79 (2021) 104-107.
- [4] Sun J., Sun J. Intracranial complications of chronic otitis media, *European Archives of Oto-Rhino-Laryngology*, 271 (2014) 2923-2926.
- [5] Mili M.K., Kalita S., Sarmah M., Talukdar S., Goswami S. Complications of chronic otitis media and their management: a study at tertiary care centre, *International Journal of Research in Medical Sciences*, 11(11) (2023) 4082.
- [6] Baysal E., Erkutlu I., Mete A., Alptekin M., Oz A., Karataş Z., Çelenk F., Mumbruç S., Kanlıkama M. Complications and Treatment of Chronic Otitis Media, *Journal of Craniofacial Surgery*, 24 (2013) 464-467.
- [7] Dhingra S., Vir D., Bakshi J., Rishi P. Mapping of audiometric analysis with microbiological findings in patients with chronic suppurative otitis media (CSOM): a neglected clinical manifestation, *Critical Reviews in Clinical Laboratory Sciences*, 60 (2023) 212 - 232.
- [8] Hutz M., Moore D., Hotaling A. Neurological Complications of Acute and Chronic Otitis Media, *Current Neurology and Neuroscience Reports*, 18 (2018) 1-7.
- [9] Khairkar M., Deshmukh P., Maity H., Deotale V. Chronic Suppurative Otitis Media: A Comprehensive Review of Epidemiology, Pathogenesis, Microbiology, and Complications, *Cureus*, 15(8) (2023) e43729.
- [10] Gkrinia E., Brotis A., Vallianou K., Ntziovara A., Hajioannou, J. Otogenic Brain Complications: A Systematic Review and Meta-analysis, *The Journal of laryngology and otology*, (2024) 1-35.
- [11] Mushi M.F., Mwalutende A.E., Gilyoma J.M., Chalya P.L., Seni J., Mirambo M.M., Mshana S.E. Predictors of disease complications and treatment outcome among patients with chronic suppurative otitis media attending a tertiary hospital, Mwanza Tanzania, *BMC Ear Nose Throat Disord*, 7 (2016) 16:1.
- [12] Laws J.C., Jordan L.C., Pagano, L.M., Wellons III J.C., Wolf M.S. Multimodal neurologic monitoring in children with acute brain injury, *Pediatric neurology*, 129 2022 62-71.
- [13] Kang J.M., Kim Y.J., Kim J.Y., Cho E.J., Lee J.H., Lee M.H., Yoo K.H. Neurologic complications after allogeneic hematopoietic stem cell transplantation in children: analysis of prognostic factors, *Biology of Blood and Marrow Transplantation*, 21(6) 2015 1091-1098.
- [14] Kaźmierczak W., Janiak-Kiszka J., Budzyńska A., Nowaczewska M., Kaźmierczak H., Gospodarek-Komkowska E. Analysis of pathogens and antimicrobial treatment in different groups of patients with chronic otitis media, *The Journal of Laryngology & Otology*, 136 (2021) 219 - 222.

- [15] Kim S.H., Kim M.G., Kim S.S., Cha S.H., Yeo S.G. Change in Detection Rate of Methicillin-Resistant *Staphylococcus aureus* and *Pseudomonas aeruginosa* and Their Antibiotic Sensitivities in Patients with Chronic Suppurative Otitis Media, *Journal of International Advanced Otolaryngology*, 11(2) (2015) 151-6.
- [16] Rubini A., Ronzani G., D'Alessandro E., Marchioni D. Management of Otogenic Meningitis: A Proposal for Practical Guidelines from a Multicenter Experience with a Systematic Review, *J Clin Med*, 13(18) (2024) 5509.
- [17] Faiz S.M., Bhargava A., Srivastava S., Gupta R. K., Parveen M., Bhatt K., Singh A. Analysis of hearing improvement by various ossiculoplasty materials (autologous versus prostheses) in chronic otitis media patients, *International Journal of Otorhinolaryngology and Head and Neck Surgery*, 9(1) (2023) 54-7.
- [18] Luers J.C., Hüttenbrink K.B. Surgical anatomy and pathology of the middle ear, *Journal of Anatomy*, 228(2) (2016) 338-353.
- [19] Schilder A., Marom T., Bhutta M., Casselbrant M., Coates H., Gisselsson-Solen M., Hall A., Marchisio P., Ruohola A., Venekamp R., Mandel E. Otitis Media: Treatment and Complications, *Otolaryngology–Head and Neck Surgery*, 156 (2017) 88-105.
- [20] Alsharif A.H., Salleh N.Z.M., Baharun R. Bibliometric analysis, *Journal of Theoretical and Applied Information Technology*, 98(15) (2020) 2948-2962.
- [21] Persson O., Danell R., Schneider J.W. How to use Bibexcel for various types of bibliometric analysis. In F. Åström, R. Danell, B. Larsen, J.W. Schneider (Eds.), *Celebrating Scholarly Communication Studies: A Festschrift for Olle Persson at his 60th Birthday*, *International Society for Scientometrics and Informetrics*, (05) (2009) 9-24.
- [22] Pritchard A. Statistical bibliography or bibliometrics, *Journal of Documentation*, 25(4) (1969) 348-349
- [23] Jacso P. As we may search-comparison of major features of the Web of Science, Scopus, and Google Scholar citation-based and citation-enhanced databases, *Current Science*, 89(9) (2005) 1537-1547.
- [24] Yadav M., Dangi A.A. Bibliometric study on Gamification and its Role in Users Engagement, *Pacific Business Review International*, 14(8) (2022) 62-72.
- [25] Hall-Stoodley L., Hu F.Z., Gieseke A., Nistico L., Nguyen D., Hayes J., Kerschner J.E. Direct detection of bacterial biofilms on the middle-ear mucosa of children with chronic otitis media, *JAMA*, 296(2) (2006) 202–211.
- [26] Gates G.A., Avery C.A., Prihoda T.J., Cooper J.C. Effectiveness of adenoidectomy and tympanostomy tubes in the treatment of chronic otitis media with effusion, *New England Journal of Medicine*, 317(23) (1987) 1444–1451.
- [27] Osma U., Cureoglu S., Hosoglu S. The complications of chronic otitis media: Report of 93 cases, *The Journal of Laryngology & Otolaryngology*, 114(2) (2000) 97–100.
- [28] Maw A. R. Chronic otitis media with effusion and adenotonsillectomy—a prospective randomized controlled study, *International Journal of Pediatric Otorhinolaryngology*, 6 (1984) 239–246.
- [29] Zinkus P.W., Gottlieb M.I., Schapiro M. Developmental and psychoeducational sequelae of chronic otitis media, *American Journal of Diseases of Children*, 132(11) (1978) 1100–1104.
- [30] Nadol J.B., Staeker H., Gliklich R. E. Outcomes assessment for chronic otitis media: The Chronic Ear Survey, *The Laryngoscope*, 110(94) (2000) 32–35.
- [31] Mandel E.M., Rockette H.E., Bluestone C.D., Paradise J.L., Nozza R.J. Efficacy of myringotomy with and without tympanostomy tubes for chronic otitis media with effusion, *The Pediatric Infectious Disease Journal*, 11(4) (1992) 270–277.
- [32] Brook I., Finegold S.M. Bacteriology of chronic otitis media, *JAMA*, 241(5) (1979) 487–488.
- [33] Riding K.H., Bluestone C.D., Michaels R.H., Cantekin E.I., Doyle W.J., Poziviak C.S. Microbiology of recurrent and chronic otitis media with effusion, *The Journal of Pediatrics*, 93(5) (1978) 739–743.
- [34] DeMaria T.F., Prior R.B., Briggs B.R., Lim D.J., Birck H.G. Endotoxin in middle-ear effusions from patients with chronic otitis media with effusion, *Journal of Clinical Microbiology*, 20(1) (1984) 15–17.
- [35] Meyerhoff W.L., Kim C.S., Paparella M.M. Pathology of chronic otitis media, *Annals of Otolaryngology, Rhinology & Laryngology*, 87(6) (1978) 749-760.
- [36] Mandel E.M., Rockette H.E., Bluestone C.D., Paradise J.L., Nozza R.J. Myringotomy with and without tympanostomy tubes for chronic otitis media with effusion, *Archives of Otolaryngology–Head & Neck Surgery*, 115(10) (1989) 1217-1224.
- [37] Zinkus P.W., Gottlieb M.I. Patterns of perceptual and academic deficits related to early chronic otitis media, *Pediatrics*, 66(2) (1980) 246-253.
- [38] Brook I. The role of anaerobic bacteria in chronic suppurative otitis media in children: implications for medical therapy, *Anaerobe*, 14(6) (2008) 297-300.
- [39] English G.M., Northern J.L., Fria T.J. Chronic otitis media as a cause of sensorineural hearing loss, *Archives of Otolaryngology*, 98(1) (1973) 18-22.
- [40] Gates G.A., Avery C.A., Prihoda T.J. Effect of adenoidectomy upon children with chronic otitis media with effusion, *The Laryngoscope*, 98(1) (1988) 58-63.
- [41] Smith J.A., Danner C.J. Complications of chronic otitis media and cholesteatoma, *Otolaryngologic Clinics of North America*, 39(6) (2006) 1237-1255.
- [42] Costa S.S.D., Rosito L.P.S., Dornelles C. Sensorineural hearing loss in patients with chronic otitis media, *European Archives of Oto-Rhino-Laryngology*, 266 (2009) 221-224.
- [43] Alles R., Parikh A., Hawk L., Darby Y., Romero J.N., Scadding G. The prevalence of atopic disorders in children with chronic otitis media with effusion, *Pediatric Allergy and Immunology*, 12(2) (2001) 102-106.
- [44] Phillips J.S., Haggard M., Yung M. A new health-related quality of life measure for active chronic otitis media (COMQ-12): development and initial validation, *Otology & Neurotology*, 35(3) (2014) 454-458.

## Isolation and Molecular Identification of Yeast Strains Causing Spoilage in Labneh Cheese

Özgür Kebabcı<sup>1,a,\*</sup>

<sup>1</sup>Department of Molecular Biology and Genetics, Faculty of Science, Sivas Cumhuriyet University, Sivas, Türkiye

\*Corresponding author

### Research Article

#### History

Received: 13/11/2024

Accepted: 17/03/2025



This article is licensed under a Creative Commons Attribution-NonCommercial 4.0 International License (CC BY-NC 4.0)

### ABSTRACT

Labneh is among the dairy products with high nutritional value in the spreadable cheese category. It is consumed together with other dairy products in domestic food consumption. It has been observed that labneh cheese purchased for consumption spoils in the refrigerator after a while. Samples taken from spoiled labneh cheese were purified by single colony cultivation method (streak-plate technique) in PDA and then purified yeast strains were identified. EurX GeneMATRIX Plant & Fungi DNA isolation kit (Poland) was used for DNA isolation in the identification. The amount and purity of the isolated DNA were measured spectrophotometrically in Thermo Scientific Nanodrop 2000 (USA). For species determination, targeted gene regions were amplified by PCR with universal primers ITS1 (5' TCCGTAGGTGAACCTGCGG 3') and ITS4 (5' TCCTCCGCTTATTGATATGC 3'). A single-step PCR process was performed to amplify the region of approximately 700 bases. The amplification results obtained by PCR were electrophoresed in 1.5% agarose gel prepared with 1x TAE buffer at 100 volts for 90 minutes and images were taken under UV light using ethidium bromide dye. The results obtained with ITS1 and ITS4 primers were evaluated using the CAP contig assembly algorithm in BioEdit software to create a consensus sequence. Species determination of yeast isolates was determined according to the closest species in NCBI. One of the two yeast species isolated from spoiled labneh cheese was identified as *Yarrowia lipolytica* with a similarity rate of 99.06% and the other as *Rhodotorula mucilaginosa* with a similarity rate of 98.42%. Evolutionary analyses were performed in MEGA11 and the evolutionary distance between the two newly isolated species was shown.

**Keywords:** Labneh cheese, Spoilage, Molecular identification, *Rhodotorula mucilaginosa*, *Yarrowia lipolytica*.

<sup>a</sup>[ozgurkebabcı@cumhuriyet.edu.tr](mailto:ozgurkebabcı@cumhuriyet.edu.tr)  <https://orcid.org/0000-0002-9404-747X>

## Introduction

The relationship between microorganisms and humans is complex. On the one hand, they provide benefits by being involved in the production of some industrial products, while on the other hand, they cause negative situations such as causing diseases in humans and spoiling food. Food spoilage causes serious economic losses worldwide. It can be said that more than 30% of the food produced every year is lost or wasted, which leads to a loss of billions of dollars [1]. It is possible for food to spoil from production to consumption. During the consumption phase, foods are stored in cooling environments such as refrigerators to prevent spoilage. However, there are many microorganisms that cause food spoilage even in the refrigerator. These microorganisms are one of the most effective causes of food spoilage. In brief, the main cause of food spoilage is contamination of food with bacteria, yeast and molds. Various factors play a role in microbial food spoilage and these factors are interconnected. First of all, the factors specific to food are internal factors and these are the nutritional composition of the food, the natural antimicrobial factors in the food and the chemical, physical and biochemical properties such as pH, aw and Eh or oxidation-reduction potential of the food. Another factor, process factors, are the factors that are effective during food processing, which are the

factors that affect microbial colonization, survival and growth during food processing. Factors such as heating or irradiation and even contamination from equipment can be added to these process factors. The last factors that are effective in microbial food spoilage are external factors [2]. These are environmental factors and are factors such as storage temperature or atmosphere. If process factors are left aside, it can be said that the factors that are effective in food products for domestic consumption are internal and external factors.

Food poisoning may come first to mind in food spoilage, but it is known that not every spoiled food causes poisoning. Food spoilage is defined as a visual, odor, taste and tactile sensory change in food, and food spoilage is expressed as a metabolic process that makes food unsuitable for human consumption due to these sensory changes [3, 4]. Although this metabolic process is sometimes chemical, it is usually carried out by microorganisms. Bacteria and fungi play an important role in food spoilage. Fungi, in particular, are involved in spoilage with their resistance. It is known that some fungal species survive even under the most extreme physico-chemical conditions and thermal processing regimes used in commercial food production [5]. Although low temperature conditions seem to prevent food spoilage in

domestic consumption, many fungal species can multiply at these low temperatures and cause food spoilage [6]. Storing foods in cold conditions can deter mesophiles but allow uncontrolled growth of psychrophiles [7]. There are also microorganisms known as psychrotrophs that can tolerate cold conditions, which are microorganisms that can grow at temperatures similar to those of mesophiles but have adapted to tolerate cold conditions. Psychrotrophs' optimum growth temperature are between +25 and +30 °C, while their minimum growth temperature is (-5)-(+7) °C, while their minimum growth temperature is (-5)-(+7) °C [8]. Both psychrophiles and psychrotrophs (facultative psychrophiles) can cause food spoilage in cold storage conditions such as refrigerators. In cultured dairy products, yeasts are the primary cause of spoilage. This is because yeasts can grow at low temperatures (such as refrigeration temperatures) and pH values. [9]. One of these dairy products is labneh. Labneh is a food product obtained by combining pasteurized milk and yogurt culture, which is in the spreadable cheese category. This product, which contains 17 g fat, 4.5 g carbohydrates, 4.9 g protein and 120 mg calcium per 100 grams, provides the nutrients necessary for the growth of microorganisms. Yeast spoilage usually manifests itself with the growth on the surface of products such as cheese and meat and the fermentation of sugars in liquid and semi-liquid products [10].

In the past, studies conducted to identify yeast species in spoiled foods were conducted using phenotypic methods that included morphological, physiological and biochemical methods [11]. Phenotypic methods, although not frequently, can give incorrect results in identifying yeasts that cause food spoilage. Liu et al. reported that some *Yarrowia* species cannot be identified based on their phenotypic characteristics alone and recommended sequencing the D1/D2 LSU rRNA gene and ITS regions in the identification of these species [12]. Nagy et al. reported that they could not observe any difference between the phenotypic characteristics of this new species and the phenotypic characteristics of *Y. deformans* and *Y. lipolytica* in their study on the new species, and reported that the new species could be identified only by the sequences of the ITS and nuclear LSU rRNA gene D1/D2 regions [13]. For these and similar reasons, the use of DNA-based genotypic methods in the identification of yeasts has become inevitable [14, 15]. Various genotypic methods come to the fore in the identification of yeast isolates isolated and purified from spoiled foods. These are; PCR-RFLP (PCR-restriction fragment length polymorphisms), rep-PCR (repetitive sequence based polymerase chain reaction), AFLPs (Amplified Fragment Length Polymorphisms), RAPD (Random Amplified Polymorphic DNA), PCR using species-specific primers, sequence analysis of the 26S rRNA gene D1/D2 region and ITS (Internal Transcribed Spacer) sequence analysis [16-21]. The last two are powerful techniques used for the accurate identification of yeast species [11].

In this study, species identification of yeast strains isolated and purified from spoiled labneh cheese was performed and after identification, the evolutionary relationship of the yeast strains was shown as a phylogenetic tree.

## Materials and Methods

### Isolation of Yeasts

It has been observed that labneh cheese purchased for consumption spoiled after a while in the refrigerator. It has been observed that labneh cheese purchased for consumption spoiled after a while in the refrigerator. The samples inoculated on petri plates were incubated at 30°C for 48 hours. After incubation, samples thought to be yeast from the microorganisms that grew as a mixed culture were inoculated again on PDA with the streak-plate technique and incubated at 30°C for 48 hours. After a few passages, yeast isolates were purified.

### DNA Isolation and PCR

DNA isolation from yeast isolates was performed using the EurX GeneMATRIX Plant & Fungi DNA isolation kit (Poland), designed for DNA isolation from different plant organs and tissues (leaves, seeds, fruits) as well as from fungi, algae and lichens [22]. In order to control the amount and purity of the DNA obtained after DNA isolation, spectrophotometric measurement was performed on the Thermo Scientific Nanodrop 2000 (USA) device. Then, PCR study of the DNA, the amount and purity of which were confirmed, was performed. For species identification of yeast isolates, targeted gene regions, nuclear ribosomal DNA 5.8S region, were amplified by PCR with universal primers ITS1 (5' TCCGTAGGTGAACCTGCGG 3') and ITS4 (5' TCCTCCGCTTATTGATATGC 3') [23-25]. PCR was performed in a single step, using Solis Biodyne (Estonia) FIREPol® DNA Polymerase Taq polymerase enzyme to amplify a region of approximately 700 bases (Table 1.). After PCR, a single band was obtained on the agarose gel, indicating that the PCR process was successful. During the purification step of the PCR product, the obtained single-band samples were purified using the MAGBIO "HighPrep™ PCR Cleanup System" (AC-60005) purification kit according to the kit's procedures. For Sanger sequencing, the ABI 3730XL Sanger sequencing device (Applied Biosystems, Foster City, CA, USA) and the BigDye Terminator v3.1 Cycle Sequencing Kit (Applied Biosystems, Foster City, CA, USA) were used in the Macrogen Netherlands laboratory. To create a consensus sequence, the results obtained with the ITS1 and ITS4 primers were turned into contigs using the CAP contig assembly algorithm in the BioEdit software [22]. In order to obtain the images of the amplification results obtained with PCR (kyratec thermocycler), electrophoresis was first carried out for 90 minutes at 100 volts in a 1.5% agarose gel prepared with 1x TAE buffer. Afterwards, the image was taken under UV light using ethidium bromide dye.



Table 1. PCR Conditions

Component	Concentration of Stock	Concentration of React.
PCR Buffer	10 x	1 x
MgCl <sub>2</sub>	25 mM	1.5 mM
DNTP mix	20 mM	0.2 mM
Forward Primer	10 μM	0.3 μM
Reverse Primer	10 μM	0.3 μM
Taq DNA polymerase	5 U/μM	2 U/μM
DNA template	3 μM	
Makeup to 35 μL with PCR-grade water		
*	95 °C, 5 min (initial denaturation)	
** 40 cycles	95 °C for 45 s (denaturation)	
	57 °C for 45 s (annealing)	
	72 °C for 60 s (extension)	
***	72 °C for 5 min (final extension)	
The temperature is reduced to 4 °C, and the PCR is completed		

### Phylogenetic Study with Maximum Likelihood Method

The evolutionary history of *R. mucilaginosa* and *Y. lipolytica*, which were isolated from spoiled labneh cheese and identified as species, was determined using the Maximum Likelihood method and the Tamura-Nei model [26]. The phylogenetic tree with the highest log probability (-3569.00) is shown (Figure 1). The initial tree(s) for the heuristic search were obtained automatically. Neighbor-Join and BioNJ algorithms were applied to a matrix of pairwise distances estimated using the Tamura-Nei model, and then the topology with the superior log probability value was selected. This analysis

included 31 nucleotide sequences and there were a total of 1081 positions in the final dataset. Evolutionary analyses were performed in MEGA11 [27].

### Results and Discussion

The identification of pure yeast strains isolated from spoiled labneh cheese was made according to the closest species in NCBI and the first yeast isolate was identified as *Rhodotorula mucilaginosa* with a similarity rate of 98.42% and the second yeast isolate was identified as *Yarrowia lipolytica* with a similarity rate of 99.06% (Table 2).

Table 2. Identification results of yeast strains isolated from spoiled labneh cheese

Yeasts	Sequence Analysis	Results
Lbn1	ACAGGGTTAGAAAGTGAGAGTTCGGACTCCAAGTTAAGTTGGACGTCCTATGT TCACTAATGATCCTTCCGTAGGTGAACCTGCGGAAGGATCATTAGTGAACATAG GACGTCCAACCTTAACCTGGAGTCCGAACCTCTCACTTTCTAACCTGTGCATTGT TTGGGATAGTAACTCTCGCAAGAGAGCGAACTCCTATTCACTTATAAACACAAA GTCTATGAATGTATTTAATTTTATAACAAAATAAACTTTCAACAACGGATCTCT TGGCTCTCGCATCGATGAAGAACGCAGCGAAATGCGATAAGTAATGTGAATTG CAGAATTCAGTGAATCATCGAATCTTTGAACGCACCTTGCGCTCCATGGTATTC CGTGGAGCATGCCTGTTTGAGTGTCATGAATACTTCAACCCTCCTCTTTCTTAAT GATTGAAGAGGTGTTTGGATTCTGAGCGCTGCTGGCCTTACGGTCTAGCTCGTT CGTAATGCATTAGCATCCGCAATCGAACTTCGGATTGACTTGGCGTAATAGACT ATTCGCTGAGGAATTCTAATCTTCGGATT	<i>Rhodotorula mucilaginosa</i> 98.42%
Lbn2	TTCTGTGGATTTCTGTGCTTATTACAGCGTCATTTTATCTCAATTATAACTATCA ACAACGGATCTCTTGGCTCTCACATCGATGAAGAACGCAGCGAACC GCGATATT TTTTGTGACTTGAGATGTGAATCATCAATCTTTGAACGCACATTGCGCGGTAT GGCATTCCGTACCGCACGGATGGAGGAGCGTGTTCCCTCTGGGATCGCATTGC TTTCTTGAAATGGATTTTTTAACTCTCAATTATTACGTCATTTACCTCCTTCAT CCGAGATTACCCGCTGAACCTAAGCATATCAATAAGGCGGAGGAAGT	<i>Yarrowia lipolytica</i> 99.06%



After species identification, the phylogenetic tree was determined using the Maximum Likelihood method and the Tamura-Nei model [26]. Evolutionary analyses were studied in MEGA11 (Figure 1.) [27]. The numbers in the

figure show the evolutionary distance of newly isolated *R. mucilaginosa* and *Y. lipolytica* strains between other *R. mucilaginosa* and *Y. lipolytica* strains and the evolutionary distance between two newly isolated species.

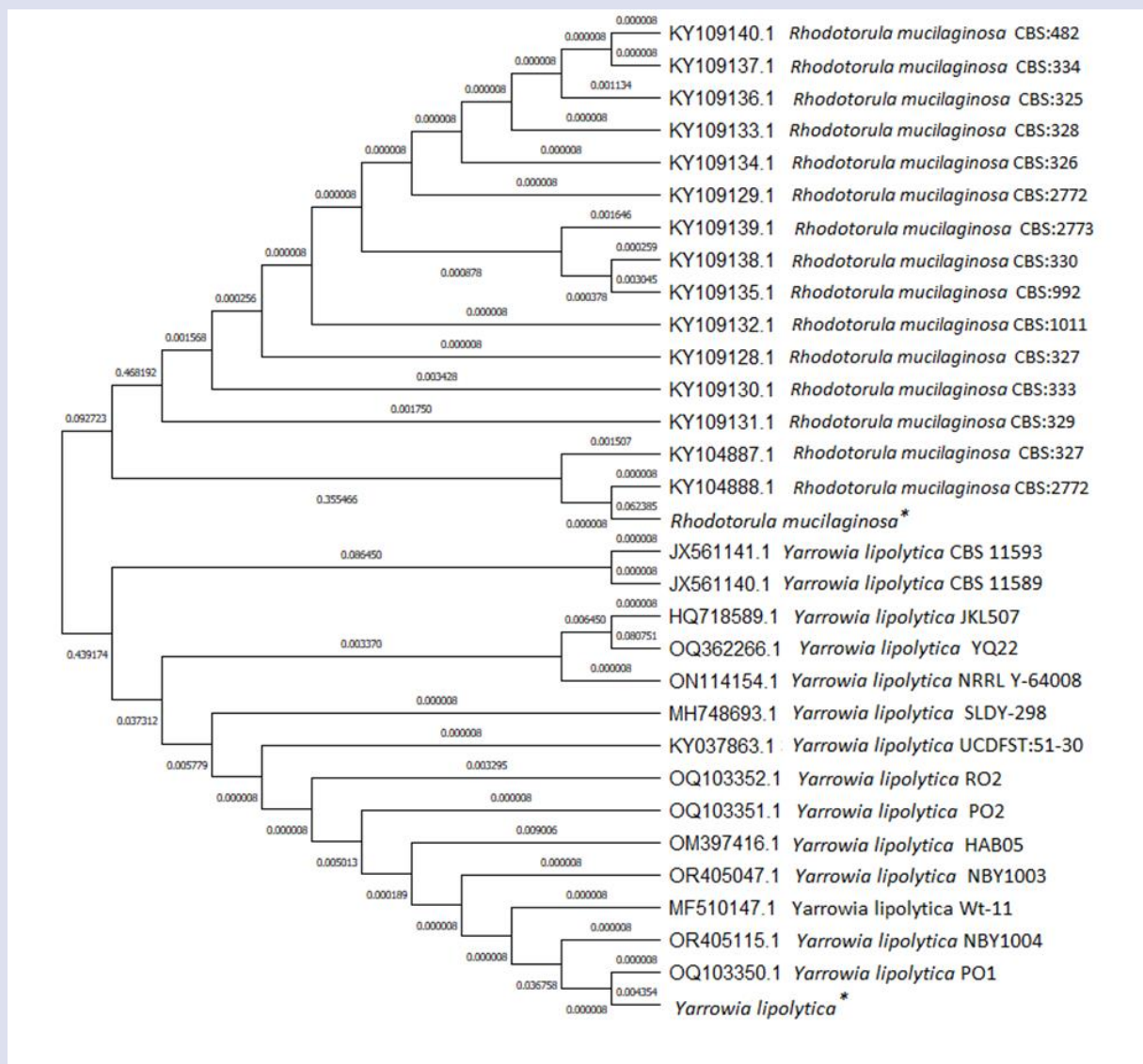


Figure 1. Phylogenetic relationships of *R. mucilaginosa* and *Y. lipolytica* to other closely related *Rhodotorula* sp and *Yarrowia* sp. (NCBI Accession number of *R. mucilaginosa* is PQ661383 and *Y. lipolytica* is PQ682298).

As a result of genetic analysis of yeast strains isolated and purified from spoiled labneh cheese, primarily named Lbn1 and Lbn2, Lbn1 was identified as *Rhodotorula mucilaginosa* with a similarity rate of 98.42%, and Lbn2 as *Yarrowia lipolytica* with a similarity rate of 99.06%. Labneh cheese is a highly nutritious food product in the spreadable cheese class. However, its nutritiousness for humans also makes this cheese type attractive to microorganisms. Yeasts are the main cause of spoilage in cultured dairy products due to their ability to grow at refrigeration temperatures and low pH values [28, 29]. Debaryomyces, *Yarrowia* and *Rhodotorula* species are frequently isolated from spoiled meat and cheese [10]. In a study, 86 samples were collected and analyzed. As a result of the analysis, 1032 yeast isolates were identified by the sequence analysis method targeting the transcript

spacer region (ITS) of ribosomal DNA. It was determined that 9 of the identified yeasts were *R. mucilaginosa* and 7 were *Y. lipolytica* [11]. In another study, 85 yeasts were isolated from different cheese samples and the results obtained showed *Y. lipolytica* and *R. mucilaginosa* strains [30]. In a study investigating the yeast content in spoiled, decorated soft cheese packaged in modified atmosphere from two different dairies, both *Y. lipolytica* and *Rhodotorula* sp. were identified. *R. mucilaginosa* was detected in the results obtained from swab samples taken from production and packaging areas [31]. Tokak et al. obtained 20 yeast isolates from dairy products such as yogurt, cream, butter, curd cheese and Antep cheese and identified one as *Yarrowia lipolytica* [32]. Budak et al. isolated and identified one *Y. lipolytica* strain from outside the samples on the 60th day and six *Y. lipolytica* strains

from outside the samples on the 120th day during the ripening of traditional Turkish Divle Cave cheese [33]. There are many other studies in the literature on *R. mucilaginosa* and *Y. lipolytica*, which cause spoilage in cheese products. However, what draws attention in the publications is where these yeasts contaminate foods before causing spoilage. Fröhlich-Wyder et al. reported that *Y. lipolytica* is among the yeast species more frequently seen in raw milk [34]. Potential contamination sources can be encountered at all stages of the cheese production process and include raw milk, equipment surfaces, and the processing environment. Both *R. mucilaginosa* and *Y. lipolytica* can be the main spoilage yeast strains not only in cheese but also in other dairy products. Milanović et al. performed molecular identification of 74 spoilage yeasts isolated from 3 different buffalo milk yogurt batches throughout their shelf life and identified *Y. lipolytica* and *Rhodotorula* sp. strains [35]. However, there are also studies that isolated *R. mucilaginosa* or *Y. lipolytica* from other foods. In a study, *R. mucilaginosa* was identified in orange fruit and juice [36]. In another study, *R. mucilaginosa* was among the yeast strains isolated and identified from apples and citrus fruits [37]. In another study on carotenoid production, *R. mucilaginosa* strains were isolated and identified from Jerusalem artichoke, tomato juice, sugar cane and agricultural soil [38]. Studies show that cheese or any other food product can be spoiled by *R. mucilaginosa* and/or *Y. lipolytica*. There are various publications in the literature on the production of labneh cheese [39, 40]. However, no publication was found on the isolation of yeast from spoiled labneh cheese. Therefore, we believe that our study will contribute to the literature.

### Conflicts of interest

The authors declare that they have no conflicts of interest in the publication.

### References

- [1] Quintieri L., Koo O.K., and Caleb, O.J., Editorial: Fight against food waste: combating contamination and spoilage, *Front. Microbiol.*, 14 (2023) 1265477.
- [2] Scott V.N., Interaction of Factors to Control Microbial Spoilage of Refrigerated Foods, *J. Food Prot.*, 52(6) (1989) 431-435.
- [3] Rawat S., Food Spoilage: Microorganisms and their prevention, *Asian J. Plant Sci.*, 5(4) (2015) 47-56.
- [4] Abdullahi A.A., Bala J.D., Kuta F.A., Adabara N.U., Liyasu U.S., and Aliu M.O., Microbial Spoilage of Food In Industry: A Review, *FUW Trends in Science & Technology Journal*, 4(2) (2019) 519-523.
- [5] Snyder A.B., and Worobo R.W., Fungal Spoilage In Food Processing, *J. Food Prot.*, 81(6) (2018) 1035-1040.
- [6] Moss M.O., General characteristics of moulds, In: Clive de W. Blackburn (Eds). Food spoilage microorganisms, Woodhead Publishing Ltd, England, (2006) 401-414.
- [7] Modi H.A., An Introduction to Microbial Spoilage of Foods, In: Modi H. A. (Eds). Microbial Spoilage of Foods, Aavishkar Publishers, Distributors, Jaipur, India, (2009) 43-66.
- [8] Erten H., Agirman B., Boyaci-Gunduz C.P., Carsanba E., and Leventdurur S., Natural Microflora of Different Types of Foods, In: Malik A., Erginkaya Z., and Erten H., (Eds). Health and Safety Aspects of Food Processing Technologies, Springer Nature, Switzerland, (2019) 51-94.
- [9] Boor K., and Fromm H., Managing microbial spoilage in the dairy industry, In: Clive de W. Blackburn (Eds). Food spoilage microorganisms, Woodhead Publishing Ltd, England, (2006) 171-193.
- [10] Kurtzman C.P., Detection, identification and enumeration methods for spoilage yeasts, In: Clive de W. Blackburn (Eds). Food spoilage microorganisms, Woodhead Publishing Ltd, England, (2006) 28-54.
- [11] Büyükkiraz M.E., Avcı E., Kahraman N., and Kesmen Z., Bazı Gıdalardaki Bozulma Etkeni Maya Türlerinin İzolasyonu ve Tanımlanması, (Identification of Spoilage Yeasts Isolated From Some Foods), *Çukurova J. Agric. Food Sci.*, 35(1) (2020) 15-28.
- [12] Liu K-F., Li X-H., and Hui F-L., *Yarrowia brassicae* f.a., sp. nov., a new yeast species from traditional Chinese sauerkraut, *Int. J. Syst. Evol. Microbiol.*, 68(6) (2018) 2024-2027.
- [13] Nagy E., Niss M., Dlauchy D., Arneborg N., Nielsen D.S., and Péter G., *Yarrowia divulgata* f.a., sp. nov., a yeast species from animal-related and marine sources, *Int. J. Syst. Evol. Microbiol.*, 63(12) (2013) 4818-4823.
- [14] Stratford M., Food and Beverage Spoilage Yeasts. In: Querol A. and Fleet G. (Eds). Yeasts in food and beverages, Springer Berlin Heidelberg, (2006) 335-379.
- [15] Hernández A., Pérez-Nevado F., Ruiz-Moyano S., Serradilla M.J., Villalobos M.C., Martín A., Córdoba M.G., Spoilage yeasts: What are the sources of contamination of foods and beverages?, *Int. J. Food Microbiol.*, 286 (2018) 98-110.
- [16] Cocolin L., Rantsiou K., Iacumin L., Zironi R., Comi G., Molecular detection and identification of *Brettanomyces/Dekkera bruxellensis* and *Brettanomyces/Dekkera anomalous* in spoiled wines, *Appl. Environ. Microbiol.*, 70(3) (2004) 1347-1355.
- [17] Pham T., Wimalasena T., Box W.G., Koivuranta K., Storgårds E., Smart K.A., Gibson B.R., Evaluation of ITS PCR and RFLP for differentiation and identification of brewing yeast and brewery 'wild' yeast contaminants, *J. Inst. Brew.*, 117(4) (2011) 556-568.
- [18] Caputo L., Quintieri L., Baruzzi F., Borcakli M., Morea M., Molecular and phenotypic characterization of *Pichia fermentans* strains found among Boza yeasts, *Food Res. Int.*, 48(2) (2012) 755-762.
- [19] Ceugniet A., Drider D., Jacques P., Coucheney F., Yeast diversity in a traditional French cheese "Tomme d'orchies" reveals infrequent and frequent species with associated benefits, *Food Microbiol.*, 52 (2015) 177-184.
- [20] Corte L., di Cagno R., Groenewald M., Roscini L., Colabella C., Gobbetti M., Cardinali G., Phenotypic and molecular diversity of *Meyerozyma guilliermondii* strains isolated from food and other environmental niches, hints for an incipient speciation, *Food Microbiol.*, 48 (2015) 206-215.
- [21] Pereira E.L., Ramalhosa E., Borges A., Pereira J.A., Baptista P., Yeast dynamics during the natural fermentation process of table olives (Negrinha de Freixo cv.), *Food Microbiol.*, 46 (2015) 582-586.
- [22] Bayazit G., Gül Ü.D., Taştan B.E., Tozoğlu F., Gurbanov R., Exploring the biotechnological prospects of a recently

- discovered fungus isolated from marine mucilage, *Biomass Conv. Bioref.*, (2024).
- [23] White T., Bruns T.D., Lee S., Taylor J., Amplification and Direct Sequencing of Fungal Ribosomal RNA Genes for Phylogenetics, *PCR Protocols*, 18 (1990) 315-322.
- [24] Gardes M., and Bruns T.D., ITS primers with enhanced specificity for basidiomycetes - Application to the identification of mycorrhizae and rusts, *Mol. Ecol.*, 2 (1993) 113-118.
- [25] Janowski D., Wilgan R., Leski T., Karliński L., Rudawska M., Effective Molecular Identification of Ectomycorrhizal Fungi: Revisiting DNA Isolation Methods, *Forests*, 10(3) (2019) 218.
- [26] Tamura K., and Nei M., Estimation of the number of nucleotide substitutions in the control region of mitochondrial DNA in humans and chimpanzees, *Mol. Biol. Evol.*, 10(3) (1993) 512-526.
- [27] Tamura K., Stecher G., and Kumar S., MEGA 11: Molecular Evolutionary Genetics Analysis Version 11, *Mol. Biol. Evol.*, 38(7) (2021) 3022-3027.
- [28] Viljoen B.C., The ecological diversity of yeasts in dairy products. In: Jakobsen et al. (Eds), *Yeasts in the Dairy Industry: Positive and Negative Aspects*, Brussels, IDF, (1998) 70-77.
- [29] Frohlich-Wyder M.T., Yeasts in dairy products, In: *Yeasts in Food Beneficial and Detrimental Aspects*, Boekhout T.A., and Robert V. (Eds), Behr's-Verlag, Hamburg, (2003) 209-237.
- [30] Prillinger H., Molnár O., Eliskases-Lechner F., Lopandic K., Phenotypic and genotypic identification of yeasts from cheese, *Antonie van Leeuwenhoek*, 75(4) (1999) 267-283.
- [31] Westall S., and Filtenborg O., Spoilage yeasts of decorated soft cheese packed in modified atmosphere, *Food Microbiol.*, 15(2) (1998) 243-249.
- [32] Tokak S., Kılıç İ.H., Yalçın H.T., and Duran T., Detection of Extracellular Lipases and Genotypic Identification from Yeast Causing Spoilage of Some Dairy Products Produced in Gaziantep, *KSU J. Agric. Nat.*, 22(1) (2019) 206-211.
- [33] Budak S.O., Figge M.J., Houbraken J., de Vries R.P., The diversity and evolution of microbiota in traditional Turkish Divle Cave cheese during ripening, *Int. Dairy J.*, 58 (2016) 50-53.
- [34] Fröhlich-Wyder M-T., Arias-Roth E., and Jakob E., Cheese yeasts, *Yeast*, 36(3) (2018) 129-141.
- [35] Milanović V., Sabbatini R., Garofalo C., Cardinali F., Pasquini M., Aquilanti L., and Osimani A., Evaluation of the inhibitory activity of essential oils against spoilage yeasts and their potential application in yogurt, *Int. J. Food Microbiol.*, 341 (2021) 109048.
- [36] Las Heras-Vazquez F.J., Mingorance-Cazorla L., Clemente-Jimenez J.M., and Rodriguez-Vico F., Identification of yeast species from orange fruit and juice by RFLP and sequence analysis of the 5.8S rRNA gene and the two internal transcribed spacers, *FEMS Yeast Res.*, 3 (2003) 3-9.
- [37] Mokhtari M., Etebarian H.R., Razavi M., Heydari A. and Mirhendi H., Identification of Yeasts Isolated from Varieties of Apples and Citrus Using PCR-Fragment Size Polymorphism and Sequencing of ITS1-5.8S-ITS2 region, *Food Biotechnol.*, 26(3) (2012) 252-265.
- [38] Šovljanski O, Saveljić A., Tomić A., Šeregelj V., Lončar B., Cvetković D., Ranitović A., Pezo L., Četković G., Markov S., and Čanadanović-Brunet J., Carotenoid-Producing Yeasts: Selection of the Best-Performing Strain and the Total Carotenoid Extraction Procedure, *Processes*, 10(9) (2022) 1699.
- [39] Gavião, E. R., Munieweg, F. R., Czarnobay, M., Dilda, A., Stefani, L. M., and Nespolo, C. R. (2021). Development and characterization of two novel formulations of Labneh cheese of sheep's milk, *Food Sci. Technol., Campinas*, 41(3) (2021) 708-715.
- [40] Tawfek M.A., Farahar E.S.A., and Shalaby S.M., Effectiveness of Myrrh Oil In Improving The Quality and Shelf Life of Labneh, *Egypt. J. Dairy Sci.*, 46(1) (2018) 79-87.

## Effect of Bortezomib, Daptomycin and Their Combination on Antiproliferation in U266 Multiple Myeloma Cell Line

Kübra Yılmaz <sup>1,a</sup>, Ahmet Ozan Kaleci <sup>2,b,\*</sup>

<sup>1</sup> Faculty of Medicine, Sivas Cumhuriyet University, Sivas, Türkiye

<sup>2</sup> Department of Pharmacology, Faculty of Medicine, Sivas Cumhuriyet University, Sivas, Türkiye

\*Corresponding author

### Research Article

#### History

Received: 28/08/2024

Accepted: 28/03/2025



This article is licensed under a Creative Commons Attribution-NonCommercial 4.0 International License (CC BY-NC 4.0)

### ABSTRACT

Multiple myeloma is the second most common hematological malignancy in adults. Although current treatment approaches extend survival to 6 to 10 years in multiple myeloma treatment, most patients relapse. This situation has led to the need for new therapeutic agents in the treatment of multiple myeloma. Daptomycin, a drug molecule isolated from *Streptomyces roseosporus* and used especially in infections caused by Gram-positive bacteria, has been shown in recent studies to suppress tumor migration and angiogenesis. Bortezomib is a chemotherapy drug currently used in the treatment of multiple myeloma. In this study, we determined the antiproliferative effect of Bortezomib and Daptomycin applications on the U266 multiple myeloma cell line by % cell viability analysis with the XTT method. In addition, we determined the apoptosis levels of U266 multiple myeloma cell lines by flow cytometry. In conclusion, we determined that the combined application of Bortezomib and Daptomycin increased the anticancer effect of Bortezomib alone in U266 multiple myeloma cell lines. In light of the data obtained from this study, we can say that the effect of Daptomycin added to Bortezomib in the treatment of multiple myeloma may contribute significantly to the treatment of the disease.

**Keywords:** Multiple Myeloma, Bortezomib, Daptomycin, Proliferation, Apoptosis.

<sup>a</sup> [kubrayyilmazy@gmail.com](mailto:kubrayyilmazy@gmail.com)

<sup>b</sup> <https://orcid.org/0009-0004-2266-5545>

<sup>\*</sup> [ahmetozankaleci@cumhuriyet.edu.tr](mailto:ahmetozankaleci@cumhuriyet.edu.tr) <sup>b</sup> <https://orcid.org/0000-0003-4514-6209>

## Introduction

Multiple Myeloma is a type of cancer characterized by clonal proliferation of malignant plasma cells in the bone marrow, accounting for 10% of hematologic malignancies. The most common abnormality in myeloma is abnormalities involving the immunoglobulin heavy chain replacement site (on the long arm of chromosome 14) [1].

There are 20,000 new diagnoses each year in the United States. The median age at diagnosis is 70 years. The primary site of involvement is the bone marrow, and involvement is usually in the form of lytic lesions throughout the skeletal system. In multiple myeloma, factors produced by neoplastic plasma cells lead to bone damage, which is the main feature of the disease. Myeloma cells disrupt normal B lymphocyte function, leaving the body vulnerable to infection. Although immunoglobulin levels are increased due to increased M protein in the plasma, functional antibody production is very low. This leads to suppression of humoral immunity in patients and an increased risk of bacterial infection [2].

Daptomycin is a natural, bactericidal antibiotic produced by a bacterium called *Streptomyces roseosporus*, which has a cyclic lipopeptide structure of 13 amino acids. This structure causes the formation of transmembrane channels in the lipoteichoic acid found abundantly in the walls of gram-positive bacteria, thus causing intracellular ions (potassium and magnesium) and ATP to leak through these channels. This leads to a rapid depolarization in the membrane potential of gram-

positive bacteria. The loss of membrane potential leads to inhibition of protein, DNA, and RNA synthesis, which quickly leads to the death of the bacteria [3]. The reason why opening holes in the membrane to allow the flow of ions during the membrane binding stage does not create toxicity for mammalian cells is that the lipid tail of the drug enters itself and creates channels that allow the flow of ions without tearing the membrane. This explains the mechanism that kills bacteria but does not create toxicity for mammalian cells [4].

Daptomycin exhibits in vitro bactericidal activity against Gram-positive pathogens, including strains with limited therapeutic alternatives. In addition, Daptomycin is an option for the treatment of pediatric infections caused by Vancomycin-resistant enterococci (VRE) such as urinary tract infection, bacteremia, sepsis, and endocarditis [5,6]. Daptomycin has weak in vitro activity against Gram-negative bacteria. Daptomycin is used as a broad-spectrum antibiotic in patients with dominant immunity [7].

Bortezomib is one of the most effective chemotherapy drugs used in the treatment of multiple myeloma. Bortezomib, a proteasome inhibitor, is widely used. In the event of recurrence of cancer, its use contributes to the treatment of the disease. Bortezomib has apoptosis-inducing effects by disrupting the cell cycle in cells. It is well tolerated in patients after use. Therefore, its use can be continued in outpatient treatment. Bortezomib is



known to have synergistic effects with some drugs. Its use together with compounds such as dexamethasone increases the efficiency of the drug with a synergistic effect. Therefore, there is a need to investigate new molecules that will synergistically increase the effect of Bortezomib [8].

In a study, it was reported that Daptomycin can bind to human ribosomal S19 protein (RPS19) and suppress tumor migration and angiogenesis. In this study, MCF7, HepG2, Huh7, SK-BR-3, MDA-MB231, A549, HeLa, HCT116, CCD-18Co, HUVECs and HEK293 cell cultures were used and it was stated that the culture with the highest sensitivity was the breast cancer cell line MCF7. Their findings show that anti-cancer drugs that will target RPS19 may be promising [9].

In this study, in order to determine whether Daptomycin has an effect on the anticancer effect of Bortezomib, which is used as a chemotherapy drug, we examined its anti-proliferative effect on U266 multiple myeloma cell lines using the XTT method and its effect on apoptosis using the Annexin V/Dead Cell kit using a flow cytometry device.

## Materials and methods

### Cell Culture

Multiple Myeloma (U266) cells obtained from ATCC were grown in RPMI (1:1) cell culture medium containing 1% L-glutamine, 1% penicillin-streptomycin and 10% fetal bovine serum in 25 cm<sup>2</sup> flasks under sterile conditions at 37°C and 5% CO<sub>2</sub> [10].

### XTT Cell Viability Test

The effect of bortezomib and daptomycin on U266 cell viability was investigated with the XTT (2,3-bis (2-methoxy-4-nitro-5-sulphophenyl)-5-[(phenylamino) carbonyl]-2H-tetrazolium hydroxide) test in accordance with the kit protocol [11].

### Evaluation of Apoptosis with Flow Cytometry

Apoptosis was evaluated with the Muse Annexin V/Dead Cell (Merck Millipore, Darmstadt, Germany) test. The procedure to be applied was determined according to the manufacturer's instructions [12].

### Statistical Analysis

Statistical evaluation of the data to be obtained and drawing of the graphics were done using the Graphpad Prism program.

## Results and Discussion

### XTT assay in Multiple Myeloma U266 cell lines

The effects of Bortezomib doses of 1600 nM, 800 nM and 400 nM and Daptomycin doses of 10 mM, 5 mM, 2.5 mM and 1.25 mM and synergistic doses of these two drugs applied to U266 Multiple Myeloma cell lines on % cell viability were investigated using the XTT method (Figures 1-3.).

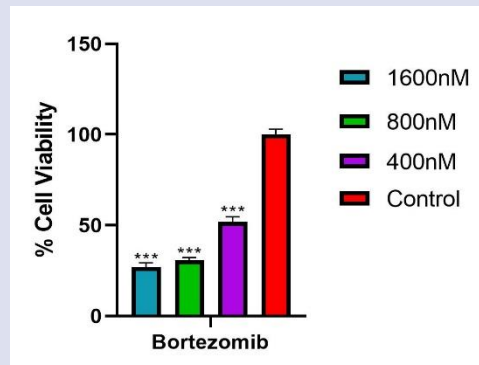


Figure 1. Viability percentages of U266 cells after 24 h Bortezomib exposure (\*\*\*P<0.001, \*\*P<0.01, \*P<0.05). IC<sub>50</sub> 392,4

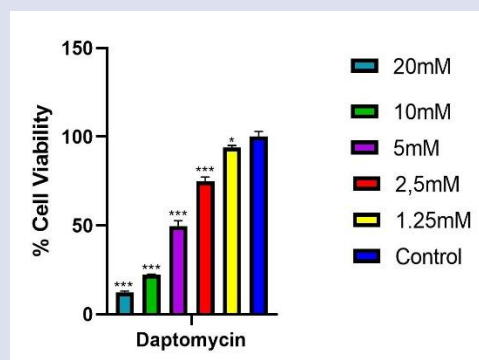


Figure 2. Viability percentages of U266 cells after 24 h Daptomycin exposure (\*\*\*P<0.001, \*\*P<0.01, \*P<0.05). IC<sub>50</sub> 4,97

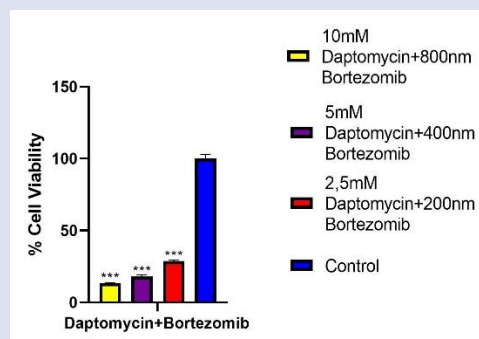


Figure 3. Viability percentages of U266 cells after 24 h Daptomycin+Bortezomib exposure (\*\*\*P<0.001, \*\*P<0.01, \*P<0.05).

The IC<sub>50</sub> values of Bortezomib and Daptomycin applied to U266 cell lines for 24 hours were determined as 392.40 nM and 4.97 mM, respectively. It was determined that Daptomycin and Bortezomib, applied separately and together to U266 Multiple Myeloma cancer cell lines for 24 hours, produced an anticancer effect on cancer cells. It was also observed that the combined application of Daptomycin and Bortezomib caused a significant decrease in cell proliferation.

### Flow Cytometry Analysis in Multiple Myeloma U266 Cell Lines

The effects of Bortezomib and Daptomycin alone and together on apoptosis in U266 Multiple Myeloma cell lines were investigated by flow cytometry (Figure 4.).



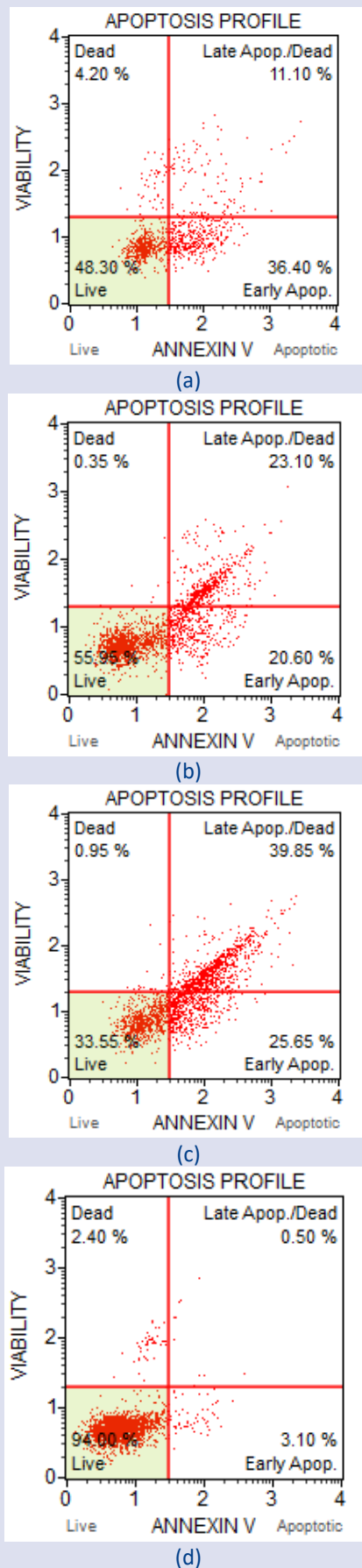


Figure 4. Flow cytometry graphs (A) IC50 dose of Bortezomib applied (B) IC50 dose of Daptomycin applied (C) IC50 doses of Bortezomib and Daptomycin applied (D) Control group U266 cell lines

Early and late apoptosis levels in U266 cell lines treated with IC50 doses of Bortezomib and Daptomycin were found to be increased compared to control group U266 cell lines. In addition, early and late apoptosis levels in U266 cell lines treated with IC50 doses of Bortezomib + Daptomycin were found to be significantly reduced compared to single drug application.

## Conclusions

In our study, we determined that even low doses of Bortezomib applied to U266 Multiple Myeloma cancer cell lines had high anticancer effects. In addition, we determined that Daptomycin, an antibiotic drug, also had anticancer effects on U266 Multiple Myeloma cancer cell lines. Interestingly, we showed that the combined use of Bortezomib and Daptomycin on U266 Multiple Myeloma cancer cell lines increased their anticancer effects.

Bortezomib, a chemotherapy drug also known as PS341, has inhibitory properties of the 26S proteasome found in cell nuclei and cytosol. This inhibition is reversible. The 26S proteasome is found in eukaryotic cells and functions in the degradation of protein molecules responsible for the continuation of the cell cycle [13,14]. Abnormal proteins are formed especially as a result of mutations that occur due to the rapid and uncontrolled division of cells, especially in Multiple Myeloma. However, there may be deformations in the folding of the synthesized proteins. The 26S proteasome mediates the elimination of these proteins. This situation mediates a decrease in the proliferation of cancer cells and constitutes the main mechanism of anti-cancer effects [15]. The ubiquitin-proteasome pathway is a pathway that regulates the biological processes of cells [16]. It is also important that bortezomib is the first drug to be approved by the US Food and Drug Administration (FDA) as a drug that inhibits this ubiquitin-proteasome pathway. The use of bortezomib mediated the direction of cells to apoptosis by suppressing the expression of proteins such as BCL-2 and BCL-XL, which are apoptosis inhibitors, in in vitro cancer cell lines. In addition, it has shown anticancer activity by regulating the expression of proteins involved in DNA repair [17]. Although bortezomib is a powerful chemotherapeutic, as with all chemotherapy drugs, resistance can develop in cancer cells against this drug [18]. However, unwanted side effects such as neuropathy may occur in its use in hematological cancers [19].

Bortezomib has anticancer effects in cancer cell lines other than Multiple Myeloma. In a study investigating its effect on drug-resistant human neuroblastoma cell lines, it was determined that apoptosis was induced in both drug-resistant and drug-resistant neuroblastoma cell lines and that it inhibited the cell cycle even at nanomolar concentrations, thus having a high anticancer activity. However, it was determined that these cell lines reduced cell proliferation after Bortezomib application after being taken into the in vivo environment. In addition, it was determined that Bortezomib inhibited new vessel formation in xenograft models [20]. It was shown that

Bortezomib was applied alone and in combination to the A549 cancer line, which is one of the non-small cell lung cancer cell lines, causing a pause in the cell cycle and reducing cell proliferation [21]. In the study examining the in vitro and in vivo effect of Bortezomib on prostate cancer, it was determined that proteasome inhibition and prostate-specific antigen modulation increased positively when the Bortezomib dose given to the patients was increased. Based on this, it has been reported that the combination of Bortezomib with radiotherapy and chemotherapy in the treatment of prostate cancer may have a higher effect on the increase of anticancer effect [22]. The use of Bortezomib also has effects on osteoblast cells that play a role in bone formation. Surprisingly, unlike other cancer cells, Bortezomib mediates an increase in the number of osteoblast cells. This also causes an increase in bone tissue [23]. The results of our study are parallel to the data in the literature that apoptosis is induced and proliferation is reduced in cancer cell lines treated with Bortezomib in vitro conditions.

Daptomycin is an antibiotic with a cyclic lipopeptide structure. It is produced by *Streptomyces roseosporus*. Its production is possible by adding decanoic acid to the growth medium of the medium. Daptomycin is used for the treatment of infections occurring in the skin and skin structures. It is also an antibiotic approved by the FDA [24,25]. Daptomycin is an effective drug used against Gram-positive bacteria, as well as in the treatment of sepsis, meningitis and many diseases such as endocarditis [5]. However, the increase in Daptomycin use causes bacteria to develop resistance to this antibiotic. It is known that *Staphylococcus aureus* in particular develops resistance to this drug [26,27].

There are very few literature studies on the relationship between Daptomycin and cancer. In a study on Daptomycin and cancer, it was shown that the binding of Daptomycin to ribosomal protein S19 has anticancer effects. It has been reported that the complex of Daptomycin and ribosomal protein S19 mediates a decrease in cell proliferation without inducing apoptosis in cell lines. When ribosomal protein S19 expression was reduced using siRNA, it was determined that the anticancer efficacy of Daptomycin application in MCF-7 cell lines increased. Daptomycin also suppressed the formation of new vessels and migration of cancer cells by suppressing VEGF expression in cancer cell lines. The data obtained from this study suggested that Daptomycin may be an alternative tool in cancer treatment [9]. In our study, we determined that Daptomycin, whose anticancer effect was reported, had a effect on the chemotherapeutic effect of Bortezomib, which is currently used in the treatment of Multiple Myeloma. We determined that Bortezomib and Daptomycin had anticancer effects on U266 cancer cell lines when used alone. However, we have shown that the combined use of Bortezomib and Daptomycin can create a great effect on U266 cell lines, making a significant contribution to the efficiency of Multiple Myeloma treatment.

## Conflicts of interest

There are no conflicts of interest in this work.

## Acknowledgement

This project is supported by TUBITAK. TUBITAK project number: 1919B012224550.

## References

- [1] Firth, J., Haematology: multiple myeloma, *Clinical Medicine*, 19(1) (2019) 58-60.
- [2] Kumar V., Abbas A.K., Aster J.C., Robin's Basic Pathology. 10th ed. Elsevier, (2020).
- [3] Anonymous, Cubicin (daptomycin) product information, Cubist Pharmaceuticals Inc., Lexington, MA, (2003).
- [4] Larkin M., Daptomycin approved for skin and skin-structure infections, *The Lancet Infectious Diseases*, 3(11) (2003) 677.
- [5] Marty F.M., Yeh W.W., Wennersten C.B., Venkataraman L., Albano E., Alyea E.P., ... & Pillai S.K., Emergence of a clinical daptomycin-resistant *Staphylococcus aureus* isolate during treatment of methicillin-resistant *Staphylococcus aureus* bacteremia and osteomyelitis, *Journal of clinical microbiology*, 44(2) (2006) 595-597.
- [6] Poutsika D.D., Skiffington S., Miller K.B., Hadley S., Snyderman, D.R., Daptomycin in the treatment of vancomycin-resistant *Enterococcus faecium* bacteremia in neutropenic patients, *Journal of Infection*, 54(6) (2007) 567-571.
- [7] Streit J.M., Jones R.N., Sader H.S., Daptomycin activity and spectrum: a worldwide sample of 6737 clinical Gram-positive organisms, *Journal of Antimicrobial Chemotherapy*, 53(4) (2004) 669-674.
- [8] Field-Smith A., Morgan G.J., Davies F.E., Bortezomib (Velcade™) in the treatment of multiple myeloma, *Therapeutics and clinical risk management*, 2(3) (2006) 271-279.
- [9] Cho S.M., Lee H.J., Karuso P., Kwon H.J., Daptomycin suppresses tumor migration and angiogenesis via binding to ribosomal protein S19 in humans, *The Journal of Antibiotics*, 74(10) (2021) 726-733.
- [10] Durusu İ.Z., Hüsnügil H.H., Ataş H., Biber A., Gerekeçi S., Güleç E.A., Özen C., Anti-cancer effect of clofazimine as a single agent and in combination with cisplatin on U266 multiple myeloma cell line, *Leukemia Research*, 55 (2017) 33-40.
- [11] Terzi H., Altun A., Şencan M., In vitro comparison of the cytotoxic effects of statins on U266 myeloma cell line, *Indian Journal of Medical Research*, 150(6) (2019) 630-634.
- [12] Bostancı H.E., Yıldız M.T., Kapancık S., Şahin Inan Z.D., Kılıç H.A., Özensoy Güler Ö., ... & Kaplancıklı Z.A., New benzimidazole derivatives containing hydrazone group as anticancer agents: Inhibition of carbonic anhydrase IX and molecular docking studies, *Archiv der Pharmazie*, 358(3) (2025) e2400930.
- [13] Roccaro A.M., Vacca A., Ribatti D., Bortezomib in the treatment of cancer, *Recent patents on anti-cancer drug discovery*, 1(3) (2006) 397-403.
- [14] Coux O., Tanaka K., Goldberg A.L., Structure and functions of the 20S and 26S proteasomes, *Annual review of biochemistry*, 65(1) (1996) 801-847.

- [15] Hideshima T., The proteasome inhibitor PS-341 inhibits growth, induces apoptosis, and overcomes drug resistance in human multiple myeloma (MM) cells, *Blood*, 96 (2000) 461a.
- [16] Ciechanover A., The ubiquitin–proteasome pathway: on protein death and cell life, *The EMBO journal*, 17(24) (1998) 7151-7160.
- [17] Mujtaba T., Dou Q.P., Advances in the understanding of mechanisms and therapeutic use of bortezomib, *Discovery medicine*, 12(67) (2011) 471.
- [18] Ruschak A.M., Slassi M., Kay L.E., Schimmer A.D., Novel proteasome inhibitors to overcome bortezomib resistance, *Journal of the National Cancer Institute*, 103(13) (2011) 1007-1017.
- [19] Argyriou A.A., Iconomou G., Kalofonos H.P., Bortezomib-induced peripheral neuropathy in multiple myeloma: a comprehensive review of the literature, *Blood, The Journal of the American Society of Hematology*, 112(5) (2008) 1593-1599.
- [20] Brignole C., Marimpietri D., Pastorino F., Nico B., Di Paolo D., Cioni M., ... & Ponzoni M., Effect of bortezomib on human neuroblastoma cell growth, apoptosis, and angiogenesis, *Journal of the National Cancer Institute*, 98(16) (2006) 1142-1157.
- [21] Mortenson M.M., Schlieman M.G., Virudachalam S., Bold R.J., Effects of the proteasome inhibitor bortezomib alone and in combination with chemotherapy in the A549 non-small-cell lung cancer cell line, *Cancer chemotherapy and pharmacology*, 54 (2004) 343-353.
- [22] Papandreou C.N., Logothetis C.J., Bortezomib as a potential treatment for prostate cancer, *Cancer research*, 64(15) (2004) 5036-5043.
- [23] Giuliani N., Morandi F., Tagliaferri S., Lazzaretti M., Bonomini S., Crugnola M., ... & Rizzoli V., The proteasome inhibitor bortezomib affects osteoblast differentiation in vitro and in vivo in multiple myeloma patients, *Blood, The Journal of the American Society of Hematology*, 110(1) (2007) 334-338.
- [24] Pillai S.K., Gold H.S., Sakoulas G., Wennersten C., Moellering Jr R.C., Eliopoulos G.M., Daptomycin nonsusceptibility in *Staphylococcus aureus* with reduced vancomycin susceptibility is independent of alterations in MprF, *Antimicrobial agents and chemotherapy*, 51(6) (2007) 2223-2225.
- [25] Tally F.P., DeBruin M.F., Development of daptomycin for gram-positive infections, *Journal of Antimicrobial Chemotherapy*, 46(4) (2000) 523-526.
- [26] Tran T.T., Munita J.M., Arias C.A., Mechanisms of drug resistance: daptomycin resistance, *Annals of the New York Academy of Sciences*, 1354(1) (2015) 32-53.
- [27] Stefani S., Campanile F., Santagati M., Mezzatesta M.L., Cafiso V., Pacini G. Insights and clinical perspectives of daptomycin resistance in *Staphylococcus aureus*: a review of the available evidence, *International journal of antimicrobial agents*, 46(3) (2015) 278-289.

## Determination of Irbesartan in Pharmaceutical Preparations by HPLC

Bilal Yılmaz<sup>1,a,\*</sup><sup>1</sup>Department of Analytical Chemistry, Faculty of Pharmacy, Ataturk University, Erzurum, Türkiye

\*Corresponding author

### Research Article

#### History

Received: 17/05/2024

Accepted: 02/04/2025



This article is licensed under a Creative Commons Attribution-NonCommercial 4.0 International License (CC BY-NC 4.0)

### ABSTRACT

In this study, a high-performance liquid chromatography (HPLC) method was developed to analyze irbesartan in both pure and pharmaceutical formulations. The mobile phase consisted of an acetonitrile-1.0 mM potassium dihydrogen phosphate solution (30:70, v/v), adjusted to pH 3.0 with phosphoric acid. The analysis was performed using an Ace C<sub>18</sub> column, and a UV detector was employed to monitor the eluent at 220 nm. With a flow rate of 1.0 mL min<sup>-1</sup>, the analysis was completed in under 6 minutes. The calibration curve was linear across the concentration range of 0.10-5.0 µg mL<sup>-1</sup>. The accuracy of the method (relative error) for irbesartan was better than 2.67%, and the intra- and inter-day precision values were below 3.23%. The mean recovery of irbesartan in pharmaceutical formulations was 101.4%. The limits of detection and quantitation were found to be 0.03 and 0.10 µg mL<sup>-1</sup>, respectively. Furthermore, the method proved to be effective for quantifying the drug and confirming the consistency of the formulation content in commercial irbesartan dosage forms.

**Keywords:** Irbesartan, HPLC, Validation, Drug analysis.<sup>a</sup>[yilmazb@atauni.edu.tr](mailto:yilmazb@atauni.edu.tr) <https://orcid.org/0000-0002-8574-7570>

## Introduction

Cardiovascular diseases account for 17.9 million deaths annually, representing approximately 30% of all deaths worldwide [1]. Hypertension is responsible for at least 45% of heart disease-related deaths. Hypertension is a major public health issue due to its widespread prevalence worldwide and the increased risk of mortality when it coexists with other diseases. Antihypertensive medications are used not only to lower blood pressure but also to mitigate the adverse effects associated with hypertension. A variety of drug classes are employed to manage hypertension, including angiotensin-converting enzyme inhibitors (ACE-I), beta-blockers, calcium channel blockers, thiazide diuretics, and angiotensin receptor blockers (ARB). In cases where monotherapy with a single class of antihypertensive drugs is insufficient, most guidelines recommend combining a thiazide diuretic with an ARB. Combination therapy, compared to monotherapy, allows for the use of lower doses of each drug, which enhances treatment effectiveness and reduces side effects. Therefore, combining medications for hypertension treatment provides a more efficient approach with fewer adverse effects than using a single drug. Various medications have been used to treat hypertension, including beta-blockers, diuretics, angiotensin-converting enzyme inhibitors, angiotensin receptor blockers, and calcium channel blockers [2].

Irbesartan belongs to the class of angiotensin II receptor antagonists. By preventing the constriction of blood vessels, irbesartan helps to lower blood pressure and enhance blood flow. It is commonly used to treat hypertension, or high blood pressure, and can be

administered either alone or in combination with other antihypertensive drugs. Irbesartan is commonly used to treat hypertension and other cardiovascular diseases. However, like any medication, irbesartan can cause some side effects. In some individuals using irbesartan, particularly those with kidney problems, heart conditions, or other serious health issues, more severe side effects may occur. Chemically, irbesartan is identified as 2-butyl-3-[p-(o-1H-tetrazol-5-yl)phenyl]benzyl]-1,3-diazaspiro[4.4]non-1-en-4-one, a non-peptide molecule. Its structural formula is shown in Figure 1, and its empirical formula is C<sub>25</sub>H<sub>28</sub>N<sub>6</sub>O. Irbesartan has a molecular weight of 428.5 g mol<sup>-1</sup> and is typically found as a crystalline powder that ranges in color from white to off-white [3].

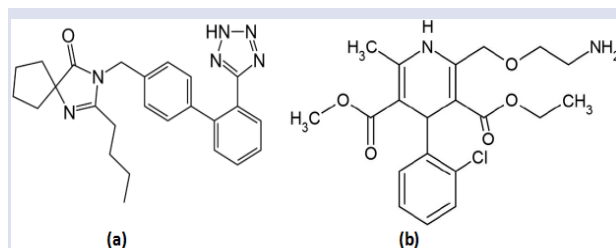


Figure 1. Chemical structures of irbesartan (a) and amlodipine (IS) (b)

Several analytical techniques have been reported for the detection of irbesartan, including UV-spectrophotometry [4-10], spectrofluorimetry [11], capillary electrophoresis [12], LC-MS [13-16] and HPLC

[17-22]. However, each of these methods presents certain challenges. Spectroscopic methods tend to have low sensitivity, while chromatographic techniques often require complex derivatization or lengthy extraction procedures, and are generally time-consuming and costly. Therefore, simpler, faster, and more affordable methods that still offer high sensitivity could provide a beneficial alternative.

HPLC is a commonly used technique for analyzing drugs in pharmaceutical formulations and biological fluids, owing to its advantages like ease of use and affordability. Only two RP-HPLC methods have been found for estimating irbesartan alone. In one method [23], the retention time of irbesartan was found to be 11.9 minutes, which is considered too long for method optimization, with a linearity range of 10-200  $\mu\text{g mL}^{-1}$ . In another method [24], the determination of irbesartan was conducted alongside other related impurities, with a reported retention time of 5.8 minutes for irbesartan. Based on the reported articles and their associated drawbacks, it can be concluded that there is a need for a clear, simple, reliable, and validated UV and HPLC method for estimating irbesartan alone, which could also be effectively used for the determination of irbesartan in marketed formulations.

Developing a novel technique for determining the concentration of irbesartan in pharmaceutical solutions or biological fluids is essential. To meet this need, the objective of the study is to propose an HPLC method with UV detection for the quantification of irbesartan in pharmaceutical products. In compliance with the International Conference on Harmonization (ICH) guidelines, the developed method was validated based on criteria such as linearity, stability, precision, accuracy, and recovery. This method offers a short six-minute run time and a simple mobile phase composition, allowing for the efficient analysis of a large number of samples.

## Materials and Methods

### Chemicals

Irbesartan, amlodipine besylate, internal standard (IS), methanol, acetonitrile and potassium dihydrogen phosphate were provided Sigma-Aldrich (St. Louis, MO, USA). The irbesartan-containing Karvea tablets were provided by the pharmacy in Erzurum, Türkiye. Every chemical was of the analytical purity.

### HPLC System and Chromatographic Conditions

The method development and validation studies were conducted using Agilent HPLC equipment from the 1260 series. A UV detector (G71144A), auto injector (G7129A), and quaternary pump (G7111A) were included in this chromatographic system's equipment. The Ace C<sub>18</sub> (250×4.60 mm ID, 5 $\mu\text{m}$ ) analytical column was used for the separations, which were carried out at 25 °C. Phosphoric acid was used to modify the acetonitrile-1.0 mM potassium dihydrogen phosphate solution (30:70, v/v, pH 3.0) for the mobile phase. Mobile phase flow rate

and UV detection of method were 1.0 mL min<sup>-1</sup> and 220 nm, respectively.

### Preparation of Standard and QC Solutions

The stock solutions of the irbesartan and IS were prepared in methanol at a concentration of 50  $\mu\text{g mL}^{-1}$  and then stored at -20 °C. Methanol was used to dilute the stock solution to prepare irbesartan standard solutions in the range of 0.10-5.0  $\mu\text{g mL}^{-1}$ . Additionally, quality control (QC) samples were prepared at concentrations of 0.75, 3.0, and 4.5  $\mu\text{g mL}^{-1}$ , along with a 5.0  $\mu\text{g mL}^{-1}$  IS solution.

### Procedure for Pharmaceutical Preparations

Using the mass of the Karvea tablets, the average tablet mass was computed. Afterward, they were subjected to homogenization, fine grinding, and the careful weighing of a portion of the powder. The necessary amount of methanol was then poured to them in a 100 mL brown measuring flask in order to dilute the powder. After sonicating the mixture for a minimum of fifteen minutes to facilitate dissolution, it was filtered using a Whatman No. 42 paper. After an appropriate volume of filtrate was taken, it was further diluted with methanol to ensure that the final solution's irbesartan concentration fell within the working range.

### Data Analysis

With the use of a computer program, SPSS 15.0 was used for the statistical analyses. The irbesartan standard line and calculations were made using regression analyses. The results' mean and standard deviation were given.

## Results and Discussion

### Development and Optimization of the Method

In recent years, the importance of the HPLC method for drug analysis in routine quality control has garnered significant attention. An appropriate technique for determining irbesartan in pharmaceutical dosage forms was proposed. For this purpose, the Ace C<sub>18</sub> column (250×4.60 mm ID, 5 $\mu\text{m}$ ) was selected. The chromatographic conditions were optimized to ensure the experiment's successful performance. The procedure utilized a mobile phase consisting of acetonitrile and 1.0 mM potassium dihydrogen phosphate solution (30:70, v/v, pH 3.0).

The retention time was observed to be 5.85 minutes. The total run time for the assay was approximately ten minutes. The mobile phase was chosen after conducting several experiments with different solvent mixtures. In selecting the mobile phase, factors such as peak properties (symmetry, tailing), run time, cost, and ease of preparation were carefully considered. A representative chromatogram obtained by applying the proposed method to the analysis of a standard irbesartan sample is shown in Figure 2. The retention time observations enabled rapid determination of the drug.



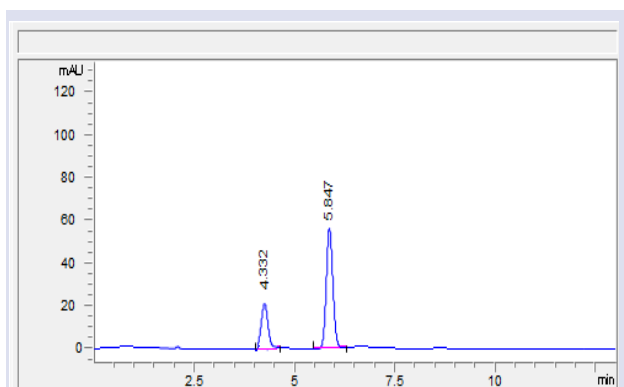


Figure 2. The chromatograms of irbesartan ( $5.0 \mu\text{g mL}^{-1}$ , Rt:5.847 min) and amplodipin (IS) ( $5.0 \mu\text{g mL}^{-1}$ , Rt:4.332 min)

### Validation of the Method

The objective of method validation is to demonstrate that the method is suitable for its intended purpose, as outlined in the ICH guidelines. The method was validated for linearity, accuracy, precision, limits of detection and quantitation, recovery, stability, selectivity and system suitability [25-27].

### Linearity

An analytical method is considered linear if it produces test results that are directly proportional to the analyte concentration in the sample within a specified range, either directly or through a well-defined mathematical transformation. Initially, this can be assessed visually by analyzing a plot of signal versus analyte concentration. If the relationship appears linear, the test results should be confirmed using appropriate statistical methods (e.g., by calculating a regression line using the least squares method). In some cases, a mathematical adjustment of the test results may be required to achieve linearity between the analyte's response and its concentration.

To mathematically assess the degree of linearity, the information derived from the regression line itself can be valuable. It is essential to report the slope of the regression line, the residual sum of squares, the y-intercept, and the correlation coefficient. Analysis was done on standard solutions containing  $5.0 \mu\text{g mL}^{-1}$  of IS and  $0.10$ - $5.0 \mu\text{g mL}^{-1}$  of irbesartan. The standard curve (Figure 3) was created by plotting the concentration of irbesartan on the X-axis and the peak area ratio of irbesartan and IS on the Y-axis.

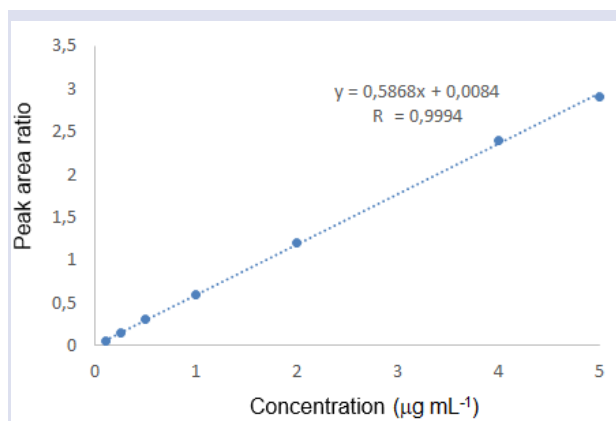


Figure 3. The standard curve of irbesartan ( $0.10$ ,  $0.25$ ,  $0.5$ ,  $1.0$ ,  $2.0$ ,  $4.0$  and  $5.0 \mu\text{g mL}^{-1}$ )

Using the least squares regression approach to construct the linear regression analysis, the linearity was assessed. The regression equation was computed from the calibration graphs (Table 1).

Table 1. Linearity of of irbesartan (n=3)

Range ( $\mu\text{g mL}^{-1}$ )	Linear regression	R <sup>2</sup>
0.10-5.0	$y=0.5868x+0.0084$	0.9988

### Accuracy and Precision

Accuracy is described as how closely test results produced by the procedure resemble the actual value. By using known, added amounts of analyte in the experiment, it is frequently stated as the percent recovery. Accuracy measures the precision of the analytical process. The true values were used to calculate the variances of the obtained results, which were subsequently reported as percentage accuracy.

Analytical procedure repeatedly to several samplings of a homogenous sample is known as its precision. The standard deviation or relative standard deviation of a set of measurements is typically used to express the precision of an analytical procedure. A measure of precision could be the analytical method's repeatability or degree of reproducibility under typical operating conditions.

The assay method's accuracy for both intra- and inter-day variations was determined by evaluating the QC samples six times. Table 2 shows the accuracy and precision values for the QC samples intra and inter-day runs. Between 2.34% and 3.23% ranged the precision, and between 1.27% and 2.67% the accuracy.

Table 2. Precision and accuracy of irbesartan

Added ( $\mu\text{g mL}^{-1}$ )	Found $\pm$ SD	Intra-day Accuracy (% relative error)	Precision RSD%	Found $\pm$ SD	Inter-day Accuracy (% relative error)	Precision RSD%
0.75	$0.73 \pm 0.019$	-2.67	2.60	$0.74 \pm 0.022$	-1.33	2.97
3.0	$3.06 \pm 0.08$	2.00	2.61	$2.98 \pm 0.07$	-0.67	2.34
4.50	$4.57 \pm 0.134$	1.27	2.93	$4.61 \pm 0.149$	2.44	3.23

### LOD and LOQ

Irbesartan's LOD and LOQ values were ascertained by evaluating various irbesartan solutions and calculating the signal-to-noise ratio for every analyte. The concentration providing a signal-to-noise ratio of roughly 3:1 is the LOD, while the concentration providing a signal-to-noise ratio of roughly 10:1 with an RSD of less than 10% with triplicate analysis is the LOQ. The HPLC technique was determined LOD and LOQ values of 0.03 and 0.10  $\mu\text{g mL}^{-1}$ , respectively.

### Recovery

Recovery values were obtained by spiking different amounts of pure drug into tablet samples that had already been pre-analyzed, within the analytical concentration range of the proposed method. Using the described procedure, the added doses of each drug were determined. The results of the recovery experiments were considered satisfactory and are presented in Table 3.

Table 3. Recovery of irbesartan in pharmaceutical preparation (n=6)

Pharmaceutical preparation	Added ( $\mu\text{g mL}^{-1}$ )	Found $\pm$ SD	Recovery (%)	RSD <sup>a</sup> (%)
Karvea	0.5	0.51 $\pm$ 0.017	102.0	3.33
tablet (1.0 $\mu\text{g mL}^{-1}$ )	2.5	2.53 $\pm$ 0.081	101.2	3.20
	3.5	3.54 $\pm$ 0.119	101.1	3.36

### Stability

Based on stability experiments, the samples remained stable for 72 hours at ambient temperature, as well as at 4°C and -20°C under refrigeration. The stability study results presented in Table 4 demonstrated that no significant degradation was observed.

Table 4. Stability of irbesartan in solutions

Added ( $\mu\text{g mL}^{-1}$ )	+25 °C stability (Recovery % $\pm$ RSD)		+4 °C stability (Recovery % $\pm$ RSD)		- 20 °C stability (Recovery % $\pm$ RSD)	
	24 h	72 h	24 h	72 h	24 h	72 h
0.50	102.1 $\pm$ 1.44	98.7 $\pm$ 3.17	99.7 $\pm$ 3.04	101.1 $\pm$ 2.94	98.3 $\pm$ 2.49	100.3 $\pm$ 2.09
2.5	101.4 $\pm$ 3.08	99.3 $\pm$ 2.71	99.4 $\pm$ 2.46	99.4 $\pm$ 3.07	101.4 $\pm$ 2.08	99.7 $\pm$ 2.65
4.5	99.4 $\pm$ 3.01	99.6 $\pm$ 2.97	101.2 $\pm$ 2.48	99.7 $\pm$ 3.19	100.4 $\pm$ 2.63	99.4 $\pm$ 3.09

### Selectivity

In this study, the potential interferences of common excipients and additives were investigated. Control samples were prepared and analyzed. At the concentrations typically found in dosage forms, no evidence of interference from these substances was observed. The excipient used in this formulation is one of the most commonly employed by the pharmaceutical industry. The selectivity of the method was evaluated by checking for any interference from common tablet ingredients such as talc, lactose, sodium chloride, titanium dioxide, and magnesium stearate. These substances did not cause any harmful impact on the proposed method. Based on the analysis results, the procedure can be regarded as selective.

### System Suitability

Prior to every validation, the chromatographic system underwent a system suitability test. Therefore, standard solutions containing 5.0  $\mu\text{g/mL}$  of internal standard (IS) and 5.0  $\mu\text{g/mL}$  of irbesartan were chosen. The efficiency, tailing factor, and area relative standard deviation were calculated for each of the five suitable injections. The average of the five suitable injections was used to quantify the check standard. The efficiency was  $\geq 2967$ , the %RSD was  $\leq 1.32\%$ , and the tailing factor was  $\leq 1.03$  for all sample analysis.

### Procedure for Pharmaceutical Preparations

The 300 mg irbesartan-containing Karvea tablet was carefully weighed and finely ground. The right amount of

powder was dissolved in 50 milliliters of methanol. Next, a balloon flask was filled to the ultimate capacity of 100 mL. After the tablet solutions were appropriately diluted, a Whatman filter was employed to filter them in order to provide a final concentration that fell between the linearity limitations of the HPLC procedure (Figure 4). Irbesartan's drug concentration was determined using the calibration curve.

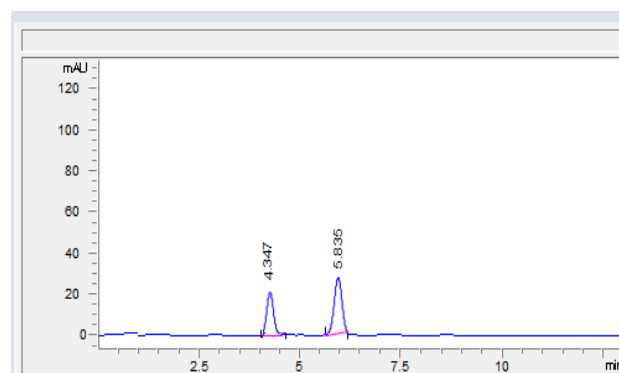


Figure 4. The chromatogram of Karvea tablet solution (2.50  $\mu\text{g mL}^{-1}$ )

### Comparison of the Methods

Irbesartan is commonly prescribed to treat chronic renal failure, congestive heart failure, and hypertension. In this study, commercial formulations used in the pharmaceutical industry were analyzed using a fast and straightforward HPLC method. The popularity of the proposed approach lies in its simplicity and ease of implementation.

Recently, voltammetry has emerged as a promising new analytical technique for the electrochemical detection of drugs. Voltammetric methods are vital for pharmaceutical analysis due to their affordability, user-friendliness, and rapid analysis times [28, 29].

The results demonstrate the excellent reproducibility and reliability of the two techniques. To statistically compare the best outcomes, a t-test was performed. The calculated t-values did not exceed the theoretical values at a 95% confidence level (Table 5).

Table 5. Comparison of the proposed and reported methods of irbesartan

Parameters	Proposed method	Official method [30]	Reported method [8]
Mean (recovery %)	101.4	100.04	99.63
SD	0.621	-	-
% RSD	0.612	0.260	0.362
Variance	0.374	-	-
SE	0.253	-	-
t-test (2.228) <sup>a</sup>	0.897	-	-
F- test (5.1) <sup>a</sup>	3.74	-	-

SE: Standard error, ( $P > 0.05$ ), <sup>a</sup>Theoretical values at  $P=0.05$ , Variance is a statistical measure that represents the spread or dispersion of a set of values.

As a result, the differences between the differential pulse polarography and square wave polarography techniques are minimal [28, 29]. The %RSD for the polarographic analysis of irbesartan tablets using the proposed methods was 1.09%. The recovery of standard additives further validated the accuracy of the methods applied to the irbesartan tablets. A mean recovery rate of 101.4% was achieved. The results from the drug analysis using the proposed techniques closely aligned with the stated values. The outcomes of the proposed methods were compared with those of the official [30] and reference methods [8]. The student t- and F-values, calculated at a 95% confidence level, indicated no significant differences in performance between the official or reference methods and the proposed techniques.

## Conclusion

In this study, a quick and simple HPLC method has been developed and validated for the quantification of irbesartan. The chromatographic approach meets all the necessary criteria, such as accuracy, linearity, recovery, and precision, ensuring its reliability and practicality. With a run time of just 6 minutes, it allows for the efficient analysis of a large number of samples. As a result, this method can be used not only for routine testing of formulations and raw materials but also for analyzing samples in accelerated stability studies.

## Conflicts of interest

The author states that did not has conflict of interests

## Acknowledgment

This study has not received financial support. Also, the author also acknowledges Semih Yilmaz for his help with the correct usage of English.

## References

- [1] Foley R.N., Parfrey P.S., Sarnak M.J., Clinical Epidemiology of Cardiovascular Disease in Chronic Renal Disease, *Am J Kidney Dis.*, (1998) S16-S23.
- [2] Nguyen Q., Dominguez J., Nguyen L., Gullapalli N., Hypertension Management: An Update, *Am Health Drug Benefits*, 3 (2010) 47-56.
- [3] Kurbanoğlu S., Yarman A., Simultaneous Determination of Hydrochlorothiazide and Irbesartan from Pharmaceutical Dosage Forms with RP-HPLC, *Turkish J Pharm Sci.*, 17(5) (2020) 523-527.
- [4] Ramakrishna S., SudhaLakshmi P.B., Rambabu C., Visible Spectrophotometric Methods for the Determination of irbesartan in Pharmaceutical Formulations, *International J Pharm Pharmaceut Sci.*, 4(3) (2012) 86-87.
- [5] Albero I., Rodenas V., Garcia S., Sánchez-Pedreno C., Determination of Irbesartan in the Presence of Hydrochlorothiazide by Derivative Spectrophotometry, *J Pharm Biomed Anal.*, 29(1-2) (2002) 299-305.
- [6] Ganesh K., Balraj C., Elango K.P., Spectroscopic and Spectrofluorimetric Studies on the interaction of Irbesartan with 2,3-dichloro-5,6-dicyano-1,4-benzoquinone and Iodine, *Spectrochim Acta Part A.*, 79(5) (2011) 1621-1629.
- [7] Abdellatef H.E., Extractive-Spectrophotometric Determination of Disopyramide and Irbesartan in their Pharmaceutical Formulation, *Spectrochim Acta Part A.*, 66(4-5) (2007) 1248-1254.
- [8] Erk N., Three New Spectrophotometric Methods Applied to the Simultaneous Determination of Hydrochlorothiazide and Irbesartan, *Pharmazie*, 58(8) (2003) 543-548.
- [9] Lakshmi S., Lakshmi K.S., H-Point Standard Addition Method for Simultaneous Spectrophotometric Determination of Irbesartan, Hydrochlorothiazide and Telmisartan in Tablets, *International J Res Pharm Chem.*, 4(2) (2014) 373-380.
- [10] Pradhan K.K., Mishra U.S., Pattnaik S., Debananda M., Ghanshyam P., Sahu K.C., Method Development, Validation and Stability Study of Irbesartan in Bulk and Pharmaceutical Dosage Form by UV-Spectrophotometric Method, *International J Pharm Biological Arch.*, 2(4) (2011) 1114-1122.
- [11] Mahmoud A., Sama H.A., Ahmed A.A., Ahmed M.A., Spectrophotometric and Spectrofluorimetric Determination of Certain Angiotensin Receptor Blockers through Complex Formation, *J Pharm Sci Research*, 3(10) (2011) 1499-1510.
- [12] Hillaert S., Van Den Bossche W., Optimization and Validation of a Capillary Zone Electrophoretic Method for the Analysis of Several Angiotensin-II-Receptor Antagonists, *J Chromatogr A.*, 979(1-2) (2002) 323-333.
- [13] Ferreiros N., Dresen S., Alonso R.M., Weinmann W., Validated Quantitation of Angiotensin II Receptor Antagonists (ARA-II) in Human Plasma by Liquid-Chromatography-Tandem Mass Spectrometry Using Minimum Sample Clean-Up and Investigation of Ion Suppression, *Therap Drug Monitor.*, 29(6) (2007) 824-834.
- [14] Gonzalez O., Alonso R.M., Ferreiros N., Weinmann W., Zimmermann R., Dresen S., Development of an LC-MS/MS Method for the Quantitation of 55 Compounds Prescribed

- in Combined Cardiovascular Therapy, *J Chromatogr B.*, 879 (2011) 243-252.
- [15] Qui X., Wang Z., Wang B., Zhan H., Pan X., Xu R., Simultaneous Determination of Irbesartan and Hydrochlorothiazide in Human Plasma by Ultra High Performance Liquid Chromatography Tandem Mass Spectrometry and its Application to the Bioequivalence Study, *J Chromatogr B.*, 957 (2014) 110-115.
- [16] Lu C.Y., Feng C.H., Quantitation of Irbesartan and Major Proteins in Human Plasma by Mass Spectrometry with Time-of-Flight Analyzer, *J Pharm Biomed Anal.*, 54(1) (2011) 100-105.
- [17] Bae S.K., Kim M.J., Shim E.J., Cho D.Y., Shon J.H., Liu K.H., Kim E.Y., Shin J.G., HPLC Determination of Irbesartan in Human Plasma: its Application to Pharmacokinetic Studies, *Biomed Chromatogr.*, 23(6) (2009) 568-572.
- [18] Rao R.N., Bompelli S., Maurya P.K., High-Performance Liquid Chromatographic Determination of Anti-Hypertensive Drugs on Dried Blood Spots Using a Fluorescence Detector-Method Development and Validation, *Biomed Chromatogr.*, 25(11) (2011) 1252-1259.
- [19] Ferreirós N., Iriarte G., Alons R.M., Jiménez R.M., Development of a Solid Phase Extraction Procedure for HPLC-DAD Determination of Several Angiotensin II Receptor Antagonists in Human Urine using Mixture Design, *Talanta*, 73(4) (2007) 748-756.
- [20] Hafez H.M., Elshanawane A.A., Abdelaziz L.M., Kamal M.M. Quantitative Determination of Three Angiotensin-II-Receptor Antagonists in Presence of Hydrochlorothiazide by RP-HPLC in their tablet preparations, *Iranian J Pharm Res.*, 12 (2013) 635-643.
- [21] Shakya A.K., Al-Hiari Y.M., Alhamami O.M.O., Liquid Chromatographic Determination of Irbesartan in Human Plasma, *J Chromatogr B.*, 848(2) (2007) 245-50.
- [22] Koyuturk S., Can N.O., Atkosar Z., Arli G., A Novel Dilute and Shoot HPLC Assay Method for Quantification of Irbesartan and Hydrochlorothiazide in Combination Tablets and Urine using Second Generation C<sub>18</sub> Bonded Monolithic Silica Column with Double Gradient Elution, *J Pharm Biomed Anal.*, 97 (2014) 103-110.
- [23] Vagamani M., Sahoo S.K., Kavitha D., Vagyalaxmi C.H., Mahapatra L., Validated RPHPLC Method for Simultaneous Estimation of Irbesartan and Hydrochlorothiazide in Tablet Dosage Form. *Int J Pharm Res and Health Sci.*, 5 (2017) 1419-23.
- [24] Rao K.T., Rao L.V., Kandepi K.M., Rapid Stability-indicating RRLC Method for Simultaneous Estimation of Irbesartan and its Related Impurities. *Indian J Pharm Sci.*, 78 (2016) 252-58.
- [25] Kissenger P.T., Heineman W.R., (Eds.), Laboratory Techniques in Electroanalytical Chemistry, 2nd Ed., Marcel Dekker, New York, (1996).
- [26] The United States Pharmacopoeia, Thirtieth Revision, and The National Formulary, 25th ed., Rockville, USA, (2007) 1802-1805.
- [27] The European Agency for the Evaluation of Medicinal Products. ICH Topic Q2B Note for Guideline on Validation of Analytical Procedures: Methodology GPMP/ICH/281/95 (1996).
- [28] El-Hefnawey G.B., El-Hallag I.S., Ghoneim E.M., Ghoneim M.M., Voltammetric Behavior and Quantification of the Sedative-Hypnotic Drug Chlordiazepoxide in Bulk Form, Pharmaceutical Formulation and Human Serum at a Mercury Electrode, *J Pharm Biomed Anal.*, 34 (2004) 75-86.
- [29] Corti P., Corbini G., Gratter P., Furlanetto S., Pinzauti S., Determination of Some Quinolones in Tablets, Human Plasma and Urine by Differential-Pulse Polarography, *International J Pharm.*, 111 (1994) 83-87.
- [30] British Pharmacopoeia, The Stationary Office, London, (2003).

## Precise Demonstration of Salt-Stress Induced Antifungal Activity of *Origanum onites* Essential Oil and *Taraxacum officinale* Extract Against Drug Resistant Isolates of *Candida albicans* and *Aspergillus fumigatus* Using Micro-Colony Method

Esra Seyran<sup>1,a,\*</sup><sup>1</sup> Department of Molecular Biology and Genetics, Faculty of Science, Sivas Cumhuriyet University, Sivas, Türkiye

\*Corresponding author

### Research Article

#### History

Received: 25/06/2024

Accepted: 02/04/2025



This article is licensed under a Creative Commons Attribution-NonCommercial 4.0 International License (CC BY-NC 4.0)

### ABSTRACT

The rise of drug-resistant fungal pathogens has intensified the need for novel antifungal agents. Plants are a significant source, although effective concentrations in extracts are often low. Accurate *in vitro* assays are essential for validating these compounds. This study uses the micro-colony method, measuring hyphal growth and cell diameter under a microscope with digital imaging, to assess antifungal activity quickly and precisely. We evaluated *Origanum onites* essential oil and *Taraxacum officinale* methanol extract against drug-resistant *Candida albicans* and *Aspergillus fumigatus* strains. Yeast cell pigmentation was also assessed using image processing tools. To enhance compound penetration, mono and divalent salts (100mM KCl, NaCl, CaCl<sub>2</sub>) were added to the media. In salt-free media, *Origanum onites* essential oil inhibited *Candida albicans* (MIC: 0.3 µl/ml; MFC: 0.03 µl/ml) and *Aspergillus fumigatus* (MIC: 0.15 µl/ml; MFC: 0.03 µl/ml), while *Taraxacum officinale* extract was ineffective. Salt stress increased *Origanum onites* activity against *Aspergillus fumigatus* (MIC: 0.075 µl/ml) but had minimal impact on *Candida albicans*. Salt stress enabled *Taraxacum officinale* extract to inhibit *Candida albicans* (EC<sub>50</sub>: 12.71 µg/ml) and reduced its pigmentation dose-dependently without affecting toxicity against *Aspergillus fumigatus*. These results demonstrate that the micro-colony assay effectively evaluates plant-derived antifungal compounds and detects subtle dose-response variations in pathogenic fungi.

**Keywords:** Antifungal drug resistance, Micro-colony method, Plant metabolites, Salt stress<sup>a</sup> [esraseyran@cumhuriyet.edu.tr](mailto:esraseyran@cumhuriyet.edu.tr)  <https://orcid.org/0000-0002-0384-4300>

## Introduction

Certain mold (e.g., *Aspergillus fumigatus* Fresenius) and yeast fungi (e.g., *Candida albicans* (C.P. Robin Berkhout) infect human tissues, causing fungal diseases (mycoses) such as aspergillosis and candidiasis, which can be fatal in some cases [1]. Synthetic antifungal drugs (azoles, echinocandins, and polyenes) are the main treatment options for mycoses [1-3]. However, fungal pathogens develop resistance to antifungal drugs through various mechanisms, including efflux proteins (ATP-binding cassette transporters and major facilitators), reduced drug penetration (selective permeability and excessive pigmentation), and modification of the drug target (point mutations hindering fungicide binding and increased transcription of the target site) [2,3].

Plants accumulate a plethora of antifungal compounds, such as alkaloids, flavonoids, and isoprenoids, with different cellular targets, including cell wall formation and protein biosynthesis [4,5]. Therefore, plants, especially endemic species, are invaluable reservoirs of novel antifungal drugs to combat resistant fungal pathogens. The European Pharmacopoeia and National Committee for Clinical Laboratory Standards (NCCLS) guidelines dictate the use of sensitive reference microorganism strains to validate prospective antimicrobial agents [6]. Given the rise of resistance,

screening potent antifungal compounds on resistant isolates is a wise strategy.

Appropriate and precise *in vitro* assays are essential for validating effective antifungal compounds. Diffusion and turbidimetric methods are two main microbiological assays of antibiotics outlined by the European Pharmacopoeia [6]. These methods have been utilized under various terminologies, such as disc diffusion halo, colony radial growth, paper disc diffusion assays, and microdilution techniques like the minimum inhibitory concentration assay outlined by NCCLS (2004) [7-9].

Previously, the micro-colony assay, which involves measuring the hyphal growth of the germinated conidium during the early incubation period using microscopy and a digital microscope camera, was developed to screen resistance to azole fungicides and dose responses to alternative oxidase inhibitors in slow-growing plant pathogens, such as the filamentous fungi *Fusicladium effusum* G. Winter and *Cercospora arachidicola* Hori [10-13]. The micro-colony method requires shorter incubation periods to validate antifungal compounds compared to other assays. Additionally, it is compatible with definitive data analysis methods, such as normal distribution tests, regression analysis, and analysis of variance tests. Data perception is based on the average growth of the



population at each concentration, which is not possible with other methods [10-12].

Hypothetically, high osmotic pressure could accelerate the influx of low molecular mass substances into fungal cells [14]. For instance, salt stress in the fungal organism *Zygosaccharomyces rouxii* (Boutroux) Yarrow induced several physiological alterations and increased nystatin toxicity [14]. In the gram-positive bacterium *Corynebacterium glutamicum*, 1.5 M NaCl-mediated osmotic pressure induced the uptake of the osmoprotectant glycine betaine, but choline uptake remained unchanged [15]. In *Escherichia coli* (Migula) Castellani and Chalmers bacteria, 0.3 M NaCl increased the cellular uptake of organic compounds containing humic substances [16]. In the oomycete *Pythium porphyrae* Takahashi and Sasaki, KCl and  $MgCl_2$  increased the membrane permeability of an anti-*Pythium* protein [17].

This study aimed to: i) validate the micro-colony assay to screen the antifungal potential of *Origanum vulgare* L. (Lamiaceae) essential oil and the endemic species *Taraxacum officinale* methanol extract against a fluconazole-resistant strain of *Candida albicans* ATCC 10231 and a drug-resistant clinical isolate of *Aspergillus fumigatus* [18]; ii) evaluate the role of salt stress during *in vitro* testing, as low molecular mass antifungal compounds might be underscored due to lack of internal penetration, and salt-mediated osmotic pressure could be used to increase the cellular penetration of substances in the plant extract; and iii) assess the pigmentation of *Candida albicans* yeast cells with images captured for the micro-colony assay.

## Material and Methods

### Plant Material

Oregano plants were purchased from a local market in Izmir, Turkey. In Western Anatolia, a common type of oregano plant is *Origanum onites* L., also known as Cretan oregano or Turkish oregano. This variety is well-known for its potent essential oils and is widely cultivated and used in the region.

### Preparation of *Origanum onites* Essential Oil

Steam distillation was performed according to the "Determination of Essential Oils in Herbal Drugs" protocol in the European Pharmacopoeia (EDQM, 2010). A total of 68.0 g of *Origanum onites* dried flowers and leaves were placed in a 2000 mL round-bottom flask with 800 mL of distilled water (EDQM, 2010). The distillation was conducted without xylene for 6 hours using a Clevenger apparatus (İldam, NS 7/5, Ankara, Turkey) and a single electric stove at 1500 W maximum power (Arçelik, Bolu, Turkey) (EDQM, 2010). The water-free *Origanum onites* essential oil was recovered using anhydrous sodium sulphate (Merck, Darmstadt, Germany) and stored at 4.0 °C in a glass container.

### Preparation of Methanolic Extracts

*Taraxacum officinale* plant material (leaves and stems) was collected in the Spring of 2024 from the rural areas surrounding the Sivas Province, Anatolia, Turkey. The collected plant material was dried at room temperature for two weeks. The dried material was then ground into a fine powder using a mechanical grinder. For the extraction process, 50 g of the powdered plant material was soaked in 500 mL of methanol (analytical grade) in a conical flask. The mixture was left to macerate at room temperature for 72 hours with occasional shaking to ensure thorough extraction of the phytochemicals. After the maceration period, the mixture was filtered using Whatman No. 1 filter paper to remove the plant residues. The filtrate was then concentrated under reduced pressure at 40°C using a rotary evaporator (Heidolph Instruments, Schwabach, Germany) to remove the methanol, yielding a semi-solid crude methanolic extract. The extract was further dried in a desiccator over anhydrous calcium chloride to obtain a constant weight. The resulting methanolic extract was stored in an airtight container at 4°C until further use.

### Micro-colony Assay

The experiments were performed in triplicate, and more than three doses were used for each substance to achieve a geometric dose-response progression (EDQM, 2010). *Origanum vulgare* essential oil was serially diluted in DMSO to reach concentrations of 0.3, 0.15, 0.1, 0.075, and 0.03 µl/ml in the media. *Taraxacum officinale* extract was serially diluted in DMSO to reach concentrations of 3.0, 1.5, 1.0, and 0.3 µg/ml in the media. *Origanum onites* essential oil is soluble in 1% DMSO, which is adequate for preparing serial dilutions for biological assays. A concentrated stock solution was prepared by dissolving 10 µL of the essential oil in 990 µL of 1% DMSO, resulting in a 1% (v/v) stock solution. To achieve serial dilutions, 500 µL of the 1% stock solution was added to 500 µL of 1% DMSO to make a 0.5% solution. This process was repeated to achieve concentrations of 0.25%, 0.125%, 0.0625%, and 0.03125%. The final working concentrations in the media were obtained by adding the appropriate volume of each diluted solution to the growth medium to reach the desired concentrations of 0.3, 0.15, 0.1, 0.075, and 0.03 µL/mL. Each concentration of the essential oil solution was thoroughly mixed with the growth medium using a magnetic stirrer for approximately 30 seconds to ensure even distribution of the essential oil in the medium. By using 1% DMSO as the solvent, the solubility of the essential oil was maintained, and the serial dilution process ensured accurate and reproducible concentrations for the antifungal assays. In a previous experiment, the azole fungicide fluconazole failed to inhibit resistant strains of *Aspergillus fumigatus* and *Candida albicans* [19]. Azole fungicides bind to key enzymes lanosterol 14 $\alpha$ -demethylase and C5-sterol desaturase, leading to the inhibition of ergosterol biosynthesis [3]. Therefore, another standard fungicide, thiabendazole, with a different mode of action, was used as a reference inhibitor. The microtubule inhibitor thiabendazole (Sigma-Aldrich, Taufkirchen, Germany) was

serially diluted in acetone to reach concentrations of 100, 10, 1.0, and 0.1 µg/ml in the medium [20].

The growth medium for the *Aspergillus fumigatus* testing was Potato Dextrose Agar (PDA) at 40 g/L (Merck, Darmstadt, Germany). The growth medium for the *Candida albicans* testing was Sabouraud Dextrose Agar (SDA) at 40 g/L (Merck, Darmstadt, Germany). The control plates were amended only with DMSO or acetone. Additionally, another group of control plates was prepared without the addition of DMSO to screen for the toxic effects of the solvent. The content of DMSO was less than 1% in all concentrations [21].

For each concentration and control, salt-amended "medium b" was prepared. In *Saccharomyces cerevisiae* Meyen ex E.C. Hansen, 100mM KCl, NaCl, and CaCl<sub>2</sub> in the medium reduced resting membrane potential and altered amiodarone toxicity [22]. To achieve osmotic pressure, 100mM concentrations of KCl, NaCl, and CaCl<sub>2</sub> were added to the media before sterilization. The autoclaved media were kept in a water bath set to 60°C throughout the experiment to prevent solidification and maintain consistent viscosity. For each concentration of *Origanum onites* essential oil, *Taraxacum officinale* extract, and thiabendazole fungicide, a separate flask with a magnetic stirrer bar was used to ensure precision in substance concentration. After serial dilution, the substances were added to the flasks and mixed with a magnetic stirrer for approximately 30 seconds to achieve thorough dispersal in the media. After mixing, 4 ml of the media was immediately introduced onto Petri plates (90x17 mm, glass) using a 5 ml capacity pipette. The plates were stored on a shelf until the medium solidified.

*Candida albicans* cells and *Aspergillus fumigatus* conidia were suspended and washed with sterile distilled water. The number of conidia and yeast cells to be inoculated on each plate was estimated using a haemocytometer (Bürker-Türk, Wertheim, Germany) to obtain final inoculums of 3 x 10<sup>6</sup> *Aspergillus fumigatus* conidia and 1 x 10<sup>5</sup> *Candida albicans* yeast cells. The *Aspergillus fumigatus* conidia and *Candida albicans* cells were introduced and spread on Petri plates with a glass rod and incubated at 27°C and 37°C for 16 and 12 hours, respectively. After the incubation period, the plates were kept at 4°C in a cold storage room. Plates were measured as separate stocks to prevent activation and further growth during the measurement process.

Images of the micro-colonies at 40X magnification were captured with Olympus Soft Imaging Solutions software under the compound microscope Olympus CX31 using model Lc 20 Micro digital microscope camera (Olympus Corp., Tokyo, Japan). The micro-colonies were measured with the Motic Images Plus 2.0 software (Motic Inc., Xiamen, China). If the fungal colonies' growth exceeded the range of the focus area, half of the diameter was measured and multiplied by two, as seen in the control plate of Figure 10.

Relative inhibition in radial growth was obtained using the equation for each concentration using the formula;  $\phi$  = micro-colony measurement on plant extract, essential oil or fungicide,  $\omega$  = micro-colony measurement on control,  $\varepsilon$  = relative inhibition in fungal growth;

$$\varepsilon = 1 - \left( \frac{\sum_{i=1}^n (\log \phi_i) / n \phi}{\sum_{i=1}^n (\log \omega_i) / n \omega} \right)$$

### Pigmentation Assay

The pigmentation of the *Candida albicans* micro-colonies was analyzed using Microsoft Paint Version 6.0 (Build 6002, Service Pack 2.0). Images captured for the micro-colony assay were opened in the Paint program. A single location on a micro-colony was selected using the "Pick Color" tool. Subsequently, the "Red, Green, and Blue" values were identified using the "Edit Colors" and "Define Custom Colors" tools.

Relative inhibition in pigmentation was obtained using the equation for each concentration using the formula;  $\beta$  = pigmentation value on plant extract, essential oil or fungicide,  $\alpha$  = pigmentation value on control, and  $\sigma$  = relative inhibition in pigmentation;

$$\sigma = \left[ \left( \frac{\sum_{i=1}^n (\log (\text{red} + \text{blue} + \text{green}) \beta_i) / n \beta}{\sum_{i=1}^n (\log (\text{red} + \text{blue} + \text{green}) \alpha_i) / n \alpha} \right) * 100 \right] - 100$$

### Data Analysis

For each concentration, fungal development was validated based on the measurement of approximately 10 distinct micro-colonies. Instead of arithmetic values, log10-transformed values of each micro-colony were used to increase the precision of growth estimation. These measurements were estimated as the growth values of the sub-population at each concentration. The normality of the population at each testing concentration was verified using the Shapiro-Wilk validity test at a significance level of P = 0.05. Additionally, differences in fungal development and pigmentation based on dose-response among the different replicates and treatments were verified with a one-way analysis of variance (ANOVA) test at a significance level of P = 0.05. However, for regression analysis and dose-response curves, the data set from one replicate was used to represent the growth or pigmentation value at each concentration. To demonstrate the influence of salt stress on radial growth and pigmentation, data sets from one replicate of salt-free and salt-amended media were compared and verified using a one-way ANOVA test at a significance level of P = 0.05. The range in growth values, minimum inhibitory concentration (MIC), i.e., the concentration that inhibits fungal development, and minimum fungicidal concentration (MFC), i.e., the concentration that reduces fungal development, were estimated (NCCLS). The fit of the dose-response curve was evaluated with linear regression analysis (critical value = 0.80). The effective concentration (EC50) that inhibits 50% of the fungal growth was estimated with the linear regression equation. Data analysis was conducted using the PAST version 2.12 software [23].

## Results

### Evaluation of Antifungal Activity of *Origanum onites* Essential Oil on *Candida albicans* Using Micro-Colony Method

In salt-free media, *Origanum onites* essential oil was toxic to *Candida albicans* in a dose-dependent manner (Figure 1). The MIC value was evaluated as 0.3 µl/ml, and the MFC was evaluated as 0.03 µl/ml (Table 1 and Figure 2). The population growth estimations in all concentrations, except for the observation at a concentration of 0.75 µl/ml, showed a log-normal

distribution (Table 1). The growth estimations of three replicates had similar mean values, except for the observation at 0.1  $\mu\text{l/ml}$  (Table 1). Salt stress altered the estimated growth of the population at all testing concentrations (Table 1 and Figure 2). In salt-amended medium (medium b), the population growth estimations at all concentrations showed a log-normal distribution (Table 1). The growth estimations of three replicates in salt-amended medium had different mean values (Table 1). However, based on relative inhibition profiling, salt

stress did not alter the MIC value, which remained at 0.3  $\mu\text{l/ml}$ . Based on linear regression validation, the relative inhibition versus concentration values fit the linear regression models for both salt-free medium ( $R^2 = 0.9175$ ) and medium b ( $R^2 = 0.8556$ ) (Figure 3). The EC50 values estimated for the salt-free medium, using the regression model equation ( $y = 371.36x - 20.026$ ), and for medium b ( $y = 344.33x - 13.82$ ) were 0.188566  $\mu\text{l/ml}$  and 0.185345  $\mu\text{l/ml}$ , respectively (Figure 3).

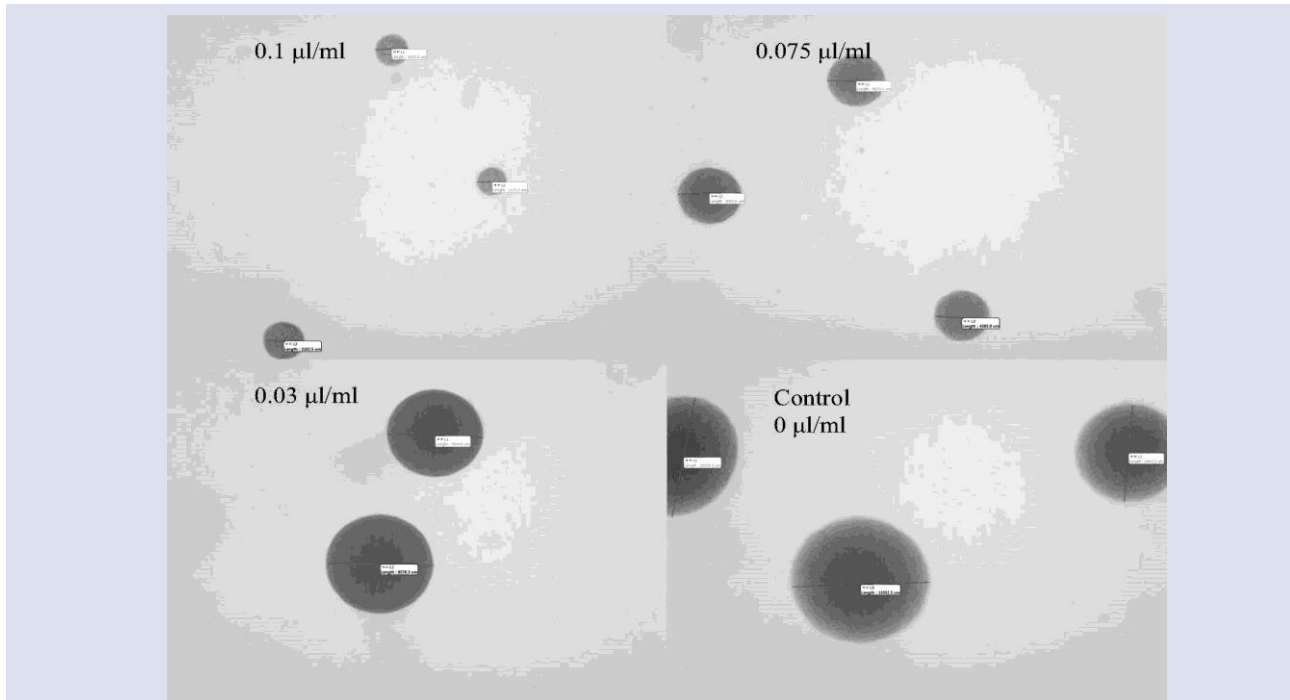


Figure 1. After 12 hours of incubation, in salt-free medium *Origanum onites* essential oil is reducing the diameter of *Candida albicans* micro-colonies in a dose-dependent, measured at 40X magnification.

Table 1. Influence of *Origanum onites* essential oil on the fungal development of *Candida albicans* using micro-colony method

Concentration ( $\mu\text{l/ml}$ )	Mean <sup>c</sup>	Range <sup>e</sup>	Shapiro-Wilk W <sup>f</sup>	F-value <sup>g</sup>	F-value <sup>h</sup>
0.3	0	0	N/A	N/A	N/A
0.15	2.38776	2.580241- 2.114611	0.9313 <sub>(n=13)</sub>	2.127 <sub>(2,23)</sub>	5.255 <sub>(1,23)</sub> <sup>a,d</sup>
0.1	2.52171	2.646011-2.427486	0.9429 <sub>(n=8)</sub>	13.69 <sub>(2,23)</sub> <sup>a,d</sup>	72.26 <sub>(1,23)</sub> <sup>a,d</sup>
0.075	2.635704	2.711807-2.521792	0.8258 <sub>a(n=10)</sub>	1.786 <sub>(2,31)</sub>	11.58 <sub>(1,18)</sub> <sup>a,d</sup>
0.03	2.836544	3.031408-2.547159	0.9287 <sub>(n=8)</sub>	0.5238 <sub>(2,27)</sub>	15.87 <sub>(1,24)</sub> <sup>a,d</sup>
0	2.908963	3.214287-2.672375	0.9709 <sub>(n=10)</sub>	0.2291 <sub>(2,25)</sub>	0.05205 <sub>(1,19)</sub>
0.3 <sup>b</sup>	0	0	N/A	N/A	
0.15 <sup>b</sup>	2.498476	2.635986-2.371068	0.9625 <sub>(n=12)</sub>	6.689 <sub>(2, 24)</sub> <sup>a,d</sup>	
0.1 <sup>b</sup>	2.267903	2.37328-2.070407	0.8503 <sub>(n=4)</sub>	5.433 <sub>(1, 9)</sub> <sup>a,d</sup>	
0.075 <sup>b</sup>	2.454632	2.559428-2.410777	0.834 <sub>(n=8)</sub>	14.9 <sub>(2, 17)</sub> <sup>a,d</sup>	
0.03 <sup>b</sup>	2.643603	2.899054-2.435526	0.9399 <sub>(n=11)</sub>	6.955 <sub>(2, 25)</sub> <sup>a,d</sup>	
0 <sup>b</sup>	2.871262	3.077622-2.602277	0.9349 <sub>(n=11)</sub>	0.06331 <sub>(2, 25)</sub>	

<sup>a</sup>  $p$  value less than 0.05 significant difference

<sup>b</sup> Medium b contains 100mM of KCl, NaCl, and CaCl<sub>2</sub>

<sup>c</sup> Mean of the Log<sub>10</sub> transformed growth values for the first replicate

<sup>d</sup> F value bigger than F value at the 0.05 significance level of the degrees of the freedom for one-way ANOVA test results

<sup>e</sup> Mean of the Log<sub>10</sub> transformed growth values for the first replicate

<sup>f</sup> Validation of the log normal distribution of the population with the Shapiro-Wilk W assay for the first

<sup>g</sup> Validation of the similarity of the log<sub>10</sub> transformed growth values of three replicates using one-way ANOVA test

<sup>h</sup> Validation of the similarity of the log<sub>10</sub> transformed growth values on salt amended and salt free medium using one-way ANOVA test

N/A; not available

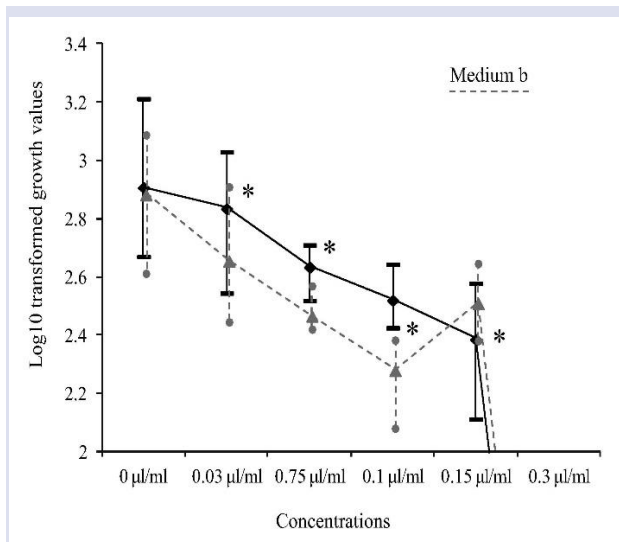


Figure 2. Dose response curve of *Candida albicans* based on the log<sub>10</sub> transformed growth values versus the different concentrations of *Origanum onites* essential oil in salt-free (medium a) and salt-amended (medium b) media. \* Sign represents the significant differences between two treatments at the corresponding concentration using one-way ANOVA.

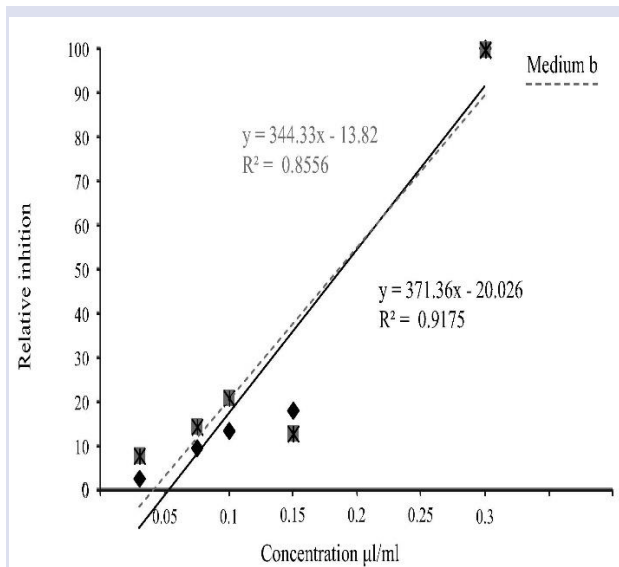


Figure 3. The linear regression models of *Candida albicans* based on the relative inhibition versus the different concentrations of *Origanum onites* essential oil in salt-free (medium a) and salt-amended (medium b) media.

### Evaluation of Antifungal Activity of *Taraxacum officinale* Extract on *Candida albicans* Using Micro-Colony Method

In salt-free medium, *Taraxacum officinale* methanol extract was not toxic to *Candida albicans* in a dose-dependent manner (Figure 4). The lethal concentration of

*Taraxacum officinale* extract was not within the testing concentration range (Table 2); therefore, the MIC value was not determined. The population growth estimations in all concentrations showed a log-normal distribution (Table 2). The growth estimations of three replicates had different mean values at all concentrations (Table 2).

In salt-amended medium, *Taraxacum officinale* extract showed toxicity at the high concentrations of 3 µg/ml and 1.5 µg/ml (Figures 4, 5, and Table 2). Salt stress altered the estimated growth of the population at these high concentrations. In salt-amended medium, the population growth estimations at all concentrations showed a log-normal distribution (Table 2). The growth estimations of three replicates in salt-amended medium had similar mean values at all concentrations (Table 2). Therefore, salt stress increased the toxicity of *Taraxacum officinale* extract and significantly reduced the variability in the response of the *Candida albicans* subpopulation (Table 2). Based on linear regression validation, in salt-free medium, the relative inhibition versus concentration values did not fit the linear regression model ( $R^2 = 0.0765$ ) (Figure 6). Conversely, in salt-amended medium, the relative inhibition versus concentration values fit the linear regression model ( $R^2 = 0.939$ ) (Figure 6). The EC<sub>50</sub> value estimated with the regression model equation ( $y = 3.828x + 1.3298$ ) was 12.71426 µg/ml.

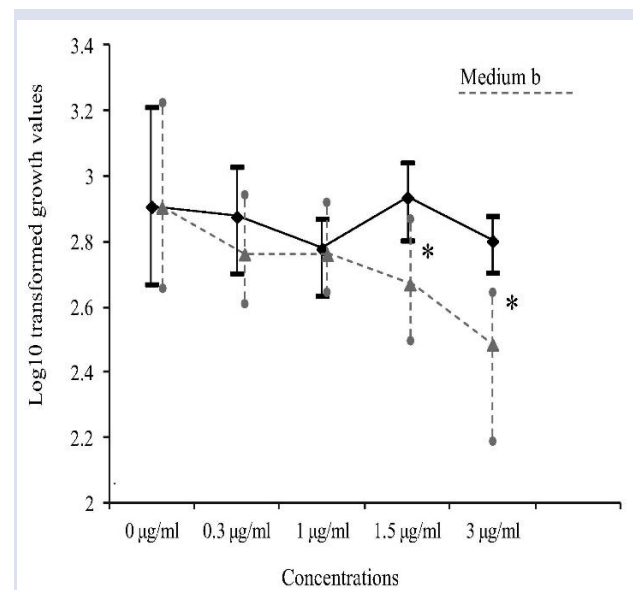


Figure 4. Dose response curve of *Candida albicans* based on the log<sub>10</sub> transformed growth values versus the different concentrations of *Taraxacum officinale* extract in salt-free (medium a) and salt-amended (medium b) media. \* Sign represents the significant differences between two treatments at the corresponding concentration using one-way ANOVA

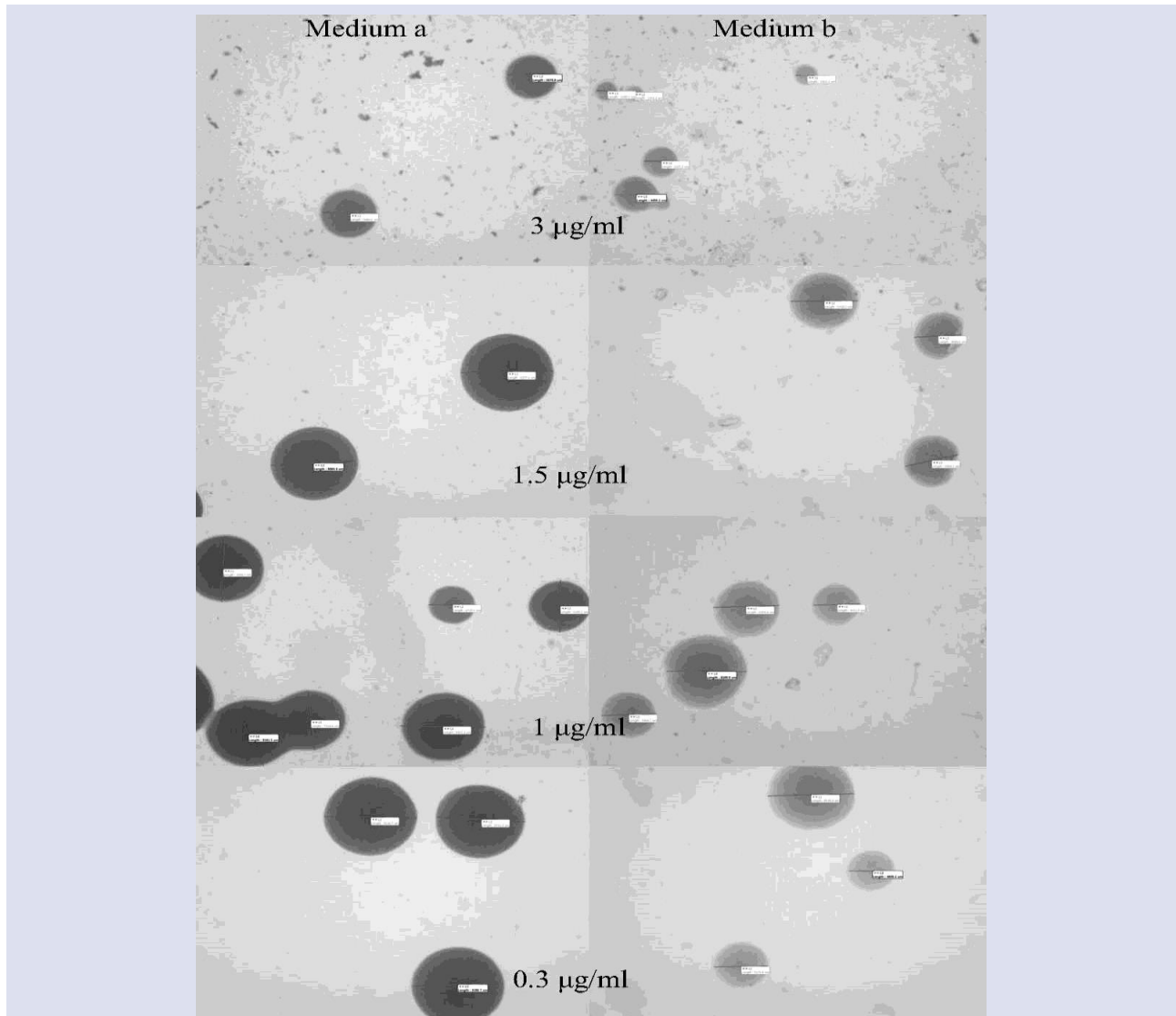


Table 2. Influence of *Taraxacum officinale* extract on the fungal development of *Candida albicans* using micro-colony method

Concentration ( $\mu\text{g/ml}$ )	Mean <sup>c</sup>	Range <sup>e</sup>	Shapiro-Wilk W <sup>f</sup>	F-value <sup>g</sup>	F-value <sup>h</sup>
3.0	2.803592	2.880814-2.70774	0.8311 <sub>(n=8)</sub>	6.408 <sub>(2,18)</sub> <sup>a,d</sup>	38.5 <sub>(1,16)</sub> <sup>a,d</sup>
1.5	2.936823	3.044344-2.806248	0.969 <sub>(n=8)</sub>	3.78 <sub>(2,23)</sub> <sup>a,d</sup>	67.71 <sub>(1,17)</sub> <sup>a,d</sup>
1.0	2.779769	2.872215-2.636789	0.904 <sub>(n=11)</sub>	3.492 <sub>(2,25)</sub> <sup>a,d</sup>	3,661 <sub>(1,17)</sub>
0.3	2.877884	3.031408-2.705864	0.9241 <sub>(n=7)</sub>	5.77 <sub>(2,19)</sub> <sup>a,d</sup>	0.007084 <sub>(1,19)</sub>
0	2.908963	3.214287-2.672375	0.9709 <sub>(n=10)</sub>	0.2291 <sub>(2,25)</sub>	0.05205 <sub>(1,19)</sub>
3.0 <sup>b</sup>	2.489879	2.631139-2.200577	0.8856 <sub>(n=10)</sub>	0.003273 <sub>(2,19)</sub>	
1.5 <sup>b</sup>	2.674407	2.854367-2.511883	0.9519 <sub>(n=10)</sub>	2.635 <sub>(2,20)</sub>	
1.0 <sup>b</sup>	2.764484	2.908485-2.658202	0.966 <sub>(n=7)</sub>	2.784 <sub>(2,18)</sub>	
0.3 <sup>b</sup>	2.76606	2.930898-2.620656	0.9431 <sub>(n=12)</sub>	0.3313 <sub>(2,25)</sub>	
0 <sup>b</sup>	2.871262	3.077622-2.602277	0.9349 <sub>(n=11)</sub>	0.06331 <sub>(2, 25)</sub>	

<sup>a</sup> *p* value less than 0.05 significant difference<sup>b</sup> Medium b contains 100mM of KCl, NaCl, and CaCl<sub>2</sub><sup>c</sup> Mean of the Log<sub>10</sub> transformed growth values for the first replicate<sup>d</sup> F value bigger than F value at the 0.05 significance level of the degrees of the freedom for one-way ANOVA test results<sup>e</sup> Mean of the Log<sub>10</sub> transformed growth values for the first replicate<sup>f</sup> Validation of the log normal distribution of the population with the Shapiro-Wilk W assay for the first<sup>g</sup> Validation of the similarity of the log<sub>10</sub> transformed growth values of three replicates using one-way ANOVA test<sup>h</sup> Validation of the similarity of the log<sub>10</sub> transformed growth values on salt amended and salt free medium using one-way ANOVA test

N/A; not available

Figure 5. After 12 hours of incubation, in salt-amended medium high concentrations (3  $\mu\text{g/ml}$  and 1.5  $\mu\text{g/ml}$ ) *Taraxacum officinale* extract is reducing the diameter and the pigmentation of *Candida albicans* micro-colonies measured at 40X magnification



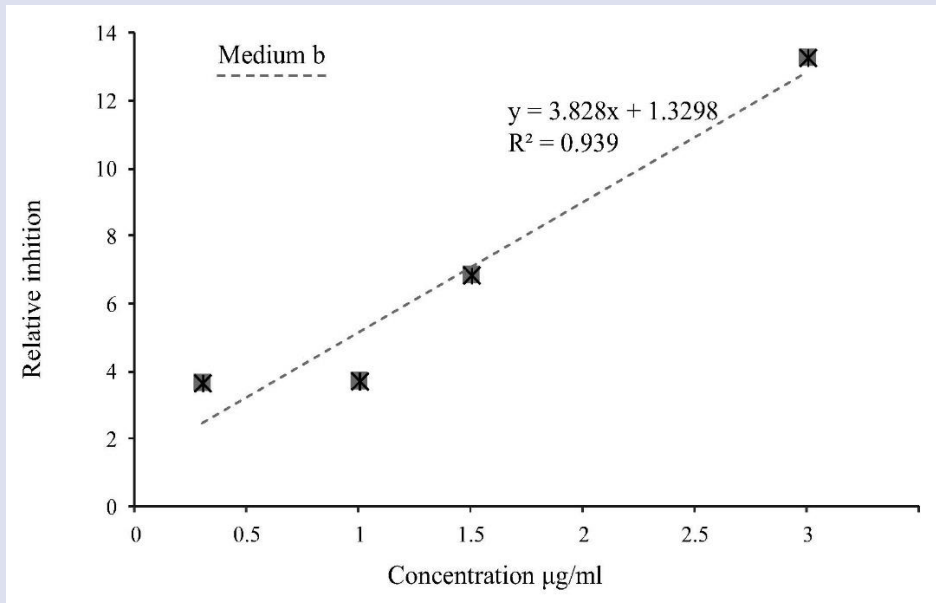


Figure 6. The linear regression model of *Candida albicans* based on the relative inhibition of the fungal growth versus the different concentrations on *Origanum onites* essential oil on salt-amended medium (medium b)

#### Evaluation of Pigmentation in *Candida albicans* in Response to *Origanum onites* Essential Oil

In salt-free medium, *Origanum onites* essential oil reduced the pigmentation of *Candida albicans* cells (Figure 7). The estimated pigmentation values at all testing concentrations showed a log-normal distribution (Table 3). The pigmentation of three replicates had similar mean values except at concentrations of 0.1 µl/ml and 0.075 µl/ml (Table 3). Salt stress altered the estimated pigmentation of the population at all testing concentrations except 0.075 µl/ml (Figure 7 and Table 3).

In salt-amended medium, the pigmentation of three replicates had similar mean values except at 0.15 µl/ml (Table 3). The relative inhibition in pigmentation versus concentration values fit the linear regression models in both salt-free ( $R^2 = 0.8616$ ) and salt-amended ( $R^2 = 0.8274$ ) media (Figure 8). The EC50 values estimated with the regression model equation for the salt-free ( $y = 393.05x - 30.121$ ) and salt-amended ( $y = 357.95x - 20.047$ ) media were 0.203844295 µl/ml and 0.195689342 µl/ml, respectively (Figure 8).

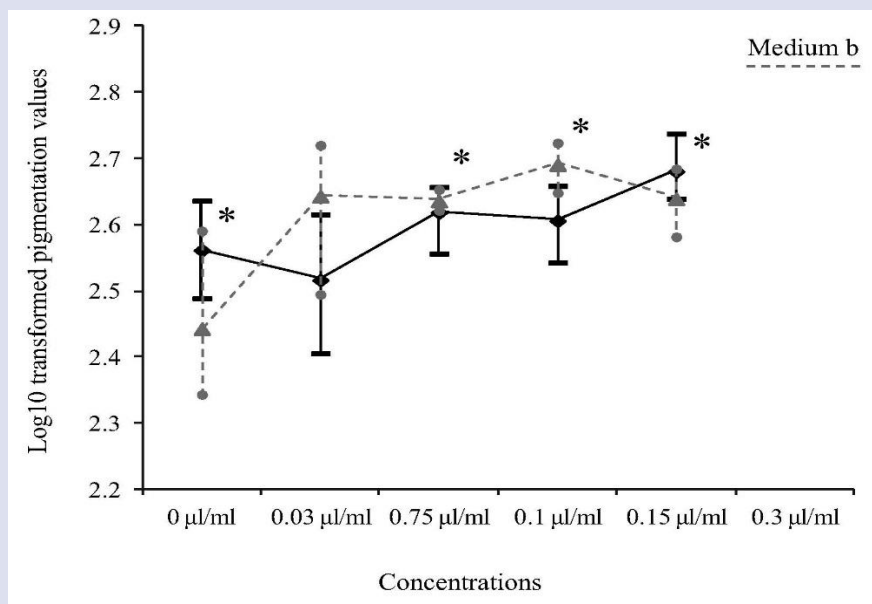


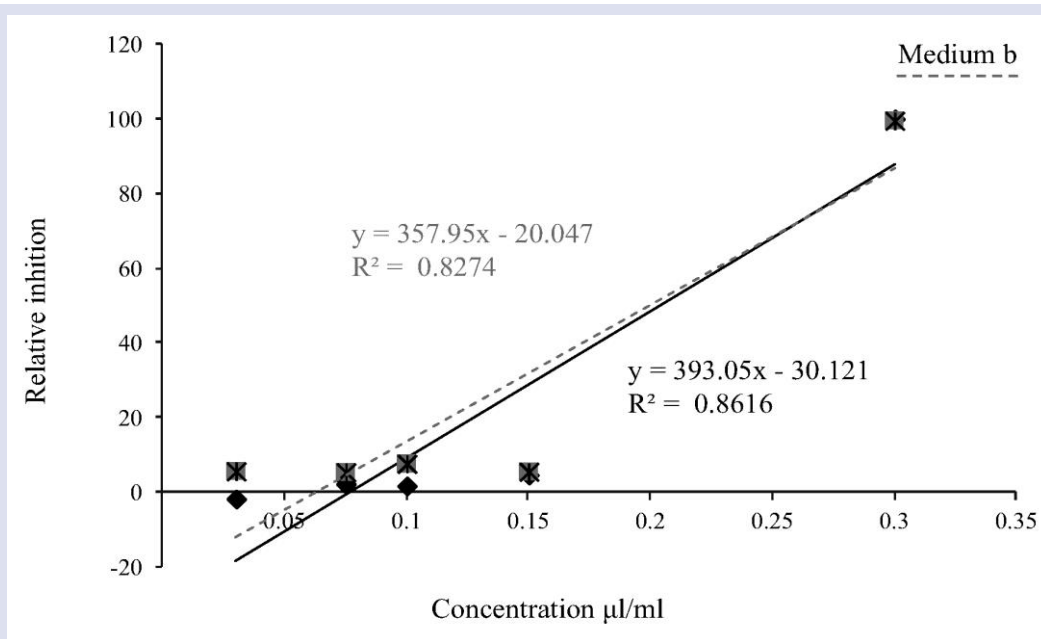
Figure 7. Dose response curve of *Candida albicans* based on the log10 transformed pigmentation values versus the different concentrations of *Origanum onites* essential oil in salt-free (medium a) and salt-amended (medium b) media. \* Sign represents the significant differences between two treatments at the corresponding concentration using one-way ANOVA

Table 3. Influence of *Origanum onites* essential oil on the pigmentation of *Candida albicans* using image processing

Concentration (µl/ml)	Mean <sup>c</sup>	Range <sup>e</sup>	Shapiro-Wilk W <sup>f</sup>	F-value <sup>g</sup>	F-value <sup>h</sup>
0.3	0	0	N/A	N/A	N/A
0.15	2.681604	2.738781-2.640481	0.9234 <sub>(n=13)</sub>	0.6505 <sub>(2,24)</sub>	7.828 <sub>(1,23)</sub> <sup>a,d</sup>
0.1	2.60703	2.659916-2.544068	0.9824 <sub>(n=8)</sub>	6.535 <sub>(2,23)</sub> <sup>a,d</sup>	29.51 <sub>(1,13)</sub> <sup>a,d</sup>
0.075	2.619661	2.658011-2.557507	0.9145 <sub>(n=10)</sub>	7.822 <sub>(2,30)</sub> <sup>a,d</sup>	2.791
0.03	2.517378	2.617000-2.40654	0.9589 <sub>(n=8)</sub>	0.07002 <sub>(1,13)</sub>	16.65 <sub>(1,17)</sub> <sup>a,d</sup>
0	2.562559	2.63749-2.489958	0.9638 <sub>(n=11)</sub>	57.59 <sub>(2,25)</sub> <sup>a,d</sup>	16.43 <sub>(1,19)</sub> <sup>a,d</sup>
0.3 <sup>b</sup>	0	0	N/A	N/A	
0.15 <sup>b</sup>	2.64394	2.689309-2.586587	0.9486 <sub>(n=12)</sub>	4.801 <sub>(2,24)</sub> <sup>a,d</sup>	
0.1 <sup>b</sup>	2.695653	2.728354-2.653213	0.9551 <sub>(n=7)</sub>	0.4435 <sub>(1,9)</sub>	
0.075 <sup>b</sup>	2.64086	2.658011-2.62634	0.9534 <sub>(n=6)</sub>	2.208 <sub>(1,17)</sub>	
0.03 <sup>b</sup>	2.64771	2.725095-2.499687	0.8801 <sub>(n=11)</sub>	2.816 <sub>(2,25)</sub>	
0 <sup>b</sup>	2.447628	2.595496-2.348305	0.9557 <sub>(n=11)</sub>	8.069 <sub>(2,25)</sub> <sup>a,d</sup>	

<sup>a</sup> p value less than 0.05 significant difference<sup>b</sup> Medium b contains 100mM of KCl, NaCl, and CaCl<sub>2</sub><sup>c</sup> Mean of the Log<sub>10</sub> transformed pigmentation values for the first replicate<sup>d</sup> F value bigger than F value at the 0.05 significance level of the degrees of the freedom for one-way ANOVA test results<sup>e</sup> Mean of the Log<sub>10</sub> transformed pigmentation values for the first replicate<sup>f</sup> Validation of the log normal distribution of the population with the Shapiro-Wilk W assay for the first<sup>g</sup> Validation of the similarity of the log<sub>10</sub> transformed pigmentation values of three replicates using one-way ANOVA test<sup>h</sup> Validation of the similarity of the log<sub>10</sub> transformed pigmentation values on salt amended and salt free medium using one-way ANOVA test

N/A; not available

Figure 8. The linear regression model of *Candida albicans* based on the relative inhibition of the fungal growth versus the different concentrations of *Origanum onites* essential oil on salt-free (medium a) and salt-amended (medium b) media

### Evaluation of Pigmentation in *Candida albicans* in Response to *Taraxacum officinale* Extract

In salt-free medium, only the highest tested concentration of *Taraxacum officinale* extract, 3.0 µg/ml, reduced the relative pigmentation of *Candida albicans* cells (Figure 5). The estimated pigmentation values at all testing concentrations showed a log-normal distribution (Table 4). The pigmentation of three replicates had similar mean values except at concentrations of 1.5 µg/ml and 1.0

µg/ml (Table 4). Salt stress altered the estimated pigmentation of the population at all testing concentrations (Table 4). In salt-amended medium, the pigmentation of three replicates had similar mean values (Table 4). However, the relative inhibition in pigmentation versus concentration values did not fit linear regression models in salt-free ( $R^2 = 0.1597$ ) and salt-amended ( $R^2 = 0.0782$ ) media.

Table 4. Influence of *Taraxacum officinale* extract on the pigmentation of *Candida albicans* using image processing

Concentration ( $\mu\text{g/ml}$ )	Mean <sup>c</sup>	Range <sup>e</sup>	Shapiro-Wilk W <sup>f</sup>	F-value <sup>g</sup>	F-value <sup>h</sup>
3.0	2.595216	2.641474-2.563481	0.9169 <sub>(n=8)</sub>	1.515 <sub>(2,18)</sub>	19.4 <sub>(1,16)</sub> <sup>a,d</sup>
1.5	2.474952	2.545307-2.428135	0.9421 <sub>(n=9)</sub>	7.466 <sub>(2,23)</sub> <sup>a,d</sup>	84.54 <sub>(1,17)</sub> <sup>a,d</sup>
1.0	2.560618	2.627366-2.465383	0.9488 <sub>(n=11)</sub>	5.785 <sub>(2,25)</sub> <sup>a,d</sup>	16.64 <sub>(1,17)</sub> <sup>a,d</sup>
0.3	2.543203	2.607455-2.481443	0.9948 <sub>(n=9)</sub>	2.937 <sub>(2,20)</sub>	81.92 <sub>(1,19)</sub> <sup>a,d</sup>
0	2.562559	2.63749-2.489958	0.9638 <sub>(n=11)</sub>	57.59 <sub>(2,25)</sub> <sup>a,d</sup>	16.43 <sub>(1,19)</sub> <sup>a,d</sup>
3.0 <sup>b</sup>	2.658418	2.70757-2.60206	0.9612 <sub>(n=10)</sub>	0.1574 <sub>(1,17)</sub>	
1.5 <sup>b</sup>	2.641549	2.710117-2.596597	0.8936 <sub>(n=10)</sub>	3.262 <sub>(2,20)</sub>	
1.0 <sup>b</sup>	2.64116	2.700704-2.604226	0.9248 <sub>(n=8)</sub>	2.683 <sub>(2,18)</sub>	
0.3 <sup>b</sup>	2.679605	2.720159-2.628389	0.9488 <sub>(n=12)</sub>	13.18 <sub>(2,25)</sub>	
0 <sup>b</sup>	2.447628	2.595496-2.348305	0.9557 <sub>(n=11)</sub>	8.069 <sub>(2,25)</sub> <sup>a,d</sup>	

<sup>a</sup> p value less than 0.05 significant difference<sup>b</sup> Medium b contains 100mM of KCl, NaCl, and CaCl<sub>2</sub><sup>c</sup> Mean of the Log<sub>10</sub> transformed pigmentation values for the first replicate<sup>d</sup> F value bigger than F value at the 0.05 significance level of the degrees of the freedom for one-way ANOVA test results<sup>e</sup> Mean of the Log<sub>10</sub> transformed pigmentation values for the first replicate<sup>f</sup> Validation of the log normal distribution of the population with the Shapiro-Wilk W assay for the first<sup>g</sup> Validation of the similarity of the log<sub>10</sub> transformed pigmentation values of three replicates using one-way ANOVA test<sup>h</sup> Validation of the similarity of the log<sub>10</sub> transformed pigmentation values on salt amended and salt free medium using one-way ANOVA test

N/A; not available

### Evaluation of Antifungal Activity of *Origanum onites* Essential Oil on *Aspergillus fumigatus* Using Micro-Colony Method

In salt-free media, *Origanum onites* essential oil was toxic to *Aspergillus fumigatus* in a dose-dependent manner (Figures 10 and 11). The MIC value was evaluated as 0.15  $\mu\text{l/ml}$ , and the MFC was evaluated as 0.03  $\mu\text{l/ml}$ . The population growth estimations in all testing concentrations showed a log-normal distribution (Table 5). The growth estimations of three replicates had different mean values except for the observation at 0.1  $\mu\text{l/ml}$  (Table 5). Salt stress drastically altered the toxicity

of *Origanum onites*, with the MIC value re-evaluated as 0.075  $\mu\text{l/ml}$  (Table 5). Salt stress affected the estimated growth of the population in all testing concentrations. The MFC concentration remained 0.03  $\mu\text{l/ml}$ , and based on a one-way ANOVA test, salt stress did not alter fungal growth at this concentration. Based on linear regression validation, in salt-free medium, the relative inhibition versus concentration values fit the linear regression model ( $R^2 = 0.9223$ ) (Figure 12). The EC<sub>50</sub> values estimated with the regression model equation ( $y = 781.24x - 26.688$ ) in salt-free medium was 0.098161896  $\mu\text{l/ml}$  (Figure 12).

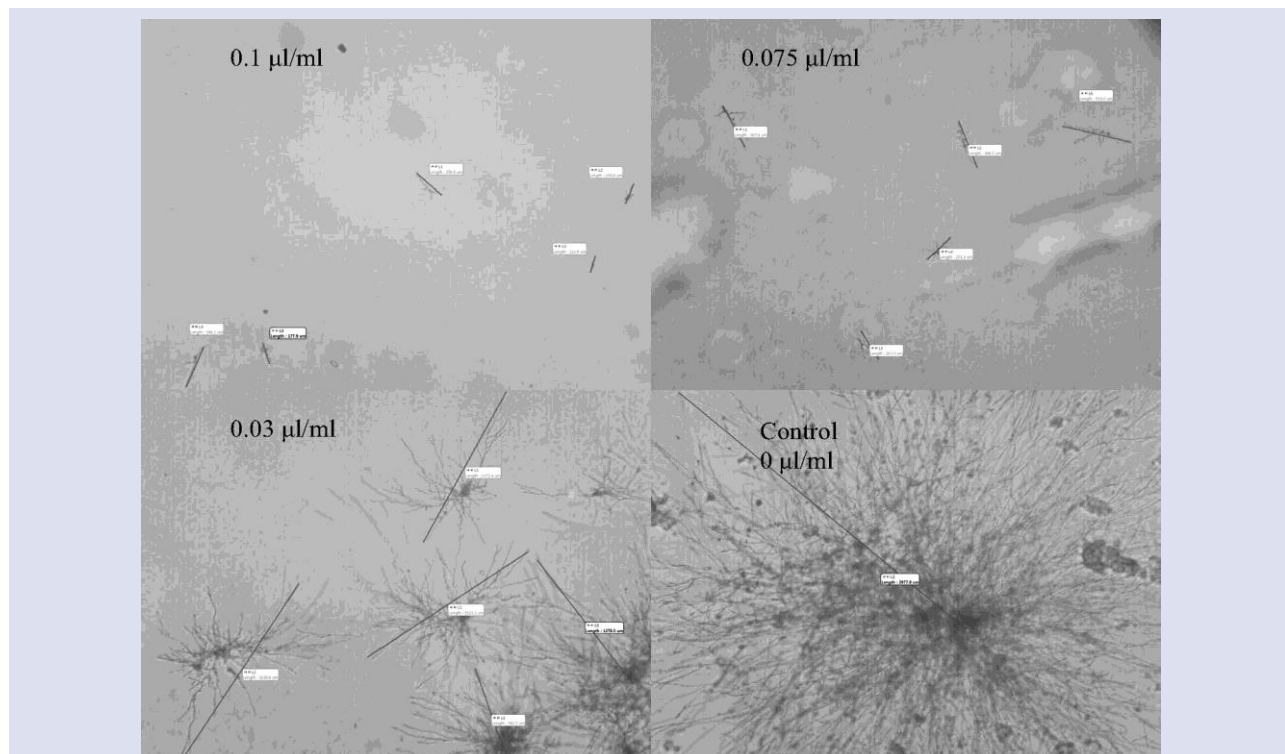


Figure 10. After 12 hours of incubation, in salt-free medium *Origanum onites* essential oil is reducing the diameter of *Aspergillus fumigatus* micro-colonies in a dose-dependent, measured at 40X magnification

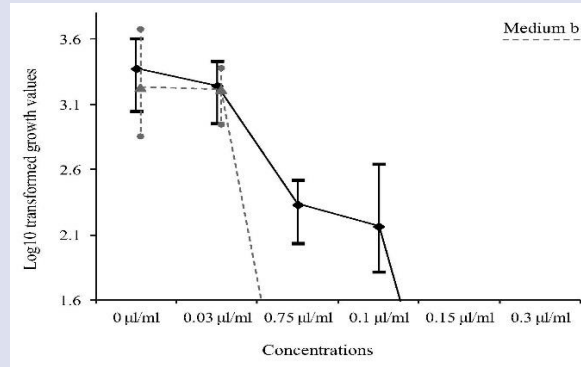


Figure 11. Dose response curve of *Aspergillus fumigatus* based on the log<sub>10</sub> transformed growth values versus the different concentrations of *Origanum onites* essential oil in salt-free (medium a) and salt-amended (medium b) media. \* Sign represents the significant differences between two treatments at the corresponding concentration using one-way ANOVA

Table 5. Influence of *Origanum onites* essential oil on the fungal development of *Aspergillus fumigatus* using micro-colony method

Concentration (µl/ml)	Mean <sup>c</sup>	Range <sup>e</sup>	Shapiro-Wilk W <sup>f</sup>	F-value <sup>g</sup>	F-value <sup>h</sup>
0.3	0	0	N/A	N/A	N/A
0.15	0	0	N/A	N/A	N/A
0.1	2.169116	2.648653-1.822168	0.9397 <sub>(n=19)</sub>	2.414 <sub>(1,27)</sub>	N/A
0.075	2.335844	2.525304-2.040602	0.9118 <sub>(n=16)</sub>	29.63 <sub>(2,31)</sub> <sup>a,d</sup>	N/A
0.03	3.247178	3.437941-2.959995	0.9586 <sub>(n=16)</sub>	5.502 <sub>(2,39)</sub> <sup>a,d</sup>	0.02817 <sub>(1,23)</sub>
0	3.379108	3.610788-3.053232	0.8893 <sub>(n=14)</sub>	5.872 <sub>(2,29)</sub> <sup>a,d</sup>	2.704 <sub>(1,24)</sub>
0.3 <sup>b</sup>	0	0	N/A	N/A	
0.15 <sup>b</sup>	0	0	N/A	N/A	
0.1 <sup>b</sup>	0	0	N/A	N/A	
0.075 <sup>b</sup>	0	0	N/A	N/A	
0.03 <sup>b</sup>	3.21874	3.386374-2.953711	0.9362 <sub>(n=9)</sub>	1.148 <sub>(2, 20)</sub>	
0 <sup>b</sup>	3.234383	3.684432-2.863025	0.9644 <sub>(n=12)</sub>	3.831 <sub>(2, 25)</sub> <sup>a,d</sup>	

<sup>a</sup> *p* value less than 0.05 significant difference

<sup>b</sup> Medium b contains 100mM of KCl, NaCl, and CaCl<sub>2</sub>

<sup>c</sup> Mean of the Log<sub>10</sub> transformed growth values for the first replicate

<sup>d</sup> F value bigger than F value at the 0.05 significance level of the degrees of the freedom for one-way ANOVA test results

<sup>e</sup> Mean of the Log<sub>10</sub> transformed growth values for the first replicate

<sup>f</sup> Validation of the log normal distribution of the population with the Shapiro-Wilk W assay for the first

<sup>g</sup> Validation of the similarity of the log<sub>10</sub> transformed growth values of three replicates using one-way ANOVA test

<sup>h</sup> Validation of the similarity of the log<sub>10</sub> transformed growth values on salt amended and salt free medium using one-way ANOVA test

N/A; not available

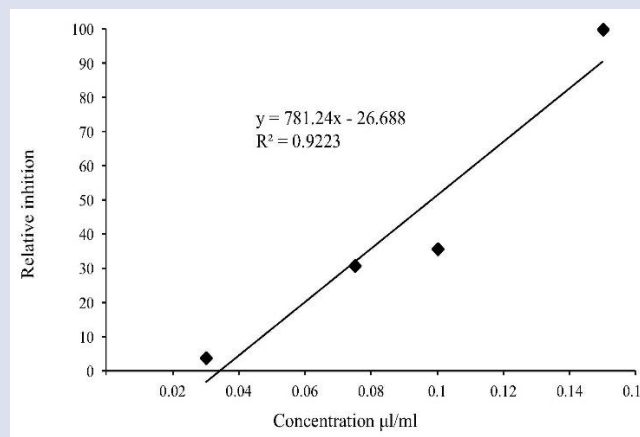


Figure 12. The linear regression model of *Aspergillus fumigatus* based on the relative inhibition of the fungal growth versus the different concentrations of *Origanum onites* essential oil on salt-free medium

### Evaluation of Antifungal Activity of *Taraxacum officinale* Extract on *Aspergillus fumigatus* Using Micro-Colony Method

In salt-free media, *Taraxacum officinale* extract was toxic to *Aspergillus fumigatus* in a dose-dependent manner (Figure 13). The population growth estimations in all concentrations showed a log-normal distribution (Table 6). The growth estimations of three replicates had different mean values except for the observation at 0.3 µg/ml (non-toxic concentration) (Table 6). Salt stress did not alter the estimated growth of the population in all testing concentrations except 0.3 µg/ml (non-toxic concentration). In salt-amended medium, the population growth estimations in all concentrations showed a log-normal distribution except at 0.1 µg/ml (non-toxic concentration) (Table 6). The growth estimations of three replicates had different mean values except for the observation at 1.5 µg/ml (non-toxic concentration) (Table 6). Unlike *Candida albicans*, salt addition did not increase the toxicity of *Taraxacum officinale* extract. The lethal concentration of *Taraxacum officinale* extract was not within the testing concentration range; therefore, the MIC value was not determined. The MFC was estimated as 3.0 µg/ml in both salt-amended and salt-free media. Based on linear regression validation, the relative inhibition versus concentration values fit the linear regression models in both salt-free ( $R^2 = 0.9324$ ) and salt-amended media ( $R^2 = 0.938$ ) (Figure 14). The EC<sub>50</sub> values estimated with the

regression model equation for salt-free ( $y = 5.4926x - 6.5695$ ) and salt-amended ( $y = 4.676x - 9.5868$ ) media were 10.29922 µg/ml and 12.74311 µg/ml, respectively (Figure 14).

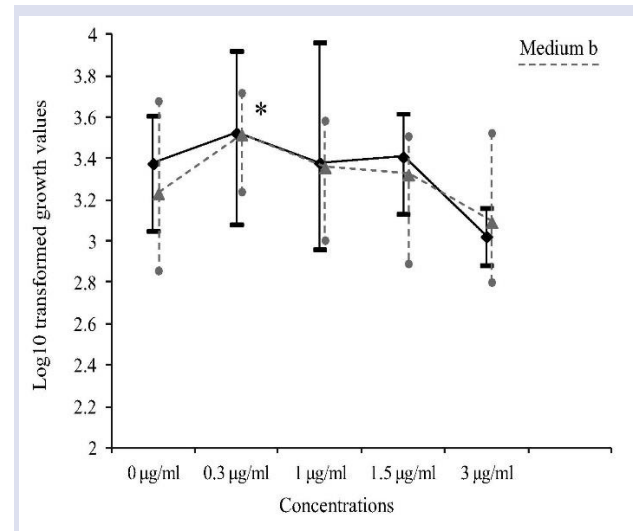


Figure 13. Dose response curve of *Aspergillus fumigatus* based on the log<sub>10</sub> transformed growth values versus the different concentrations of *Taraxacum officinale* extract in salt-free (medium a) and salt-amended (medium b) media. \* Sign represents the significant differences between two treatments at the corresponding concentration using one-way ANOVA

Table 6. Influence of *Taraxacum officinale* extract on the fungal development of *Aspergillus fumigatus* using micro-colony method

Concentration (µg/ml)	Mean <sup>c</sup>	Range <sup>e</sup>	Shapiro-Wilk W <sup>f</sup>	F-value <sup>g</sup>	F-value <sup>h</sup>
3.0	3.025688	3.164353-2.88773	0.9772 <sub>(n=11)</sub>	9.53 <sub>(2,28)</sub> <sup>a,d</sup>	0.7891 <sub>(1,21)</sub>
1.5	3.410988	3.620864-3.135673	0.9626 <sub>(n=15)</sub>	4.911 <sub>(2,28)</sub> <sup>a,d</sup>	2.352 <sub>(1,24)</sub>
1.0	3.381992	3.966264-2.96459	0.9429 <sub>(n=11)</sub>	6.386 <sub>(2,18)</sub> <sup>a,d</sup>	0.05602 <sub>(1,22)</sub>
0.3	3.526891	3.925291-3.085219	0.9774 <sub>(n=10)</sub>	2.887 <sub>(2,24)</sub>	34.29 <sub>(1,18)</sub> <sup>a,d</sup>
0	3.379108	3.610788-3.053232	0.8893 <sub>(n=14)</sub>	5.872 <sub>(2,29)</sub> <sup>a,d</sup>	2.704 <sub>(1,24)</sub>
3.0 <sup>b</sup>	3.095654	3.529456-2.807332	0.8897 <sub>(n=12)</sub>	5.311 <sub>(2,28)</sub> <sup>a,d</sup>	
1.5 <sup>b</sup>	3.326025	3.514056-2.897022	0.8159 <sub>(n=11)</sub> <sup>a</sup>	2.333 <sub>(2,24)</sub>	
1.0 <sup>b</sup>	3.359797	3.589279-3.01013	0.8971 <sub>(n=13)</sub>	12.76 <sub>(2,28)</sub> <sup>a,d</sup>	
0.3 <sup>b</sup>	3.519158	3.723685-3.245192	0.9745 <sub>(n=6)</sub>	21.93 <sub>(2,22)</sub> <sup>a,d</sup>	
0 <sup>b</sup>	3.234383	3.684432-2.863025	0.9644 <sub>(n=12)</sub>	3.831 <sub>(2,25)</sub> <sup>a,d</sup>	

<sup>a</sup> p value less than 0.05 significant difference

<sup>b</sup> Medium b contains 100mM of KCl, NaCl, and CaCl<sub>2</sub>

<sup>c</sup> Mean of the Log<sub>10</sub> transformed growth values for the first replicate

<sup>d</sup> F value bigger than F value at the 0.05 significance level of the degrees of the freedom for one-way ANOVA test results

<sup>e</sup> Mean of the Log<sub>10</sub> transformed growth values for the first replicate

<sup>f</sup> Validation of the log normal distribution of the population with the Shapiro-Wilk W assay for the first

<sup>g</sup> Validation of the similarity of the log<sub>10</sub> transformed growth values of three replicates using one-way ANOVA test

<sup>h</sup> Validation of the similarity of the log<sub>10</sub> transformed growth values on salt amended and salt free medium using one-way ANOVA test

N/A; not available



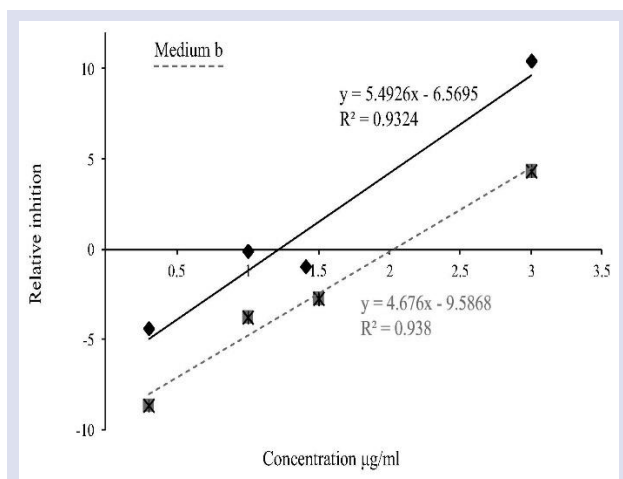


Figure 14. The linear regression models of *Aspergillus fumigatus* based on the relative inhibition versus the different concentrations of *Origanum onites* essential oil in salt-free (medium a) and salt-amended (medium b) media

## Discussion

Based on our *in vitro* assays with *Candida albicans* and *Aspergillus fumigatus* at different concentrations of *Origanum onites* essential oil and *Taraxacum officinale* extract in salt-free (medium A) and salt-amended (medium B) treatments, the micro-colony method provides data on relative inhibition, log-normal distribution of growth values, significant similarities in growth values, linear regression models, EC50 values, and differences using mathematical and statistical models. Thus, the micro-colony assay meets the requirements (validity of mathematical model and verification of the dose response with a linear model) set for a microbiological assay by the European Pharmacopeia [6].

The main advantage of the micro-colony method is its unbiased and detailed perception of fungal development at the population level at each concentration using definitive data analysis methods. The micro-colony method has similarities with diffusion methods (e.g., disc diffusion halo assay, disc diffusion method, radial growth) which use a graduated ruler for measurement [6]. However, the micro-colony method is less time-consuming in preparation and requires a significantly shorter incubation period to obtain growth values, which is important, especially for mold fungi that must be incubated for 3-7 days [8]. The MIC assay in liquid medium is a reference and popular method which could be conducted without spectrometric instruments, and many scholars utilize visual observations and state as “sharp or obvious” decrease based on the decision of the observer [8,9,21]. Thus, in the MIC method, growth could be evaluated solely based on a two-level scheme, i.e., growth or inhibition at each concentration. Therefore, NCCLS has efforts to define “more reproducible reference testing methods” [21]. Conversely, the micro-colony method is more compatible with the fundamental concepts of instrumental analysis due to the measurement of growth using microscopic instruments.

The micro-colony method can demonstrate the impact of medium salinity causing slight alterations in the dose response. Additionally, the images of the colony growth could be stored for future experiments and shared with other research groups. However, the drawbacks of the method are the laborious and time-consuming process of micro-colony measurements and data analysis.

Our preliminary assays suggest that the yeast cell images captured for the micro-colony assays could be used to screen pigmentation in yeast cells. Pigmentation was significantly higher in the control of the salt-amended medium compared to the salt-free control. *Origanum onites* essential oil inhibited the pigmentation of the *Candida albicans* cells. Both *Origanum onites* essential oil and *Taraxacum officinale* extract, in combination with salt, reduced the relative pigmentation significantly in all testing concentrations. Melanin is the major pigment in fungi, which plays roles in pathogenicity and antioxidant activity [24]. Additionally, pigments incorporate with the fungal cell wall and hamper the penetration of toxins into the fungal cells. Therefore, compounds capable of inhibiting pigmentation are prospective reagents in antifungal drug co-formulations.

The toxicity of *Origanum onites* essential oil was proven with the micro-colony method on *Candida albicans* and *Aspergillus fumigatus*. The essential oil was more toxic to the filamentous fungus *Aspergillus fumigatus*. In several studies, an isopropyl cresol terpenoid molecule, carvacrol, was found to be the major component of *Origanum onites* essential oil, which could reach up to 86.9% of its overall content. The multi-site antifungal activity of the carvacrol molecule derives from its hydroxyl moiety and hydrophobicity [7,25]. In fungi, carvacrol is capable of inhibiting ergosterol biosynthesis, disrupting the cell membrane, altering its fatty acid composition, inducing  $\text{Ca}^{2+}$  burst, and triggering specific cellular events similar to rapamycin [7,25,26]. Thus, carvacrol and *Origanum onites* essential oil demonstrate broad-spectrum antimicrobial and toxic activity, capable of inhibiting mold fungi (*Penicillium roqueforti* Thom.), yeast fungi (*S. cerevisiae*), bacteria (*E. coli* and *Pseudomonas aeruginosa* (Schröter) Migula), and insect larvae (*Ochlerotatus caspius* Pallas) [26,27]. Based on the micro-colony assay, *Taraxacum officinale* extract did not exert strong antifungal activity. In our experiments, salt stress altered the response of *Candida albicans* to *Origanum onites* essential oil; however, the estimated relative inhibition was unchanged.

## Conflicts of interest

There are no conflicts of interest in this work.

## References

- [1] Warrell D.A., Cox T.M., Weatherall D., Benz Jr E.J., Firth J.D, Oxford textbook of Medicine, Oxford university press., (2003).
- [2] Chandrasekar P.H., Manavathu E.K., Antifungal resistance: aspergillus. In: Antimicrobial Drug Resistance: Clinical and Epidemiological Aspects, Totowa, NJ: Humana Press., (2009) 953–65.

- [3] Akins R.A., Sobel J.D., Antifungal targets, mechanisms of action, and resistance in *Candida albicans*, In: Antimicrobial Drug Resistance: Mechanisms of Drug Resistance., (2009) 347–407.
- [4] Vicente M.F., Basilio A., Cabello A., Peláez F., Microbial natural products as a source of antifungals, *Clin. Microbiol. Infect.*, 9(1) (2003) 15–32.
- [5] Evans W.C., Trease and Evans Pharmacognosy, 15th ed. W.B. Saunders., (2002) 585.
- [6] European Pharmacopoeia Commission, European Directorate for the Quality of Medicines & Healthcare, European pharmacopoeia, Council of Europe., 1 (2010).
- [7] Ahmad A., Khan A., Akhtar F., Yousuf S., Xess I., Khan L.A., Fungicidal activity of thymol and carvacrol by disrupting ergosterol biosynthesis and membrane integrity against *Candida*, *Eur. J. Clin. Microbiol. Infect. Dis.*, 30 (2011) 41–50.
- [8] Kim J.H., Campbell B.C., Mahoney N., Chan K.L., May G.S., Targeting antioxidative signal transduction and stress response system: control of pathogenic *Aspergillus* with phenolics that inhibit mitochondrial function, *J. Appl. Microbiol.*, 101 (2006) 181–9.
- [9] Koroishi A.M., Foss S.R., Cortez D.A., Ueda-Nakamura T., Nakamura C.V., Dias Filho B.P., In vitro antifungal activity of extracts and neolignans from *Piper regnellii* against dermatophytes, *J. Ethnopharm.*, 117 (2008) 270–7.
- [10] Seyran M., Development of rapid in vitro assays and current status of fungicide sensitivity in the pecan scab pathogen *Fusicladium effusum* [Doctoral dissertation], University of Georgia., (2008).
- [11] Qui J., Detection and mechanism of resistance to sterol demethylation inhibiting fungicides in *Cercospora arachidicola* [MSc Thesis], University of Georgia., Department of Plant Pathology., (2010).
- [12] Seyran M., Brenneman T.B., Stevenson K.L., In vitro toxicity of alternative oxidase inhibitors salicylhydroxamic acid and propyl gallate on *Fusicladium effusum*, *J. Pest Sci.*, 83 (2010) 421–7.
- [13] Hosono K., Effect of nystatin on the release of glycerol from salt-stressed cells of the salt-tolerant yeast *Zygosaccharomyces rouxii*, *Arch. Microbiol.*, 173 (2000) 284–7.
- [14] Farwick M., Siewe R.M., Krämer R., Glycine betaine uptake after hyperosmotic shift in *Corynebacterium glutamicum*, *J. Bacteriol.*, 177 (1995) 4690–5.
- [15] Kulikova N.A., Perminova I.V., Badun G.A., Chernysheva M.G., Koroleva O.V., Tsvetkova E.A., Estimation of uptake of humic substances from different sources by *Escherichia coli* cells under optimum and salt stress conditions by use of tritium-labeled humic materials, *Appl. Environ. Microbiol.*, 76 (2010) 6223–30.
- [16] Woo J.H., Kamei Y., Antifungal mechanism of an anti-Pythium protein (SAP) from the marine bacterium *Streptomyces* sp. strain AP77 is specific for *Pythium porphyrae*, a causative agent of red rot disease in *Porphyra* spp, *Appl. Microbiol. Biotech.*, 62 (2003) 407–13.
- [17] Zore G.B., Thakre A.D., Rathod V., Karuppaiyl S.M., Evaluation of anti-*Candida* potential of geranium oil constituents against clinical isolates of *Candida albicans* differentially sensitive to fluconazole: inhibition of growth, dimorphism and sensitization, *Mycoses.*, 54 (2011) 99-109.
- [18] Katiyar S.K., Gordon V.R., McLaughlin G.L., Edlind T.D., Antiprotozoal activities of benzimidazoles and correlations with beta-tubulin sequence, *Antimicrob. Agents Chemother.*, 38 (1994) 2086–90.
- [19] Maresova L., Muend S., Zhang Y.Q., Sychrova H., Rao R., Membrane hyperpolarization drives cation influx and fungicidal activity of amiodarone, *J. Biol. Chem.*, 284 (2009) 2795–802.
- [20] Hammer Ø., Harper D.A., Past: paleontological statistics software package for education and data analysis, *Palaeontol. Electron.*, 4 (2001) 1.
- [21] Jacobson E.S., Hove E., Emery H.S., Antioxidant function of melanin in black fungi, *Infect. Immun.*, 63 (1995) 4944–5.
- [22] Ben Arfa A., Combes S., Preziosi-Belloy L., Gontard N., Chaliar P., Antimicrobial activity of carvacrol related to its chemical structure, *Lett. Appl. Microbiol.*, 43 (2006) 149–54.
- [23] Rao A., Zhang Y., Muend S., Rao R., Mechanism of antifungal activity of terpenoid phenols resembles calcium stress and inhibition of the TOR pathway, *Antimicrob. Agents Chemother.*, 54 (2010) 5062–9.
- [24] Bakkali F., Averbeck S., Averbeck D., Idaomar M., Biological effects of essential oils—a review, *Food Chem. Toxicol.*, 46 (2008) 446–75.
- [25] Seyran M., Brenneman T.B., Stevenson K.L., A rapid method to monitor fungicide sensitivity in the pecan scab pathogen, *Fusicladium effusum*, *Crop Prot.*, 29 (2010) 1257–63.
- [26] National Committee for Clinical Laboratory Standards (NCCLS), Performance standards for antimicrobial susceptibility testing: eight international supplement M100-S14, Wayne, PA: NCCLS., (2004).
- [27] Hosono K., Effect of nystatin on the release of glycerol from salt-stressed cells of the salt-tolerant yeast *Zygosaccharomyces rouxii*, *Arch. Microbiol.* 173 (2000) 284–7.

## Theoretical Investigation about Inhibition Performance of Acyclovir (ACV) Molecule on Corrosion of Fe (1 1 0) Surface in Acidic Medium: DFT, MC, Toxicity and Solubility Analyses

Dilara Özbakır Işın<sup>1,a,\*</sup>, Savaş Kaya<sup>1,b</sup>

<sup>1</sup> Department of Chemistry, Faculty of Science, Sivas Cumhuriyet University, 58140, Sivas, Türkiye

\*Corresponding author

### Research Article

#### History

Received: 18/12/2024

Accepted: 21/04/2025



This article is licensed under a Creative Commons Attribution-NonCommercial 4.0 International License (CC BY-NC 4.0)

### ABSTRACT

In the present paper, mechanistic insights for the corrosion inhibition efficiency of a drug, namely 2-amino-9-[(2-hydroxyethoxy) methyl]-6,9-dihydro-1H-purin-6-one (Acyclovir) for Fe (1 1 0) surface in acidic medium are reported by means of Density Functional Theory and Molecular Dynamic Simulation calculations. Intercalarly, some useful information about toxicity and solubility of the mentioned chemical system is presented. For Acyclovir, many popular global and local reactivity descriptors of Conceptual DFT were calculated for the studied molecule, and how these parameters affect the inhibition efficiency of the molecule was discussed in detail. The calculations of the parameters were done via B3lyp/SVP, CAM-B3lyp/TZVP and  $\omega$ B97XD/Def2-TZVP calculation level in both gas phase and aqueous media. Adsorption behaviors of the mentioned molecule on Fe (1 1 0) surface was checked with the help of Monte Carlo (MC) simulation approach. The results of both DFT and MC approaches are in good agreement with the experimental results reported previously in the literature. Also, the reactivity of the molecule was evaluated in terms of well-known electronic structure principles such as Maximum Hardness and Minimum Electrophilicity Principles. In terms of toxicity, the ACV molecule having log IGC50 value of 0.91 mmol/L exhibits good solubility and the highly negative calculated adsorption energy value for the interaction between Fe (1 1 0) surface and ACV implies the good inhibition performance of this molecule.

**Keywords:** Acyclovir, DFT, MDS, Corrosion, Toxicity.

<sup>a</sup> [dozbakir@cumhuriyet.edu.tr](mailto:dozbakir@cumhuriyet.edu.tr)

<sup>b</sup> <https://orcid.org/0000-0002-3919-9462>

<sup>c</sup> [savaskaya@cumhuriyet.edu.tr](mailto:savaskaya@cumhuriyet.edu.tr)

<sup>d</sup> <https://orcid.org/0000-0002-0765-9751>

## Introduction

Corrosion can be simply defined as the wearing away and deterioration of metals by the influence of environmental conditions or by reaction with environmental components [1,2]. Corrosion is among the factors that negatively affect the costs of industrial investments and production activities. Safe and high-efficiency work can only be achieved by taking the necessary precautions against corrosion. Interest in experimental and theoretical studies involving the design and synthesis of cheap and effective inhibitor molecules for the protection of metals from corrosion is increasing day by day. It has been frequently reported that organic molecules containing electron-donating atoms such as nitrogen, sulfur, oxygen, conjugated pi bonds, and electron-donating functional groups interact strongly with metal surfaces because of electron transfer between inhibitor and metal and significantly prevent corrosion [3,4]. In this field, researchers, in parallel with experimental studies, present studies on the design and development of effective inhibitors with quantum chemical calculations and molecular dynamics simulation-based analyses to the literature [5,6].

Acyclovir (ACV), one of the purine derivatives, has been reported as a drug frequently used in the effective treatment of varicella zoster and herpes simplex infections. In addition to studies proving that purine derivatives exhibit high biological activity against various biological systems, studies proving that this group of molecules is an effective corrosion inhibitor are frequently encountered in the literature [7,8]. In the experimental study conducted by C. Verma et al. [9], acyclovir was reported to be a good inhibitor against the corrosion of mild steel in 1 M HCl solution. Another study penned by Abdallah and coworkers [10] tested the corrosion inhibition efficiency against Sabic iron corrosion of Acyclovir (ACV) and Omeprazole (OMP) drugs with required comparisons made through weight loss, electrochemical impedance and polarization measurements. In our previously published paper [11], we theoretically investigated the corrosion inhibition efficiency of omeprazole and tinidazole drugs presenting required mechanistic insights and with the help of B3lyp/SVP, CAM-B3lyp/TZVP and  $\omega$ B97XD/Def2-TZVP computation levels of the theory. In a recent study including experimental and theoretical insights, Zhang

and coworkers [12] analyzed the inhibitive performance of two purine derivatives (FAP and N-BAP) for mild steel corrosion and proved high inhibition efficiency of the mentioned molecules in acidic medium.

This study includes important explanations about the reactivity, toxicity and solubility of Acv, a purine derivative, while the interaction modes of the mentioned molecule with the Fe (110) surface will be given through MDS simulations. In the highlighting of the chemical reactivity, the popular parameters and principles of the Conceptual DFT will be considered. The main scope of this article is to present nontoxic and highly soluble nature of ACV molecule in addition its high inhibition performance against the corrosion of Fe (110) surface. Additionally, the results obtained will be compared with the results of previously published theoretical papers about the studied molecule.

### Computational Details and Equations Used in DFT Studies

In the present study, all computational studies were performed with the help of Density Functional Theory (DFT) methods having GD3 corrections. The optimizations of the structures were made through B3LYP [24], CAM-B3LYP and  $\omega$ B97XD methods and valance polarization (SVP), triple- $\zeta$  valance polarization (TZVP) and valance triple- $\zeta$  polarization (def2-TZVP) basis sets. In such studies, basis sets and functionals that provide more accurate results with the approaches they contain should be used to reliably analyze the reactivity of the studied molecule. The reason of the selecting of three different calculation level showing this property is to compare the results obtained via different levels of the calculation. To see the solvent effect, polarizable continuum model (PCM) [30] was preferred. In the solvent-based calculations, the dielectric constant of  $\epsilon = 78.36$  and a refractive index of  $n = 1.33$  were used. Geometry optimizations were performed using equilibrium solvation for the respective state ( $S_0$ ). To check the stability of the optimized structures, frequency computations were made. All calculations were made via the Gaussian09 program suite. Conceptual Density Functional Theory (CDFT) is one of the most popular theoretical tools selected for corrosion inhibition studies. This theory presents the following mathematical relations for the parameters like chemical potential ( $\mu$ ), electronegativity ( $\chi$ ), hardness ( $\eta$ ) and softness ( $\sigma$ ) [13].

$$\mu = -\chi = \left[ \frac{\partial E}{\partial N} \right]_{v(r)} \quad (1)$$

$$\eta = \left[ \frac{\partial^2 E}{\partial N^2} \right]_{v(r)} \quad (2)$$

$$\sigma = 1/\eta \quad (3)$$

By means of the finite differences method, the aforegiven mathematical relations including the total electronic energy ( $E$ ) and total number of the electrons ( $N$ ) of the studied chemical systems turn into ionization energy ( $I$ ) and electron affinity ( $A$ ) based equations as [14].

$$\mu = -\chi = -\left( \frac{I + A}{2} \right) \quad (4)$$

$$\eta = I - A \quad (5)$$

Electrophilicity index ( $\omega$ ) is one of the most used parameters to highlight the organic reaction mechanisms. Parr's electrophilicity index [15] (or first electrophilicity index) ( $\omega_1$ ), second electrophilicity index ( $\omega_2$ ) and net electrophilicity ( $\omega^+$ ) of a molecular chemical system are calculated as [16,17]:

$$\omega_1 \equiv \frac{\chi^2}{2\eta} \quad (6)$$

$$\omega_2 = I \cdot A / I - A \quad (7)$$

$$\Delta\omega^\pm = \omega^+ - (-\omega^-) = \omega^+ + \omega^- \quad (8)$$

In this study, to predict the ionization energy and electron affinity of Acv molecule, we considered Koopmans Theorem [18] giving the relations  $I = -E_{\text{HOMO}}$  and  $A = -E_{\text{LUMO}}$ , where  $E_{\text{HOMO}}$  and  $E_{\text{LUMO}}$  are the energies of HOMO and LUMO orbitals, respectively.

The Fukui function at a point,  $r$ , in the space around the molecule is mathematically presented as the first derivative with respect to the number of electron density at a constant external potential.

$$f(r) = \left( \frac{\partial \rho(r)}{\partial N} \right)_v = \left( \frac{\partial \mu}{\partial v(r)} \right)_N \quad (9)$$

Using Eq. 9, one can write the Fukui indices for nucleophilic (+) and electrophilic (-) attacks as:

$$f^+(r) = \left( \frac{\partial \rho(r)}{\partial N} \right)_v^+ \quad (10)$$

$$f^-(r) = \left( \frac{\partial \rho(r)}{\partial N} \right)_v^- \quad (11)$$

As is known, Fukui functions [19] are often preferred in the analysis of which regions or atoms a molecule uses for nucleophilic, electrophilic and radical attacks when interacting with another system. The Fukui functions for nucleophilic, electrophilic and radical attacks are calculated as follows, respectively, where  $q_k$  represents the charge on atom  $k$  in the molecule.

$$f_k^+ = q_k(N+1) - q_k(N) \quad (12)$$

$$f_k^- = q_k(N) - q_k(N-1) \quad (13)$$

$$f_k^0 = [q_k(N+1) - q_k(N-1)] / 2 \quad (14)$$

It should be noted that in the calculations of Fukui functions, we used Mulliken charges on atoms considering the published papers in literature.

### Monte Carlo (MC) Simulation

Using Monte Carlo Simulation approach, adsorption behavior of Acv molecule on Fe (110) was checked. The mode of the interaction between Acv and Fe (110) surface was analyzed with the help of adsorption locator module of Materials Studio 2017 software [20]. Optimization of the adsorption system designed was done with Forcite module through COMPASS force field. There were three dimensions to the slab model: 19.859 Å × 19.859 Å × 14.187 with an enclosed addition of a 30 Å edge creating (12×12) supercell. In the calculation process, an inhibitor molecule, 180 water molecules, 4H<sub>3</sub>O<sup>+</sup> and 4 Cl<sup>-</sup> ions were used. Calculations were performed at 298 Kelvin temperature (NVT) canonical ensemble with a simulation duration of 600 ps (1 fs time step). In the light of the analysis, the most stable adsorption mode of the inhibitor on Fe (110) surface and how high the adsorption energy for the interaction were determined.

### Environmental Toxicity and Solubility Prediction of Acyclovir Molecule

Toxicity and solubility of the Acv molecule that its structure is given in Fig. 1 were estimated with the help of the chemical databases given in modeling environment website [21].

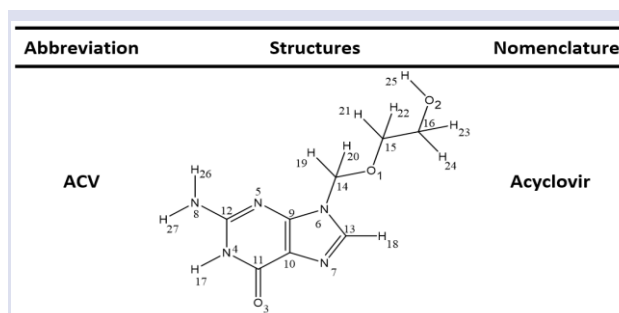


Figure 1. Molecular structure, name and abbreviations of studied inhibitor

## Results and Discussion

### Toxicity and Solubility Analysis

Toxicity and solubility results obtained for ACV molecule are given in Table 1. From the values given in this table, Log (IGC50) is known as the toxic potency of the molecules to provide 50% inhibitory growth of species. This value is generally reported for like *Tetrahymena pyriformis* or *Daphnia magna*. Log P values presented for molecules imply their lipophilic character. The more negative the Log P value is, the more soluble the molecule is in water. According to calculated Log P value for ACV molecule, it can be said that this molecule has good solubility in water media. It should be noted that in the paper mentioned in the introduction part, Abdallah and coworkers experimentally studied the efficiency of ACV in hydrochloric acid solution at the concentration range between 100 ppm and 500 ppm. The IGC50 value determined for Acv molecule is less than the concentration used in experimental analysis. If so, we can say that ACV is an environmentally friendly compound at the studied concentration range

Table 1. Predicted toxicity and solubility values for ACV molecule

Inhibitor Molecule	Log (IGC50) (mmol/L)	Log P (mol/L)
ACV	0.91	-2.1

### DFT Calculations

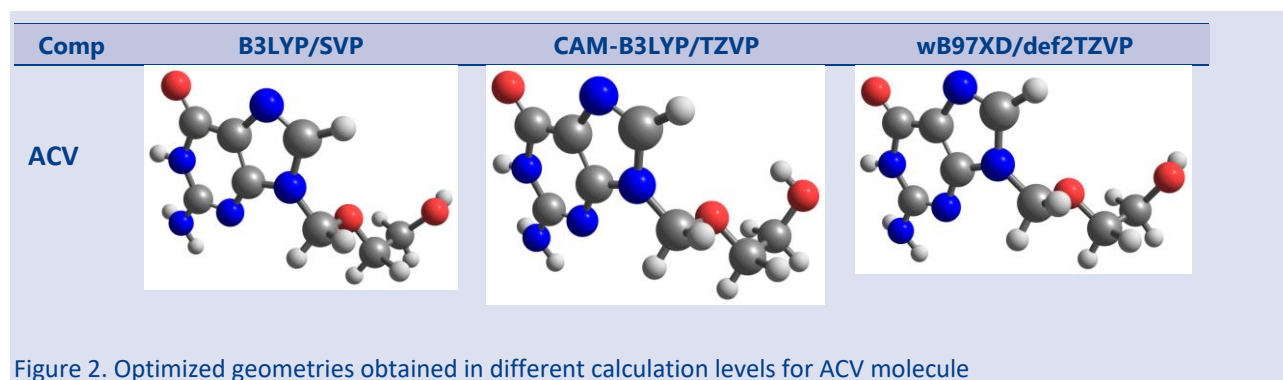


Figure 2. Optimized geometries obtained in different calculation levels for ACV molecule

Figure 2. includes optimized geometries obtained at different calculation levels for ACV molecule while calculated reactivity descriptors for ACV molecule in both gas phase and aqueous phase are presented in Table 2. Chemical reactivity descriptors such as frontier orbital

energies, hardness, electronegativity, first electrophilicity index, second electrophilicity index, electrodonating/accepting powers, dipole moment and polarizability obtained via Density Functional Theory calculations are widely used in the estimation of the



corrosion inhibition efficiency of the molecules [22]. HOMO and LUMO orbital energies used in chemical reactivity analysis in Molecular Orbital Theory (MOT) reflect the corrosion inhibition performances also of the molecules. The molecules with higher HOMO energies are good corrosion inhibitors because such molecules are effective electron donors. Chemical hardness concept [23] introduced by R.G. Pearson is a measure of the resistance against polarization of chemical systems. According to

Maximum Hardness Principle [24], this quantity reflects the stability of the molecules. Hard molecules exhibiting high stability cannot give the electrons easily to metal surfaces and are not good corrosion inhibitors. If so, it should be noted that good corrosion inhibitors should be soft molecules with high reactivity. Considering electronegativity, it can be said that effective corrosion inhibitors should have low electronegativity.

Table 2. Calculated reactivity descriptors for ACV molecule in both gas phase and aqueous phase

Parameter	B3LYP/SVP		CAM-B3LYP/TZVP		$\omega$ B97XD/Def2-TZVP	
	Gas	Water	Gas	Water	Gas	Water
$E_{\text{HOMO}}$ (eV)	-5.656	-5.826	-7.472	-7.518	-7.792	-7.976
$E_{\text{LUMO}}$ (eV)	-0.244	-0.340	0.681	0.636	1.567	1.330
$I$	5.656	5.826	7.472	7.518	7.792	7.976
$A$	0.244	0.340	-0.681	-0.636	-1.567	-1.330
$\chi$	2.950	3.083	4.077	4.077	4.680	4.653
$\eta$	5.412	5.486	6.791	6.882	6.225	6.646
$\omega_1$	0.804	0.866	1.224	1.208	1.759	1.629
$\omega_2$	0.255	0.361	0.749	0.695	1.961	1.596
$\omega^-$	3.421	3.617	4.910	4.884	6.247	6.000
$\omega^+$	0.471	0.534	0.833	0.807	1.567	1.347
Net electrophilicity	3.892	4.151	5.743	5.691	7.814	7.347
Polarizability ( $\alpha.u$ )	128.466	163.444	136.252	177.917	139.921	183.825
Dipole moment (Debye)	11.421	7.848	10.931	8.220	12.127	11.421

Especially, the electronegativity and chemical hardness values determined for ACV molecule in B3LYP/SVP level is smaller than the data obtained via CAM-B3LYP/TZVP and  $\omega$ B97XD/Def2-TZVP levels. Polarizability is a property minimized in stable states [25]. If so, a good corrosion inhibitor should have high polarizability. Noting that the dipole moment is a measure of the polarizability of molecules, some researchers proved that the molecules with high dipole moment are good corrosion inhibitors. Both calculated polarizability and calculated dipole moment support that ACV is an effective corrosion inhibitor as reported by Abdallah and coworkers [10].

As given in computational details section, net electrophilicity is the sum of electrodonating power ( $\omega^-$ ) and electroaccepting power ( $\omega^+$ ) of the molecules. For the calculating of  $\omega^-$  and  $\omega^+$ , we used the following equations derived by Gazquez and coworkers [26].

$$\omega^- = (3I + A)^2 / (16(I - A)) \quad (15)$$

$$\omega^+ = (I + 3A)^2 / (16(I - A)) \quad (16)$$

Electrodonating power reflects the electron donating ability of the chemical systems. It is noteworthy that the calculated values of this parameter for the Acv molecule at various computational levels are quite high.

Fukui indices can provide insight into the anti-corrosion mechanism of a compound. For example, a high positive Fukui index value ( $f^+$ ) in a reactive region of a molecule indicates that the frontier electron density in that region is high, thus the potential for nucleophilic attack is high. Knowing the reactive sites can help determine which sites are most effective in inhibiting the corrosion process.

Acyclovir compound has 27 reactive sites, which are labelled from 1O to 27H. The Fukui indices of the acyclovir compound were calculated in the gas phase and in water at different calculation levels and are presented in Tables 3-5.

Table 3 shows the order of reactive sites, as determined by the Fukui indices, for the Acyclovir compound using DFT/B3LYP/SVP method both in the gas and in water. The most reactive site for nucleophilic attack is the 2O atom in the gas phase. For electrophilic attacks, the most reactive site is the 26H atom. In water, the most reactive site is the 12C for nucleophilic attack and is the 13C for electrophilic attack.

Table 1. Fukui indices of reactive sites of the *Acyclovir* compound by using DFT/B3LYP/SVP method in both gas and in solvent (water). See figure 1 for numbering.

compound ACV	B3LYP/SVP Gas			B3LYP/SVP Water		
	$f^+$	$f^-$	$f^0$	$f^+$	$f^-$	$f^0$
1O	-0.001	-0.007	-0.004	0.003	0.000	0.001
2O	0.118	0.068	0.093	0.100	0.103	0.102
3O	0.003	-0.005	-0.001	0.001	0.001	0.001
4N	-0.002	0.006	0.002	-0.008	-0.007	-0.007
5N	0.049	0.030	0.039	0.048	0.043	0.045
6N	0.079	0.013	0.046	0.092	0.021	0.057
7N	-0.002	0.011	0.004	-0.005	0.024	0.009
8N	0.064	0.016	0.040	0.078	0.030	0.054
9C	0.058	0.068	0.063	0.074	0.148	0.111
10C	-0.008	-0.017	-0.012	0.002	0.009	0.005
11C	0.064	0.038	0.051	0.093	0.023	0.058
12C	0.107	0.065	0.086	0.121	0.059	0.090
13C	0.075	0.052	0.064	0.096	0.190	0.143
14C	-0.028	-0.043	-0.036	-0.005	-0.006	-0.005
15C	0.053	0.104	0.078	0.074	0.107	0.090
16C	-0.001	-0.029	-0.015	0.000	-0.001	0.000
17H	0.026	0.043	0.034	0.024	0.033	0.028
18H	0.038	0.069	0.054	0.022	0.027	0.025
19H	0.078	0.067	0.073	0.058	0.045	0.052
20H	0.020	0.047	0.034	0.007	0.009	0.008
21H	0.025	0.047	0.036	0.007	0.011	0.009
22H	0.047	0.050	0.049	0.036	0.059	0.047
23H	0.028	0.061	0.045	0.004	0.005	0.004
24H	0.005	0.022	0.014	0.003	0.004	0.003
25H	0.044	0.057	0.050	0.038	0.033	0.036
26H	0.047	0.105	0.076	0.037	0.030	0.033
27H	0.013	0.060	0.037	0.001	0.002	0.001

According to Table 4, the most reactive site is the 11C atom with a positive Fukui index value of 0.131, followed by the 2O atom with value of 0.126. The least reactive sites are 14C and 1O atoms, both with negative values

indicating electrophilic character. In water, the most reactive site is the 11C atom for nucleophilic attack and are the 2O and 13C atoms for electrophilic attack.

Table 4. Fukui indices of reactive sites of compound *Acyclovir* by using DFT/ CAM-B3LYP/TZVP method both in the gas phase and in water.

Compound ACV	CAM-B3LYP/TZVP Gas			CAM-B3LYP/TZVP Water		
	$f^+$	$f^-$	$f^0$	$f^+$	$f^-$	$f^0$
1O	-0.003	-0.006	-0.004	0.004	-0.001	-0.280
2O	0.126	0.074	0.100	0.110	0.130	-0.412
3O	0.024	0.024	0.024	0.002	0.002	-0.432
4N	0.002	0.001	0.001	0.010	-0.002	-0.048
5N	0.038	0.012	0.025	0.049	0.050	-0.106
6N	0.084	0.010	0.047	0.103	0.038	-0.160
7N	0.007	0.025	0.016	0.011	0.025	-0.264
8N	0.072	0.028	0.050	0.091	0.022	-0.336
9C	0.037	0.079	0.058	0.039	0.109	-0.086
10C	0.021	0.000	0.011	0.013	0.027	-0.037
11C	0.131	0.100	0.116	0.181	0.060	-0.045
12C	0.111	0.075	0.093	0.118	0.085	-0.016
13C	0.048	0.050	0.049	0.048	0.248	0.018
14C	-0.040	-0.045	-0.042	-0.004	-0.005	-0.120
15C	0.038	0.110	0.074	0.046	0.048	0.239
16C	-0.003	-0.004	-0.003	-0.001	-0.002	-0.084
17H	0.014	0.037	0.025	0.016	0.017	0.153
18H	0.029	0.052	0.041	0.014	0.014	0.154
19H	0.071	0.070	0.070	0.042	0.032	0.174
20H	0.019	0.023	0.021	0.006	0.006	0.135
21H	0.027	0.037	0.032	0.006	0.007	0.132
22H	0.045	0.054	0.050	0.029	0.045	0.290
23H	0.027	0.030	0.028	0.003	0.003	0.136
24H	0.005	0.006	0.006	0.002	0.003	0.128
25H	0.038	0.057	0.048	0.030	0.020	0.287
26H	0.042	0.109	0.075	0.029	0.016	0.286
27H	-0.011	-0.008	-0.009	0.000	0.002	0.293

According to Table 5, the most reactive site is the 2O atom with a positive Fukui index value of 0.134, followed by the 11C atom with value of 0.121 in the gas phase. In water, the most reactive site is the 11C atom for

nucleophilic attack with a positive Fukui index value of 0.169 followed by the 2O atom with value of 0.117 and are the 2O and 13C atoms for electrophilic attack.

Table 5. Fukui indices of reactive sites of compound Acyclovir by using DFT/ $\omega$ B97XD/def2-TZVP method both in the gas phase and in water.

Compound ACV	$\omega$ B97XD/def2-TZVP Gas			$\omega$ B97XD/def2-TZVP Water			
	$f^+$	$f^-$	$f^0$	$f^+$	$f^-$	$f^0$	
1O		-0.003	-0.004	-0.003	0.004	0.000	0.002
2O		0.134	0.086	0.110	0.117	0.152	0.135
3O		0.000	0.000	0.000	0.001	0.001	0.001
4N		0.014	0.021	0.018	0.020	0.005	0.012
5N		0.055	0.010	0.033	0.062	0.048	0.055
6N		0.084	0.009	0.046	0.102	0.040	0.071
7N		0.014	0.049	0.031	0.020	0.038	0.029
8N		0.078	0.041	0.059	0.097	0.022	0.059
9C		0.050	0.084	0.067	0.060	0.091	0.075
10C		-0.003	-0.014	-0.008	-0.002	0.010	0.004
11C		0.121	0.111	0.116	0.169	0.066	0.118
12C		0.103	0.065	0.084	0.110	0.099	0.104
13C		0.037	0.033	0.035	0.037	0.243	0.140
14C		-0.029	-0.030	-0.030	-0.005	-0.006	-0.005
15C		0.027	0.095	0.061	0.036	0.036	0.036
16C		-0.008	-0.008	-0.008	-0.002	-0.002	-0.002
17H		0.019	0.035	0.027	0.018	0.018	0.018
18H		0.035	0.055	0.045	0.017	0.016	0.017
19H		0.068	0.065	0.066	0.039	0.029	0.034
20H		0.017	0.018	0.018	0.006	0.006	0.006
21H		0.025	0.031	0.028	0.006	0.007	0.006
22H		0.044	0.055	0.049	0.026	0.042	0.034
23H		0.026	0.028	0.027	0.003	0.003	0.003
24H		0.003	0.003	0.003	0.002	0.002	0.002
25H		0.036	0.053	0.045	0.028	0.018	0.023
26H		0.042	0.100	0.071	0.028	0.015	0.021
27H		0.011	0.012	0.011	0.001	0.001	0.001

It is worth nothing that the relative reactivity of the atomic sites can be significantly affected by the solvent environment, as seen in the differences between in the gas phase and in water results. The results show that the order of reactive sites varies depending on the method and solvent used.

#### Monte Carlo Simulation Results

To test the corrosion inhibition efficiency of Acv molecule against the corrosion of Fe (110) surface, in

addition to DFT calculations, we made a Monte Carlo Simulation based analysis also [27,28]. Then, we checked whether the results of MC simulation based analysis are in good agreement with experimental data. As a result of the calculations made, the most stable (low energy) adsorption mode was determined for Fe (110)-Acv interaction. Fig. 3 visually presents the most stable low energy configuration for the adsorption of Acv on Fe (110) surface. In this figure, the top and side views of the most stable adsorption mode are seen.

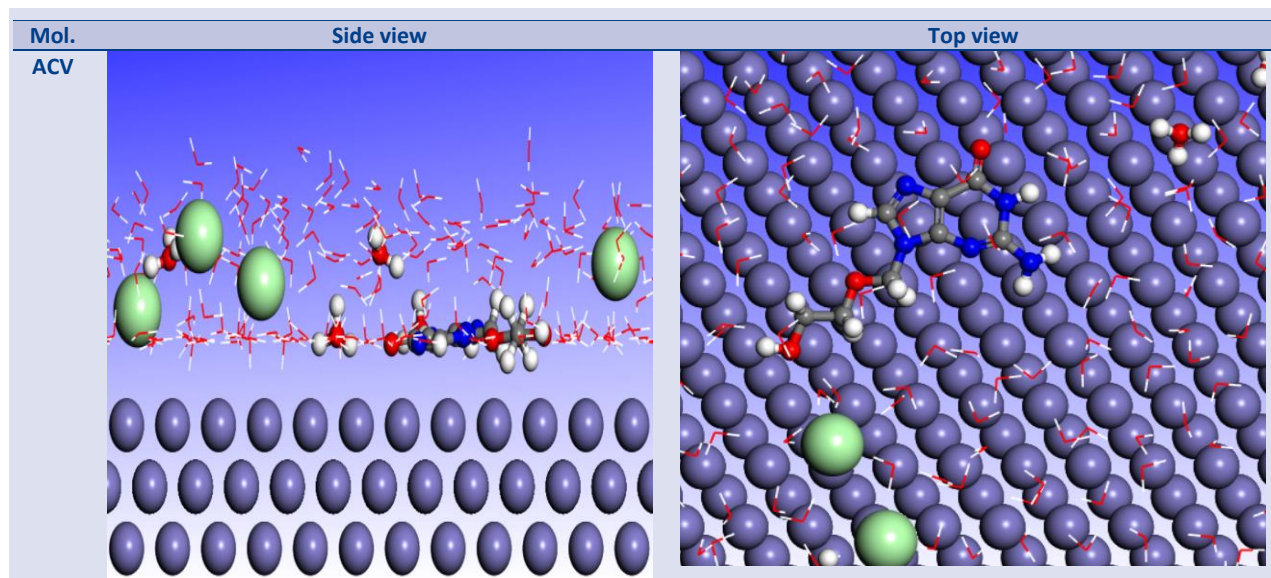


Figure 3. The most stable /low energy configuration for the adsorption of Acv on Fe (110) surface

With the help of Monte Carlo Simulations based calculations, in addition to the most stable adsorption mode of the inhibitor, the power of the interaction between metal surface and inhibitor can be also determined via adsorption energy prediction. As can be seen from Fig 3 that inhibitor has an orientation parallel to the metal surface. In this way, the surface interacts more strongly with the heteroatoms in its structure. Adsorption energy (Eads) is a parameter reflecting the power of the interaction between metal and inhibitor and corrosion inhibition efficiency of the studied molecule. The more negative the calculated adsorption energy for the metal-inhibitor interaction, the more effective the inhibitor is in protecting the considered surface from corrosion. In the acidic medium designed via Monte Carlo method, the adsorption energy value calculated for Fe (110)-ACV interaction is -3352.92 kcal/mol. This value is the proof that Acv is an effective inhibitor against steel corrosion. Additionally, it implies that adsorption is chemical as compatible with previously published experimental study. In a recent paper, Anadebe and coworkers [29] analyzed the corrosion inhibition mechanism of ACV molecule on Fe (110) using computational model based on DFT, RDF and MD simulation. Our study includes toxicity analysis and solubility study also for same molecule. Quantum chemical parameters calculated at B3LYP/SVP calculation level in this paper are in good agreement with the values presented by Anadebe and coworkers.

## Conclusions

Density Functional Theory based calculations illuminate the reactive or stable behaviors of the molecules while Monte Carlo Simulation based analyses effectively explain the natures of the interactions between metal surfaces and corrosion inhibitors. While the strength of inhibitor-metal interactions can be easily analyzed in Monte Carlo Simulation based analyses the orientation of the inhibitor molecule in these interactions can also be easily explained. This paper includes Density Functional Theory (DFT) calculations to highlight the chemical reactivity of Acv molecule. In addition, adsorption behaviors of the molecule on Fe (110) surface were explained in the light of Monte Carlo Simulations. Regarding to the corrosion inhibition performance of the Acv molecule with high solubility and non-toxic nature, the following conclusions can be given.

1. Studied molecule is effective corrosion inhibitor against the corrosion of mild steel in acidic medium
2. Theoretically predicted reactivity descriptors at different calculation levels are in good agreement with experimental observations.
3. The presented data here will provide important clues to experimental corrosion scientists in terms of the design of new and effective purine derivatives.
4. The studied molecules exhibit nontoxic nature and high solubility in aqueous media as expected from good corrosion inhibitor.
5. The heteroatoms of the studied inhibitor molecule are positioned parallel to the metal surface to maximize their interaction with the surface.

## Conflict of Interest

We declare that we have no conflicts of interest related to this study. We have no personal or financial relationships that could influence our work.

## Acknowledgments

This research was made possible by TUBITAK ULAKBIM, High Performance and Grid Computing Center (TR-Grid e-Infrastructure). We thank Farhan Siddique who made some calculations for us.

## References

- [1] Kadhim A., Betti N., Al-Bahrani H. A., Al-Ghezi M. K. S., Gaaz T., Kadhum A. H., Alamiery A., A mini review on corrosion, inhibitors and mechanism types of mild steel inhibition in an acidic environment, *International Journal of Corrosion and Scale Inhibition*, 10(3) (2021) 861-884.
- [2] Kumar H., Yadav V., Saha S. K., Kang N., Adsorption and inhibition mechanism of efficient and environment friendly corrosion inhibitor for mild steel: Experimental and theoretical study, *Journal of Molecular Liquids*, 338 (2021) 116634.
- [3] Ansari K. R., Quraishi M. A., Singh A., Schiff's base of pyridyl substituted triazoles as new and effective corrosion inhibitors for mild steel in hydrochloric acid solution, *Corros. Sci.*, 79 (2014) 5-15.
- [4] Verma C., Quraishi M. A., Recent developments in sustainable corrosion inhibitors: design, performance and industrial scale applications, *Mater. Adv.*, 2(12) (2021) 3806-3850.
- [5] Chauhan D. S., Verma C., Quraishi M. A., Molecular structural aspects of organic corrosion inhibitors: Experimental and computational insights, *J. Mol. Struct.*, 1227 (2021) 129374.
- [6] Guo L., Obot I. B., Zheng X., Shen X., Qiang Y., Kaya S., Kaya C., Theoretical insight into an empirical rule about organic corrosion inhibitors containing nitrogen, oxygen, and sulfur atoms, *Applied surface science*, 406 (2017) 301-306.
- [7] Matić J., Stanisavljević G., Kovačević M., 6-Morpholino-and 6-amino-9-sulfonyl-purine derivatives, Synthesis, computational analysis, and biological activity, *Nucleosides Nucleotides Nucleic Acids*, 40(4) (2021) 470-503.
- [8] Jiang Z., Li Y., Zhang Q., Hou B., Xiong W., Liu H., Zhang, G., Purine derivatives as high efficient eco-friendly inhibitors for the corrosion of mild steel in acidic medium: Experimental and theoretical calculations, *Journal of Molecular Liquids*, 323 (2021) 114809.
- [9] Verma C., Quraishi M. A., Verma P., Electrochemical studies of 2-amino-1, 9-dihydro-9-((2-hydroxyethoxy) methyl)-6H-purin-6-one as green corrosion inhibitor for mild steel in 1.0 M hydrochloric acid solution, *Int. J. Electrochem. Sci.*, 8(5) (2013) 7401-7413.
- [10] Abdallah M., Fawzy A., Al Bahir A., The effect of expired acyclovir and omeprazole drugs on the inhibition of Sabc iron corrosion in HCl solution, *Int. J. Electrochem. Sci.*, 15(5) (2020) 4739-4753.

- [11] Kaya S., Lgaz H., Thakkur A., Kumar A., Özbakır Işın D., Karakuş N., Ben Ahmed S., Molecular insights into the corrosion inhibition mechanism of omeprazole and tinidazole: a theoretical investigation, *Molecular Simulation*, 49(17) (2023) 1632-1646.
- [12] Jiang Z., Li Y., Zhang Q., Hou B., Xiong W., Liu H., Zhang G., Purine derivatives as high efficient eco-friendly inhibitors for the corrosion of mild steel in acidic medium: Experimental and theoretical calculations, *Journal of Molecular Liquids*, 323 (2021) 114809.
- [13] Aktas A. B., Dastan T., Gorgun S., Gunlu A., Ercan E., Katin K. P., Kaya S., IR spectra simulations by anharmonic DFT and CDFT-saturated and unsaturated fatty acids of Siberian sturgeon (*Acipenser baerii* Brandt, 1869), *Journal of Food Composition and Analysis*, 136 (2024) 106776.
- [14] Kaya Y., Erçağ A., Serdaroğlu G., Kaya S., Grillo I. B., Rocha G. B., Synthesis, spectroscopic characterization, DFT calculations, and molecular docking studies of new unsymmetric bishydrazone derivatives, *Journal of Molecular Structure*, 1244 (2021) 131224.
- [15] Parr R. G., Szentpály L. V., Liu S., Electrophilicity index. *Journal of the American Chemical Society*, 121 (1999) 1922-1924.
- [16] von Szentpály L., Kaya S., Karakuş N., Why and when is electrophilicity minimized? New theorems and guiding rules. *The Journal of Physical Chemistry A*, 124(51) (2020) 10897-10908.
- [17] Chattaraj P. K., Chakraborty A., Giri S., Net electrophilicity. *The Journal of Physical Chemistry A*, 113 (2009) 10068-10074.
- [18] Koopmans, T. Über die Zuordnung von Wellenfunktionen und Eigenwerten zu den einzelnen Elektronen eines Atoms. *Physica*, 1(1-6) (1934) 104-113. Contreras, R. R., Fuentealba, P., Galván, M., & Pérez, P. A direct evaluation of regional Fukui functions in molecules. *Chemical Physics Letters*, 304(5-6) (1999) 405-413.
- [19] Verma, C., Lgaz, H., Verma, D. K., Ebenso, E. E., Bahadur, I. and Quraishi, M. A. Molecular dynamics and Monte Carlo simulations as powerful tools for study of interfacial adsorption behavior of corrosion inhibitors in aqueous phase: a review. *Journal of Molecular Liquids*, 260 (2018) 99-120.
- [20] Leeson P. D., Springthorpe B., The influence of drug-like concepts on decision-making in medicinal chemistry, *Nat. Rev. Drug Discov.*, 6(11) (2007) 881-890.
- [21] Islam N., Kaya S., *Conceptual Density Functional Theory and its Application in the Chemical Domain*, CRC Press, 2018.
- [22] Kaya, S., Kaya, C., A new equation for calculation of chemical hardness of groups and molecules, *Molecular Physics*, 113(11) (2015) 1311-1319.
- [23] Kaya S., Kaya C., A simple method for the calculation of lattice energies of inorganic ionic crystals based on the chemical hardness, *Inorganic Chemistry*, 54(17) (2015) 8207-8213.
- [24] Chattaraj P. K., Sengupta S., Popular electronic structure principles in a dynamical context, *The Journal of Physical Chemistry*, 100(40) (1996) 16126-16130.
- [25] Gázquez J. L., Cedillo A., Vela A., Electrodonating and electroaccepting powers, *The Journal of Physical Chemistry A*, 111 (2007) 1966-1970.
- [26] Saraswat V., Yadav M., Obot I. B., Investigations on eco-friendly corrosion inhibitors for mild steel in acid environment: Electrochemical, DFT and Monte Carlo Simulation approach, *Colloids and Surfaces A: Physicochemical and Engineering Aspects*, 599 (2020) 124881.
- [27] Madkour L. H., Kaya S., Obot I. B., Computational, Monte Carlo simulation and experimental studies of some arylazotriazoles (AATR) and their copper complexes in corrosion inhibition process, *Journal of Molecular Liquids*, 260 (2018) 351-374.
- [28] Anadebe V.C., Surface interaction and inhibition mechanism prediction of Aciclovir molecule on Fe (110) using computational model based on DFT, RDF and MD simulation, *Computational and Theoretical Chemistry*, 1238 (2024) 114702.



## Molecular pKa Prediction with Deep Learning and Chemical Fingerprints

Fatih Mehmet Avcu<sup>1,a,\*</sup><sup>1</sup> Department of Informatics, İnönü University, 44280, Malatya, Türkiye

\*Corresponding author

### Research Article

#### History

Received: 31/10/2024

Accepted: 28/04/2025



This article is licensed under a Creative Commons Attribution-NonCommercial 4.0 International License (CC BY-NC 4.0)

### ABSTRACT

Today, drug discovery and design, the determination of molecular properties, in particular the determination of a molecule's pKa value, is essential for understanding and optimising the biological activity of drugs. In this context, in addition to traditional chemical methods, artificial intelligence techniques such as machine learning and deep learning are increasingly used to predict molecular properties and drug design processes. In this paper, we present an approach that investigates the effect of molecular properties on pKa prediction and implements this prediction using a deep learning model. The model considers molecular weight together with chemical fingerprinting methods such as Morgan fingerprinting to represent molecular structures. The dataset used in this study contains 2093 molecular data points obtained from PubChem. The method presented in the paper predicts the pKa values of many molecules with 96.66% accuracy. This can save time and money in the drug discovery, design process, and provide valuable guidance for experimental studies. The paper also presents a comprehensive analysis of the training process, accuracy metrics and performance of the deep learning model. Finally, this paper presents research that evaluates the impact of molecular features on pKa prediction and demonstrates the success of the deep learning model in these predictions.

**Keywords:** SMILES, pKa, Machine Learning, Deep Learning.<sup>a</sup> [fatih.avcu@inonu.edu.tr](mailto:fatih.avcu@inonu.edu.tr) <https://orcid.org/0000-0002-1973-7745>

## Introduction

The pKa values of molecules determine many important properties such as the direction and rate of chemical reactions, solubility, biological activity and environmental behaviour. The determination of pKa values by conventional methods requires laboratory experiments. Therefore, rapid and accurate estimation of pKa values is of great importance in chemistry and biochemistry.

In recent years, the application of artificial intelligence and machine learning techniques to chemistry has led to significant advances in the prediction of molecular properties. These techniques can model complex properties of molecular structures by learning from large data sets and predict them with high accuracy. In particular, deep learning models have the potential to make successful predictions by processing the structural information of molecules.

In this study, a deep learning model was developed to predict the pKa values of molecules using Simplified Molecular Input Line Entry System (SMILES) codes. SMILES is a common notation system that represents the structures of molecules in text format and is widely used in chemical information processing. The model developed uses Morgan fingerprinting to represent molecular structures, taking into account molecular weight.

This paper details the steps taken to develop the model, the data sets used, the training and validation processes, and the performance analyses of the model.

## Related Works

Estimating the pKa of molecules is a topic that has long been studied in chemistry and biochemistry. Traditionally, pKa values are determined by laboratory methods such as titration experiments. These methods provide high accuracy but are time consuming and costly. Therefore, in recent years there has been a great deal of interest in computational estimation methods.

### Quantum chemistry and molecular dynamics approaches

Quantum chemical calculations and molecular dynamics simulations attempt to predict pKa values by calculating molecular structures and energy levels. Gao et al (2009) successfully predicted the pKa values of several organic molecules using quantum mechanical and molecular mechanical (QM/MM) approaches [1]. Ho and Coote studied the prediction of acidity in the gas and solution phases from the first principles [2]. Cramer and Truhlar developed methods for transition metal chemistry using density functional theory [3].

### Machine learning approaches

Machine learning techniques, especially deep learning models, have revolutionised the prediction of molecular properties. Xu et al. predicted pKa values on a large dataset using machine learning algorithms and achieved high accuracy [4]. Wang et al. improved the accuracy of pKa predictions by combining deep learning models and chemical fingerprinting methods [5]. Mayr et al. investigated toxicity prediction using deep learning and developed a model called DeepTox [6]. Ramsundar et al.

presented a comprehensive review of the use of deep learning in life sciences [7]. Feinberg et al. achieved significant success in molecular feature prediction using a model called PotentialNet [8]. Gilmer et al. developed highly accurate models for quantum chemistry using neural message passing techniques [9]. Wu et al. evaluated molecular machine learning models using a benchmark called MoleculeNet [10]. Rupp et al. quickly and accurately modelled molecular atomisation energies using machine learning [11]. Faber et al. showed that molecular machine learning models have lower prediction errors than hybrid DFT errors [12]. Schütt et al. developed a convolutional neural network with a continuous filter called SchNet for modelling quantum interactions [13]. De Cao and Kipf introduced a generative model called MolGAN for small molecular graphs [14]. Kearnes et al. managed to go beyond fingerprints using molecular graph convolutions [15]. Winter et al. learned continuous and data-driven molecular descriptors by transforming equivalent chemical representations [16]. Altae-Tran et al. used one-shot learning techniques for low-data drug discovery [17]. Ragoza et al. achieved significant success in protein-ligand scoring using convolutional neural networks [18].

#### *SMILES and chemical fingerprinting methods*

SMILES codes are a common notation system that represents the structures of molecules in a compact and understandable form. Chemical fingerprinting methods are widely used to numerically represent the structural properties of molecules. Rogers and Hahn provided a detailed encoding of molecular structures using the Morgan fingerprinting method and showed that this method provides important input for machine learning models [19].

In this study, a deep learning model was developed to predict the pKa values of molecules using SMILES codes and chemical fingerprinting methods. The developed model aims to increase the accuracy of pKa predictions by taking into account traditional molecular properties. Considering previous studies in the literature, it seems that this approach provides a significant improvement in pKa predictions and can be a valuable tool for chemical research.

## **Materials and Methods**

### *Data Collection*

The data used in this study were obtained from the PubChem database. PubChem is an open-access resource providing comprehensive information on chemical compounds, biomolecules and biological activities. The PubChemPy library developed for this purpose was used.

### *SMILES and its Implementation*

SMILES is a naming system designed to represent the structure of chemical molecules in text format. This representation consists of a sequence of characters without spaces. SMILES has found wide application in chemical information processing by expressing the atomic

and bonding structures of molecules in human-readable and writable strings. The SMILES format is widely used in chemical databases due to its ability to efficiently encode both simple and complex molecules. This convenience of SMILES allows chemical data to be efficiently stored, searched and compared [20]. Furthermore, the flexibility and ease of use of the SMILES format have led to its preference in many chemical data processing software and databases [21]. These features make SMILES an important tool in the field of chemical information systems.

Table 1 compares the the International Union of Pure and Applied Chemistry (IUPAC) names of various molecules with their SMILES representations. For example, the SMILES representation of the water molecule called 'oxidane' is 'O'. The more complex molecule 6-(hydroxymethyl)oxane-2,3,4,5-tetrol is represented as 'C(C1C(C(C(C(O1)O)O)O)O)O'. This table clearly demonstrates the ability of the SMILES format to represent both simple and complex molecules.

Table 1. IUPAC names of molecules, SMILES representations

IUPAC Names	SMILES Representations
Oxidane	O
Ethanol	CCO
Acetic acid	CC(=O)O
Benzene	c1ccccc1
6-(hydroxymethyl)oxane-2,3,4,5-tetrol	C(C1C(C(C(C(O1)O)O)O)O)O
2-acetyloxybenzoic acid	CC(=O)Oc1ccccc1C(=O)O
Metan	C
Propan	CCC

### *Chemical Fingerprinting Methods*

The Morgan Fingerprint is a molecular descriptor widely used in chemoinformatics. It represents the structural properties of molecules in a numerical format that is ideal for comparing molecular similarities and predicting molecular properties in machine learning models. Morgan FingerPrint takes into account the chemical environment within a certain radius from the atoms of the molecules and encodes this environment as a unique bit sequence. This method, commonly known as Extended-Connectivity FingerPrints (ECFP), captures the topological properties of molecules, effectively representing the environmental information of chemical bonds and atoms. For example, the Morgan fingerprint of a molecule is calculated based on the chemical bonding pattern of atoms within a given radius, and this information is uniquely encoded in a bit string. In this way, Morgan fingerprints can be used quickly and efficiently for molecular similarity searches in large chemical databases and for predicting associated biological activities.

Table 2 compares the representation of several molecules in the SMILES format with the 64-bit Morgan FingerPrint representation of these molecules. The table shows how Morgan FingerPrint encodes chemical structures into a numerical format and captures the topological properties of molecules. Örneğin,

'OC=1(N(N=C(C=1)C2(=CC=CC=C2))C)' The molecule represented by the SMILES notation is encoded as a bit string in the Morgan FingerPrint format '1010010010000000010010101000000111001001100110010011010001100000'. This table helps to understand the use of Morgan FingerPrint for calculating molecular similarities and for fast searching in chemical databases.

Table 2. SMILES and 64-bit Morgan FingerPrint Representations of Molecules

SMILES Demonstration	64-bit Morgan FingerPrint
OC=1(N(N=C(C=1)C2(=CC=CC=C2))C)	10100100100000000100101000000111001001100110010011010001100000
S(=O)(=O)(NC1(=NC(=CC=N1)C))C2(=CC=C(N)C=C2)	10011000011110001101011000010010010010000000101001001010100001
ON=C1(C(=NO)CCCC1)	00111000001000000010010100000010000000100000000
O=[N+](O)C1(=CC(=CC=C1)[CH])[N+](=CC=C(C(=O)CC2(=CC=CC=C2))C=C3))	100101100011001111101010101001100010100101110111010000100100100
O=C(O)C=1(OC=2(C=CC=CC=2(C=1OC)))	1000110011100100110001100010001001001101100001011000000100000101

### Deep Learning Model

Deep learning, a subset of machine learning, is a technique that uses artificial neural networks to learn and make decisions from data. When supported by large data sets and high computing power, this method is capable of solving complex problems and achieving high accuracy rates. Deep learning models use artificial neural networks consisting of many layers and learn complex relationships in the data through these layers [22].

The basic building block of deep learning is the artificial neural network. Artificial neural networks are inspired by biological neural networks and consist of interconnected artificial neurons (Fig. 1). Each neuron receives inputs multiplied by a given weight, processes them through an activation function, and produces an output. The network is organised in layers; the input layer receives the data, hidden layers process the data and the output layer produces the final prediction or classification result. This multi-layer structure forms 'deep' neural networks, and deeper networks are generally capable of learning more complex and abstract features [23].

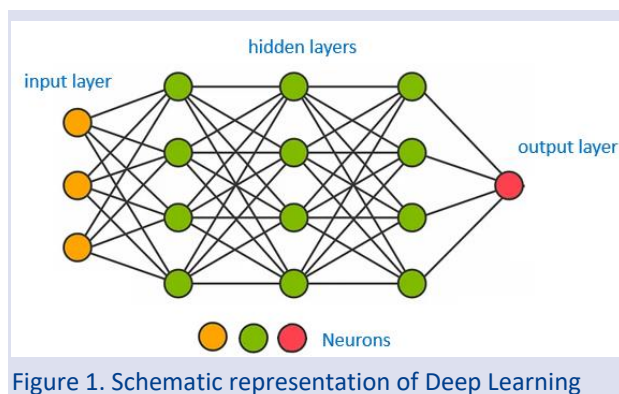


Figure 1. Schematic representation of Deep Learning

Deep learning models are trained on large datasets. The training process involves optimising the parameters (weights) of the model. This is done by minimising the difference (loss) between the model's predicted values and the actual values. Optimisation algorithms such as Stochastic Gradient Descent (SGD) or Adam are used to minimise this loss [24]. In each training cycle, the model learns from the data and updates its parameters.

Deep learning becomes more effective as the amount of data and computing power increases. Today, thanks to GPUs and specialised hardware (e.g. TPUs), deep learning models can be trained quickly and efficiently on large datasets [25]. The development of this technology is enabling artificial intelligence to achieve results close to or better than human performance in several areas.

### Metrics Used

Mean Absolute Error (MAE) is a performance metric that measures the average absolute difference between a model's predicted and actual values. The MAE is used to assess the accuracy of predictions and is calculated as follows:

$$MAE = \frac{1}{n} \sum_{i=1}^n |\hat{y}_i - y_i| \quad (1)$$

In Eq.1,  $\hat{y}_i$  is the predicted value,  $y_i$  is the true value and  $n$  is the total number of data points. The MAE shows the average error of the model's predictions and is easy to interpret. Low MAE values indicate that the model is predicting with high accuracy.

Mean Squared Error (MSE) is a performance metric that measures the average of the squares of the differences between a model's predicted and actual values. The MSE is used to assess the amount of error in the model's predictions and the magnitude of these errors and is calculated as follows:

$$MSE = \frac{1}{n} \sum_{i=1}^n (\hat{y}_i - y_i)^2 \quad (2)$$

In Eq.2,  $\hat{y}_i$  is the predicted value,  $y_i$  is the true value and  $n$  is the total number of data points. The MSE squares and magnifies errors, so that large errors are penalised

more. Low MSE values indicate that the model is predicting with high accuracy.

### Software and Algorithm

Computations were performed on an Intel 8700 processor computer running Ubuntu 24.04 LTS Linux with kernel version 5.4.0-12.15-generic. All computations were performed using Python 3.12.4, Scikit-learn 1.4.2, Tensorflow 2.17.0 and Keras 3.4.1. A schematic representation of the developed software is shown in Figure 2.

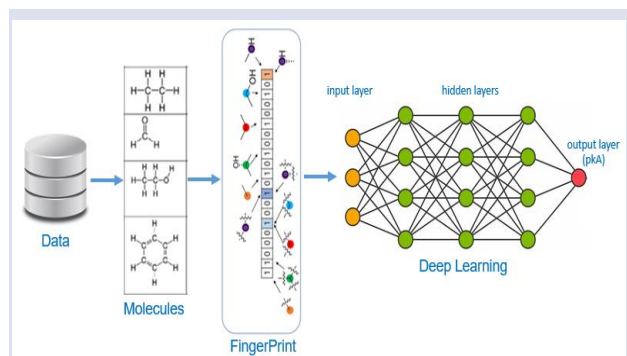


Figure 2. Schematic representation of algorithm

### Analysis and Results

In machine learning, all data features must be on the same scale [26]. Differences between the original features in the dataset can cause problems for many machine learning models. Variables measured at different scales do not contribute equally to the model fit and learning function, which can lead to biased results. For example, if a feature in the dataset is numerically large, it will become dominant. To avoid this, I scale the data using standardisation or z-score normalisation. To do this, I use the StandardScaler function in the Sklearn.Preprocessing library in Python. StandardScaler sets the mean of each column in the data set to 0 and the standard deviation to 1.

To evaluate the performance of the model during the classification process, 30% of the dataset was randomly selected as test data. The remaining 70% was used to train the model. This split of the dataset allows a more general and reliable evaluation of the model's performance. This was done using the 'train\_test\_split' function in the 'sklearn.model\_selection' library in the Python programming language. This function allows the model to be accurately evaluated on both training and test data, while randomly splitting the data set. In this way, the overall validity and generalisability of the model is tested.

In order to prevent overfitting during the development of the model, the "Dropout" technique was applied to each hidden layer. This technique increases the generalisation capability of the model and reduces the risk of overfitting by randomly disabling neurons at certain rates during the learning process of the model[27-28]. In this study, 30% of the neurons were randomly disabled for each hidden layer.

In the optimisation process, the Adaptive Moment Estimation (Adam) algorithm was used, which is widely preferred and provides effective results[29]. By adapting the learning rate for each parameter separately, Adam provides successful results, especially in deep learning models[30]. The deep learning model was trained for a total of 750 epochs; this number of epochs was chosen to allow the model to learn and generalise sufficiently. MAE and MSE functions were used to evaluate and optimise the performance of the model. In understanding the error distribution, MAE treats all errors equally, while MSE penalises large errors more. Using these two metrics together, one can evaluate both the overall error size (MAE) and the sensitivity of the model to large errors (MSE). In performance balancing, using MAE and MSE together ensures that the model performs well against both small and large errors. For example, if a model avoids making very large errors, this may result in a large improvement in MSE, but not necessarily the same improvement in MAE. A low MAE and MSE function is an indication that the model is being better optimised by making accurate predictions. Therefore, minimising the loss function during the training process is critical to the overall performance of the model.

The model created in this study consists of 5 layers in total. These consist of 1 input, 1 output and 3 hidden layers. The structure used 128 input neurons and a hidden layer of 256 neurons. The rectified linear unit (ReLU) function was preferred as the activation function of the input and hidden layers. A linear function was used to activate the output layer. The output layer of the pKa prediction system was configured as 1 neuron.

Table 3. Performance Metrics across Different Hidden Layers and Epochs

HL	Epoch	MAE	MSE	Accuracy
1	100	0.0317	0.0092	0.8559
1	250	0.0229	0.0092	0.7889
1	500	0.0187	0.0093	0.7978
1	750	0.0179	0.0092	0.748
1	1000	0.0179	0.0094	0.7684
2	100	0.0394	0.0099	0.9508
2	250	0.0239	0.0086	0.9611
2	500	0.0175	0.0081	0.9303
2	750	0.0177	0.008	0.9413
2	1000	0.0177	0.0082	0.9549
3	100	0.0353	0.009	0.9598
3	250	0.021	0.0079	0.9545
3	500	0.0172	0.0076	0.9659
3	750	0.0166	0.0076	0.9666
3	1000	0.0178	0.0079	0.9666

The main objective in choosing the different hidden layer configurations listed in Table 3 is to balance the complexity of the model with the overall accuracy. Increasing the number of hidden layers allows the model to learn more parameters and better represent complex relationships in the dataset, while at the same time it may



increase the risk of overfitting. Although fewer hidden layers allow the model to learn faster and have a higher generalisation capacity, the accuracy level may be lower for more complex data. The experiments conducted in the study showed that the model with three hidden layers gave the best results in terms of both accuracy and error rates. For example, this structure showed the highest performance with an accuracy of 96.66% between 750 and 1000 epochs, while at the same time increasing the capacity to learn complex relationships with low error rates (MAE and MSE). After 750 epochs, the performance stabilised, indicating the optimal learning limit for this structure and avoiding the risks of adding more layers. These results show that deep structures offer better generalisation capacity in pKa estimation and allow for a balanced optimisation of small and large errors. These results are more clearly visualised in Figures 3, 4 and 5.

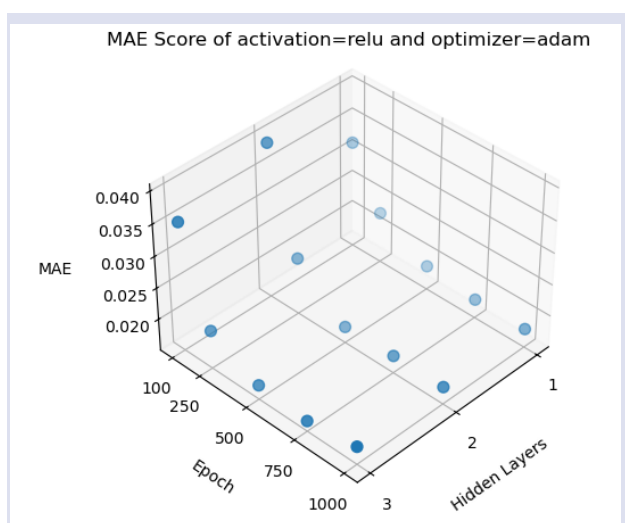


Figure 3. MAE Results: Change with Number of Layers and Epoch

Figure 3 shows the (MAE) performance of the model for different number of layers and epoch values. In this figure, the sensitivity of the MAE, which reflects the average magnitude of the model's prediction errors, to the model's configuration parameters is examined. It is clear from the figure that adding more hidden layers generally leads to lower MAE values. In particular, the three-layer model provided the lowest MAE values at all epoch values, indicating that the model can make more accurate predictions with a deeper structure. This indicates the capacity of deep learning models to learn more complex relationships in the data. With the increase in the number of epochs, a significant decrease in MAE values was observed at first. However, after 750 epochs, the improvement in MAE values came to a halt and fluctuations occurred from time to time. This trend indicates that the learning reaches a saturation point when the model is trained further and additional training processes do not significantly reduce the error. Furthermore, no signs of overlearning were observed up to 1000 epochs, indicating that the generalization capacity of the model is high.

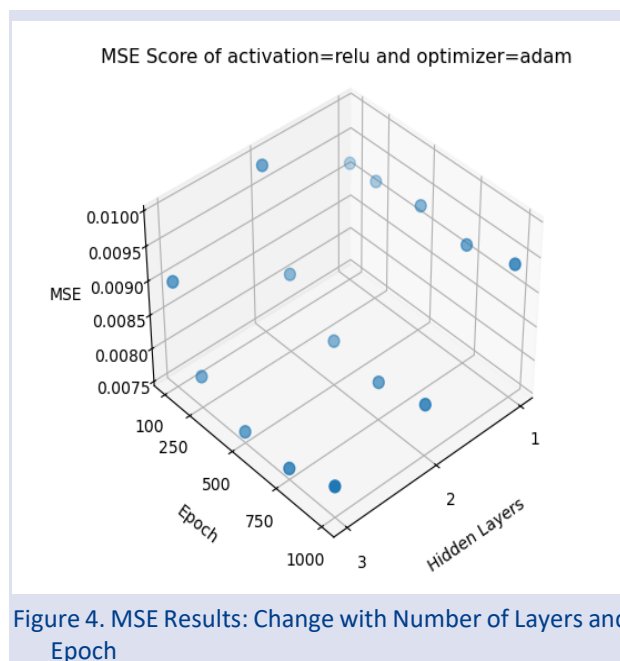


Figure 4. MSE Results: Change with Number of Layers and Epoch

Figure 4. shows the mean square error (MSE) performance of the model for different number of layers and epoch values. This graph examines the sensitivity of the model to the squared prediction errors and its dependence on the reconstruction parameters. It is observed that there is a significant decrease in the MSE values with increasing number of layers. In particular, the three-layer model provides the lowest MSE values at all epoch levels, proving that prediction accuracy improves with more complex structures. While the MSE initially decreases rapidly with the increase in the number of epochs, this decrease slows down after approximately 750 epochs and the values start to stabilize. This suggests that the model reaches a saturation point during the training process and the performance does not improve significantly with additional training. Furthermore, the absence of signs of overlearning up to 1000 epochs demonstrates the robustness of both the generalization ability and the learning process of the model.

Figure 3 and Figure 4 show an overall improvement in both MAE and MSE values as the number of layers increases, indicating that deeper models provide better learning. With a single layer structure, the model achieves 76.84% accuracy and 0.00179 MAE in 1000 epochs with 0.00178 MAE. Furthermore, the MSE values ranged from 0.00076 to 0.00094, indicating that the overall performance of the model is high.

Although increasing the number of epochs will initially improve performance, the improvement will plateau or slightly deteriorate in the 750-1000 epoch range. The epoch value is not increased further as the model may overfit after a certain point with more training. The agreement between MSE and MAE shows that the model improves similarly for small and large errors.



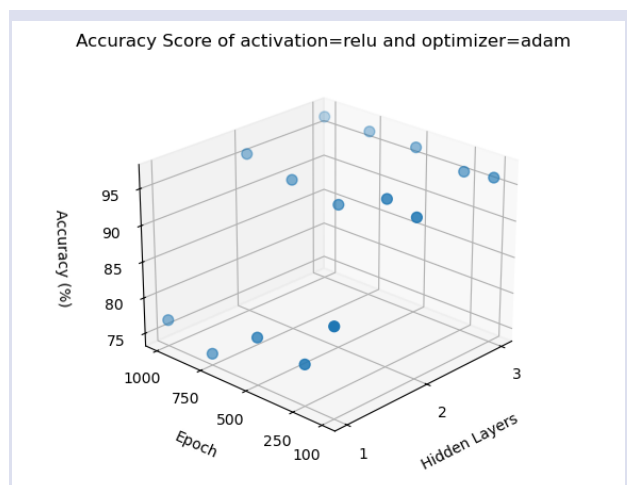


Figure 5. Accuracy Results: Comparison of Model Performance

Figure 5. shows that the three-layer model performs best in the range of 750-1000 epochs and reaches 96.66% accuracy in pKa predictions. This proves that the model can be successfully trained and predicted with both low error rates (MAE and MSE) and high accuracy. The superior performance of the three-layer model points to the capacity of deep learning models to learn complex relationships. A deeper structure allowed the model to learn the fine details in the data, producing more consistent and accurate results. In particular, both MAE and MSE values are low, indicating that the model improves small and large prediction errors similarly. It is observed that increasing the number of epochs initially improves the performance, but the improvement slows down after 750 epochs and stabilizes up to 1000 epochs. This suggests that the model reaches a saturation point at this point and additional training runs do not significantly reduce the error rates. Furthermore, the absence of signs of overfitting (overlearning) in the model proves that the model has a good generalization capacity in general and that this configuration is a reliable forecasting tool.

## Conclusions

This study has shown that molecular pKa values can be predicted with high accuracy using a deep learning model. The model was trained on a dataset of 2093 molecules and achieved a prediction accuracy of 96.66%. The results show that deep learning methods are an effective tool for predicting chemical properties. In particular, careful selection and modelling of molecular features play a critical role in improving the accuracy of pKa predictions.

The results of the study can contribute to a wide range of practical applications in chemistry and biochemistry. For example, in the drug discovery and design process, rapid and accurate estimation of pKa values can be an important step in optimising the biological activities of new drug molecules. These methods can also be used in environmental chemistry to model processes such as the dispersion and biodegradability of pollutants.

For future studies, the effect of different combinations of molecular features on deep learning models can be investigated in more detail. In addition, the generalisation ability of the model can be tested and improved by using larger and more diverse data sets. Such improvements can increase the usability of the model not only in academic research, but also in industrial applications.

## Conflicts of interest

There are no conflicts of interest in this work.

## References

- [1] Gao J., Truhlar D.G., Quantum mechanical methods for enzyme kinetics, *Annu Rev Phys Chem.*, 53 (2002) 467-505.
- [2] Ho J., Coote M.L., First-principles prediction of acidities in the gas and solution phase, *WIREs Comput Mol Sci.* 1(5) (2011) 649-60.
- [3] Cramer C.J., Truhlar D.G., Density functional theory for transition metals and transition metal chemistry, *Phys Chem Chem Phys.* 11(46) (2009) 10757-10816.
- [4] Xu Y., Dai Z., Chen F., Gao S., Pei J., Lai L., Deep learning for drug-induced liver injury, *J Chem Inf Model.* 55(10) (2015) 2085-2093.
- [5] Wang S., Guo Y., Wang Y., Sun H., Huang J., SMILES-BERT: Large scale unsupervised pre-training for molecular property prediction. *Proc 10th ACM Int Conf Bioinformatics, Comput Biol Health Inform.*, (2019) 429-436.
- [6] Mayr A., Klambauer G., Unterthiner T., Hochreiter S., DeepTox: Toxicity prediction using deep learning, *Front Environ Sci.*, (2016)
- [7] Ramsundar B., Eastman P., Walters P., Pande V., Deep learning for the life sciences, Sebastopol (CA): O'Reilly Media, (2015).
- [8] Feinberg E.N., Sur D., Wu Z., Husic B.E., Mai H., Li Y., PotentialNet for molecular property prediction, *ACS Cent Sci.*, 4(11) (2018) 1520-1530.
- [9] Gilmer J., Schoenholz S.S., Riley P.F., Vinyals O., Dahl G.E., Neural message passing for quantum chemistry. In: Proceedings of the 34th International Conference on Machine Learning, (2017) 1263-1272.
- [10] Wu Z., Ramsundar B., Feinberg E.N., Gomes J., Geniesse C., Pappu A.S., MoleculeNet: A benchmark for molecular machine learning, *Chem Sci.*, 9 (2018) 513-530.
- [11] Rupp M., Tkatchenko A., Müller K.R., von Lilienfeld O.A., Fast and accurate modeling of molecular atomization energies with machine learning, *Phys Rev Lett.*, 108(5) (2012) 058301.
- [12] Faber F.A., Hutchison L., Huang B., von Lilienfeld O.A., Baitz G.J., Prediction errors of molecular machine learning models lower than hybrid DFT error, *J. Chem. Theory Comput.*, 13(11) (2017) 5255-5264.
- [13] Schütt K.T., Kindermans P.J., Sauceda H.E., Chmiela S., Tkatchenko A., Müller K.R., SchNet: A continuous-filter convolutional neural network for modeling quantum interactions. In: Proceedings of the 31st Conference on Neural Information Processing Systems, (2017) 991-1001.

- [14] De Cao N., Kipf T., MolGAN: An implicit generative model for small molecular graphs. *arXiv Preprint arXiv:1805.11973*, (2018).
- [15] Kearnes S., McCloskey K., Berndl M., Pande V., Riley P., Molecular graph convolutions: Moving beyond fingerprints, *J. Comput. Aided Mo.l Des.*, 30 (2016) 595-608.
- [16] Winter R., Montanari F., Noé F., Clevert D.A., Learning continuous and data-driven molecular descriptors by translating equivalent chemical representations, *Chem. Sci.*, 10(6) (2019) 1692-701.
- [17] Altae-Tran H., Ramsundar B., Pappu A.S., Pande V., Low data drug discovery with one-shot learning, *ACS Cent. Sci.*, 3(4) (2017) 283-93.
- [18] Ragoza M., Hochuli J., Idrobo E., Sunseri J., Koes D.R., Protein-ligand scoring with convolutional neural networks, *J. Chem. Inf. Model.*, 57(4) (2017) 942-957.
- [19] Rogers D., Hahn M., Extended-connectivity fingerprints, *J. Chem. Inf Model*, 50(5) (2010) 742-54.
- [20] Weininger D., SMILES, a chemical and information system. 1. Introduction to methodology and encoding rules, *J. Chem. Inf. Model*, 28(1) (1988) 31-6.
- [21] Daylight Chemical Information Systems. SMILES: Simplified molecular input line entry system. Available at: <https://www.daylight.com/smiles/>. Retrieved October 2, 2023.
- [22] LeCun Y., Bengio Y., Hinton G., Deep learning. *Nature*, 521(7553) (2015) 436-44.
- [23] Goodfellow I., Bengio Y., Courville A., Deep learning, Cambridge (MA): MIT Press, (2016).
- [24] Avcu F.M., Clustering honey samples with unsupervised machine learning methods using FTIR data, *An. Acad. Bras. Cienc.*, 96(1) (2024).
- [25] Jouppi N.P., Young C., Patil N., Patterson D., Agrawal G., Bajwa R., In-datacenter performance analysis of a tensor processing unit, In: Proceedings of the 44th Annual International Symposium on Computer Architecture, (2017) 1-12.
- [26] Jain A.K., Murty M.N., Flynn P.J., Data clustering: a review. *ACM Comput Surv.*, 31(3) (1999) 264-323.
- [27] Srivastava N., Hinton G., Krizhevsky A., Sutskever I., Salakhutdinov R., Dropout: a simple way to prevent neural networks from overfitting, *J. Mach. Learn. Res.*, 15 (2014) 1929–1958.
- [28] Zaremba W., Recurrent neural network regularization. *arXiv preprint arXiv:1409.2329* (2014).
- [29] Ruder S., An overview of gradient descent optimization algorithms, *arXiv Preprint arXiv:1609.04747* (2017).
- [30] Karakaplan M., Avcu F.M., Classification of some chemical drugs by genetic algorithm and deep neural network hybrid method, *Concurr Comput Pract Exp.*, 33(13) (2021).

## Detection of Biochemical, Cytotoxic, and Genotoxic Damage Caused by Glufosinate-Ammonium on the Zebrafish Cell Line

Harika Eylül Esmer Duruel<sup>1,a,\*</sup>, Figen Esin Kayhan<sup>2,b</sup>

<sup>1</sup> Department of Veterinary, Elbistan Vocational School, Kahramanmaraş İstiklal University, Kahramanmaraş, Türkiye.

<sup>2</sup> Department of Biology, Faculty of Science, Marmara University, İstanbul, Türkiye.

\*Corresponding author

### Research Article

#### History

Received: 03/12/2024

Accepted: 03/05/2025



This article is licensed under a Creative Commons Attribution-NonCommercial 4.0 International License (CC BY-NC 4.0)

### ABSTRACT

Pesticides widely used in agriculture can enter aquatic ecosystems and threaten non-target organisms in the environment. In this study, sublethal toxic effects of glufosinate-ammonium on Zebrafish (*Danio rerio*) liver fibroblast cell line (ZFL) were investigated. Cytotoxicity and genotoxicity tests; MTT, neutral red uptake, lactate dehydrogenase, trypan blue tests were observed at 24 hours, 48 hours, 72 hours and 96 hours; apoptosis and necrosis detection at 48 and 96 hours, cell proliferation detection at 72 hours, micronucleus test at 96 hours. A sublethal dose of 2000 mgL<sup>-1</sup> was determined as the initial concentration and there are dilution differences between the tests. As a result of the tests; Decreases were observed in all applications compared to the negative control in MTT, neutral red uptake, trypan blue, % necrosis and cell proliferation detection tests; in lactate dehydrogenase and % apoptosis tests, an increase were observed in all applications compared to the negative control. In the micronucleus test, it was determined that glufosinate-ammonium application stimulated micronucleus formation compared to the negative control. Biochemical tests were performed in ZFL cell lines with 96-hour application. Selected groups; control group, 250 mgL<sup>-1</sup>, 500 mgL<sup>-1</sup> and 1000 mgL<sup>-1</sup> glufosinate-ammonium doses. Evaluated biochemical parameters; lipid peroxidation determination, reduced glutathione determination, catalase enzyme activity determination, acetylcholinesterase enzyme activity determination and total protein determination. As a result of biochemical experiments; lipid peroxidation level at 1000 mgL<sup>-1</sup>; catalase enzyme activity 250 mgL<sup>-1</sup>; total protein levels in all concentrations increased compared to the control. lipid peroxidation level at 250 mgL<sup>-1</sup> and 500 mgL<sup>-1</sup>; catalase enzyme activity 500 mgL<sup>-1</sup> and 1000 mg/L; GSH level and AChE enzyme activity decreased at all glufosinate-ammonium dose applications. It is thought that the obtained results will provide important contributions to the literature and shed light on further research.

**Keywords:** Pesticide, Zebrafish, Oxidative stress, Cytotoxicity, Genotoxicity.

<sup>a</sup> [heyul.esmerduruel@istiklal.edu.tr](mailto:heyul.esmerduruel@istiklal.edu.tr)  <https://orcid.org/0000-0002-0792-2062>

<sup>b</sup> [feekayhan@marmara.edu.tr](mailto:feekayhan@marmara.edu.tr)  <https://orcid.org/0000-0001-7754-1356>

<sup>b</sup> <https://orcid.org/0000-0001-7754-1356>

## Introduction

The rapid increase in the world population and the development of technology have led to the widespread use of pesticides that aim to protect plants and animals from unwanted pests. This practice is considered a part of integrated farming. The extensive use of pesticides should be regarded as a global phenomenon [1]. Despite its numerous advantages, pesticide use has raised many concerns in terms of public health and environmental pollution. [2]. Pesticides used to protect the target organism and control pests are usually found in aquatic ecosystems [3]. According to Mellanby, pesticides can lead to bioaccumulation in both aquatic and terrestrial flora and fauna through the food chain, often resulting in undesirable consequences for the ecosystem [4]. Pesticide residues are generally considered harmful to fish in most cases [5]. Excessive pollutants reaching surface and groundwater from various sources contribute to water pollution, becoming one of the major environmental issues worldwide [5]. There are four main ways pesticides reach water: they can drift outside the intended area during spraying, percolate from the soil to

groundwater, be transported towards surface waters, or accidental over-discharge can occur [6].

Many studies have reported changes in lipid metabolism in aquatic organisms due to external stress factors such as pesticides [7,8]. The liver has a vital role in maintaining lipid homeostasis. Changes in lipid functions can lead to metabolic problems and damage to other potential pathways [7]. Additionally, the liver takes responsibility for part of the reproductive system in fish, along with the gonads, pituitary, and brain. In case of damage, the ability to reproduce in these creatures will be affected [9]. Glufosinate-ammonium (D, L-phosphinothricin or 2-amino-4-(hydroxymethylphosphinyl) butanoic acid) is a broad-spectrum herbicide belonging to the organophosphorus chemical family. It is used to control various weeds or for vegetation control in non-cropped areas [10]. Glufosinate disrupts photorespiration, leading to reduction of molecular oxygen, which generates reactive oxygen species. It has an unusual physicochemical profile compared to most herbicides currently used worldwide and is the most important herbicide targeting glutamine

synthetase (GS) [11]. Environmental conditions can significantly affect the performance of glufosinate-ammonium used in the field, and only a few weed species worldwide have developed glufosinate resistance. The European Commission has suggested glufosinate-ammonium as "one of the few alternatives to glyphosate" currently used in the world. Since there are very few studies evaluating the effects of glufosinate-ammonium in the literature, it was thought that it was necessary to examine them.

Zebrafish liver cell line (ZFL) is used to simulate the metabolic processes of toxins entering the liver. The zebrafish genome is preferred for generating preliminary hypotheses about human disease mechanisms since it shares many orthologs of human genes [12]. The use of cell lines is beneficial for obtaining toxicological data by measuring parameters such as cell metabolism, morphology, viability, cell membrane permeability, cell adhesion/detachment, and proliferation or growth kinetics in order to simulate the metabolic processes of toxins entering the liver [13]. In numerous cytotoxicity studies, a positive correlation has been established between *in vitro* and *in vivo* EC50 (Effective Concentration 50) values in fish exposed to different pollutants. These studies emphasize the value of using fish cell lines in the field of toxicology [12,13]. Furthermore, the advantages of using cell lines, such as facilitating mechanistic studies, producing less toxic waste, and reducing animal use, should be increasingly emphasized. Fish cell lines are gaining increasing importance in ecotoxicology and genotoxicology as they represent standardized laboratory systems that are conducted in a controlled environment, providing rapid, cost-effective, and ethically sound results [14]. In this study, the use of cell lines as an alternative method to animal experiments was preferred. The use of cell lines together with the evaluation of oxidative stress parameters, cell survival/damage results, and genotoxic parameters brings the study to a valuable point in the field.

The purpose of this study is to examine the effects of exposure to various doses of glufosinate-ammonium on the ZFL cell line. In order to gain more insight into the potential mechanisms of action of the glufosinate-ammonium compound, unlike many studies, various parameters such as DNA damage, cell proliferation, cell viability and oxidative stress levels were simultaneously selected and evaluated.

## Materials and Methods

### Chemicals and Reagents

Chemicals were supplied by the following companies: ZFL CRL 2643 cell line from ATCC; MTT test solution from Biofrox; LDH Test kit and Neutral Red Uptake Test kit from Abcam; BrdU Cell Proliferation Assay Kit from Biovision; Propidium Iodide from Sigma-Aldrich; Hoechst 33342, Trypan blue solution, DMSO, Trypsin-EDTA, dPBS and Colchicine from ThermoFisher Scientific; Giemsa

solution, Thio Barbituric Acid, Trichloroacetic acid, H<sub>2</sub>O<sub>2</sub>, DTNB, Bradford reagent from Merck.

### Cell Culture

The zebrafish liver cell line (ZFL), which is considered as a model organism, was preferred to determine the metabolic processes of possible toxicological effects of Glufosinate ammonium, was obtained from the American Type Culture Collection (ZFL-CRL- 2643). The culture medium was prepared according to the manufacturer's instructions (consisting of; 50% L-15, 35% DMEM, 15% Ham's F12, 0.15g L<sup>-1</sup> sodium bicarbonate, 15mM HEPES, 10µg mL<sup>-1</sup> bovine insulin, 50ng mL<sup>-1</sup> mouse EGF, 5% FBS, and 0.5% Trout Serum). The cells were incubated in 75 cm<sup>2</sup> flasks at 28°C 100% air. The doubling time for adherent cells was determined to be 72 hours under laboratory conditions. At the end of 72 hours, when the cells were examined under a microscope and it was understood that they reached 75-80% confluency, the plate was first washed with dPBS to remove cellular waste. After removing dPBS, adherent cells were trypsinized and the cells were removed from the surface. Cells separated from the flasks were stained with 0.4% trypan blue stain (50 trypan blue: 50 cell line %) and total cell count was performed in the Thoma chamber. Cell viability was expressed as the percentage of live cells, and when cell viability was equal to or greater than 80%, further experiments were conducted. A stock solution of glufosinate-ammonium was prepared in the culture medium and diluted in wells. Negative and positive controls were also prepared in the same culture medium for each test. For cytotoxicity tests, including cell proliferation, apoptosis, necrosis, cell viability, and survival, 10<sup>4</sup> cells/well were seeded in a 96-well plate. Measurements were taken at 24, 48, 72, and 96 hours according to the experimental plan. For oxidative stress experiments, 10<sup>6</sup> cells/well were seeded in a 6-well plate. The application was terminated after 96 hours to measure the endpoint. Negative and positive controls were examined in parallel (Figure 1).

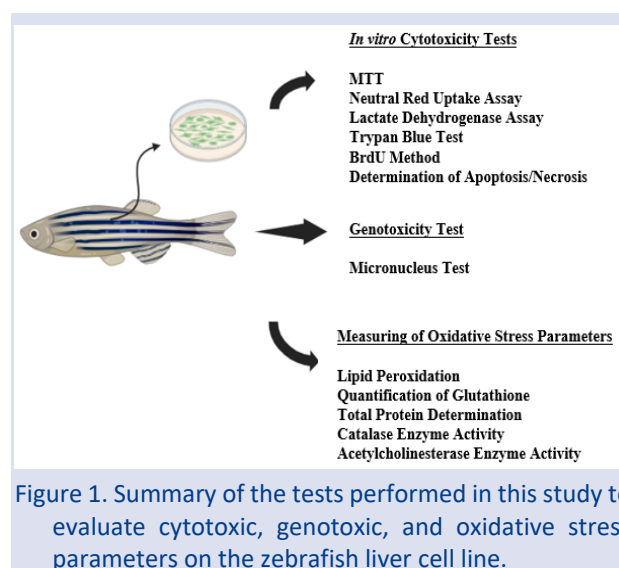


Figure 1. Summary of the tests performed in this study to evaluate cytotoxic, genotoxic, and oxidative stress parameters on the zebrafish liver cell line.

## ***In vitro cytotoxicity tests***

### ***MTT***

The MTT test is based on the conversion of the yellow tetrazolium salt into the blue-purple colored soluble formazan product by the enzyme mitochondrial succinate dehydrogenase [15]. Cells were seeded in a 96-well, 4-plate format with  $10^4$  cells per well. Glufosinate-ammonium application doses were added to the wells, and as a positive control 2.5% DMSO solution was added. Plates were incubated at 28°C for screening every 24 hours. At the end of the incubation period, the medium was removed. All wells were washed with dPBS. Fresh medium (100 µL) was added to each well. In a dark environment, 10 µL MTT solution (Biofroxx) was added to each well. Plates wrapped in aluminum foil were shaken at 200 rcf for 2 minutes at room temperature. They were then incubated at 28°C for 4 hours. After 4 hours, the solution was removed. For the dissolution of formazan crystals, 100 µL DMSO was added and shaken at 200 rcf. Formazan crystals were observed under an inverted microscope. Measurements were taken at 570 nm wavelength and 650 nm reference wavelength. The viability rate of the negative control group was considered to be 100%.

### ***Neutral Red Uptake Assay***

Lysosomal integrity was evaluated using the Neutral Red Uptake (NRU) method. Damaged cells exhibit differential uptake of Neutral Red, while dead cells cannot retain the dye [16]. In a 96-well, 4-plate format,  $10^4$  cells were seeded in each well. After adherent cells attached to the surface, the wells were washed with dPBS. Glufosinate-ammonium application doses were added to the wells, and as a positive control 20 mM doxorubicin (Abcam, ab234039) was added. Plates were incubated at 28°C for screening every 24 hours. At the end of the incubation period, the medium was removed. Each well was washed with 200 µL washing solution as per the kit procedure. Subsequently, 150 µL of Neutral Red dye was added, and the plates were incubated at 28°C for 2 hours. After the incubation, the plate was examined under an inverted microscope. The dye was removed, and each well was washed with washing solution. Then, 150 µL of the dissolution liquid was added, and the plate was shaken for 20 minutes at room temperature and 200 rcf in a shaker. At the end of this period, measurements were taken at an absorbance of 540 nm.

### ***Lactate Dehydrogenase Assay***

The Lactate Dehydrogenase (LDH) test measures the release of the LDH enzyme from the cytoplasm of cells to the cell medium. When cells are exposed to toxic agents that damage the membrane, LDH reduces membrane integrity to keep LDH in the cytoplasm. The more damage a cell membrane suffers, the greater the LDH leakage [17]. In a 96-well, 4-plate format,  $10^4$  cells were seeded in each well. After adherent cells attached to the surface, the wells were washed with dPBS. Glufosinate-ammonium application doses were added to the wells, and a 5 µL

positive control solution (Abcam, ab197004) included in the kit was added. Plates were incubated at 28°C for screening every 24 hours. Thirty minutes before measurement, 10 µL of the lysate control solution was added, shaken for 1 minute, and incubated. At the end of the incubation period, the plates were initially shaken at 200 rcf in a shaker. 5 µL of the supernatant were transferred to a new white 96-well plate. Then, 95 µL of the reaction mixture was added to each well according to the kit's instructions. All of these processes were performed in a dark environment to prevent potential interference from light. The plate wrapped in aluminum foil was shaken for 10 minutes at 200 rcf. Fluorescence measurements were taken at Ex/Em = 535/587 nm. The blank wells did not contain cells.

### ***Trypan Blue Test***

To determine cell viability, one of the most commonly used methods is the Trypan Blue (TB) method. Due to the integrity of the live cell membrane, Trypan Blue dye cannot pass through; it can only pass through dead cell membranes and stain them [18]. In a 24-well, 4-plate format,  $5 \times 10^4$  cells were seeded in each well. After adherent cells attached to the surface, the wells were washed with dPBS. Glufosinate-ammonium application doses were added to the wells, and as a positive control 2.5% DMSO was added. Plates were incubated at 28°C for screening every 24 hours. At the end of the incubation period, the medium was removed, dPBS was used for washing, and Trypsin- EDTA solution was added to the wells. The cells were incubated for 5 minutes at 28°C. Growth medium was added to stop the effect of Trypsin-EDTA, and it was aspirated by gentle pipetting. To remove the Trypsin-EDTA solution, the cell suspension was centrifuged at 125 rcf for 5 minutes. The supernatant was discarded, and the cell pellet was resuspended with growth medium. To count cells, 10 µL of the cell suspension and 10 µL of Trypan Blue were mixed. In the use of Trypan Blue, cells that take up the blue color are considered dead, while those that do not are considered live. Cell counting was performed for each well in triplicate using a Thoma chamber.

### ***5-bromo-2-deoxyuridine (BrdU) Method***

Cell proliferation experiments are widely used in life sciences. 5-bromo-2-deoxyuridine (BrdU) is a pyrimidine analog that incorporates into the newly synthesized DNA of proliferating cells in place of thymidine. In a 96-well plate,  $10^4$  cells were seeded in each well. After adherent cells attached to the surface, the wells were washed with dPBS. Glufosinate-ammonium application doses were added to the wells, and as a positive control 2.5% DMSO was added. The plate was incubated at 28°C for 96 hours. At the end of the incubation period, the steps outlined in the kit procedure were followed (BioVision, K306-200). Measurements were taken at 650 nm absorbance between 5-30 minutes. Then, the stop solution was added, and measurements were taken at 450 nm absorbance.



### **Determination of Apoptosis/Necrosis**

Hoechst 33342 (HOE) is a fluorescent dye that can penetrate both intact and fragmented cell membranes and has a strong binding ability to specific areas in DNA (Adenine-Thymine). When the dye binds to DNA, it emits blue light in fluorescent imaging, allowing the counting of all cells (both living and dead) [19]. Propidium iodide (PI) is a fluorescent dye with the ability to penetrate damaged cell membranes and bind to nuclear DNA by circulating among DNA bases, specifically in dead or damaged cells. In a 96-well, 2-plate format,  $10^4$  cells were seeded in each well. After adherent cells attached to the surface, the wells were washed with dPBS. Glufosinate-ammonium application doses were added to the wells, and as a positive control 2.5% DMSO was added. The plates were incubated at 28°C for 2 different hours (48 hours and 96 hours). The treated cells were washed with dPBS. HOE prepared as a stock solution (ThermoFisher Scientific) was added to each well (100  $\mu$ L per well) and incubated at 28°C for 20 minutes. Just before taking measurements, 10  $\mu$ L of PI solution (Sigma-Aldrich) was added to the wells. Fluorescent imaging was obtained with Texas Red, DAPI, and Brightfield filters using a multi-plate reader. During the area scan, photographs were taken, and a percentage evaluation was made based on 200 counted cells.

### **In vitro genotoxicity test**

#### **Micronucleus test**

Micronuclei are formed from chromosomes or fragments of chromosomes. An increase in their numbers indicates genomic instability and damage occurring during the cell cycle [20]. In a 96-well plate,  $5 \times 10^3$  cells were seeded in each well. After adherent cells attached to the surface, the wells were washed with dPBS. Glufosinate-ammonium application doses were added to the wells, and as a positive control 2.5% DMSO was added. The plates were incubated for 72 hours, which is the doubling time. At the 50th hour after dose application, colchicine was added to each well at a concentration of  $0.20 \mu\text{g mL}^{-1}$ . Incubation continued until 72 hours had elapsed. After incubation, the colchicine-containing medium was removed. Each well received 100  $\mu$ L of hypotonic solution and was incubated for 10 minutes. After centrifugation at 1200 rpm for 15 minutes, the supernatant was removed. The cells were treated with a fixation solution and allowed to dry. Upon drying, 30  $\mu$ L of Giemsa staining solution (Merck) was added to the cells. After waiting for 15 minutes, the cells were rinsed three times with distilled water and allowed to dry. At the end of the process, cells with two or more nuclei and cells with micronuclei were counted and recorded using an inverted microscope.

### **Measuring the Oxidative Stress Parameters**

The imbalance between oxidants and antioxidants causes oxidative stress by resulting in the formation of reactive oxygen species (ROS). Fish are equipped with a defense system to against the effects of ROS, which result from the breakdown of xenobiotics [21].

### **Lipid Peroxidation**

According to the Ledwozyw method, the spectrophotometric evaluation of the pink color produced as a result of the reaction between Malondialdehyde (MDA) and thiobarbituric acid (TBA) at 532 nm will allow the assessment of lipid peroxidation [22].

### **Quantification of Glutathione**

The Ellman reagent is based on the ability of DTNB (5,5'-dithiobis 2-nitrobenzoic acid) to react with compounds containing sulfhydryl groups to form a mixed disulfide (GS-TNB) and 2-nitro-5-thiobenzoic acid (TNB) [23]. This method evaluates reduced glutathion (GSH) levels spectrophotometrically at 412 nm.

### **Total Protein Determination**

Protein determination in tissues based on the Bradford method relies on the measurement of the absorbance at 595 nm of the color solutions formed as a result of Coomassie Brilliant Blue dye binding to proteins [24].

### **Catalase Enzyme Activity**

A quantitative spectrophotometric method defined by Aebi monitors the breakdown of hydrogen peroxide catalyzed by catalase (CAT) by observing a reduction in ultraviolet absorbance of a hydrogen peroxide solution. This decomposition is determined by the decrease in absorbance at 240 nm after the tissue in the experimental solution is allowed to stand for 1 minute [25].

### **Acetylcholinesterase Enzyme Activity**

In the aftermath of oxidative damage, acetylcholinesterase (AChE) enzyme activity is often affected, resulting in an excessive accumulation of acetylcholine. The degree of AChE enzyme activity impairment is measured through spectrophotometric measurements at 412 nm, aiming to determine the damage resulting from oxidative stress [26].

### **Statistical Analysis**

Experiments were carried out with a minimum of three replicates. The SPSS 23 software package was utilized for statistical analyses. The experiments were evaluated using one-way analysis of variance (ANOVA), Tukey's post hoc comparison method, and factorial ANOVA. Differences within the confidence intervals of  $p < 0.05$  were considered statistically significant. Data is presented as mean  $\pm$  standard error.

## **Results**

While pesticides tend to become diluted when they enter aquatic ecosystems, they often remain toxic through various mechanisms. For aquatic vertebrates like fish, acute toxicity occurs at low mg/L concentrations. However, the effects of environmentally relevant chronic exposure have not been fully assessed, which is taken into

consideration in our study. Glufosinate-ammonium, classified among non-selective herbicides and widely used in agriculture, has been chosen for this study.

### MTT Test

To assess the potential toxicity and genotoxicity at the cellular level induced by glufosinate-ammonium, in vitro cytotoxicity tests were employed. These tests aimed to provide detailed information on cell viability, causes of cell death (apoptosis, necrosis), protein/DNA synthesis processes, and cell division.

The MTT assay revealed a consistent decrease in viability at all time points compared to the group of negative control (Figure 2a). After a 24-hour exposure, statistically significant decreases in viability were observed compared to the group of negative control ( $p < 0.05$ ). At 48 hours, a statistically non-significant decrease was identified only at the 500 mg L<sup>-1</sup> dose. However, viability at all other doses exhibited a statistically significant reduction compared to the group of negative control ( $p < 0.05$ ). Significant differences were found between the 24-hour application and the subsequent time points (48, 72, and 96 hours) according to factorial ANOVA ( $p < 0.001$ ). Additionally, statistically significant differences were identified within the 48-hour and 96-hour applications ( $p < 0.001$ ).

### NRU Test

The NRU assay results indicated a decrease in neutral red uptake at all time points and doses compared to the group of negative control (Figure 2b). After a 24-hour application, statistically non-significant decreases were observed at doses of 2000 mg L<sup>-1</sup> to 31.25 mg L<sup>-1</sup> compared to the group of negative control ( $p > 0.05$ ). At 48 hours, only the 2000 mg L<sup>-1</sup> dose showed a statistically significant decrease compared to the group of negative control. All other doses exhibited a decrease in comparison to the group of negative control. After 72 hours, a decrease was observed at all doses compared to the group of negative control. A statistically significant difference was found at doses of 250 mg L<sup>-1</sup> and 31.25 mg L<sup>-1</sup> after 96 hours ( $p < 0.05$ ). Significant differences were identified between the 24-hour and 48-hour applications ( $p < 0.01$ ) and between the 48-hour and 72-hour applications ( $p < 0.05$ ) according to factorial ANOVA.

### LDH Test

The LDH assay results, evaluated at 24, 48, 72, and 96 hours after glufosinate-ammonium application, indicated an increase in lactate dehydrogenase (LDH) activity at all time points and doses compared to the group of negative control (Figure 2c). After a 24-hour application, statistically non-significant increases were observed at doses of 2000 mg L<sup>-1</sup> to 31.25 mg L<sup>-1</sup> compared to the group of negative control ( $p > 0.05$ ). At 48 hours, only the 1000 mg L<sup>-1</sup> dose showed a statistically significant increase compared to the group of negative control. All other doses exhibited a non-significant increase compared to the group of negative control. After 72 hours, an increase was observed at all doses compared to the group of negative

control, with statistically significant increases at doses of 500 mg L<sup>-1</sup> and 250 mg L<sup>-1</sup>. After 96 hours, a statistically significant difference was identified only at the 250 mg L<sup>-1</sup> dose compared to the group of negative control ( $p < 0.05$ ). Significant differences were identified between the 24-hour application and subsequent time points (48, 72, and 96 hours) according to factorial ANOVA ( $p < 0.001$ ).

### Trypan Blue Test

The trypan blue test results, evaluated at 24, 48, 72, and 96 hours after glufosinate-ammonium application, indicated a decrease in cell viability at all time points compared to the group of negative control (Figure 2d). After a 24-hour application, statistically significant decreases in viability were observed at doses of 2000 mg L<sup>-1</sup> to 250 mg L<sup>-1</sup> compared to the group of negative control ( $p < 0.05$ ). At 48 hours, statistically significant decreases were identified only at doses of 2000 mg L<sup>-1</sup> and 1000 mg L<sup>-1</sup> compared to the group of negative control. All other doses showed a non-significant decrease in cell viability compared to the group of negative control ( $p > 0.05$ ). After 72 hours, statistically significant decreases were observed at doses of 2000 mg L<sup>-1</sup> to 500 mg L<sup>-1</sup> compared to the group of negative control ( $p < 0.05$ ). All other doses continued to exhibit a decrease in cell viability compared to the group of negative control. After 96 hours, statistically significant decreases were identified at doses of 2000 mg L<sup>-1</sup> and 1000 mg L<sup>-1</sup> compared to the group of negative control ( $p < 0.05$ ). According to factorial ANOVA, there was a statistically significant difference only between the 48-hour and 96-hour applications ( $p < 0.05$ ).

### BrdU Cell Proliferation Test

The results of the bromodeoxyuridine (BrdU) cell proliferation test were evaluated after a 96-hour application of glufosinate-ammonium. A decrease in all doses was observed compared to the group of negative control (Figure 2e). After the 96-hour application, a statistically non-significant decrease was identified compared to the group of negative control ( $p > 0.05$ ). This suggests that cell proliferation was not significantly affected.

### Hoechst 33342 and Propidium Iodide Dual Staining Test

The results of the apoptosis/necrosis test were evaluated after 48 and 96 hours of glufosinate-ammonium application. The % Apoptosis test showed an increase at all time points compared to the group of negative control (Figure 2f). After a 48-hour application, a statistically significant increase in the percentage of apoptosis was observed at the 2000 mg L<sup>-1</sup> dose compared to the group of negative control ( $p < 0.05$ ). In all other doses, the percentage of apoptosis increased non-significantly compared to the group of negative control ( $p > 0.05$ ). After the 96-hour glufosinate-ammonium application, a statistically significant increase was identified at doses of 2000 mg L<sup>-1</sup> to 250 mg L<sup>-1</sup> compared to the group of negative control ( $p < 0.05$ ). Statistically non-significant increases were observed at doses of 125 mg L<sup>-1</sup> and 62.5 mg L<sup>-1</sup>. According to factorial ANOVA for the % Apoptosis

test, a statistically significant difference was found between the 48-hour and 96-hour applications ( $p < 0.05$ ).

The % Necrosis test showed a change at all time points compared to the group of negative control (Figure 2g). After a 48-hour application, a statistically significant decrease in the percentage of apoptosis was identified at the 2000 mg L<sup>-1</sup> dose compared to the group of negative control ( $p < 0.05$ ). While doses of 1000 mg L<sup>-1</sup>, 500 mg L<sup>-1</sup>, and 62.5 mg L<sup>-1</sup> showed statistically non-significant decreases compared to the group of negative control, doses of 250 mg L<sup>-1</sup> and 125 mg L<sup>-1</sup> exhibited statistically non-significant increases ( $p > 0.05$ ). After the 96-hour glufosinate-ammonium application, a statistically significant decrease was identified at doses of 2000 mg L<sup>-1</sup> to 250 mg L<sup>-1</sup> compared to the group of negative control ( $p < 0.05$ ). Statistically non-significant decreases were observed at doses of 125 mg L<sup>-1</sup> and 62.5 mg L<sup>-1</sup>. According to factorial ANOVA for the % Necrosis test, a statistically

significant difference was found between the 48-hour and 96-hour applications ( $p < 0.01$ ).

### Micronucleus Test

The results of the micronucleus test were evaluated after a 72-hour application of glufosinate-ammonium, corresponding to the doubling time of ZFL cells. A change in micronucleus rates was observed in doses compared to the group of negative control (Figure 2h). After the 2000 mg L<sup>-1</sup> and 1000 mg L<sup>-1</sup> applications, a statistically significant increase in % micronucleus rates was identified compared to the group of negative control ( $p < 0.05$ ). Increases continued at doses of 500 mg L<sup>-1</sup>, 250 mg L<sup>-1</sup>, and 125 mg L<sup>-1</sup> compared to the control, but these increases were not statistically significant. The lowest dose application, 62.5 mg L<sup>-1</sup>, showed a statistically non-significant decrease compared to the control.

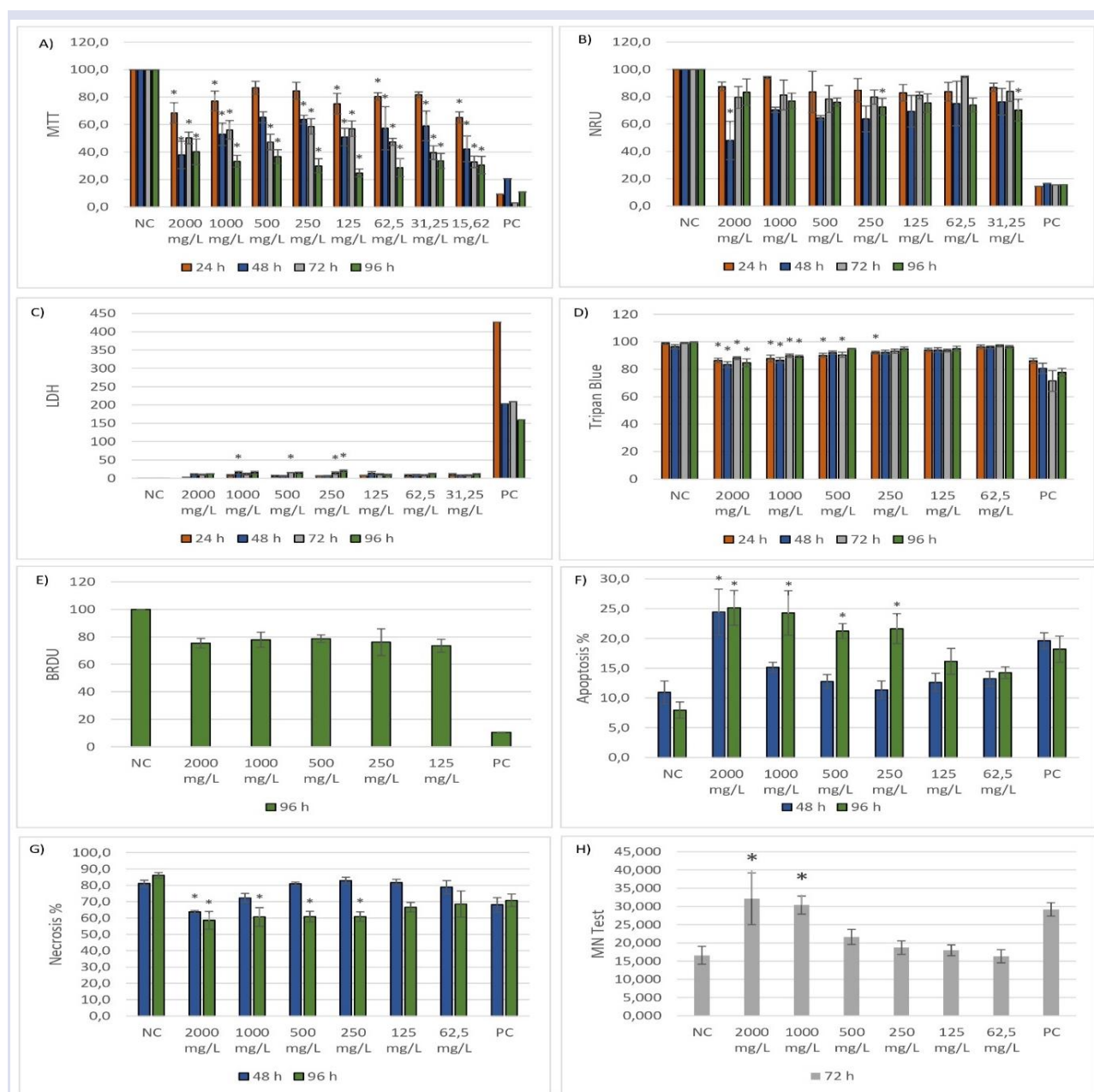


Figure 2. Analysis Findings of ZFL Cells Over Time; A) MTT Analysis Results B) NRU Analysis Results C) LDH Analysis Results D) Trypan Blue Analysis Results E) BrdU Method for Cell Proliferation Analysis Results F) % Apoptosis Analysis Results G) % Necrosis Analysis Results H) % Micronucleus Analysis Results (\*  $p < 0.05$ )

### Oxidative Stress Tests

In order to assess potential biochemical changes in the ZFL cell line, measurements of total protein, MDA, and GSH levels, as well as CAT and AChE enzyme activities, were conducted. Sublethal exposure doses of 250 mg L<sup>-1</sup>,

500 mg L<sup>-1</sup>, and 1000 mg L<sup>-1</sup> were selected. The evaluation of biochemical test parameters is presented as mean values ( $\pm$  standard error). Statistically significant results ( $p < 0.05$ ) were observed in the low and medium doses for total protein and GSH (Table 1).

Table 1. Biochemical Analysis Findings of ZFL Cells (\*  $p < 0.05$ )

Parameters	Control	250 mg L <sup>-1</sup>	500 mg L <sup>-1</sup>	1000 mg L <sup>-1</sup>
MDA	0,018 $\pm$ 0,002	0,017 $\pm$ 0,004	0,015 $\pm$ 0,003	0,019 $\pm$ 0,005
GSH	0,037 $\pm$ 0,007	0,008 $\pm$ 0,006*	0,016 $\pm$ 0,001*	0,025 $\pm$ 0,005
CAT	9,759 $\pm$ 0,421	10,097 $\pm$ 0,478	8,786 $\pm$ 0,243	8,519 $\pm$ 0,492
AChE	0,103 $\pm$ 0,009	0,088 $\pm$ 0,002	0,099 $\pm$ 0,010	0,091 $\pm$ 0,006
Total Protein	13,571 $\pm$ 0,304	15,899 $\pm$ 0,309*	15,443 $\pm$ 0,274*	14,769 $\pm$ 0,452

### Discussion

In our study, the ZFL cell line was chosen as a suitable model because it has the genotypic and phenotypic features of liver cells that have the ability to metabolize many xenobiotics to a large extent. The exposure durations applied in our study were kept broad to provide a reliable estimate of glufosinate-ammonium toxicity. Similar to our research, some studies also identified time-dependent effects. A study conducted in 2007 shows a five-fold increase in differential toxicity between the active ingredient glyphosate and a formulation of Roundup after 72 hours of exposure [27]. Additionally, short-term exposures were hypothesized to result in different effects on tested compounds' direct toxicity compared to long-term exposures [28].

In our study, a reduction in cell viability compared to the group of the control has been observed in all hours and doses where glufosinate-ammonium application was administered. In a study related to determining the cytotoxicity of apigenin at different concentrations on CHO-K1 cells, our results similarly indicate a dose-dependent decrease in cell viability [29].

In another study similar to ours, Bonomo et al. (2019) exposed the ZFL cell line to various doses (1, 10, 100, and 1000 ng mL<sup>-1</sup>) of the flavonoid metal-insecticide magnesium-hesperidin complex (MgHP) for 24 hours, and the mitochondrial activity (MTT test) of ZFL cells showed a dose-dependent decrease. When the exposure time was extended to 96 hours, a decrease in mitochondrial activity was reported at the concentration of 10 ng mL<sup>-1</sup> and higher concentrations of MgHP. However, no significant difference was found in the trypan blue and LDH tests assessing cell membrane integrity compared to the control group [30]. Goulart et al. conducted a study on ZFL cells, exposing the cell line to various doses of the herbicide glyphosate, the insecticide carbofuran, and a combination of these pesticides. In the ZFL cell line treated with glyphosate, a significant decrease in plasma membrane integrity (i.e., viability) was observed even at the lowest tested concentration (67.7  $\mu$ g L<sup>-1</sup>, 94%  $\pm$  0.7) ( $p < 0.05$ ). At higher tested concentrations a decrease in cell viability was determined in correlation with the integrity of the plasma membrane. Additionally, a significant decrease in medium viability was observed at

medium and high concentrations due to mitochondrial activity. Regarding the integrity of the plasma membrane in ZFL cells exposed to the insecticide carbofuran, when compared to the control, cytotoxicity was found to cause a significant reduction in cell viability for three tested concentrations ( $p < 0.05$ ). In the case of mixed application, the effects on membrane integrity exhibited a statistically significant reduction in cell viability compared to the group of the control, although no statistically significant difference was observed compared to separate application of the mixture [31].

Our study aligns with a study conducted by Kanat and Selmanoğlu in 2020, which produced results similar to our NRU test findings. In their research, the effects of the organochlorine insecticide fipronil on the human neuroblastoma cell line SH-SY5Y were evaluated at different durations (24 and 48 hours) and concentrations (125, 250, and 500  $\mu$ M). Similar to our NRU test results, this study also demonstrated a dose-dependent decrease in cell viability. The most significant decrease in cell viability was observed in the group with the highest application dose of 500  $\mu$ M. The lowest cell viability was calculated as 52.22% for 24 hours and 30.77% for 48 hours. In the same study, the LDH test conducted after 24-hour and 48-hour applications revealed a significant increase in each concentration group compared to the group of the negative control. The highest cytotoxicity was observed at the highest dose (500  $\mu$ M) [32].

Our study indicates an increased LDH leakage compared to the group of negative control. It has been noted that there may be a significant difference between time-dependent applications. In a study, Karacaoğlu conducted MTT and LDH leakage tests to evaluate the cytotoxic effects of the triazole fungicide flusilazole at concentrations of 25, 100, and 200  $\mu$ M on the SerW3 cell line. Similar to our study results, this research also showed a dose-dependent reduction in SerW3 cell viability based on the results of the MTT test during a 24-hour incubation period of flusilazole application. Cell viability statistically decreased in all flusilazole application groups compared to the group of the control. Moreover, the cell viability in the group treated with the highest flusilazole dose (200  $\mu$ M) was statistically different from the group treated with 25  $\mu$ M flusilazole. In the same study, an LDH test was conducted. The results revealed that increasing



concentrations of flusilazole caused cell membrane damage. While the percentage of LDH leakage increased during 25 and 100  $\mu\text{M}$  flusilazole applications, it did not show a statistically significant difference from the control group. However, the percentage of LDH leakage in the 200  $\mu\text{M}$  flusilazole application group was found to be statistically significantly different from the control group [33].

In a study conducted in 2019, it was determined that ZFL cells exposed to various doses of MgHP (1, 10, 100, and 1000 ng mL<sup>-1</sup>) for 10, 24, and 96 hours did not show a significant impact on apoptotic or necrotic processes. Furthermore, when comparing exposure durations of 24 hours and 96 hours, it was observed that the effects of MgHP after 96 hours were not as severe as those observed after 24 hours. The researchers associated this phenomenon with the adaptive capacity developed by the cells against stressful conditions or the xenobiotic metabolism capability of liver cells [30]. In a study, Karacaoğlu utilized the Acridine Orange/Propidium Iodide (AO/PI) staining method to determine the type of cell death induced by the fungicide flusilazole in SerW3 cells. The evaluation of this staining method revealed that the 24-hour application of flusilazole induced concentration-dependent apoptotic cell death. The increase in the percentage of apoptotic cell death in all treatment groups showed statistical significance when compared to the control group. It was also determined that necrotic cell death occurred at high concentrations of flusilazole [33].

The potential of substances to induce toxicity is known to cause harm to the cellular DNA structure. In this regard, our study aims to determine cell proliferation using the Bromodeoxyuridine (BrdU) method. Following a 96-hour application, a decrease in cell proliferation compared to the group of negative control was observed. In a thesis conducted by Orta Yılmaz in 2017, various concentrations of fluoride (0.01, 0.05, 0.1, 1, 5, 10, 50, 100, and 200 ppm) were applied to TM3 Leydig cells for 24 hours, and BrdU test results were evaluated. According to this study's findings, a decrease was observed in all concentrations compared to the control group. With the exception of the lowest dose, all administered doses demonstrated statistical significance [34].

In another study conducted in 2020, it was observed that as the concentration of the flavonoid metal-insecticide magnesium-hesperidin complex increased, genotoxicity also increased, leading to nuclear abnormalities after 24 hours of exposure. When the exposure period was extended to 96 hours, improvements in nuclear abnormalities were detected, along with the stimulation of DNA repair mechanisms. In the same study, at high concentrations, it influenced cell stability by increasing ROS levels in both exposure durations (24 and 96 hours). After 24 hours of exposure, CAT enzyme activity decreased, while GSH levels increased. Consistent with our findings, it was determined in this study that there was no deviation from the group of negative control when examining lipid peroxidation levels [35].

In a study conducted on *Cnesterodon decemmaculatus* in 2019, chlorpyrifos and glyphosate were administered to the fish separately and in combination for a duration of 42 days. It was observed that the formation of micronuclei in fish was not statistically significantly affected, while nuclear abnormalities showed a significant increase [3].

ROS formation is associated with oxidative damage and can occur when the antioxidant and detoxification systems are out of balance. It becomes particularly significant when active intermediates produced by xenobiotics and their metabolites need to be neutralized. Lipid peroxidation is a valuable indicator of cellular components resulting from oxidative stress [36]. Furthermore, variations in antioxidant responses can be explained to some extent by differences in the intensity of oxidative stress. ROS may induce the biosynthesis of antioxidant enzymes and GSH to enhance antioxidant capacity. Additionally, significantly higher ROS levels may also lead to inactivation of antioxidant enzymes. Following increased ROS production, a moderate oxidative stress may occur, characterized by a further increase in oxidatively modified components but a decrease in ROS-sensitive parameters due to enzyme inactivation caused by the ROS source. GSH, non-protein thiol, serves as a primary reducer in cells. It is the most abundant antioxidant and is commonly reported as a focal point in assessing oxidative stress in zebrafish. Typically, the concentration of GSH decreases upon induction of oxidative stress.

Consistent with our findings, Gasnier et al. study in 2010 on glyphosate-based herbicides reported that the treatment of a human hepatic cell line with glyphosate and four formulations led to a decrease in glutathione transferase levels [37].

Lipid peroxidation is likely the most reliable indicator of the systemic damage caused by ROS and, therefore, is implicated in the toxicity of pesticides through this mechanism. In our study, no statistically significant differentiation in MDA levels was observed. Similarly, Larsen et al. (2012) in their research noted that, akin to our study, rats exposed to glyphosate through drinking water did not show significant changes in lipid peroxidation levels, although TBARS production tended to be lower. They suggest that one reason for this could be the absence of cell damage or cell death, and another reason might be the creation of specific oxidative radical groups by glyphosate that do not attack lipids [38].

CAT, located in peroxisomes, is an enzyme that facilitates the removal of hydrogen peroxide by metabolizing it into molecular oxygen and water. The SOD-CAT system provides the first line of defense against oxygen toxicity and is often used as a biological indicator of ROS production [39]. A study conducted by Karacaoğlu in 2022 has reported similar results to our research. After applying the fungicide flusilazole to SerW3 cells at doses of 25, 100, and 200  $\mu\text{M}$ , a spectrophotometric method was employed to determine CAT enzyme activity. Compared to the control group, statistically insignificant decreases in CAT activities were observed at low and



medium flusilazole concentrations, while a significant decrease occurred at high concentrations [33].

## Conclusion

With the contribution of the increasing world population and developing technology, pesticide use has become more widespread. Despite the many contributions of pesticides, the view that they are also an important public health problem has begun to spread. In addition to affecting target organisms throughout the ecosystem, they also cause non-target organisms to be affected. In this study, the cytotoxic, genotoxic, and oxidative stress effects of glufosinate-ammonium on the zebrafish liver cell line were evaluated. The zebrafish liver cell line was used to simulate the metabolic processes of toxins entering the liver. It is of critical importance due to its role as a biological model organism. The findings show that agents used to support production, such as glufosinate-ammonium, can trigger oxidative stress in non-target organisms and potentially strain the antioxidant defense system of this organism. As a result of the resulting stress, cell survival may decrease, DNA breaks may occur, and micronucleus formation may be stimulated.

These results, which can be seen in non-target organisms, can tell us that we need to be more careful about pesticide use and that the smallest change that can occur in nature can affect the survival of all organisms with the butterfly effect. The application of a holistic approach will make it easier for all living things to live in prosperity. In order to investigate the toxic effects of glufosinate-ammonium on aquatic organisms more comprehensively, its chronic effects should be evaluated by including different methods.

## Conflicts of interest

There are no conflicts of interest in this work.

## Acknowledgement

This article is a part of the Harika Eylül ESMER DURUEL's doctoral thesis. Thanks to Marmara University Scientific Research Commission (BAPKO) project number FEN-C-DRP-230119-0010 for funding.

## References

- [1] Saeed T., Sawaya W.N., Ahmad N., Rajagopal S., Al-Omair A., Organophosphorus pesticide residues in the total diet of Kuwait. *Arab J Sci Eng*, 30 (2005) 17–28.
- [2] Kumar V., Kumar P., Pesticides in agriculture and environment: Impacts on human health, In *Contaminants in Agriculture and Environment: Health Risks and Remediation*, 1 (2019) 76–95.
- [3] Bonifacio A.F., Hued A.C., Single and joint effects of chronic exposure to chlorpyrifos and glyphosate based pesticides on structural biomarkers in *Cnesterodon decemmaculatus*. *Chemosphere*, 236 (2019) 124311.
- [4] Mellanby K., Pesticides and pollution. *Pesticides and Pollution*, 1967.
- [5] Hashmi T.A., Qureshi R., Tipre D., Menon S., Investigation of pesticide residues in water, sediments and fish samples from Tapi River, India as a case study and its forensic significance. *Environ Forensics*, 21 (2020) 1–10.
- [6] Rahman M.Z., Hossain Z., Mollah M.F.A., Ahmed G.U., Effect of Diazinon 60 EC on *Anabas testudineus*, *Channa punctatus* and *Barbodes gonionotus*, *Naga, The ICLARM Quarterly*, 25 (2) (2002).
- [7] Natesan V., Kim S.J., Lipid metabolism, disorders and therapeutic drugs—review. *Biomol Ther (Seoul)*, 29 (2021) 596.
- [8] Kayhan F., Esmer Duruel H.E., Kızılkaya Ş., Dinç S., Kaymak G., Akbulut C., Yön Ertuğ N.D., Toxic effects of herbicide tribenuron-methyl on liver tissue of zebrafish (*Danio rerio*). *Fresenius Environ Bull*, 29 (12A) (2020) 11175–11179.
- [9] Villeneuve D.L., Larkin P., Knoebel I., Miracle A.L., Kahl M.D., Jensen K.M., et al., A graphical systems model to facilitate hypothesis-driven ecotoxicogenomics research on the teleost brain–pituitary–gonadal axis. *Environ Sci Technol*, 41 (2007) 321–30.
- [10] Halim N., Kuntom A., Determination of glufosinate ammonium in crude palm oil: use of the modified quechers method and LC-MS/MS detection. *J Oil Palm Res*, 25 (2013) 84–91.
- [11] Dayan F.E., Barker A., Bough R., Ortiz M., Takano H., Duke S.O., *Herbicide mechanisms of action and resistance*, In *Comprehensive Biotechnology*, 3rd Ed. (2019) 36–48.
- [12] Kwok M.L., Hu X.L., Meng Q., Chan K.M., Whole-transcriptome sequencing (RNA-seq) analyses of the zebrafish liver cell line, ZFL, after acute exposure to Cu<sup>2+</sup> ions. *Metallomics*, 12 (2020) 732–51.
- [13] Bols N.C., Dayeh V.R., Lee L.E.J., Schirmer K., Use of fish cell lines in the toxicology and ecotoxicology of fish. *Piscine cell lines in environmental toxicology. Biochemistry and Molecular Biology of Fishes*, 6 (2005) 43–84.
- [14] Žegura B., Filipič M., The application of the Comet assay in fish cell lines. *Mutation Research/Genetic Toxicology and Environmental Mutagenesis*, 842 (2019) 72–84.
- [15] Mosmann T., Rapid colorimetric assay for cellular growth and survival: application to proliferation and cytotoxicity assays. *J Immunol Methods*, 65 (1983) 55–63.
- [16] Krone P.H., Blechinger S.R., Evans T.G., Ryan J.A., Noonan E.J., Hightower L.E., Use of fish liver PLHC-1 cells and zebrafish embryos in cytotoxicity assays. *Methods*, 35 (2005) 176–87.
- [17] Alberts B., Johnson A., Lewis J., Raff M., Roberts K., Walter P., *Molecular Biology of the Cell*, Garland Science Textbooks 2007.
- [18] Strober W., Trypan blue exclusion test of cell viability. *Curr Protoc Immunol*, 111 (2015) A3-B.
- [19] Parrilla I., Vazquez J.M., Cuello C., Gil M.A., Roca J., Di Bernardino D., et al., Hoechst 33342 stain and uv laser exposure do not induce genotoxic effects in flow-sorted boar spermatozoa. *Reproduction*, 128 (2004) 615–21.
- [20] Şekeroğlu V., Atlı-Şekeroğlu Z., Genotoksik hasarın belirlenmesinde mikronükleus testi. *Türk Hijyen ve Deneysel Biyoloji Dergisi*, 68 (2011) 241–52.
- [21] Wang Y., Tang M., Review of in vitro toxicological research of quantum dot and potentially involved mechanisms. *Science of the Total Environment*, 625 (2018) 940–62.
- [22] Ledwożyw A., Michalak J., Stępień A., Kądziołka A., The relationship between plasma triglycerides, cholesterol, total lipids and lipid peroxidation products during human atherosclerosis. *Clinica Chimica Acta*, 155 (1986) 275–83.

- [23] Beutler E., Glutathione in red blood cell metabolism. A Manuel of Biochemical Methods, (1975).
- [24] Bradford M.M., A rapid method for the quantitation of microgram quantities of protein utilizing the principle of protein dye binding. *Anal Chem*, 72 (1973) 249–54.
- [25] Aebi H., Catalase in vitro Methods of Enzymatic Analysis. 2nd Ed, FL 121 (1974).
- [26] Ellman G.L, Courtney KD, Andres Jr V, Featherstone RM., A new and rapid colorimetric determination of acetylcholinesterase activity. *Biochem Pharmacol*, 7 (1961) 88–95.
- [27] Benachour N., Sipahutar H., Moslemi S., Gasnier C., Travert C., Seralini G.E., Time-and dose-dependent effects of roundup on human embryonic and placental cells. *Arch Environ Contam Toxicol*, 53 (2007) 126–33.
- [28] Mesnage R., Defarge N., Spiroux de Vendômois J., Seralini G.E., Major pesticides are more toxic to human cells than their declared active principles. *Biomed Res Int*, 26 (2014) 179691.
- [29] Nenni M., Toksikolojide in vitro Hücre Temelli Sitotoksosite Çalışmaları. Ege Üniversitesi Sağlık Bilimleri Enstitüsü Yüksek Lisans tezi (2019).
- [30] Bonomo M.M., Fernandes J.B., Carlos R.M., Fernandes M.N., Mitochondrial and lysosomal dysfunction induced by the novel metal-insecticide [Mg (hesp) 2 (phen)] in the zebrafish (*Danio rerio*) hepatocyte cell line (ZF-L). *Chem Biol Interact*, 307 (2019) 147–53.
- [31] Goulart T.L.S., Boyle R.T., Souza M.M., Cytotoxicity of the association of pesticides Roundup Transorb® and Furadan 350 SC® on the zebrafish cell line, ZF-L. *Toxicology in Vitro*, 29 (2015) 1377–84.
- [32] Kanat Ö.N., Selmanoğlu G., Neurotoxic effect of fipronil in neuroblastoma SH-SY5Y cell line. *Neurotox Res* 2020;37:30–40.
- [33] Karacaoğlu E., Flusilazole-induced damage to SerW3 cells via cytotoxicity, oxidative stress and lipid metabolism: An in vitro study. *Pestic Biochem Physiol*, 180 (2022) 104998.
- [34] Orta Yılmaz B., Sodyum florürün leydig hücrelerinde steroidogenik yolak üzerinde in vitro etkileri, İstanbul Üniversitesi, Fen Bilimleri Enstitüsü, Doktora tezi, (2017).
- [35] Bonomo M.M., Fernandes J.B., Carlos R.M., Fernandes M.N., Biochemical and genotoxic biomarkers and cell cycle assessment in the zebrafish liver (ZF-L) cell line exposed to the novel metal-insecticide magnesium-hesperidin complex. *Chemosphere*, 250 (2020) 126416.
- [36] Repetto M., Semprine J., Boveris A., Lipid peroxidation: chemical mechanism, biological implications and analytical determination. *Lipid Peroxidation*, 1 (2012) 3–30.
- [37] Gasnier C., Benachour N., Clair E., Travert C., Langlois F., Laurant C., et al., Dig1 protects against cell death provoked by glyphosate-based herbicides in human liver cell lines. *Journal of Occupational Medicine and Toxicology*, 5 (2010) 1–13.
- [38] Larsen K., Najle R., Lifschitz A., Virkel G., Effects of sub-lethal exposure of rats to the herbicide glyphosate in drinking water: glutathione transferase enzyme activities, levels of reduced glutathione and lipid peroxidation in liver, kidneys and small intestine. *Environ Toxicol Pharmacol*, 34 (2012) 811–8.
- [39] Van der Oost R., Beyer J., Vermeulen N.P.E., Fish bioaccumulation and biomarkers in environmental risk assessment: a review. *Environ Toxicol Pharmacol*, 13 (2003) 57–149.

## Temperature-Dependent Biochemical Alterations in *Oreochromis niloticus* exposed to Pendimethalin and Fluometuron

Derya Kocamaz<sup>1,a,\*</sup>, Mine Beyazaslan<sup>1,b</sup>, Aşkın Barış Kaya<sup>1,c</sup>

<sup>1</sup> Department of Biology, Faculty of Science and Arts, Cukurova University, 01330, Adana, Türkiye

\*Corresponding author

### Research Article

#### History

Received: 31/01/2025

Accepted: 11/05/2025



This article is licensed under a Creative Commons Attribution-NonCommercial 4.0 International License (CC BY-NC 4.0)

### ABSTRACT

Pesticides contamination and global warming are significant environmental challenges that threaten aquatic ecosystems. Aquatic organisms are often exposed to pesticide mixtures rather than individual compounds, leading to complex toxicological interactions that may enhance adverse effects. Additionally, temperature increase due to climate change can influence pesticide persistence and toxicity. This study aimed to investigate the combined biochemical effects of pendimethalin and fluometuron mixtures under different temperature conditions in the blood of *Oreochromis niloticus*. Fish were exposed to environmentally relevant low (0.1 ppb) and high concentrations (1 ppb) of herbicide mixtures for 96 hours at 22°C and 28°C. Results demonstrated significant interactions between pesticide concentration and temperature for all measured parameters. Cortisol level increased at 22°C in both pesticide-exposed groups compared to control, while it decreased at 28°C. Estradiol and testosterone levels were reduced 28°C in both exposure concentrations. Thyroid hormones (triiodothyronine (T<sub>3</sub>) and thyroxine (T<sub>4</sub>)) were reduced in the high concentration group at both temperatures. Alanine aminotransferase (ALT) and aspartate aminotransferase (AST) enzyme activities were decreased across both pesticide concentrations at both temperatures, except in the low concentration group at 28°C. Ion levels were also reduced in the high pesticide concentration at 28°C. Principal component analysis (PCA) confirmed that the most pronounced biochemical alterations were observed in the high concentration group at 28°C, reflecting the synergistic effect of both stressors. These findings suggest that elevated temperature exacerbates the toxic effect of pesticide mixtures, emphasizing the need to examine interactive stressors to better predict the impacts of climate change on non-target organisms.

**Keywords:** Aquatic toxicology, Biochemical biomarkers, Fish, Global warming, Pesticide mixtures.

<sup>a</sup> [drykocamaz@gmail.com](mailto:drykocamaz@gmail.com)

<sup>c</sup> [askinbaris@hotmail.com](mailto:askinbaris@hotmail.com)

<sup>b</sup> <https://orcid.org/0000-0002-0705-4672>

<sup>d</sup> <https://orcid.org/0009-0001-9274-7237>

<sup>e</sup> [minebeyazaslan@gmail.com](mailto:minebeyazaslan@gmail.com)

<sup>f</sup> <https://orcid.org/0009-0008-3899-0288>

## Introduction

Global warming, which significantly alters the Earth's climate through rising temperatures, represents one of the significant challenges in today's. Simultaneously, pesticide toxicity poses another serious threat to life on Earth, with profound implications for both environmental and public health [1]. A key question is how global warming, as a thermal stressor, and environmental pollution, as a chemical stressor interact to impact ecosystems. Some studies have reported the interactive effects of rising temperatures and pesticides on biota [2-3]. Research indicates that elevated temperatures enhance the uptake of pesticides and lead to alterations in the stress response and maintenance of homeostasis in organisms [4]. Researchers also predict an increase in pesticide usage in the coming decades due to the accelerated degradation of pesticides and the proliferation of pest species as a consequence of global warming [5]. Pesticides can also reach surface waters through agricultural runoff and spray drift, affecting non-target organisms such as fish. In addition to the widespread and indiscriminate use of pesticides in agriculture, unregulated domestic applications may also impact non-target organisms [6].

Pendimethalin is a dinitroaniline herbicide widely used to control weeds in both aquaculture and agriculture. It has a molecular weight of 281.3 g/mol, high lipophilicity (log KOW: 5.4 for pH:6.5 at 20°C), and low water solubility (0.33 mg/L at 20°C), which reflect a strong tendency to adsorb to sediments and may bioaccumulate in aquatic organisms [7-8]. Pendimethalin is environmentally persistent, with a hydrolysis half-life exceeding 365 days and photolysis half-lives reported approximately 21 days under continuous exposure [8]. Although its Groundwater Ubiquity Score (GUS) index indicates low leaching potential; environmental monitoring has detected pendimethalin concentrations of up to 0.9 µg/L in groundwater and ranging from 0.01 µg/L to 17.6 µg/L in surface water [9]. Notably, a recent study in Spain waters reported a mean concentration of 0.255±0.148 µg/L, exceeding the upper limit for human drinking water set by the European Union [10]. Pendimethalin has also been classified as a potential human carcinogen by the United States Environmental Protection Agency, increasing further concern about its environmental impact [11-12]. In aquatic organisms, reported effects of pendimethalin include erythrocyte abnormalities in *Cyprinus carpio*, a reduction in protein content in tissues such as the testes

and ovaries of spotted snakehead (*Channa punctata*), reproductive impairment through decreased testosterone levels, and oxidative stress in walking catfish (*Clarias batrachus*) due to altered antioxidant defense enzymes [10-12]. Fluometuron is a phenylurea herbicide widely used to control broadleaf weeds and grasses in agricultural crops [13]. It has a molecular weight of 232.2 g/mol, moderate lipophilicity (log KOW: 2.3) and relatively high-water solubility (110 mg/L at 20°C), reflecting greater mobility in aquatic environments [14]. Its GUS suggests a moderate to high leaching potential, raising concerns about contamination of water resources. Fluometuron is considered environmentally persistent, with a photolysis half-life of approximately 3 days in water and its hydrolysis half-life varies with pH, remaining stable at neutral pH. Reported concentrations of fluometuron range from 6.42-18.36 µg/L in surface waters of Spain, and from 1.95 to 317.6 µg/L in surface waters of North Greece [14-15]. Acute toxicity test report 96-hour LC<sub>50</sub> values of 170 mg/L for carp, 55 mg/L for catfish and 30 mg/L for rainbow trout [16]. Although fluometuron is classified as slightly toxic to aquatic organisms according to U.S. Environmental Protection Agency, fish may still exhibit high sensitivity to fluometuron through various mechanisms. Previous studies have demonstrated that phenylurea herbicides can disrupt endocrine function, including anti-androgenic effects in *Tilapia nilotica* and cause neurotoxic responses in zebra fish [17-20].

Selected pesticides, pendimethalin and fluometuron, are extensively used in Cukurova region, Southern Anatolia, predominantly for pest control in cotton agriculture. Previous studies have primarily focused on evaluating the individual effects of these pesticides on non-target organisms like fish. However, environmentally realistic assessments that consider multiple stressors simultaneously, such as pesticide mixtures combined with elevated temperatures, remain scarce in the current literature. Addressing this gap is necessary for understanding ecological impacts under realistic environmental scenarios and for improving environmental risk assessment. Therefore, this study aimed to investigate how elevated temperatures might influence the toxicity of pesticide mixtures. We hypothesized that higher temperature could increase the toxicity of pesticide mixture in fish. To test this hypothesis, we analyzed biochemical parameters in *O. niloticus* exposed to environmentally relevant concentrations of pendimethalin and fluometuron mixture at 22°C and 28°C for 96 hours. Specifically, we assessed reproductive hormone levels (cortisol, estradiol, testosterone), thyroid hormones (T<sub>3</sub> and T<sub>4</sub>), liver enzyme activities (ALT and AST) and ion concentrations (Na<sup>+</sup>, K<sup>+</sup>, Cl<sup>-</sup>) indicative of kidney function.

## Materials and Methods

### Animals

*O. niloticus* (33.67±1.57 g, 11.47±0.95 cm) samples were obtained from the Cukurova University Fish Culture Farm. Fish were acclimated for one month in 140 L glass aquaria filled with dechlorinated and aerated tap water. Water quality parameters were maintained as follows:

temperature 20±2°C, pH 8.01±0.73, dissolved oxygen 7.40±0.22 mg/L, alkalinity 261 mg/L CaCO<sub>3</sub>, and total hardness 285 mg/L CaCO<sub>3</sub>. A 12:12 h light-dark photoperiod was used throughout. Water was renewed daily by transferring the fish to freshly prepared aquaria, in accordance with standard protocols (APHA, AWWA, WPCF, 1998). Fish were fed ad libitum once daily with commercial pellets (Pınar, İzmir, Türkiye), and uneaten feed was removed to prevent water quality deterioration. All fish used in the experiments were maintained under identical laboratory conditions. All procedures were conducted in accordance with the Helsinki Declaration and approved by the local ethics committee (31.10.2023; 8).

### Experimental Design

In this study, the commercial formulations of pendimethalin [(N-(1-ethylpropyl)-3,4-dimethyl-2,6-dinitrobenzenamine), Stomp®, BASF, 450 g/L] and fluometuron [(1,1-dimethyl-3-(3-(trifluoromethyl)phenyl)urea), Cottonex®, ADAMA, 500 g/L], were used. Environmentally relevant, sublethal nominal concentrations were selected based on levels previously reported in surface waters [15,21]. Fish were exposed to these pesticides under semi-static conditions, in which test solutions were daily renewed by transferring fish into freshly prepared pesticide solutions to compensate for loss. Water temperature in the aquarium was maintained by an in-line chiller and a submerged heater set to 22°C and 28°C. Fish were not acclimated to the higher test temperature prior to pesticide exposure. No mortality was observed in any treatment groups during the exposure period. The experimental groups were arranged as follows:

**Control:** Fish maintained in pesticide-free tap water at 22°C and 28°C (n=6 per group).

**Low concentration pesticide mixture:** Fish exposed to a mixture of 0.1 ppb pendimethalin + 0.1 ppb fluometuron at 22°C and 28°C for 96 hours.

**High concentration pesticide mixture:** Fish exposed to a mixture of 1 ppb pendimethalin + 1 ppb fluometuron mixture at 22°C and 28°C for 96 hours.

The experiments were combined from three replicated independent experiments.

### Blood Collection and Analysis

At the end of the experiment, blood samples were collected from the caudal vein of each fish. Plasma was separated by centrifuging the blood samples at 4000 rpm for 15 minutes. Biochemical parameters, including reproductive hormone levels (cortisol, estradiol and testosterone), thyroid hormones (T<sub>3</sub> and T<sub>4</sub>), liver enzyme activities (ALT and AST) and ion concentrations (Na<sup>+</sup>, K<sup>+</sup> and Cl<sup>-</sup>) were performed using a Roche Cobas Integra 800 autoanalyzer. All analyses were performed on the same day that the blood samples were collected.

### Statistics

A Two-Way Analysis of Variance (ANOVA) was performed to assess the effects of pesticide concentration and temperature, as well as their interaction, on the measured biochemical parameters. Significant differences

between experimental groups were determined using the Student Newman-Keuls (SNK) post hoc test, with statistical significance set at  $P \leq 0.05$ . In addition, PCA analysis was conducted using standardized biochemical data to explore group separation patterns and to identify the variables contributing to pesticide-induced toxicity. All statistical analyses were conducted by GraphPad Prism 9.0 software. Data are presented as mean  $\pm$  standard deviation (SD).

## Results and Discussion

### Hormones

A Two-Way ANOVA conducted for all hormones revealed significant main effects for both concentration ( $P \leq 0.0001$ ) and temperature ( $P \leq 0.0001$ ), as well as for their interaction ( $P \leq 0.0001$ ). The SNK post-hoc test for individual group comparisons indicated that both pesticide exposures significantly increased cortisol levels at 22°C compared to the control group, while both low and high concentration exposures decreased cortisol levels at 28°C relative to the control group. No significant differences were observed between the two control groups (Table 1). The primary stress response in fish includes endocrinological changes, such as elevated

corticosteroid levels. Cortisol, a glucocorticoid hormone secreted by the adrenal glands, is widely recognized as a significant stress-related hormone in fish and is commonly used to evaluate the effects of various stressors, including xenobiotics, temperature, and photoperiod [22]. Cortisol also plays a key role in ion regulation and energy metabolism. In our study, elevated cortisol levels at 22°C were observed in response to both pesticide mixtures. Similarly, significant increases in cortisol levels have been reported in various fish species, including *O. mossambicus* exposed to chlorpyrifos, *Chanos chanos* exposed to endosulfan, *Labeo rohita* exposed to deltamethrin, and *Carassius auratus* exposed to a combination of pendimethalin and linuron [23-25]. In contrast, we found that elevated temperatures led to a reduction in cortisol levels in tilapia exposed to both pesticide mixtures for 96 hours. Few studies in the literature have demonstrated increased cortisol levels in response to elevated temperature [26]. However, a tendency for decreased cortisol levels in goldfish after 16 days of pesticide exposure at 32°C has also been reported [27]. This result suggests that thermal stress may disrupt the normal functioning of the hypothalamic-pituitary-adrenal axis in fish, altering the induction of a stress response to the pesticides.

Table 1. The results of hormone levels in *O. niloticus* exposed to pendimethalin and fluometuron mixtures at 22°C and 28°C for 96 hours.

Cortisol (ug/dL)	Control	Low Concentration	High Concentration
22 °C	9.01 $\pm$ 0.19 <sup>abx</sup>	10.20 $\pm$ 0.60 <sup>aby</sup>	14.12 $\pm$ 0.79 <sup>az</sup>
28 °C	9.68 $\pm$ 0.35 <sup>abw</sup>	1.91 $\pm$ 0.16 <sup>bt</sup>	8.59 $\pm$ 0.38 <sup>abv</sup>
Estradiol (pmol/L)			
22 °C	2012 $\pm$ 2.16 <sup>ax</sup>	1113 $\pm$ 3.59 <sup>ay</sup>	2217 $\pm$ 6.27 <sup>az</sup>
28 °C	5527 $\pm$ 4.65 <sup>bw</sup>	854.70 $\pm$ 5.47 <sup>bt</sup>	1476 $\pm$ 5.31 <sup>bv</sup>
Testosterone(ng/dL)			
22 °C	216.6 $\pm$ 2.66 <sup>ax</sup>	206.10 $\pm$ 4.19 <sup>ay</sup>	170.60 $\pm$ 1.71 <sup>az</sup>
28 °C	614.9 $\pm$ 4.14 <sup>bw</sup>	ND	245.90 $\pm$ 4.62 <sup>bv</sup>
T <sub>3</sub> (pg/mL)			
22 °C	9.33 $\pm$ 0.06 <sup>ax</sup>	9.22 $\pm$ 0.08 <sup>ax</sup>	7.56 $\pm$ 0.65 <sup>az</sup>
28 °C	11.61 $\pm$ 0.75 <sup>bw</sup>	ND	2.55 $\pm$ 0.09 <sup>bv</sup>
T <sub>4</sub> (ng/dL)			
22 °C	0.31 $\pm$ 0.01 <sup>ax</sup>	0.47 $\pm$ 0.00 <sup>aby</sup>	0.27 $\pm$ 0.00 <sup>az</sup>
28 °C	0.48 $\pm$ 0.01 <sup>abw</sup>	0.60 $\pm$ 0.01 <sup>bt</sup>	0.38 $\pm$ 0.00 <sup>bv</sup>

Different letters (x, y, z, w, t, v) in each row indicate statistically significant differences between concentrations and a-b letters in each column indicate statistically significant differences between temperatures ( $P \leq 0.05$ ). ND: Not Determined.

According to the post-hoc test, a reduction in estradiol levels was observed in the low concentration group at 22°C compared to the control, while estradiol levels increased in the high concentration group. Additionally, both low and high concentrations decreased estradiol levels at 28°C compared to the control group. On the other hand, estradiol levels were higher in the 28°C control group than in the 22°C control group. For testosterone

levels, the SNK post-hoc test revealed that both pesticide mixtures at 22°C and high concentration exposure at 28°C reduced testosterone levels compared to their respective control groups. However, testosterone levels were found to be higher in the 28°C control group than in the 22°C control group. Testosterone levels at the 28°C low concentration group were not detected due to being outside the reference range. Similar findings have been reported in previous studies. For instance, decreased testosterone levels were observed in *C. batrachus* exposed to pendimethalin, in Nile tilapia exposed to the phenylurea herbicide diuron, and in tilapia exposed to pesticide mixtures, which also showed decreased



estradiol and testosterone levels. Lower levels of estradiol and testosterone have also been observed in fish species exposed to temperatures higher than optimal [28]. The timing of spawning in several fish species is directly influenced by temperature and photoperiod. Temperature plays a significant role in gonadal development, gametogenesis, gamete quality, and embryo development [29]. Studies have shown that high temperatures can modify gonadotropin-releasing hormone secretion and gonadal steroidogenesis in fish [30]. In the present study, a possible explanation for the decreased steroid hormone levels in fish is that the pesticide mixture and elevated temperatures alter the gonadal biosynthetic capacity through the suppression of gonadotropin secretion.

The SNK post-hoc test revealed that  $T_3$  levels significantly decreased in the high concentration exposure for both temperatures compared to their respective controls (Table 1). No significant differences were observed between the low concentration exposure at 22°C and its control group. Additionally,  $T_3$  levels at the 28°C low concentration group were not detected due to out of reference range. For  $T_4$ , the SNK post-hoc test indicated that  $T_4$  levels increased in the low concentration group at both temperatures compared to the controls, whereas  $T_4$  levels decreased in the high concentration group at both temperatures.  $T_3$  and  $T_4$  levels were also found to be higher in the 28°C control group than in the 22°C control group. Thyroid hormones play a crucial role in brain development, growth, energy metabolism, immunity, and reproduction in fish. Pesticide exposure and temperature can affect thyroid function in fish. For example, high temperatures have been shown to increase the  $T_4$  degradation rate to  $T_3$  in trout, and combined pesticide exposure has been shown to alter circulating thyroid hormone levels in zebrafish, as well as decrease thyroid hormone levels in humans exposed to pesticides [31-33]. In this study, we found that  $T_3$  and  $T_4$  levels were more affected by both high concentration of pesticide mixtures and high temperature exposure compared to the optimal temperature condition. These findings suggest that changes in thyroid hormone levels may significantly

impact fish health by altering energy metabolism, immunity, and reproduction.

### Enzymes

For ALT and AST levels, a Two-Way ANOVA revealed significant main effects for both concentration ( $P \leq 0.0001$ ) and temperature ( $P \leq 0.0001$ ), as well as for their interaction ( $P \leq 0.0001$ ). The SNK post-hoc test for individual group comparisons showed that ALT levels decreased in both pesticide concentrations at 22°C and in the high concentration group at 28°C compared to their respective controls, whereas ALT levels increased in the low concentration group at 28°C compared to the control (Table 2). On the other hand, AST levels significantly decreased in both low and high concentration exposures at both temperatures compared to their controls. ALT and AST are primarily found in the liver and play key roles in transamination, which involves amino acid synthesis and the deamination pathway. These processes enable interconversion between carbohydrate and protein metabolism, especially during stress when organisms experience high energy demands [34]. The liver, as the main organ for detoxification, is highly sensitive to stress, making these enzymes important biomarkers in toxicological studies for evaluating fish health [35]. In this study, decreased levels of ALT and AST enzymes were observed in all experimental groups, except for the low concentration pesticide mixture at 28°C. Both enzymes were most affected under the combined conditions of high concentration and high temperature, with a 43% decrease in ALT and a 30% decrease in AST. The literature presents conflicting results regarding ALT and AST levels in fish exposed to stressors. Some studies have reported increased ALT and AST levels in catfish, carp, and tilapia exposed to pesticides, as well as in spotted seabass and rainbow trout subjected to thermal stress [35-38]. Conversely, other studies have shown decreased levels of these enzymes in fish exposed to pesticides [35-39]. In this study, the observed changes suggest that liver damage caused by pesticide toxicity likely alters the circulating levels of ALT and AST enzymes, which are critical indicators of hepatic function and fish health.

Table 2. The results of liver enzymes levels in *O. niloticus* exposed to pendimethalin and fluometuron mixtures at 22°C and 28°C for 96 hours.

ALT (U/L)	Control	Low Concentration	High Concentration
22 °C	43.30±1.74 <sup>ax</sup>	31.08±0.45 <sup>bwy</sup>	37.39±0.47 <sup>az</sup>
28 °C	32.24±0.34 <sup>bwy</sup>	40.03±0.17 <sup>bct</sup>	18.09±0.31 <sup>bcv</sup>
AST (U/L)			
22 °C	347.9±1.53 <sup>ax</sup>	254±3.90 <sup>ay</sup>	329.6±1.79 <sup>az</sup>
28 °C	423.3±2.05 <sup>bw</sup>	416.9±1.49 <sup>bt</sup>	292.5±3.46 <sup>bv</sup>

Different letters (x, y, z, w, t, v) in each row indicate statistically significant differences between concentrations and a-c letters in each column indicate statistically significant differences between temperatures ( $P \leq 0.05$ ).

### Ions

For ion levels, a Two-Way ANOVA revealed significant main effects for concentration ( $P \leq 0.0001$ ) and temperature ( $P \leq 0.0001$ ), as well as their interaction ( $P \leq 0.0001$ ). The SNK post-hoc test for individual group comparisons showed that  $Na^+$  levels increased in the low

concentration group at 28°C compared to the control, while they decreased in the high concentration group (Table 3). However, no significant differences were detected between groups at 22°C. Potassium levels significantly decreased in the low concentration group at 22°C and in both concentration groups at 28°C compared to their respective controls, whereas they increased in the high concentration group at 22°C. Chloride levels increased in the low concentration group at 28°C compared to the control but decreased in the high concentration group. No significant differences in Cl<sup>-</sup> levels were observed between groups at 22°C. Additionally, Na<sup>+</sup> and Cl<sup>-</sup> levels were lower in the 28°C control group than in the 22°C control group, while K<sup>+</sup> levels were higher in the 28°C control group than in the 22°C control group. Ion levels are widely recognized as bioindicators used to assess the homeostatic mechanisms

of organisms. Na<sup>+</sup>, K<sup>+</sup>, and Cl<sup>-</sup> levels play critical roles in osmoregulation and homeostasis in fish [37]. Specifically, Na<sup>+</sup> and K<sup>+</sup> are predominant ions that regulate acid-base balance, thereby maintaining ionic sufficiency for tissue function [37]. K<sup>+</sup> also plays a significant role in the nervous, secretory, and digestive systems [39]. Previous studies have demonstrated that pesticide exposure and temperature changes can alter ion levels in fish [38]. In our study, Na<sup>+</sup> and Cl<sup>-</sup> levels were not significantly affected by pesticide exposure at 22°C. However, significant changes in ion levels were observed in fish exposed to both pesticide concentrations at 28°C. These findings suggest that temperature significantly influences pesticide toxicity on the ion regulation, leading to abnormalities in ion levels and disrupting osmoregulatory mechanisms in fish.

Table 3. The results of ion levels in *O. niloticus* exposed to pendimethalin and fluometuron mixtures at 22°C and 28°C for 96 hours

Na <sup>+</sup> (mmol/L)	Control	Low Concentration	High Concentration
22 °C	154.80±2.98 <sup>abx</sup>	155.80±3.30 <sup>ax</sup>	151.00±2.94 <sup>abx</sup>
28 °C	135.00±2.58 <sup>bw</sup>	148.00±2.16 <sup>abt</sup>	125.30±3.86 <sup>bv</sup>
K <sup>+</sup> (mmol/L)			
22 °C	5.45±0.21 <sup>ax</sup>	4.71±0.12 <sup>ay</sup>	6.23±0.32 <sup>abz</sup>
28 °C	7.90±0.15 <sup>bw</sup>	6.97±0.12 <sup>bt</sup>	6.49±0.12 <sup>abv</sup>
Cl <sup>-</sup> (mmol/L)			
22 °C	137.70±1.12 <sup>abx</sup>	139.50±2.51 <sup>abx</sup>	135.90±2.52 <sup>abx</sup>
28 °C	122.00±2.16 <sup>bw</sup>	135.50±2.67 <sup>abt</sup>	114.00±2.96 <sup>bv</sup>

Different letters (x, y, z, w, t, v) in each row indicate statistically significant differences between concentrations and a-c letters in each column indicate statistically significant differences between temperatures (P≤0.05).

To integrate the biochemical alterations and understanding of the overall patterns of group separation, a PCA test was performed. The first two principal components explained a total of 66.1% of the variance in the dataset, with PC1 accounting for 37.9% and PC2 for 28.2%. The control group at 22°C clustered tightly, indicating physiological homeostasis under optimal conditions, whereas control group at 28°C exhibits clear shift along PC1, characterized by increased ions and sex hormones, suggesting that temperature alone may induce endocrine and ionic parameter changes. PCA results clearly showed that the high concentration mixture group at 28°C showed the most notable separation, indicating a synergistic effect of pesticide exposure and elevated temperature, likely leading to disruption in biochemical parameters. Interestingly, the low concentration exposure group at 28°C clustered unexpectedly close to the control group at 22°C rather than other groups at 28°C. This pattern may reflect adaptive mechanisms, compensatory physiological responses or individual variation. On the other hand, low and high concentration groups at 22°C showed intermediate separation, indicating concentration-dependent but thermally moderated biochemical changes. These findings

demonstrate that temperature is a critical modulator of concentration-dependent pesticide toxicity and may disrupt biochemical parameters (Figure 1).

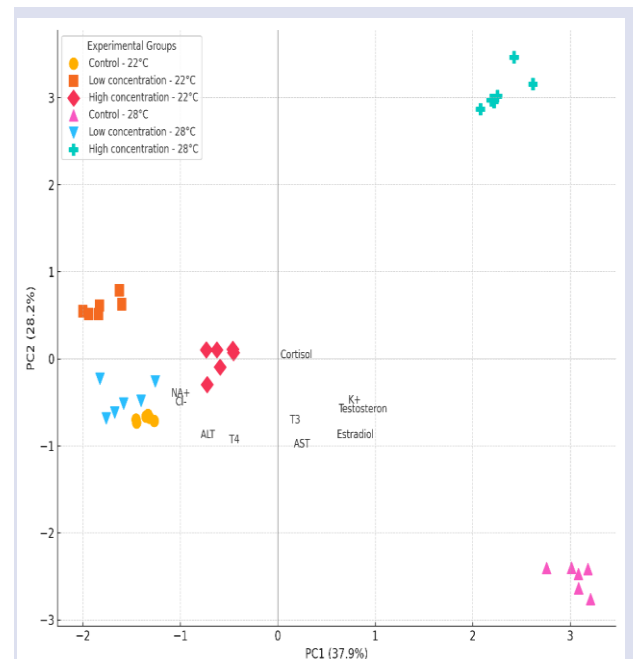


Figure 1. Principal component analysis (PCA) of biochemical alterations in *O. niloticus* exposed to pendimethalin and fluometuron mixtures at 22°C and 28°C for 96 hours.

## Conclusion

In summary, elevated temperatures exacerbated the toxicity of pendimethalin and fluometuron mixtures in *O. niloticus*. The interactive effects of acute exposure to multiple stressors disrupted endocrine function, detoxification mechanisms, and osmoregulatory processes. These findings were further supported by PCA, which confirmed clear group separation and identified important key biochemical markers contributing to concentration and temperature-dependent stress effects. This highlights the importance of assessing multiple environmental stressors, particularly under climate change conditions. Therefore, it is important to evaluate the effects of multiple stressors in non-target organisms are affected by ongoing global warming to take precautions.

## Limitations

Although this study provides important insights into the acute effects of pesticide mixtures and elevated temperature on blood biochemical parameters in *O. niloticus*, several limitations should be considered. First, the current findings reflect acute exposure outcomes and may not fully represent chronic or long-term physiological responses. Second, the study investigated only two temperature conditions; however, natural aquatic environments experience a broader range of thermal fluctuations, which may affect pesticide toxicity in different ways. Finally, although the selected biochemical parameters offer fast and practical indicators of environmental impact, additional analyses such as molecular and/or histological assessments could provide a more detailed understanding of the underlying mechanisms of pesticide toxicity. Future research should consider chronic, long-term, or seasonal exposure across broader temperature gradients and include additional analyses to enhance environmental risk assessment.

## Conflict of Interest

The authors declare no conflicts of interest.

## Acknowledgments

The author would like to thank Cukurova University (FBA-2025-17441).

## Ethical Approval

The experimental protocol was conducted in compliance with the Helsinki Declaration and approved by the ethics committee of the Cukurova University according to the guidelines for the care and use of animals in laboratory research (31.10.2023; 8).

## References

- [1] Muralikrishna I.V., Manickam V., Environmental Policies and Legislation, *Environmental Management*, (2017) 37–55.
- [2] Noyes P.D., Lema S.C., Forecasting the impacts of chemical pollution and climate change interactions on the health of wildlife, *Current Zoology*, 61(4) (2015) 669–689.
- [3] Marchand A., Haddad S., Simultaneous exposures to heat and chemicals and the impact on toxicokinetic and biomonitoring, *Current Opinion in Toxicology*, 4 (2017) 22–27.
- [4] Jacquin L., Gandar A., Aguirre-Smith M., Perrault A., Le Hénaff M., De Jong L., Paris-Palacios S., Laffaille P., Jean S., High temperature aggravates the effects of pesticides in goldfish, *Ecotoxicology and Environmental Safety*, 172 (2019) 255–263.
- [5] Choudhury P.P., Saha S., Dynamics of pesticides under changing climatic scenario, *Environmental Monitoring and Assessment*, 192(S1) (2021).
- [6] Philippe C., Thore E.S.J., Verbesselt S., Gregoir A.F., Brendonck L., Pinceel T., Combined effects of global warming and chlorpyrifos exposure on the annual fish *Nothobranchius furzeri*, *Ecotoxicology and Environmental Safety*, 248 (2022) 114290.
- [7] Luks A.-K., Zegarski T., Nowak K.M., Miltner A., Kästner M., Matthies M., Schmidt B., Schäffer A., Fate of Pendimethalin in Soil and Characterization of Non-Extractable Residues (Ner), *Science of the Total Environment*, 753 (2021).
- [8] Vighi M., Matthies M., Solomon K.R., Critical assessment of pendimethalin in terms of persistence, bioaccumulation, toxicity, and potential for long-range transport, *J. Toxicol. Environ. Health Part B*, 20(1) (2016) 1–21.
- [9] European Food Safety Authority, Peer review of the pesticide risk assessment of the active substance pendimethalin, *EFSA J.*, (2016).
- [10] Herrero-Hernandez E., Simon-Egea A.B., Sanchez-Martin M.J., Rodriguez-Cruz M.S., Andrades M.S., Monitoring and environmental risk assessment of pesticide residues and some of their degradation products in natural waters of the Spanish vineyard region included in the Denomination of Origin Jumilla, *Environmental Pollution*, 264 (2020) 114666.
- [11] Asman W.A., Jorgensen A., Bossi R., Vejrup K.V., Mogensen B.B., Glasius M., Wet deposition of pesticides and nitrophenols at two sites in Denmark: measurements and contributions from regional sources, *Chemosphere*, 59(7) (2005) 1023–1031.
- [12] Barba-Briosio C., Fernandez-Caliani J.C., Miras A., Cornejo J., Galan E., Multi-source water pollution in a highly anthropized wetland system associated with the estuary of Huelva (SW Spain), *Marine Pollution Bulletin*, 60(8) (2010) 1259–1269.
- [13] Udarbe Zamora E., Fluometuron, *Encyclopedia of Toxicology*, 340–342 (2005).
- [14] Gikas G.D., Vryzas Z., Koshis Z., Experiments on fluometuron removal from simulated agricultural wastewater in porous media filters, *Environ. Process.*, 9(1) (2021).
- [15] Coupe R.H., Welch H.L., Pell A.B., Thurman E.M., Herbicide and degradate flux in the Yazoo River Basin, *Int. J. Environ. Anal. Chem.*, 85 (2005) 1127–1140 [16] U.S. E.P.A., Chemical Information Fact Sheet Number 88:

- Fluometuron, *Office of Pesticides and Toxic Substances*, Washington, DC (1985).
- [16] de Almeida M.D., Pereira T.S.B., Batlouni S.R., Boscolo C.N.P., de Almeida E.A., Estrogenic and anti-androgenic effects of the herbicide tebuthiuron in male Nile tilapia (*Oreochromis niloticus*), *Aquatic Toxicology*, 194 (2018) 86–93.
- [17] Maharaj S., El Ahmadie N., Rheingold S., El Chehouri J., Yang L., Souders C.L., Martyniuk C.J., Sub-lethal toxicity assessment of the phenylurea herbicide linuron in developing zebrafish (*Danio rerio*) embryo/larvae, *Neurotoxicology Teratology*, 81 (2020) 106917.
- [18] Bojarski B.L., Swadźba-Karbowy M., Makulska J., Jakubiak M., Pawlak K., Tombarkiewicz B., Witeska M., Effects of herbicides pendimethalin and ethofumesate on common carp (*Cyprinus carpio*) erythrocyte morphology, *Folia Biologica*, 66(3) (2018) 143–149.
- [19] Gupta P., Verma S.K., Impacts of herbicide pendimethalin on sex steroid level, plasma vitellogenin concentration and aromatase activity in teleost *Clarias batrachus* (Linnaeus), *Environmental Toxicology and Pharmacology*, 75 (2020) 103324.
- [20] Herrero-Hernández E., Andrades M.S., Álvarez-Martín A., Pose-Juan E., Rodríguez-Cruz M.S., Sánchez-Martín M.J., Occurrence of pesticides and some of their degradation products in waters in a Spanish wine region, *J. Hydrol.*, 486 (2013) 234–245.
- [21] Lemos L.S., Angarica L.M., Hauser-Davis R.A., Quinete N., Cortisol as a stress indicator in fish: Sampling methods, analytical techniques, and organic pollutant exposure assessments, *International Journal of Environmental Research and Public Health*, 20(13) (2023).
- [22] Kumar N., Ambasankar K., Krishnani K., Gupta S., Bhushan S., Minhas P., Acute toxicity, biochemical, and histopathological responses of endosulfan in *Chanos chanos*, *Ecotoxicology and Environmental Safety*, 131 (2016) 79–88.
- [23] Suvetha L., Saravanan M., Hur J.H., Ramesh M., Krishnapriya K., Acute and sublethal intoxication of deltamethrin in an Indian major carp, *Labeo rohita*: Hormonal and enzymological responses, *Journal of Basic and Applied Zoology*, 72 (2015) 58–65.
- [24] Ghayyur S., Tabassum S., Ahmad M.S., Akhtar N., Khan M.F., Effect of chlorpyrifos on hematological and seral biochemical components of fish *Oreochromis niloticus*, *Pakistan Journal of Zoology*, 51(3) (2019) 1047–1052.
- [25] Chadwick J.G., Nislow K.H., McCormick S.D., Thermal onset of cellular and endocrine stress responses correspond to ecological limits in brook trout, *Conservation Physiology*, 3(1) (2015) cov017.
- [26] Gandar A., Laffaille P., Canlet C., Trembay-Franco M., Gautier R., Perrault A., Gress L., Mormede P., Tapie N., Budzinski H., Jean S., Adaptive response under multiple stress exposures in fish: From the molecular to the individual level, *Chemosphere*, 188 (2017) 60–72.
- [27] Alix M., Kjesbu O.S., Anderson K.C., From gametogenesis to spawning: How climate-driven warming affects teleost reproductive biology, *Fish Biology*, 97(3) (2020) 607–632.
- [28] Servili A., Canario A.V.M., Mouchel O., Munoz-Cueto J.A., Climate change impacts on fish reproduction are mediated at multiple levels of the brain-pituitary-gonad axis, *General and Comparative Endocrinology*, 291 (2020) 113439.
- [29] Pankhurst N.W., Thomas P.M., Maintenance at elevated temperature delays the steroidogenic and ovulatory responsiveness of rainbow trout (*Oncorhynchus mykiss*) to luteinizing hormone-releasing hormone analogue, *Aquaculture*, 166(1–2) (1998) 163–177.
- [30] Guo D., Liu W., Qiu J., Li Y., Chen L., Wu S., Qian Y., Changes in thyroid hormone levels and related gene expressions in embryo-larval zebrafish exposed to binary combinations of bifenthrin and acetochlor, *Ecotoxicology*, 29(5) (2020) 584–593.
- [31] Kongtip P., Nankongnab N., Pundee R., Kallayanatham N., Pengpumpkiat S., Chungcharoen J., Woskie S., Acute changes in thyroid hormone levels among Thai pesticide sprayers, *Toxics*, 9(1) (2021).
- [32] Little A.G., Kunisue T., Kannan K., Seebacher F., Thyroid hormone actions are temperature-specific and regulate thermal acclimation in zebrafish (*Danio rerio*), *BMC Biology*, 11 (2013) 26.
- [33] Samanta P., Pal S., Mukherjee A.K., Ghosh A.R., Evaluation of metabolic enzymes in response to Excel Mera 71, a glyphosate-based herbicide, and recovery pattern in freshwater teleostean fishes, *Biomed Research International*, (2014) 425159.
- [34] Qin H., Long Z., Huang Z., Ma J., Kong L., Lin Y., Li Z., A comparison of the physiological responses to heat stress of two sizes of juvenile spotted seabass (*Lateolabrax maculatus*), *Fishes*, 8(7) (2023) 340.
- [35] Sapana Devi M., Gupta A., Sublethal toxicity of commercial formulations of deltamethrin and permethrin on selected biochemical constituents and enzyme activities in liver and muscle tissues of *Anabas testudineus*, *Pesticide Biochemistry and Physiology*, 115 (2014) 48–52.
- [36] Phinrub W., Lunjirapan T., Srirum T., Kumjurnern K., Srisuttha P., Panase A., Panase P., Alterations of serum electrolytes and biochemical indices of *Pangasianodon gigas* subjected to different water temperatures and the appropriate temperature range for sustaining life, *Journal of Applied Animal Research*, 51(1) (2023) 342–349.
- [37] Davis K.B., Temperature affects physiological stress responses to acute confinement in sunshine bass (*Morone chrysops* × *Morone saxatilis*), *Comparative Biochemistry and Physiology A: Molecular & Integrative Physiology*, 139(4) (2004).
- [38] Pillans R.D., Anderson W.G., Good J.P., Hyodo S., Takei Y., Hazon N., Franklin C.E., Plasma and erythrocyte solute properties of juvenile bull sharks (*Carcharhinus leucas*) acutely exposed to increasing environmental salinity, *Journal of Experimental Marine Biology and Ecology*, 331(2) (2006) 145–157.



## Morphological, Transcriptional, and Epigenetics Alterations due to L-arginine and L-methionine Treatment in *Fusarium culmorum*

Fatma Berra Yücesan<sup>1,a</sup>, Özlem Sefer<sup>1,b</sup>, Emre Yörük<sup>1,c,\*</sup><sup>1</sup> Department of Molecular Biology and Genetics, Faculty of Sciences and Literature, Istanbul Yeni Yüzyıl University, Istanbul, Türkiye

\*Corresponding author

### Research Article

#### History

Received: 13/02/2025

Accepted: 11/05/2025



This article is licensed under a Creative Commons Attribution-NonCommercial 4.0 International License (CC BY-NC 4.0)

### ABSTRACT

*Fusarium culmorum* is a worldwide phytopathogenic fungus of small-grain cereals. Struggling strategies such as fungicide treatment and biocontrol agent usage are not long-term solutions due to the potential adverse effects on ecological environment and resistance development in fungal pathogens. In this study, potential suppressive effects of amino acid supplementation on *F. culmorum* were investigated. Potato dextrose agar (PDA) medium amended with 1 mg mL<sup>-1</sup> and 2 mg mL<sup>-1</sup> concentrations of L-arginine and L-methionine were used as experimental sets. PDA with no supplement and PDA amended with nicotinamide of 1 mg mL<sup>-1</sup> and 2 mg mL<sup>-1</sup> concentrations were used as negative and positive control sets, respectively. While L-arginine treatment led to significant increase in linear growth rate (LGR) with  $p < 0.01$ , L-methionine decreased LGR values ( $p < 0.001$ ). Coupled Restriction Enzyme Digestion-Random Amplification (CRED-RA) essays yielded very similar alterations in terms of genomic template stability within the experiment groups of L-arginine and L-methionine treated sets. UPGMA-dendrogram (unweighted pair group method with arithmetic mean) revealed co-clustering of L-methionine and nicotinamide treated sets. Methylation-specific PCR (MSP) analysis showed that there was Type-II and Type-III methylation present in 2 mg mL<sup>-1</sup> L-methionine treated sets. Gene expression analysis showed that L-methionine and L-arginine treatment led to contrast alteration in expressions of *tri6* and *FcStuA* genes with significant differences ( $p < 0.05$ - $p < 0.0001$ ). Our results showed that L-methionine treatment could suppress potential aggressiveness of *F. culmorum* at phenotypic, epigenetics, and transcriptional levels.

**Keywords:** *Fusarium culmorum*, Gene expression, CRED-RA, L-arginine, L-methionine.<sup>a</sup> [berrayucesan@gmail.com](mailto:berrayucesan@gmail.com)<sup>b</sup> <https://orcid.org/0009-0007-3289-8731><sup>c</sup> [emre.yoruk@yeniuyuzil.edu.tr](mailto:emre.yoruk@yeniuyuzil.edu.tr)<sup>d</sup> <https://orcid.org/0000-0003-2770-0157><sup>e</sup> [ozlem.sefer@yeniuyuzil.edu.tr](mailto:ozlem.sefer@yeniuyuzil.edu.tr)<sup>f</sup> <https://orcid.org/0000-0002-2711-5938>

## Introduction

Phytopathogenic fungi are responsible for various diseases of cereals, contamination of cereals by mycotoxins and associated risks to human and animal health [1,2]. Mycotoxins are natural secondary metabolites produced by various fungal species. These compounds are significantly different from most synthetic food contaminants. Their presence in food is almost inevitable and largely depends on climatic conditions that are difficult to control [2-4]. The only way to keep these substances in food at the lowest possible level is to observe good agricultural practices, ensure proper storage conditions, ensure crop diversity, use plant varieties resistant to fungal diseases, and apply fungicides [5-8]. Furthermore, fungus-infected seed grains are of lower quality and have lower yields, so the economic consequences must also be seriously considered.

*Fusarium* species are known worldwide as the causal agent of devastating diseases, especially in cereal crops of economic value (such as barley, wheat, maize, rice, rye, and oats), but they also infect a wide variety of plant species [9,10,8]. In Turkey and worldwide, *Fusarium* spp. infect cereal crops such as barley (*Hordeum vulgare* L.), wheat (*Triticum aestivum* L.), and maize (*Zea mays* L.), causing economic losses by causing head blight and crown rot. *F. culmorum* Schwabe is one of the most important

agents of spike blight and root rot [9, 11-13]. *F. culmorum* produces different types of mycotoxins including deoxynivalenol (DON), acetylated derivatives of DON, zearalenone, and fusarins, and these phytopathogenic fungi have been reported to present moderate- and high-level genetic diversity among different populations worldwide. Since there is still failure in disease management and increased epidemics, struggling with diseases caused by *F. culmorum* (and also *F. graminearum*) has been still interest of plant pathologist for management of head blight and crown rot [13-18].

*Fusarium* species have been reported to cause increasing adverse effects over larger areas due to climate changes caused by global warming [19-21]. Thus, disease epidemics should be monitored every year and precautions must be taken. In this context, different disease management strategies have been carried out for head blight and crown rot diseases including fungicide management, biocontrol agent usage, and resistant plant cultivation [6,11,22,23]. However, fungicide resistance development, increased genomic plasticity, adverse effects on environment, high labor efforts, long periods, and some other reasons could yield with failure in management of head blight and crown rot in fields [7,11,24]. Considering this situation, it is almost inevitable



to use alternative chemicals or to develop new approaches to control spike blight and root rot diseases.

In recent years, researches have been increasingly focused on understanding the molecular mechanisms underlying *Fusarium* pathogenicity and toxin production to develop more targeted control strategies. *FcStuA*, an APSES-type transcription factor in the phytopathogenic fungus *F. culmorum*, plays a crucial role in regulating fungal development, virulence, and secondary metabolism. Functional analyses have demonstrated that *FcStuA* is essential for the proper formation of reproductive structures and conidia, and its deletion results in significant morphological abnormalities [25,26]. Moreover, *FcStuA* contributes to the biosynthesis of the trichothecene mycotoxin deoxynivalenol (DON) by facilitating the transcriptional activation of *tri6* via recruitment of the SAGA (Spt-Ada-Gcn5 acetyltransferase) complex. The acetylation of *FcStuA* enhances its affinity for the *tri6* promoter, thereby promoting gene expression critical to mycotoxin production [27]. *FcStuA* regulates the expression of *tri6*, thereby indirectly controlling DON biosynthesis. This regulatory relationship is crucial for the pathogenicity of *F. culmorum* and its ability to produce trichothecene toxins *in planta*. Consequently, both *FcStuA* and *tri6* are considered key molecular targets in the development of strategies aimed at controlling Fusarium head blight (FHB) and reducing trichothecene contamination in cereal crops.

In this study, an alternative approach was investigated to combat the resistance of the *F. culmorum* pathogen to conventional agrochemicals by exploring epigenetic control strategies using adjuvant compounds on a reference strain of *F. culmorum*. Specifically, the study aimed to reveal potential suppressive effects of L-arginine and L-methionine amino acids on *F. culmorum* FcUK99 reference strain. The morphological, transcriptional, and epigenetics alterations by their treatment through various analytical approaches.

## Materials and Methods

### *In vitro* Growth Assays

*Fusarium culmorum* FcUK99 reference strain was kindly provided by Dr. Pierre Hellin (Walloon Agricultural Research Centre, Belgium). The fungal cultures were grown on the PDA (potato dextrose agar) media for 7 days at  $28 \pm 2^\circ\text{C}$ . PDA medium amended with  $1 \text{ mg mL}^{-1}$  and  $2 \text{ mg mL}^{-1}$  concentrations of L-arginine and L-methionine were used as experimental sets. PDA with no supplement and PDA amended with nicotinamide of  $1 \text{ mg mL}^{-1}$  and  $2 \text{ mg mL}^{-1}$  concentrations were used as negative and positive control groups, respectively. control and experimental sets were named as follows due to PDA medium content: FCC (Control set), FCARG1(PDA-amended with  $1 \text{ mg mL}^{-1}$  L-arginine), FCARG2 (PDA-amended with  $2 \text{ mg mL}^{-1}$  L-arginine), FCMET1 (PDA-amended with  $1 \text{ mg mL}^{-1}$  L-methionine), FCMET2 (PDA-amended with  $2 \text{ mg mL}^{-1}$  L-methionine), FCNIC1 (PDA-amended with  $1 \text{ mg mL}^{-1}$  nicotinamide), and FCNIC2 (PDA-

amended with  $2 \text{ mg mL}^{-1}$  nicotinamide). *In vitro* growth capacities of fungal cultures were analyzed by measuring the linear growth rate (LGR) on the 4<sup>th</sup> and 7<sup>th</sup> days. Each experiment set included at least three repeats. Statistical changes were tested using GraphPad Prism 9.0 software with confidence intervals of 0.05 and Dunnett's post-test.

### Coupled Restriction Enzyme Digestion-Random Amplification (CRED-RA) Assays

The genomic template stability (GTS) and genetic polymorphisms in L-arginine and L-methionine-treated *F. culmorum* were investigated via CRED-RA assay. First, genomic DNA (gDNA) was extracted from 7-day-old mycelia cultures. Then, diluted gDNA molecules were used in CRED-RA assays. A commercial kit (Anatolia Geneworks, Türkiye) was used to obtain gDNA. 50 mg fresh mycelium was homogenized using liquid nitrogen, a sterile pestle, and a sterile mortar. For binding, washing, and elution steps, the recommendations of the manufacturer were followed. 1.0% agarose gels and spectrophotometer (Thermo Fisher Scientific-Multiskan Go, U.S.A.) were used for the qualitative and quantitative gDNA analyses, respectively.

*MspI* and *HpaII* restriction enzymes were used to digest the gDNA of control and experimental sets. Digestion reactions were carried out in a volume of 50  $\mu\text{L}$  including 10 U of digestion enzyme (Thermo Fisher Scientific, U.S.A.), 1X reaction buffer with 0.1X BSA, and 500 ng gDNA. The digestion reaction was performed by two-step incubation processes including  $37^\circ\text{C}$  for 75 min and  $80^\circ\text{C}$  for 10 min. Non-digested gDNA of 50 ng  $\mu\text{L}^{-1}$  was used to form internal control set of CRED-RA. PCRs were carried out using common OPERON primers given in Table 1. The cycling conditions were as follows: Initial denaturation ( $94^\circ\text{C}$  for 5 min), 45 cycles of three steps (1 min at  $94^\circ\text{C}$ , 1 min at  $40^\circ\text{C}$ , and 2 min at  $72^\circ\text{C}$ ), and final elongation ( $72^\circ\text{C}$  for 10 min). PCR bands were separated using 1.7% agarose gels and visualized with a U.V. transilluminator. Bands were scored as "0" or "1" as being related to their absence or presence on the experimental set. GTS, similarity matrix, and unweighted pair group method with arithmetic mean (UPGMA) dendrogram was obtained using MVSP software combined with Nei and Li's coefficient [28].

### Methylation Specific PCR (MSAP)

Alteration in methylation on *FcStuA* and *tri6* genes which are related to asexual growth and trichothecene biosynthesis process were evaluated by MSA-PCR. Primers were designed in this study (Table 2). gDNA molecules which were non-digested (by any restriction enzyme), *MspI*-digested, and *HpaII*-digested were used in PCR assays. PCRs were conducted in a reaction volume of 25  $\mu\text{L}$  containing 50 ng gDNA, 1X PCR buffer, 2.5 mM  $\text{MgCl}_2$ , 0.1 mM dNTP mix, 10 pmol of each primer, 0.04 U  $\mu\text{L}^{-1}$  *Taq* DNA polymerase (Nepenthe, Türkiye). The cycling conditions included initial denaturation at  $94^\circ\text{C}$  for 5 min, a loop of 35 cycles ( $94^\circ\text{C}$  for 45 s,  $61^\circ\text{C}$  for 45 s,  $72^\circ\text{C}$  for 2

min), and final extension at 72°C for 5 min. PCR bands were separated on 1.7% agarose gels as described above.

### Quantitative Real-Time PCR (qRT-PCR) Assays

*tri6* (a zinc finger transcription factor) involved in DON biosynthesis and *FcStuA* (APSES protein) related to asexual growth, were used as target genes in qRT-PCR

assays. *β-tubulin* was used as an endogenous gene (Table 2).

Sybr Green-I reagent, QuantStudio 5.0 (Applied BioSystems-Thermo F.S., U.S.A.), and  $2^{-\Delta\Delta CT}$  formula [29] were used as dsDNA binding dye, thermal cycler, and fold change calculation formula, respectively. For this purpose, the total RNA was first extracted, and then the total RNA was converted to cDNA. cDNA was used in qRT-PCR assays.

Table 2. MSAP and qRT-PCR primers used in this study

Aim	Target gene	Primer set	5'-3' sequence (forward/ reverse)	Band size
MSAP	<i>FcStuA</i>	2SPANSTUA-F/R	ttccccaattgctagacctg / aaacacttcgcttgacctga	2001 bp
MSAP	<i>tri6</i>	spantri6F/R	taccaatcgtgtccctctc / cgccaaactcgtcatcattt	874 bp
qRT-PCR	<i>FcStuA</i>	stuartf/r	gcccctactggatacgatca / ttgccttctaggacattgg	100 bp
qRT-PCR	<i>tri6</i>	tri6qpcrf/r	acggtggattcaaccaagac / tggctactcgtccaacagtc	117 bp

The total RNA was extracted from 7-day-old fungal mycelium of 50 mg. Mycelium was extracted by using liquid nitrogen and 0.8 mL of NucleoZOL compound (Macherey-Nagel, Germany). The recommendations of the manufacturer were followed to obtain total RNA. After the qualitative (1% agarose gel) and quantitative (spectrophotometer, Thermo Fisher Scientific Inc.) analyses of RNA, cDNA conversion (from 1000 ng total RNA) was performed by a commercial cDNA synthesis kit following the protocol of the manufacturer (Nepenthe, Türkiye). The reactions were conducted in a 12 µL volume containing cDNA amount corresponding to 50 ng total RNA, 5 pmol of each primer, and 1X SYBR Green Mix (Episozyme, Türkiye). The cycling conditions were as follows: the pre-denaturation at 95°C for 2 min, the amplification with 40 cycles of 95°C for 15 s, 57°C for 20 s, and 72°C for 20 s, and the melting curve temperature scan step. Each Cp and fold change was recorded for each gene and experimental set separately.

## Results and Discussion

### In vitro Growth Assays

Linear growth rate (LGR) values were recorded in *F. culmorum* FcUK99 strain treated with L-arginine, L-methionine, and nicotinamide with two concentrations sets of 1 mg mL<sup>-1</sup> and 2 mg mL<sup>-1</sup>. The control set grown on PDA medium yielded 11.55±0.14 mm/day LGR values. LGR values for FCARG1 and FCARG2 were recorded as 13.40±0.31 and 13.42±0.30, respectively. In contrast to increased LGR values, L-methionine treatment decreased growth rate with LGR values of 9.01±0.23 (FCMET1) and 7.04±0.23 (FCMET2). Similar results were obtained from nicotinamide treatment with 8.51±0.23 (FCNIC1) and 7.39±0.18 (FCMET2). All comparisons among control and experimental sets by Dunnett's post-hoc test yielded significant changes from p<0.05 to p<0.0001 (Figure 1). These findings led to knowledge about the contrary effects of L-arginine and L-methionine on the *in vitro* growth capacity of *Fusarium* spp. Our findings align with previous studies on fungal organisms, which indicate that L-arginine treatment may serve as a positive regulator of asexual and/or sexual growth while acting as a negative

regulator of mycotoxin biosynthesis in fungi, including *Coniothyrium* spp., *Alternaria* spp., and *Fusarium* spp. [30–32]. Additionally, L-methionine's adverse effect on fungal growth, mycotoxin production, and plant-protective effect against fungal phytopathogenic species were present in previous studies.

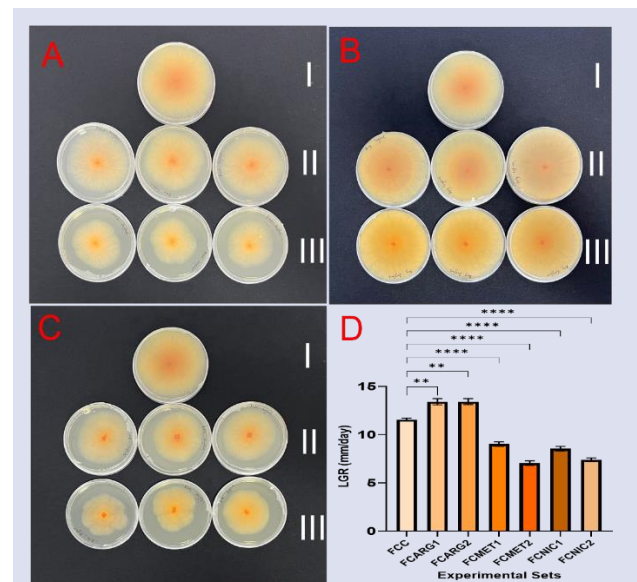


Figure 1 *in vitro* growth profile of L-methionine (A), L-arginine (B), and nicotinamide (C) treated *F. culmorum* FcUK99 strain on petri dishes (A, B, and C) and boxplot graphic (D). I, II, and III show 0 mg mL<sup>-1</sup>, 1 mg mL<sup>-1</sup>, and 2 mg mL<sup>-1</sup> concentrations of supplements, respectively. “\*\*\*” means significant changes with p<0.01 and “\*\*\*\*” means p<0.0001.

Our study revealed similar data on decreased fungal growth [33,34]. However, further studies could include *in planta* analysis including plant protective effects of L-methionine for *Fusarium* spp. and its plant host.

### CRED-RA Analysis

After checking the quality and the quantity of gDNA molecules, CRED-RA assays were carried out. In CRED-RA assays, 10 primers were used in PCRs. OPA3 and OPB9 yielded no amplicon in all experimental sets (Table 1).

Table 1. OPERON primers used in CRED-RA analysis

Primer	5'-3' sequence	GC%	Highest no of bands in any sample	Total band no	Polymorphic band no
OPM1	gttggtggtc	60	21	25	1
OPM4	ggcgttgtc	60	12	14	0
OPM7	ccgtgactca	60	17	18	0
OPM8	tctgttcccc	60	6	6	1
OPB9	tgggggactc	60	0	0	0
OPB13	ttccccgct	70	9	9	1
OPB14	tccgctctgg	70	11	11	1
OPG13	ctctccgcca	70	10	12	0
OPC5	gatgaccgcc	70	17	20	1
OPA3	agtcagccac	60	0	0	0

By excluding OPB9 from CRED-RA analysis, the amplicon numbers ranged from 6 (OPM8) to 25 (OPM1). Figure 2.A shows CRED-RA band profiling of OPG13 primer.

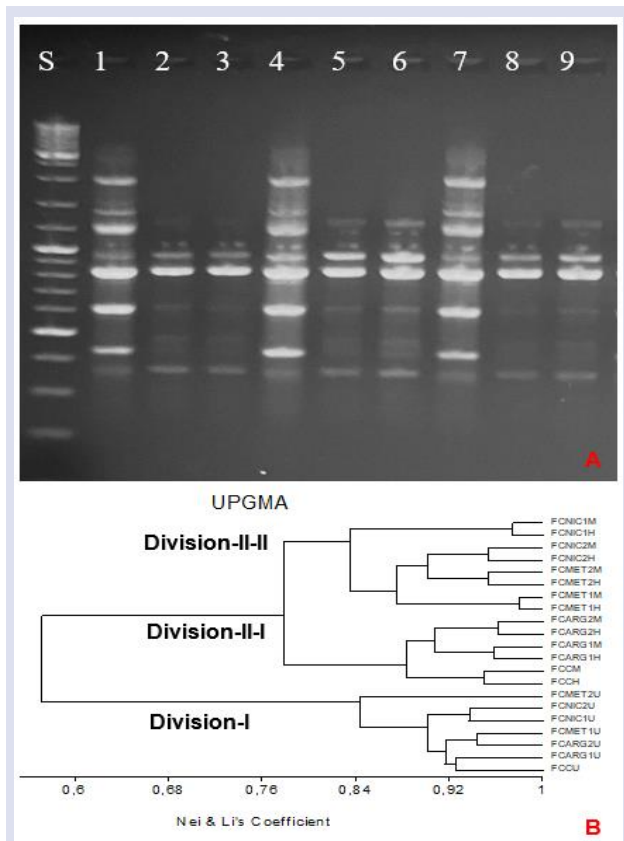


Figure 2. Agarose gel profiling of OPG13 primer (A) and UPGMA dendrogram of CRED-RA assay. U, M, and H means undigested, *MspI*-digested, and *HpaII*-digested samples, respectively. S: 1kb plus DNA ladder (Thermo, U.S.A.). Samples from "1" to "9" mean FCCU, FCCH, FCCM, FCNIC1U, FCNIC1H, FCNIC1M, FCNIC2U, FCNIC2H, FCNIC2M, respectively. U, H, and M also mean "undigested", "*HpaII*-digested", and "*MspI*-digested" samples.

The GTS values were recorded between 75.5% (FCMET2) and 100% (FCARG1). These findings were very consistent with the LGR analysis. L-arginine and L-

methionine yielded contrasting GTS values. In comparison to previous studies, a relatively moderate level of genomic template stability level was present in this study. Prednisone and Nair reported that prednisone treatment yielded up to a 66.6% decrease in GTS for *F. oxysporum* [35]. Similar findings with more than 50% GTS decrease were reported from studies including biotic and abiotic stress factors against *Fusarium* spp. [36,37].

Genetic diversity analysis combined with similarity matrix and UPGMA dendrogram showed that digestion type is decisive for the distribution and clustering of experimental sets into sub-divisions. According to the similarity matrix, the minimum genetic similarity value was 46.5% for FCARG2U, and FCNIC2H. The maximum genetic similarity value was recorded as 98% for FCMET1H and FCMET1M (data not shown). The almost homogenous distribution of enzyme-digestion profiling for experimental sets was detected via the UPGMA dendrogram (Figure 2.B). All the undigested samples were co-clustered in division I, while a nearly homogenous distribution of *HpaII* and *MspI* digested samples were clustered in sub-divisions II-I and II-II. In comparison to previous studies including *Fusarium* spp., nearly perfect, consistent, and very clear clustering of *F. culmorum* experimental sets present in this study [32-35]. However, in comparison to those investigations, methylation changes were analyzed via MSAP in this study.

### MSAP Analysis

*FcStuA* and *tri6* genes were amplified using the MSAP technique in undigested, *HpaII*-digested, and *MspI*-digested *F. culmorum* FcUK99 strains. The *FcStuA* gene was amplified from each experimental set at approximately 2 kb (Figure 3).

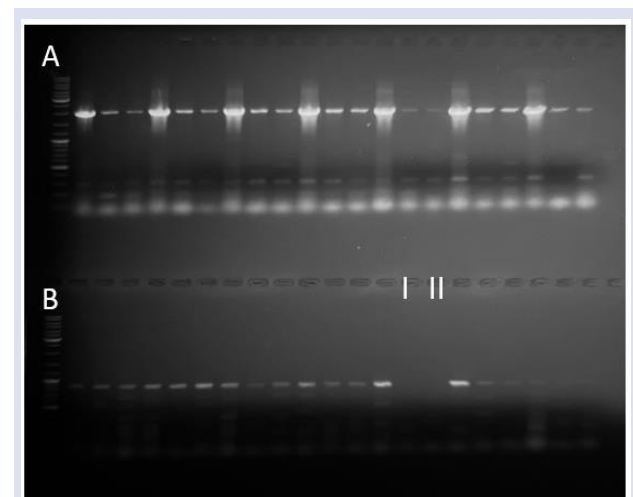


Figure 3. Agarose gel profiling of *FcStuA* (A) and *tri6* (B) MSAP assays. I: FCMET2H and II: FCMET2M. Samples were run on agarose gels with the same loading order as illustrated on Figure 2.

However, each set excluding FCMET2H and FCMET2M yielded amplicon for the *tri6* gene. This data is very important in terms of supporting our findings obtained

from LGR analysis. Increased concentrations of L-methionine resulted in an alteration in Type-II and Type-III methylation in the *F. culmorum* FcUK99 strain. However, no methylation alteration was detected for L-arginine-treated fungal samples. Type-II and Type-III methylation changes were detected in fungal genomes subjected to biotic or abiotic stress factors in previous studies[35–37]. Similar to the findings from a previous report of Albayrak et al. (2023), mycotoxin-related gene *tri5* showed Type-III methylation alteration in response to myrcene treatment [38]. It could be concluded that Type-II or Type-III methylation differentiation studies on fungal organism which are subjected to biotic and/or abiotic stress factors would be evaluated in terms of mycotoxin biosynthesis related genes.

### Gene Expression Analysis

After quality and quantity control of total RNAs extracted from experimental sets, qRT-PCR analysis was performed. *tri6* and *FcStuA* expression were normalized to the expression of  $\beta$ -tubulin (Table 3). *FcStuA* expression resulted in significantly altered expression between control and experimental sets (Figure 4).

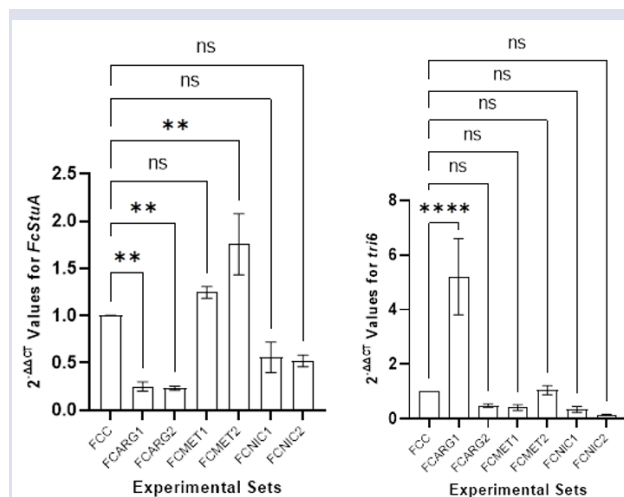


Figure 4. Fold changes in *FcStuA* (left-sided) and *tri6* (right-sided) gene expression levels in 7 experimental sets of *F. culmorum* treated with L-arginine, L-methionine, and nicotinamide. “ns” means “no significant changes- $p>0.05$ ”, “\*\*” means “significant changes with  $p<0.01$ ”, and “\*\*\*\*” means “significant changes with  $p>0.0001$ ”.

The upregulation in *FcStuA* expression could be evaluated as a positive regulator for stress factor presence in *Fusarium* spp [39,40]. Our findings revealed that L-methionine treatment led to increased expression of *FcStuA* gene in *F. culmorum* FcUK99 strain. In concordance with LGR data, it can be concluded that *FcStuA*, as a transcription factor, plays a crucial role in regulating responses to environmental changes and stress factors. Additionally, *tri6*, a zinc finger transcription factor involved in regulating DON biosynthesis, exhibited contrasting expression profiles between the FCARG and FCMET groups. As a result of gene expression analysis for

*tri6* toxin gene, it was determined that *tri6* expression level decreased with increasing concentrations of L-arginine, while the *tri6* expression level increased with increasing concentrations of L-methionine. It seems that 1 mg mL<sup>-1</sup> of L-methionine treatment *in vitro* and/or *in vivo* would be enough to decrease the DON biosynthesis. This concentration could be accepted as a relatively low or moderate level of potential antifungal treatment in comparison to previous investigations [38,41–43].

### Conclusion

*F. culmorum* reduces the quality and yield of the product in the cereal economy. In an effort to prevent this situation, the number of studies carried out to increase the quality and yield of the product is increasing. In this study, it was observed that L-arginine amino acid had a growth promoting effect on *F. culmorum*, while L-methionine had a growth suppressing effect. The potential antifungal effect of L-methionine treatment has been confirmed at morphological, epigenetic, and transcriptional levels with scientifically significant data. However, *in planta* studies are needed to confirm the usefulness of L-methionine supplements or combinations in the control of phytopathogenic organisms. Studies conducted on wheat and barley plants have demonstrated that the amino acids L-arginine and L-methionine can enhance plant growth and physiological responses under abiotic stress conditions such as drought. These amino acids appear to support the stress response mechanisms of plants, thereby exhibiting potential to improve agricultural productivity.

### Acknowledgments

This study was supported by Scientific and Technological Research Council of Türkiye (TUBITAK) under Grant Number 1919B012310447 (2209-A). The authors thank TUBITAK for their support.

### Conflict of Interest

The authors declare that they have no conflicts of interest for this work.

### References

- [1] Dean R., Van Kan J.A.L., Pretorius Z.A., Hammond-Kosack K.E., Di Pietro A., Spanu P.D., Rudd J.J., Dickman M., Kahmann R., Ellis J., Foster G.D., The Top 10 fungal pathogens in molecular plant pathology, *Mol. Plant Pathol.*, 13 (2012) 414–30.
- [2] Oğuz H., Mikotoksinler ve önemi, *Türk Klin. J. Vet. Sci. Pharmacol Toxicol-Spec Top.*, 3 (2017) 113–9.
- [3] Oruç H.H., Mikotoksinler ve tanı yöntemleri, *Uludağ Üniversitesi Vet. Fakültesi Derg.*, 24 (2005) 105–110.
- [4] Bakır Ö., Sekonder metabolitler ve rolleri, *Uluslar Anadolu Ziraat Mühendisliği Bilim Derg.*, 2 (2020) 39–45.



- [5] Cook R.J., Making Greater Use of Introduced Microorganisms for Biological Control of Plant Pathogens, *Annu. Rev. Phytopathol.*, 31 (1993) 53–80.
- [6] Moya-Elizondo E.A., Jacobsen B.J., Integrated management of Fusarium crown rot of wheat using fungicide seed treatment, cultivar resistance, and induction of systemic acquired resistance (SAR). *Biol. Control*, 92 (2016) 153–163.
- [7] Zubrod J.P., Bundschuh M., Arts G., Brühl C.A., Imfeld G., Knäbel A., Payraudeau S., Rasmussen J.J., Rohr J., Scharmüller A., Smalling K., Stehle S., Schulz, R., Schäfer, R.B., Fungicides: An Overlooked Pesticide Class? *Environ. Sci. Technol.*, 53 (2019) 3347–3365.
- [8] Alisaac E., Mahlein A.K., Fusarium head blight on wheat: biology, modern detection and diagnosis and integrated disease management, *Toxins* 15 (2023) 192.
- [9] Matny O.N., Fusarium head blight and crown rot on wheat & barley: losses and health risks, *Adv. Plants Agric. Res.*, 2 (2015) 00039.
- [10] Rampersad S.N., Pathogenomics and management of Fusarium diseases in plants, *Pathogens*, 9 (2020) 340.
- [11] Bai G., Shaner G., Management and resistance in wheat and barley to fusarium head blight, *Annu. Rev. Phytopathol.*, 42 (2004) 135–161.
- [12] Beccari G., Covarelli L., Nicholson P., Infection processes and soft wheat response to root rot and crown rot caused by *Fusarium culmorum*, *Plant Pathol.*, 60 (2011) 671–684.
- [13] Çepni E., Tunalı B., Gürel F., Genetic diversity and mating types of *Fusarium culmorum* and *Fusarium graminearum* originating from different agro-ecological regions in Turkey: Genetic diversity of *Fusarium* spp., *J. Basic Microbiol.*, 53 (2013) 686–694.
- [14] Wang H., Hwang S.F., Eudes F., Chang K.F., Howard R.J., Turnbull G.D., Trichothecenes and aggressiveness of *Fusarium graminearum* causing seedling blight and root rot in cereals, *Plant Pathol.*, 55 (2006) 224–230.
- [15] Desjardins A.E., Proctor R.H., Molecular biology of Fusarium mycotoxins, *Int. J. Food Microbiol.*, 119 (2007) 47–50.
- [16] Foroud N.A., Eudes F., Trichothecenes in cereal grains, *Int. J. Mol. Sci.*, 10 (2009) 147–173.
- [17] [Wang C., Zhang S., Hou R., Zhao Z., Zheng Q., Xu Q., Zheng, D., Wang, G., Liu H., Gao X., Ma J.W., Kistler H.C., Kang Z., Zu J.R., Functional analysis of the kinome of the wheat scab fungus *Fusarium graminearum*, *PLoS Pathog.*, 7 (2011) e1002460.
- [18] Yli-Mattila T., Rämö S., Hietaniemi V., Hussien T., Carlobos-Lopez A.L., Cumagun C.J.R., Molecular quantification and genetic diversity of toxigenic *Fusarium* species in Northern Europe as compared to those in Southern Europe, *Microorganisms* 1 (2013) 162–174.
- [19] Saharan M.S., Kumar J., Sharma A.K., Nagarajan S., Fusarium head blight (FHB) or head scab of wheat-a review, *PNAS Biol. Sci.*, 70(3) (2004) 255-268.
- [20] Yli-Mattila T., Gagkaeva T., Ward T.J., Aoki T., Kistler H.C., O'Donnell K., A novel Asian clade within the *Fusarium graminearum* species complex includes a newly discovered cereal head blight pathogen from the Russian Far East, *Mycologia*, 101 (2009) 841–852.
- [21] Saharan M.S., Current status of resistant source to Fusarium head blight disease of wheat: a review, *Indian Phytopathol.*, 72 (2020) 3–9.
- [22] Bolanos-Carriel C., Wegulo S.N., Baenziger P.S., Funnell-Harris D., Hallen-Adams H.E., Eskridge K.M., Effects of fungicide chemical class, fungicide application timing, and environment on Fusarium head blight in winter wheat, *Eur. J. Plant Pathol.*, 158 (2020) 667–79.
- [23] Noel Z.A., Roze L.V., Breunig M., Trail F., Endophytic Fungi as a Promising Biocontrol Agent to Protect Wheat from *Fusarium graminearum* Head Blight, *Plant Dis.*, 106 (2022) 595–602.
- [24] Różewicz M., Wyzińska M., Grabiński J., The most important fungal diseases of cereals—Problems and possible solutions, *Agronomy*, 11 (2021) 714.
- [25] Lysøe E., Pasquali M., Breakspear A., Kistler H.C., The Transcription Factor FgStuAp Influences Spore Development, Pathogenicity, and Secondary Metabolism in *Fusarium graminearum*, *Mol. Plant-Microbe Interactions*, 24 (2011) 54–67.
- [26] Xu C., Wang J., Zhang Y., Luo Y., Zhao Y., Chen Y., Ma, Z., The transcription factor FgStuA regulates virulence and mycotoxin biosynthesis via recruiting the SAGA complex in *Fusarium graminearum*, *New Phytol.*, 240 (2023) 2455–2467.
- [27] Niu G., Yang Q., Liao Y., Sun D., Tang Z., Wang G., Xu M., Wang C., Kang J., Advances in understanding *Fusarium graminearum*: Genes involved in the regulation of sexual development, pathogenesis, and deoxynivalenol biosynthesis, *Genes*, 15 (2024) 475.
- [28] Nei M., Li W.H., Mathematical model for studying genetic variation in terms of restriction endonucleases, *Proc. Natl. Acad. Sci.*, 76 (1979) 5269–5273.
- [29] Livak K.J., Schmittgen T.D., Analysis of relative gene expression data using real-time quantitative PCR and the 2- $\Delta\Delta CT$  method, *Methods*, 25 (2001) 402–408.
- [30] Gong X., Fu Y., Jiang D., Li G., Yi X., Peng Y., L-arginine is essential for conidiation in the filamentous fungus *Coniothyrium minitans*, *Fungal Genet. Biol.*, 44 (2007) 1368–1379.
- [31] Wang D., Meng L., Zhang H., Liu R., Zhu Y., Tan X., Wu Y., Gao Q., Ren X., Kong Q., Exogenous L-Arginine Enhances Pathogenicity of *Alternaria alternata* on Kiwifruit by Regulating Metabolisms of Nitric Oxide, Polyamines, Reactive Oxygen Species (ROS), and Cell Wall Modification, *J. Fungi*, 10 (2024) 801.
- [32] Wenhao L., Shikai H.U., Zhonghua S., Xiangjin W.E.I., Gui'ai J., Gaoneng S., Effects of Exogenous Amino Acids on the Mycelial Growth and Fumonisin Production of *Fusarium proliferatum*, *China Rice*, 30 (2024) 47.
- [33] Alwan A.H., Twaij B.M., Alwan B.H., Induction of *Allium sativum* tissue culture by L-methionine and gibberellic acid and study of the effect of extract against fungal plant pathogens, *Plant Arch.*, 20 (2020) 2839–2844.
- [34] El-Fawy M.M., Abdel-Fatah B.E., Saeed A.S., Abo-Elnaga H.I.G., Ameen A.M.M., Effect of soil drenching with humic acid, L-methionine and phosphoric acid on *Fusarium* wilt and induction of enzymes related to oxidative stress and defense in tomato plants, *Arch. Phytopathol. Plant Prot.*, 54 (2021) 1876–1895.
- [35] Harshitha K., Nair R.A., Evaluation of DNA Methylation Changes by CRED–RA Analysis Following Prednisone Treatment of Endophyte, *Fusarium oxysporum*, *Indian J. Microbiol.*, 60 (2020) 254–258.
- [36] Gazdağlı A., Sefer Ö., Yörük E., Varol G.İ., Tekler T., Albayrak G., Investigation of camphor effects on *Fusarium graminearum* and *F. culmorum* at different molecular levels, *Pathogens*, 7 (2018) 90.
- [37] Yörük E., Özkale E., Sefer Ö., Özsoy E., Trichoderma atroviride triggers alterations at epigenetics, transcripts, oxidative stress, and apoptosis levels on *Fusarium graminearum*, *J. Plant Pathol.*, 104 (2022) 1039–1047.



- [38] Albayrak G., Yörük E., Teker T., Sefer Ö., Investigation of antifungal activities of myrcene on *Fusarium* reference strains. *Arch. Microbiol.*, 205 (2023) 82.
- [39] Pasquali M., Spanu F., Scherm B., Balmas V., Hoffmann L., Hammond-Kosack K.E., Beyer M., Migheli Q., FcStuA from *Fusarium culmorum* controls wheat foot and root rot in a toxin dispensable manner, *PLoS One*, 8 (2013) e57429.
- [40] Rath M., Crenshaw N.J., Lofton L.W., Glenn A.E., Gold S.E., FvSTUA is a Key Regulator of Sporulation, Toxin Synthesis, and Virulence in *Fusarium verticillioides*, *Mol. Plant-Microbe Interactions*, 33 (2020) 958–971.
- [41] Pinson-Gadais L., Richard-Forget F., Frasse P., Barreau C., Cahagnier B., Richard-Molard D., Bakan B., Magnesium represses trichothecene biosynthesis and modulates Tri5, Tri6, and Tri12 genes expression in *Fusarium graminearum*, *Mycopathologia*, 165 (2008) 51–59.
- [42] Boutigny A.L., Barreau C., Atanasova-Penichon V., Verdal-Bonnin M.N., Pinson-Gadais L., Richard-Forget F., Ferulic acid, an efficient inhibitor of type B trichothecene biosynthesis and Tri gene expression in *Fusarium* liquid cultures, *Mycol Res.*, 113 (2009) 746–753.
- [43] Covarelli L., Turner A.S., Nicholson P., Repression of deoxynivalenol accumulation and expression of Tri genes in *Fusarium culmorum* by fungicides *in vitro*, *Plant Pathol.*, 53 (2004) 22–28.

## Non-Competitive Inhibition of Xanthine Oxidase by N-Nitrosomorpholine: An In Vitro Study

Deniz BAKIR <sup>1,a</sup>, Serkan KAPANCIK <sup>2,b,\*</sup>

<sup>1</sup> Biochemistry Laboratory, Medical Faculty Hospital, Sivas Cumhuriyet University, Sivas, Türkiye

<sup>2</sup> Department of Biochemistry, Faculty of Medicine, Sivas Cumhuriyet University, Sivas, Türkiye

\*Corresponding author

### Research Article

#### History

Received: 16/05/2024

Accepted: 13/05/2025




This article is licensed under a Creative Commons Attribution-NonCommercial 4.0 International License (CC BY-NC 4.0)


### ABSTRACT

Nitrosamines can be formed from nitrate. Nitrate is not actually toxic to mammals but can be reduced to nitrite. Nitrite, on the other hand, reacts with amino groups to form the carcinogenic N-nitroso compound. N-nitrosomorpholine (NMOR) is a carcinogenic compound that is included in the nitrosamine class and is the most common type of nitrosamines. Xanthine oxidase (XO) is an enzyme that catalyzes the hydroxylation of hypoxanthine to xanthine and xanthine to uric acid in purine metabolism. Excessive production and/or inadequate excretion of uric acid causes hyperuricemia. This condition is associated with kidney and cardiovascular diseases, especially gout. In order to prevent hyperuricemia and therefore gout, suppressing the activity of the XO enzyme is one of the main targets. In our study, the possible inhibitory effects of NMOR on the activity of the XO enzyme were investigated by spectrophotometric method. XO activity was evaluated in the presence of different concentrations of NMOR and analyzed using Lineweaver-Burk plot. The  $K_m$  value was determined as 0.55 mM and the  $V_{max}$  value was determined as 2.45 U/ml. Finally, it was determined that the XO enzyme was inhibited non-competitively by NMOR. Inhibition of XO enzyme with the help of NMOR may lead to functional deficiencies by disrupting the pathway in which purines are metabolized, as well as mediating the control of the production of uric acid formed in purine metabolism. More advanced methods and in vivo studies are needed to better understand the effects of NMOR on the organism and XO enzyme.

**Keywords:** Xanthine Oxidase, Nitrosamine, Nitrosomorpholine, Non-competitive inhibition, Purine metabolism.

 [denizbakir1314@hotmail.com](mailto:denizbakir1314@hotmail.com)

 <https://orcid.org/0000-0002-9255-3301>

 [serkankapancik@gmail.com](mailto:serkankapancik@gmail.com)

 <https://orcid.org/0000-0003-3019-4275>

## Introduction

Nitrosamines can be formed from nitrate. Nitrate is not actually toxic to mammals but can be reduced to nitrite. Nitrite reacts with amino groups to form the carcinogenic N-nitroso compound. Nitrosamines are known as amine derivatives containing the  $R_1R_2N-N=O$  functional group. Nitrosamine has been reported to be carcinogenic to humans by the International Institute for Research on Cancer [1,2]. In order to maintain the freshness of meat products and preserve their color and flavor, nitrate and nitrite salts are added to them during production. Thus, although the microbial load is reduced and the shelf life of meat products is improved due to its effects on *Salmonella*, *Clostridium botulinum*, and mesophilic bacteria, this process also brings some risks. Especially nitrites and nitrates added to meat products form N-Nitrosamine compounds as a result of reactions involving nitrosating agents. Therefore, consumption of meat products produced with the addition of additives such as nitrite and nitrate can result in the formation of N-nitrosamine through nitrosating agents in the presence of stomach acid. Nitrosamine formation causes the risk of diseases such as cancer and negatively affects public health [3,4].

NMOR is a carcinogenic compound that is included in the nitrosamine class and is the most common type of

nitrosamines. It is the nitrosamine with the fastest formation reaction. It can be formed as a result of the nitrosation reaction between morpholine and  $NaNO_2$ . The in-vivo synthesis of NMOR in the human body is quite high compared to its direct intake from the environment [5]. NMOR has been detected in sewage systems where wastewater is discharged, in workplace air, in tobacco products, and in drugs [6-9]. When NMOR was given to rats with drinking water, it was determined that it mediated hepatocarcinogenic formation, and also mediated changes in the expression of pyruvate kinase L and M2 isoenzymes, and the expression of pyruvate kinase L shifted towards the expression of pyruvate kinase M2 [10]. It was determined that morphological changes occurred in the bronchial epithelial cells of Syrian golden hamsters exposed to NMOR and that NMOR exposure mediated lung tumor formation in these animals [11]. However, in another study examining the development of oncogenic cells in the thyroid, adrenal gland, pituitary gland, pancreas, testis and femur bone of mice exposed to NMOR, oncogenic cells were detected in different endocrine tissues in more than half of the mice exposed to NMOR. Although the endocrine tissues in which these cells were observed varied from mouse to mouse, the thyroid, adrenal gland, pituitary gland and pancreas were

determined as the endocrine tissues in which these cells were observed [12].

The XO enzyme is an enzyme that catalyzes the hydroxylation of hypoxanthine to xanthine and xanthine to uric acid. It was first purified from cow's milk. It is found in nature in a highly protected form. This is because organisms in nature need to metabolize purines. However, the enzyme is found as a dehydrogenase in most organisms except mammals. Excessive production and/or inadequate excretion of uric acid causes hyperuricemia, which is a significant health problem worldwide. Hyperuricemia is caused by excess uric acid in the blood as a result of the destruction of nucleic acids such as adenine and guanine. This can cause kidney function losses, metabolic disorders, gouty arthritis and cardiovascular diseases. Since the uricase enzyme, which is found in many organisms and allows uric acid to be broken down into allantoin, is not found in humans, the XO enzyme, which is responsible for the synthesis of uric acid, is the main target for the treatment of hyperuricemia and gout caused by hyperuricemia. Although some compounds, especially allopurinol, topiroxostat and febuxostat, which have XO inhibition, have been discovered and used for therapeutic purposes in medicine, these compounds have undesirable side effects. Therefore, studies on new compounds that mediate XO inhibition are useful for human health. These inhibition studies of the enzyme are important for the determination of effective compounds or extracts that have the potential to be used in the treatment of diseases caused by the activity of XO [13-15].

In our study, we aimed to look at the effects of NMOR, which is one of the nitroso compounds we are exposed to through different factors in our environment, on purine metabolism. In line with this purpose, we examined the effect of NMOR on the activation of the XO enzyme in vitro.

## Materials and Methods

### XO Activity Determination

The basis of this method is the formation of uric acid from xanthine by the enzyme xanthine oxidase and the measurement of the formed uric acid spectrophotometrically at a wavelength of 293 nm. Xanthine oxidase activity is calculated from the amount of uric acid formed per unit time by the formula. 1  $\mu$ mol of urate formed per minute at pH 7.5 and 25°C was determined as one unit activity [16].

### NMOR Interaction with XO

In order to find the in vitro effect of NMOR on XO activity, enzyme activities were determined against 2, 1, 0.5 and 0.3 mM substrate concentrations. NMOR was added to 4 different substrate concentrations as an inhibitor at 0, 20, 40 and 60 mM concentrations and enzyme activity was determined. Vmax and Km values of XO enzyme were calculated by drawing Lineweaver-Burk plot.

## Results

Michaelis-Menten Plot was drawn according to the data obtained in vitro by using 4 different concentrations of XO enzyme substrate (2, 1, 0.5, 0.3 mM) (Figure 1) (Table 1).

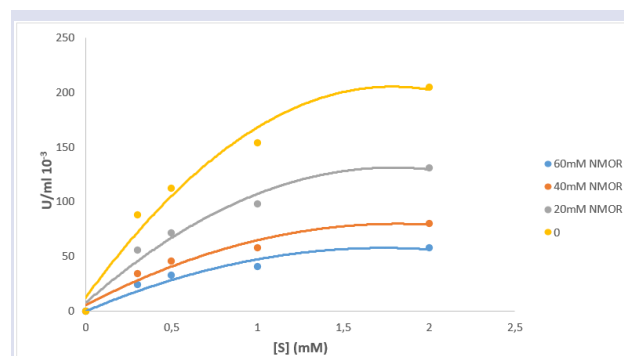


Figure 1. Michaelis-Menten Plot on inhibition of XO by NMOR

Lineweaver-Burk plot was drawn according to the data obtained in vitro by using 4 different concentrations of XO enzyme substrate (2, 1, 0.5, 0.3 mM). Vmax and Km values were calculated with the help of Lineweaver-Burk plot (Figures 2) (Table 2).

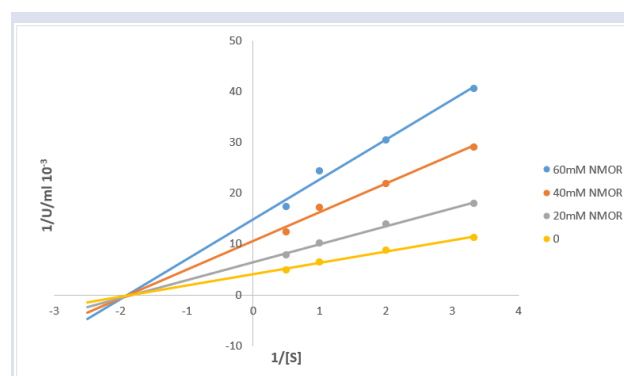


Figure 2. Lineweaver-Burk plot on inhibition of XO by NMOR

Table 2. Effects of NMOR on XO enzyme

	Inhibitor-free	20 mM NMOR	40 mM NMOR	60 mM NMOR
Vmax(U/ml).10 <sup>-4</sup>	2,45	1,59	0,95	0,67
Km(mM)	0,55	0,57	0,55	0,53

According to the data obtained from the Lineweaver-Burk curve, when NMOR inhibitor was not added to the reaction medium, Km of XO enzyme was determined as 0.55 mM and Vmax was determined as 2.45 U/ml 10<sup>-4</sup>. When 20 mM NMOR inhibitor is added, the Km of the XO enzyme is 0.57 mM, Vmax is 1.59 U/ml 10<sup>-4</sup>. When 40 mM NMOR inhibitor is added, the Km of the XO enzyme is 0.55 mM, Vmax is 0.95 U/ml 10<sup>-4</sup>. When 60 mM NMOR inhibitor is added, the Km of the XO enzyme is 0.53 mM, Vmax is 0.67 U/ml 10<sup>-4</sup> (Figure 2) (Table 2).

When the apparent  $K_m$  value ( $K_m$  value in the presence of inhibitor) and  $V_{max}$  values of the enzyme were determined for each NMOR concentration with the help of these curves, a remarkable decrease was detected in the  $V_{max}$  values of the enzyme with increasing NMOR concentration, as seen in Figure 2 and Table 2. In conclusion, non-competitive inhibition was confirmed as the  $V_{max}$  values decreased while the  $K_m$  values remained relatively unchanged.

## Discussion

NMOR is a nitrosamine with carcinogenic effects. In particular, it plays a role in the formation of hepatocellular carcinomas [17]. It is known that nitrosamines inhibit the activity of many enzymes involved in the regulation of metabolism [18]. However, the literature study investigating the effects of NMOR on metabolism-regulating enzymes is quite limited.

It is known that the XO enzyme is responsible for purine destruction. Hyperuricemia, which occurs as a result of an increase in the activity of the enzyme, causes neurodegenerative diseases, especially gout, as well as chronic diseases such as cardiovascular diseases, diabetes, and persistent wounds. Therefore, XO enzyme is the main target for eliminating hyperuricemia. Inhibitors of this enzyme are currently used in the clinic for the treatment of diseases. However, these inhibitors have serious side effects that can be fatal. Therefore, research on XO inhibitors that cause minimal toxicity in the organism and have high inhibitory activity is important [19,20]. Therefore, in our study, due to the limited literature on the roles of NMOR on enzymes involved in metabolism; in order to contribute to the potential inhibitor studies of XO enzyme, the in vitro effect of NMOR on XO enzyme was investigated. In this study, XO was interacted with NMOR in the reaction medium containing different concentrations of xanthine substrate. The activities found were graphed with Lineweaver-Burk. In the graph, it was seen that NMOR inhibited XO non-competitively. It was determined that the enzyme interacting with NMOR lost its activity. The reason for this may be that NMOR mediated the suppression of its activity by binding to the enzyme protein when released into the medium.

In non-competitive inhibition, the inhibitor interacts with the enzyme to prevent product formation, whether the substrate molecule is bound or not. The inhibitor binds to a region separate from the substrate. It changes the conformation of the enzyme. The enzyme and the inhibitor are not similar in structure. There is no competition in enzyme binding. Since the EIS complex is degraded more slowly than the ES complex, the product yield and enzyme speed slow down. In non-competitive inhibition,  $V_{max}$  values decrease while  $K_m$  values remain relatively unchanged [21]. As a result of our study, since  $V_{max}$  values decrease while  $K_m$  values remain relatively unchanged, it was concluded that XO enzyme inhibition via NMOR is non-competitive inhibition in vitro. The in

vitro results obtained from this study may indicate that NMOR can also inhibit purine degradation via XO enzyme in vivo. Thus, we can say that NMOR can prevent hyperuricemia in the body and the emergence of patients with hyperuricemia. However, in order to speak more definitively about the in vivo effects of NMOR on the XO enzyme, in vivo studies are needed on this subject.

## Conclusions

We can say that NMOR has a non-competitive inhibitory effect on the purine metabolism enzyme XO in in vitro conditions, and that in this respect, NMOR may mediate the suppression of uric acid synthesis resulting from purine destruction in the body, and thus the hyperuricemia state. However, in vivo studies are needed to be sure about this issue.

## Conflicts of interest

There are no conflicts of interest in this work.

## Acknowledgement

There is no acknowledgement.

## References

- [1] Swann P.F., The toxicology of nitrate, nitrite and n-nitroso compounds, *Journal of the Science of Food and Agriculture*, 26 (11) (1975) 1761-1770.
- [2] Ozbay S., Sireli U.T., Filazi A., Nitrosamines, their chemistries and effects on health, *Int. J. Sci. Technol. Res.*, 5 (4) (2019) 124-133.
- [3] Deveci G., Tek N.A., N-Nitrosamines: a potential hazard in processed meat products. *Journal of the Science of Food and Agriculture*, 104 (5) (2024) 2551-2560.
- [4] Xie Y., Geng Y., Yao J., Ji J., Chen F., Xiao J., ... & Ma L., N-nitrosamines in processed meats: Exposure, formation and mitigation strategies. *Journal of Agriculture and Food Research*, 13 (2023) 100645.
- [5] Li Y., Hecht S.S., Metabolic activation and DNA interactions of carcinogenic N-nitrosamines to which humans are commonly exposed, *International journal of molecular sciences*, 23 (9) (2022) 4559.
- [6] Zhao B., Zhou J., Nakada N., Ihara M., Liu Y., Wong Y.J., ... & Tanaka H., COVID-19 impacts on characterization of N-nitrosamines and their precursors during transport in sewer systems, *Water Research*, 279 (2025) 123439.
- [7] Meng X.J., Liu X.D., Zhang X.M., Hu Y., Guo Q.F., Determination of 8 N-nitrosamines in the workplace air by GC-MS/MS method, *Chinese journal of industrial hygiene and occupational diseases*, 42 (8) (2024) 616-620.
- [8] Brunnemann K.D., Hoffmann D., Decreased concentrations of N-nitrosodiethanolamine and N-nitrosomorpholine in commercial tobacco products, *Journal of agricultural and food chemistry*, 39 (1) (1991) 207-208.
- [9] Schmidtsdorff S., Neumann J., Schmidt A.H., Parr M.K., Prevalence of nitrosamine contaminants in drug samples: Has the crisis been overcome?, *Archiv der Pharmazie*, 356 (2) (2023) 2200484.

- [10] Steinberg P., Klingelhöffer A., Schäfer A., Wüst G., Weisse G., Oesch F., Eigenbrodt E., Expression of pyruvate kinase M 2 in preneoplastic hepatic foci of N-nitrosomorpholine-treated rats, *Virchows Archiv*, 434 (1999) 213-220.
- [11] Reznik-Schüller H., Sequential morphologic alterations in the bronchial epithelium of Syrian golden hamsters during N-nitrosomorpholine-induced pulmonary tumorigenesis, *The American Journal of Pathology*, 89 (1) (1977) 59.
- [12] Gezer E., Özer C., Şimşek T., Yaprak Bayrak B., Turan G., Çetinarslan B., ... & Köksalan D., N-Nitrosomorpholine-induced oncogenic transformation in rat endocrine organs, *European Journal of Medical Research*, 29 (1) (2024) 64.
- [13] Kostić D.A., Dimitrijević D.S., Stojanović G.S., Palić I.R., Đorđević A.S., Ickovski J.D., Xanthine oxidase: isolation, assays of activity, and inhibition, *Journal of chemistry*, 2015 (1) (2015) 294858.
- [14] Hille R., Xanthine oxidase—a personal history, *Molecules*, 28 (4) (2023) 1921.
- [15] Ullah Z., Yue P., Mao G., Zhang M., Liu P., Wu X., ... & Yang L., A comprehensive review on recent xanthine oxidase inhibitors of dietary based bioactive substances for the treatment of hyperuricemia and gout: Molecular mechanisms and perspective, *International Journal of Biological Macromolecules*, (2024) 134832.
- [16] Massey V., Brumby P E., Komai H., Palmer G., Studies on milk xanthine oxidase: some spectral and kinetic properties, *Journal of Biological Chemistry*, 244 (7) (1969) 1682-1691.
- [17] Masui T., Nakanishi H., Inada K.I., Imai T., Mizoguchi Y., Yada H., ... & Tatematsu M., Highly metastatic hepatocellular carcinomas induced in male F344 rats treated with N-nitrosomorpholine in combination with other hepatocarcinogens show a high incidence of p53 gene mutations along with altered mRNA expression of tumor-related genes, *Cancer letters*, 112 (1) (1997) 33-45.
- [18] Alston T.A., Porter D.J., Bright H.J., Enzyme inhibition by nitro and nitroso compounds, *Accounts of Chemical Research*, 16 (11) (1983) 418-424.
- [19] Singh A., Singh K., Sharma A., Kaur K., Chadha R., Bedi P.M.S., Past, present and future of xanthine oxidase inhibitors: design strategies, structural and pharmacological insights, patents and clinical trials, *RSC Medicinal Chemistry*, 14 (11) (2023) 2155-2191.
- [20] Yu D., Du J., He P., Wang N., Li L., Liu Y., ... & Li Y., Identification of natural xanthine oxidase inhibitors: Virtual screening, anti-xanthine oxidase activity, and interaction mechanism, *International Journal of Biological Macromolecules*, 259 (2024) 129286.
- [21] Onat T., Emerk K., Sözmén E., İnsan biyokimyası, Palme yayıncılık, (2002) 208.



## The Effect of NKCC1 Inhibitor Azosemide on Emotional Behaviors and Hippocampal GABA Levels in a Rat Model of Post-traumatic Stress Disorder

Sebahattin Karabulut<sup>1,a,\*</sup>, Sumeysra Koc<sup>1,b</sup>, Aysegul Ozturk<sup>1,c</sup>

<sup>1</sup> Department of Medical Services and Techniques, Vocational School of Health Services, Sivas Cumhuriyet University, Sivas, Türkiye

\*Corresponding author

### Research Article

#### History

Received: 22/01/2025

Accepted: 13/05/2025



This article is licensed under a Creative Commons Attribution-NonCommercial 4.0 International License (CC BY-NC 4.0)

### ABSTRACT

Post-traumatic stress disorder (PTSD) is an anxiety disorder that can occur immediately or years after exposure to a traumatic event. Despite extensive research, the etiology of PTSD is largely unknown, but it is thought that impaired GABAergic transmission may play a role in the disease process. Using a single prolonged stress (SPS) procedure, we aimed to determine the effect of azosemide, a sodium-potassium-chloride cotransporter (NKCC1) inhibitor, on anxiety and memory-related behaviors and hippocampal GABA level in rats. Behavioral tests were performed by open field test and passive avoidance test, while hippocampal GABA levels were determined by ELISA. We found that azosemide treatment partially improved emotional behavior and significantly improved memory performance in rats with PTSD, without affecting the decline in hippocampal GABA levels induced by a SPS exposure. These findings suggest that azosemide may offer partial therapeutic benefits for symptoms of PTSD, particularly cognitive deficits. However, they underscore the necessity for multimodal approaches to address the various neurobiological underpinnings of the disorder.

**Keywords:** Post-traumatic stress disorder, Azosemide, Hippocampus, Rat.

<sup>a</sup> [skkarabulut@yandex.com](mailto:skkarabulut@yandex.com)

<sup>b</sup> <https://orcid.org/0000-0002-3261-4125>

<sup>c</sup> [skoc8747@gmail.com](mailto:skoc8747@gmail.com)

<sup>d</sup> <https://orcid.org/0009-0004-7328-788X>

<sup>e</sup> [aysegulozturk@cumhuriyet.edu.tr](mailto:aysegulozturk@cumhuriyet.edu.tr)

<sup>f</sup> <https://orcid.org/0000-0001-8130-7968>

## Introduction

Posttraumatic stress disorder (PTSD) is a psychological condition that can develop following exposure to a traumatic event, such as war, natural disasters, sexual assault or serious accidents [1]. PTSD is characterized by a constellation of symptoms, including intrusive memories, hyperarousal, avoidance behaviors, and negative changes in cognition and mood [2]. These symptoms significantly impair individuals' daily functioning and overall quality of life. PTSD has been recognized as a distinct psychiatric disorder since its inclusion in the Diagnostic and Statistical Manual of Mental Disorders (DSM-III) in 1980 [3]. The estimated prevalence of PTSD in the general population ranges from 6 to 8 percent; however, specific populations, such as military veterans and first responders, demonstrate significantly higher rates [4]. For instance, it is estimated that up to 30 percent of military veterans may experience PTSD because of combat-related trauma. In recent years, the significance of PTSD has garnered increased attention, particularly following the COVID-19 pandemic, which has highlighted its effects on healthcare professionals and individuals who have suffered loss [5].

The pathophysiology of PTSD is complex and multifactorial, involving dysregulation of the hypothalamic-pituitary-adrenal (HPA) axis, alterations in neurotransmitter systems, and both structural and functional changes in key brain regions, including the amygdala, hippocampus, and prefrontal cortex [6], [7]. These neurobiological changes are believed to underlie the hallmark symptoms of PTSD, including increased

reactivity to trauma-related cues and a diminished ability to regulate emotions and manage stress. Recent advancements in neuroimaging and molecular genetics underscore the significant role of both genetic and environmental factors in the development of PTSD. Contemporary treatment approaches generally involve a combination of pharmacotherapy-primarily selective serotonin reuptake inhibitors (SSRIs) and GABAergic medications-along with trauma-focused cognitive behavioral therapy, which is the primary modality of psychotherapy [3]. Recently, emerging modalities, including psychedelics, ketamine, and neuromodulation techniques, have been investigated as potential interventions for treatment-resistant PTSD [8]. Despite the availability of various treatments, many individuals diagnosed with PTSD do not achieve complete recovery. This highlights the necessity for ongoing research into novel therapeutic approaches.

Azosemide is a loop diuretic primarily used to treat conditions characterized by fluid overload, such as heart failure, renal failure, and hypertension [9]. Azosemide operates by inhibiting the sodium-potassium-chloride cotransporter (NKCC1) in the ascending thick limb of the loop of Henle, resulting in increased excretion of sodium, chloride, and water [10]. This inhibition leads to an increased excretion of sodium, chloride, and water. The diuretic effect of azosemide decreases plasma volume and alleviates symptoms associated with fluid retention. Azosemide demonstrates a powerful diuretic effect and

has a longer duration of action compared to furosemide, another loop diuretic. This property allows azosemide to be an effective tool in the clinical treatment of edema and hypertension. However, azosemide has also garnered attention for its ability to restore neurotransmission balance, presenting a novel therapeutic strategy [11], [12]. Specifically, the capacity of azosemide to inhibit NKCC1 within the central nervous system may have broader implications for its application in psychiatric disorders. NKCC1 plays a crucial role in regulating the intracellular chloride concentration ( $[Cl^-]_i$ ) within neurons, functioning as a cation-chloride cotransporter that facilitates the accumulation of  $Cl^-$  ions in the neuronal cytosol [13]. Consequently, NKCC1 is integral to the maintenance of the chloride gradient in neurons, which is essential for the proper functioning of gamma-aminobutyric acid (GABA) receptors. The dysregulation of this gradient may play a significant role in the pathophysiology of PTSD, particularly concerning altered inhibitory neurotransmission and increased neuronal excitability [14]. Azosemide may facilitate the restoration of normal chloride homeostasis through the inhibition of NKCC1, which may subsequently alleviate symptoms of hyperarousal and anxiety associated with PTSD by enhancing GABAergic inhibition. Considering this information, we conducted an investigation into the effects of azosemide treatment on emotional behavior and hippocampal GABA levels in a rat model of PTSD to elucidate the potential preventive role of azosemide in alleviating symptoms associated with PTSD.

## Material and Method

### Animals and Treatments

Eighteen male Wistar Albino rats, each weighing between 200-250 grams, were utilized in this study. The experimental subjects were divided into three distinct groups:

- 1) Control group; it was not exposed to any stressors,
- 2) Post-traumatic stress disorder (PTSD) group; it consisted of subjects that were subjected to a SPS exposure,
- 3) PTSD + Azosemide (PTSD + AZO) group; it consisted of animals that were administered azosemide at a dosage of 5 mg/kg i.p. after trauma exposure.

To create an animal model of PTSD, rats underwent a SPS exposure protocol (Figure 1). Among the various animal models of PTSD that have been used to imitate the basic symptoms, such as anxiety and fear-related behaviors, the SPS protocol has consistently demonstrated good face validity for the PTSD condition in humans. In this model, anxiety-related behavioral disorders are used as an indicator of the severity of the PTSD-like phenotype, and this provides us with a reliable measure to assess the possible contribution of posttraumatic azosemide treatment to the development of PTSD. Initially, the animals were confined in an apparatus that immobilized them for two hours. Subsequently, they were placed in a tank (124 cm in diameter and 32 cm in depth) filled with water at 22°C, where they experienced 20 minutes of forced swimming.

Following this, they were placed in an isolated apparatus where they were exposed to ether until unconsciousness occurred [15].

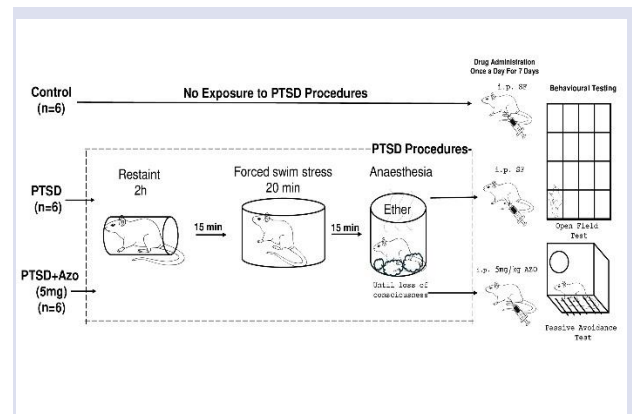


Figure 1. Experimental protocol.

The animals except for the control group were subjected to 2 hours of restraint, 20 minutes of forced swimming stress and ether until unconsciousness, respectively. AZO: Azosemide, PTSD: Post-traumatic stress disorder, PTSD + AZO: Post-Traumatic Stress Disorder + Azosemide.

Previous studies have shown that NKCC inhibitors, including azosemide, penetrate the brain by crossing the blood-brain barrier and act by binding to these receptors [12], [16]. The rats in the PTSD + AZO group were administered azosemide at a dose of 5 mg/kg i.p. for 7 days following exposure to a traumatic event. On the 8th day, behavioral assessments, including open field and passive avoidance tests, were conducted on all subjects. After the 9th day, all animals were euthanased by ethical guidelines, and hippocampal tissue samples were collected under sterile surgical conditions for the subsequent measurement of GABA levels. All procedures involving the animals were conducted with the approval of the Sivas Cumhuriyet University Animal Experiments Local Ethics Committee (Decision No: 65202830-050.04.04-72).

### Open Field Test

This experiment was conducted to evaluate the emotional behavior and locomotor activity of animals within a platform measuring 100 cm×100 cm×30 cm, which was subdivided into 16 equal squares. Individual rats were placed in the center of the platform and permitted to move freely for 5 min. During this period, the activities of the animals were recorded via video, and subsequent analyses were performed on the number of frames traversed, as well as instances of rearing and grooming behavior [17].

### Passive Avoidance Test

The passive avoidance test is a procedure designed to evaluate fear-related memory in rodents. This test utilizes an apparatus comprising two chambers: one illuminated and the other darkened, which are separated by an

automatically closing door. The floors of both chambers are constructed from stainless steel bars. In the initial phase of the two-day experiment, the rats were situated in a brightly illuminated room, and the door was opened after 10 seconds. Considering that rodents exhibit an inherent preference for darker environments and tend to avoid brightly lit areas, the subjects were observed to progressively move towards the dark chamber of the apparatus. Upon their entry into the dark chamber, the door was subsequently closed, and the animal was administered a single low-intensity foot shock of 0.5 mA for 5 seconds. On the subsequent day, during the retention phase, the rats underwent the same procedure following a 24-hour interval; however, no shock was administered when the animals entered the dark chamber. The transition time of the rats from the light chamber to the dark chamber was recorded on both day one and day two. Learning performance was assessed by measuring the increase in the time delay during the retention trial in comparison to the acquisition trial [18].

#### Measurement of GABA Levels in the Hippocampus

In the assessment of the impact of azosemide treatment on hippocampal GABA levels, GABA concentrations in hippocampal tissue samples from the subjects were quantified using the enzyme-linked immunosorbent assay (ELISA) method [19]. The hippocampal tissue samples were homogenized in sterile phosphate-buffered saline (PBS) utilizing a mechanical homogenizer (SpeedMill PLUS; Analytik Jena). Subsequently, the homogenates were centrifuged at 4000

rpm for 10 min at a temperature of 4°C. Following the centrifugation, the supernatant was collected for further analysis, and the Bradford protein assay was employed to determine protein concentration. The ELISA protocol was conducted according to the manufacturer's instructions.

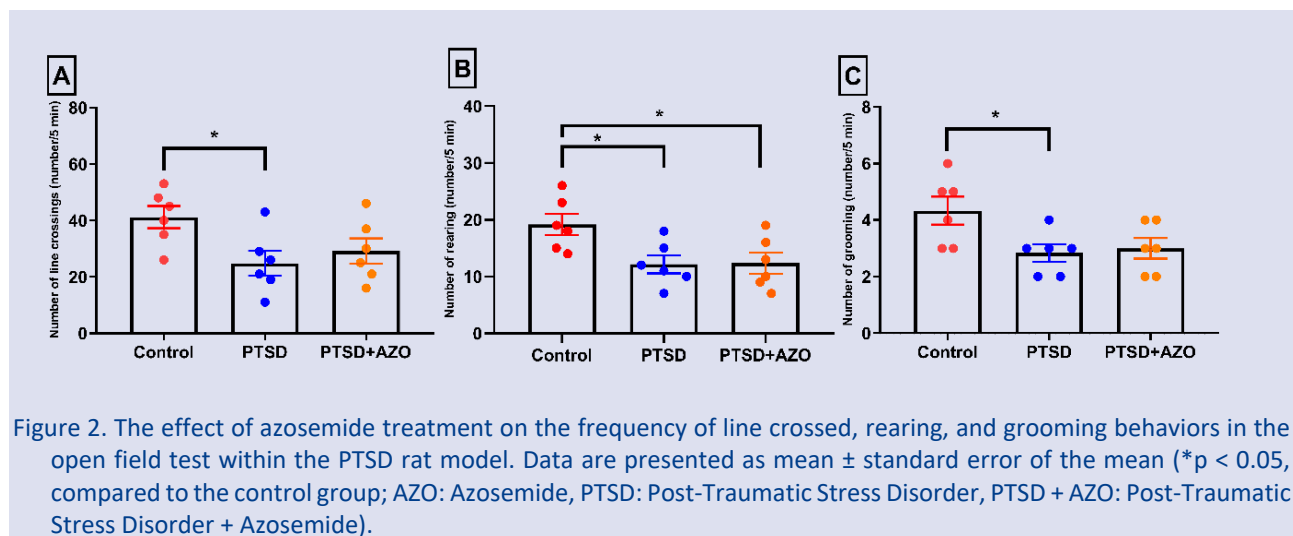
#### Statistical Analysis

GraphPad Prism (version 8.0) software was utilized to analyze the data collected during the study. The data are presented as mean  $\pm$  standard error of the mean (SEM) and were subjected to a one-way analysis of variance (ANOVA) followed by a post-hoc Tukey test. Results with a p-value of less than 0.05 were deemed statistically significant.

#### Results and Discussion

##### Effect of Azosemide on Number of Line Crossed, Grooming and Rearing in the Open Field Test

The effect of azosemide treatment on the number of line crossed, rearing and grooming behavior during the open field test in rats subjected to a SPS is illustrated in Figure 2. It was observed that the number of line crossed by the rats with PTSD was significantly lower than that of the control group ( $p < 0.05$ ). Furthermore, the number of rearing behaviors was significantly reduced in both the PTSD and PTSD + AZO groups when compared to the control group ( $p < 0.05$ ). In addition, the frequency of grooming behaviors was statistically significantly lower in the PTSD group when compared to the control group ( $p < 0.05$ ).



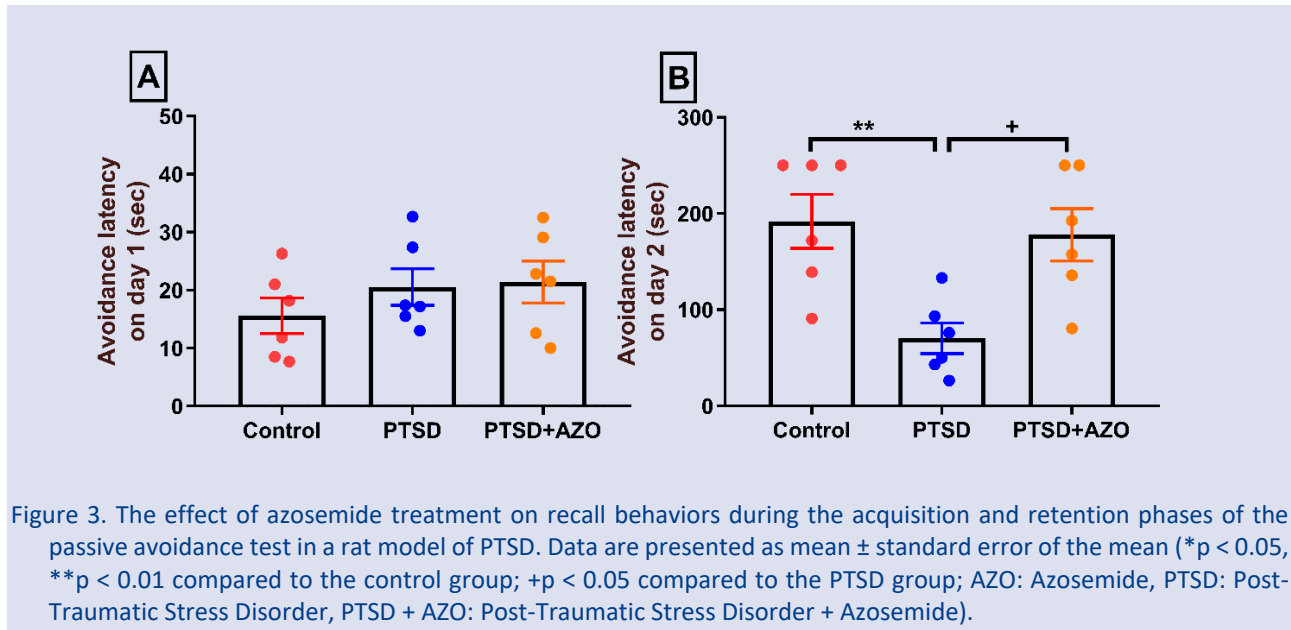
#### Effect of Azosemide on Emotional Memory Performance in Passive Avoidance Test

The effect of azosemide treatment on emotional memory in rats subjected to SPS was evaluated using the passive avoidance test. During the acquisition phase on

the initial day, no statistically significant differences were observed between the groups regarding the time taken to transition from the bright area to the dark area. On the other hand, after 24 hours, during the retention phase on the second day, a significant reduction in the escape time

from the bright area to the dark area was observed in the rats belonging to the PTSD group when compared to those

in both the control group and the PTSD + AZO group (Figure 3).



#### Effect of Azosemide on Hippocampal GABA Levels

The effect of azosemide treatment on hippocampal GABA levels was investigated using the ELISA method in rats subjected to prolonged stress. As shown in Figure 4, hippocampal GABA levels were significantly reduced in both the PTSD and PTSD+AZO groups compared to the control group (Figure 4).

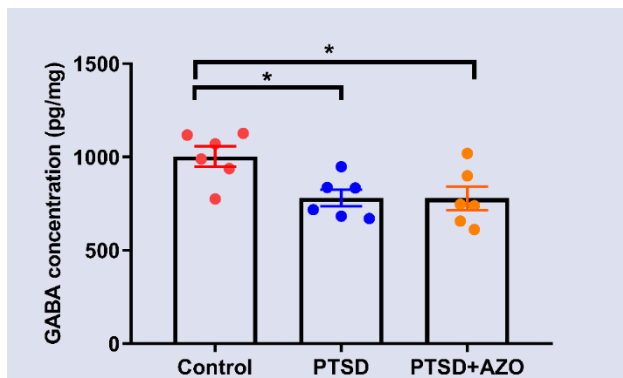


Figure 4. The effect of azosemide treatment on hippocampal GABA levels in the PTSD rat model. The data are presented as mean  $\pm$  standard error (\* $p < 0.05$  compared to the control group; AZO: Azosemide, PTSD: Post-Traumatic Stress Disorder, PTSD + AZO: Post-Traumatic Stress Disorder + Azosemide).

Overall, our results indicate that azosemide treatment partially improves emotional behavior and significantly improves memory performance in PTSD rats and has no effect on the decrease in hippocampal GABA levels induced by SPS. These results provide insight into the potential therapeutic benefits and limitations of azosemide in PTSD.

Our observation of a partial improvement in emotional behavior suggests that azosemide may modulate specific neurobiological pathways underlying emotional dysregulation in PTSD. The ability of azosemide to cross the blood-brain barrier and inhibit the NKCC1 in the brain may explain its effect on the emotional behavior of rats exposed to SPS. Indeed, it is possible that azosemide may restore impaired chloride homeostasis by inhibiting NKCC1 in the brain, thereby increasing GABAergic inhibition and reducing the symptoms of hyperarousal and anxiety associated with PTSD. It is suggested that proper regulation of chloride homeostasis may help prevent neuropsychiatric disorders due to improper chloride homeostasis and GABA shift abnormalities, such as PTSD [20]. Previous research has implicated dysregulated stress response systems, such as the hypothalamic-pituitary-adrenal (HPA) axis, in the pathophysiology of PTSD [7], [21]. Also, allopregnanolone, a neurosteroid involved in the regulation of the HPA axis, has been reported to be reduced in PTSD and is a potential target for treatment [22]. Thus, the effects of azosemide on brain chloride balance could potentially attenuate some aspects of increased emotional reactivity by indirectly influencing HPA axis activity. However, the partial nature of this improvement suggests that other central mechanisms, such as altered amygdala function or impaired prefrontal-limbic connectivity, remain unaffected by azosemide treatment [21], [23]. In addition, efflux transport across the blood-brain barrier, which limits the penetration of azosemide into the brain, may also play a role in this result [12]. The same researchers reported that systemic administration of NKCC inhibitors such as Azosemide, Torademide and Bumetanide increased the effect of phenobarbital in epileptic mice by crossing the blood brain barrier [16]. Further research is needed to identify these mechanisms and to investigate



whether azosemide treatments that target emotional regulation may be beneficial.

Cognitive deficits, including impaired memory, are hallmarks of PTSD and have been associated with hippocampal dysfunction [24]–[26]. Therefore, our finding that azosemide-treated rats showed improved memory compared with the untreated group is remarkable. It is possible that azosemide improves memory through mechanisms unrelated to hippocampal GABAergic signaling, such as suppressing neuroinflammation by regulating nuclear factor  $\kappa$ B (NF- $\kappa$ B) activity, which affects the release of inflammatory factors. It is known that neuroinflammation is positively correlated with memory impairment and that inflammation plays a role in the pathogenesis and pathophysiology of PTSD [27], [28]. Gong et al. reported that inhibition of NKCC1 downregulated inflammatory molecules such as p-p65-NF- $\kappa$ B, IL-6, IL-1 $\beta$  and TNF- $\alpha$  and suppressed neuroinflammation in an surgical brain injury rat model [29]. Although these findings highlight the potential utility of azosemide in improving cognitive impairment in PTSD, the underlying mechanisms require further investigation.

Interestingly, we found that azosemide did not reverse the reduction in hippocampal GABA levels induced by SPS. This finding is consistent with previous evidence suggesting that GABAergic dysfunction in PTSD is driven by complex, multifaceted processes, including not only reduced GABA synthesis, but also altered GABA receptor expression or increased excitatory input [14], [30], [31]. Furthermore, the pharmacological profile of azosemide does not directly target these GABAergic abnormalities, which may explain its lack of effect in restoring hippocampal GABA levels. Indeed, the effect of azosemide on GABAergic activation is indirect in that it reduces the amount of intracellular Cl<sup>-</sup> ions in neuronal cells, thereby increasing the activity of GABA.

All in all, this study highlights both the therapeutic promise and the limitations of azosemide in the treatment of PTSD. While azosemide appears to be effective in improving memory performance and partially ameliorating emotional disturbance, its inability to restore hippocampal GABA levels highlights the need for multimodal approaches that target the multiple pathophysiological features of PTSD. On the other hand, considering that the application of azosemide treatment for 7 days after the first trauma in our study coincided with the period during which new and permanent brain plasticity related to the stabilization of PTSD occurs in this process, the study points in the direction of elucidating the possible protective role of azosemide treatment in PTSD. In addition, extending this work to include molecular analyses of HPA axis components, inflammatory markers and indicators of oxidative stress may provide a more comprehensive understanding of the mechanisms of action of azosemide in PTSD.

### Conflicts of interest

There are no conflicts of interest in this work.

### Acknowledgments

We would like to thank the Sivas Cumhuriyet University, School of Medicine, CUTFAM Research Center, Sivas, Turkey, for providing the necessary facilities to conduct this study. This study is funded by TUBITAK 2209-A Research Project Support Programme for Undergraduate Students under grant number 1919B012305656.

### References

- [1] Pai A., Suris AM., North CS, Posttraumatic Stress Disorder in the DSM-5: Controversy, Change, and Conceptual Considerations, *Behav Sci.*, 7(1) (2017) 7.
- [2] Schöner J., Heinz A., Endres M., Gertz K., Kronenberg G, Post-traumatic stress disorder and beyond: an overview of rodent stress models, *J Cell Mol Med.*, 21(10) (2017) 2248-2256.
- [3] Bryant RA, Post-traumatic stress disorder: a state-of-the-art review of evidence and challenges, *World Psychiatry.*, 18(3) (2019) 259-269.
- [4] Hitchcock C., Goodall B., Sharples O, Population Prevalence of the Posttraumatic Stress Disorder Subtype for Young Children in Nationwide Surveys of the British General Population and of Children in Care, *J Am Acad Child Adolesc Psychiatry.*, 60(10) (2021) 1278-1287.
- [5] Abdalla S.M., Ettman C.K., Rosenberg, SB, Post-traumatic stress disorder during the Covid-19 pandemic: a national, population-representative, longitudinal study of U.S. adults, *npj Mental Health Res.*, 3 (2024) 20.
- [6] Yehuda R., Hoge CW., McFarlane AC, Post-traumatic stress disorder, *Nat Rev Dis Primers.*, 1 (2015) 15057
- [7] Simeon D., Knutelska M., Yehuda R., Putnam F., Schmeidler J., Smith LM, Hypothalamic-pituitary-adrenal axis function in dissociative disorders, post-traumatic stress disorder, and healthy volunteers, *Biol Psychiatry.*, 61(8) (2007) 966-973.
- [8] Astill L., Sijbrandij M., Sinnerton R., Lewis C., Roberts N.P., Bisson JI, Pharmacological prevention and early treatment of post-traumatic stress disorder and acute stress disorder: a systematic review and meta-analysis., *Transl Psychiatry.*, 9(1) (2019) 334.
- [9] Löscher W., Kaila K, CNS pharmacology of NKCC1 inhibitors, *Neuropharmacology.*, 205 (2022) 108910.
- [10] Suh O.K., Kim S.H., Lee MG, Pharmacokinetics and pharmacodynamics of azosemide, *Biopharm Drug Dispos.*, 24(7) (2003) 275-297.
- [11] Kaila K., Price T.J., Payne J.A., Puskarjov M., Voipio J, Cation-chloride cotransporters in neuronal development, plasticity and disease, *Nat Rev Neurosci.*, 15(10) (2014) 637-654.
- [12] Hampel P., Römermann K., MacAulay N., Löscher W, Azosemide is more potent than bumetanide and various other loop diuretics to inhibit the sodium-potassium-chloride-cotransporter human variants hNKCC1A and hNKCC1B, *Sci Rep.*, 8(1) (2018) 9877.
- [13] Muñoz A., Méndez P., DeFelipe J., Alvarez-Leefmans FJ, Cation-chloride cotransporters and GABA-ergic innervation in the human epileptic hippocampus, *Epilepsia.*, 48(4) (2007) 663-673.
- [14] Huang J., Xu F., Yang L, Involvement of the GABAergic system in PTSD and its therapeutic significance, *Front Mol Neurosci.*, 20(16) (2023) 1158825.



- [15] Souza R.R., Noble L.J., McIntyre CK, Using the Single Prolonged Stress Model to Examine the Pathophysiology of PTSD, *Front Pharmacol.*, 8 (2017) 615.
- [16] Hampel P., Römermann K., Gailus B, Effects of the NKCC1 inhibitors bumetanide, azosemide, and torasemide alone or in combination with phenobarbital on seizure threshold in epileptic and nonepileptic mice, *Neuropharmacology*, 185 (2021) 108449.
- [17] Filiz A.K., Gumus E., Karabulut S., Tastemur Y., Taskiran AS, Protective effects of lamotrigine and vitamin B12 on pentylene-tetrazole-induced epileptogenesis in rats, *Epilepsy Behav.*, 118 (2021) 107915.
- [18] Sahin B., Karabulut S., Filiz AK, Galium aparine L. protects against acetaminophen-induced hepatotoxicity in rats, *Chem Biol Interact.*, 366 (2022) 110119.
- [19] Yulak F., Joha Z., Öztürk A., İnan D.Ş., Taşkıran AŞ, Enoxaparin Protects C6 Glioma Cells from Glutamate-Induced Cytotoxicity by Reducing Oxidative Stress and Apoptosis, *Mol Neurobiol.*, 62(4) (2025) 4631-4640.
- [20] Hui K.K., Chater T.E., Goda Y., Tanaka M, How Staying Negative Is Good for the (Adult) Brain: Maintaining Chloride Homeostasis and the GABA-Shift in Neurological Disorders, *Front Mol Neurosci.*, 15 (2022) 893111.
- [21] Whitaker A.M., Farooq M.A., Edwards S., Gilpin NW, Post-traumatic stress avoidance is attenuated by corticosterone and associated with brain levels of steroid receptor co-activator-1 in rats, *Stress.*, 19(1) (2016) 69-77.
- [22] Almeida F.B., Pinna G., Barros HMT, The Role of HPA Axis and Allopregnanolone on the Neurobiology of Major Depressive Disorders and PTSD, *Int J Mol Sci.*, 22(11) (2021) 5495.
- [23] Whitaker A.M., Gilpin N.W., Edwards S, Animal models of post-traumatic stress disorder and recent neurobiological insights, *Behav Pharmacol.* 25(56) (2014) 398-409.
- [24] Acheson D.T., Gresack J.E., Risbrough VB, Hippocampal dysfunction effects on context memory: possible etiology for posttraumatic stress disorder, *Neuropharmacology.*, 62(2) (2012) 674-685.
- [25] Devignes Q., Ren B., Clancy KJ, Trauma-related intrusive memories and anterior hippocampus structural covariance: an ecological momentary assessment study in posttraumatic stress disorder, *Transl Psychiatry*, 14 (2024) 74.
- [26] Postel C., Mary A., Dayan J, Variations in response to trauma and hippocampal subfield changes, *Neurobiol Stress.*, 15 (2021) 100346.
- [27] Grigoryan GA, Neuroinflammation and Reconsolidation of Memory, *Neurochem. J.*, 16 (2022) 109-120.
- [28] Lee D.H., Lee J.Y., Hong DY, Neuroinflammation in Post-Traumatic Stress Disorder, *Biomedicines.*, 10(5) (2022) 953.
- [29] Gong Y., Wu M., Shen J, Inhibition of the NKCC1/NF-κB Signaling Pathway Decreases Inflammation and Improves Brain Edema and Nerve Cell Apoptosis in an SBI Rat Model, *Front Mol Neurosci.*, 14 (2021) 641993.
- [30] Kelmendi B., Adams T.G., Yarnell S., Southwick S., Abdallah C.G., Krystal JH, PTSD: from neurobiology to pharmacological treatments, *Eur J Psychotraumatol.*, 7 (2016) 31858.
- [31] Fang Q., Li Z., Huang GD, Traumatic Stress Produces Distinct Activations of GABAergic and Glutamatergic Neurons in Amygdala, *Front Neurosci.*, 12 (2018) 387.

## Investigation of a Stable Interaction of Levothyroxine with AFP through Molecular Modelling

Emel Akbaba<sup>1,a</sup>, Deniz Karataş<sup>2,b,\*</sup>, Ataman Gönel<sup>3,c</sup>, Ezgi Soylu<sup>2,d</sup>, Beste Kiraz<sup>2,e</sup>, Yusur Almahdi<sup>2,f</sup>

<sup>1</sup>Department of Medical Biology, Faculty of Medicine, Kırıkkale University, Kırıkkale, 71450, Türkiye

<sup>2</sup>Department of Bioengineering, Faculty of Engineering and Natural Sciences, Manisa Celal Bayar University, Manisa, 45140, Türkiye

<sup>3</sup>Department of Biochemistry, Faculty of Medicine, Sanko University, Gaziantep, 27580, Türkiye

\*Corresponding author

### Research Article

#### History

Received: 12/12/2024

Accepted: 19/05/2025



This article is licensed under a Creative Commons Attribution-NonCommercial 4.0 International License (CC BY-NC 4.0)

### ABSTRACT

Thyroid dysfunctions are common all over the world, and accordingly, the use of thyroid drugs has increased. Incorrect measurement of tumor markers may lead to missed cases of cancer. We hypothesized that the interaction between tumor markers and thyroid medications could lead to decreasing measurement of tumor markers in serum. The most used cancer markers are CA19-9, CA125, CEA, PSA, and AFP molecules. In this study, the molecular interactions of these markers with the thyroid medications of levothyroxine, methimazole, and propylthiouracil were investigated via molecular docking and dynamics simulations. In the molecular docking studies, levothyroxine was shown to interact with AFP, CEA, and CA15-3 in low concentrations. As a result of the MD simulations, the AFP/LEVO model exhibited the highest level of interaction. For instance, while the RMSD values of AFP/Levothyroxine complex were consistently around 0.7, and for the others they were observed above 1. This tight binding was reflected in interaction energies, with the total interaction in the AFP/Levothyroxine model computed as -192.04 kJ/mol. In contrast, for CA15-3/Levothyroxine and CEA/Levothyroxine complexes, these values were calculated as -135.26 and -88.56 kJ/mol, respectively. The SASA analysis also suggested the superiority of AFP/Levothyroxine complex due to ligand masking and a decrease in standard deviation, as the SASA mean difference area was found to be -0.46. This unique and only study elucidates the interactions between drugs used in thyroid cancer and biomarkers at the atomistic level. This clarity suggests a potential to mitigate misunderstandings that may arise in clinical and experimental studies.

**Keywords:** Levothyroxine, AFP, CEA, CA 15-3, Molecular modelling.

<sup>a</sup>[emakbaba@kku.edu.tr](mailto:emakbaba@kku.edu.tr)

<sup>c</sup>[catamangonel@gmail.com](mailto:catamangonel@gmail.com)

<sup>e</sup>[160323017@ogr.cbu.edu.tr](mailto:160323017@ogr.cbu.edu.tr)

<sup>b</sup><https://orcid.org/0000-0003-4915-5153>

<sup>d</sup><https://orcid.org/0000-0001-7200-1537>

<sup>f</sup><https://orcid.org/0009-0003-0125-8791>

<sup>b</sup>[deniz.karatas@cbu.edu.tr](mailto:deniz.karatas@cbu.edu.tr)

<sup>d</sup>[211208006@ogr.cbu.edu.tr](mailto:211208006@ogr.cbu.edu.tr)

<sup>e</sup>[221290005@ogr.cbu.edu.tr](mailto:221290005@ogr.cbu.edu.tr)

<sup>b</sup><https://orcid.org/0000-0002-8176-4883>

<sup>d</sup><https://orcid.org/0000-0003-1322-580X>

<sup>e</sup><https://orcid.org/0009-0003-9569-3777>

## Introduction

Thyroid function abnormalities are commonly encountered in general practice. Hypothyroidism and hyperthyroidism commonly arise from pathological processes within the thyroid gland. The diagnosis of thyroid dysfunction is predominantly based on biochemical confirmation [1]. Thyroid disfunction occurs much more often in females than males, with close to a million people being treated for hypothyroidism [2]. In iodine-replete populations, thyroid dysfunction is most commonly due to thyroid autoimmunity. The established treatment of hypothyroidism is carried out with levothyroxine [3]. Hyperthyroidism, on the other hand, is an excessive concentration of thyroid hormones in tissues causing a characteristic clinical state [4]. Hyperthyroidism caused by overproduction of thyroid hormones are commonly treated with antithyroid medications, methimazole and propylthiouracil [5].

Alteration of glycosylation, which occurs early in cancer, results in the production of tumor-associated glycans or glycoproteins. These molecules are subsequently secreted or membrane-shed into the blood

stream and thus serve as tumor-associated markers. These glycosylation markers, applicable for detection and monitoring of cancer, include CA 19-9, CA 125, CEA, PSA, and AFP. Because of their specific affinity to distinct sugar moieties, lectins are useful for developing assays to detect these tumors associated with glycans and glycoproteins in clinical samples. As such, various enzyme-linked lectin assays have been developed for diagnosis, monitoring and prognosis [6].

Carbohydrate antigen 19-9 (CA 19-9) is a cell surface glycoprotein complex, most commonly associated with pancreatic ductal adenocarcinoma. Structurally, it is a tetrasaccharide carbohydrate with a transmembrane protein skeleton and extensively glycosylated extracellular oligosaccharide chains. CA 19-9 is also used as a biomarker for gastrointestinal (such as colorectal and oesophageal cancers), urological, gynecological, pulmonary, and thyroid cancers [7]. CEA and CA 15-3 are generally associated with breast cancer [8]. Furthermore, CA 125 has been a valuable indicator for evaluating the efficacy of treatment and prognosis in ovarian cancer [9]. Alpha-fetoprotein (AFP) is considered as a diagnostic and prognostic cancer marker for

hepatocellular carcinoma which is one of the most common malignant tumors in the World [10]. Prostate specific antigen (PSA) is generally known as prostate cancer antigen [11]. Therefore, the specificity of cancer antigens is variable.

Molecular docking is a method which analyses the conformation and orientation of molecules (ligands) into a macromolecular target (receptor). Molecular docking is extensively used to hypothesize interaction modes and better characterize the ligand-receptor interactions [12]. Indeed, molecular docking is among one of the most popular and successful structure-based *in silico* methods, which help predict the interactions occurring between molecules and biological targets. Based on the protein structures, many possible poses of ligand are generated. Therefore, the first step is predicting the molecular orientation of a ligand within a receptor, and then estimating their complementarity through the use of a scoring function [13]. This molecule/protein complex must form a stable complex [14]. The binding free energy directly mirrors the ability of the ligand to interact with the protein, and is, therefore, regarded as the key quantity in studies of molecular recognition and association phenomena. The lowest the binding energy, the highest the binding affinity is [15]. The important energetic factors for protein–ligand binding, such as hydrogen bonds, and hydrophobic effects are also used to predict binding affinity [16]. Molecular dynamics (MD) simulations, on the other hand, predict how every atom in a protein or other molecular system will move over time, based on a general model of the physics governing interatomic interactions. These simulations can capture a wide variety of important biomolecular processes, including conformational change, ligand binding, and protein folding, revealing the positions of all the atoms at femtosecond temporal resolution [17]. In this study, MD simulations were performed to evaluate the stability of ligand/receptor complexes. Recently, the molecular interactions between propylthiouracil and thyroid peroxidase, a key enzyme in thyroid hormone synthesis has investigated with MD and docking. The aim is to elucidate the binding mechanism of propylthiouracil as an inhibitor of thyroid peroxidase at the atomic level. The study clarifies the key interactions, like hydrogen bonds, and hydrophobic interactions, that contribute to propylthiouracil's inhibitory activity [18]. In another recent study utilizes an integrated computational approach to explore the molecular mechanisms by which perfluorooctane sulfonic acid induces thyroid toxicity. Molecular docking and molecular dynamics simulations revealed the potential binding interactions between perfluorooctane sulfonic acid and key thyroid-related proteins, such as thyroid peroxidase and thyroid hormone receptors [19]. Another paper used molecular dynamics simulations to investigate the molecular mechanisms behind the resistance to resmetirom, a selective thyroid hormone receptor beta agonist, in certain contexts. The simulations identified key amino acid residues and interactions that are crucial for resmetirom binding and how these are affected in resistant variants [20]. Another

paper suggested that two common anti-thyroid drugs, methimazole and propylthiouracil, inhibited the enzymatic activity of thyroid peroxidase in the results which obtained through computational study [21]. One another theoretical and experimental study showed the interaction between levothyroxine, and bovine serum albumin [22]. *In silico* studies on biomarkers and thyroid cancer have also become popular in recent years. One comparative modelling study investigated the role of Iron-Sulfur Cluster Assembly 1 (ISCA1) across various cancer types, with a specific focus on its correlation with ferroptosis-related genes and its potential as a biomarker in thyroid carcinoma. [23]. Another study investigated a multi-omics network approach to identify systems biomarkers for papillary thyroid cancer prognosis and treatment. [24]. Another study employed gene-expression profile analysis to identify potential biomarkers for thyroid carcinoma. [25]. In the meantime, another study combined network pharmacology and molecular docking to investigate the mechanisms by which polybrominated diphenyl ethers to induce thyroid dysfunction. [26]. Another study performed a comprehensive, large-scale transcriptomic analysis of RNAs in thyroid cancer to identify pathological biomarkers related to the tumor immune microenvironment and to explore potential target therapies [27]. Although there is a body of research on the interactions between thyroid cancer therapeutics and diverse protein targets, theoretical studies pertaining to the interaction of these drugs with glycosylation markers are notably absent from the current literature. Therefore, in this study, our hypothesis was as follows: The medications used for thyroid disorders may interact with tumor markers, preventing their detection in blood tests. Given the widespread use of thyroid medications in the population, the suppression of tumor markers could adversely affect cancer diagnosis or follow-up treatments. The interactions of thyroid drugs with tumor markers may alter the serum levels of tumor antigens, which may cause a possible case of cancer to be missed as a result. Therefore, we investigated the interactions between certain thyroid medications and the tumor markers through the use of molecular docking, and dynamics simulations.

## Materials and Methods

### Protein Preparation

The molecular structures of tumor markers were imported from PDB (Protein Data Bank). The chosen tumor markers are AFP (PDB id: 3MRK), CA125 (PDB id: 1IVZ), CEA (PDB id: 5DZL), PSA (PDB id: 1GVZ), and CA15-3 (PDB id: 6BSC). Only CA19-9 was imported from PubChem (PubChem CID: 643993). All macromolecules were exhibited in alpha helixial and beta sheet structures, except CA19-9 which is the only non-protein cancer marker studied in this research. CA19-9 is a carbohydrate antigen; therefore, it is displayed in sticks with the colors specific to atom type (Figure 1).

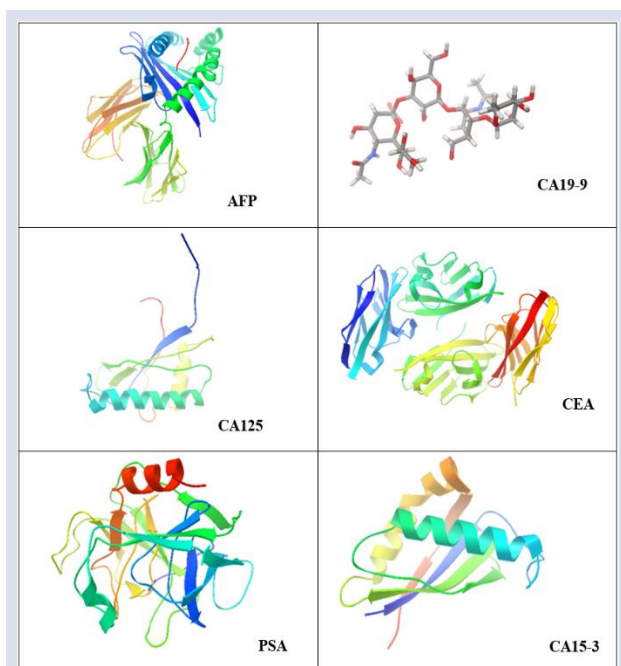


Figure 1. The structures of tumor markers are shown in rainbow form except CA19-9 of which is displayed in balls and sticks. Grey, red, white, and blue colors for CA19-9 represent carbon (C), oxygen (O), hydrogen (H) and nitrogen (N), respectively.

Before starting docking, water molecules and other irrelevant ligands were removed. Then marker molecules were prepared as a PDBQT file format using AUTODOCK TOOLS [28]. The missing residuals were checked and repaired. Hydrogen atoms were added to the dangling bonds. In the following step, Kollman charges were assigned and added to the marker molecules.

### Ligand Preparation

The molecular structures of all drugs were imported from the PubChem databank, saved in .sdf format. The file in SDF format was converted to PDBQT format using the

OpenBabelGUI (ObGUI) program [29]. The structures of the ligands (drugs) are shown in the Figure 2.

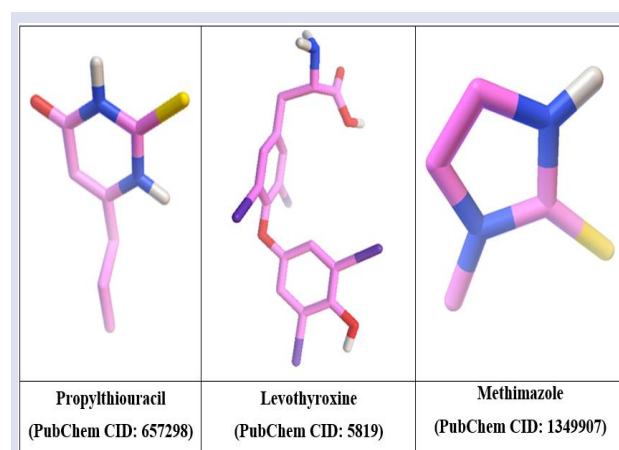


Figure 2. The structures of drugs are shown in ball-stick model. White, red, pink, purple, blue, and yellow colors represent hydrogen (H), oxygen (O), carbon (C), iodine (I), nitrogen (N), and sulfur (S), respectively.

### Launching Autogrid

The number of grid box points and xyz coordinates adjusted that completely cover the macromolecule structure entered from the grid box section. The grid parameter file (GPF) was saved with the entered values. All GPF parameters were illustrated in Table 1. These parameters are the default values generated by the AutoDock Tools software subsequent to the definition of the grid box. Before selecting, GPF file to run autogrid, autogrid4.exe program was launched. As GPF file was selected from working directory, at the same time a grid log file (GLG) with the same name was automatically generated. After the running finished all parameters, such as atom types, grid box details, dielectric constants, and lowest pairwise-atomic interaction energies.

Table 1. GPF parameters for ligand/marker models.

DRUG	MARKER	# of Grid Points (xyz)	Spacing	xyz Grid Center Coordinates(Å)
Propylthiouracil	AFP	126 126 126	0.55	7.391 x -0.582 x 9.49
	CA 19-9	50 50 50	0.375	-1.154 x 5.576 x -2.915
	CA 125	126 126 126	0.55	-1.929 x 11.891 x -4.083
	CEA	126 126 126	0.575	11.566 x -10.159 x 1.684
	PSA	126 126 126	0.5	11.3 x 23.915 x 24.743
	CA 15-3	100 100 100	0.375	-19.265 x 11.673 x 4.338
Levothyroxine	AFP	126 126 126	0.55	7.391 x -0.582 x 9.49
	CA 19-9	50 50 50	0.375	-1.154 x 5.576 x -2.915
	CA 125	126 126 126	0.55	-1.929 x 11.891 x -4.083
	CEA	126 126 126	0.575	11.566 x -10.159 x 1.684
	PSA	126 126 126	0.5	11.3 x 23.915 x 24.743
	CA 15-3	110 110 110	0.5	-19.265 x 11.673 x 4.338
Methimazole	AFP	126 126 126	0.55	7.391 x -0.582 x 9.49
	CA 19-9	50 50 50	0.375	-1.154 x 5.576 x -2.915
	CA 125	126 126 126	0.55	-1.929 x 11.891 x -4.083
	CEA	126 126 126	0.575	11.566 x -10.159 x 1.684
	PSA	126 126 126	0.5	11.3 x 23.915 x 24.743
	CA 15-3	100 100 100	0.375	-19.265 x 11.673 x 4.338



All the values of grid points, spacing, and grid center coordinates of propylthiouracil and methimazole are identical as shown in Table 1. However, values of grid center points and spacing of CA15-3/levothyroxine complex are different from that of CA15-3/propylthiouracil and CA15-3/levothyroxine complexes. The reason for this exceptional situation is molecular size and structural complexity of Levothyroxine.

### Molecular Docking

Apolar hydrogens cannot be read in XRD. To get exact results with XRD, nonpolar hydrogens were neglected. OpenBabel GUI (ObGUI) was used to calculate the minimum (most stable) charges. The codes of the drugs were inserted into the input format section of the ObGUI. The file type was selected as SDF. The output file was then saved as ".pdbqt" format in the relevant drug folder. Then the AutoDock program was started. Before submitting docking, macromolecule was selected to set receptor molecules as rigid body. Genetic algorithm (GA) was selected as search parameters. The number of runs and population size were selected as 100, and 300, respectively. Furthermore, the number of evals was chosen as long level. Hybrid Lamarckian and GA parameters were assigned, and the input file was saved as docking parameter file (DPF) (Table 2). Finally, DPF was selected to launch docking [30].

Table 2. DPF parameters for ligand/marker models.

Program	Autodock4.exe
Search Parameters	Lamarckian Genetic Algorithm
# of Run	100
# of Generations	27000
Maximum # of Energy Evaluations (Long level)	25000000
Population Size	300

For the analysis of the results, the run number where the lowest binding energy occurs should be entered in the conformations section and visualized. In the result pop out, all RMSD results were exhibited in detail.

The free binding energy (BE) calculation was carried out as follows.

Estimated Free Energy of Binding = (1) + (2) + (3) - (4)

(1): Final Intermolecular Energy = [vdW + Hbond + desolvation Energy] + Electrostatic Energy; (2): Final Total Internal Energy; (3): Torsional Free Energy; (4): Represents Unbound System's Energy = [(2) Final Total Internal Energy].

### Molecular Dynamics (MD)

The ligand/receptor complexes with the highest binding affinities were further evaluated via MD simulations which were conducted using the GROMACS program to elucidate the interaction regions and energies in aqueous environments with full atomic mobilities as compared to molecular docking. Prior to initiating MD

simulations, all atoms in the model were assigned using the CHARMM36 force field recommended for protein-ligand complexes. The TIP3P water model was selected for the solvent environment. Subsequently, a simulation box in the form of a dodecahedron was constructed, considering the protein structure, after merging the ligand molecule prepared on the swissParam website with the protein. Ion addition was performed to neutralize the ligand/protein simulation boxes containing water, followed by sufficient minimization using the steepest descent algorithm in 3D periodicity to reduce over-accessed energy on atoms and prepare the supercell for simulation. Next, equilibration was carried out in NVT and NPT ensembles for each of the three boxes, with 100 picoseconds (ps) each, followed by independent 50-nanosecond (ns) simulations. Moreover, temperature and pressure were maintained constant during the simulation via a modified Berendsen thermostat and the Parrinello-Rahman barostat. A temperature of 300 K and a pressure of 1 bar were applied. Short-range van der Waals forces were truncated at a cutoff distance of 1.2 nm, and long-range electrostatic forces were computed employing the Particle Mesh Ewald summation [23, 31]. To analyze molecular interactions and sizes between protein and ligand, RMSD, RMSF, radius of gyration, SASA, RDF, and interaction energy analyses were successively performed. In all relevant analyses, the entire ligand molecule was selected in contrast to the protein backbone for thorough examination.

### Results and Discussion

*In silico* studies revealed new insights about the possible binding mode of different compounds with receptors [32]. This research aimed to study possible interactions of the selected drugs used in hyperthyroidism or hypothyroidism with the serum tumor markers via molecular docking analysis. Propylthiouracil (PRO) and methimazole (MET), the drugs used in hyperthyroidism, and levothyroxine (LEVO) which is used in hypothyroidism were chosen as the ligand molecules. On the other hand, AFP, CA19-9, CA125, CA15-3, CEA, and PSA were selected as the receptors which are commonly known as tumor antigens routinely used to predict various cancers. The elevated levels of tumor markers could be a sign of cancer, therefore, should not be underestimated. Tumor markers can be evaluated by a blood test which is an easy and inexpensive method. This study aims to question the reliability of tumor marker measurement tests in people using the selected thyroid medications. The possible interactions of tumor markers and thyroid drugs are possibly change the serum levels of the antigens. One of the possible outcomes of the tumor marker with drug interaction is a decrease in serum tumor marker levels, which may be interpreted as ignoring the cancer, which may have devastating outcomes. Thyroid disease is common in older adults. Up to 5%, and 2.3% of older people are diagnosed with hypothyroidism and hyperthyroidism, respectively [33]. It is obvious that



cancer cases also increase with age. The interactions of thyroid medications with cancer markers could result in the elimination or delay of cancer diagnosis in the case of an elderly using thyroid drugs with no symptoms of cancer, who only has cancer marker bioassays. Therefore, it is essential to make certain that the medications used to treat thyroid diseases do not have any kind of interaction with the cancer markers.

In all the selected tumor markers, the simplest and smallest marker is CA19-9 whereas AFP, CEA and PSA are more complex and bulkier than others (Figure 1). All

examined ligand molecules with the polar hydrogens were depicted in Figure 2. Four iodine atoms just exist covalently in LEVO, the biggest, bulkiest, and longest ligand whereas sulfur belongs to the other drugs, relatively smaller and simpler structures (Figure 2).

### Molecular Interactions of Markers and PRO

The molecular interactions of marker and PRO from the total 100 runs are shown in Table 3.

Table 3. Molecular interactions of markers and PRO.

MODEL	BE from Lowest to Highest (kcal/mol)	IC From Lowest to Highest (mM)	Number of Clustering	Lowest Binding Run	Detected H-bonds (Å)
AFP/PRO	(-5.51)	(0.09)	8	72	No H-Bond formed
CA19-9/PRO	(-4.79)	(0.31)	2	11	(1.971)
CA125/PRO	(-3.88)	(1.44)	2	11	(2.131)
CA125/PRO	(-3.70)	(1.95)	15	15	No H-Bond formed
CEA/PRO	(-3.95)	(1.28)	15	15	No H-Bond formed
CEA/PRO	(-3.57)	(2.42)	19	18	ASP82:A(2.133)
PSA/PRO	(-4.40)	(0.59)	19	18	ASP82:A(2.133)
PSA/PRO	(-3.80)	(1.65)	10	16	LYS95F:A(1.965)
PSA/PRO	(-5.39)	(0.11)	10	16	LYS95F:A(1.965)
PSA/PRO	(-4.00)	(1.16)	9	3	PHE1094:A (2.234)
CA15-3/PRO	(-4.67)	(0.37)	9	3	PHE1094:A (2.234)
CA15-3/PRO	(-3.78)	(1.70)			

The amino acids contributing to the H-bonds which are listed in Table 3 are also shown in Figure 3. The lowest and highest binding energies of AFP/PRO model were determined to be -5.51 and -4.79 kcal/mol, respectively. Clearly, less than 1 kcal/mol difference was obtained between the lowest and highest binding energies of AFP/PRO model. Furthermore, AFP/PRO complex was found to be clustered in 8 sites out of 100 conformations. No hydrogen (H) bond was observed in this model, however, hydrophobic interactions with PHE22 and PRO20 which exist on A chain of AFP with PRO were determined. Also, other intermolecular interactions were observed in PRO with the residues SER11A, GLU19A, SER38A, SER71A, GLN72A, and ARG75A of AFP. Furthermore, a low inhibition constant (IC) value (0.09 mM) was found in AFP/PRO complex. Therefore, all these factors contributed to the low binding energy, suggesting AFP as the most favorable tumor marker with the interaction of PRO. A recently published study reported docking scores for Propylthiouracil spanning from -4.485 to -5.144 kcal/mol across ten distinct models, which closely align with the results obtained in our current research [18]. The aforementioned study highlighted the substantial interaction exhibited by the Propylthiouracil molecule with the thyroid hormone receptor. Another study, employing not only docking but also MD simulations, demonstrated a considerably strong interaction between the same drug and the same receptor [21].

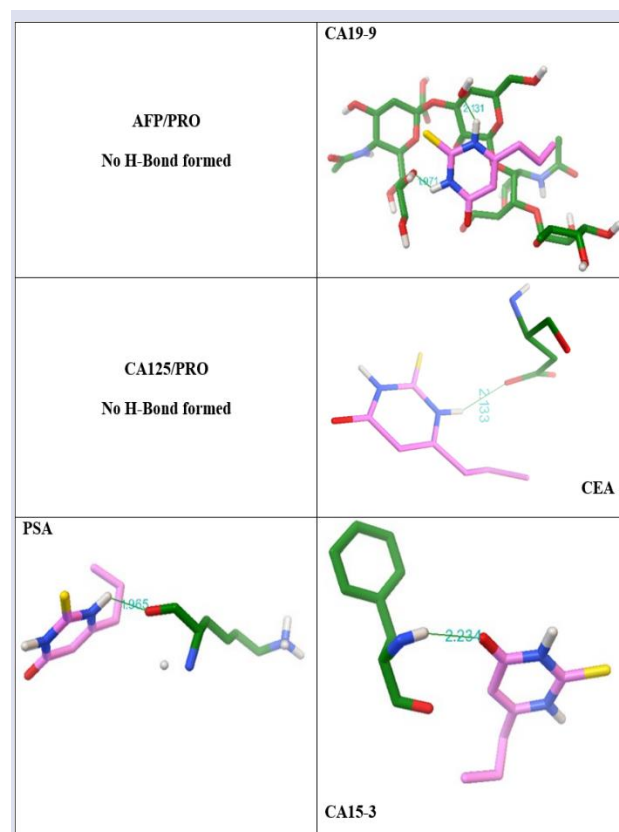


Figure 3. The marker/PRO interaction poses. The amino acids contributing to H-bonds are shown in green. Propylthiouracil (PRO) is shown in pink.

PSA/PRO model was also found to have low binding free energy (-5.39 kcal/mol) with one H-bond interaction. The IC value of this model was shown to be 0.11 mM. Furthermore, CA15-3/PRO model which has a binding energy of -4.67 kcal/mol displayed one H-bond as well as low IC value (0.37 mM).  $\pi$ -cation interactions were also observed in PRO with LYS1093A, in addition to hydrophobic interactions with PHE1054A, PRO1061A, and PRO1096A of CA 15-3. Furthermore, other intermolecular interactions were predicted between PRO and CA 15-3 with GLU1059A, TYR1066A, and ARG1095A residues. The marker/PRO poses displaying the lowest binding energies are shown in Figure 3. H-bonds were determined in all models except AFP/PRO and CA125/PRO. The effective driving forces in AFP/PRO and CA125/PRO models were determined as van der Waals interactions (-5.92 and -4.41

kcal/mol, respectively), while electrostatic interactions remained at minimum levels (-0.19 and -0.05 kcal/mol, respectively). However, in the other marker/PRO models, the effective driving forces were determined to be H-bonds and van der Waals interactions, with the minimum electrostatic contribution. Such hydrogen bonding and hydrophobic interactions have also been identified by using molecular docking and dynamics investigations involving PRO, which have further elucidated their function in regulating the interactions with the receptor [18, 21].

### Molecular Interactions of Markers and LEVO

Molecular interactions of markers and LEVO are shown in Table 4.

Table 4. Molecular interactions of markers and LEVO.

MODEL	Binding Energy (kcal/mol)	Inhibition Constant (mM)	Number of Clustering	Lowest Binding Run	Number of Detected H-bonds (Å)
AFP/LEVO	(-8.10) (-4.54)	(0.001) (0.4)	60	83	ASP30:A(2.084) GLY237:A(1.968) ARG12:B(1.992)
CA19-9/LEVO	(-4.53) (-3.01)	(0.478) (6.21)	22	36	2.239
CA125/LEVO	(-5.30) (-3.16)	(0.063) (4.86)	67	73	ASP95:A(2.129) ARG120:A(2.168) ARG96:A(2.152) THR4:B(2.131) THR101:B(1.813) SER6:C(2.103)
CEA/LEVO	(-8.60) (-4.51)	(0.0004) (0.494)	51	78	LYS95F:A(1.722) ARG150:A(2.068)
PSA/LEVO	(-7.16) (-4.48)	(0.005) (0.5)	57	48	
CA15-3/LEVO	(-8.35) (-5.73)	(0.0008) (0.06)	37	8	No H-Bond formed

Clearly seen from Table 4 that low binding energies were determined in all models of LEVO/marker. Figure 4 shows the best conformations of LEVO with the markers. A combined experimental and computational study into the molecular interplay between levodopa and thyroid hormones revealed a considerably high degree of interaction. Moreover, the binding affinity of the lowest energy conformer was determined to be -6.4 kcal/mol through docking simulations. The underlying interactions responsible for this affinity were illustrated as predominantly involving hydrogen bonds and hydrophobic forces [22].

The highest affinity between LEVO and tumor markers was determined to be in LEVO/CEA model which displayed an incredibly low binding free energy as -8.60 kcal/mol. H-bond interactions were predicted in LEVO with the residues THR4B, THR 101B, and SER6C of CEA. Furthermore, hydrophobic interactions with LEU2B, PHE9C, and ALA100B residues as well as other intermolecular interactions with ASN42A, GLN1B, GLU99B, THR3C, THR4C, GLN103C of CEA also contributed to the low binding energy. IC value of LEVO/CEA complex was found to be 0.0004 mM which is the lowest in all LEVO/marker models.

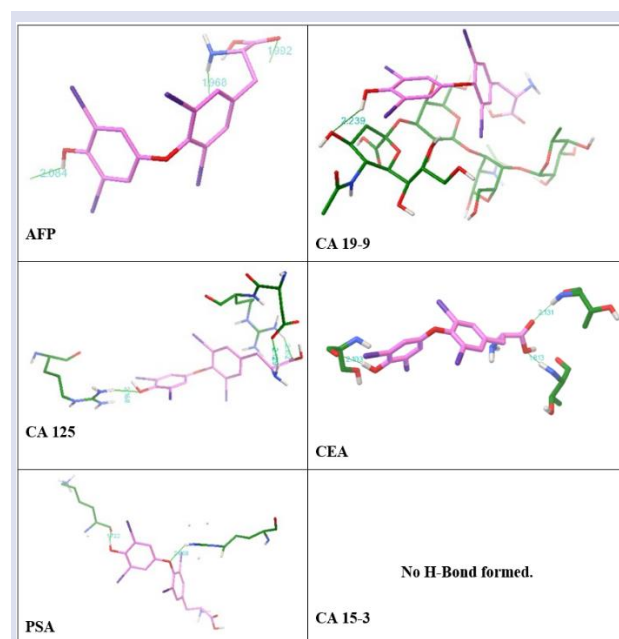


Figure 4. The LEVO/marker interaction poses. The amino acids are shown in green. Levodopa (LEVO) is shown in pink.

On the other hand, LEVO/CA 15-3 model was shown to display the second lowest binding energy (-8.35 kcal/mol). Although no H-bonds were predicted in LEVO with CA 15-3, hydrophobic interactions were observed with PHE1042A, LEU1078A, GLY1088A, LEU1089A, ALA1106B and ALA1106B, in addition to other intermolecular interactions with GLN1070A, SER1074A, SER1090A, ASN1091A, THR1104B amino acids of CEA. The low IC value of LEVO/CEA complex was noticed as 0.0008 mM. Therefore, CEA and CA 15-3 were suggested as the most favorable tumor markers in the interactions with LEVO. Furthermore, LEVO displayed low binding free energies of -8.10 kcal/mol and -7.16 kcal/mol with AFP and PSA, respectively. ASP30A, GLY237A, and ARG12B residues of AFP constituted H-bond interactions. Also, hydrophobic interactions in LEVO with TRY27A, LEU65B, and TYR67B were determined, in addition to other intermolecular interactions with THR31A, GLN32A, ARG48A, and SER52B residues of AFP. On the other hand, H-bond interactions in LEVO with LYS 95FA and ARG 150 A of PSA were observed. MET60, and LEU95I residues of PSA were observed to form hydrophobic interactions with LEVO. Also, other intermolecular interactions were observed between LEVO and PSA with HIS35, HIS39, GLN41, HIS57, and LYS95G residues. Therefore, the above-mentioned interactions of LEVO with AFP and PSA contributed to the low binding energies.

Among all LEVO/marker models, a relatively low binding affinity between LEVO and CA125 was observed as -5.30 kcal/mol binding energy. However, many bonding interactions were predicted in this complex such as H-bond interactions with residues ASP95A, ARG120A and ARG96A at high distances. On the other hand, hydrophobic interactions in LEVO were observed with VAL97, TYR100, PHE124, and VAL125, in addition to intermolecular interactions with ASP95, TYR100, and ARG120 residues of CA125. Therefore, although binding score of LEVO/CA125 complex was shown to be relatively low, many bonding interactions in this complex suggest good binding affinity.

As it can be seen from Table 4, high number of clustering in all LEVO/marker models were obtained. For example, in LEVO/CEA model, number of clustering was determined to be 51 in 100 conformations, suggesting many binding sites of the markers. Although LEVO is the bulkiest ligand in this study, substantially low binding energies with the markers were shown. LEVO is the only ligand in this study, possessing iodine residue and many polar hydrogens. Probably, these factors increased the affinity of LEVO to tumor markers, especially CA15-3, CEA, AFP, and PSA.

H-bonds and van der Waals interactions were found to be the effective driving forces in the interactions of LEVO with tumor markers. However, electrostatic interactions remained at minimum levels in all LEVO/marker complexes.

### Molecular Interactions of Markers and MET

Molecular interactions of markers and MET are given in Table 5. The binding energy of MET with PSA was observed to be -3.70 kcal/mol which is the lowest value within all MET/marker complexes. No H-bond interactions of MET with PSA were predicted. Furthermore, MET was found to represent a binding energy of -3.22 kcal/mol with CA125 which is also considered as low binding affinity. A H-bond interaction of MET was observed with VAL 125A of CA 125. Also, the IC value (4.39 mM) was determined to be moderately higher than PSA/MET model (1.94 mM). Figure 5 illustrates the best conformations of MET with the tumor markers. Clearly, MET did not reveal good binding affinities with any of the tumor markers in 100 conformations. Therefore, MET is not considered to be a favorable ligand for the studied tumor markers. With only one polar hydrogen, MET is the smallest ligand in this study. Possibly, the interactions of MET with the chosen markers are constrained by the presence of a single polar hydrogen. *In silico* study involving methimazole have demonstrated its interaction with thyroid peroxidase enzymes, mediated by hydrogen bonds and hydrophobic forces [21].

Table 5. Molecular interactions of markers and MET.

MODEL	Binding Energy (kcal/mol)	Inhibition Constant (mM)	Number of Clustering	Lowest Binding Run	Number of Detected H-bonds (Å)
AFP/MET	(-3.10) (-2.87)	-5.37 -7.88	4	39	HIS70:A (1.521)
CA19-9/MET	(-2.58)	12.85	1	65	-2.134
CA125/MET	(-3.22) (-2.84)	-4.39 -8.27	3	83	VAL125:A (1.825)
CEA/MET	(-3.06) (-2.74)	-5.73 -9.76	12	97	No H bond
PSA/MET	(-3.7) (-3.32)	-1.94 -3.67	7	95	No H Bond
CA15-3/MET	(-3.09) (-2.93)	-5.46 -7.11	2	84	ASN1091:A (2.021)

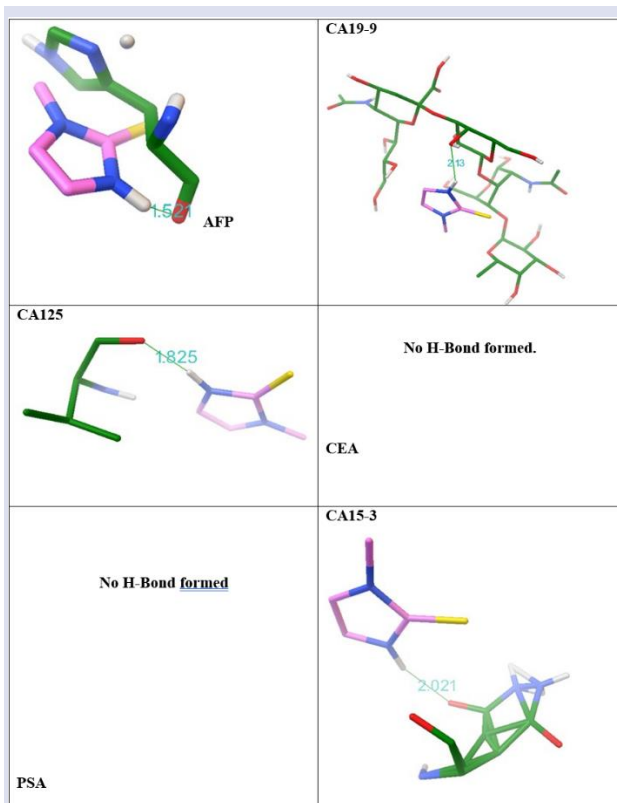


Figure 5. The marker/MET conformations with the lowest binding energies. The amino acids are shown in green. Methimazole (MET) is shown in pink.

Other forces affecting the molecular interactions between the tumor markers and the drugs, apart from the H-bond interactions, are given in Figure 6. The van der Waals spheres forming the molecular surface and close contacts of the left images are removed in the right images so that the  $\pi$ -cation yellow light beam can be seen. Two  $\pi$ -cation interactions occurred in the CA15-3/PRO model, while one was formed in CA15-3/LEVO. As a result of the docking, it was observed that the other parameters affecting the molecular interactions apart from the H-bond were  $\pi$ -cation and van der Waals interactions.

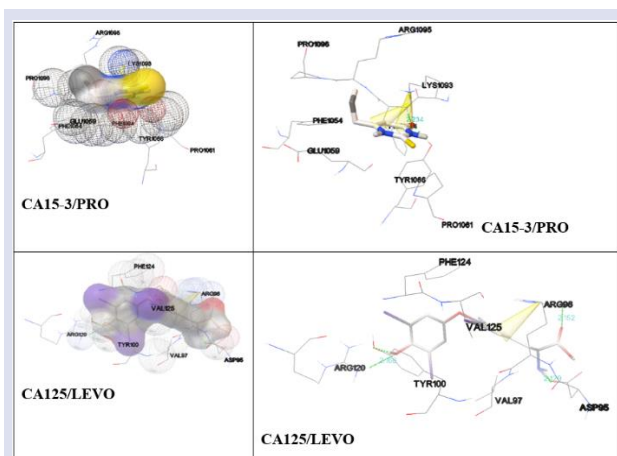


Figure 6. The molecular shape of CA15-3/PRO model shows amino acids causing hydrophobic interactions. The grey van der Waals spheres are carbonaceous region; red wireframe spheres are oxygen; the yellow region is sulfur, the purple spheres are iodine region, and the white spheres are hydrogenous region.

As a result, molecular docking analyzes revealed high binding affinities of LEVO to AFP, CA15-3, and CEA tumor marker proteins. Further, MD simulations were performed to support the stability of the aforementioned ligand/receptor interactions. ARG96 residue constituted  $\pi$ -cation interaction between LEVO and CA125, as well.

### Structural and Dynamic Analyses

RMSD, RMSF and Rg graphs, which are indicators of structural changes and protein stability of LEVO, are given in Figure 7.

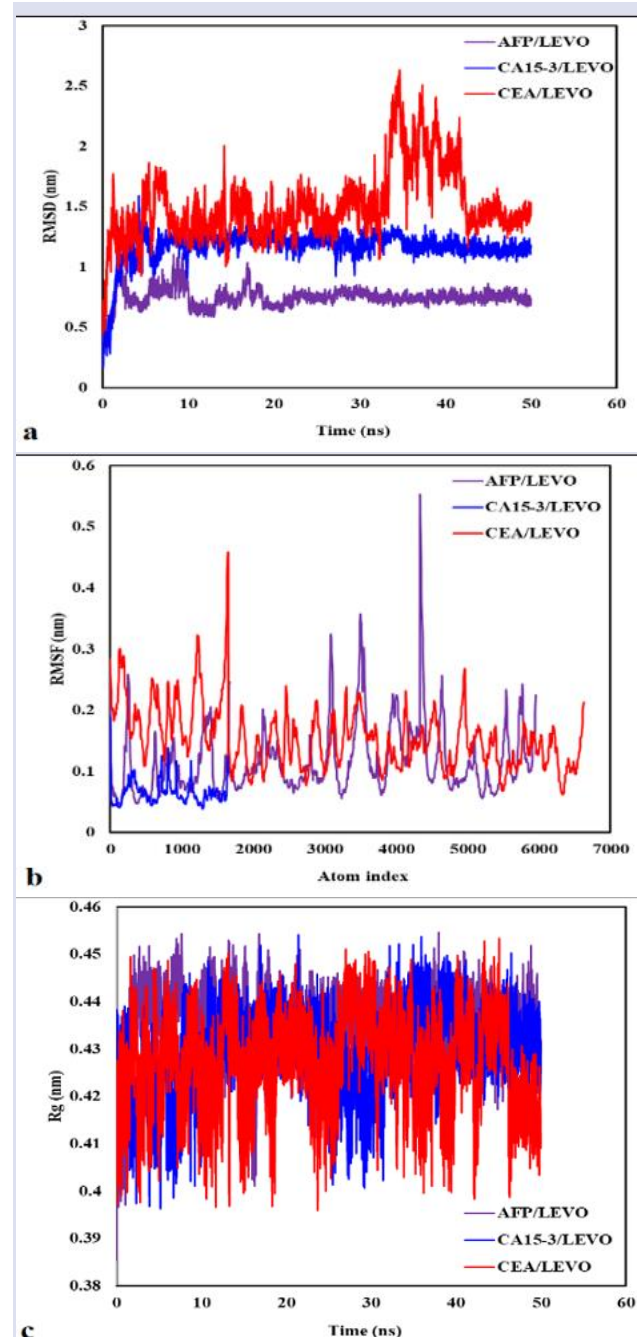


Figure 7. RMSD (a), RMSF (b), and Rg (c) graphs of AFP/LEVO, CA15-3/LEVO, and CEA/LEVO models.

RMSD (Root Mean Square Deviation) is the average measurement of atomic positions between two structures. In MD simulations, RMSD is employed to assess the similarity or dissimilarity between the generated protein and ligand complex and a reference



structure by comparing the variations in their positional alignment [34]. RMSD graphs facilitate the analysis of structural variations and stabilities in proteins and ligands. Additionally, they enable the interpretation of interactions between the ligand and protein throughout the simulation, as well as the observation and analysis of structural conformational changes during the binding of the ligand to the receptor [35].

It is a crucial type of graph for determining the equilibrium of the structure and dynamic stability. Figure 7a shows the RMSD graphs of AFP/LEVO, CA15-3/LEVO and CEA/LEVO complexes during a 50-nanosecond duration of MD simulation. The AFP/LEVO model exhibits a stable simulation, converging around 0.7 nm after the initial 10 ns and continuing steadily until completion. Similarly, the CA15-3/LEVO model stabilizes around 1.25 nm and continues consistently. In contrast, the CEA/LEVO model shows relatively larger fluctuations, reaching approximately 1.5 nm, with oscillations exceeding 2 nm observed between 35-45 ns of the simulation interval. This variation can be attributed to the presence of four chains in CEA, unlike the other models which have only one chain, and the stability of CEA appears to be influenced by the presence of the ligand. Indeed, in a study reporting the resolution as 3.4 Å in the X-Ray PDB validation report properties, it was observed that the resolution was notably lower, especially when compared to CA15-3 [36]. It is evident that the presence of the ligand affects the stability of the protein-ligand complex.

Root Mean Square Fluctuation (RMSF) denotes the calculation of atomic fluctuations in protein-ligand complexes generated during MD simulations over a specified time interval. The RMSF value allows for calculations regarding the extent to which the average positions of each structure deviate [34]. In MD simulations, the RMSF value provides information about the flexibility and conformational changes in specific regions of the protein, such as the binding site [37]. Figure 7b shows the RMSF graphs of AFP/LEVO, CA15-3/LEVO and CEA/LEVO complexes. Clearly, the CEA/LEVO model exhibits the highest fluctuations, attributed to the bulkier and more flexible nature of the CEA structure. The ordering of atom indices from large to small is a consequence of the CEA molecule having the longest total sequence length, followed by the sequence length of the single chain in AFP. The prominent peaks in AFP/LEVO correspond to atoms at indices 3088, 3503, and 4335. In CEA/LEVO, the most distinct peak is at index 1653, measuring 0.46 nm.

The gyration radius is utilized in MD simulations to discern the compactness of the protein-ligand complex, aiming to observe the shape and stability of the complex [38] [39]. This type of graph enables the assessment of the compactness of the protein-ligand complex. Gyration radius graphs corresponding to AFP/LEVO, CA15-3/LEVO and CEA/LEVO complexes are presented in Figure 7c. When examining the averages of the gyration radius (Rg) results, it is noted that their numerical average is approximately 0.43 nm for all models. However, as evident in Figure 7c, the CEA/LEVO complex exhibits a notably lower Rg value, especially in the last 4 ns of the simulation, compared to the others. This suggests that CEA is more flexible and disordered confirming the RMSD and RMSF results.

### Solvent Accessible Surface Area (SASA)

SASA is the surface area accessible to the solvent molecules in a molecular system. SASA enables the measurement of the area accessible to the solvent in protein-ligand complexes. The determination of SASA is crucial for understanding protein folding and stability. Additionally, SASA reflects the hydrophobic compactness of protein structures [40].

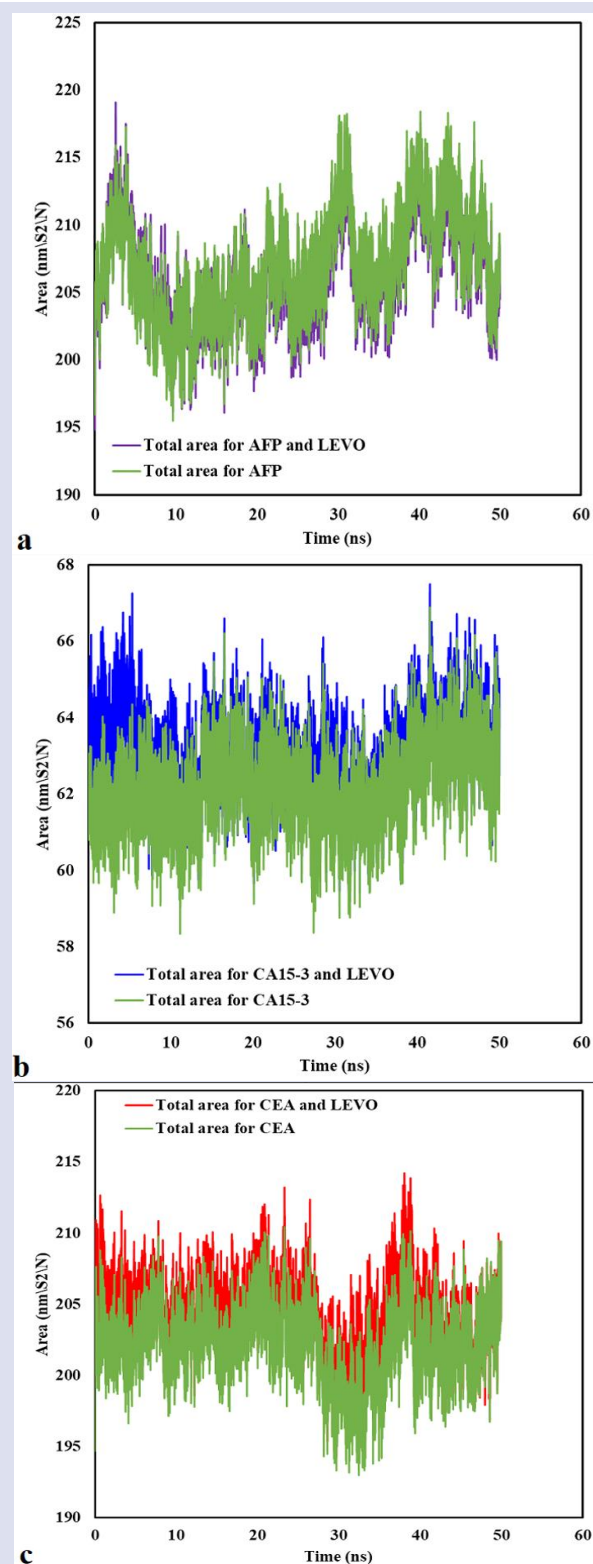


Figure 8. SASA curves for protein and protein/ligand models for the complexes of AFP/LEVO (a), CA15-3/LEVO (b), and CEA/LEVO (c).



In Figure 8, SASA graphs of protein-ligand complexes have been obtained to illustrate their behavior concerning solvent interactions. A slight decrease in SASA is observed in the presence of LEVO in the AFP/LEVO complex shown in Figure 8a. Indeed, the calculated difference in average areas is -0.46. Conversely, in the other two models, opposite results are obtained, with differences calculated as +0.80 and +2.13 for CA15-3/LEVO and CEA/LEVO complexes, respectively. According to these results, it can be inferred that the ligand masks the surface accessibility of the protein. On the other hand, the reason for the higher overall fluctuation areas in AFP is due to its having the shortest sequence length (57 amino acids) among the proteins. In the others, these fluctuation ranges are relatively less, especially in CA15-3. These minor fluctuations may suggest the formation of a stable complex between the ligand and the protein.

### Radial Distribution Function (RDF) Analyses and Interaction Energies

The term RDF refers to measuring the distance distribution of a specific molecule with reference molecules. In MD simulations, the RDF graph enables the interpretation of protein-ligand interaction sites, interaction dynamics, binding regions, and stabilities [41]. In Figure 9, the RDF graph for LEVO with the receptors' backbone is provided.

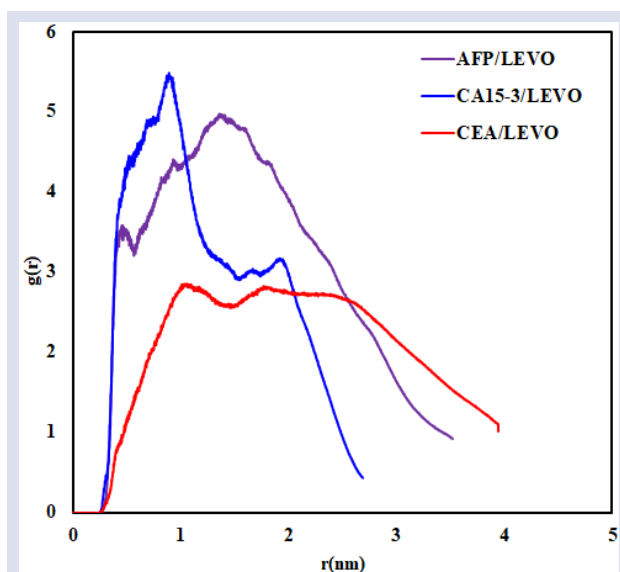


Figure 9. RDF graphs for AFP/LEVO, CA15-3/LEVO, and CEA/LEVO models.

The ligand exhibited its highest peak around 1 nm with the CA15-3 receptor, as indicated by the RDF results, highlighting this region as the most frequently occupied. In the AFP/LEVO model, the highest peak was observed around 1.6 nm, while in CEA/LEVO, a dominant and broad peak occurred in the range of 1-3 nm. These peaks and regions serve as clear evidence of the interaction between the ligand and the protein. To quantify these interactions, interaction energies between protein and ligand molecules were calculated, and the results are provided in Table 6.

Table 6. Total short range interaction energies and their contributions.

Energy, kJ/mol	AFP/LEVO	CA15-3/LEVO	CEA/LEVO
Coulombic	-78.13	-25.26	-23.17
Lenard-Jones	-113.91	-110	-65.39

Upon examining the results in Table 6, it can be asserted that the LJ parameter, and thus van der Waals interactions, are more effective. Regarding electrostatic interactions, the contribution is -78.13 kJ/mol in AFP/LEVO complex. In molecular docking results, however, CEA/LEVO exhibits the lowest total interaction energy. This observation may suggest that one of the influential parameters here is the hydrogen bonding.

Molecular docking and dynamics investigations were performed in this study, and the results showed that LEVO has a high affinity in low concentrations for binding to CEA, CA15-3, and AFP, which are all tumor markers. In particular, the MD results demonstrated that the LEVO/AFP complex exhibited a significant degree of stability while being simulated for fifty nanoseconds. As a result, we propose that the thyroid medicine LEVO interacts with AFP, which may result in a change in the amount of AFP that is present in the blood serum. The molecular structure of the protein will almost certainly undergo a change, whether it is in a single form or contained within a complex. That being the case, it is quite possible that the complex form of AFP is not detectable in blood serum. As a consequence of this, the amount of AFP that is present in the serum can appear to be quite low, which might lead to inaccurate findings.

### Conclusion

In this study, molecular docking and dynamic studies have revealed the interactions of levothyroxine used in thyroid dysfunction with tumor markers of CEA, CA 15-3, and AFP. Other than H-bond and van der Waals interactions, hydrophobic and  $\pi$ -cation interactions were also found to contribute this interaction. According to the results of MD simulations, the stability of levothyroxine to AFP is quite remarkable. As a result of the interaction between tumor markers and drugs, molecular changes may complicate the detection of these molecules. The molecular changes in the structure of AFP in the AFP/levothyroxine complex quite possibly decrease the detection of serum AFP levels. Levothyroxine's interaction with CEA, CA 15-3, and especially with AFP molecules at low concentrations suggests that it may produce erroneous results in cancer patients undergoing diagnosis and treatment. The limitations of the study is that we only performed *in silico* analysis to show the binding of levothyroxine to the studied tumor markers. Experimental studies are necessary to validate the findings of the study, particularly those examining the effect of levothyroxine on the serum concentrations of CEA, CA 15-3, and AFP. Moreover, although this research hypothesizes a potential reduction in serum AFP levels due to

levothyroxine, this conclusion is exclusively derived from computational analyses. Therefore, experimental corroboration, including techniques like ELISA and immunological assays, is essential to ascertain its clinical relevance. As a consequence of this study, the amount of AFP that is present in the serum could appear to be quite low, which might lead to inaccurate findings. The misleading results of serum AFP levels in patients under diagnosis and cancer follow-up treatment could result in devastating outcomes.

### Conflicts of interest

There are no conflicts of interest in this work.

### Acknowledgements

Computing resources for Molecular Docking studies calculations reported in this paper were fully performed at Harran University High Performance Computing Center (Harran HPC resources). Computing resources used in this work for MD simulations were totally provided by the National Center for High Performance Computing of Turkey (UHeM) under grant number 1013972022.

### References

- [1] Taylor P.N., Global epidemiology of hyperthyroidism and hypothyroidism, *Nat. Rev. Endocrinol.*, 14(5) (2018) 301-316.
- [2] Chiovato L., Magri F., Carlé A., Hypothyroidism in Context: Where We've Been and Where We're Going, *Advances in Therapy*, 36(S2) (2019) 47-58.
- [3] Hughes K., Eastman C., Thyroid disease: Long-term management of hyperthyroidism and hypothyroidism, *Aust. J. Gen. Pract.*, 50(1-2) (2021) 36-42.
- [4] Guerri G., *Hypothyroidism and hyperthyroidism*, Acta Biomed., 90(10-S) (2019) 83-86.
- [5] Kravets I., Hyperthyroidism: Diagnosis and Treatment, *Am. Fam. Physician.*, 93(5) (2016) 363-70.
- [6] Silsivani A., Glycosylation Markers in Cancer, *Adv. Clin. Chem.*, 89(2019) 189-213.
- [7] Lee T., Teng T.Z.J., Shelat V.G., Carbohydrate antigen 19-9 - tumor marker: Past, present, and future, *World J. Gastrointest Surg.*, 12(12) (2020) 468-490.
- [8] Seale K.N., Tkaczuk K.H.R., Circulating Biomarkers in Breast Cancer, *Clin Breast Cancer*, 22(3) (2022) e319-e331.
- [9] Zhang M., Roles of CA125 in diagnosis, prediction, and oncogenesis of ovarian cancer, *Biochim. Biophys. Acta. Rev. Cancer*, 1875(2) (2021) 188503.
- [10] Zheng Y., Zhu M., Li M., Effects of alpha-fetoprotein on the occurrence and progression of hepatocellular carcinoma, *J. Cancer Res. Clin. Oncol.*, 146(10) (2020) 2439-2446.
- [11] Carlsson S.V., Vickers A.J., Screening for Prostate Cancer, *Med. Clin. North Am.*, 104(6) (2020) 1051-1062.
- [12] Torres P.H.M., Key Topics in Molecular Docking for Drug Design, *Int. J. Mol. Sci.*, 20(18) (2019).
- [13] Pinzi L., Rastelli G., Molecular Docking: Shifting Paradigms in Drug Discovery, *Int. J. Mol. Sci.*, 20(18) (2019).
- [14] Akbaba E., Improvement of memory deficits via acetylcholinesterase inhibitory activity of *Nepeta nuda* ssp. *nuda* essential oil in rats, *Kuwait Journal of Science*, 48(3) (2021).
- [15] Fu H., Accurate determination of protein:ligand standard binding free energies from molecular dynamics simulations, *Nat Protoc.*, 17(4) (2022) 1114-1141.
- [16] Li J., Fu A., Zhang L., An Overview of Scoring Functions Used for Protein-Ligand Interactions in Molecular Docking, *Interdiscip Sci.*, 11(2) (2019) 320-328.
- [17] Hollingsworth S.A., Dror R.O., Molecular Dynamics Simulation for All, *Neuron*, 99(6) (2018) 1129-1143.
- [18] Suryandari D.A., Molecular Insights into Propylthiouracil as a Thyroid Peroxidase Inhibitor: A Computational Study Approach, *Indonesian Journal of Medical Chemistry and Bioinformatics*. 3(1) (2024).
- [19] Li H., Integrated computational analysis of molecular mechanisms underlying perfluorooctane sulfonic acid induced thyroid toxicity, *Sci Rep.*, 15(1) (2025) 7920.
- [20] Lu Y., Molecular Dynamic Simulation To Reveal the Mechanism Underlying MGL-3196 Resistance to Thyroxine Receptor Beta, *ACS Omega*, 9(19) (2024) 20957-20965.
- [21] Pradhan S., Comparative Study on the Binding Affinity of Methimazole and Propylthiouracil to Thyroid Peroxidase as an Anti-Thyroid Drug: An Insilico Approach, *Journal of Molecular Imaging & Dynamics*, 07(01) (2017).
- [22] Sandu N., Evaluation of the interaction of levothyroxine with bovine serum albumin using spectroscopic and molecular docking studies, *J. Biomol. Struct. Dyn.*, 40(3) (2022) 1139-1151.
- [23] Xiong D., Comprehensive Analysis Reveals That ISCA1 Is Correlated with Ferroptosis-Related Genes Across Cancers and Is a Biomarker in Thyroid Carcinoma, *Genes (Basel)*, 15(12) (2024).
- [24] Gulfidan G., Systems biomarkers for papillary thyroid cancer prognosis and treatment through multi-omics networks, *Arch Biochem Biophys*, 715(2022) 109085.
- [25] Mahmud S., Gene-expression profile analysis to disclose diagnostics and therapeutics biomarkers for thyroid carcinoma, *Comput Biol Chem.*, 113(2024) 108245.
- [26] He Q., Combining Network Pharmacology with Molecular Docking for Mechanistic Research on Thyroid Dysfunction Caused by Polybrominated Diphenyl Ethers and Their Metabolites, *Biomed. Res. Int.*, 2021(2021) 2961747.
- [27] Shih M.L., Large-scale transcriptomic analysis of coding and non-coding pathological biomarkers, associated with the tumor immune microenvironment of thyroid cancer and potential target therapy exploration, *Front Cell Dev. Biol.*, 10(2022) 923503.
- [28] Morris G.M., AutoDock4 and AutoDockTools4: Automated docking with selective receptor flexibility, *J. Comput. Chem.*, 30(16) (2009) 2785-91.
- [29] O'Boyle, Open Babel: An open chemical toolbox, *J. Cheminform*, 3(2011) 33.
- [30] Akbaba E., Karatas D., Phytochemicals of *Hibiscus sabdariffa* with Therapeutic Potential against SARS-CoV-2: A Molecular Docking Study, *J. Inst. Sci. Technol.*, 13(2) (2023).
- [31] Tang S., Sun L., Wang F., Identification of highly active natural thyroid hormone receptor agonists by pharmacophore-based virtual screening, *J. Biomol. Struct. Dyn.*, 39(3) (2021) 901-910.
- [32] Bagci E., Evaluation of anti-amnesic activity of *Salvia multicaulis* essential oil on scopolamine-induced amnesia in rats: in vivo and in silico approaches, *Heliyon*, 5(8) (2019) e02223.
- [33] Dedon J., Thyroid Disease in Aging, *Mo. Med.*, 119(4) (2022) 351-353.

- [34] Hirasawa M., Interaction of Nevirapine with the Peptide Binding Groove of HLA-DRB1\*01:01 and Its Effect on the Conformation of HLA-Peptide Complex, *Int. J. Mol. Sci.* 19(6) (2018).
- [35] Behera S.K., In Silico Analysis Determining the Binding Interactions of NAD(P)H: Quinone Oxidoreductase 1 and Resveratrol via Docking and Molecular Dynamic Simulations, *Eur. J. Biol.*, 82(2) (2023) 280-288.
- [36] Huang Y.H., CEACAM1 regulates TIM-3-mediated tolerance and exhaustion, *Nature*, 517(7534) (2015) 386-U566.
- [37] Huang H.J., Lee C.C., Chen C.Y., Lead discovery for Alzheimer's disease related target protein RbAp48 from traditional Chinese medicine, *Biomed. Res. Int.*, 2014(2014) 764946.
- [38] Rampogu S., Molecular Docking and Molecular Dynamics Simulations Discover Curcumin Analogue as a Plausible Dual Inhibitor for SARS-CoV-2, *International Journal of Molecular Sciences*, 23(3) (2022).
- [39] Shoaib T.H., Exploring the potential of approved drugs for triple-negative breast cancer treatment by targeting casein kinase 2: Insights from computational studies, *Plos One*. 18(8) (2023).
- [40] Zhang D., Lazim R., Application of conventional molecular dynamics simulation in evaluating the stability of apomyoglobin in urea solution, *Sci Rep.*, 7(2017) 44651.
- [41] Johnson K.J., Cygan R.T., Fein J.B., Molecular simulations of metal adsorption to bacterial surfaces, *Geochimica Et Cosmochimica Acta.*, 70(20) (2006) 5075-5088.

## Biogenic Synthesis and Characterization of Silver Nanoparticles Using *Hoya Carnosa* Flower Extract

Halil İbrahim Çetintaş<sup>1,a,\*</sup>

<sup>1</sup> Advanced Technology Research and Application Center, Sivas Cumhuriyet University, Sivas, Türkiye

\*Corresponding author

### Research Article

#### History

Received: 12/25/2024

Accepted: 19/05/2025



This article is licensed under a Creative Commons Attribution-NonCommercial 4.0 International License (CC BY-NC 4.0)

### ABSTRACT

Silver nanoparticles (AgNPs) are important metallic nanomaterials thanks to their superior antibacterial properties and wide application areas; however, conventional synthesis methods are quite limiting in terms of environmental and economic aspects. This situation causes green synthesis methods to be investigated more and more. *Hoya carnosa* plant have the potential to be an alternative biogenic synthesis agent to traditional methods thanks to their rich phytochemical content. In this study, biogenic AgNPs were synthesized for the first time using *Hoya carnosa* flower extract. The reaction was completed in a short time, such as 15 min under room conditions. AgNPs were comprehensively characterized by UV-Vis, FTIR, XRD, SEM, TEM and EDX analyses. According to the obtained results, the average size of AgNPs was calculated as 16 nm by the Debye Scherrer equation and 21 nm by TEM analysis. This study demonstrates that the use of *Hoya carnosa* flower extract can be a successful alternative to traditional methods by contributing to the synthesis of AgNPs in an environmentally friendly and rapid manner.

**Keywords:** Green synthesis, Biogenic synthesis, Silver nanoparticles, *Hoya carnosa*, Plant.

<sup>a</sup> [hcetintas@cumhuriyet.edu.tr](mailto:hcetintas@cumhuriyet.edu.tr)

<sup>ib</sup> <https://orcid.org/0000-0003-1769-0098>

## Introduction

Nanotechnology attracts attention as one of the most important fields that has been frequently mentioned in recent years, and research on the development and use of nanosized materials is gaining momentum day by day. In this context, metal nanoparticles serve numerous purposes in different areas—from environmental [1] and biomedical [2] fields to electronics [3], energy [4], food [5], agriculture [6], textile [7], and cosmetics [8]—thanks to their unique optical, magnetic, electrical, biological, and chemical properties [9,10]. Especially silver nanoparticles (AgNPs) have attracted great attention in healthcare and many other industries due to their antimicrobial, anti-inflammatory, and anticarcinogenic impacts [11,12]. However, conventional chemical and physical AgNPs synthesis techniques bring with them potential dangers in terms of the use of toxic chemicals, high energy consumption, and environmental sustainability [13,14].

In recent years, biogenic synthesis methods have attracted considerable attention as an eco-friendly and sustainable alternative to reduce the negative effects of conventional methods. Biogenic synthesis is based on the utilization of bio-based reducing agents such as plant extracts, bacteria, yeast, fungi, and algae and offers safe and sustainable solutions in terms of health, environment, energy, and economy [15,16]. Plant extracts, especially due to their rich phytochemical content such as phenolic compounds, flavonoids, terpenoids, alkaloids, and saponins, effectively reduce silver ions and ensure the formation of stable AgNPs [17]. The function of these phytochemicals as reducing and stabilizing agents provides the opportunity to control the size, shape, and surface properties of nanoparticles.

*Hoya carnosa* is a plant belonging to the Asclepiadaceae family and is generally grown for ornamental purposes, and is used in traditional medicine for various therapeutic purposes due to its antioxidant, antimicrobial, and anti-inflammatory effects [18–22]. The flowers have a pentamerous corolla with a prominent star-shaped gynostegium formed by fused male and female organs at the center (Figure 1) [23]. Extracts obtained from its leaves and flowers serve as potential therapeutic agents in biomedical applications due to their rich phytochemical content [21]. However, current studies have generally focused on the biological processes and pharmacological properties of *Hoya carnosa*, and no study has yet been found that has investigated its potential use in nanoparticle synthesis.



Figure 1. *Hoya carnosa* flowers.



In this study, for the first time in the literature, AgNPs were synthesized by biogenic methods using *Hoya carnosa* flower extract. This method is quite simple and provides biocompatible production of nanoparticles in accordance with green chemistry principles without using any toxic chemicals. In addition, the chemical, morphological, and structural properties of the synthesized AgNPs were characterized by detailed examination with advanced spectroscopic and microscopic approaches, including UV-Vis, FTIR, XRD, SEM, TEM, and EDX.

## Materials and Methods

### Materials

*Hoya carnosa* flowers were freshly collected in May from a mature potted plant grown in a local home in Sivas, Türkiye. Silver nitrate ( $\text{AgNO}_3$ ) was obtained from Carlo Erba Reagents (Italy). MilliQ ultrapure water (Millipore Synergy UV, Merck, Germany) was used in all stages of the experiments.

### Preparation of Flower Extract

*Hoya carnosa* flowers were freshly collected and washed first with water and then with ultrapure water to remove dirt and dust. After the flowers were separated from their stems, they were chopped into small pieces. 20 g of fresh *Hoya carnosa* flowers were extracted by boiling in 250 ml of ultrapure water for 30 min. The resulting pink extraction solution was allowed to cool and filtered first with a simple strainer and then with Whatman No. 1 filter paper. The extract obtained was stored in the refrigerator at 4 °C.

### Biogenic Synthesis of AgNPs

10 ml of *Hoya carnosa* flower extract was taken into a skirted centrifuge tube. Instead of preparing a separate silver solution, 1 mmol of  $\text{AgNO}_3$  was directly added to the extract solution and mixed briefly with a vortex mixer until all solids were dissolved. After shaking the tube at 100 rpm for 15 min at room temperature in an orbital shaker, a dark colloidal solution was formed, indicating that the reduction reaction had taken place and successfully ensured the nucleation and growth of spherical AgNPs, as reported in the literature (Figure 2) [24]. The synthesis mechanism begins with coordination of  $\text{Ag}^+$  ions by phenolic –OH groups, followed by electron donation that reduces  $\text{Ag}^+$  to  $\text{Ag}^0$ , nucleation and growth of silver seeds, and final stabilization of the nanoparticles through capping by oxidized phytochemicals [25]. The AgNPs solution was centrifuged at 6000 rpm for 10 min to precipitate the particles. This procedure was repeated three times by adding ultrapure water instead of the drained supernatant, and finally pure AgNPs were obtained. The obtained nanoparticles were dried at 50 °C. The yield of synthesized AgNPs was determined using Equation 1.

$$\% \text{ Yield} = \frac{\text{Actual Yield}}{\text{Theoretical Yield}} \times 100 \quad (1)$$

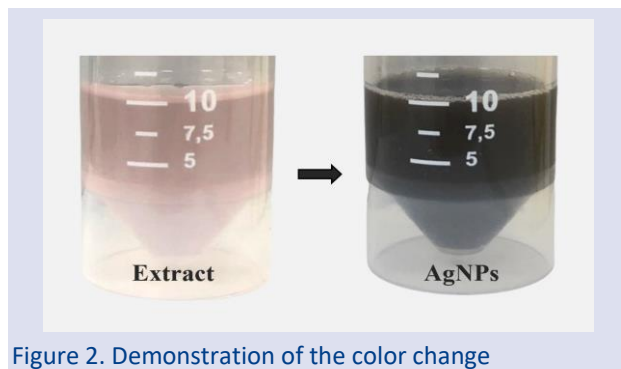


Figure 2. Demonstration of the color change

### Characterization of AgNPs

The characterizations of AgNPs synthesized by biogenic methods using *Hoya carnosa* flower extract were carried out by UV-Vis, FTIR, XRD, SEM, EDX and TEM techniques. The presence of AgNPs was confirmed by UV-Vis spectrophotometer (Evolution 201, Thermo Scientific, USA) and the chemical structure analysis was determined by FTIR-ATR (Tensor II ATR, Bruker, USA). XRD (Mini Flex 600, Rigaku, Japan) was used for the determination of crystal structure and theoretical particle size calculations. The size, morphology and elemental analyses of nanoparticles were characterized using SEM (Mira 3, Tescan, Czech Republic) integrated with S-TEM and EDX (X-act, Oxford Instruments, UK) detectors.

## Results

### UV-Vis Analysis

UV-Vis absorption spectroscopy is a highly effective method for the detection of the presence of many metallic nanoparticles, especially silver and gold nanoparticles, using Surface Plasmon Resonance (SPR) peaks [26]. The presence of AgNPs synthesized by biogenic method using *Hoya carnosa* flower extract was analyzed by observing the SPR peak using UV-Visible spectrophotometer in the wavelength range of 350 to 800 nm and shown in Figure 3. The analysis was performed in a quartz cuvette with a 1 cm light path and at 25 °C. The  $\lambda_{\text{max}}$  value at 436 nm wavelength resulting from the SPR effect confirms the successful formation of AgNPs in the extract solution. In previous studies in the literature, the maximum wavelength of AgNPs has generally been reported in the range of 400–450 nm [27].

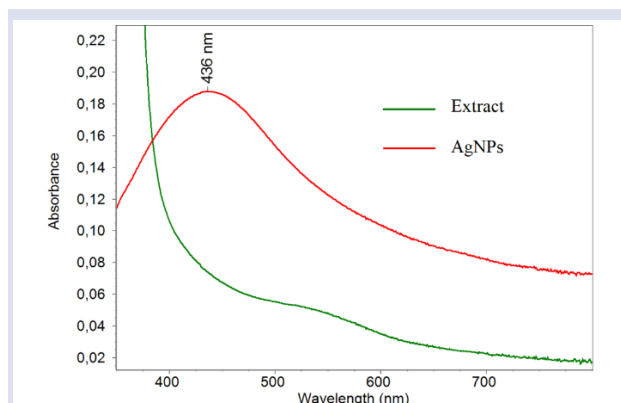


Figure 3. UV-visible spectra of *Hoya carnosa* Extract and AgNPs.

### FTIR Analysis

Fourier Transform Infrared Spectroscopy (FTIR) is one of the most fundamental techniques used to investigate the presence of functional groups in metallic nanoparticles. The synthesized AgNPs were characterized with 16 scan numbers in the wavenumber range of 4000-400  $\text{cm}^{-1}$  and the FTIR-ATR spectrum is presented in Figure 4. The strong band at 3450  $\text{cm}^{-1}$  is attributed to the O-H stretching vibrations of phenols and the N-H stretching vibrations of proteins [28, 29]. The medium sharp band centered at 1633  $\text{cm}^{-1}$  is assigned to the N-H bending vibrations originating from the amines in the protein structure [28]. The weak band at 1384  $\text{cm}^{-1}$  is attributed to the O-H bending vibrations of phenols [30]. The synthesis of the nanoparticles occurred via a reduction reaction, especially with the phenolic compounds in the plant extract acting as both reducing and stabilizing agents and thus constituting the main phytochemical group responsible for this process [31]. The broad bands at 1112  $\text{cm}^{-1}$  and 559  $\text{cm}^{-1}$  may be due to the C-N stretching vibrations of the amine groups and halo compounds, respectively.

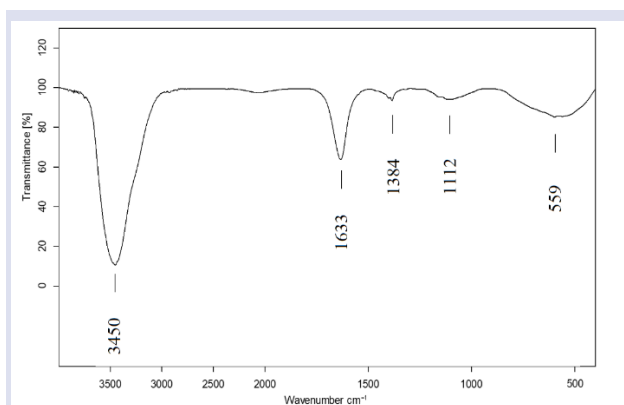


Figure 4. FTIR spectra of the biogenic synthesized AgNPs.

### XRD Analysis

XRD analysis was carried out at a voltage of 40 kV and a current of 15 mA with Cu K $\alpha$  radiation in the region of 2 $\theta$  from 20° to 80° and the spectrum of AgNPs are shown in Figure 5. The diffraction peaks at 2 $\theta$  values of 37.90°, 44.13°, 64.36°, and 77.38° are attributed to (1 1 1), (2 0 0), (2 2 0) and (3 1 1) planes, respectively. X-ray diffraction (XRD) patterns of silver nanoparticles show that its structure is face-centered cubic and match well with standard patterns of silver (JCPDS file no. 04-0783) [32, 33]. Since the analysis was performed with a low amount of AgNPs, the remaining peaks belong to the silicon originating from the sample holder. The average crystalline size of the AgNPs was calculated using the Debye Scherrer equation shown in Equation 2.

$$D = \frac{K\lambda}{\beta \cos \theta} \quad (2)$$

Here,  $D$  is the crystalline size of the nanoparticles,  $K$  is the Debye Scherrer constant (0.98),  $\lambda$  is the wavelength of Cu K $\alpha$  radiation (0.154 nm), and  $\beta$  is the full width at half

maximum (FWHM) [34]. The theoretical average crystalline size ( $D$ ) of the biogenic synthesized AgNPs was determined as 16 nm according to the Debye-Scherrer equation.

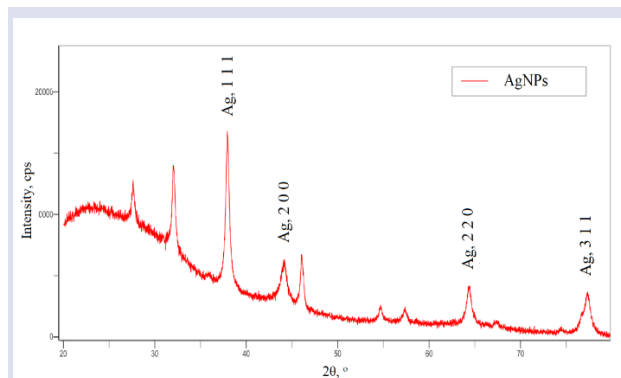


Figure 5. Powder XRD pattern of the biogenic synthesized AgNPs.

### SEM, TEM and EDX Analyses

Scanning electron microscopy (SEM) is undoubtedly the most widely used technique for characterizing the shape, size and surface morphology of nano-sized materials. AgNPs, synthesized using *Hoya carnosa* flower extract using a very simple, fast, economical and environmentally friendly method, were examined under 100 kx magnification using a secondary electron (SE) detector at 20 kV and shown in Figure 6.a. It is clearly seen that the nanoparticles, which are highly agglomerated due to drying process, are mostly spherical in shape and their sizes are below 100 nm.

Transmission electron microscopy (TEM) is another powerful technique that provides much higher resolution than other techniques due to the high voltage values it uses. Since the nanoparticles are dispersed in the liquid, agglomeration is largely eliminated and thus the size distribution and morphological properties of the nanoparticles can be measured directly. In this study, TEM analyses were examined under 250 kx magnification at 30 kV with an S-TEM module connected to the SEM device and the resulting image is presented in Figure 6.b. It was also confirmed by TEM that AgNPs were mostly spherical in shape and had a size below 100 nm. The diameters of 90 individual nanoparticles were measured from the SEM image (Figure 6.a) using the Mira TC software, and the average particle size was determined to be 21 nm. In addition, this value is very close to the theoretically calculated size of 16 nm from the XRD peaks.

Energy-dispersive X-ray spectroscopy (EDX) is a useful analysis technique for elemental and compositional characterization of the materials using the characteristic X-rays of electrons. EDX spectrum of AgNPs is given in Figure 6.c. The results show that approximately 93% of the nanoparticles by weight consist of silver element. The carbon and oxygen content in the material are thought to originate from phytochemicals bound to silver ions and residues of uncleaned *Hoya carnosa* flower extract. Similarly, the phytochemical content is also found in the FTIR spectrum, indicating that the results are consistent.

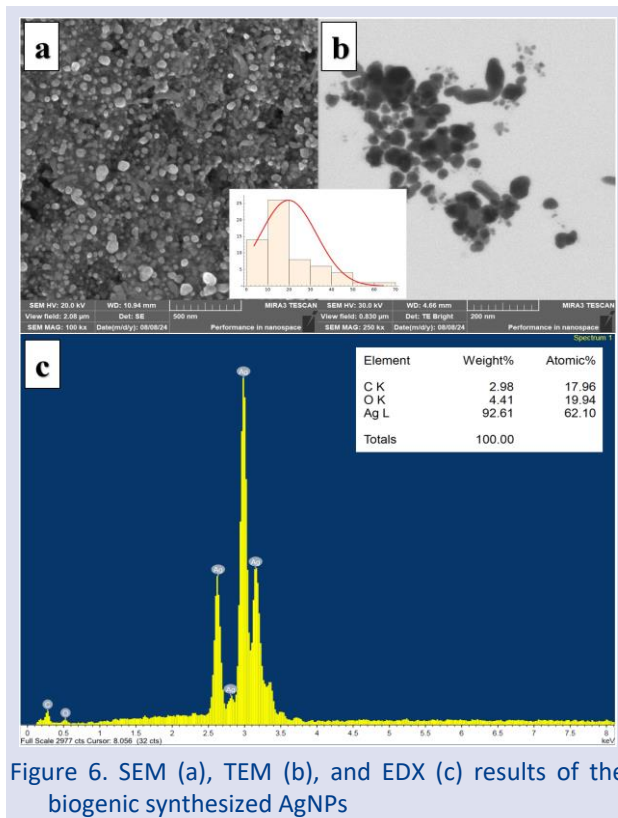


Figure 6. SEM (a), TEM (b), and EDX (c) results of the biogenic synthesized AgNPs

The synthesis of silver nanoparticles from flower extracts, like other parts of plants including leaves, stems, and roots, has recently become a widely researched topic. In this context, a comparative list of studies conducted in the literature on AgNP synthesis using flower extracts is presented in Table 1. When compared to other studies, it is clearly seen that AgNP synthesis from *Hoya carnosa* flower extract is a successful method with its very short reaction time and the possibility of synthesis under room conditions. In addition, the nanoparticle size measured at 21 nm is at a level that is competitive with AgNPs produced from other flower extracts reported in the literature.

Table 1. Recent studies on AgNP synthesis using flower extracts.

	Flower used for extract	Reaction duration	Reaction temperature	AgNPs size (nm)	Reference
1.	<i>Ferulago macrocarpa</i>	2.5 h	80 °C	14-25	[35]
2.	<i>Plumeria alba</i>	30 min	Room temp.	36.19	[36]
3.	<i>Caesalpinia pulcherrima</i>	24 h	Room temp.	12	[37]
4.	<i>Fritillaria</i>	2 h	Room temp.	10	[38]
5.	<i>Moringa oleifera</i>	30 min	-	8	[39]
6.	<i>Ipomoea digitata</i>	10 min	80 °C	<100	[40]
7.	<i>Madhuca longifolia</i>	20 min	40 °C	30-50	[41]
8.	<i>Tussilago farfara</i>	4 h	80 °C	13.57 ±3.26	[42]
9.	<i>Malva sylvestris</i>	4 h	25 °C	20-40 nm	[43]
10.	<i>Hoya carnosa</i>	15 min	Room temp.	21 nm	This study

## Conclusion

In this study, AgNPs were synthesized via a biogenic method using *Hoya carnosa* flower extract, which represents a low-cost, environmentally sustainable, and non-toxic green synthesis approach. The synthesis was completed under room conditions within a short time of 15 min, achieving a 64 % yield. The AgNPs were analyzed using UV-Vis, FTIR, XRD, SEM, TEM, and EDX analyses. The successful synthesis of the AgNPs was confirmed by the SPR peak at 436 nm in the UV-Vis analysis, while FTIR verified the presence of phytochemical components attached to the nanoparticles. XRD analysis revealed the face-centered cubic crystal structure of the AgNPs, and the size was calculated as 16 nm using the Debye Scherrer equation. SEM and TEM analyses demonstrated that the nanoparticles were spherical, with a particle size of 21 nm. EDX results further confirmed the presence of silver and phytochemical content. This study is the first report of the biogenic synthesis of AgNPs from *Hoya carnosa* flower extract, demonstrating that this plant can serve as a successful alternative to conventional AgNPs synthesis methods. Future studies may explore the antibacterial, antioxidant, and antifungal properties of these biogenic AgNPs, potentially expanding the use of *Hoya carnosa* in scientific research.

## Conflicts of interest

There are no conflicts of interest in this work.

## Acknowledgments

The author extends heartfelt gratitude to Assoc. Prof. Dr. Serap ÇETİNKAYA for her invaluable support and to Necla SÖZÜBATMAZ for generously providing the *Hoya carnosa* flowers used in this study.

## References

- [1] Saravanan A., Kumar P. S., Karishma S., Vo D.-V. N., Jeevanantham S., Yaashikaa P. R., George C. S., A Review on Biosynthesis of Metal Nanoparticles and Its Environmental Applications, *Chemosphere*, 264 (2021) 128580.
- [2] Malik A., Khan J. M., Alhomida A. S., Ola M. S., Alshehri M. A., Ahmad A., Metal Nanoparticles: Biomedical Applications and Their Molecular Mechanisms of Toxicity, *Chem. Pap.*, 76(10) (2022) 6073–6095.
- [3] Sosna-Głębska A., Szczecińska N., Znajdek K., Sibiński M., Review on Metallic Oxide Nanoparticles and Their Application in Optoelectronic Devices, *Acta Innov.*, 30 (2019) 5–15.
- [4] Gupta N., Kumar A., Dhawan S. K., Dhasmana H., Kumar A., Kumar V., Verma A., Jain V. K., Metal Nanoparticles Enhanced Thermophysical Properties of Phase Change Material for Thermal Energy Storage, *Mater. Today: Proc.*, 32 (2020) 463–467.
- [5] Dos Santos C. A., Ingle A. P., Rai M., The Emerging Role of Metallic Nanoparticles in Food, *Appl. Microbiol. Biotechnol.*, 104 (2020) 2373–2383.

- [6] Cruz-Luna A. R., Cruz-Martínez H., Vásquez-López A., Medina D. I., Metal Nanoparticles as Novel Antifungal Agents for Sustainable Agriculture: Current Advances and Future Directions, *J. Fungi*, 7(12) (2021) 1033.
- [7] Bhandari V., Jose S., Badanayak P., Sankaran A., Anandan V., Antimicrobial Finishing of Metals, Metal Oxides, and Metal Composites on Textiles: A Systematic Review, *Ind. Eng. Chem. Res.*, 61(1) (2022) 86–101.
- [8] Arroyo G. V., Madrid A. T., Gavilanes A. F., Naranjo B., Debut A., Arias M. T., Angulo Y., Green Synthesis of Silver Nanoparticles for Application in Cosmetics, *J. Environ. Sci. Health A*, 55(11) (2020) 1304–1320.
- [9] Joudeh N., Linke D., Nanoparticle Classification, Physicochemical Properties, Characterization, and Applications: A Comprehensive Review for Biologists, *J. Nanobiotechnology*, 20(1) (2022) 262.
- [10] Batlle X., Moya C., Escoda-Torroella M., Iglesias Ò., Rodríguez A. F., Labarta A., Magnetic Nanoparticles: From the Nanostructure to the Physical Properties, *J. Magn. Magn. Mater.*, 543 (2022) 168594.
- [11] Ratan Z. A., Haidere M. F., Nurunnabi M. D., Shahriar S. M., Ahammad A. S., Shim Y. Y., Reaney M. J., Cho J. Y., Green Chemistry Synthesis of Silver Nanoparticles and Their Potential Anticancer Effects, *Cancers*, 12(4) (2020) 855.
- [12] Bamal D., Singh A., Chaudhary G., Kumar M., Singh M., Rani N., Mundlia P., Sehrawat A. R., Silver Nanoparticles Biosynthesis, Characterization, Antimicrobial Activities, Applications, Cytotoxicity and Safety Issues: An Updated Review, *Nanomater.*, 11(8) (2021) 2086.
- [13] Ahmed S. F., Mofijur M., Rafa N., Chowdhury A. T., Chowdhury S., Nahrin M., Islam A. S., Ong H. C., Green Approaches in Synthesising Nanomaterials for Environmental Nanobioremediation: Technological Advancements, Applications, Benefits and Challenges, *Environ. Res.*, 204 (2022) 111967.
- [14] Rosman N. S. R., Harun N. A., Idris I., Wan Ismail W. I., Nanobiotechnology: Nature-Inspired Silver Nanoparticles towards Green Synthesis, *Energy Environ.*, 32(7) (2021) 1183–1206.
- [15] Akhtar M. S., Panwar J., Yun Y.-S., Biogenic Synthesis of Metallic Nanoparticles by Plant Extracts, *ACS Sustain. Chem. Eng.*, 1(6) (2013) 591–602.
- [16] Sharma D., Kanchi S., Bisetty K., Biogenic Synthesis of Nanoparticles: A Review, *Arab. J. Chem.*, 12(8) (2019) 3576–3600.
- [17] Ritu, Verma K. K., Das A., Chandra P., Phytochemical-Based Synthesis of Silver Nanoparticle: Mechanism and Potential Applications, *BioNanoScience*, 13(3) (2023) 1359–1380.
- [18] Fistiana F. A., Evanita E., Riadi A. A., Sistem Pendukung Keputusan Pemilihan Tanaman Hias Hoya Carnosa Berbasis Android Menggunakan Metode TOPSIS, *Jurasik*, 6(2) (2021) 305–311.
- [19] Alam N., Siddique W., Mishra M. K., Pandey A., Purshottam D. K., Singh K. J., Tewari S. K., Chakrabarty D., Micropropagation of *Hoya Carnosa*, *H. Kerrii*, *H. Parasitica*, and *H. Longifolia* Using Tray-Based Floating and Stationary Hydroponic Systems, *Sci. Hortic.*, 311 (2023) 111804.
- [20] Ab-Rahim N., Ismail W. I., Rosdan M. N. F., Mail M. H., Lamin R. A. C., Ismail S., Antibacterial Activity of Hoya Diversifolia Ethanolic Leaves Extract, *Biomed. Pharmacol. J.*, 12(2) (2019) 857–862.
- [21] Rumaling M. K., Fong S. Y., Rao P. V., Gisil J., Sani M. H. M., Wan Saudi W. S., Pharmacological Properties of Hoya (Apocynaceae): A Systematic Review, *Nat. Prod. Res.*, (2024) 1–17.
- [22] Rahayu M. L., Bakta I. M., Suardana W., Astawa N. M., Arijana I. G. K., Tunas I. K., Ethanol Extraction of Hoya Carnosa Leaves Improved Stroma of Middle Ear Epithelium Infected by *Pseudomonas Aeruginosa*, *Biomed. Pharmacol. J.*, 12(1) (2019) 171.
- [23] Mochizuki K., Furukawa S., Kawakita A., Pollinia Transfer on Moth Legs in Hoya Carnosa (Apocynaceae), *Am. J. Bot.*, 104(6) (2017) 953–960.
- [24] Rodríguez-León, E., Iñiguez-Palomares, R., Navarro, R. E., Herrera-Urbina, R., Tánori, J., Iñiguez-Palomares, C., Maldonado, A., Synthesis of Silver Nanoparticles Using Reducing Agents Obtained From Natural Sources (*Rumex hymenosepalus* Extracts), *Nanoscale Res. Lett.*, 8 (2013) 1–9.
- [25] Bhardwaj, A., Gupta, N., Green Synthesis and Characterization of Silver Nanoparticles Using Seed Extract of *Zanthoxylum armatum* and Their Kinetic Study, *Chem. Afr.*, (2025) 1-19.
- [26] Fan J., Cheng Y., Sun M., Functionalized Gold Nanoparticles: Synthesis, Properties and Biomedical Applications, *Chem. Rec.*, 20(12) (2020) 1474–1504.
- [27] Chand K., Cao D., Eldin Fouad D., Hussain Shah A., Qadeer Dayo A., Zhu K., Nazim Lakhani M., Mehdi G., Dong S., Green Synthesis, Characterization and Photocatalytic Application of Silver Nanoparticles Synthesized by Various Plant Extracts, *Arab. J. Chem.*, 13(11) (2020) 8248–8261.
- [28] Abraham J., Saraf S., Mustafa V., Chaudhary Y., Sivanangam S., Synthesis and Evaluation of Silver Nanoparticles Using Cymodocea Rotundata against Clinical Pathogens and Human Osteosarcoma Cell Line, *J. Appl. Pharm. Sci.*, 7(6) (2017) 055–061.
- [29] Jyoti K., Baunthiyal M., Singh A., Characterization of Silver Nanoparticles Synthesized Using *Urtica Dioica* Linn. Leaves and Their Synergistic Effects with Antibiotics, *J. Radiat. Res. Appl. Sci.*, 9(3) (2016) 17–227.
- [30] Kumar B., Smita K., Cumbal L., Debut A., Green Synthesis of Silver Nanoparticles Using Andean Blackberry Fruit Extract, *Saudi J. Biol. Sci.*, 24(1) (2017) 45–50.
- [31] Sivaraman, S. K., Elango, I., Kumar, S., Santhanam, V., A Green Protocol for Room Temperature Synthesis of Silver Nanoparticles in Seconds, *Curr. Sci.*, 97(7) (2009) 1055–1059.
- [32] Vidhu V. K., Philip D., Spectroscopic, Microscopic and Catalytic Properties of Silver Nanoparticles Synthesized Using *Saraca Indica* Flower, *Spectrochim. Acta - A: Mol. Biomol. Spectrosc.*, 117 (2014) 102–108.
- [33] Padalia H., Moteriya P., Chanda S., Green Synthesis of Silver Nanoparticles from Marigold Flower and Its Synergistic Antimicrobial Potential, *Arab. J. Chem.*, 8(5) (2015) 732–741.
- [34] Prashanth Kumar P. G., Shoukat Ali R. A., Jagadisha A. S., Umesh S. D., Synthesis and Studies of Cr Doped Zn Ferrites, *Mater. Today: Proc.*, 36 (2021) 837–840.
- [35] Azarbani F., Shiravand S., Green Synthesis of Silver Nanoparticles by *Ferulago Macrocarpa* Flowers Extract and Their Antibacterial, Antifungal and Toxic Effects, *Green Chem. Lett. Rev.*, 13(1) (2020) 41–49.
- [36] Mata R., Reddy Nakkala J., Rani Sadras S., Catalytic and Biological Activities of Green Silver Nanoparticles Synthesized from *Plumeria Alba* (Frangipani) Flower Extract, *Mater. Sci. Eng. C*, 51 (2015) 216–225.
- [37] Moteriya P., Chanda S., Synthesis and Characterization of Silver Nanoparticles Using Caesalpinia Pulcherrima Flower Extract and Assessment of Their in Vitro Antimicrobial, Antioxidant, Cytotoxic, and Genotoxic Activities, *Artif. Cells, Nanomed., Biotechnol.*, 45(8) (2017) 1556–1567.
- [38] Hemmati S., Rashtiani A., Zangeneh M. M., Mohammadi P.,



- Zangeneh A., Veisi H., Green Synthesis and Characterization of Silver Nanoparticles Using *Fritillaria* Flower Extract and Their Antibacterial Activity against Some Human Pathogens, *Polyhedron*, 158 (2019) 8–14.
- [39] Bindhu M. R., Umadevi M., Esmail G. A., Al-Dhabi N. A., Arasu M. V., Green Synthesis and Characterization of Silver Nanoparticles from *Moringa Oleifera* Flower and Assessment of Antimicrobial and Sensing Properties, *J. Photochem. Photobiol. B: Biol.*, 205 (2020) 111836.
- [40] Varadavenkatesan T., Selvaraj R., Vinayagam R., Dye Degradation and Antibacterial Activity of Green Synthesized Silver Nanoparticles Using *Ipomoea Digitata* Linn. Flower Extract, *Int. J. Sci. Environ. Technol.*, 16(5) (2019) 2395–2404.
- [41] Patil M. P., Singh R. D., Koli P. B., Patil K. T., Jagdale B. S., Tipare A. R., Kim G.-D., Antibacterial Potential of Silver Nanoparticles Synthesized Using *Madhuca Longifolia* Flower Extract as a Green Resource, *Microb. Pathog.*, 121 (2018) 184–189.
- [42] Lee Y. J., Song K., Cha S.-H., Cho S., Kim Y. S., Park Y., Sesquiterpenoids from *Tussilago Farfara* Flower Bud Extract for the Eco-Friendly Synthesis of Silver and Gold Nanoparticles Possessing Antibacterial and Anticancer Activities, *Nanomater.*, 9(6) (2019) 819.
- [43] Mahmoodi Esfanddarani H., Abbasi Kajani A., Bordbar A.-K., Green Synthesis of Silver Nanoparticles Using Flower Extract of *Malva Sylvestris* and Investigation of Their Antibacterial Activity, *IET Nanobiotechnol.*, 12(4) (2018) 412–416.

## Determination of Total Phenolic Amounts of Chloroform, Acetone and Methanol Extracts of *Sargassum sp.*, *Ulva sp.* and *Schizochytrium sp.*

Mehmet Naz <sup>1,a,\*</sup><sup>1</sup> Aquaculture, Marine Sciences and Technology Faculty, Iskenderun Technical University, Hatay, Türkiye.

\*Corresponding author

### Research Article

#### History

Received: 30/01/2024


Accepted: 27/05/2025

### ABSTRACT

The present study was aimed to determine the total phenolic amounts of the bioactive contents resulting from the extraction of *Sargassum sp.*, *Ulva sp.* and *Schizochytrium sp.* with different solvents such as chloroform, acetone and methanol. Total phenolic content was determined using the Folin-Ciocalteu method. Samples (12.5%) were extracted with chloroform, acetone, and methanol, then filtered and the solvents were evaporated. Absorbance was measured at 760 nm. Total phenolic content was expressed as gallic acid equivalents (GAE). The total phenolic contents obtained from chloroform, acetone and methanol extracts of *Sargassum sp.*, *Ulva sp.* and *Schizochytrium sp.* were determined as 136.40±1.93 mg GAE/g extract -3.61±0.18 mg GAE/g extract -7.83±0.03 mg GAE/g extract, 5.25±0.07 mg GAE/g extract -4.27±0.1 mg GAE/g extract -14.5±0.06 mg GAE/g extract and 15.7±0.27 mg GAE/g extract -2.6±0.04 mg GAE/g extract -14.84±0.11 mg GAE/g extract, respectively. Differences between total phenolic values were found to be statistically significant ( $p<0.05$ ). The extraction yields obtained from chloroform, acetone and methanol extracts of *Sargassum sp.*, *Ulva sp.* and *Schizochytrium sp.* were determined as 2.2±0.06%-4.35±0.07%-6.68±0.14%, 2.96±0.02%-4.33±0.09%-9.74±0.16% and 14.96±0.24%-10.03±0.004%-19.03±0.3%, respectively ( $p<0.05$ ). Biochemical parameters such as dry matter, protein, ash and lipid of *Sargassum sp.*, *Ulva sp.* and *Schizochytrium sp.* were found to be 94.05±0.01% -20.92±0.35% -26.55±1.77% -1.36±0.01%, 94.1±0.005%-17.04±0.04%-28.11±0.06% -2.66±0.05% and 95.1±0.05%-23.01±0.07%-9.59±0.787%-25.5±0.21%. The soluble protein concentrations of *Sargassum sp.*, *Ulva sp.* and *Schizochytrium sp.* in distilled water were determined as 66.45±0.5mg/g, 83.38±0.88 mg/g and 115.95±0.89 mg/g, respectively. In conclusion, chloroform and methanol extracts of *Schizochytrium sp.* had good extraction yield and phenolic content. On the other hand, the chloroform extract of *Sargassum sp.* had the highest phenolic content, while the extraction yield was at the lowest level. Acetone extracts of the 3 species tested exhibited low phenolic activity.

**Keywords:** *Sargassum sp.*, *Ulva sp.*, *Schizochytrium sp.*, Different solvents, Total phenolics.

This article is licensed under a Creative Commons Attribution-NonCommercial 4.0 International License (CC BY-NC 4.0)

<sup>a</sup> [mehmet.naz@iste.edu.tr](mailto:mehmet.naz@iste.edu.tr) <https://orcid.org/0000-0002-5129-8498>

## Introduction

Algae and their secondary metabolites, as primary producers in the aquatic ecosystem, play a crucial role in the environmental cycle and are widely utilized across various sectors. Macroalgae are known as three groups depending on pigmentation, namely brown (2000 species), red (7300 species) and green (1500 species) [1]. FAO stated that 28.6% (122.58 million tons) of world aquaculture production is macroalgae cultivation [2]. Cai et al. revealed that the tonnage and economic contributions of brown algae and other algae such as red and green to the world macroalgae production are 47.3%-52% and 52.7%-48%, respectively [3]. Additionally, the researcher has shown that green macroalgae contribute the lowest (less than 1%) to the world macroalgae production. Yu et al. stated that *Schizochytrium sp.* is an important source of antioxidant compounds such as phenolics and DHA product [4]. La et al. stated that phenolic compounds and n-3 PUFAs in *Schizochytrium sp.* can regulate the antioxidant function of animals [5].

Since macroalgae are exposed to various abiotic and biotic stresses during their life cycle in the ecosystem, they

produce secondary metabolites to have strong defense systems. Phenolic compounds are indicators of stress algae metabolism [6]. Jégou et al. pointed out that macroalgae are rich in phytochemicals including antioxidants [7]. Researchers have reported that macroalgae contain carotenoids, lipids, dietary fiber, proteins, minerals, vitamins, and phenolic compounds, which are biologically active metabolites [8]. Wang et al. revealed that strong relations between phenolic compounds and antioxidant activities were found [9]. Phenolic compounds having antioxidant potential have been intensely investigated in recent years. Phenolic compounds are considered one of the most important classes of natural antioxidants [10]. Researchers have stated that phenolic compounds increase the antioxidant capacity of algae and that algae also contain phenolic compounds that are beneficial to human health [7]. Sadeghi et al. showed that applications of extracted phenolic compounds were pharmaceutical, biomedical, cosmetic industry, packaging industry, food industry and textile industry [11].

Algae attract attention due to their bioactive properties. The study aimed to reveal the total phenolic contents as well as their biochemical compositions, extraction yields and soluble protein concentrations of *Ulva sp.* (Chlorophyta), *Sargassum sp.* (Ochrophyta) and *Schizochytrium sp.*

## Materials and Methods

The *Sargassum sp.*, *Ulva sp.*, and *Schizochytrium sp.* meals used in this study was sourced from commercial suppliers, namely Akuamaks (Turkey) and Fuzhou Wonderful Biological Technology Co. Ltd. (China). Solvents with varying polarities, including chloroform, acetone, and methanol, were employed for the extraction of *Sargassum sp.*, *Ulva sp.*, and *Schizochytrium sp.* meals.

### Total Phenolic Content

The total phenolic content was determined using the Folin-Ciocalteu method as described by Singleton et al.

[12]. Briefly, the samples were extracted with chloroform, acetone, and methanol at a concentration of 12.5 g/100 mL by stirring at room temperature for 24 hours. The resulting extracts were filtered through Whatman No. 1 filter paper, and the solvents were evaporated using a rotary evaporator. Each extract (1 mg/ml) was added to a universal bottle, followed by 1 mL of Folin-Ciocalteu reagent. The mixture was thoroughly mixed, and after 3 minutes, 3 mL of sodium carbonate solution was added. The mixture was then left to stand in the dark at room temperature (25°C) for 2 hours, as the reaction is sensitive to light. Absorbances were measured at 760 nm using a UV-1280 Shimadzu spectrophotometer. A gallic acid (GA) standard curve (0.0625, 0.125, 0.25, 0.5 and 1 mg GA/ml) shown in Figure 1, was used in the calculations. Total phenolic content was expressed as gallic acid equivalents (mg GAE/g extract). Extraction yield (w/w) was used as an indicator of solvent efficiency. Total phenolic contents of *Sargassum sp.*, *Ulva sp.* and *Schizochytrium sp.* were determined in triplicate.

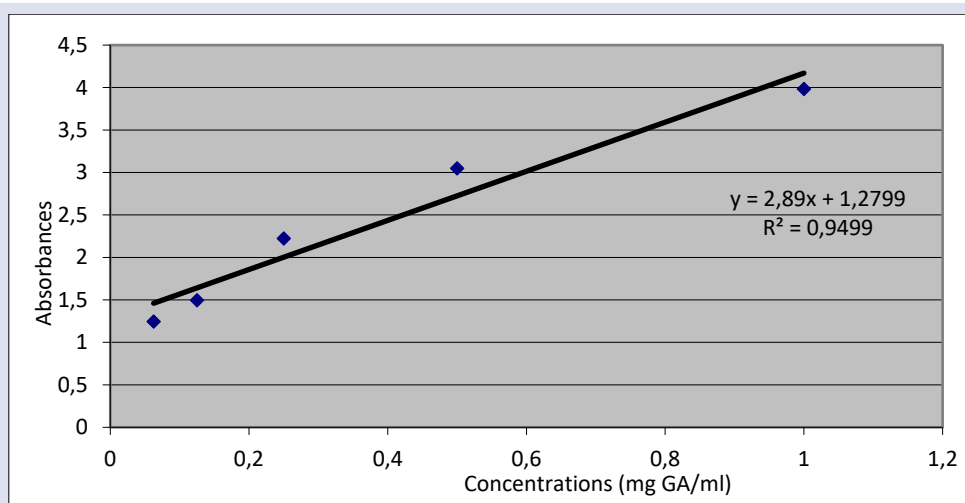


Figure 1. Standard curve obtained from different concentrations of GA.

### Biochemical Compositions

Dry matter analysis was based on the principle of evaporating the moisture in the samples at 105 °C. For ash analysis, the samples were incinerated at 550 °C for 4 hours, cooled in a desiccator, and then weighed using a scale with a sensitivity of 0.0001 g. Lipid analysis was conducted using the chloroform–methanol extraction method described by Bligh and Dyer [13]. Protein content was determined following standard AOAC procedures [14], which involve three main steps: digestion, distillation, and titration. During digestion, the samples were incinerated at 420 °C. This was followed by the distillation step, and finally, titration was carried out using 0.1 N HCl. The volume of 0.1 N HCl consumed during titration was used in the calculations. Biochemical compositions of *Sargassum sp.*, *Ulva sp.* and *Schizochytrium sp.* were determined in triplicate

### Soluble Protein Contents

Soluble protein concentrations of *Sargassum sp.*, *Ulva sp.* and *Schizochytrium sp.* were determined in triplicate using the dye-binding method developed by Bradford [15]

(Bio-Rad Protein Assay, Cat. No: 5002). Following the procedure provided with the Bio-Rad kit, absorbance was measured at 595 nm using a Shimadzu UV–1280 spectrophotometer. The absorbance values were calculated based on a BSA (Bovine Serum Albumin) standard curve.

### Statistical Analyses

Analyses were performed in triplicate. Statistical analyses were performed using SPSS 17.0 software. Duncan's multiple comparison test was applied at a 5% significance level. The results were expressed as mean ± standard error (SE).

## Results

In current study, the total phenolic amounts of the bioactive extracts obtained with different solvents such as chloroform, acetone and methanol from *Sargassum sp.*, *Ulva sp.* and *Schizochytrium sp.* were determined and the

results are given in Table 1. Also, the biochemical compositions, extraction yields obtained from different solvents and the soluble protein concentrations of *Sargassum sp.*, *Ulva sp.* and *Schizochytrium sp.* were determined.

Table 1. Total phenolic contents of algae extracted in different solvents (mg GAE/g extract)

Species	Solvents		
	Chloroform	Acetone	Methanol
<i>Sargassum sp.</i>	136.40±1.93 <sup>c</sup>	3.61±0.18 <sup>a</sup>	7.83±0.03 <sup>b</sup>
<i>Ulva sp.</i>	5.25±0.07 <sup>b</sup>	4.27±0.1 <sup>a</sup>	14.5±0.06 <sup>c</sup>
<i>Schizochytrium sp.</i>	15.7±0.27 <sup>c</sup>	2.6±0.04 <sup>a</sup>	14.84±0.11 <sup>b</sup>

a,b,c show statistical differences (p<0.05)

The total phenolic contents obtained from chloroform, acetone and methanol extracts of *Sargassum sp.*, *Ulva sp.* and *Schizochytrium sp.* were determined as 136.40±1.93 mg GAE/g extract-3.61±0.18 mg GAE/g extract-7.83±0.03 mg GAE/g extract, 5.25±0.07 mg GAE/g extract-4.27±0.1 mg GAE/g extract-14.5±0.06 mg GAE/g extract and 15.7±0.27 mg GAE/g extract-2.6±0.04 mg GAE/g extract-14.84±0.11 mg GAE/g extract, respectively. Differences between total phenolic values were found to be statistically significant (p<0.05). The highest total phenolic content was observed in the chloroform extract of *Sargassum sp.* while the lowest total phenolic contents were in the acetone extracts of all tested species. The lowest total phenolic content was found in acetone group of *Schizochytrium sp.* The extraction yields of *Sargassum*

*sp.*, *Ulva sp.* and *Schizochytrium sp.* extracted with different solvents are given in Table 2. The extraction yields obtained from chloroform, acetone and methanol extracts of *Sargassum sp.*, *Ulva sp.* and *Schizochytrium sp.* were determined as 2.2±0.06%-4.35±0.07%-6.68±0.14%, 2.96±0.02%-4.33±0.09%-9.74±0.16% and 14.96±0.24%-10.03±0.004%-19.03±0.3%, respectively (p<0.05). The highest extraction yield was determined in the methanol extract of *Schizochytrium sp.* The all extracts of *Schizochytrium sp.* have higher extraction yields according to the extracts of *Sargassum sp.* and *Ulva sp.*

In study, the biochemical compositions of *Sargassum sp.*, *Ulva sp.* and *Schizochytrium sp.* were also determined (Table 3). Biochemical parameters such as dry matter, protein, ash and lipid of *Sargassum sp.*, *Ulva sp.* and *Schizochytrium sp.* were found to be 94.05±0.01%-20.92±0.35%-26.55±1.77%-1.36±0.01%, 94.1±0.005%-17.04±0.04%-28.11±0.06%-2.66±0.05% and 95.1±0.05%-23.01±0.07%-9.59±0.787%-25.5±0.21% (p<0.05). The highest dry matter, protein, ash and lipid amounts were observed in *Schizochytrium sp.* (95.1±0.05%), *Schizochytrium sp.* (23.01±0.07%), *Ulva sp.* (28.11±0.06%) and *Schizochytrium sp.* (25.5±0.21%).

Table 2. The extracted yields of algae extracted in different solvents (%)

Species	Solvents		
	Chloroform	Acetone	Methanol
<i>Sargassum sp.</i>	2.2±0.06 <sup>a</sup>	4.35±0.07 <sup>b</sup>	6.68±0.14 <sup>c</sup>
<i>Ulva sp.</i>	2.96±0.02 <sup>a</sup>	4.33±0.09 <sup>b</sup>	9.74±0.16 <sup>c</sup>
<i>Schizochytrium sp.</i>	14.96±0.24 <sup>b</sup>	10.03±0.004 <sup>a</sup>	19.03±0.3 <sup>c</sup>

a,b,c show statistical differences (p<0.05)

Table 3. Biochemical compositions of algae (% dry basis)

Species	Biochemical Compositions			
	Dry Matter	Protein	Ash	Lipid
<i>Sargassum sp.</i>	94.05±0.01 <sup>a</sup>	20.92±0.35 <sup>b</sup>	26.55±1.77 <sup>b</sup>	1.36±0.01 <sup>a</sup>
<i>Ulva sp.</i>	94.1±0.005 <sup>a</sup>	17.04±0.04 <sup>a</sup>	28.11±0.06 <sup>c</sup>	2.66±0.05 <sup>b</sup>
<i>Schizochytrium sp.</i>	95.1±0.05 <sup>b</sup>	23.01±0.07 <sup>c</sup>	9.59±0.787 <sup>a</sup>	25.5±0.21 <sup>c</sup>

a,b,c show statistical differences (p<0.05)

The soluble protein concentrations of *Sargassum sp.*, *Ulva sp.* and *Schizochytrium sp.* in distilled water were determined as 66.45±0.5mg/g, 83.38±0.88 mg/g and 115.95±0.89 mg/g, respectively (p<0.05). The lowest and highest amounts of the soluble protein concentrations were *Sargassum sp.* (66.45±0.5mg/g) and *Schizochytrium sp.* (115.95±0.89 mg/g), respectively.

## Discussions

In the present study, the total phenolic contents of bioactive extracts obtained from *Sargassum sp.*, *Ulva sp.*, and *Schizochytrium sp.* using different solvents such as chloroform, acetone, and methanol were determined. In addition, the biochemical compositions, extraction yields from different solvents, and soluble protein concentrations of *Sargassum sp.*, *Ulva sp.*, and *Schizochytrium sp.* were investigated.

El-Baky et al. [16] found that total phenolic content of *Ulva lactuca* was 4.6±0.58 mg GAE/g extract. Kumar et al. [17] determined phenolic contents in three green algae

were 32.57-61.69 mg/g dry weight. Gaffney et al. [18] found that the highest total phenol content of *Schizochytrium sp.* was 3.1 ± 0.1 mg GAE/g. Çelenk [19] revealed that total phenolic contents of Chlorophyta and Ochrophyta species were 126.3-6.3 mg GAE/g and 477.2-3.3 mg GAE/g, respectively. Puspita et al. [20] found that soluble total phenolic content of viscozyme extract of the brown alga *Sargassum muticum* was 6.4% of dry weight. Güner [21] determined that total phenolic contents of brown and green macroalgae were 33.20±1.41 mg GAE/g methanol extract and 2.34±0.1 mg GAE/g (chloroform extract)-25.58±1 mg GAE/g (methanol extract), respectively. Yılmaz et al. determined that the highest and lowest phenolic contents of *Gongolaria barbata* (Ochrophyta) were 2.29±0.01 mg GAE/g extract and 0.41±0.01 mg GAE/g extract, respectively [8]. The total phenolic contents of *Sargassum vulgare* and *Ulva intestinalis* extracted using acetone, ethanol, chloroform, and methanol were determined to be 0.004 mg GAE/100 g-0.003 mg GAE/100 g-0.003 mg GAE/100 g-0.003 mg GAE/100 g and 0.003 mg GAE/100 g-0.002 mg GAE/100 g-



0.003 mg GAE/100 g-0.004 mg GAE/100 g, respectively [22]. Gür and Polat [23] found that phenolics ranged between 34.6-106.05 mg GAE/g dry weight. Santos et al. [24] determined that the lowest and highest total phenolic contents of *Sargassum muticum* were  $1752 \pm 46.3$  mg GAE/L and  $440.8 \pm 20.4$  mg GAE/L, respectively. Researchers have indicated that the observed differences in total phenolic content can be attributed to multiple factors, including environmental conditions, algal species, geographical origin, physiological variations, the choice of solvents, extraction conditions, nutrient availability, and the growing season [22].

Elnabris et al. [25] found that extraction yields of *Ulva lactuca*, *Enteromorpha compressa* *Padina pavonica* were 17%, 7.3% and 5.2%, respectively. Güner [21] showed that extraction yields of brown and green macroalgae were 228 mg (%0,21-chloroform)-3902 mg (%3,6-methanol) and 195 mg (%0,22-chloroform)- 927 mg (%1,1-methanol), respectively. Puspita et al. [20] revealed that extraction yields of aqueous extract and enzyme extract were  $26.5 \pm 4.7\%$  of dry algal material and  $32.6 \pm 4.9\%$  of dry algal material, respectively. Park et al. [26] showed that the extraction yields of brown macroalgae varied from 68.40% to 81.88%. Hashem et al. [27] showed that the extraction yield depends on the solvent polarity.

Researcher showed that biochemical compositions such as ash, lipid and protein of *Ulva sp.* and *Sargassum sp.* were 28.77-29.6% ; 0.38-3.4% ; 9.24-33.6% and 26.95-27.94% ; 0.91-1.37% ; 20.6-20.69%, respectively [28,29]. Øverland et al. [30] showed that ash, lipid and protein changes of green, brown and red macroalgae were 11-55% ; 0.3-2.8% ; 3.2-35.2%, 15-45% ; 0.3- 9.6% ; 2.4-16.8% and 12-42.2% ; 0.2-12.9% ; 6.4-37.6%, respectively. Naz et al. [31] showed that ash, lipid and protein amounts of green and brown macroalgae were 12.19-17.68% ; 1.74-4.84% ; 5.56-6.70% and 13.19 - 21.38% ; 4.31-5.83% ; 9.75-11.45%, respectively. Gür and Polat [23] determined ash, lipid and protein values of macroalgae were 3.12-77%, 0.25 - 6.35% and 2.94 - 6.15%. Allen et al. [32] revealed that *Schizochytrium sp.* is rich source of lipid and docosahexaenoic acid (DHA). Researcher showed that lipid, PUFA, EPA and DHA amounts of *Schizochytrium sp.* were 46-78%, 46.96%, 0.72% and 37.63%, respectively [33]. De Lima Valença et al. [34] revealed that protein, lipid, DHA and EPA amounts of the genus *Schizochytrium sp.* were 17% , 53% , 27.20% DHA and 0.28% EPA, respectively. Park et al. [26] showed that ash contents of macroalgae ranged from 16.79% to 26.02%.

Literatures showed that ash contents of macroalgae depend on the species, geographical, environmental factors, the presence of various mineral components and the amount of mineral absorbed [35]. Chakraborty and Bhattacharya [36] pointed out that the lipid contents of macroalgae can change according to the amounts of the elements in their environment. Ahmad et al. [37] revealed that brown macroalgae have high lipid contents than those of red and green macroalgae species. The differences in the protein amounts obtained from macroalgae could be due to factors such as geographic

area, species, maturity and seasons [38]. Macroalgae contain between 8% and 47% protein by dry weight. Øverland et al. [30] showed that protein amounts of green and red macroalgae were higher than that of brown macroalgae. The researcher has demonstrated that biochemical differences can exist even within the same species. Variations in the ash, lipid, and protein contents of macroalgae may be attributed to factors such as species type, geographical location, season, sampling site, water quality, light intensity, salinity, temperature, and species-specific characteristics. [29]. Bernaerts et al. [39] stated that the observed differences may be due to the difference in the analysis methods used in the studies.

The soluble protein concentrations of *Sargassum sp.*, *Ulva sp.* and *Schizochytrium sp.* in distilled water were determined as  $66.45 \pm 0.5$  mg/g,  $83.38 \pm 0.88$  mg/g and  $115.95 \pm 0.89$  mg/g, respectively ( $p < 0.05$ ). The lowest and highest amounts of the soluble protein concentrations were *Sargassum sp.* ( $66.45 \pm 0.5$  mg/g) and *Schizochytrium sp.* ( $115.95 \pm 0.89$  mg/g), respectively. El-Sayed et al. [40] reported that soluble protein concentrations can vary depending on factors such as harvest time and cell degradation. Soluble proteins are associated with an increase in nitrogenous compounds, including nitrates, free amino acids, ammonia, nitrites, and short-chain peptides.

In conclusion, the chloroform and methanol extracts of *Schizochytrium sp.* demonstrated good extraction yields and notable phenolic content. Conversely, the chloroform extract of *Sargassum sp.* exhibited the highest phenolic content, despite having the lowest extraction yield. The acetone extracts of all three tested species showed low phenolic activity. Algae are globally recognized as sustainable resources with high bioactive potential. In this context, further optimization studies are needed on culturable algae, taking into account the factors that influence phenolic compound levels, extraction efficiency, soluble protein content, and overall biochemical composition. The data generated from such studies will enhance industrial interest in algae and broaden their range of applications.

## Conflicts of interest

There are no conflicts of interest in this work.

## Ethical Approval Statement

Since no human or animal subjects were used in this study, ethical approval was not required.

## References

- [1] Guiry M.D., *AlgaeBase GGM*, World-wide Electronic Publication, National University of Ireland, Galway, (2021).
- [2] FAO, *The State of World Fisheries and Aquaculture. Towards Blue Transformation*, Rome: FAO, (2022).
- [3] Cai, J., Lovatelli, A., Aguilar-Manjarrez, J., Cornish, L., Dabbadie, L., Desrochers, A., Diffey, S., Garrido Gamarro,

- E., Geehan, J., Hurtado, A., Lucente, D., Mair, G., Miao, W., Potin, P., Przybyla, C., Reantaso, M., Roubach, R., Tauati, M., Yuan, X., *Seaweeds and microalgae: an overview for unlocking their potential in global aquaculture development*, FAO Fisheries and Aquaculture Circular No. 1229, Rome: FAO, (2021).
- [4] Yu, J. H., Wang, Y., Sun, J., Bian, F., Chen, G., Zhang, Y., Wu, Y. J., Antioxidant activity of alcohol aqueous extracts of *Cryptocodinium cohnii* and *Schizochytrium* sp., *Journal of Zhejiang University. Science. B*, 18(9) (2017) 797.
  - [5] La, A. L. T. Z., Pierce, K. M., Liu, W. H., Gao, S. T., Bu, D. P., Ma, L., Supplementation with *Schizochytrium* sp. enhances growth performance and antioxidant capability of dairy calves before weaning, *Animal Feed Science and Technology*, 271 (2021) 114779.
  - [6] Stengel, D. B., Connan, S., Popper, Z. A., Algal chemodiversity and bioactivity: sources of natural variability and implications for commercial application, *Biotechnology Advances*, 29(5) (2011) 483–501.
  - [7] Jégou, C., Connan, S., Bihannic, I., Céranola, S., Guérard, F., Stiger-Pouvreau, V., Phlorotannin and pigment content of native canopy-forming Sargassaceae species living in intertidal rockpools in Brittany (France): any relationship with their vertical distribution and phenology?, *Marine Drugs*, 19(9) (2021) 504–524.
  - [8] Yılmaz, M., Türker, G., Ak, İ., The effect of different solvents on antioxidant properties of *Gongolaria barbata* (Phaeophyceae), *Çanakkale Onsekiz Mart University Journal of Marine Sciences and Fisheries*, 4(2) (2021) 197–201.
  - [9] Wang, B. G., Zhang, W. W., Duan, X. J., Li, X. M., In vitro antioxidative activities of extract and semipurified fractions of the marine red alga, *Rhodomela confervoides* (Rhodomelaceae), *Food Chemistry*, 113 (2009) 1101–1105.
  - [10] Andrade, L. M., Andrade, C. J., Dias, M., Nascimento, C., Mendes, M. A., Chlorella and spirulina microalgae as sources of functional foods, nutraceuticals, and food supplements, *Nutraceuticals and Food Supplements*, 6(1) (2018) 45–58.
  - [11] Sadeghi, A., Rajabiyan, A., Nabizade, N., Meygolinezhad, N., Ahmady, A. Z., Seaweed-derived phenolic compounds as diverse bioactive molecules: A review on identification, application, extraction and purification strategies, *International Journal of Biological Macromolecules*, (2024) 131147.
  - [12] Singleton, V. L., Orthofer, R., Lamuela-Raventós, R. M., Analysis of total phenols and other oxidation substrates and antioxidants by means of Folin-Ciocalteu reagent. In: *Methods in Enzymology*, Academic Press, 299 (1999) 152–178.
  - [13] Bligh, E. G., Dyer, W. J., A rapid method of total lipid extraction and purification, *Canadian Journal of Biochemistry and Physiology*, 37(8) (1959) 911–917.
  - [14] AOAC, *Animal Feed*. In: *Official Methods of Analysis*, (1997), 30 pp.
  - [15] Bradford, M. M., A rapid and sensitive method for the quantitation of microgram quantities of protein utilizing the principle of protein dye binding, *Analytical Biochemistry*, 72 (1976) 248–254.
  - [16] El-Baky, H. H. A., El-Baz, F. K., El-Baroty, G. S., Natural preservative ingredient from marine alga *Ulva lactuca* L., *International Journal of Food Science and Technology*, 44(9) (2009) 1688–1695.
  - [17] Kumar, M., Gupta, V., Kumari, P., Reddy, C. R. K., Jha, B., Assessment of nutrient composition and antioxidant potential of Caulerpaceae seaweeds, *Journal of Food Composition and Analysis*, 24 (2011) 270–278.
  - [18] Gaffney, M., O'Rourke, R., Murphy, R., Manipulation of fatty acid and antioxidant profiles of the microalgae *Schizochytrium* sp. through flaxseed oil supplementation, *Algal Research*, 6 (2014) 195–200.
  - [19] Çelenk, F. G., Investigation of antioxidant, cytotoxic, hypoglycemic and hypolipidemic effects of some macroalgae from the coasts of İzmir Gulf, PhD Thesis, Ege University, Graduate School of Natural and Applied Sciences, 2014.
  - [20] Puspita, M., Déniel, M., Widowati, I., Radjasa, O. K., Douzenel, P., Marty, C., Bourgoignon, N., Total phenolic content and biological activities of enzymatic extracts from *Sargassum muticum* (Yendo) Fensholt, *Journal of Applied Phycology*, 29 (2017) 2521–2537.
  - [21] Güner, A., Investigation of the protective effects and biological activities of hexane, chloroform and methanol extracts of brown algae (*Halopteris scoparia* Sauvageau), green (*Enteromorpha linza* J. Agardh) and red (*Gracilaria gracilis* M. Steentoft, L. M. Irvine & W. F. Farnham) collected from İzmir Gulf (Urla), PhD Thesis, Ege University, Graduate School of Natural and Applied Sciences, 2017.
  - [22] Peksezer, B., Alp, M. T., Ayas, D., *Ulva intestinalis* (Linnaeus 1753) ve *Sargassum vulgare* (F. Furcatum (Kützinger) J. Agardh 1889) ekstraktlarının bazı patojen mikroorganizmalar üzerindeki antimikrobiyal etkileri, *Mediterranean Fisheries and Aquaculture Research*, 5(2) (2022) 54–64.
  - [23] Gür, İ., Polat, S., Seasonal changes in proximate and bioactive compounds of brown and red seaweeds from İskenderun Bay, the North-Eastern Mediterranean Sea, *Çanakkale Onsekiz Mart University Journal of Marine Sciences and Fisheries*, 6(1) (2023) 33–43.
  - [24] Santos, J. M., Jesus, B. C., Ribeiro, H., Martins, A., Marto, J., Fitas, M., Marrucho, I. M., Extraction of macroalgae phenolic compounds for cosmetic application using eutectic solvents, *Algal Research*, 79 (2024) 103438.
  - [25] Elnabris, K. J., Elmanama, A. A., Chihadeh, W. N., Antibacterial activity of four marine seaweeds collected from the coast of Gaza Strip, Palestine, *Mesopotamian Journal of Marine Sciences*, 28(1) (2013) 81–92.
  - [26] Park, J. S., Han, J. M., Shin, Y. N., Park, Y. S., Shin, Y. R., Park, S. W., Chun, B. S., Exploring bioactive compounds in brown seaweeds using subcritical water: A comprehensive analysis, *Marine Drugs*, 21(6) (2023) 328.
  - [27] Hashem, S. M., El-Lahot, A., Helal, A. M., Massoud, M. I., Evaluation of the phytochemicals and nutritional characteristics of some microalgae grown in Egypt as healthy food supplements, *Egyptian Journal of Food Science*, 49(1) (2021) 173–185.
  - [28] Diken, G., Determination using in vitro assay of inhibition values of different feed ingredients on the protease activities of meagre, *Argyrosomus regius* (Asso, 1801) larvae and production of species-specific microdiet, PhD Thesis, Süleyman Demirel University, Graduate School of Natural and Applied Sciences, 2018.
  - [29] Yenmiş, A. M., Naz, M., The determination of the leaching ratios of microdiets containing algae used as direct and indirect in aquaculture, *Journal of Applied Animal Research*, 46(1) (2018) 1496–1504.
  - [30] Øverland, M., Mydland, L. T., Skrede, A., Marine macroalgae as sources of protein and bioactive compounds in feed for monogastric animals, *Journal of the Science of Food and Agriculture*, 99(1) (2019) 13–24.

- [31] Naz, M., Sayın, S., Çetin, Z., Saygılı, E. İ., Taşkın, E., Söyler, O., The changes in biochemical compositions of five different macroalgae and seagrass (*Halophila stipulacea* (Forsskal) Ascherson 1867) collected from Iskenderun Bay, *Journal of Advanced Research in Natural and Applied Sciences*, 8(4) (2022) 796–804.
- [32] Allen, K. M., Habte-Tsion, H. M., Thompson, K. R., Filer, K., Tidwell, J. H., Kumar, V., Freshwater microalgae (*Schizochytrium* sp.) as a substitute to fish oil for shrimp feed, *Scientific Reports*, 9(1) (2019) 6178.
- [33] Chi, G., Xu, Y., Cao, X., Li, Z., Cao, M., Chisti, Y., He, N., Production of polyunsaturated fatty acids by *Schizochytrium* (*Aurantiochytrium*) spp., *Biotechnology Advances*, 55 (2022) 107897.
- [34] De Lima Valença, R., da Silva Sobrinho, A. G., Silva, L. G., Borghi, T. H., de Andrade, N., Soares, M., Meza, D. A. R., Bezerra, L. R., Performance, carcass traits, physicochemical properties and fatty acids composition of lamb's meat fed diets with marine microalgae meal (*Schizochytrium* sp.), *Livestock Science*, 243 (2021) 104387.
- [35] Serrano Jr, A. E., Declarador, R. S., Tumbokon, B. L. M., Proximate composition and apparent digestibility coefficient of *Sargassum* spp. meal in the Nile tilapia, *Oreochromis niloticus*, *Animal Biology & Animal Husbandry*, 7(2) (2015) 159–168.
- [36] Chakraborty, S., Bhattacharya, T., Nutrient composition of marine benthic algae found in the Gulf of Kutch coastline, Gujarat, India, *Journal of Algal Biomass Utilization*, 3(1) (2012) 32–38.
- [37] Ahmad, F., Sulaiman, M. R., Saimon, W., Yee, C. F., Matanjun, P., Proximate compositions and total phenolic contents of selected edible seaweed from Semporna, Sabah, Malaysia, *Borneo Science*, 31 (2012) 85–96.
- [38] Gressler, V., Yokoya, N. S., Fujii, M. T., Colepicolo, P., Mancini Filho, J., Torres, R. P., Pinto, E., Lipid, fatty acid, protein, amino acid and ash contents in four Brazilian red algae species, *Food Chemistry*, 120(2) (2010) 585–590.
- [39] Bernaerts, T. M., Gheysen, L., Kyomugasho, C., Kermani, Z. J., Vandionant, S., Foubert, I., Van Loey, A. M., Comparison of microalgal biomasses as functional food ingredients: Focus on the composition of cell wall related polysaccharides, *Algal Research*, 32 (2018) 150–161.
- [40] El-Sayed, A. E. K. B., Reda, M. M., Almutairi, A. W., Mavromatis, C., Biomass production and biochemical composition of *Chlorella vulgaris* grown in Net-House Photobioreactor (NHPBR) using sugarcane press mud waste, *Journal of Taibah University for Science*, 17(1) (2023) 2194843.

## The Role of Systemic Inflammation and Haematological Parameters in Autism

Elif Abanoz<sup>1,a,\*</sup>, Merve Soyhan Bal<sup>1,b</sup>, Ayla Uzun Cicek<sup>1,c</sup>, Ali Güven Say<sup>1,d</sup>, Serkan Bolat<sup>2,e</sup><sup>1</sup>Department of Child and Adolescent Psychiatry, Sivas Cumhuriyet University Faculty of Medicine, Sivas, Türkiye<sup>2</sup>Department of Medical Biochemistry, Sivas Cumhuriyet University Faculty of Medicine, Sivas, Türkiye

\*Corresponding author

### Research Article

#### History

Received: 13/02/2025

Accepted: 11/06/2025



This article is licensed under a Creative Commons Attribution-NonCommercial 4.0 International License (CC BY-NC 4.0)

### ABSTRACT

Autism spectrum disorder (ASD) is a neurodevelopmental condition characterized by challenges in social communication and repetitive behaviors. Emerging evidence suggests that ASD may also involve systemic inflammatory processes. This study aimed to assess systemic inflammation in children with ASD using hematological biomarkers and to investigate the association between these markers and autism severity. A total of 75 children with ASD (mean age: 4.37±1.01 years) and 75 age- and sex-matched healthy controls (mean age: 4.41±1.06 years) were included. Complete blood count data were used to calculate neutrophil-to-lymphocyte ratio (NLR), platelet-to-lymphocyte ratio (PLR), systemic immune-inflammation index (SII), and systemic inflammation response index (SIRI). Compared to controls, the ASD group showed significantly higher levels of leukocytes ( $p=0.011$ ), neutrophils ( $p=0.001$ ), monocytes ( $p<0.001$ ), NLR ( $p=0.005$ ), SII ( $p=0.001$ ), and SIRI ( $p<0.001$ ). Moreover, CARS scores, indicating autism severity, were positively correlated with these inflammatory markers (e.g., SIRI:  $r=0.403$ ,  $p<0.001$ ; monocyte:  $r=0.362$ ,  $p<0.001$ ). These findings suggest that systemic inflammation may contribute to the pathophysiology of ASD and that hematological indices could serve as accessible biomarkers for clinical evaluation.

**Keywords:** ASD, SII, SIRI, Inflammation, Haematological biomarkers.<sup>a</sup>[elifabanoz\\_17@hotmail.com](mailto:elifabanoz_17@hotmail.com)<sup>b</sup><https://orcid.org/0000-0002-9214-4735><sup>c</sup>[dr.f.ayla@hotmail.com](mailto:dr.f.ayla@hotmail.com)<sup>d</sup><https://orcid.org/0000-0003-2274-3457><sup>e</sup>[drsbolat@gmail.com](mailto:drsbolat@gmail.com)<sup>e</sup><https://orcid.org/0000-0002-8669-8782><sup>b</sup>[merve.soyhan1996@gmail.com](mailto:merve.soyhan1996@gmail.com)<sup>d</sup><https://orcid.org/0009-0001-9238-5256><sup>e</sup>[dr.aliguven say@gmail.com](mailto:dr.aliguven say@gmail.com)<sup>e</sup><https://orcid.org/0009-0009-4413-1145>

## Introduction

Autism spectrum disorder (ASD) is a lifelong neurodevelopmental disorder that affects social communication and interaction, accompanied by repetitive and restrictive behavioral patterns [1]. Recent epidemiological research has indicated a notable rise in the prevalence of ASD [2]. Although its precise etiology remains unclear, genetic, neurophysiological, neuroanatomical, immunological, and environmental factors are thought to contribute to its pathogenesis [3]. Growing evidence suggests that, beyond being a neurodevelopmental disorder, ASD may also be associated with immunological and inflammatory processes [4, 5].

Inflammation serves as a defense mechanism of the immune system against infections, tissue damage, and stress [6]. Low-grade systemic inflammation has been implicated in various psychiatric disorders, including psychotic, mood, and personality disorders [7]. While blood-based biomarkers are commonly used to investigate inflammation in psychiatric research, many of these markers are costly and not suitable for routine clinical application. Consequently, there is a need for more cost-effective and practical alternatives. Among these, the neutrophil-to-lymphocyte ratio (NLR) has emerged as a simple and efficient marker for assessing systemic inflammation and has recently been investigated in psychiatric populations [8]. Similarly, the platelet-to-

lymphocyte ratio (PLR) has been explored as an indicator of subclinical inflammation, with studies demonstrating elevated PLR levels in individuals with bipolar disorder and schizophrenia [9].

Serum inflammation biomarkers are increasingly recognized as valuable tools for the early identification and etiological investigation of psychiatric disorders. In addition to NLR and PLR, several novel hematological indices, including the systemic immune-inflammation index (SII) and systemic inflammation response index (SIRI) have been proposed [10]. These indices, derived from complete blood count and biochemical analyses, provide cost-effective and practical measures of systemic inflammation and immune response [11].

SII, a novel inflammatory biomarker, is calculated as (platelet count × neutrophil count) / lymphocyte count, while SIRI is determined using the formula (neutrophil count × monocyte count) / lymphocyte count. These indices are considered comprehensive indicators of inflammation, reflecting both neutrophil-mediated inflammatory activity and the suppression of lymphocyte-driven immune responses [12-14]. Despite their potential utility, the diagnostic value of these biomarkers in psychiatric disorders remains insufficiently explored.

The present study aims to assess systemic inflammation in individuals with ASD through hematological biomarkers and to investigate the



association between these parameters and autism severity. Current literature lacks sufficient data on the use of novel hematological markers such as SII and SIRI in evaluating ASD severity. Therefore, this study seeks to compare these markers between individuals with ASD and healthy controls and to examine their potential correlations with autism severity. These results are anticipated to improve insights into the immunological mechanisms involved in ASD and support the assessment of inflammation-related biomarkers in both diagnostic and clinical decision-making.

## Materials and Methods

In this study, the records of patients who applied to the Child and Adolescent Mental Health and Diseases Outpatient Clinic of Sivas Cumhuriyet University Faculty of Medicine Hospital between January 2023 and January 2024 were retrospectively analysed. The study included children diagnosed with autism spectrum disorder (ASD) as a result of clinical interviews based on DSM-5 diagnostic criteria, family interviews and diagnostic psychiatric evaluation performed in the infant/child play observation room. The study group consisted of 75 children diagnosed with ASD, aged between 3 and 6 years, who did not have any accompanying psychiatric, neurological or medical disease and whose haemograms were performed. The control group consisted of 75 healthy children who did not have any psychiatric diagnosis, who underwent haemogram examinations and were matched with the patient group in terms of age and gender. In order to support the diagnosis and differential diagnosis, routine blood tests were requested from all participants to evaluate their current metabolic status and to monitor drug side effects in case of possible need for pharmacological treatment. Children with recent infections, chronic medical conditions, recent vaccinations, or current medication use were excluded from both groups in order to minimize potential confounding effects on inflammatory parameters. The Childhood Autism Rating Scale (CARS) was used to assess the severity of autism and the relevant data were retrospectively scanned from the patient files. Sociodemographic data of the children in the study were obtained from the hospital registration system. Complete Blood Count (CBC) analyses were performed in the hospital biochemistry laboratory using a MINDRAY BC-6200 device. From the CBC parameters, two systemic inflammatory indices were calculated: the SII, defined as  $(\text{Platelet} \times \text{Neutrophil}) / \text{Lymphocyte}$ , and the SIRI, defined as  $(\text{Neutrophil} \times \text{Monocyte}) / \text{Lymphocyte}$ . These indices were used to assess systemic inflammatory status based on peripheral blood parameters. Approval for this study was obtained from Sivas Cumhuriyet University Non-

Interventional Clinical Research Ethics Committee dated 17.10.2024 and numbered 2024-10/17.

### *Childhood Autism Rating Scale (CARS)*

The ASRS is a behavioural rating scale developed by Schopler et al. (1980) and is used for screening and differential diagnosis of autism spectrum disorders [15]. The scale consists of 15 items and classifies the severity of autism as 'mild-moderate' and 'severe'. The severity of 15 behaviours such as 'Relationship with People', 'Imitation', 'Emotional Reactions', 'Use of Body', 'Object Use', 'Visual Reaction', 'Adaptation to Change', 'Listening Reaction', 'Taste, Smell, Touch Reaction and Use', 'Verbal Communication', 'Fear or Irritability', 'Nonverbal Communication', 'Activity Level', 'Level and Consistency of Mental Reactions', 'General Impressions' are evaluated. The severity of each behaviour is evaluated on a 1-4, half-point scale. The total score obtained from the scale varies between 15-60, and 30 points and above support the diagnosis of autism. According to the scoring, autism symptoms are not present in children between 15-29.5 points. Children with a score range of 30-36.5 are considered 'mild-moderately autistic'; children with a score range of 37-60 are considered 'severely autistic'. The Turkish validity and reliability study of the CARS was conducted by Gassaloğlu, Baykara et al. (2016) [16].

### *Statistical Analysis*

SPSS software (IBM SPSS, Version 22.0, IBM Corporation, Armonk, NY, USA) was used for the statistical analyses of the data. The Kolmogorov-Smirnov test was performed to determine normality. The numerical and categorical data were given as mean  $\pm$  standard deviation (SD), medians (25th, 75th), number (n), and percentage (%) as appropriate. Normally distributed data were analyzed using Independent Samples t-test and non-normally distributed data were analyzed using the Mann-Whitney U test. The comparison of categorical variables between the groups was analysed by Chi-square ( $\chi^2$ ) test. Correlations were evaluated using Pearson correlation analysis. A p-value of  $<0.05$  was considered statistically significant in all analyses.

## Results

### *Socio-demographic and Familial Characteristics of Participants*

The mean age of the ASD group was  $4.37 \pm 1.01$  years and the mean age of the control group was  $4.41 \pm 1.06$  years. Age, gender, family income, place of residence, parental age and education did not differ significantly between the ASD and control groups (all p values  $>0.05$ ). Table 1 shows the sociodemographic and familial characteristics of the participants.

Table 1. Socio-demographic and familial characteristics of participants. Data were given as mean±standard deviation or number (percent%).

	ASD group (n=75)	Control group (n=75)	p-value*
Age (mean-years±SD)	4.37±1.01	4.41±1.06	0.935
Gender (n, %)			0.119
Male	62 (82.7)	54 (72.0)	
Female	13 (17.3)	21 (28.0)	
Family income level (n, %)			0.577
The minimum wage/less than minimum wage	18 (24)	21 (28)	
Above the minimum wage	57 (76)	54 (72)	
Place of residence (n, %)			0.666
Urban	61 (81.3)	63 (84)	
Rural	14 (18.7)	12 (16)	
Maternal age (mean-years±SD)	30.73±3.45	30.56±4.08	0.356
Level of education of the mother (n, %)			0.578
Primary and secondary school	13 (17.3)	18 (24)	
High school	51 (68)	48 (64)	
University	11 (14.7)	9 (12)	
Paternal age (mean-years±SD)	35.47±4.19	34.96±4.02	0.757
Level of education of the father (n,%)			0.733
Primary and secondary school	9 (12)	12 (16)	
High school	41 (54.7)	41 (54.7)	
University	25 (33.3)	22 (29.3)	

Notes: \*The chi-square test for categorical variables and the Mann-Whitney U for continuous variables were used to test group differences. Bold font indicates statistical significance:  $p < 0.05$ .

Abbreviations: ASD, Autism Spectrum Disorder; SD, Standard Deviation.

#### Comparison of CBC, Systemic Inflammatory Indices and Scale Scores Used between ASD and Control Groups

In the evaluation of blood parameters, no statistically significant difference was found between ASD and control groups in terms of haemoglobin, lymphocyte, platelet and PLR values. On the other hand, leucocyte, neutrophil,

monocyte, NLR, SII and SICI values were significantly higher in the ASD group compared to the control group ( $p=0.011$ ,  $p=0.001$ ,  $p<0.001$ ,  $p=0.005$ ,  $p=0.001$ ,  $p<0.001$ , respectively). Similarly, it was determined that the mean scores of the CARS were statistically significantly higher in the ASD group compared to the control group ( $p<0.001$ ). The results are displayed in Table 2.

Table 2. Comparison of CBC, systemic inflammatory indices and scale scores used between ASD and control groups

	ASD group (n=75)	Control group (n=75)	p-value*
Hemoglobin mean ± SD	13.2±0.9	12.9±1.2	0.060
Leukocyte mean ± SD	8.6±2.4	7.6±2.1	<b>0.011</b>
Neutrophil median (25th-75th)	3.9 (2.8-4.8)	3.2 (2.5-4.1)	<b>0.001</b>
Lymphocyte median (25th-75th)	3.3 (2.8-4.2)	3.3 (2.7-3.8)	0.549
Monocyte mean ± SD	0.5±0.2	0.4±0.1	<b>&lt;0.001</b>
Platelet mean ± SD	358.3±94.2	354.2±66.4	0.754
NLR median (25th-75th)	1.1 (0.8-1.7)	1.0 (0.7-1.1)	<b>0.005</b>
PLR mean ± SD	110.2±44.5	108.0±32.6	0.721
SII mean ± SD	514.2±441.5	338.4±131.7	<b>0.001</b>
SIRI median (25th-75th)	0.6 (0.4-0.9)	0.4 (0.3-0.5)	<b>&lt;0.001</b>
CARS median (25th-75th)	38.5 (35.5-47.5)	17 (16-17)	<b>&lt;0.001</b>

Notes: \* The chi-square test was used for categorical variables, while the Mann-Whitney U test or the Independent Samples t-test was applied to continuous variables, depending on their distribution, to test group differences. **Bold font** indicates statistical significance:  $p < 0.05$ .

Abbreviations: ASD, Autism Spectrum Disorder; NLR, Neutrophil-to-Lymphocyte Ratio; PLR, Platelet-to-Lymphocyte Ratio; SII, Systemic Immune Inflammation Index; SIRI, Systemic Inflammation Response Index; CARS, Childhood Autism Rating Scale; SD, Standard Deviation

#### Correlations between CARS Mean Score and CBC and Systemic Inflammatory Indices

According to the correlation analysis, there was a significant positive correlation between the mean of the

CARS total score and the values of leukocyte, neutrophil, monocyte, NLR, SII and SICI ( $p=0.01$ ,  $p=0.008$ ,  $p<0.001$ ,  $p<0.001$ ,  $p=0.001$ ,  $p<0.001$ , respectively). The results are shown in Table 3.

Table 3. Correlations between CARS mean score and CBC and systemic inflammatory indices

	CARS- Total Scores	
	r*	p*
Hemoglobin	0.120	0.143
Leukocyte	0.210	<b>0,01</b>
Neutrophil	0.215	<b>0,008</b>
Lymphocyte	0.019	0.819
Monocyte	0.362	<b>&lt;0.001</b>
Platelet	-0.021	0.795
NLR	0.285	<b>&lt;0.001</b>
PLR	0.037	0,656
SII	0.264	<b>0,001</b>
SIRI	0.403	<b>&lt;0.001</b>

\*Pearson correlation analysis was used. **Bold font** indicates statistical significance:  $p < 0.05$ .

Abbreviations: NLR, Neutrophil-to-Lymphocyte Ratio; PLR, Platelet-to-Lymphocyte Ratio; SII, Systemic Immune-inflammation Index; SIRI, Systemic Inflammation Response Index; CARS, Childhood Autism Rating Scale; SD, Standard Deviation

Notes: \* The chi-square test was used for categorical variables, while the Mann-Whitney U test or the Independent Samples t-test was applied to continuous variables, depending on their distribution, to test group differences. Bold font indicates statistical significance:  $p < 0.05$ .

Abbreviations: ASD, Autism Spectrum Disorder; NLR, Neutrophil-to-Lymphocyte Ratio; PLR, Platelet-to-Lymphocyte Ratio; SII, Systemic Immune-inflammation Index; SIRI, Systemic Inflammation Response Index; CARS, Childhood Autism Rating Scale; SD, Standard Deviation

## Discussion

In this study, systemic inflammatory markers were analysed in children with ASD and the relationship between these markers and autism severity was evaluated. Results showed that leukocyte, neutrophil, monocyte, NLR, SII and SRI values were significantly higher in children with ASD compared to healthy control group. In addition, a positive correlation was found between CARS scores and these inflammatory markers.

Recent studies suggest that ASD should not only be considered as a neurodevelopmental disorder, but may also be closely related to immunological and inflammatory mechanisms. Indeed, postmortem analyses have demonstrated elevated levels of proinflammatory cytokines, including interleukin-6 (IL-6), interleukin-8 (IL-8), interferon-gamma (IFN- $\gamma$ ), tumor necrosis factor-alpha (TNF- $\alpha$ ), and monocyte chemoattractant protein-1 (MCP-1), in the cerebellum and frontal cortex of individuals with autism. It has been reported that IL-6 in particular is associated with a decrease in dendritic branching and granule cell number and may contribute to excitatory-inhibitory synaptic imbalances [17-19]. TNF- $\alpha$  has been suggested to be a potential biomarker in the early diagnosis of autism [20]. Meta-analyses on this topic indicate that individuals with ASD exhibit significantly higher proinflammatory cytokine levels compared to healthy controls [21]. These findings support that

inflammation may interact with the neurodevelopmental processes of ASD.

Biomarkers used in the evaluation of systemic inflammation are generally expensive and not suitable for routine clinical use. Therefore, the need for affordable and accessible inflammatory markers is increasing. NLR, a low-cost and reliable parameter, was initially developed to measure the level of inflammation and stress in critically ill patients. Later studies have indicated that NLR is linked to unfavorable outcomes in conditions such as pancreatitis, cardiovascular diseases, and liver disorders. Elevated NLR levels have also been found to correlate with increased C-reactive protein (CRP) and cytokine concentrations [22]. Similarly, PLR is an important marker used to evaluate the level of inflammation [8]. Studies have reported that NLR and PLR show significant changes in various neuropsychiatric diseases such as mood disorders, schizophrenia and Parkinson's disease [23, 24].

Although studies examining inflammatory biomarkers in childhood and adolescence are limited, high NLR and PLR levels have been shown to be associated with major depressive disorder and obsessive-compulsive disorder in adolescents [25, 26]. Higher NLR and PLR levels were reported in children with attention deficit hyperactivity disorders (ADHD) compared to healthy controls, but lymphocyte counts were found to be lower [27, 28]. Studies conducted in individuals with ASD have revealed similar findings. For example, it has been reported that neutrophil counts and NLR values were significantly higher compared to the healthy control group, but PLR levels remained similar and lymphocyte counts were lower [29]. It was also reported that monocyte levels increased and there was a positive correlation between autism severity and NLR [30]. The findings of our study, consistent with the existing literature, suggest that inflammation may be an important component in understanding the neurodevelopmental mechanisms of autism.

SII and SIRI, which are among the biomarkers of systemic inflammation, are inflammatory markers calculated using neutrophil, platelet, monocyte and lymphocyte from peripheral blood parameters. In the literature, SII and SIRI have been shown to have higher prognostic value compared to other inflammatory markers such as NLR and PLR [12, 13]. These parameters, which were first evaluated as a prognostic indicator in neurological and cardiovascular diseases, have started to be examined in the context of psychiatric disorders in recent years [14, 31]. It has been reported that SII and SIRI levels are significantly higher in individuals diagnosed with schizophrenia, bipolar disorder and anxiety disorder compared to healthy controls. However, studies addressing the role of these inflammatory markers in childhood psychiatric disorders are quite limited [32-34]. This study revealed that individuals with ASD had significantly elevated SII and SIRI levels compared to healthy controls. These results suggest that inflammation could be involved in the etiology of ASD and highlight the potential of these inflammatory markers as biomarkers in the assessment of ASD.

The relationship between neurodevelopmental disorders and inflammatory processes has been addressed especially through the role of proinflammatory cytokines such as IL-6. Monocytes may contribute to neuroinflammation by producing high levels of IL-6 with the activation of inflammatory processes [35]. Studies in the literature indicate that IL-6 levels are significantly elevated in individuals with ASD compared to healthy controls. Additionally, higher IL-6 levels have been found to be positively correlated with repetitive behaviors and behavioral issues, which are core symptoms of ASD. In addition, it was found that not only IL-6 but also other proinflammatory cytokines increased in individuals with ASD and this was associated with more severe behavioural symptoms [35, 36].

In a study using the CARS, the relationship between ASD severity and inflammatory markers was examined and it was reported that IL-12p40 levels were higher in individuals with mild ASD and TNF- $\alpha$  levels were higher in individuals with moderate ASD [37]. In addition, it was discovered that there was a strong positive link between NLR and social interaction issues, and that this ratio tended to correlate with the overall severity of ASD symptoms [38]. Other studies in the literature also indicates that in people with neurodevelopmental issues, inflammatory markers may be linked to significant attention and social difficulties, as well as an increase in aggressive behaviors and hostility [39, 40]. In this study, a significant positive correlation was found between inflammatory markers and autism severity. This finding suggests that systemic inflammation may be associated not only with the presence of ASD but also with the clinical severity of the disease. In particular, the relationship between inflammatory response and autism symptom severity was observed to be significant.

Although our findings emphasise the role of inflammatory processes in ASD, our study has some limitations. Due to the retrospective design of the study, temporal changes of inflammatory markers could not be evaluated. Furthermore, cytokine analyses assessing specific immune responses in individuals with ASD were not performed. In addition, the relatively small sample size may limit the generalisability of our findings. Future prospective and longitudinal studies with larger populations are needed to examine the impact of inflammation on the course of ASD symptoms in more detail.

In conclusion, this study shows that markers of systemic inflammation are increased in children with ASD and that these markers are positively associated with autism severity. Our findings suggest that ASD is not only a neurodevelopmental disorder, but may also be linked to immunological mechanisms. In the future, we emphasise the need for large-scale studies investigating the potential role of inflammation-targeted therapeutic approaches in the management of ASD.

## Conflicts of interest

The authors declared no potential conflicts of interest with respect to the research, authorship, and/or publication of this article.

## Ethical Approval Statement

This study was approved by the local Ethics Committee of the Medical Faculty of Sivas Cumhuriyet University. (Date: 17.10.2024, No: 2024-10/17).

## References

- [1] American Psychiatric Association, Diagnostic and Statistical Manual of Mental Disorders DSM 5 TR (5th ed, text revision), 2022.
- [2] Maenner M.J., Prevalence and characteristics of autism spectrum disorder among children aged 8 years—Autism and Developmental Disabilities Monitoring Network, 11 sites, United States, 2020, *MMWR. Surveill. Summ.*, 72 (2023).
- [3] Limperopoulos C., Bassan H., Sullivan N.R., Soul J.S., Robertson R.L. Jr., Moore M., Ringer S.A., Volpe J.J., du Plessis A.J., Positive screening for autism in ex-preterm infants: prevalence and risk factors, *Pediatrics*, 121 (4) (2008) 758-765.
- [4] Gładysz D., Krzywdzińska A., Hozyasz K.K., Immune abnormalities in autism spectrum disorder—could they hold promise for causative treatment?, *Mol. Neurobiol.*, 55 (2018) 6387-6435.
- [5] Masi A., Quintana D., Glozier N., Lloyd A., Hickie I., Guastella A., Cytokine aberrations in autism spectrum disorder: a systematic review and meta-analysis, *Mol. Psychiatry*, 20 (4) (2015) 440-446.
- [6] Xiao T.S., Innate immunity and inflammation, *Cell. Mol. Immunol.*, 14 (1) (2017) 1-3.
- [7] Osimo E.F., Cardinal R.N., Jones P.B., Khandaker G.M., Prevalence and correlates of low-grade systemic inflammation in adult psychiatric inpatients: an electronic health record-based study, *Psychoneuroendocrinology*, 91 (2018) 226-234.
- [8] Mazza M.G., Lucchi S., Tringali A.G.M., Rossetti A., Botti E.R., Clerici M., Neutrophil/lymphocyte ratio and platelet/lymphocyte ratio in mood disorders: a meta-analysis, *Prog. Neuropsychopharmacol. Biol. Psychiatry*, 84 (2018) 229-236.
- [9] Catak Z., Uzmez E., Ozturk N., Ugur K., Comparison of neutrophil-to-lymphocyte, platelet-to-lymphocyte, and monocyte-to-lymphocyte ratios in patients with schizophrenia, bipolar disorder, and major depressive disorder, *Int. J. Med. Biochem.*, 1 (3) (2018) 106-110.
- [10] Song Y., Zhao Y., Shu Y., Zhang L., Cheng W., Wang L., Shu M., Xue B., Wang R., Feng Z., Combination model of neutrophil to high-density lipoprotein ratio and system inflammation response index is more valuable for predicting peripheral arterial disease in type 2 diabetic patients: A cross-sectional study, *Front. Endocrinol.*, 14 (2023) 1100453.
- [11] Jin Z., Wu Q., Chen S., Gao J., Li X., Zhang X., Zhou Y., He D., Cheng Z., Zhu Y., The associations of two novel inflammation indexes, SII and SIRI with the risks for cardiovascular diseases and all-cause mortality: a ten-year follow-up study in 85,154 individuals, *J. Inflamm. Res.*, (2021) 131-140.
- [12] Hu B., Yang X.R., Xu Y., Sun Y.F., Sun C., Guo W., Zhang X., Wang W.M., Qiu S.J., Zhou J., Systemic immune-inflammation index predicts prognosis of patients after curative resection for hepatocellular carcinoma, *Clin. Cancer Res.*, 20 (23) (2014) 6212-6222.



- [13] Qi Q., Zhuang L., Shen Y., Geng Y., Yu S., Chen H., Liu L., Meng Z., Wang P., Chen Z., A novel systemic inflammation response index (SIRI) for predicting the survival of patients with pancreatic cancer after chemotherapy, *Cancer*, 122 (14) (2016) 2158-2167.
- [14] Ninla-Aesong P., Kietdumrongwong P., Neupane S.P., Puangsri P., Jongkriak H., Chotipong P., Kaewpijit P., Relative value of novel systemic immune-inflammatory indices and classical hematological parameters in predicting depression, suicide attempts and treatment response, *Sci. Rep.*, 14 (1) (2024) 19018.
- [15] Schopler E., Reichler R.J., DeVellis R.F., Daly K., Toward objective classification of childhood autism: Childhood Autism Rating Scale (CARS), *J. Autism Dev. Disord.*, (1980).
- [16] Gassaloğlu S.I., Baykara B., Avcil S., Demiral Y., Çocukluk Otizmi Derecelendirme Ölçeği Türkçe formunun geçerlik ve güvenilirlik çalışması, *Türk Psikiyatri Derg.*, 27 (4) (2016) 266-274.
- [17] Xu N., Li X., Zhong Y., Inflammatory cytokines: potential biomarkers of immunologic dysfunction in autism spectrum disorders, *Mediators Inflamm.*, 2015 (1) (2015) 531518.
- [18] Careaga M., Van de Water J., Ashwood P., Immune dysfunction in autism: a pathway to treatment, *Neurotherapeutics*, 7 (3) (2010) 283-292.
- [19] Masi A., Glozier N., Dale R., Guastella A.J., The immune system, cytokines, and biomarkers in autism spectrum disorder, *Neurosci. Bull.*, 33 (2017) 194-204.
- [20] Anastasescu C.M., Gheorman V., Stoicanescu E.-C., Popescu F., Gheorman V., Udriștoiu I., Immunological biomarkers in Autism Spectrum Disorder: the role of TNF-Alpha and dependent trends in serum IL-6 and CXCL8, *Life*, 14 (9) (2024) 1201.
- [21] Saghazadeh A., Ataeinia B., Keynejad K., Abdolalizadeh A., Hirbod-Mobarakeh A., Rezaei N., A meta-analysis of pro-inflammatory cytokines in autism spectrum disorders: Effects of age, gender, and latitude, *J. Psychiatr. Res.*, 115 (2019) 90-102.
- [22] Zulfic Z., Weickert C.S., Weickert T.W., Liu D., Myles N., Galletly C., Neutrophil-lymphocyte ratio—a simple, accessible measure of inflammation, morbidity and prognosis in psychiatric disorders?, *Australas. Psychiatry*, 28 (4) (2020) 454-458.
- [23] Bhikram T., Sandor P., Neutrophil-lymphocyte ratios as inflammatory biomarkers in psychiatric patients, *Brain Behav. Immun.*, 105 (2022) 237-246.
- [24] Hosseini S., Shafiabadi N., Khanzadeh M., Ghaedi A., Ghorbanzadeh R., Azarhomayoun A., Bazrgar A., Pezeshki J., Bazrafshan H., Khanzadeh S., Neutrophil to lymphocyte ratio in Parkinson's disease: A systematic review and meta-analysis, *BMC Neurol.*, 23 (1) (2023) 333.
- [25] Özyurt G., Binici N.C., Increased neutrophil-lymphocyte ratios in depressive adolescents is correlated with the severity of depression, *Psychiatry Res.*, 268 (2018) 426-431.
- [26] Özyurt G., Binici N.C., The neutrophil-lymphocyte ratio and platelet-lymphocyte ratio in adolescent obsessive-compulsive disorder: Does comorbid anxiety disorder affect inflammatory response?, *Psychiatry Res.*, 272 (2019) 311-315.
- [27] Avcil S., Evaluation of the neutrophil/lymphocyte ratio, platelet/lymphocyte ratio, and mean platelet volume as inflammatory markers in children with attention-deficit hyperactivity disorder, *Psychiatry Clin. Neurosci.*, 72 (7) (2018) 522-530.
- [28] Önder A., Gizli Çoban Ö., Sürer Adanır A., 'Elevated neutrophil-to-lymphocyte ratio in children and adolescents with attention-deficit/hyperactivity disorder, *Int. J. Psychiatry Clin. Pract.*, 25 (1) (2021) 43-48.
- [29] Kutlu A., Binici N.C., Does increased neutrophil-lymphocyte ratio predict autism spectrum disorder?, *Anadolu Psikiyatri Derg.*, 19 (6) (2018) 607-614.
- [30] Tural Hesapcioglu S., Kasak M., Cıtaç Kurt A.N., Ceylan M.F., High monocyte level and low lymphocyte to monocyte ratio in autism spectrum disorders, *Int. J. Dev. Disabil.*, 65 (2) (2019) 73-81.
- [31] Dziedzic E.A., Gaşior J.S., Tuzimek A., Paleczny J., Junka A., Dąbrowski M., Jankowski P., Investigation of the associations of novel inflammatory biomarkers—Systemic Inflammatory Index (SII) and Systemic Inflammatory Response Index (SIRI)—With the severity of coronary artery disease and acute coronary syndrome occurrence, *Int. J. Mol. Sci.*, 23 (17) (2022) 9553.
- [32] İnaltekin A., Yağcı İ., Evaluation of simple markers of inflammation and systemic immune inflammation index in schizophrenia, bipolar disorder patients and healthy controls, *Türk. J. Psychiatry*, 34 (1) (2021) 11.
- [33] Canlı D., Evaluation of systemic immune-inflammation index, systemic inflammatory response index and hematologic inflammatory parameters in generalized anxiety disorder: a controlled study, *Anatol. Curr. Med. J.*, 6 (2) (2024) 161-167.
- [34] Aşar P.A., Kara T., Kocaman O., Akkuş M., Evaluation of primary markers of inflammation and the systemic inflammation index in specific learning disabilities, *Biomark. Med.*, 18 (20) (2024) 907-916.
- [35] Hughes H.K., Onore C.E., Careaga M., Rogers S.J., Ashwood P., Increased monocyte production of IL-6 after toll-like receptor activation in children with autism spectrum disorder (ASD) is associated with repetitive and restricted behaviors, *Brain Sci.*, 12 (2) (2022) 220.
- [36] Ashwood P., Krakowiak P., Hertz-Picciotto I., Hansen R., Pessah I., Van de Water J., Elevated plasma cytokines in autism spectrum disorders provide evidence of immune dysfunction and are associated with impaired behavioral outcome, *Brain Behav. Immun.*, 25 (1) (2011) 40-45.
- [37] Inga Jácome M.C., Morales Chacón L.M., Vera Cuesta H., Maragoto Rizo C., Whilby Santiesteban M., Ramos Hernandez L., Noris García E., González Fragueta M.E., Fernandez Verdecia C.I., Vegas Hurtado Y., Peripheral inflammatory markers contributing to comorbidities in autism, *Behav. Sci.*, 6 (4) (2016) 29.
- [38] Topal Z., Tufan A.E., Karadağ M., Gökçen C., Akkaya C., Sarp A.S., Bahsi I., Kilinc M., Evaluation of peripheral inflammatory markers, serum B12, folate, ferritin levels and clinical correlations in children with autism spectrum disorder (ASD) and attention deficit hyperactivity disorder (ADHD), *Nord. J. Psychiatry*, 76 (2) (2022) 150-157.
- [39] Marsland A.L., Prather A.A., Petersen K.L., Cohen S., Manuck S.B., Antagonistic characteristics are positively associated with inflammatory markers independently of trait negative emotionality, *Brain Behav. Immun.*, 22 (5) (2008) 753-761.
- [40] Krefft M., Frydecka D., Zalsman G., Krzystek-Korpacka M., Śmigiel R., Gębura K., Bogunia-Kubik K., Misiak B., A pro-inflammatory phenotype is associated with behavioural traits in children with Prader-Willi syndrome, *Eur. Child Adolesc. Psychiatry*, 30 (2021) 899-908.

## Comparative Analysis of Sciatic Nerve Ligation and Oxaliplatin-Induced Neuropathic Pain Models: Thermal Nociception and Inflammatory Mechanisms

Emre Gedikli<sup>1,a</sup>, Aysegül Öztürk<sup>2,b,\*</sup>, Şahin Yıldırım<sup>1,c</sup>

<sup>1</sup>Departments of Pharmacology, Medicine Faculty, Sivas Cumhuriyet University, Sivas, Türkiye

<sup>2</sup>Departments of Therapy and Rehabilitation, Vocational School of Health Services, Sivas Cumhuriyet University, Sivas, Türkiye

\*Corresponding author

### Research Article

#### History

Received: 16/12/2024

Accepted: 15/06/2025



This article is licensed under a Creative Commons Attribution-NonCommercial 4.0 International License (CC BY-NC 4.0)

### ABSTRACT

Neuropathic pain, resulting from damage or dysfunction of the nervous system, presents significant clinical challenges due to its chronic nature and resistance to treatment. This study compared the thermal nociception and inflammatory mechanisms of two neuropathic pain models: Sciatic nerve ligation (SNL) and oxaliplatin-induced peripheral neuropathy. Male Wistar Albino rats were randomly assigned to control, SNL, and oxaliplatin-induced neuropathy. The SNL model was established through partial sciatic nerve ligation, while oxaliplatin (4 mg/kg) was administered intraperitoneally twice weekly for four weeks. Thermal nociception was evaluated using tail-flick and hot-plate tests, and inflammatory markers (TNF- $\alpha$  and IL-1 $\beta$ ) were measured in dorsal root ganglia (DRG) tissue and serum using ELISA. Thermal analgesia tests revealed that neuropathic pain symptoms appeared from the second week in the oxaliplatin group and the fourth week in both models ( $p < 0.05$ ). TNF- $\alpha$  and IL-1 $\beta$  levels were significantly elevated in the SNL and oxaliplatin groups compared to controls, with the highest TNF- $\alpha$  levels observed in the oxaliplatin group ( $p < 0.05$ ). These findings indicate that both models effectively induce neuropathic pain, with notable increases in pro-inflammatory cytokines in DRG and serum. The study examines the inflammatory mechanisms underlying neuropathic pain, providing insights into its pathophysiology and potential therapeutic approaches.

**Keywords:** Neuropathic pain, Sciatic nerve ligation, Oxaliplatin-induced neuropathy, Thermal nociception, Pro-inflammatory cytokines.

<sup>a</sup>[eczalb@gmail.com](mailto:eczalb@gmail.com)

<sup>c</sup>[syildirim1965@gmail.com](mailto:syildirim1965@gmail.com)

<sup>b</sup><https://orcid.org/0000-0001-5593-2073>

<sup>c</sup><https://orcid.org/0000-0003-1312-7283>

<sup>b</sup>[aysegulozturk@cumhuriyet.edu.tr](mailto:aysegulozturk@cumhuriyet.edu.tr) <sup>b</sup><https://orcid.org/0000-0001-8130-7968>

## Introduction

Neuropathic pain is a clinical condition that results from damage or dysfunction in the nervous system. It significantly impacts patients' quality of life and is often challenging to treat (1). This type of pain can impact both the peripheral and central nervous systems, often becoming chronic and leading to physical, emotional, and social challenges (2,3). The fundamental mechanisms underlying neuropathic pain include peripheral and central sensitization, inflammation, and neurotransmitter imbalances. Therefore, the strategies used in the treatment of neuropathic pain are typically complex and multifaceted (4).

Several experimental models have been developed to enhance our understanding neuropathic pain's underlying mechanisms and to formulate effective treatment strategies. These models simulate various etiological processes and are crucial for investigating pain's neurophysiological, biochemical, and behavioral characteristics. The most used models for studying neuropathic pain include spinal nerve ligation (SNL), oxaliplatin-induced neuropathy, and chronic constriction injury (CCI) (5–7). Each model simulates distinct mechanisms of neuropathic pain, aiding researchers in understanding the development of pain and its response to treatment.

Sciatic nerve injury is a commonly used method to model injuries in peripheral nerves and the pain syndromes they cause (8). This model is induced by various methods, including nerve compression, transection, or partial ligation, and it mimics the mechanical allodynia, thermal hyperalgesia, and motor dysfunction that result from peripheral nerve damage. Models that utilize sciatic nerve injury are often preferred for elucidating the molecular mechanisms underlying peripheral neuropathies (9–11). On the other hand, oxaliplatin is a platinum-based chemotherapeutic agent utilized in cancer treatment, and peripheral neuropathy is a frequently observed side effect (12). Oxaliplatin-induced neuropathic pain models have been developed to enhance our understanding of chemotherapy-induced neuropathy. These models reflect clinical symptoms such as cold sensitivity, mechanical allodynia, and sensorimotor dysfunction (6,13). This model facilitates the simultaneous examination of both central and peripheral components of neuropathic pain, allowing for a comprehensive assessment of the underlying pathophysiological processes in this domain.

The dorsal root ganglion (DRG) is a crucial structure involved in transmitting sensory information from peripheral nerves to the central nervous system (14,15). In

the development of neuropathic pain, both peripheral nerve injury and chemotherapy-induced neurotoxicity have been shown to induce significant molecular and cellular changes in the DRG. In the literature, alterations in gene expression, neuronal hyperexcitability, and inflammatory processes at the DRG level have been prominently observed in models of chemotherapeutic agents, such as oxaliplatin-induced peripheral neuropathies and sciatic nerve injuries. This underscores the DRG as a critical structural and functional center in the mediation of neuropathic pain(16,17).

The role of inflammation in the pathogenesis of neuropathic pain is garnering increasing attention. Nerve damage and chemotherapy agents increase pro-inflammatory cytokines in the peripheral and central nervous systems. In this process, tumor necrosis factor- $\alpha$  (TNF- $\alpha$ ) and interleukin-1 beta (IL-1 $\beta$ ) levels are significantly elevated (18,19). These cytokines play a critical role in activating the molecular pathways that initiate neuropathic pain. TNF- $\alpha$  can increase oxidative stress and cause neuronal damage in nerve cells by binding to TNF receptors on the cell surface. In contrast, IL-1 $\beta$  can intensify pain by promoting microglial activation and central sensitization processes(18). Therefore, the examination of inflammatory markers is crucial for enhancing our understanding of the molecular basis of neuropathic pain and for developing targeted treatment strategies.

This study aims to compare the similarities and differences between a peripheral neuropathy model based on sciatic nerve injury and an oxaliplatin-induced neuropathic pain model. By examining the inflammatory molecular mechanisms that mediate pain, as well as the sensory and behavioral changes in both models, this research seeks to provide a more comprehensive understanding of the pathophysiology of neuropathic pain.

## Material Method

### Animals

The necessary authorization for this research was obtained from the Local Animal Experiments Ethics Committee of Sivas Cumhuriyet University, under approval number 13.02.2024-16. The study utilized a sample of 18 male Wistar Albino rats, each four months old and weighing between 230 and 250 grams. The rats were housed in cages designed to minimize stress, according to international guidelines. The animals were maintained in a climate-controlled environment that provided a 12-hour light/dark cycle, with a temperature range of  $22 \pm 2^\circ\text{C}$  and a relative humidity of  $53 \pm 5\%$ . The room was equipped with sound insulation to minimize external disturbances. The research was conducted between 9:00 AM and 5:00 PM, during which light and sound levels were continuously monitored. In our research, we chose to euthanize the animals using the

method of decapitation without anesthesia. The primary reason for this choice was to prevent potential interactions between the administered anesthesia and our biochemical findings.

### Oxaliplatin-Induced Peripheral Neuropathy

Oxaliplatin was obtained from Fortius Pharmaceutical Health Products Ltd. Co. (İstanbul, Türkiye). The effects of oxaliplatin on thermal analgesia were investigated using tail-flick and hot-plate tests. Oxaliplatin (4 mg/kg) was administered intraperitoneally twice a week for 4 weeks, specifically on the 1<sup>st</sup>, 2<sup>nd</sup>, 8<sup>th</sup>, 9<sup>th</sup>, 15<sup>th</sup>, 16<sup>th</sup>, 22<sup>nd</sup>, and 23<sup>rd</sup> days. Thermal analgesia tests were conducted before the initial drug application (Day 0, pre-test) and on the 2<sup>nd</sup>, 9<sup>th</sup>, 16<sup>th</sup>, 23<sup>rd</sup> and 30<sup>th</sup> days thereafter (6).

### Surgical Intervention

A neuropathic pain model was established through the partial ligation of the sciatic nerve. The surgical procedures were performed in the Experimental Animals Laboratory at Sivas Cumhuriyet University. Anaesthesia was administered via intramuscular injections of ketamine at a dosage of 90 mg/kg and xylazine at a dosage of 3 mg/kg. A surgical incision approximately 1 cm in length was made on the biceps femoris under aseptic conditions. Subsequently, the sciatic nerve was accessed at the mid-thigh level of the right leg. The sciatic nerve was meticulously dissected from the surrounding connective tissues and securely ligated using a 4-0 chromic catgut. The incision was then closed with 4-0 silk sutures (7,20).

### Analgesia Tests

Thermal nociception was assessed using the tail-flick and hot plate methods (May TF 0703 Tail-flick Unit, AHPi 0603 Analgesic HP, Commat). The tail-flick test was conducted by positioning the stimulus 3 cm from the tips of the rats' tails to evaluate the functionality of the spinal reflex arc. The duration of the tail-flick response was then measured in seconds (21). A cutoff latency of 30 seconds was established to minimize the risk of tissue damage. The subjects were placed on a heated surface maintained at a temperature of  $53 \pm 0.6^\circ\text{C}$  for the hot-plate test. The latency to the first behavioral response, either licking or jumping, was recorded as an indicator of the pain threshold. A cutoff time of 50 seconds was established to prevent potential injury to the paw. Measurements in rats treated with oxaliplatin were taken at 30 and 60 minutes, while measurements in rats with sciatic nerve ligation were conducted at 60 minutes (22,23).

### Experimental Protocol

Rats were randomly divided into three groups. To establish a neuropathic pain model, oxaliplatin (administered i.p. at a dose of 4 mg/kg) and the sciatic nerve ligation method were applied to the rats. The progression of neuropathic pain in the rats was subsequently monitored over four weeks using thermal analgesia tests.

### Determination of TNF- $\alpha$ and IL-1 $\beta$ Levels in DRG and Serum

Following the completion of the experimental measurements, the rats were sacrificed via cervical dislocation, and the DRG was extracted from the L4-S5 region of the spinal column. The DRG tissues were placed in petri dishes and subjected to three washes with cold phosphate-buffered saline (PBS) at a pH of 7.4. The samples were then homogenized in cold PBS using a mechanical homogenizer (SpeedMill PLUS; Analytik Jena) to ensure thorough mixing. Subsequently, the homogenized samples were centrifuged at 4000 rpm for 10 minutes at a temperature of 4°C. The resulting supernatants were employed for biochemical analyses, with total protein concentrations determined using the Bradford protein assay kit (SERVA, Heidelberg, Germany) (24). Blood samples were collected into serum tubes and centrifuged at 2000 rpm for 10 minutes. The resulting yellowish serum was then carefully separated.

### Data Analysis

The outcomes were assessed using one-way analysis of variance (ANOVA) and repeated measures ANOVA, followed by a Tukey post hoc test (SPSS version 23.0 for Windows) to enable multiple group comparisons. All findings are presented as mean  $\pm$  standard error of the mean (SEM). The threshold for statistical significance was set at  $p < 0.05$ .

## Results

### Effects of Sciatic Nerve Ligation and Oxaliplatin-Induced Neuropathic Pain Model on Thermal Analgesia

The nociceptive pain threshold in each rat was assessed using thermal analgesia tests, including the Tail Flick and Hot Plate methods.

It has been determined that signs of neuropathy in animals appeared after the administration of oxaliplatin, beginning in the second week and starting from the 60<sup>th</sup> minute ( $p < 0.05$ ; Figure 1). From the third week of oxaliplatin administration, neuropathic symptoms were observed in the Tail Flick test conducted at both the 30-minute and 60-minute marks ( $p < 0.05$ ; Figure 1). Neuropathic pain symptoms were observed in both the sciatic nerve ligation and oxaliplatin-induced groups beginning in the fourth week ( $p < 0.01$ ; Figure 1). In the control group, the values on day 9 increased significantly compared to those on day 2 ( $p = 0.013$ ). However, no significant differences were observed between day 16 and day 2 ( $p = 0.226$ ) or between day 16 and day 9 ( $p = 0.145$ ). Therefore, the significant changes observed on days 9 and 16 are believed to be attributable to the decrease in the neuropathic groups rather than to transient fluctuations in the control group. In the hot-plate test, it was observed that neuropathic symptoms developed in all groups within

the neuropathic pain model, beginning in the second week ( $p < 0.05$ ; Figure 2).

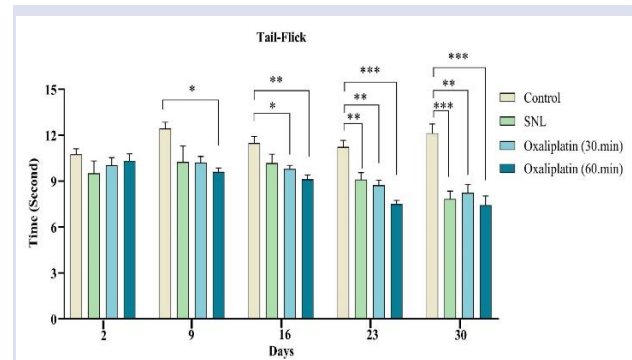


Figure 1. The data demonstrate the impact of SNL and oxaliplatin-induced neuropathic pain on nociception, as evaluated through tail flick tests. The values are presented as means  $\pm$  SEM ( $n = 6$ ). \* $p < 0.05$ , \*\* $p < 0.01$ , \*\*\* $p < 0.001$ , reflecting a significant difference compared to the control group.

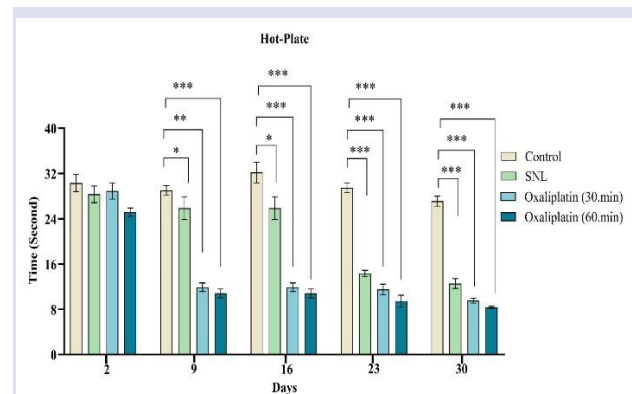


Figure 2. The data demonstrate the impact of SNL and oxaliplatin-induced neuropathic pain on nociception, as evaluated through hot plate tests. The values are presented as means  $\pm$  SEM ( $n = 6$ ). \* $p < 0.05$ , \*\* $p < 0.01$ , \*\*\* $p < 0.001$ , reflecting a significant difference compared to the control group.

### The Effect of Sciatic Nerve Ligation and Oxaliplatin-Induced Neuropathic Pain Models on Inflammatory Markers

The TNF- $\alpha$  level, measured in DRG tissue as an inflammatory marker, shows a significant difference between groups according to the statistical analysis results ( $p < 0.05$ ; Figure 3A). It has been determined that the group with the highest level of TNF- $\alpha$  is the one that received oxaliplatin treatment ( $p < 0.001$ ; Figure 3A). Comparing TNF- $\alpha$  levels between the SNL and oxaliplatin groups, it was observed that TNF- $\alpha$  levels were elevated in the oxaliplatin group ( $p < 0.05$ ; Figure 3A). When examining serum TNF- $\alpha$  levels, a significant increase was observed in both the SNL group and the Oxaliplatin group compared to the control group ( $p < 0.01$ ; Figure 3B).



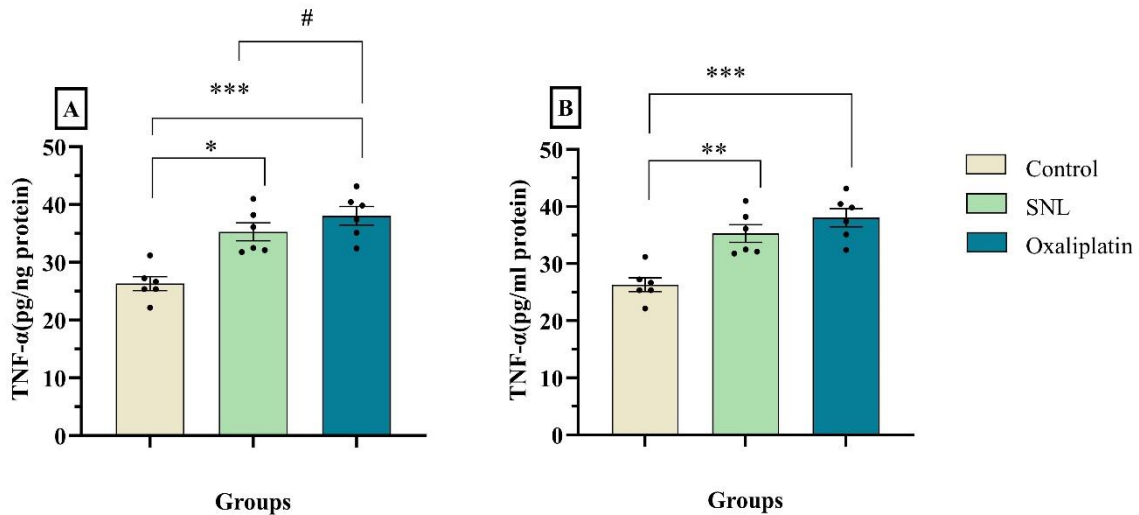


Figure 3. The data demonstrate the effects of SNL and oxaliplatin-induced neuropathic pain on (A) DRG and (B) serum levels of TNF- $\alpha$ , as assessed by ELISA. The values are presented as means  $\pm$  SEM (n = 6). \*p < 0.05, \*\*p < 0.01, \*\*\*p < 0.001, reflecting a significant difference compared to the control group.

IL-1 $\beta$  measured using the ELISA method in DRG tissue demonstrated a significant difference between the groups (p<0.05; Figure 4A). The analysis revealed that the concentrations of IL-1 $\beta$  were significantly elevated in both the SNL and oxaliplatin groups compared to the control

group (p<0.05; Figure 4A). Serum IL-1 $\beta$  levels were assessed across the groups, showing significantly elevated levels in both the SNL and Oxaliplatin groups (p<0.05; Figure 4B).

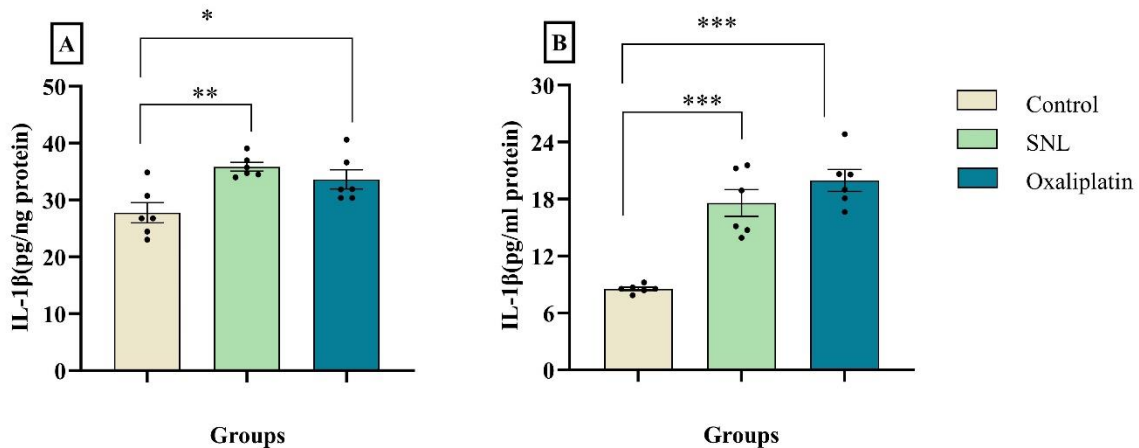


Figure 4. The data demonstrate the effects of SNL and oxaliplatin-induced neuropathic pain on (A) DRG and (B) serum levels of IL-1 $\beta$ , as assessed by ELISA. The values are presented as means  $\pm$  SEM (n = 6). \*p < 0.05, \*\*p < 0.01, \*\*\*p < 0.001, reflecting a significant difference compared to the control group.

## Discussion

This study demonstrates that thermal analgesia tests (Tail Flick and Hot Plate methods) conducted in models of sciatic nerve ligation and oxaliplatin-induced neuropathic pain indicate that symptoms of neuropathic pain began to develop in both models starting from the second week. The oxaliplatin group (second week) showed neuropathic symptoms earlier than the SNL group (fourth week).

Inflammatory markers, specifically TNF- $\alpha$  and IL-1 $\beta$ , were significantly elevated in both models within the DRG and serum when compared to the control group. Furthermore, the oxaliplatin group demonstrated higher levels of TNF- $\alpha$  than the SNL group.

Our data suggest that the earlier onset of neuropathic symptoms in the oxaliplatin group aligns with the established toxic effects of oxaliplatin on peripheral nerves. This indicates that nociceptive pathways are

affected and altered more rapidly. Several studies in the literature have emphasized the ability of oxaliplatin to disrupt axonal integrity and induce peripheral nerve dysfunction (25,26). Research findings reveal that oxaliplatin causes damage to peripheral nerves, and this effect is mediated through mechanisms including inflammation, oxidative stress, mitochondrial dysfunction, and disruptions in axonal transport (27–29). These mechanisms can lead to rapid energy depletion and dysfunction in nerve cells. Sciatic nerve ligation typically results in more localized damage, while oxaliplatin exerts a systemic effect. This distinction can influence both the onset duration and the distribution of pain (30). This may consequently accelerate the onset of neuropathic symptoms in oxaliplatin-induced neuropathy by influencing both the timing of onset and the distribution of pain. Furthermore, oxaliplatin leads to cellular hyperactivity, particularly by affecting voltage-dependent  $\text{Na}^+$  and  $\text{Ca}^{2+}$  channels (31,32). This alteration can result in abnormal electrical signalling in nerve cells and increased pain sensitivity. Consequently, these effects may lead to a more rapid onset of neuropathic pain compared to the ligation model.

Studies have demonstrated that inflammation plays a crucial role in the development of neuropathic pain, as indicated by elevated levels and activation of pro-inflammatory cytokines such as  $\text{TNF-}\alpha$  and  $\text{IL-1}\beta$ . These cytokines contribute to the sensitization of pain pathways by promoting neuroinflammatory processes in both the peripheral and central nervous systems, thereby exacerbating pain perception and neuronal dysfunction (19). The data obtained from the study indicate that elevated levels of  $\text{TNF-}\alpha$  and  $\text{IL-1}\beta$  are associated with a strong pro-inflammatory response in both models. These cytokines are known mediators of neuropathic pain and contribute to sensitization and hyperalgesia by activating immune and glial cells in the DRG (19,33). The considerable increase in inflammatory cytokines, particularly  $\text{TNF-}\alpha$  and  $\text{IL-1}\beta$ , observed in both models underscores the potential benefits of anti-inflammatory therapies that target these pathways. The observed differences in  $\text{TNF-}\alpha$  levels between SNL and oxaliplatin models suggest potential variations in the mechanisms underlying neuropathy in traumatic and chemotherapy-induced pain models. These findings suggest that, although similar inflammatory responses are observed in both models, different pathways may be involved. This distinction could play an important role in the development of treatments for neuropathic pain.

In conclusion, the elevation of inflammatory cytokines, such as  $\text{TNF-}\alpha$  and  $\text{IL-1}\beta$ , in both models suggests the potential advantages of anti-inflammatory therapies. Additionally, the rapid onset of neuropathic symptoms associated with oxaliplatin treatment emphasises the necessity for early intervention. While this study concentrated on  $\text{TNF-}\alpha$  and  $\text{IL-1}\beta$  to characterize the inflammation profile, analyses of other cytokines and chemokines could yield further insights. Moreover, long-

term studies are needed to explore the progression and chronic effects of neuropathy.

## Conflicts of interest

There are no conflicts of interest in this work.

## Acknowledgments

The authors would like to thank the Sivas Cumhuriyet University, School of Medicine, CUTFAM Research Center, Sivas, Türkiye, for providing the necessary facilities to conduct this study.

## Ethical Approval Statement

The necessary authorization for this research was obtained from the Local Animal Experiments Ethics Committee of Sivas Cumhuriyet University, under approval number 13.02.2024-16.

## References

- [1] Koetsier E., Franken G., Debets J., Heijmans L., van Kuijk S. M. J., Linderth B., Joosten E. A., Maino P., Mechanism of dorsal root ganglion stimulation for pain relief in painful diabetic polyneuropathy is not dependent on GABA release in the dorsal horn of the spinal cord, *CNS Neuroscience & Therapeutics*, 26(1) (2020) 136–143.
- [2] Ozturk A., Sabanciogullari V., Tastemur Y., Oztoprak I., Evaluation of thalamus volumes in patients with diabetic polyneuropathy using magnetic resonance imaging method. *Cumhuriyet Science Journal*, 43(4) (2022) 569–576.
- [3] Devor M., Neuropathic pain and injured nerve: Peripheral mechanisms, *British Medical Bulletin*, 47(3) (1991) 619–630.
- [4] Kocot-Kępska M., Zajączkowska R., Mika J., Wordliczek J., Dobrogowski J., Przeklasa-Muszyńska A., Peripheral mechanisms of neuropathic pain—The role of neuronal and non-neuronal interactions and their implications for topical treatment of neuropathic pain, *Pharmaceuticals*, 14(2) (2021) 77.
- [5] Fonseca-Rodrigues D., Laranjeira I., Barbosa J., Lamas N. J., Amorim D., Almeida A., Nociceptive, emotional, electrophysiological, and histological characterization of the chronic constriction injury model in female Wistar Han rats, *Brain Research Bulletin*, 167 (2021) 56–70.
- [6] Sakurai M., Egashira N., Kawashiri T., Yano T., Ikeshue H., Oishi R., Oxaliplatin-induced neuropathy in the rat: Involvement of oxalate in cold hyperalgesia but not mechanical allodynia, *Pain*, 147(1) (2009) 165–174.
- [7] Joha Z., Yıldırım Ş., Hacısüleyman L., Taşkıran A.Ş., Investigation of the analgesic properties L-759,633 and SER 601 in experimental neuropathic pain model in rats and their comparison with pregabalin, *Cumhuriyet Science Journal*, 44(1) (2023) 41–45.
- [8] Hacısüleyman L., Saraç B., Joha Z., Analgesic effects of vilazodone, indatraline, and talsupram in a rat model of neuropathic pain, *Turkish Journal of Pharmaceutical Sciences*, 19(3) (2022) 336–342.
- [9] Wang B. B., Guo C., Sun S. Q., Zhang X. N., Li Z., Li W. J., Li Z., Schumacher M., Liu S., Comparison of the nerve

- regeneration capacity and characteristics between sciatic nerve crush and transection injury models in rats, *Biomedical and Environmental Sciences*, 36(2) (2023) 160–173.
- [10] Suter M. R., Papaloizos M., Berde C. B., Woolf C. J., Gilliard N., Spahn D. R., Decosterd I., Development of neuropathic pain in the rat spared nerve injury model is not prevented by a peripheral nerve block, *Anesthesiology*, 99(6) (2003) 1402–1408.
  - [11] Medeiros P., Dos Santos I. R., Júnior I. M., Palazzo E., da Silva J. A., Machado H. R., Ferreira S. H., Maione S., Coimbra N. C., de Freitas R. L., An adapted chronic constriction injury of the sciatic nerve produces sensory, affective, and cognitive impairments: A peripheral mononeuropathy model for the study of comorbid neuropsychiatric disorders associated with neuropathic pain in rats. *Pain Medicine*, 22(2) (2021) 338–351.
  - [12] Cersosimo R. J., Oxaliplatin-associated neuropathy: A review, *Annals of Pharmacotherapy*, 39(1) 128–135.
  - [13] Egashira N., Pathological mechanisms and preventive strategies of oxaliplatin-induced peripheral neuropathy, *Frontiers in Pain Research*, 2.
  - [14] Ozsoy S., Ozdemir E., Gunes H., Gevrek F., Gulmez K., Ondansetron and AS19 attenuate morphine tolerance by modulating serotonin 5-HT<sub>3</sub> and 5-HT<sub>7</sub> receptor expressions in rat dorsal root ganglia, *J. Radiat Res. Appl. Sci.*, 16(4) (2023) 100682.
  - [15] Ciltas A.C., Ozdemir E., Gunes H., Ozturk A., Inhibition of the TRPM2 cation channel attenuates morphine tolerance by modulating endoplasmic reticulum stress and apoptosis in rats, *Neurosci Lett.*, 851 (2025) 138168.
  - [16] Zhao L., Jiang C., Yu B., Zhu J., Sun Y., Yi S., Single-cell profiling of cellular changes in the somatic peripheral nerves following nerve injury, *Front Pharmacol.*, (2024) 15.
  - [17] Sun W., Hao Y., Li R., Ho I.H.T., Wu S., Li N., Comparative Transcriptome of Dorsal Root Ganglia Reveals Distinct Etiologies of Paclitaxel- and Oxaliplatin-induced Peripheral Neuropathy in Rats. *Neuroscience*, 516 (2023) 1–14.
  - [18] Nadeau S., Filali M., Zhang J., Kerr B. J., Rivest S., Soulet D., Iwakura Y., de Rivero Vaccari J. P., Keane R. W., Lacroix S., Functional recovery after peripheral nerve injury is dependent on the pro-inflammatory cytokines IL-1 $\beta$  and TNF: Implications for neuropathic pain, *The Journal of Neuroscience*, 31(35) (2011) 12533–12542.
  - [19] Leung L., Cahill C. M., TNF- $\alpha$  and neuropathic pain: A review. *Journal of Neuroinflammation*, 7(1) (2010) 27.
  - [20] Malmberg A. B., Basbaum A. I., Partial sciatic nerve injury in the mouse as a model of neuropathic pain: Behavioral and neuroanatomical correlates, *Pain*, 76(1) (1998) 215–222.
  - [21] Baser T., Ozdemir E., Filiz A. K., Taskiran A. S., Ghrelin receptor agonist hexarelin attenuates antinociceptive tolerance to morphine in rats, *Canadian Journal of Physiology and Pharmacology*, 99(5) (2021) 461–47.
  - [22] Çetindağ Çiltaş A., Öztürk A. Effect of thiamine on morphine analgesia and tolerance in rats, *Cumhuriyet Medical Journal*, (2023).
  - [23] Dirik H., Taşkıran, A.Ş., Joha Z., Ferroptosis inhibitor ferrostatin-1 attenuates morphine tolerance development in male rats by inhibiting dorsal root ganglion neuronal ferroptosis, *Korean Journal of Pain*, 36(3) (2023) 233–246.
  - [24] Avcı O., Ozdemir E., Taskiran A. S., Inan Z. D. S., Gursay S., Metformin prevents morphine-induced apoptosis in rats with diabetic neuropathy: A possible mechanism for attenuating morphine tolerance, *Naunyn-Schmiedeberg's Archives of Pharmacology*, 395(11) (2022) 1449–1462.
  - [25] Park S. B., Cetinkaya Fisgin A., Argyriou A. A., Höke A., Cavaletti G., Alberti P., Axonal degeneration in chemotherapy-induced peripheral neurotoxicity: Clinical and experimental evidence, *Journal of Neurology, Neurosurgery & Psychiatry*, 94(11) (2023) 962–972.
  - [26] Argyriou A. A., Bruna J., Park S. B., Cavaletti G., Emerging pharmacological strategies for the management of chemotherapy-induced peripheral neurotoxicity (CIPN), based on novel CIPN mechanisms, *Expert Review of Neurotherapeutics*, 20(10) (2020) 1005–1016.
  - [27] Schellingerhout D., LeRoux L. G., Hobbs B. P., Bredow S., Impairment of retrograde neuronal transport in oxaliplatin-induced neuropathy demonstrated by molecular imaging, *PLoS One*, 7(9) (2012) e45776.
  - [28] Zheng H., Xiao W. H., Bennett G. J., Functional deficits in peripheral nerve mitochondria in rats with paclitaxel- and oxaliplatin-evoked painful peripheral neuropathy, *Experimental Neurology*, 232(2) (2012) 154–161.
  - [29] Fumagalli G., Monza L., Cavaletti G., Rigolio R., Meregalli C. Neuroinflammatory process involved in different preclinical models of chemotherapy-induced peripheral neuropathy, *Frontiers in Immunology*, 11 626687.
  - [30] Park S. B., Lin C. S. Y., Krishnan A. V., Goldstein D., Friedlander M. L., Kiernan M. C., Oxaliplatin-induced neurotoxicity: Changes in axonal excitability precede development of neuropathy, *Brain*, 132(10) (2009) 2712–2723.
  - [31] Grolleau F., Gamelin L., Boisdron-Celle M., Lapied B., Pelhate M., Gamelin E., A possible explanation for a neurotoxic effect of the anticancer agent oxaliplatin on neuronal voltage-gated sodium channels, *Journal of Neurophysiology*, 85(5) (2001) 2293–2297.
  - [32] Kawashiri T., Egashira N., Kurobe K., Tsutsumi K., Yamashita Y., Ushio S., L-type Ca<sup>2+</sup> channel blockers prevent oxaliplatin-induced cold hyperalgesia and TRPM8 overexpression in rats, *Molecular Pain*, 8 (2012) Article 7.
  - [33] Karabulut S., Filiz A. K., Akkaya R., Thiamine alleviates cognitive impairment and epileptogenesis by relieving brain inflammation in PTZ-induced kindling rat model, *Neurological Research*, 44(10) (2022) 902–909.



## Eco-Friendly and Durable Sponge with In Situ Formed Silver Nanoparticles for Antimicrobial Filtration

Furkan Sahin<sup>1,a,\*</sup>

<sup>1</sup> Department of Biomedical Engineering, Faculty of Engineering and Architecture, Beykent University, 34398, Istanbul, Türkiye

\*Corresponding author

### Research Article

#### History

Received: 09/03/2024

Accepted: 15/05/2025



This article is licensed under a Creative Commons Attribution-NonCommercial 4.0 International License (CC BY-NC 4.0)

### ABSTRACT

Microbial contamination poses a significant challenge to the management of water resources and biomedical applications. In this study, the development of a biogenic antimicrobial filtration system has been successfully achieved. This system utilizes a plant extract-mediated synthesis approach for in situ formation of silver nanoparticles (AgNPs) within a porous sponge matrix. The fabrication process involved the immersion of a commercial sponge in an aqueous solution of AgNO<sub>3</sub> and plant extract, followed by a thermal treatment. The structural and chemical properties of the Ag@Sponge were then confirmed via a range of analytical methods, including scanning electron microscopy (SEM), energy-dispersive X-ray spectroscopy (EDX), X-ray diffraction (XRD), and X-ray photoelectron spectroscopy (XPS). These results indicated the successful incorporation of AgNPs within the sponge, with a predominant spherical morphology and an average size of 54 ± 14 nm. Antimicrobial activity tests demonstrated that Ag@Sponge exhibited significant bacterial and fungal inactivation, achieving >99.99999% microbial reduction against *Escherichia coli* (*E. coli*), *Staphylococcus aureus* (*S. aureus*), and *Candida albicans* (*C. albicans*) ( $R > 7$ ). Furthermore, the results of filtration experiments demonstrated that microbial removal efficiency increased progressively over six cycles, reaching final reductions of 6.2–6.4 log CFU/mL for *E. coli*, *S. aureus*, and *C. albicans*. Mechanical durability tests confirmed that Ag@Sponge retained >6 log CFU/mL reduction after 5000 cm abrasion (down to 6.6 ± 0.5) and 400 bending cycles (down to 6.1 ± 1.2), indicating strong mechanical resilience and in situ nanoparticle stability. These findings highlight the potential of Ag@Sponge as a sustainable and efficient antimicrobial filtration material for practical applications in water purification and medical decontamination.

**Keywords:** Disinfection, Green fabrication, Ag nanoparticles, Antimicrobial, Sponge.

<sup>a</sup> [furkansahin@beykent.edu.tr](mailto:furkansahin@beykent.edu.tr)

<https://orcid.org/0000-0001-5409-3925>

## Introduction

Microbial contamination continues to pose a significant challenge to the sustainable management of water resources and biomedical applications [1]. Hospital-based liquid waste, in particular, poses considerable risks to both the environment and public health due to its high levels of pathogenic microorganisms, antibiotic residues, and pharmaceutical components [2,3]. Inadequate treatment of such waste accelerates the spread of antibiotic resistance and causes irreversible damage to ecosystems [1]. The World Health Organization (WHO) reports that approximately 1.5 million people die each year from complications related to diseases originating from unsafe water sources, and that antibiotic resistance further exacerbates this situation [4]. In response, the United Nations (UN) has emphasized the importance of safe water resource management and pathogen load reduction through Sustainable Development Goal 6 (Clean Water and Sanitation) and Sustainable Development Goal 3 (Good Health and Well-being) within the broader framework of the Sustainable Development Goals (SDGs) [5,6]. In this context, the development of low-cost and sustainable disinfection technologies that do not leave antibiotic residues has become a global necessity [7].

A review of the extant literature reveals a plethora of methodologies for liquid disinfection, including chlorination, ozonation and UV radiation, which are notable for their strong oxidation effects [8–10]. However, a significant disadvantage of these methods is that by-products formed during disinfection (e.g., chlorinated organic compounds) can cause secondary pollution, resulting in environmental toxicity and health risks [8,9]. This situation highlights the necessity for the development of alternative strategies [8]. In recent years, the integration of antimicrobial materials into disinfection systems has emerged as an innovative approach [11,12], but certain disadvantages persist, including the risk of antibiotic or chemical residues in the liquid and the limited effectiveness against diverse microorganisms [13]. An alternative and more sustainable approach involves the incorporation of metallic nanoparticles, known for their broad-spectrum antimicrobial properties, into filtration systems [14]. Metal nanoparticles have been shown to exhibit high activity against microorganisms and to enhance the performance of disinfection systems through mechanisms such as the production of reactive oxygen species and the disruption of cell membranes [15–17]. AgNPs in particular have a proven track record of



effectiveness and reliability over time [15]. In contrast to essential metals such as copper, silver is not required for bacterial physiology and therefore lacks associated homeostatic regulation [15]. As a result, Ag<sup>+</sup> ions irreversibly bind to critical thiol-containing biomolecules, including cysteine residues in enzymes and membrane proteins, leading to irreversible enzyme inactivation and disruption of respiratory electron transport chains [15]. Furthermore, the catalytic generation of reactive oxygen species (ROS), particularly H<sub>2</sub>O<sub>2</sub>, contributes to oxidative stress and further compromises bacterial viability [15,17]. The synergy of these characteristics results in AgNPs demonstrating exceptional potency at low concentrations, while concurrently minimizing the risk of resistance development. This positions silver as one of the most efficient and reliable antimicrobial agents among metallic nanoparticles.

Nonetheless, a number of fundamental issues inherent in systems developed with metal nanoparticles have yet to be resolved. Chief among these is the propensity of nanoparticles to readily detach from the carrier surface [18], a phenomenon that precipitates a swift decline in the efficiency of the filtration system [19]. Moreover, the utilization of chemical reagents in nanoparticle production has the potential to engender environmental toxicity and escalate production costs [20–22]. Consequently, there is a compelling imperative to explore the development of cost-effective, sustainable, and high-performance materials that are synthesized in an environmentally friendly manner [23].

The present study set out to cultivate AgNPs directly on the surface of a sponge by means of an eco-friendly method that utilized plant extracts. Almond shell extracts were employed as a means to reduce Ag ions and stabilize nanoparticles, a process that is environmentally friendly and reduces reliance on chemical reagents. It is well established that such plant-based reductants contain polyphenols, flavonoids and organic acids, which facilitate the reduction of metal ions and provide surface functional groups for stabilization [21]. In the preceding literature, a number of plant sources, including tea leaves, citrus peels and other agricultural residues, have been documented for analogous purposes [16,21]. However, the present study elected to utilize almond shells on the basis of their elevated phenolic content, local availability and potential for valorization as a waste-derived material [24]. The sponge was used as a carrier matrix for nanoparticles due to its high surface area and durability. This approach resulted in the development of a low-cost, sustainable and durable filtration system. The Ag@Sponge material was thoroughly characterized using a range of analytical techniques, including scanning electron microscopy (SEM), X-ray diffraction (XRD), and X-ray photoelectron spectroscopy (XPS). Furthermore, the material's effectiveness in reducing microbial load in liquid waste and its long-term performance was comprehensively investigated.

## Materials and Methods

### *Fabrication of Ag@Sponge*

The Ag@Sponge platform was synthesized through a strategy of in situ growth of Ag nanostructures on the sponge surface. The synthesis process involved a biogenic reduction method that was used in an environmentally friendly manner, with almond shell extract serving as the reducing agent of choice.

To prepare the almond shell extract, 10 g of washed and dried almond shell at 40 °C was kept in 100 mL of double distilled water at 80 °C for 6 hours. The resulting solution was then filtered using a filter paper (M&Nagel MN 640 m, pore size 4–12 µm, medium flow rate) to remove solid content, thereby yielding the aqueous almond shell extract. The prepared almond shell extract was then utilized for the reduction of Ag ions and the formation of Ag@Sponge. To this end, a 1.5 mM AgNO<sub>3</sub> aqueous solution was prepared and 20 mL of AgNO<sub>3</sub> solution and 10 mL of almond extract were added to a 50 mL Falcon tube, resulting in a final solution concentration of 1 mM. Thereafter, the sponge sample was placed in the solution and gently shaken to ensure homogeneous distribution. In situ AgNPs growth was then performed by keeping the tube in a water bath at 90 °C for 1 hour. Subsequent to the completion of the process, the sponge sample was removed from the solution and dried in an oven at 50 °C, resulting in the formation of a platform that was designated Ag@Sponge.

### *Characterization of Ag@Sponge*

Morphological analysis of the produced nanostructured Ag@Sponge and the control surface was performed using a scanning electron microscope (SEM, Zeiss EVO LS10, 25 kV). In order to determine the composition of the surface, elemental analysis was performed with energy dispersive X-ray spectroscopy (EDX, XFlash 6110, Bruker) integrated into the SEM system. The size distribution of the particles on the surface was calculated using ImageJ software from the obtained SEM images. The chemical composition and bonding structure of the produced surfaces were analyzed using X-ray photoelectron spectroscopy (XPS, K-alpha, Thermo Scientific) equipped with a monochromatic Al Kα (1486.7 eV) X-ray source. X-ray diffraction (XRD) analysis was performed to examine the crystal structure, and the measurements were performed with the Panalytical Empyrean XRD system at 45 kV and 40 mA operating conditions, using Cu K-α1 (λ = 1.5406 Å) X-ray source. The XRD data were processed using OriginPro (OriginLab Corp., USA), with a 100-point Savitzky-Golay smoothing algorithm applied in order to reduce noise and enhance peak clarity without distorting peak shape. The average size of the crystallites was calculated from the XRD data using the Debye–Scherrer equation (Eq. 1).

$$D = \frac{K * \lambda}{\beta * \cos\theta} \quad (1)$$

In this calculation, the Bragg angle ( $\theta$ ), X-ray wavelength ( $\lambda$ ) and full width at half maximum (FWHM) peak width ( $\beta$ ) parameters were used. The degree of crystallinity (CI) was calculated by taking the ratio of the crystalline peak areas within the total area under the diffraction curve (Eq. 2).

$$CI = \frac{\text{Area of all the crystalline peaks}}{\text{Area of all the crystalline and amorphous peaks}} \quad (2)$$

### Antimicrobial Assay

Antimicrobial, antibacterial and antifungal activity were evaluated by following the AATCC test protocol with slight modifications. Bactericidal activity was investigated on Gram-negative *E. coli* (ATCC 25922) and Gram-positive *S. aureus* (ATCC 25923) bacteria, while fungicidal activity was tested on *C. albicans*. Mueller-Hinton liquid (broth) and solid (agar) media were utilized for bacterial strains, while Sabouraud Dextrose Broth and Sabouraud Dextrose Agar were employed for fungal strains. 100  $\mu$ L each of fungal and bacterial suspension at 0.5 McFarland turbidity was taken and inoculated onto Ag@Sponge and control surfaces of approximately  $1 \times 1 \text{ cm}^2$  in size. Untreated sponge was used as the control surface. After 24 hours of incubation at 37 °C, the surfaces were placed in 10 mL of PBS and 5 minutes of sonication and 5 minutes of vortexing were applied to transfer the microorganisms on the surfaces to the PBS medium. A volume of 100  $\mu$ L of the resulting suspension was then inoculated onto solid media, after which the number of colonies on agar plates was enumerated following a 24-hour incubation period at 37 °C. The antimicrobial activity was then calculated according to equation 3.

$$\text{Antimicrobial Activity (R)} = \log(Ut) - \log(At) \quad (3)$$

In this equation, *At* represents the average number of colonies surviving on the developed Ag@Sponge platform, while *Ut* represents the average number of colonies surviving on the untreated sponge.

### Microbial Retention and Inactivation Performance Test

In order to evaluate the performance of microbial filtration of the Ag@Sponge platform, the microorganism *E. coli*, *S. aureus* and *C. albicans* were utilized. The microorganism suspensions were prepared in sterile phosphate-buffered saline (PBS) by adjusting to 1 McFarland turbidity standard. A total of 20 mL of PBS solution was used for each microorganism.

The prepared PBS-microorganism suspension was then passed through sponge samples that had been prepared in advance at a flow rate of 2 mL/min. The liquid that had been filtered was collected in a sterile beaker, and the sponge was left for one hour to ensure that the liquid absorbed by the sponge was completely released. At the conclusion of this period, the final liquid retained by the sponge, which did not drip freely, was added to the

filtrate collected in the beaker by gently compressing the sponge. 100  $\mu$ L of the waste liquid accumulated in the beaker after filtration was taken and inoculated on solid medium and incubated at 37 °C for 24 hours. The microorganism retention and inactivation performance were then evaluated by taking wastewater and restarting the filtration process. This procedure was repeated six times. After each filtration cycle, the colonies formed on the solid media were counted and the number of microorganisms removed was compared to the initial microorganism load using Equation 3.

### Antimicrobial Robustness Test

In order to evaluate the durability of the produced samples in the context of antimicrobial activity under mechanical stress, a series of abrasion and bending tests were conducted. The abrasion test involved subjecting the samples to friction against an aluminum foil surface over specific distances, with a weight of approximately 200 g applied. The samples were shifted by 500 cm, 1000 cm, 2500 cm and 5000 cm to assess the impact of surface abrasion and material erosion on their antimicrobial activity. The bending test involved subjecting the samples to repeated bending cycles, with the number of cycles ranging from 50 to 400, to simulate the durability of the sponges under mechanical loads such as tension and flexion. Following each test stage, the samples were subjected to antimicrobial tests, as outlined in section 2.3, to evaluate the effect of mechanical stresses on microorganism inhibition capacity.

## Results and Discussion

A biogenic antimicrobial filtration system was developed through a plant extract-mediated synthesis approach for the in situ formation of AgNPs within a porous sponge matrix (Figure 1A). The fabrication process involved the immersion of a commercial sponge in an aqueous solution of AgNO<sub>3</sub> and plant extract, followed by a thermal treatment at 90°C for 60 minutes. The color change from pale yellow to dark brown indicated the successful reduction of Ag<sup>+</sup> ions and in situ formation of AgNPs. To evaluate the potential application of Ag@Sponge in microbial filtration, a conceptual schematic is presented in Figure 1B. Contaminated liquid waste passes through the Ag@Sponge, where microbial retention and inactivation occur due to the antimicrobial properties of AgNPs, resulting in a disinfected liquid effluent.

The morphological characteristics of the pristine sponge and Ag@Sponge were examined using scanning electron microscopy (SEM) (Figure 1C). While the unmodified sponge exhibited a clean and uniform porous structure, the Ag@Sponge showed embedded nanoparticles throughout the surface, as highlighted in the magnified regions. SEM images revealed that the nanoparticles on the surface were predominantly spherical; however, spiky structures were also observed in certain regions (e.g. area marked yellow). The distribution

of the particles was found to be nonuniform, with partial aggregations evident as surface clusters. This morphology is attributed to the spontaneous and progressive reduction of metal ions directly on the substrate, where nucleation occurs randomly and continues over time, which is typically observed in similar in situ formation processes [16,25]. Consequently, the newly formed nanoparticles have the capacity to emerge on top of existing ones, thus giving rise to the formation of layered or aggregated structures. The particle size distribution, based on distinguishable spherical domains within these aggregates, revealed an average diameter of  $54 \pm 14$  nm (Figure 1D). The presence of Ag in the modified sponge

was further confirmed by EDX analysis (Figure 1E). A comparison of the spectrum of the pristine sponge, primarily composed of carbon and oxygen [26], with that of the Ag@Sponge revealed the presence of additional peaks corresponding to Ag (15.6 wt%), along with minor contributions from Na, K, and Cl, which may have originated from the almond shell extract [24]. The findings, when considered collectively, indicate the successful synthesis of Ag@Sponge via a green chemistry approach, with its structural and chemical properties supporting its potential use in antimicrobial liquid filtration applications.

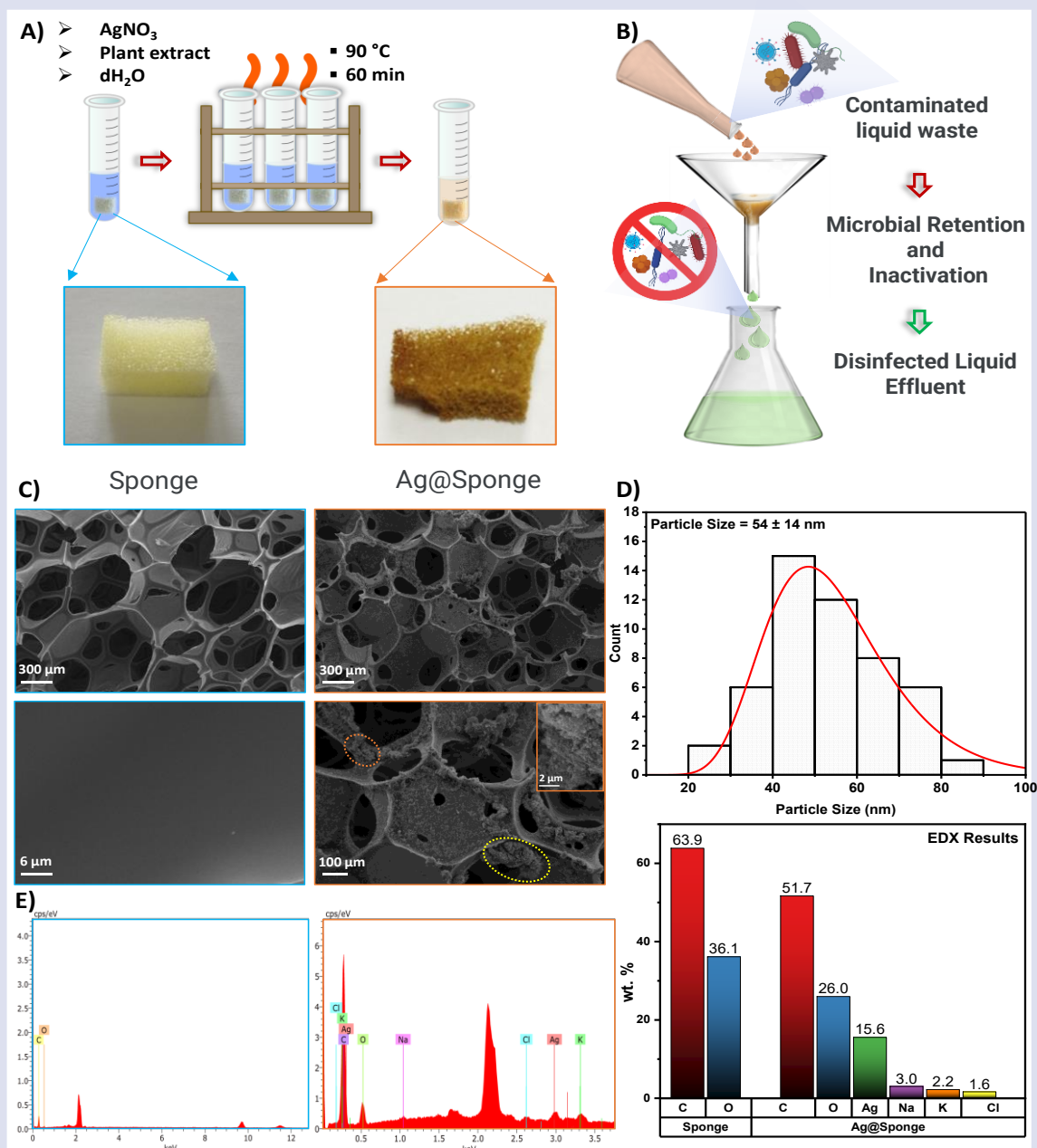


Figure 1. Schematic representation of the process of in situ formation of AgNPs on the sponge (A) and the disinfection of contaminated liquid waste using the developed Ag@Sponge (B). SEM images (C), particle size distribution graph (D), and EDX results (E) of the sponge and Ag@Sponge.

EDX results confirmed exclusively the presence of Ag; however, they did not provide any information regarding its chemical state or crystalline form. Therefore, XRD and XPS analyses were conducted to elucidate the structural and chemical characteristics of Ag within the sponge matrix.

In order to investigate the crystalline structure of the AgNPs incorporated into the sponge matrix, XRD analysis was performed. As demonstrated in Figure 2A, characteristic diffraction peaks were identified at  $2\theta = 38.1^\circ, 44.2^\circ, 64.8^\circ, 77.3^\circ$ , and  $81.2^\circ$ , which correspond to the (111), (200), (220), (311), and (222) planes of face-centered cubic (fcc) metallic silver ( $\text{Ag}^0$ ) (JCPDS #No. 04-0783) [27]. The presence of these peaks confirmed the successful formation of metallic Ag within the porous sponge structure. The average crystallite size of the AgNPs was determined using the Debye–Scherrer equation, based on the full width at half maximum (FWHM) of the peaks, yielding average crystallite sizes of 6.5 nm (111), 5.1 nm (200), 5.1 nm (220), 5.4 nm (311), and 4 nm (222) for the respective diffraction peaks. A comparison of these values with those of previously reported monometallic AgNPs synthesized via green chemistry approaches suggests that the former exhibit a relatively smaller crystal size distribution [27,28]. This reduction in crystallite size can be attributed to the specific synthesis conditions, including the interaction of silver precursors with the

sponge matrix. It is hypothesized that this interaction may have influenced the nucleation rate and inhibited the growth of larger crystallites [29]. The selection of the matrix and the growth environment is likely to have played a crucial role in limiting the crystal size [29], resulting in a higher surface-to-volume ratio that is often desirable for applications such as catalysis and antimicrobial activity [30]. Furthermore, the crystallinity index (CI) was calculated as 25.24%. CI values exceeding 40% have been reported for certain bimetallic and trimetallic nanoparticle systems [16]. Nevertheless, direct comparison is constrained by the disparities in substrate materials and synthesis conditions.

To further confirm the chemical state of Ag in the synthesized Ag@Sponge, high-resolution XPS analysis was conducted; the Ag 3d spectrum (Figure 2B) exhibiting two prominent peaks at binding energies of 368.3 eV and 374.3 eV, corresponding to Ag 3d<sub>5/2</sub> and Ag 3d<sub>3/2</sub>, respectively. The observed spin-orbit splitting of 6.0 eV was in good agreement with literature reports for metallic silver ( $\text{Ag}^0$ ) [27,31], confirming that the silver present in the sponge was in its reduced, elemental form rather than in an oxidized state. These XPS results are consistent with the XRD findings, reinforcing the conclusion that AgNPs were successfully synthesized and incorporated into the sponge matrix through the plant extract-mediated reduction of  $\text{Ag}^+$  ions.

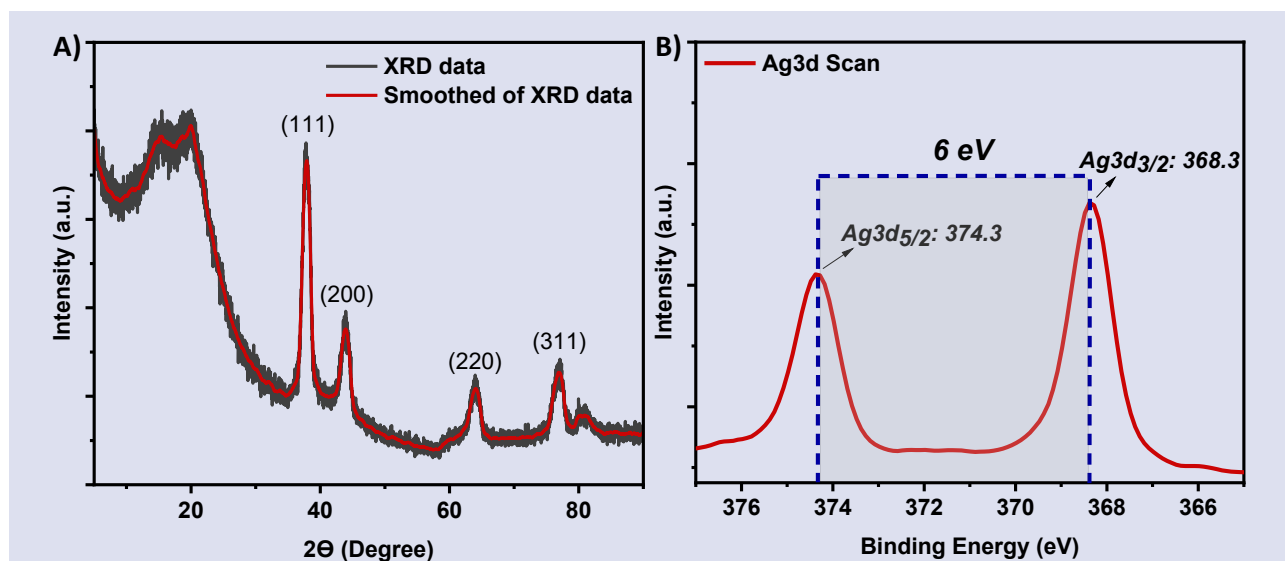


Figure 2. Chemical characterization of the Ag@Sponge platform. A) XRD patterns of Ag@Sponge. B) High-resolution XPS spectra of Ag 3d in Ag@Sponge.

The antimicrobial activity of Ag@Sponge was evaluated against a range of common pathogenic microorganisms, including the Gram-positive bacteria *S. aureus*, the Gram-negative bacteria *E. coli*, and the fungal pathogen *C. albicans*. According to the test results, Ag@Sponge effectively inactivated nearly all inoculated microorganisms. In comparison with the untreated sponge material, Ag@Sponge demonstrated logarithmic reductions (R) of  $7.2 \pm 0.2$ ,  $7.6 \pm 0.3$ , and  $7.5 \pm 0.2$  against *E. coli*, *S. aureus*, and *C. albicans*, respectively. The R value,

which is indicative of antimicrobial efficacy, significantly exceeded the critical threshold of 2 [32], indicating an inactivation rate of >99.99999%. It is noteworthy that Ag@Sponge exhibited higher antibacterial efficacy against Gram-positive bacteria compared to Gram-negative bacteria. This phenomenon can be attributed to the structural differences in their cell walls. Gram-positive bacteria possess a thick peptidoglycan layer, whereas Gram-negative bacteria have an additional outer membrane composed of phospholipids and



polysaccharides that surrounds the peptidoglycan layer [33]. This outer membrane may act as a barrier, limiting the penetration of metallic nanoparticles into the bacterial cell, thereby reducing bactericidal efficacy. In addition, inorganic oxide nanoparticles exhibit a heightened adsorption affinity for distinctive components within the cell wall of Gram-positive bacteria, including teichoic acids, predominantly via  $\pi$ - $\pi$  interactions [34]. Differences in the isoelectric points of their membranes result in Gram-negative *E. coli* having a less negative surface charge compared to Gram-positive *S. aureus* [35], which may contribute to the enhanced inhibitory activity of metallic nanoparticles against Gram-positive bacteria [16]. However, it is important to note that the calculated R values are relative to the control surface, and variations in microbial growth on the control samples could influence the final antimicrobial efficacy values.

Beyond its antibacterial effects, Ag@Sponge also exhibited excellent antifungal activity against *C. albicans*, a leading cause of nosocomial infections. One possible mechanism underlying this strong antimicrobial activity is the ability of AgNPs to enhance reactive oxygen species (ROS) generation, leading to oxidative stress-induced apoptosis [35]. The generation of ROS by metallic

nanoparticles is known to cause oxidative damage to microbial cells through mechanisms such as DNA/RNA strand breakage, protein oxidation, membrane disruption, and lipid peroxidation, ultimately leading to cell death [25,35]. Additionally, Ag ions released from the nanoparticles have the capacity to penetrate cells via ion channels and/or purines, bind to lipopolysaccharides, peptidoglycans, and carboxyl groups, and alter the electrochemical potential of intracellular and extracellular components [36]. This can result in membrane depolarization and instability, leading to nuclear membrane deformation, cytoplasmic leakage, and damage to essential cellular processes, including DNA replication and transcription [17,36]. Furthermore, the nanoscale spherical morphology of the AgNPs likely enhanced the antimicrobial effect due to their high surface area-to-volume ratio, which promotes greater interaction with microbial cells [37]. In summary, the potent antimicrobial activity observed in Ag@Sponge is most likely a consequence of nano/micro-scale metallic particles encountering pathogens, disrupting cell membranes, penetrating microbial cells, and interfering with critical biomolecular structures such as proteins and DNA.

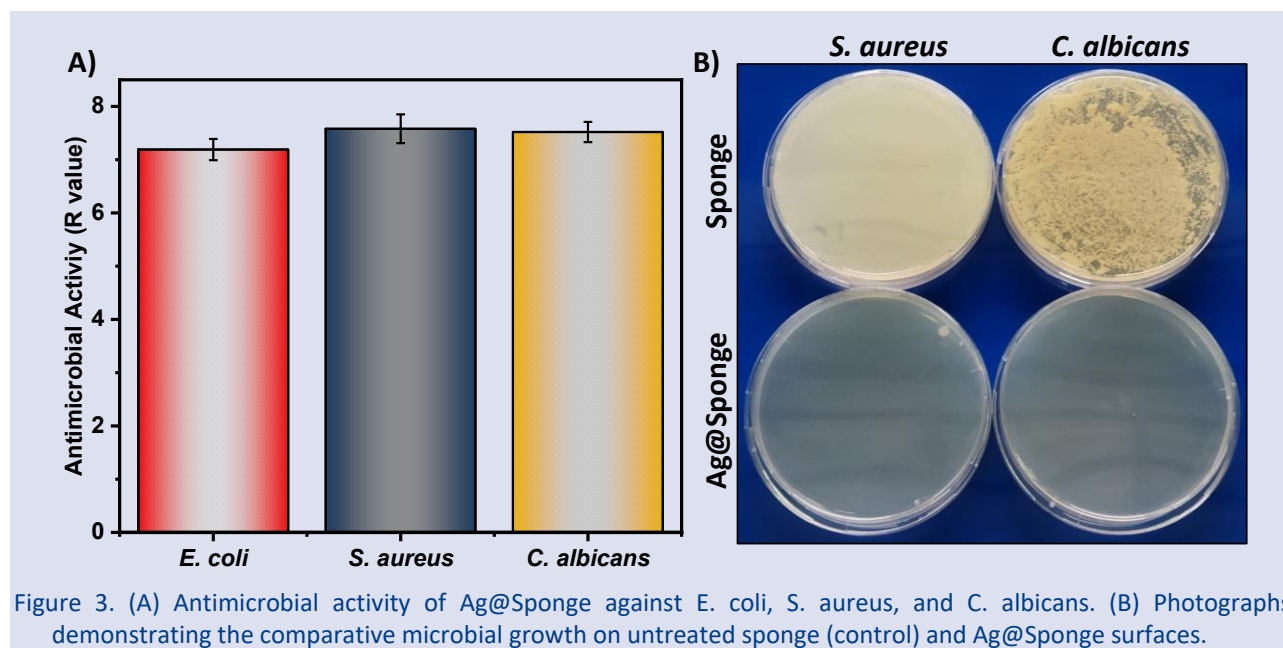


Figure 3. (A) Antimicrobial activity of Ag@Sponge against *E. coli*, *S. aureus*, and *C. albicans*. (B) Photographs demonstrating the comparative microbial growth on untreated sponge (control) and Ag@Sponge surfaces.

The microbial removal performance of the developed Ag@Sponge material was evaluated using a simple filtration setup (Figure 1B and 4). The results demonstrate that microbial removal gradually increases with the filtration process, with a significant removal observed for all microorganism species in the first filtration stage, resulting in a decrease of approximately >4 log CFU/mL in all microbial strains. As the number of filtrations increased, the removal rate continued to increase, although at a rate that was lower compared to the first filtration.

This phenomenon can be attributed to the combined impact of multiple factors during the filtration process.

Initially, microorganisms interact with the Ag@Sponge surface, resulting in a rapid removal due to the high surface activity of AgNPs [38]. Additionally, the initial stage of filtration facilitates the retention of free and large microorganism clusters in the suspension, contributing to an enhanced filtration efficiency. However, as the filtration progresses, the removal rate becomes more limited due to a decrease in the concentration of microorganisms remaining in the system. Furthermore, the accumulation of microbial residues and biological materials on the surface may partially reduce the binding areas of new microorganisms [38]. Additionally, due to the controlled release of silver ions ( $\text{Ag}^+$ ), the more intense

effect of free ions in the initial stages may cause this interaction to gradually balance in the subsequent cycles [39].

In the final filtration stage, microbial removal was achieved at approximately 6-7 log CFU/mL levels in the 6th cycle, and it was revealed that the Ag@Sponge

material offers high and stable antimicrobial activity. These results show that the developed sponge-based filter material exhibits effective performance in multi-stage filtrations and offers a strong alternative for the removal of microbial contamination.

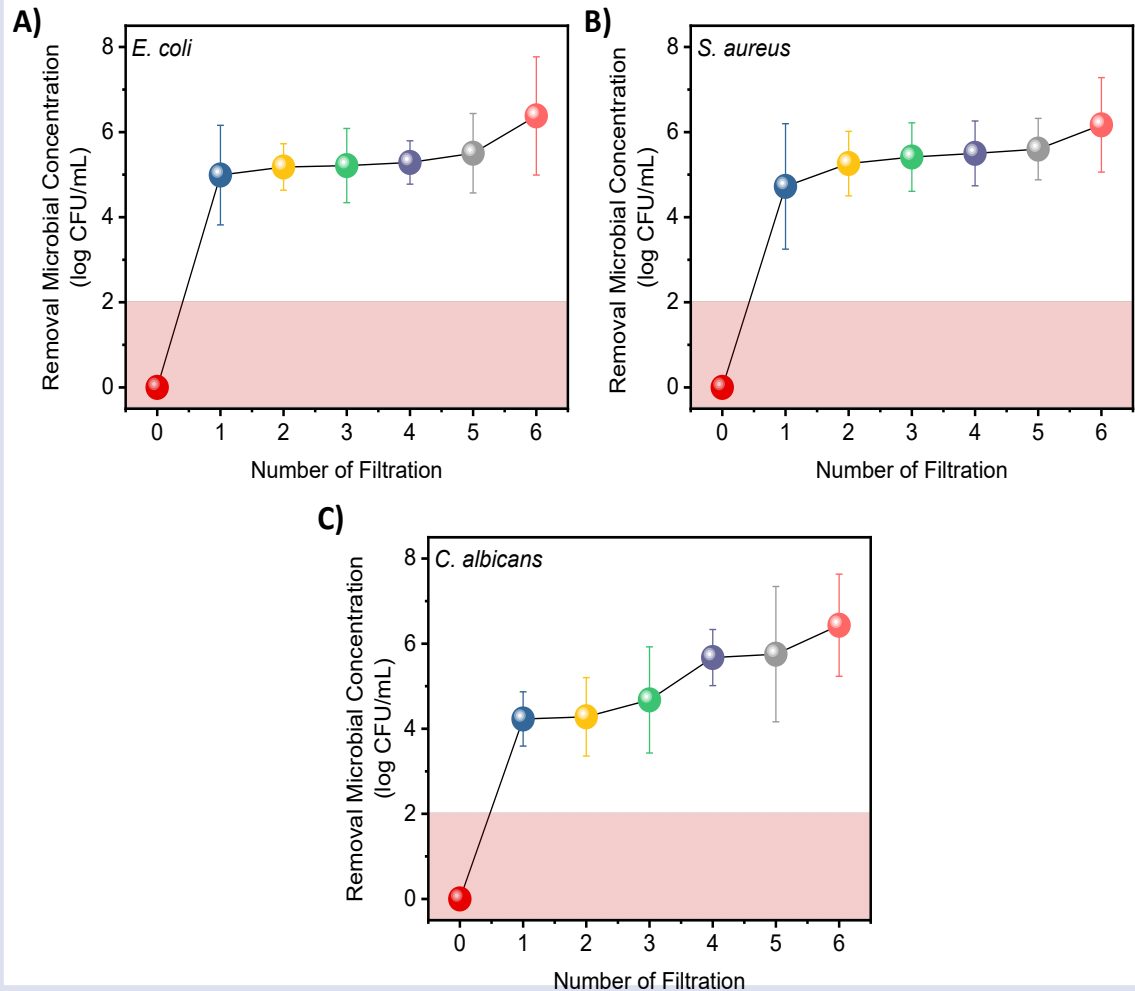


Figure 4. Filtration performance of the developed Ag@Sponge material on A) *E. coli*, B) *S. aureus* and C) *C. albicans* microorganisms. Microbial removal concentration (log CFU/mL) was investigated throughout the filtration cycle. The shaded red area in the figure represents the safe limit zone required for microbial filtration.

The long-term effectiveness of materials utilized in filtration processes is contingent not only on their antimicrobial performance but also on their mechanical strength and structural stability. In this context, the antimicrobial activity preservation performance of the developed Ag@Sponge material was evaluated following abrasion and bending tests (Figure 5).

As demonstrated in Figure 5A, the R value exhibited minimal decline against *E. coli*, *S. aureus*, and *C. albicans* microorganisms across the range of abrasion distances from 500 cm to 5000 cm. The material's initial high antimicrobial activity was retained, suggesting that the AgNPs on the Ag@Sponge surface maintained strong bonding against mechanical effects and did not readily separate from the material surface. The bending strength test results, presented in Figure 5B, demonstrate that

after 50 to 400 bending cycles, the antimicrobial activity against all microorganisms was significantly preserved. Notably, even after 400 bending cycles, the decrease in the R value was minimal, and it was observed that the flexibility properties of the material did not have a negative impact on the antimicrobial activity. This outcome demonstrates that the Ag@Sponge material possesses a flexible and durable structure, capable of retaining its functionality under mechanical stresses. In general, the results of the abrasion and bending tests demonstrate that the developed Ag@Sponge material exhibits a level of robustness (mechanical durability) that renders it suitable for long-term use. This feature confirms that the material can provide sustainable antimicrobial activity in real-life applications and can demonstrate stable performance in repeated filtration processes [40].

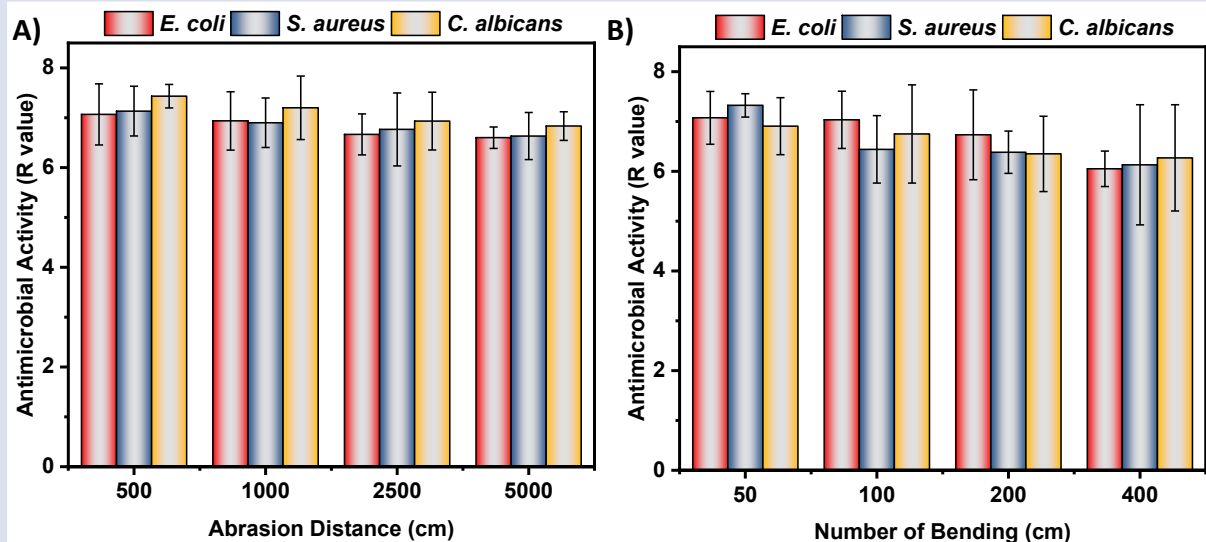


Figure 5. Preservation performance of antimicrobial activity under mechanical strength of the developed Ag@Sponge material. (A) Antimicrobial activity (R value) against *E. coli*, *S. aureus* and *C. albicans* microorganisms after different abrasion distances (500–5000 cm). (B) Evaluation of antimicrobial activity after different bending cycles (50–400 times).

## Conclusion

In this study, a biogenic antimicrobial filtration system, Ag@Sponge, was successfully synthesized via a green chemistry approach utilizing plant extract-mediated formation of AgNPs. The utilization of almond shell extract facilitated the in situ formation of AgNPs within a porous sponge matrix, thereby obviating the requirement for hazardous chemical reagents and ensuring a sustainable fabrication process. Structural analysis confirmed the effective incorporation of AgNPs into the porous sponge matrix, while antimicrobial tests demonstrated exceptional efficacy against bacterial and fungal pathogens, achieving microbial inactivation rates exceeding 99.99%. The filtration experiments further validated the system's effectiveness, demonstrating significant microbial removal across multiple filtration cycles ( $R > 6$ ). Additionally, mechanical durability assessments confirmed that Ag@Sponge retained its antimicrobial properties even after extensive abrasion and bending tests. The material's sustained antimicrobial activity and structural robustness position it as a promising candidate for real-world water purification and biomedical applications. The findings highlight the potential of Ag@Sponge as a cost-effective and environmentally friendly solution for microbial contamination in liquid waste treatment systems. Future studies may focus on optimizing the material's scalability, regeneration capabilities, and real-world performance under complex environmental conditions.

## Conflict of Interest

There are no conflicts of interest in this work.

## Acknowledgment

This study did not receive funding from any public, commercial, or non-profit organizations.

## References

- [1] Abosse J.S., Megersa B., Zewge F., Eregno F.E., Healthcare waste management and antimicrobial resistance: a critical review, *Journal of Water and Health*, 22 (2024) 2076–2093.
- [2] Chand S., Shastry S., Hiremath S., Joel J., Bhat C., Uday V., Water, sanitation, hygiene and biomedical waste disposal in the healthcare system: A review, *Biomedicine*, 40 (2020) 14.
- [3] Singh H., YT K., Mishra A.K., Singh M., Mohanto S., Ghumra S., Seelan A., Mishra A., Kumar A., Pallavi J., Ahmed M.G., Sangeetha J., Thangadurai D., Harnessing the foundation of biomedical waste management for fostering public health: strategies and policies for a clean and safer environment, *Discov Appl Sci*, 6 (2024) 89.
- [4] Pal M., Ayele Y., Hadush A., Panigrahi S., Jadhav V., Public Health Hazards Due to Unsafe Drinking Water, *Air Water Borne Dis.*, 7 (2018) 1000138.
- [5] Matta G., Kumar P., Uniyal D.P., Joshi D.U., Communicating Water, Sanitation, and Hygiene under Sustainable Development Goals 3, 4, and 6 as the Panacea for Epidemics and Pandemics Referencing the Succession of COVID-19 Surges, *ACS EST Water*, 2 (2022) 667–689.
- [6] Tyagi I., Kumar V., Tyagi K., Water pollution—sources and health implications of the environmental contaminants on the aquatic ecosystem and humans: approach toward sustainable development goals, In: Dehghani M.H., Karri R.R., Tyagi I., Scholz M. (Eds.), *Water, The Environment, and the Sustainable Development Goals*, 1st ed. Elsevier, (2024) 35–66.
- [7] Rajapakse J., Otoo M., Danso G., Progress in delivering SDG6: Safe water and sanitation, *Cambridge Prisms: Water*, 1 (2023) e6.
- [8] Bharti B., Li H., Ren Z., Zhu R., Zhu Z., Recent advances in sterilization and disinfection technology: A review, *Chemosphere*, 308 (2022) 136404.

- [9] Da Costa J.B., Rodgher S., Daniel L.A., Espíndola E.L.G., Toxicity on aquatic organisms exposed to secondary effluent disinfected with chlorine, peracetic acid, ozone and UV radiation, *Ecotoxicology*, 23 (2014) 1803–1813.
- [10] Kong J., Lu Y., Ren Y., Chen Z., Chen M., The virus removal in UV irradiation, ozonation and chlorination, *Water Cycle*, 2 (2021) 23–31.
- [11] Mandal T.K., Nanomaterial-Enhanced Hybrid Disinfection: A Solution to Combat Multidrug-Resistant Bacteria and Antibiotic Resistance Genes in Wastewater, *Nanomaterials*, 14 (2024) 1847.
- [12] Cai Y., Sun T., Li G., An T., Traditional and Emerging Water Disinfection Technologies Challenging the Control of Antibiotic-Resistant Bacteria and Antibiotic Resistance Genes, *ACS EST Eng.*, 1 (2021) 1046–1064.
- [13] Sanganyado E., Gwenzi W., Antibiotic resistance in drinking water systems: Occurrence, removal, and human health risks, *Science of The Total Environment*, 669 (2019) 785–797.
- [14] Castro-Muñoz R., The Role of New Inorganic Materials in Composite Membranes for Water Disinfection, *Membranes*, 10 (2020) 101.
- [15] Slavin Y.N., Asnis J., Häfeli U.O., Bach H., Metal nanoparticles: understanding the mechanisms behind antibacterial activity, *J Nanobiotechnol*, 15 (2017) 65.
- [16] Demirel Sahin G., Sahin F., Barlas F.B., Onses M.S., Acar S., Antimicrobial, anti-biofouling, antioxidant, and biocompatible fabrics with high durability via green growth of trimetallic nanoparticles, *Materials Today Communications*, 41 (2024) 110807.
- [17] Sahin F., Camdal A., Demirel Sahin G., Ceylan A., Ruzi M., Onses M.S., Disintegration and Machine-Learning-Assisted Identification of Bacteria on Antimicrobial and Plasmonic Ag–Cu<sub>2</sub>O Nanostructures, *ACS Appl. Mater. Interfaces*, 15 (2023).
- [18] Carrillo J.-M.Y., Dobrynin A.V., Contact Mechanics of Nanoparticles, *Langmuir*, 28 (2012) 10881–10890.
- [19] Wang H., Zhang W., Zeng S., Shen C., Jin C., Huang Y., Interactions between nanoparticles and fractal surfaces, *Water Research*, 151 (2019) 296–309.
- [20] Besha A.T., Liu Y., Bekele D.N., Dong Z., Naidu R., Gebremariam G.N., Sustainability and environmental ethics for the application of engineered nanoparticles, *Environmental Science & Policy*, 103 (2020) 85–98.
- [21] Saravanan A., Kumar P.S., Karishma S., Vo D.-V.N., Jeevanantham S., Yaashikaa P.R., George C.S., A review on biosynthesis of metal nanoparticles and its environmental applications, *Chemosphere*, 264 (2021) 128580.
- [22] Kirubakaran D., Wahid J.B.A., Karmegam N., Jeevika R., Sellapillai L., Rajkumar M., SenthilKumar K.J., A Comprehensive Review on the Green Synthesis of Nanoparticles: Advancements in Biomedical and Environmental Applications, *Biomedical Materials & Devices*, (2025) 1-26.
- [23] Wei F., Zhao X., Li C., Han X., A novel strategy for water disinfection with a AgNPs/gelatin sponge filter, *Environ Sci Pollut Res*, 25 (2018) 19480–19487.
- [24] Queirós C.S.G.P., Cardoso S., Lourenço A., Ferreira J., Miranda I., Lourenço M.J.V., Pereira H., Characterization of walnut, almond, and pine nut shells regarding chemical composition and extract composition, *Biomass Conv. Bioref.*, 10 (2020) 175–188.
- [25] Sahin F., Celik N., Ceylan A., Ruzi M., Onses M.S., One-step Green Fabrication of Antimicrobial Surfaces via In Situ Growth of Copper Oxide Nanoparticles, *ACS Omega*, 7 (2022) 26504–26513.
- [26] Khan M.S.J., Kamal T., Ali F., Asiri A.M., Khan S.B., Chitosan-coated polyurethane sponge supported metal nanoparticles for catalytic reduction of organic pollutants, *International Journal of Biological Macromolecules*, 132 (2019) 772–783.
- [27] Sahin F., Celik N., Camdal A., Sakir M., Ceylan A., Ruzi M., Onses M.S., Machine Learning-Assisted Pesticide Detection on a Flexible Surface-Enhanced Raman Scattering Substrate Prepared by Silver Nanoparticles, *ACS Appl. Nano Mater.*, 5 (2022) 13112–13122.
- [28] Elemike E.E., Onwudiwe D.C., Fayemi O.E., Botha T.L., Green synthesis and electrochemistry of Ag, Au, and Ag–Au bimetallic nanoparticles using golden rod (*Solidago canadensis*) leaf extract, *Appl. Phys.*, A 125 (2019) 42.
- [29] Meldrum F.C., O'Shaughnessy C., Crystallization in Confinement, *Advanced Materials*, 32 (2020) 2001068.
- [30] Makvandi P., Wang C., Zare E.N., Borzacchiello A., Niu L., Tay F.R., Metal-Based Nanomaterials in Biomedical Applications: Antimicrobial Activity and Cytotoxicity Aspects, *Advanced Functional Materials*, 30 (2020) 1910021.
- [31] Cheng D., Zhang Y., Liu Y., Bai X., Ran J., Bi S., Deng Z., Tang X., Wu J., Cai G., Wang X., Mussel-inspired synthesis of filter cotton-based AgNPs for oil/water separation, antibacterial and catalytic application, *Materials Today Communications*, 25 (2020) 101467.
- [32] ISO 20743:2021, ISO (n.d.). <https://www.iso.org/standard/79819.html> (accessed March 8, 2025).
- [33] Vaiwala R., Sharma P., Ganapathy Ayappa K., Differentiating interactions of antimicrobials with Gram-negative and Gram-positive bacterial cell walls using molecular dynamics simulations, *Biointerphases*, 17 (2022) 061008.
- [34] Wang M., Li Z., Zhang Y., Li Y., Li N., Huang D., Xu B., Interaction with teichoic acids contributes to highly effective antibacterial activity of graphene oxide on Gram-positive bacteria, *Journal of Hazardous Materials*, 412 (2021) 125333.
- [35] Modi S.K., Gaur S., Sengupta M., Singh M.S., Mechanistic insights into nanoparticle surface-bacterial membrane interactions in overcoming antibiotic resistance, *Front. Microbiol.*, 14 (2023) 1135579.
- [36] Mikhailova E.O., Green Silver Nanoparticles: An Antibacterial Mechanism, *Antibiotics*, 14 (2025) 5.
- [37] Duman H., Eker F., Akdaşçı E., Witkowska A.M., Bechelany M., Karav S., Silver Nanoparticles: A Comprehensive Review of Synthesis Methods and Chemical and Physical Properties, *Nanomaterials*, 14 (2024) 1527.
- [38] Yu Y., Zhou Z., Huang G., Cheng H., Han L., Zhao S., Chen Y., Meng F., Purifying water with silver nanoparticles (AgNPs)-incorporated membranes: Recent advancements and critical challenges, *Water Research*, 222 (2022) 118901.
- [39] Sukhorukova I.V., Sheveyko A.N., Shvindina N.V., Denisenko E.A., Ignatov S.G., Shtansky D.V., Approaches for Controlled Ag<sup>+</sup> Ion Release: Influence of Surface Topography, Roughness, and Bactericide Content, *ACS Appl. Mater. Interfaces*, 9 (2017) 4259–4271.
- [40] Saud A., Gupta S., Allal A., Preud'homme H., Shomar B., Zaidi S.J., Progress in the Sustainable Development of Biobased (Nano)materials for Application in Water Treatment Technologies, *ACS Omega*, 9 (2024) 29088–29113.



## Potential Application of Al Doped Carbon Nanotubes for Tretinoin: a Theoretical Study

Fatma Genç <sup>1,a,\*</sup>, Serap Senturk Dalgic <sup>2,b</sup>, Fatma Kandemirli <sup>3,c</sup>

<sup>1</sup> Department of Pharmaceutical Chemistry, Faculty of Pharmacy, Istanbul YeniYuzuil University, Istanbul, Türkiye

<sup>2</sup> Department of Physics, Atomic and Molecular Physics, Faculty of Science, Trakya University, Edirne-Türkiye

<sup>3</sup> Department of Biomedical Engineering, Faculty of Engineering & Architecture, Kastamonu University, Kastamonu, Türkiye

\*Corresponding author

### Research Article

#### History

Received: 28/02/2025

Accepted: 17/04/2025



This article is licensed under a Creative Commons Attribution-NonCommercial 4.0 International License (CC BY-NC 4.0)

### ABSTRACT

In this research, a Density Functional Theory (DFT) calculation was performed to study the interaction of Tretinoin drug (TRE) known as a valuable medication in treating mild, moderate, and severe acne that can be used topically or systemically into Al-doped carbon nanotube (Al-CNT) with the use of M062X/6-31G(d) level of theory in the gas, n-octanol and water environment. The Quantum Theory of Atoms in Molecules (QTAIM) study was performed for complexes in gas, n-octanol and water environments. The contributions of atomic orbitals to the Highest Occupied Molecular Orbital (HOMO) and Lowest Unoccupied Molecular Orbital (LUMO) for TRE and its complex with Al-CNT in gas, n-octanol and water environment were found using the multifunctional wavefunction analyzer program (Multiwfn). Surface analysis, global minimum and global maximum of TRE and its complexity in different environments were performed. The adsorption, interaction, and deformation energies of TRE drug on Al-CNT have been calculated, along with the changes in the enthalpy and Gibbs-free energy in different environments. Calculations indicate that Al-CNT is a promising device for drug carriers for TRE drugs due to the more negative adsorption energies. The Gibbs free energy for adsorption of TRE on Al-CNTs is also more favorable in water.

**Keywords:** Quantum theory of atoms in molecules (QTAIM), Quantum theory, Density functional theory (DFT), Al doped carbon nanotube, Integral equation formalism PCM (IEFPCM).

<sup>a</sup> [ftmgenc@yahoo.com](mailto:ftmgenc@yahoo.com)

<sup>b</sup> <https://orcid.org/0000-0002-5304-5347>

<sup>c</sup> [serapd@trakya.edu.tr](mailto:serapd@trakya.edu.tr)

<sup>d</sup> <https://orcid.org/0000-0003-2541-9214>

<sup>e</sup> [fatma\\_kandemirli@yahoo.com](mailto:fatma_kandemirli@yahoo.com)

<sup>f</sup> <https://orcid.org/0000-0001-6097-2184>

## Introduction

Acne, also known as Acne Vulgaris, is a chronic and persistent skin inflammation of hairy sebaceous follicles that affects people worldwide. Acne is estimated to affect 9.4 % of the global population and ranks eighth among skin diseases [1]. TRE is a generic name for a medication derivative of vitamin A (retinol), also commonly known as all-trans retinoic acid (ATRA). TRE can be given systemically or topically for various indications [2]. Historically used as a comedolytic agent to treat mild to moderate acne, TRE can stimulate the growth of new cells, unclog pores, and support the normal flow of sebum when used both as a standalone treatment and in combination with antibacterials [3].

Nano emulsions and colloidal nano-sized particles increase the therapeutic efficacy of TRE and minimize side effects. The number of acne lesions and the size and intensity of porphyrin production were significantly reduced after topical application of TRE-loaded Nano emulsions in a pilot clinical study of nanoparticles developed in the form of a stable oil-in-water emulsion with a particle size of approximately 150 nm and containing circular and separated particles [4].

TRE is an important component of topical treatments because it causes the loss of comedones and eliminates the lesions they form. TRE also stimulates collagen

formation, aggregation of sebaceous glands and control of cell proliferation and differentiation, although it has typical side effects such as skin irritation, burning and erythema [5]. Recently, new drug delivery systems such as solid Lipid Nanoparticles (SLNs) and Nanostructured Lipid Carriers (NLCs) have been designed to increase the therapeutic efficacy of TRE [6-8].

They studied the interaction of a nanotube with an anticancer agent named TRE in methanol, ethanol, and water using quantum mechanics and semi-empirical methods and revealed that these composites are more stable in water than in the other solvents [9]. The main objective of developing Nanocarrier drug delivery systems using cylindrical molecules made of carbon atoms such as CNTs is to increase the therapeutic effect or reduce the toxicity of therapeutically active materials [10].

Features such as efficient and augmented tumour targeting, thanks to the improved permeability and retention effect of CNTs, are among the advantages of using a CNT-supported drug delivery system [11].

Al doping increases the surface reactivity of CNTs, allowing stronger interactions and better adsorption of drug molecules. The presence of Al atoms increases loading efficiency by creating active sites that enable covalent and non-covalent binding of a wide range of drug

molecules. To our knowledge, no computational studies have included an analysis of TRE and its complexes with Al-CNT or the solvent effects for the TRE and Al-CNT/TRE complex.

## Materials and Methods

### Computational methods

The molecular geometries of TRE and its complex with Al-CNT ( $\text{AlC}_{35}\text{H}_{12}$ , composed of one aluminum, 35 carbon, and 12 hydrogen atoms) were optimized in a vacuum, n-octanol, and water environment at the M062X/6-31G(d) level of theory [12]. The M062X/6-31G(d) method was selected as the main level of theory because recent works [13-16] indicate that the M062X level in DFT calculations successfully describes intermolecular interactions by comparison with other traditional functionals. The M062X model is due to the long-range corrected energy, which can successfully investigate drug adsorption [13-16]. The M062X function/6-31G(d) method has been provide more

reliable results for recent drug delivery applications by describing non-covalent and weak interactions [17]. The obtained geometries of isolated molecules were subsequently optimized in the presence of gas, n-octanol and water environment, using the same level and Integral Equation Formalism Polarizable Continuum Models (IEFPCM) solvation model [18].

## Results and Discussion

### Molecular Geometry, Molecular Electrostatic Potentials (ESP), HOMO-LUMO and Surface Analysis

The optimized form with atomic number of TRE and Al-CNT and HOMO, LUMO and electrostatic potential (ESP) shape of TRE calculated at M062X level with 6-31G(d) basis set with the generated via Gauss view 5.0 [19] for gas environment are represented in Fig.1. Besides the percentage composition of atoms to HOMO and LUMO for TRE are given in Table 1 in gas, water and n-octanol environment.

Table 1. Contribution of atoms orbitals to HOMO and LUMO for TRE in gas, water and n-octanol environment

Atoms	Gas	Water	n-octanol	Atoms	Gas	Water	n-octanol
HOMO (eV)				LUMO (eV)			
C6	4.76	5.59	5.47	O2	4.74	4.99	5.02
C8	9.04	10.14	9.96	C8	2.44	2.42	2.45
C11	14.18	13.91	13.97	C11	10.07	9.62	9.57
C13	7.40	8.12	8.02	C13	2.82	2.45	2.41
C14	11.31	10.40	10.53	C14	12.74	12.58	12.55
C16	14.61	15.00	14.96	C16	5.86	5.06	4.96
C17	5.46	4.58	4.69	C17	13.96	14.46	14.50
C18	13.90	13.68	13.72	C18	11.47	10.49	10.34
C21	9.96	9.17	9.27	C19	11.44	12.67	12.82
				C21	13.46	13.18	13.12
				C22	6.09	6.99	7.11

HOMO of the TRE consist of mainly C6, C8, C11, C13, C14, C16, C17, C18, C21 atoms of TRE for gas, water and n-octanol form. The contributios of these atoms as a percentage are 4.76, 9.04, 14.18, 7.40, 11.31, 14.61, 5.46, 13.90, 9.96 in gas environment. The contributios of these atoms change due to the media used. As seen in Table 1. LUMO of the TRE consist of mainly O2, C8, C11, C13, C14, C16, C17, C18, C19, C21 and C22 atoms of TRE for gas, water and n-octanol form. The contributios of these atoms as a percentage are 4.74, 2.44, 10.07, 2.82, 12.74, 5.86, 13.96, 11.47, 11.44, 13.46, 6.09. The contributios of these atoms changes due to the media used as seen in Table 1.

The theoretical basis of the molecular electrostatic potential (ESP), which has been widely used for predicting nucleophilic and electrophilic sites and for the mode of molecular recognition, is that molecules always approach each other in a complementary manner. ESP on TRE van der Waals (vdW) surface for the gas environment is given in Fig.1. The molecular structure of TRE and surface extrema, which pink and green spheres correspond to minima and maxima, respectively, are given in Figure 2.

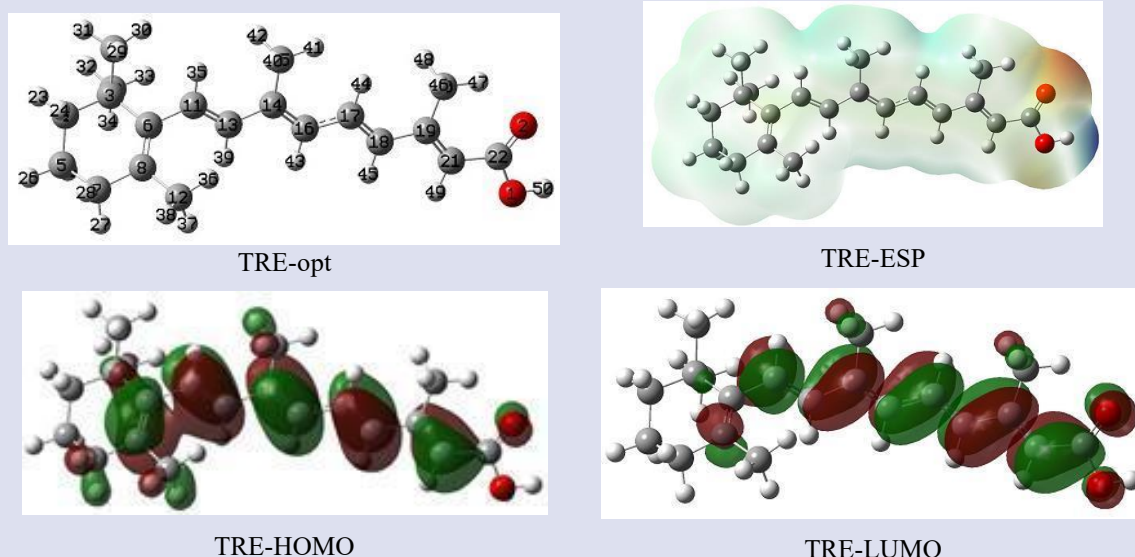


Figure 1. HOMO, LUMO and ESP shape of TRE and optimized form of TRE

The number of surface maxima and minima for TRE in a gas environment is 24 and 20. A minimum of 20 (-34.02 kcal/mol) of TRE is the global minimum on the surface for the gas environment (Figure 2). This large negative value is due to the lone pair of oxygen in the carbonyl group for gas, n-octanol and water environments. Maximum energy for gas, n-octanol and water environment 47.79, 50.66 and 51.13 kcal/mol, respectively (Table 2). The global maximum arises from a hydroxyl group's positively charged H atom.

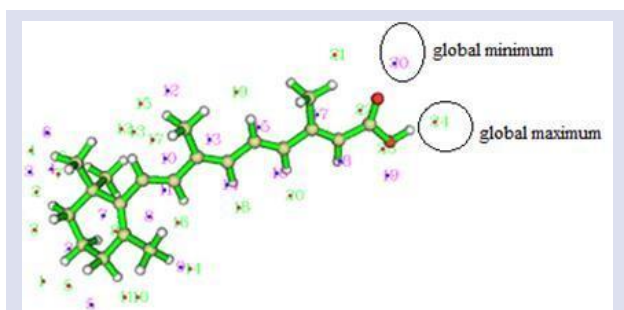


Figure 2. Molecular structure and surface extrema for TRE in gas environment (pink and green spheres correspond to maxima and minima)

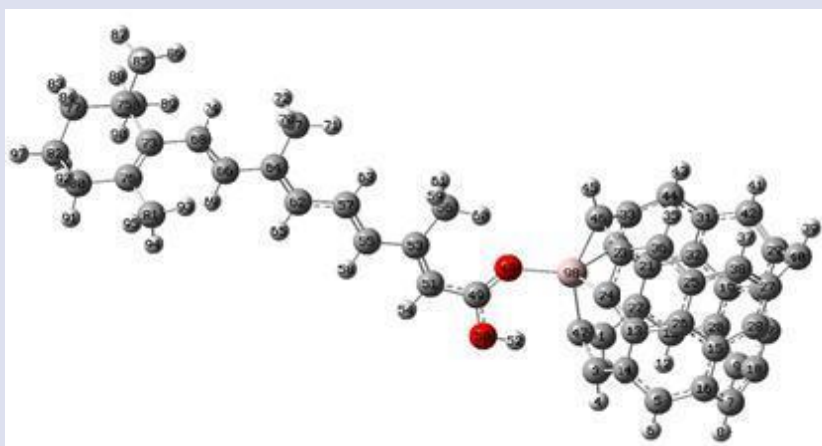
Summary of surface analysis of TRE global minimum (Gmin) and global maximum (Gmax) energy values are given in Table 2 with the surface maxima and minima for gas, n-octanol and water environment. Surface analysis was evaluated according to Volume (V) in Bohr<sup>3</sup> unit, Overall surface area (OSA), Positive surface area (PSA), Negative surface area (NSA) in Bohr<sup>2</sup> unit, Overall average value (OAV), Positive average value (PAV) Negative average value (NAV) in kcal/mol unit, Overall variance (OV), Positive variance (PV), Negative variance (NV) in (kcal/mol)<sup>2</sup> unit, Balance of charges (BC) in mui unit, Product of and Miu (PSM) in (kcal/mol)<sup>2</sup> unit, Internal charge separation (ICS) in kcal/mol unit.

Table 2. Summary of surface analysis of TRE

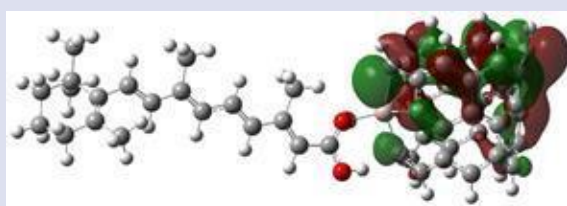
Properties	Gas	n-octanol	Water
V	2852.57	2848.67	2848.00
OSA	1366.40	1364.96	1364.65
PSA	881.93	881.45	880.95
NSA	484.47	483.51	483.71
OAV	1.23	1.28	1.28
PAV	6.66	7.50	7.65
NAV	-8.64	-10.05	-10.32
OV	100.52	125.08	129.28
PV	34.93	39.26	40.18
NV	65.59	85.82	89.10
BC	0.23	0.22	0.21
PSM	22.79	26.94	27.69
ICS	7.08	8.09	8.28
Gmin	-34.02	-38.90	-39.67
Gmax	47.79	50.66	51.13

As seen from Table 2, the summarized values change with the change in the environment. The results show that the presence of a solvent lowers the Global minimum value of TRE and increases the Global maximum value of TRE. The order of Gmin according to medium for TRE is gas>n-octanol>water. However, the order of Gmax according to medium for TRE is gas<n-octanol<water.

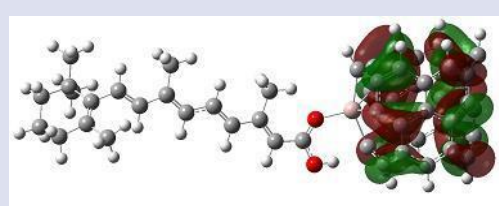
HOMO, LUMO and ESP shape and the optimized form with an atomic number of complex calculated at M062X level with 6-31G(d) basis set with the generated via Gauss view 5.0 for the gas environment are represented in Fig.3. Besides the percentage composition of atoms to HOMO and LUMO for the complex are given in Table 3 in gas, water and n-octanol environment. HOMO and LUMO are given as  $\alpha$ -HOMO,  $\beta$ -HOMO,  $\alpha$ -LUMO, and  $\beta$ -LUMO due to the spin multiplicity of the complex is 2. As seen from the Table 3, the contribution of atoms to  $\alpha$ -HOMO,  $\beta$ -HOMO are different.  $\alpha$ -HOMO consist of C17, C24, C27, C29, C34, C36, C38, C40, C42, C44 and C46 atoms belonging to Al-CNT,  $\beta$ -HOMO consist of C1, C3, C7, C9, C13, C15, C19, C21, C28, C30, C36, C38, C42, C44 atoms belonging to Al-CNT, but the contribution to  $\beta$ -HOMO is made by atoms other than those contributing to the  $\alpha$ -HOMO.



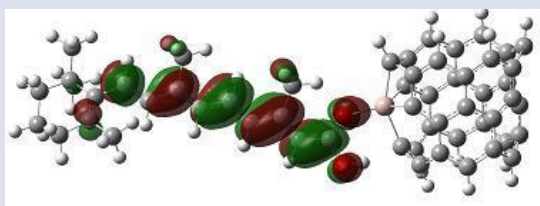
Al-CNT/TRE-opt



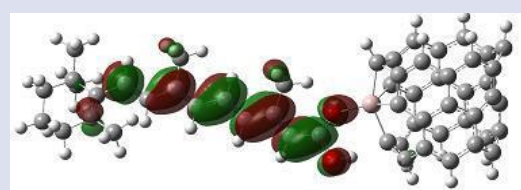
$\alpha$ -HOMO



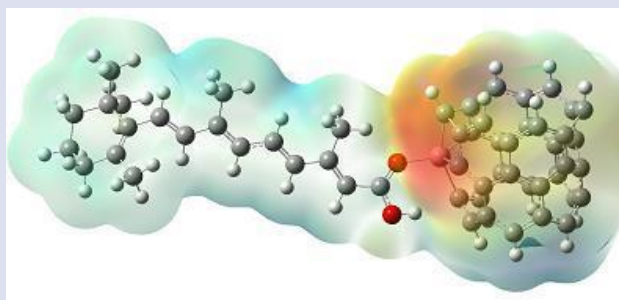
$\beta$ -HOMO



$\alpha$ -LUMO



$\beta$ -LUMO



Al-CNT/TRE-ESP

Figure 3.  $\alpha$ -HOMO,  $\beta$ -HOMO,  $\alpha$ -LUMO, and  $\beta$ -LUMO and ESP shape of complex and optimized form of complex



Table 3. Percentage contribution of atoms orbitals to HOMO and LUMO for Al-CNT/TRE complex in gas, water and n-octanol form

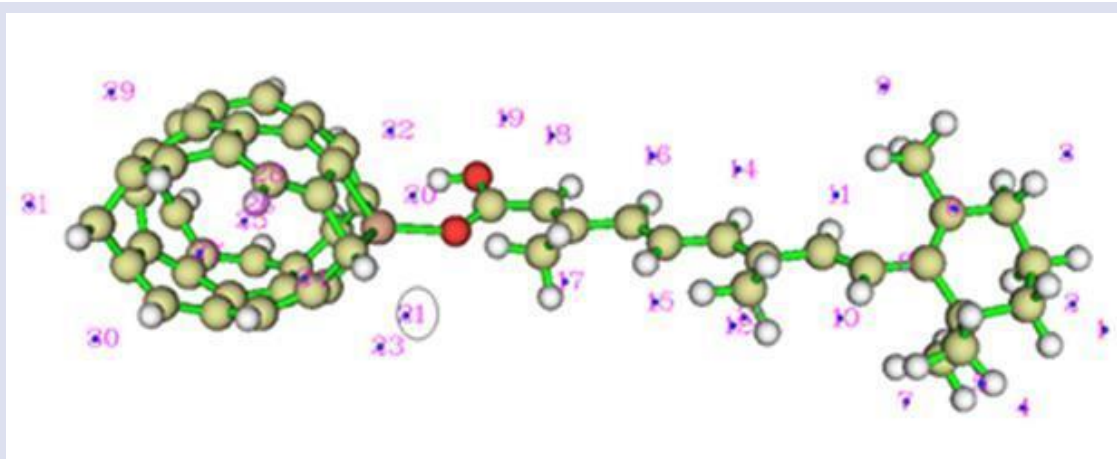
Atoms	Gas	Wat	n-oct	Gas	Wat	n-oct	Gas	Wat	n-oct	Gas	Wat	n-oct
	$\alpha$ -HOMO			$\beta$ -HOMO			$\alpha$ -LUMO			$\beta$ -LUMO		
C17	3.1	3.4	3.3	C1	3.7	3.7	C1	4.1	4.9		9.2	10.4
C24	4.6	4.7	4.7	C3	3.1	3.5	C3	4.1	4.9		8.9	10.1
C27	4.5	4.6	4.6	C7	6.4	6.3	C5	3.8	4.6		8.4	9.5
C29	3.0	3.3	3.2	C9	5.9	6.1	C7	3.0	3.6		6.9	7.8
C34	4.5	4.9	4.8	C13	7.0	6.6	C9	3.2	3.9		7.4	8.2
C36	6.5	7.4	7.2	C15	4.8	4.8	C11	3.9	4.7		8.8	9.8
C38	25.3	27.6	27.1	C19	5.1	4.9						
C40	6.5	7.1	7.0	C21	7.4	6.7	O48	4,7	3.6	3.4	4.7	2.1
C42	4.5	4.6	4.6	C28	4.7	5.0	C49	12,3	11.1	10.2	12.3	6.7
C44	12.8	8.4	9.4	C30	4.7	5.0	O50	3,3	2.8	2.5	3.3	5.6
C46	4.4	3.4	3.6	C36	7.7	7.2	C51	10.0	6.6	6.2	9.9	3.8
Al98	4.39	3.37	3.58	C38	5.4	5.6	C53	16,8	14.1	13.1	16.7	8.5
				C42	5.5	5.6	C55	7,0	4.2	4.0	7.0	2.4
				C44	7.5	7.1	C57	15,4	11.9	11.1	15.4	7.1
							C64	11,5	8.4	7.9	11.4	5.0
							C68	7,7	5.5	5.1	7.7	3.2

A summary of surface analysis of Al-CNT/TRE complex global minimum (Gmin) and global maximum (Gmax) energy value is given in Table 4 with the surface maxima and minima number for gas, n-octanol and water environment. The number of surface minima and maxima for complexes in gas environments is 21 and 33. The complex's minimum 21 (-36.37, -49.59, and -53.34 kcal/mol) is the global minimum on the surface for gas, n-octanol and water environment (Figure 4 and Table 4).

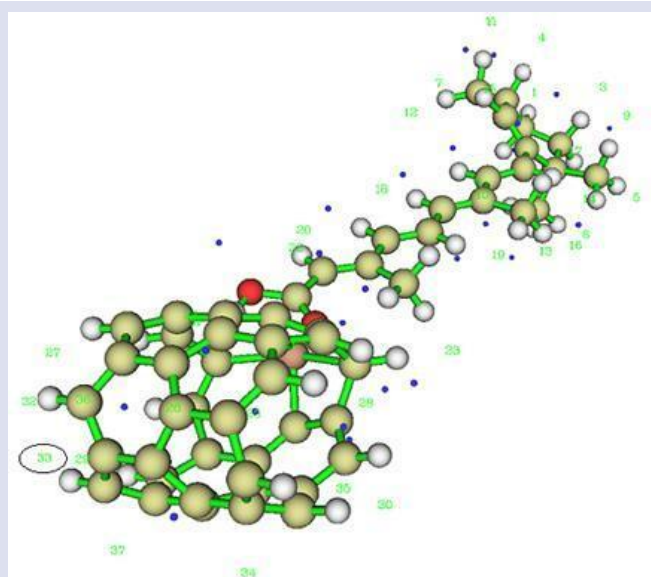
This large negative value is due to the lone pair of oxygen in the carbonyl group for gas, n-octanol and water

environments. Maximum energy for gas, n-octanol and water environment 28.88, 41.76 and 45.45 kcal/mol, respectively. The global maximum arises from the positively charged H atom belonging to Al-CNT.

The results show that the presence of a solvent lowers the Global minimum value of the complex and increases the global maximum value. The order of Gmin, according to the complex, is gas>n-octanol >water. However, The order of Gmax according to medium is gas<n-octanol <water in Table 4.



a-minima



b-maxima

Figure 4. Molecular structure and surface extrema (pink and green spheres correspond to maxima and minima) for complex

Table 4. Summary of surface analysis of Al-CNT/TRE complex

Properties	Gas	n-octanol	Water
V	6038.97	6030.80	6028.96
OSA	2400.99	2401.49	2400.81
PSA	1432.51	1420.81	1413.62
NSA	968.48	980.69	987.19
OAV	0.42	-0.06	-0.23
PAV	9.79	11.96	12.48
NAV	-13.44	-17.49	-18.45
OV	130.73	261.31	305.62
PV	43.01	87.64	104.55
NV	87.72	173.68	201.08
BC	0.22	0.22289574	0.22505901
PS	28.86	58.24	68.78
ICS	11.18	14.23	14.98
Gmin	-36.37	-49.59	-53.34
Gmax	28.88	41.76	45.45

### Stability and Energetics

Adsorption energy resulting from the interaction of TRE and Al-CNT in the gas, n-octanol, and water environments is -40.70, -40.36, and -40.65 kcal/mol, and

negative adsorption energy indicates that TRE / Al-CNT systems are stable in these environments (Table 5). In addition to the bond lengths and angles, the electronic properties of TRE changed in all three environments with the interaction of the TRE molecule with the Al-CNT.

The Fermi energy, known as the midpoint of the HOMO–LUMO energy gap at a temperature equal to 0 K, is calculated, and The fermi energy of Al-CNT in gas, n-octanol and water environment found as -4.79, -4.87, -4.91 eV.  $E_{HOMO}$  of the drug in gas, n-octanol and water environment are -6.570, -6.569, and -6.573 eV. It is likely that electrons are transferred from the TRE drug to the Al-CNT because the Fermi level of the Al-CNT is higher (less negative) than the HOMO energy of the TRE drug. The energy difference between the Fermi level of Al-CNT and the HOMO of the drug acts as the driving force for charge transfer. The driving force increases with the increase of the dielectric constant of the media. TRE is a hydrophobic drug. Since hydrophobic drug molecules try to escape from the aqueous environment in water, they adsorb more easily on CNTs and in n-octanol, hydrophobic interactions with the solvent reduce adsorption on CNTs, so the adsorption energy calculated in the n-octanol environment is lower than the adsorption energy calculated in the water environment. As seen from Table 5, Gibbs free energy in adsorption is negative, indicating a spontaneous process in gas, n-octanol and water environment. The Gibbs free energy for adsorption of TRE on Al-CNTs is more favourable in water than in n-octanol due to the hydrophobic nature of the drug.

Table 5. Adsorption, interaction and deformation energies in terms of Sum of electronic and zero-point Energies, Sum of electronic and thermal Enthalpies, Sum of electronic and thermal Free Energies in Kcal/mol unit for the formation of Al-CNT / TRE complex in gas, water and n-octanol environment, charged values and recovery time ( $\tau$ ) in sec.

Environment		$\Delta E$	$\Delta H$	$\Delta G$	Charge transfer TRE $\rightarrow$ Al-CNT	$\tau(sec)$
Gas	Eads	-40.70	-40.55	-27.77	0.205888	2.13x10 <sup>13</sup>
	Eads*	-27.31*	-32.61*	-21.20*	0.2113*	1.75x10 <sup>4</sup>
	Eint	-37.96	-36.99	-26.16		
n-octanol	Edef	-2.74	-3.57	-1.61		
	Eads	-40.36	-40.25	-27.06	0.23192	1.203x10 <sup>13</sup>
	Eint	-37.31	-36.37	-25.80		
	Edef	-3.05	-3.87	-1.26		
Water	Eads	-40.65	-40.47	-27.65	0.237163	1.961x10 <sup>13</sup>
	Eint	-37.61	-36.62	-26.38		
	Edef	-3.03	-3.84	-1.27		

\*Those values calculated for BMSF-BENZ drug adsorption O<sub>35</sub>/Al-CNT as given in Ref [16].

The adsorption process for TRE drug/Al-CNT complex is in chemisorption nature with higher adsorption energy value in the gas phase of -40.70 kcal/mol (-1.76492 eV) than 1 eV as given in Table 5. Thus, it indicates that the strong interactions between O atom (in TRE) and Al (in CNT) with considerable negative adsorption energy is considered to occur and compared with those obtained from BMSF-BENZ drug/Al-CNT for O<sub>35</sub>/Al-CNT as -1.184 eV [16].

The more negative the adsorption energy, representing a higher stable system. For drug delivery sensor devices, the adsorption process is expected to negatively value adsorption energy, thus the adsorbent must have a strong interaction with the drug. We have found that O/Al-CNT configuration have more negative adsorption energy than others for both drug. Thus Al-CNT can be used as a drug carrier device [16] because of the high recovery time values which was obtained in vacuum UV light conditions with frequency  $3 \times 10^{16} \text{ s}^{-1}$  at room temperature in the gas phase have given in Table 5 by

$$\tau = \nu^{-1} \exp\left(\frac{-E_{ads}}{kT}\right) \quad (1)$$

Where temperature and the attempt frequency are defined by T in K and  $\nu$ , respectively. K is Boltzman constant. The desorption time values for TRE(O)/Al-CNT in gas, n-octanol and water are  $2.13 \times 10^{13}$ ,  $1.203 \times 10^{13}$  and  $1.961 \times 10^{13}$  sec, respectively. Thus, it can be extended as drug delivery system with reasonable recovery times.

### Mulliken Charge Analysis

Geometric parameters such as bond length are critical in interpreting drug interactions with nanotubes in drug delivery systems. Table 6 gives some bond lengths and Mulliken charges of free TRE and its complex with Al-CNT for the gas, n-octanol, and water environments. According to the results, some bond lengths of the TRE drug change after interaction with Al-CNT. The bond lengths of C18-C19, C19-C20, C19-C21, C21-H49, C21-C22, C22-O1, O1-H50, and C22-O2 in the molecule TRE are 1.46099 Å, 1.50451 Å, 1.35188 Å, 1.08582 Å, 1.47317 Å, 1.35368 Å, 0.97242 Å, and 1.21193 Å in gas environment and after the interaction Al-CNT with TRE drug change to 1.45620 Å, 1.50510 Å, 1.36067 Å, 1.08500 Å, 1.44729 Å, 1.31498 Å, 0.98973 Å, 1.24848 Å, 1.90598 Å respectively (Table 6).

Table 6. Some Bond lengths and Mulliken charges for TRE and its complex with Al-CNT

TRE				Al-CNT / TRE complex			
	Gas	n-octanol	Water		Gas	n-octanol	Water
Atoms	Bond-Length (Å)			Atoms	Bond-Length (Å)		
C18-C19	1.46099	1.46062	1.46057	C55-C53	1.45620	1.45396	1.45350
C19-C20	1.50451	1.50432	1.50433	C53-C56	1.50510	1.50395	1.50385
C19-C21	1.35188	1.35366	1.35397	C53-C51	1.36067	1.36359	1.36400
C21-H49	1.08582	1.08579	1.08579	C51-H54	1.08500	1.08482	1.08481
C21-C22	1.47317	1.47130	1.47106	C51-C49	1.44729	1.44326	1.44265
C22-O1	1.35368	1.35068	1.35021	C49-O50	1.31498	1.31511	1.31465
O1-H50	0.97242	0.97356	0.97374	O50-H52	0.98973	0.98838	0.98800
C22-O2	1.21193	1.21540	1.21592	C49-O48	1.24848	1.25352	1.25494
				O48-Al98	1.90598	1.89636	1.89584
Mulliken charges (e)				Mulliken charges (e)			
O1	-0.61632	-0.62433	-0.62535	O50	-0.60539	-0.60742	-0.606314
O2	-0.50047	-0.52982	-0.53432	O48	-0.55411	-0.57264	-0.576618
C18	-0.19216	-0.2086	-0.21167	C55	-0.19901	-0.21427	-0.216746
C19	0.174503	0.169024	0.167682	C53	0.180032	0.182693	0.181782
C20	-0.57373	-0.57551	-0.57581	C57	-0.13363	-0.1416	-0.14343
C21	-0.29252	-0.30424	-0.30625	C51	-0.29161	-0.30532	-0.30647
C22	0.589938	0.595185	0.596024	C49	0.671515	0.683415	0.684315
H49	0.176347	0.18552	0.187164	H54	0.1891	0.203317	0.20644
H50	0.430826	0.448969	0.451763	H52	0.472336	0.478688	0.481551
				Al	0.478181	0.468809	0.457716

The bond length of C18-C19, C19-C20, C21-H49, C21-C22, C22-O1 and C22-O2 of molecule TRE in gas environment decreased in n-octanol and water environment, whereas C19-C21, O1-H50 bond length increased. The Mulliken charge of O1, O2, C18, C20, C21, C22 of TRE in gas environment increased in n-octanol and water environment as a negative and H49 and H50 atoms of the TRE increased as a positive. Mulliken charges of these atoms have also changed in the interaction with Al-CNT.

The negative charge on the O1, C20, and C21 atoms in Al-CNT TRE is smaller than that of the bond length, which was 1.21193 in free TRE and increased to 1.24848 in the Al-CNT / TRE complex. This increase is due to the interaction between TRE and the Al-CNT / TRE complex. Free TRE, however, on the O2, C18 atoms in Al-CNT/TRE is larger than that of free TRE. Since aluminium is an electropositive element with lower electronegativity than

carbon and oxygen, in Al-CNT, the Al atom offers electron deficient sites that can interact with the oxygen atom of the C=O group and due to the interaction, charge transfer from the carbonyl oxygen to the Al-CNT decreases the electron density around the oxygen, and this means at the same time carbon becomes more electron-deficient. Therefore, the bond between the attached carbonyl carbon groups can gain more electron density, leading to the shortening and strengthening of the C22-O1 and C22-C21 bonds. The bond lengths of C22-O1 and C22-C21 bonds in free TRE are 1.35368 and 1.47317, while they are 1.31498 and 1.44729 in Al-CNT.



## Topology Analysis: Quantum Theory of Atoms in Molecules (QTAIM)

The nature of interactions and bonding characteristics between TRE and Al-CNT have been investigated using the QTAIM [20] method, which was employed with the MULTIWFN program [21]. They are obtained in terms of electron densities at bond critical points (BCPs) between

two neighbouring atoms [15]. Thus, the topology parameters of QTAIM theory, which are the Lagrangian kinetic energy (GBCP), electron density ( $\rho_{BCP}$ ), energy density (HBCP), potential energy density (VBCP), Laplacian ( $\nabla^2\rho_{BCP}$ ),  $|V_{BCP}|/G_{BCP}$  values of complex in gas, n-octanol, and water environments, are given in Table 7 (they are given in Hartrees).

Table 7. Potential Energy Density, Total Energy Density, Lagrangian Kinetic Energy, Electron Density, Laplacian of  $\nabla^2\rho_{BCP}$  of Al-CNT / TRE complex (in a.u. units)

Structure	Gas	n-octanol	Water
$\rho_{BCP}$ (a.u.)	0.05426	0.05554	0.05572
GBCP (a.u.)	0.08954	0.09286	0.09317
VBCP	-0.08091	-0.08380	-0.08415
HBCP	0.00863	0.00906	0.00902
$\nabla^2\rho_{BCP}$	0.39267	0.40769	0.40874
$ V_{BCP} /G_{BCP}$	0.90362	0.90243	0.90319

In QTAIM analysis for the studied complex, the electron density of the bond formed by the interaction of TRE and Al-CNT was analyzed to understand this interaction. In this interaction, the electron density in BCP was found to be 0.05426, which means that a moderate electron density can be suitable for controlled release and moderate stability of the drug in the system.

The Lagrangian kinetic energy of the drug complex plays an important role in drug delivery as it affects the system's stability, transport and release dynamics. Table 7 shows the (GBCP)Lagrangian kinetic energy of the Al-CNT/TRE complex at BCP is 0.08954 a.u. (56.19 kcal/mol) in the gas environment and those in the n-octanol and water environment are 0.09286 and 0.09317, indicating that the Lagrangian kinetic energy increases with the increase of the dielectric constant of the solvent.

The energy density values at the BCP, including Potential Energy Density  $V(r)$  and Total Energy Density  $H(r)$ , provide insight into the nature and strength of interactions. A negative VBCP value indicates that the interaction is stabilizing and attractive. VBCP -0.08091 means moderate binding strength, likely due to  $\pi$ - $\pi$  stacking (Table 7).

HBCP>0 and a negative VBCP value show weak interactions, meaning the drug will be easily released from the carrier. This means that it is beneficial for rapid drug delivery, where you need the drug to be released quickly upon reaching the target.  $\rho_{BCP}$ , GBCP, VBCP, and HBCP values increase with the increase of the dielectric coefficient of the solvent.

In QTAIM, BCPs also separate attractive (negative  $\nabla^2\rho$ ) and repulsive (positive  $\nabla^2\rho$ ) interactions that are critical for drug binding. The Laplacian reveals regions of electron density accumulation and depletion and helps classify

hydrogen bonding, van der Waals interactions, and charge transfer interactions. Positive ( $\nabla^2\rho > 0$ )  $\rightarrow$  Electron density is locally depleted, e.g., closed-shell interactions like hydrogen bonds, van der Waals forces, ionic interaction  $\nabla^2\rho_{BCP}$  values of the complex in gas, n-octanol, and water media are 0.39267, 0.40769, 0.40874 means that suggests a closed-shell interaction (Table 7).

## Conclusion

The interaction of TRE with Al-doped carbon nanotubes (Al-CNT) has been thoroughly analyzed at the level of M062X theory and 6-31G(d) basis set in gas, n-octanol and water environments. In this paper, our investigations show that the polarity of solvent has effect in the percentage composition of atoms to HOMO and LUMO, charge transfer interaction energy for TRE and its complex. The adsorption energy found in the n-octanol environment is lower than the adsorption energy in the water environment. The complex can be suitable for controlled release and moderate stability of the drug in the system. Gibbs free energy values indicate that the process is a spontaneous process in gas, n-octanol and water environment. The Gibbs free energy for adsorption of TRE on Al-CNTs is more favorable in water. The results indicate that Al-CNT serves as an effective carrier for TRE, with stable interactions confirmed by adsorption energy calculations and charge transfer analysis. The study provides valuable insights into the molecular-level interactions between the drug and nanotubes, demonstrating how environmental factors, such as solvent type, influence the stability and electronic properties of the complex.

## Conflicts of interest

The authors declare that there is no conflict of interest

## References

- [1] Hazarika N., Acne Vulgaris: New Evidence in Pathogenesis and Future Modalities of Treatment, *Journal of dermatological treatment*, 32(3) (2021) 277-285.
- [2] Yoham A.L., Casadesus D., Tretinoin, In *StatPearls [Internet]*, StatPearls Publishing: Tampa, FL, USA, (2023).
- [3] Schmidt N., Eugene H. G., Tretinoin: a Review of Its Anti-inflammatory Properties in the Treatment of Acne, *The Journal of Clinical and Aesthetic Dermatology*, 4(11) (2011) 22-29.
- [4] Sabouri M., Samadi A., Nasrollahi S.A., Farboud E.S., Mirrahimi B., Hassanzadeh H., Kashani M.N., Dinarvand R., Firooz A., Tretinoin Loaded Nanoemulsion for Acne Vulgaris: Fabrication, Physicochemical and Clinical Efficacy Assessments, *Skin Pharmacology and Physiology*, 31 (6) (2018) 316-323.
- [5] Thielitz A., Abdel-Naser M. B., Fluhr J. W., Zouboulis C. C., Gollnick H., Topical Retinoids in Acne—an Evidence-based Overview, *JDDG: Journal der Deutschen Dermatologischen Gesellschaft*, 6(12) (2008) 1023-1031.
- [6] Amidouche D., Montassier P., Poelman M. C., Duchêne, D., Evaluation by Laser Doppler Velocimetry of The Attenuation of Tretinoin Induced Skin Irritation by  $\beta$ -cyclodextrin Complexation, *International Journal of Pharmaceutics*, 111(2) (1994) 111-116.
- [7] Naseri N., Valizadeh H., Zakeri-Milani P., Solid Lipid Nanoparticles and Nanostructured Lipid Carriers: Structure, Preparation and Application, *Advanced Pharmaceutical Bulletin*, 5(3) (2015) 305.
- [8] Falcocchio S., Ruiz C., Pastor F. J., Saso L., Diaz P., Propionibacterium Acnes GehA Lipase, an Enzyme Involved in Acne Development, can be Successfully Inhibited by Defined Natural Substances, *Journal of Molecular Catalysis B: Enzymatic*, 40 (3-4) (2006) 132-137.
- [9] Ghadamgahi M., Ajloo D., Molecular Dynamic Insight into the Ethanol Effect on Tretinoin Drug Delivery Through Carbon Nanotubes, *Journal of Nanostructure in Chemistry*, 4 (2014) 1-11.
- [10] Chen Q., Wang Q., Liu Y. C., Wu T., Kang Y., Moore J. D., Gubbins K. E., Energetics Investigation on Encapsulation of Protein/Peptide Drugs in Carbon Nanotubes, *The Journal of Chemical Physics*, 131 (1) (2009).
- [11] Bianco A., Kostarelos K., Prato M., Applications of Carbon Nanotubes in Drug Delivery, *Current Opinion in Chemical Biology*, 9 (6) (2005) 674-679.
- [12] Hariharan P. C., Pople J. A., The Influence of Polarization Functions on Molecular Orbital Hydrogenation Energies, *Theoretica Chimica Acta*, 28(3) (1973) 213-222.
- [13] Sayiner H. S., Kandemirli F., Dalgic S. S., Monajjemi M., Mollaamin F., Carbazochrome Carbon Nanotube as Drug Delivery Nanocarrier for Anti-bleeding Drug: Quantum Chemical Study, *Journal of Molecular Modeling*, 28 (1) (2022) 11.
- [14] Al-Sawaff Z. H., Dalgic S. S., Kandemirli F., Monajjemi M., Mollaamin F., DFT Study Adsorption of Hydroxychloroquine for Treatment COVID-19 by SiC Nanotube and Al, Si Doping on Carbon Nanotube Surface: A Drug Delivery Simulation, *Russian Journal of Physical Chemistry A*, 96 (13) (2022) 2953-2966.
- [15] Dalgic S. S., Al-Sawaff Z. H., Dalgic S., Kandemirli, F., A Comparative DFT Study on Al-and Si-doped Single-Wall Carbon Nanotubes (SWCNTs) for Ribavirin Drug Sensing and Detection, *Materials Science in Semiconductor Processing*, 158 (2023) 107360.
- [16] Al-Sawaff Z. H., Dalgic S. S., Kandemirli F., Theoretical study of the adsorption of BMSF-BENZ drug for osteoporosis disease treatment on Al-doped carbon nanotubes (Al-CNT) as a drug vehicle, *European Journal of Chemistry*, 12 (3) (2021) 314-322.
- [17] Dalgic Senturk S, Burucu DK, Dalgic S, Kandemirli F., A comparative DFT study on the interaction of Aldara drug molecule with SiC and Si-carbon nanotubes, *Journal of Applied Physics*, 137 (3) (2025) 135104.
- [18] Tomasi J., Mennucci B., Cammi R., Quantum Mechanical Continuum Solvation Models, *Chemical Reviews*, 105 (8) (2005) 2999-3094.
- [19] Frisch M. J., Trucks G. W., Schlegel H. B., Scuseria G. E. Et al., Gaussian 09, Gaussian Inc., Wallingford, (2013).
- [20] Bader R.F.W., Atoms in molecules, *Accounts of Chemical Research*, 18 (1985) 9–15.
- [21] Lu T., Chen F., Multiwfn: a multifunctional wave function analyser, *Journal of Computational Chemistry*, 33 (2012) 580–592.

## Natural Remedies for Type 2 Diabetes: Evaluation of Phytochemicals with Bioinformatics and Molecular Approaches/ ADME/T Analysis

Adem Necip <sup>1,a,\*</sup>

<sup>1</sup>Department of Pharmacy Services, Vocational School of Health Services, Harran University, Sanliurfa, Türkiye

\*Corresponding author

### Research Article

#### History

Received: 21/02/2025

Accepted: 24/04/2025



This article is licensed under a Creative Commons Attribution-NonCommercial 4.0 International License (CC BY-NC 4.0)

### ABSTRACT

Diabetes mellitus (DM) is a rapidly spreading chronic disease worldwide, affecting more than 10% of the adult population. Type 2 diabetes (T2DM) accounts for the vast majority of DM cases and can lead to serious health complications. While current treatment options such as  $\alpha$ -Glucosidase inhibitors are effective, new alternatives need to be explored due to absorption problems and side effects. In this context, natural compounds have significant potential. The antioxidant, anti-inflammatory and insulin sensitizing effects of phytochemicals offer a promising option in diabetes management. The therapeutic efficacy of phytochemicals can be determined using computational approaches, systems biology and network pharmacology. In this study, the interactions between important diabetes target proteins (1RE1, 5NJK, 5VK1, 5WBL and 6B1E) and phytochemicals (Catechine, 3',4'-Di-O-benzyl-7-O-(2-hydroxyethyl)-3-O-methylquercetin, Retusapurpurin\_A, Sakuranetin and Thevetiaflavone) were analyzed by molecular docking methods. The highest docking score values of -6.710, -6.173, -5.806 and -5.779 kcal/mol were found between 5VK1/catechine, 5NJK/3',4'-Di-O-benzyl-7-O-(2-hydroxyethyl)-3-O-methylquercetin 6B1E/catechine and 5WBL/catechine, respectively. Furthermore, ADME/T calculations were performed to evaluate the pharmacokinetic properties of these compounds. The findings reveal the potential of natural compounds in the treatment of diabetes and aim at additional contributions of natural products to the treatment in the future.

**Keywords:** Diabetes mellitus, Phytochemicals, Molecular docking,  $\alpha$ -Glucosidase inhibitors, ADME/T analysis.

<sup>a</sup>[ademnecip@harran.edu.tr](mailto:ademnecip@harran.edu.tr)

<https://orcid.org/0000-0002-2092-7829>

## Introduction

DM is a leading cause of death, affecting 530 million people worldwide. This corresponds to a prevalence of 10.5% of adults aged 20-79 years who are caught. Diabetes is a rapidly growing chronic disease affecting more than 10% of adults worldwide and more than 90% of patients with diabetes have T2DM. Without effective intervention, the global prevalence of diabetes is projected to skyrocket to 643 million people by 2030 and 783 million by 2045 [1]. Diabetes mellitus (DM) is a chronic metabolic disease associated with insufficient and/or defective insulin production or insulin resistance [2]. It causes hyperglycemia, which is a high level of glucose in the bloodstream, a condition that, if left untreated, leads to severe damage to various organs such as the kidneys, eyes, blood vessels, heart and nerves [3].  $\alpha$ -Glucosidase inhibitor is a class of drugs clinically approved to help regulate the glycemic index in diabetic patients [4]. The enzyme  $\alpha$ -Glucosidase metabolizes disaccharides and oligosaccharides in the gut, resulting in elevated blood glucose levels [5]. Molecules that inhibit  $\alpha$ -glucosidase help improve blood glucose levels in type-2 diabetes patients [6]. Deoxynojirimycin, acarbose, voglibos and miglitol are the main drugs used to inhibit  $\alpha$ -glucosidase to a large extent; however, these molecules have absorption problems and are associated with many side effects such as cramping, diarrhea and colonic gas

production [7]. There is no permanent cure for diabetes, leaving patients dependent on a combination of healthy lifestyle choices and timely medication [8]. In this context, the investigation of natural products as a potential source of antidiabetic drugs holds great promise. Natural compounds have been used for medicinal purposes for thousands of years and offer unique advantages such as easy availability, minimal side effects and compatibility with conventional practices [9].

Recent studies have demonstrated that plant-derived phytochemicals found in fruits, vegetables, and spices offer promising alternatives for diabetes management. These naturally occurring compounds are well recognized for their ability to modulate various biochemical signaling pathways and can be seamlessly integrated into modern therapeutic approaches that target multiple physiological processes with a single drug. Flavonols and steroid saponins, in particular, exhibit antioxidant and anti-inflammatory properties, contribute to glycemic regulation, and enhance insulin sensitivity—key factors in diabetes management. These complex bioactive molecules function through multiple molecular pathways, exerting dual effects in modulating diabetes-related mechanisms [10]. Phytochemicals, particularly those derived from medicinal plants, have demonstrated significant potential in regulating intricate biochemical

networks. Recent research highlights that certain natural compounds, including flavonoids, alkaloids, terpenoids, and saponins, possess antioxidant and anti-inflammatory properties while also enhancing insulin sensitivity. These effects are mediated through direct interactions with protein signaling pathways involved in glucose metabolism. Furthermore, advanced computational techniques such as AI-assisted predictive modeling, systems biology, and network pharmacology facilitate the rapid screening of phytochemicals for their therapeutic potential. The integration of these cutting-edge tools enhances algorithmic performance, enabling a systematic evaluation of phytochemical interactions with key protein targets. This approach aids in the identification and prioritization of small molecules with superior specificity and binding affinity toward crucial drug targets in type 2 diabetes mellitus (T2DM). By merging traditional medicinal plant knowledge with modern diagnostic technologies, a more holistic and sustainable treatment strategy for diabetes can be developed. Such strategies reduce reliance on synthetic drugs, which may cause adverse effects, and contribute to patient-centered, long-term therapeutic solutions.

Propolis is a resinous substance collected by bees from plant sources and has various pharmacological uses thanks to its rich flavonoid and phenolic plant content. These products include plants such as Catechin, Thevetiaflavone and 3',4'-Di-O-benzyl-7-O-(2-hydroxyethyl)-3-O-methylquercetin. It is important to investigate the lives of these plants on diabetes and to maintain the anti-diabetic potential of propolis [11]. A study in rats induced with streptozotocin diabetes showed that catechin treatment lowered blood glucose levels and alleviated complications associated with diabetes. These effects are attributed to the antioxidant properties of catechin [12]. Although specific studies on thevetiaflavone are limited, it is known that the flavonoids contained in propolis generally exhibit anti-diabetic effects. Propolis supplementation has been shown to improve glycemic control and antioxidant status in patients with type 2 diabetes in randomized controlled trials [13]. Quercetin derivatives are known for their strong antioxidant and anti-inflammatory properties. The positive effects of propolis-derived flavonoids on obesity and diabetes have been demonstrated in cellular and animal models [14]. Catechine, Thevetiaflavone, and 3',4'-Di-O-benzyl-7-O-(2-hydroxyethyl)-3-O-methylquercetin were made to better understand the potential therapeutic effects of propolis on diabetes and to elucidate the mechanisms of these compounds. These studies support the role of propolis and its components in diabetes management.

The application of network pharmacology in phytoconstituent research has transformed conventional drug discovery processes, offering a more comprehensive methodology for identifying bioactive compounds. By integrating genetic, proteomic, and metabolomic data, scientists can construct molecular interaction networks that provide insights into protein and RNA interactions

with plant-derived compounds or their respective targets within the human system. This systems biology-driven approach enables a deeper understanding of the mechanisms underlying phytochemical functions and their associated therapeutic benefits. Additionally, computational techniques such as molecular docking and dynamic simulations play a crucial role in predicting the binding affinity and stability of plant-derived compounds with target proteins. These technologies significantly enhance the efficiency of identifying lead drug candidates with the highest therapeutic potential [15].

In this study, we analyzed the interactions between key diabetes-related target proteins and crucial regulators of blood glucose levels, including CASP3 (1RE1), MDM2 (5VK1), AKT1 (5WBL), HSP90AA1 (5NJX), and dipeptidyl peptidase IV (PDB ID: 6B1E), alongside alpha-amylase and alpha-glucosidase, using a reference compound [16]. Additionally, ADME/T (Absorption, Distribution, Metabolism, Excretion, and Toxicity) calculations were performed to assess the pharmacokinetic and metabolic interactions of these molecules in the human body. The findings of this study provide valuable insights for the future development of novel antidiabetic drugs.

## Materials and Methods

### Molecular Docking Calculation

An important method used to identify molecules with high activity against biological materials is docking. The crystal structures of crystal structure of caspase-3 with a nicotinic acid aldehyde inhibitor (PDB ID: 1RE1, Method: X-ray Diffraction, Resolution: 2.50 Å), Human FKBP51 protein in complex with C-terminal peptide of Human HSP 90-alpha (PDB ID: 5NJX, Method: X-ray Diffraction, Resolution: 2.49 Å), Crystal structure of human MDM4 in complex with a 12-mer lysine-cysteine side chain dithiocarbamate stapled peptide inhibitor PMI (PDB ID: 5VK1, Method: X-ray Diffraction, Resolution: 2.69 Å), Crystal structure of the Arabidopsis thaliana Raptor in complex with the TOS peptide of human PRAS40 alpha (PDB ID: 5WBL, Method: X-ray Diffraction, Resolution: 3.35 Å) and The structure of DPP4 in complex with Vildagliptin (PDB ID: 6B1E, Method: X-ray Diffraction, Resolution: 2.69 Å), were retrieved from the PDB database (<http://www.rcsb.org/pdb>). Molecular docking calculations were performed with Schrödinger's Maestro Molecular modeling platform. First, the protein preparation module is used to prepare the protein and then the LigPrep module is used to prepare the molecule. The prepared proteins and molecules are also interacted with each other by Glide ligand docking (Schrödinger Release 2022-4).

### ADME Analysis

ADME analysis of catechin, epicatechin gallate, epigallocatechin gallate, gallic acid, and isoquercitrin was carried out using the Swiss ADME online tool (<http://www.swissadme.ch/>) and Admetlab (<https://admetmesh.scbdd.com/>). The canonical SMILES



representations of these compounds were generated using ChemDraw, followed by an assessment of their physicochemical properties. This evaluation included parameters such as lipophilicity, drug-likeness, pharmacokinetics, topological polar surface area (TPSA), the number of rotatable bonds, and compliance with Lipinski's rule of five [17]. Additionally, ADME/T analysis was conducted to investigate how these molecules interact within human metabolism and to assess their pharmacokinetic and toxicological profiles.

## Result and Discussion

Molecular docking calculations are commonly employed to complement experimental studies and to identify the active sites of molecules. Molecular modeling serves as a crucial tool for examining how molecules interact with proteins, providing insights into binding

mechanisms through docking simulations [18]. This computational approach evaluates the affinity of molecules for specific protein targets, with stronger interactions typically correlating with higher biological activity. Various parameters are generated as a result of docking analyses, each offering unique insights into the molecular properties under investigation [19, 20]. Among these, the docking score is considered the primary determinant of molecular activity, as it reflects the strength and stability of the molecular-protein interaction. We can say that the lower the docking score value, the stronger the connection [21]. The values between Catechine, 3',4'-Di-O-benzyl-7-O-(2-hydroxyethyl)-3-O-methylquercetin, Retusapurpurin\_A, Sakuranetin and Thevetiaflavone with docking score values of 1RE1, 5NJK, 5VK1, 5WBL and 6B1E proteins are given in Table 1.

Tablo 1. Catechine, 3',4'-Di-O-benzyl-7-O-(2-hydroxyethyl)-3-O-methylquercetin, Retusapurpurin\_A, Sakuranetin and Thevetiaflavone with docking score values of 1RE1, 5NJK, 5VK1, 5WBL and 6B1E proteins

	docking score values (kcal/mol)				
	1RE1	5NJK	5VK1	5WBL	6B1E
Catechine	-4.991	-5.352	-6.710	-5.779	-5.806
3',4'-Di-O-benzyl-7-O-(2-hydroxyethyl)-3-O-methylquercetin	-4.160	-6.173	-5.731	-4.993	-5.841
Retusapurpurin_A	-4.419	-5.518	-5.626	-5.578	-4.340
Sakuranetin	-4.360	-5.358	-5.410	-4.849	-5.377
Thevetiaflavone	-4.837	-5.726	-6.095	-5.183	-5.364
Acarbose	-5.855	-6.647	-4.892	-6.593	-6.538

In this study, the binding affinities of various bioactive compounds (Catechine, 3',4'-Di-O-benzyl-7-O-(2-hydroxyethyl)-3-O-methylquercetin, Retusapurpurin\_A, Sakuranetin and Thevetiaflavone) with different protein targets (1RE1, 5NJK, 5VK1, 5WBL and 6B1E proteins) were examined using molecular docking analysis. Docking scores were calculated in terms of binding free energy (kcal/mol), with negative values indicating higher binding affinity. Docking scores express the binding energy (kcal/mol) of ligands to protein; more negative values indicate stronger binding affinity.

When the results of molecular docking analysis against 1RE1 protein are analyzed; Acarbose shows the strongest interaction with a binding energy of -5.855 kcal/mol. It can be said that Acarbose has a high binding affinity and is a suitable positive control for evaluating the activity of other compounds. Although Catechine (-4.991 kcal/mol) and Thevetiaflavone (-4.837 kcal/mol) have higher binding energy (less negative) compared to Acarbose, they show better binding compared to other compounds. This suggests that Catechine in particular may interact strongly with the 1RE1 protein. Retusapurpurin\_A (-4.419 kcal/mol), Sakuranetin (-4.360 kcal/mol) and 3',4'-Di-O-benzyl-7-O-(2-hydroxyethyl)-3-O-methylquercetin (-4.160 kcal/mol) have lower binding affinity values. These compounds show weaker interactions than Catechine and Thevetiaflavone. However, binding scores below -4.0

kcal/mol suggest that these compounds may still show some affinity with 1RE1.

When the results of the molecular docking analysis against the 5NJK protein are analyzed; Acarbose (-6.647 kcal/mol) is the compound with the lowest binding energy, i.e. the molecule that shows the strongest interaction with the 5NJK protein. 3',4'-Di-O-benzyl-7-O-(2-hydroxyethyl)-3-O-methylquercetin (-6.173 kcal/mol) has the highest binding affinity among the other compounds and gives the best result after Acarbose. Although it has a lower affinity compared to Acarbose, it is thought that this compound may show a significant interaction with the 5NJK protein. Thevetiaflavone (-5.726 kcal/mol) has a high binding energy, suggesting that it could be a potentially effective ligand. Retusapurpurin\_A (-5.518 kcal/mol), Sakuranetin (-5.358 kcal/mol) and Catechine (-5.352 kcal/mol) have close binding energies.

When the results of molecular docking analysis against 5VK1 protein are analyzed; Acarbose (-4.892 kcal/mol) is the compound with the weakest binding energy in this study. While it is generally expected to be the strongest binding compound, the compounds tested in this study appear to have higher binding affinity than Acarbose. This result suggests that some of the compounds may have stronger inhibitory potential than Acarbose. Catechine (-6.710 kcal/mol) has the lowest binding energy and shows the highest affinity for the 5VK1 protein. Thevetiaflavone

(-6.095 kcal/mol) also shows strong binding and ranks second. Catechine is the compound showing the strongest binding for the 5VK1 protein and can be considered as the best inhibitor candidate. Thevetiaflavone is the compound with the second highest binding affinity and could be a strong alternative inhibitor. Acarbose has the weakest binding energy, indicating that the tested compounds may be more effective inhibitors for the 5VK1 protein.

When the results of the molecular docking analysis against the 5WBL protein are analyzed; Acarbose (-6.593 kcal/mol) is the compound with the lowest binding energy and the molecule showing the strongest binding. The other compounds tested have higher binding energies and show lower affinities compared to Acarbose. Catechine (-5.779 kcal/mol) is the compound with the lowest binding energy and has the best binding affinity after Acarbose. Retusapurpurin\_A (-5.578 kcal/mol) shows a similarly strong binding. These two compounds show better interaction with the 5WBL protein than the other compounds and can be considered as potential inhibitor candidates.

When the results of the molecular docking analysis against the 6B1E protein are analyzed; Acarbose (-6.538 kcal/mol) is the compound with the lowest binding energy and is the reference point as the compound showing the highest affinity for the 6B1E protein. 3',4'-Di-O-benzyl-7-O-(2-hydroxyethyl)-3-O-methylquercetin (-5.841 kcal/mol) and Catechine (-5.806 kcal/mol) have the best binding affinity among the other compounds. These two compounds, although not as strong as Acarbose, can be considered as potential inhibitor candidates due to their high binding affinity. Sakuranetine (-5.377 kcal/mol) and Thevetiaflavone (-5.364 kcal/mol) have very close binding energies and show moderate binding affinity. Although these two compounds have lower binding energies compared to Acarbose and the strongest binding compounds, they may still have some inhibitory potential.

When the binding energies of molecular docking analyses with five different proteins (1RE1, 5NJK, 5VK1, 5WBL, 6B1E) are evaluated together; Acarbose has the lowest binding energy overall in terms of docking scores and shows the strongest binding with 5NJK (-7.012 kcal/mol) and 5WBL (-6.593 kcal/mol) proteins. It has the weakest binding affinity with the 5VK1 protein (-4.892 kcal/mol), meaning that for this protein the binding strength of other compounds is higher than Acarbose. These results suggest that Acarbose may be a potent inhibitor for 5NJK and 5WBL proteins, but may show lower inhibitory activity for 5VK1. Catechine shows the strongest binding with the 5VK1 protein (-6.710 kcal/mol) and binds much better than Acarbose. We can say that there is a strong binding between Catechine and 6B1E (-5.806 kcal/mol) and 5WBL (-5.779 kcal/mol) proteins. Catechine may be a better inhibitor than Acarbose, especially for the

5VK1 protein. 3',4'-Di-O-benzyl-7-O-(2-hydroxyethyl)-3-O-methylquercetin has the lowest binding energy with 5NJK protein (-6.173 kcal/mol) and can be considered as a strong inhibitor for this protein. 3',4'-Di-O-benzyl-7-O-(2-hydroxyethyl)-3-O-methylquercetin has variable binding affinity depending on the protein type. For the protein 5VK1 (-6.095 kcal/mol), Thevetiaflavone showed a relatively strong binding.

Acarbose has the strongest binding affinity with most proteins. Catechine and Thevetiaflavone have the best binding energy among the natural compounds tested and can be considered as potential inhibitor candidates. However, Catechine has stronger binding affinity for the 5VK1 protein. This suggests that Catechine may be a better inhibitor for this protein than Acarbose. Catechine has better binding affinity than other compounds in general. It has a higher inhibitory potential than Acarbose, especially for the 5VK1 protein and binds well with other proteins. 3',4'-Di-O-benzyl-7-O-(2-hydroxyethyl)-3-O-methylquercetin showed high binding with 5NJK and 6B1E proteins, indicating that it may have inhibitory potential for these proteins. These findings should be supported by biological activity tests and ADMET assays. Especially the biological activity of Catechine and 3',4'-Di-O-benzyl-7-O-(2-hydroxyethyl)-3-O-methylquercetin should be tested experimentally.

Thevetiaflavone interacts with the target protein 1RE1 by forming one hydrogen bonds with the backbone residues Arg341. The hydroxyl (OH) group probably acts as a hydrogen bond donor and interacts with polar amino acids.

The carbonyl (C=O) group acts as a bond acceptor and provides bonds with polar groups in the protein. 3',4'-Di-O-benzyl-7-O-(2-hydroxyethyl)-3-O-methylquercetin interacts with the target protein 5NJK by forming two hydrogen bonds and one Pi bonds with the backbone residues Arg53, Lys113 and Phe162. Catechine interacts with the target protein 5VK1 by forming five hydrogen bonds with the backbone residues Gln58, Gln71, His54. Different OH groups Gln58 and Gln71 made two hydrogen bonds each. Catechine interacts with the target protein 5WBL by forming five hydrogen bonds with the backbone residues Asp352, Arg379, Asn334, Gln333, respectively. 3',4'-Di-O-benzyl-7-O-(2-hydroxyethyl)-3-O-methylquercetin interacts with the target protein 6B1E by forming four hydrogen bonds and one pi bağı with the backbone residues His 740, Asp709, Lys122, Lys 554 and Trp627, respectively. All 2D and 3D interactions are shown in Figures 1 and 2.

The presence of different groups in the catechine, epicatechin gallate, epigallocatechin gallate gallic acid and isoquercitrin may enhance their activity by modifying their physicochemical properties and pharmacokinetic parameters to increase their bioavailability and metabolic stability as well as their binding affinity to receptors.

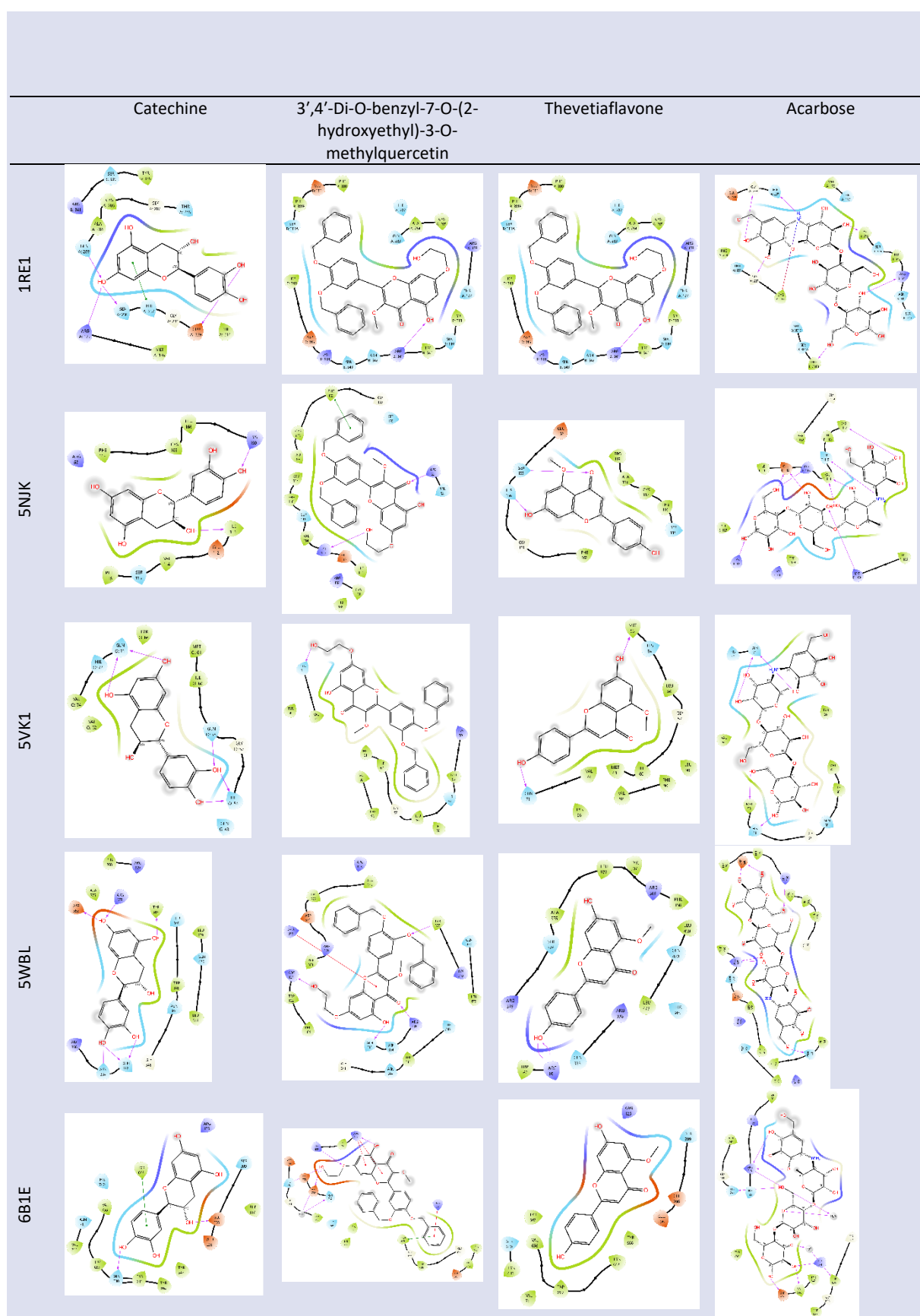


Figure 1. 2D bond interactions of catechine, 3',4'-Di-O-benzyl-7-O-(2-hydroxyethyl)-3-O-methylquercetin, Thevetiaflavone and Acarbose



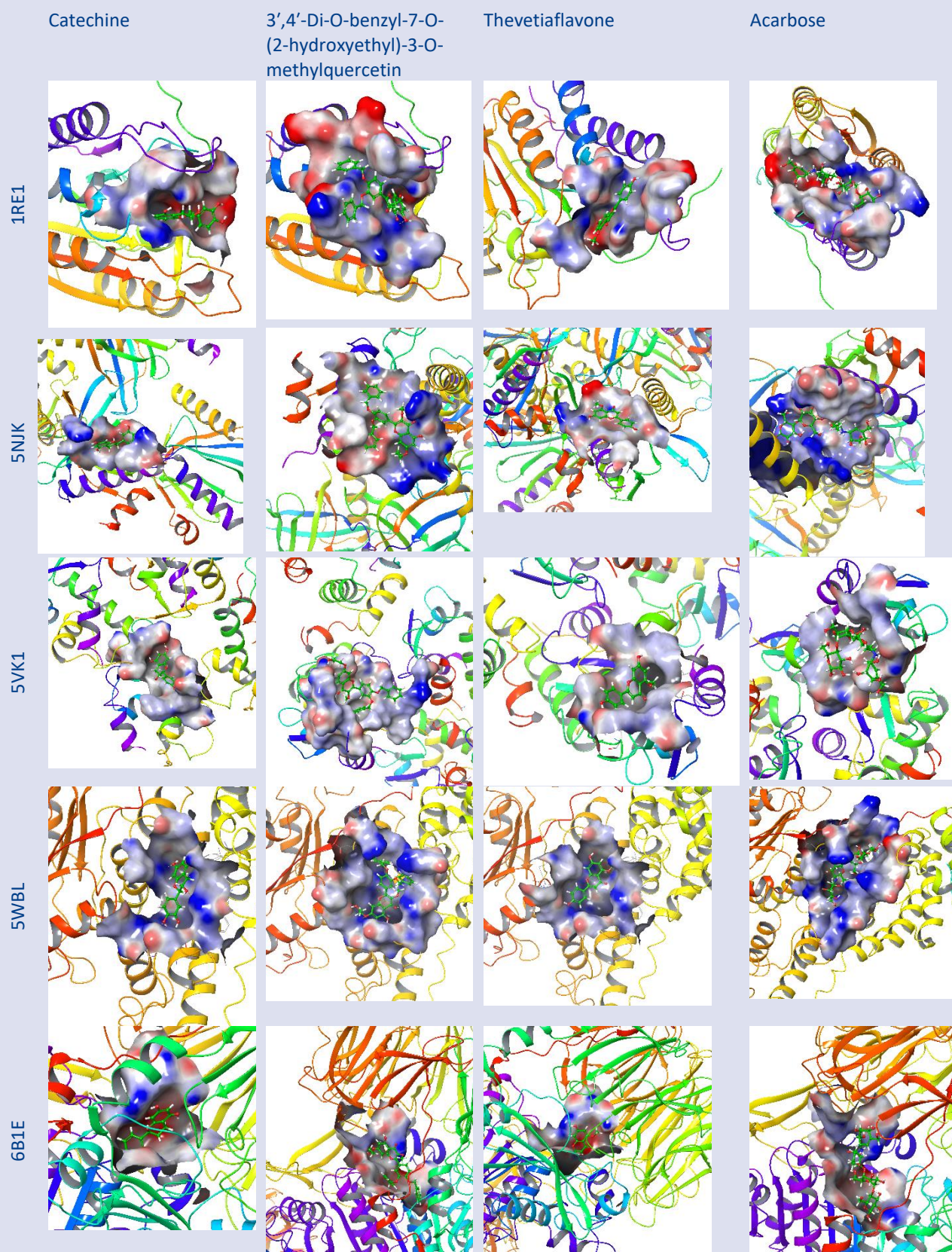


Figure 2. 3D bond interactions of catechine, 3',4'-Di-O-benzyl-7-O-(2-hydroxyethyl)-3-O-methylquercetin, Thevetiaflavone and Acarbose



To evaluate the effects and interactions of the studied molecules within human metabolism, an ADME/T (Absorption, Distribution, Metabolism, Excretion, and Toxicity) analysis was conducted. This analysis provided insights into how these molecules are absorbed, distributed, metabolized, and eventually eliminated from the body, along with an assessment of their potential toxicity. By examining these parameters, a comprehensive understanding of the molecules' pharmacokinetic and toxicological properties was obtained. Many parameters that analyze the chemical properties of molecules are calculated, such as mol\_MW (molar mass of molecules), Molecular Weight (MW), Volume (molecular volume), LogP (The degree of lipophilicity of the molecule), TPSA (Total Polar Surface Area, Refers to the polar surface area of the molecule, affects bioavailability), nRot (Number of

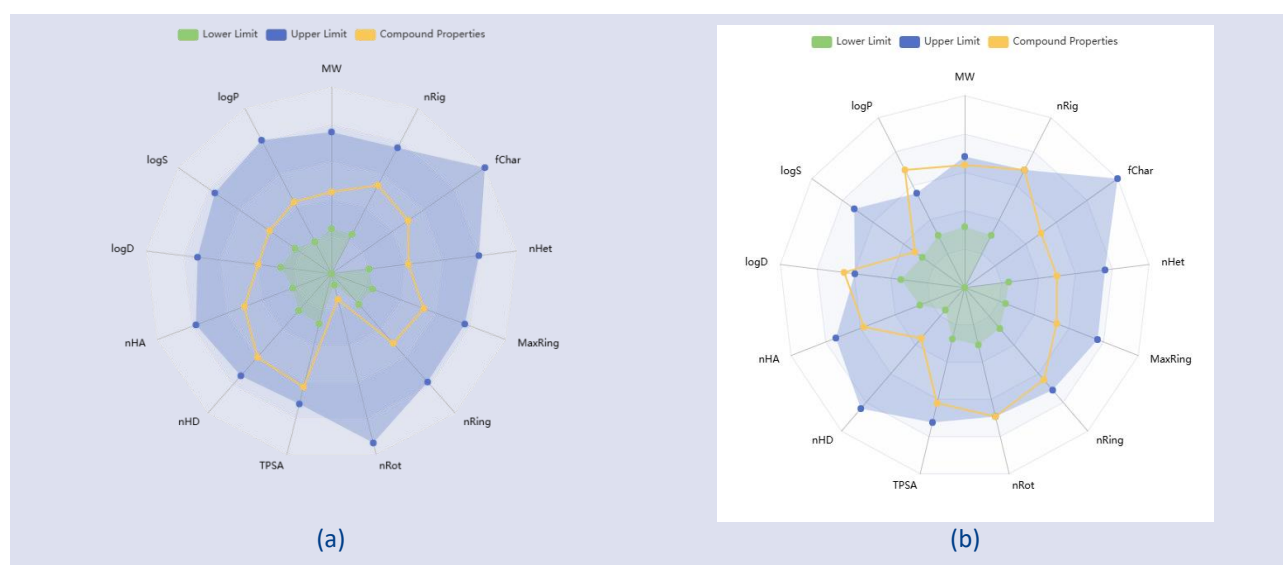
rotationally free bonds), LogS (Degree of water solubility), nHA and nHD (Refers to the number of atoms that accept and give hydrogen bonds). The physicochemical and ADME properties of the catechine, 3',4'-Di-O-benzyl-7-O-(2-hydroxyethyl)-3-O-methylquercetin, Thevetiaflavone and Acarbose are given in Table 2.

The molecular weights of all compounds are in the range of 100-600 Da, within the accepted limits for drug-like molecules. Although the number of atoms capable of hydrogen bonding generally complies with Lipinski's rules, it exceeds the limit values in some compounds. In particular, catechine, 3',4'-Di-O-benzyl-7-O-(2-hydroxyethyl)-3-O-methylquercetin, Thevetiaflavone and Acarbose (nHA=12, nHD=8) may violate Lipinski rules due to its high hydrogen bonding capacity.

Table 2. Physicochemical and ADME properties of catechine, 3',4'-Di-O-benzyl-7-O-(2-hydroxyethyl)-3-O-methylquercetin, Thevetiaflavone and Acarbose

	Catechine	3',4'-Di-O-benzyl-7-O-(2-hydroxyethyl)-3-O-methylquercetin	Thevetiaflavone	Acarbose	Optimal
Molecular Weight (MW)	290.08	540.18	284.07	645.25	100-600
Volume	279.249	552.657	282.482	573.315	
Density	1.039	0.977	1.006	1.125	
nHA	6	8	5	19	0-12
nHD	5	2	2	14	0-7
nRot	1	11	2	9	0-11
nRing	3	5	3		0-6
MaxRing	10	10	10	4	0-18
nHet	6	8	5	6	1-15
fChar	0	0	00	0	-1
nRig	17	30	18	24	0-30
Flexibility	0.059	0.367	0.11	0.375	
Stereo Centers	2	0	0	19	<2
TPSA	110.38	107.59	79.9	321.17	0-140
logS	-2.581	-3.512	-3.889	0.533	
logP	1.173	4.651	2.507	-4.808	0-3
logD7.4	1.537	3.465	2.45	-3.652	1-3
Lipinski Rule	**	**	**	*	
Pfizer Rule	**	**	**	**	
GSK Rule	**	*	**	*	

\* Rejected \*\*Accepted



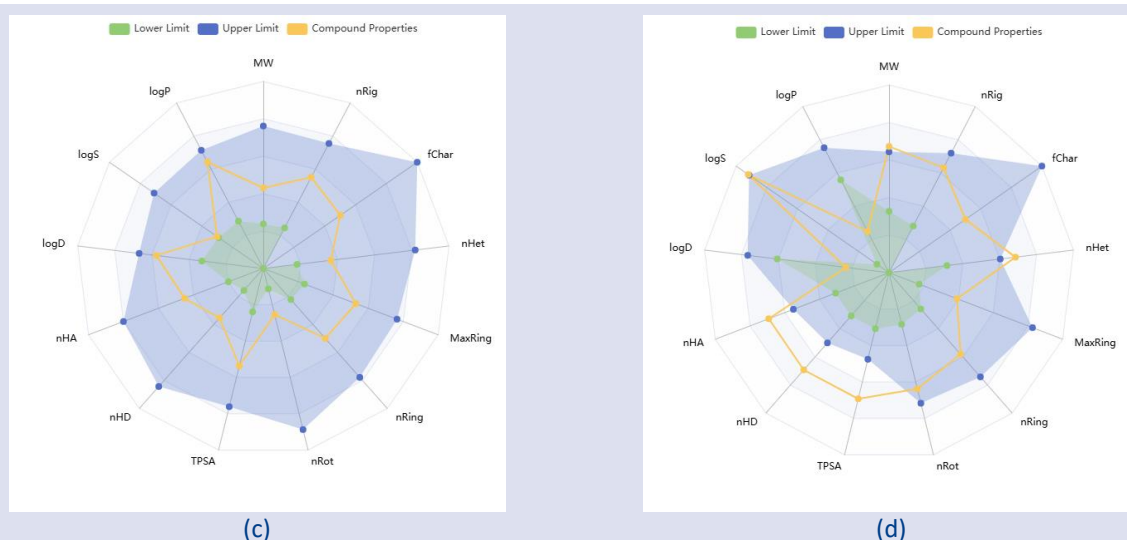


Figure 3. Radar graph showing the chemical structure and physicochemical properties of catechine (A), 3',4'-Di-O-benzyl-7-O-(2-hydroxyethyl)-3-O-methylquercetin (B), Thevetiaflavone (C) and Acarbose (D)

Catechine (290.08 Da), Thevetiaflavone (284.07 Da) and 3',4'-Di-O-benzyl-7-O-(2-hydroxyethyl)-3-O-methylquercetin (540.18 Da) fall within this range. Acarbose (645.25 Da) exceeds the optimal limit and may be disadvantageous in terms of absorption due to the large molecular weight. The TPSA values for Catechine, 3',4'-Di-O-benzyl-7-O-(2-hydroxyethyl)-3-O-methylquercetin, Thevetiaflavone and Acarbose were 110.38, 107.59, 79.9 and 321.17, respectively. Acarbose (321.17 Å) may be difficult to pass through the cell membrane by passive diffusion due to its high TPSA value. The logP values of the compounds are in the range of 0-3 and are at acceptable levels in terms of drug design. This indicates that the lipophilic properties of the compounds are sufficient and membrane permeability may be appropriate. Although the water solubility (logS) of the compounds is relatively low for catechine (-2.581), 3',4'-Di-O-benzyl-7-O-(2-hydroxyethyl)-3-O-methylquercetin (-3.512), Thevetiaflavone (-3.889) and Acarbose 0.533) it is critical in terms of bioavailability. Catechine and Thevetiaflavone stand out as the most favorable compounds in terms of their pharmacokinetic properties. 3',4'-Di-O-benzyl-7-O-(2-hydroxyethyl)-3-O-methylquercetin can be considered even though its logP value is high.

## Conclusion

This study investigated the molecular docking interactions of various bioactive compounds, including Catechine, 3',4'-Di-O-benzyl-7-O-(2-hydroxyethyl)-3-O-methylquercetin, Retusapurpurin\_A, Sakuranetin, and Thevetiaflavone, with five different protein targets (1RE1, 5VK1, 5WBL, and 6B1E). Acarbose served as a positive control due to its strong binding affinity. The results demonstrated that Catechine exhibited the highest binding affinity for the 5VK1 protein (-6.710 kcal/mol), indicating its potential as a strong inhibitor. Thevetiaflavone also displayed strong interactions with

5VK1, while 3',4'-Di-O-benzyl-7-O-(2-hydroxyethyl)-3-O-methylquercetin showed high affinity for 5NJK and 6B1E proteins. These findings suggest that these natural compounds could serve as promising inhibitors for their respective targets.

Hydrogen bonding and  $\pi$  interactions played a key role in stabilizing ligand-protein complexes, with Catechine forming multiple hydrogen bonds with 5VK1 and 5WBL. The results highlight the importance of structural features such as hydroxyl and carbonyl groups in enhancing binding affinity. However, to confirm these computational findings, biological activity assays and ADMET studies are necessary. In particular, Catechine and 3',4'-Di-O-benzyl-7-O-(2-hydroxyethyl)-3-O-methylquercetin should be further evaluated for their potential inhibitory effects. These findings provide valuable insights into the development of natural inhibitors, contributing to future research in drug discovery and biotechnological applications.

## Conflicts of interest

The authors report no conflicts of interest in this work

- [1] I.D. Atlas, t.E. Committee, International Diabetes Federation: Brussels, Belgium, (2015).
- [2] W. Benalla, S. Bellahcen, M. Bnouham, Antidiabetic medicinal plants as a source of alpha glucosidase inhibitors, *Current Diabetes Reviews*, 6 (2010) 247-254.
- [3] W.H. Organization, Global Report on Diabetes, World Health Organization, (2016).
- [4] Malaguarnera, Giugno, Ruello, Rizzo, Motta, Mazzoleni, Acarbose is an effective adjunct to dietary therapy in the treatment of hypertriglyceridaemias, *British Journal Of Clinical Pharmacology*, 48 (1999) 605-609.
- [5] Y.-J. Shim, H.-K. Doo, S.-Y. Ahn, Y.-S. Kim, J.-K. Seong, I.-S. Park, B.-H. Min, Inhibitory effect of aqueous extract from the gall of *Rhus chinensis* on alpha-glucosidase activity and postprandial blood glucose, *Journal of Ethnopharmacology*, 85 (2003) 283-287.

- [6] M. Nawaz, M. Taha, F. Qureshi, N. Ullah, M. Selvaraj, S. Shahzad, S. Chigurupati, A. Waheed, F.A. Almutairi, Structural elucidation, molecular docking,  $\alpha$ -amylase and  $\alpha$ -glucosidase inhibition studies of 5-amino-nicotinic acid derivatives, *Bmc Chemistry*, 14 (2020) 1-11.
- [7] A. Reuser, H. Wisselaar, An evaluation of the potential side-effects of  $\alpha$ -glucosidase inhibitors used for the management of diabetes mellitus, *European journal of clinical investigation*, 24 (1994) 19-24.
- [8] Z.-J. Lin, L.-P. He, C.-P. Li, Research Progress of Risk Factors Associated with Gestational Diabetes Mellitus, *Endocrine, Metabolic & Immune Disorders-Drug Targets*, 25 (2025) 99-108.
- [9] M.S. Hossain, M.A. Kader, K.W. Goh, M. Islam, M.S. Khan, M. Harun-Ar Rashid, D.J. Ooi, H.D. Melo Coutinho, Y.M. Al-Worafi, S. Moshawih, Herb and spices in colorectal cancer prevention and treatment: A narrative review, *Frontiers in Pharmacology*, 13 (2022) 865801.
- [10] W. Zhang, Y. Bai, Y. Wang, W. Xiao, Polypharmacology in drug discovery: a review from systems pharmacology perspective, *Current Pharmaceutical Design*, 22 (2016) 3171-3181.
- [11] A. Necip, I. Demirtas, S.E. Tayhan, M. Işık, S. Bilgin, İ.F. Turan, Y. İpek, Ş. Beydemir, Isolation of phenolic compounds from eco-friendly white bee propolis: Antioxidant, wound-healing, and anti-Alzheimer effects, *Food Science & Nutrition*, 12 (2024) 1928-1939.
- [12] S. Samarghandian, M. Azimi-Nezhad, T. Farkhondeh, Catechin treatment ameliorates diabetes and its complications in streptozotocin-induced diabetic rats, *Dose-response*, 15 (2017) 1559325817691158.
- [13] F. Afsharpour, M. Javadi, S. Hashemipour, Y. Koushan, Propolis supplementation improves glycemic and antioxidant status in patients with type 2 diabetes: A randomized, double-blind, placebo-controlled study, *Complementary Therapies in Medicine*, 43 (2019) 283-288.
- [14] H. Kitamura, Effects of propolis extract and propolis-derived compounds on obesity and diabetes: knowledge from cellular and animal models, *Molecules*, 24 (2019) 4394.
- [15] G.M. Morris, M. Lim-Wilby, Molecular docking, Molecular modeling of proteins, (2008) 365-382.
- [16] E. Gayathiri, P. Prakash, S.Y. Chaudhari, S. Sabarathinam, S.D. Priyadarshini, M.K. Al-Sadoon, J. Panneerselvam, S.W. Chang, B. Ravindran, R.R. Mani, Interaction of molecular mechanisms of plant-derived metabolites in Type 2 diabetes mellitus: A network pharmacology, docking and molecular dynamics approach on AKT1 kinase, *Energy Nexus*, 17 (2025) 100351.
- [17] M. Yildirim, E. Yasar, A. Necip, M. Cimentepe, B. Demirbağ, A. Kilic, Facile synthesis and spectral analysis of the bioactive spiroborate compounds as a novel therapeutic agent for computational insights, biological evaluation, and applications, *Journal of Organometallic Chemistry*, (2025) 123510.
- [18] M. Yildirim, A. Kilic, M. Cimentepe, A. Necip, S. Turedi, Synthesis of bioactive quercetin-boronate esters as a novel biological agent: Enzyme inhibition, anti-microbial properties, computational insights and anti-cancer activity, *Journal of Molecular Structure*, 1321 (2025) 140216.
- [19] M. Yildirim, K. Dogan, A. Necip, M. Cimentepe, Naringenin-loaded pHEMA cryogel membrane: preparation, characterization, antibacterial activity and in silico studies, *Chemical Papers*, (2024) 1-10.
- [20] A. Necip, Kardiyovasküler Hastalıklarda Doğal Ürünler: Kurkumin ve Quercetin Moleküler Docking, *Mehes Journal*, 2 (2024) 1-9.
- [21] T.G. Dikme, A. Necip, R. Dikme, S. Güneş, Effect of Phytosterols in Apricot Kernel on Cholesterol: Molecular Docking, *Mehes Journal*, 2 (2024) 28-38.

## Investigation of the Activity of Benzenesulfonamide Derivative Molecules Against Gastric Cancer Proteins with Gaussian Calculations and Docking Analysis

**Burak Tüzün<sup>1,a,\*</sup>**<sup>1</sup> Plant and Animal Production Department, Technical Sciences Vocational School of Sivas, Sivas Cumhuriyet University, Sivas, Türkiye

\*Corresponding author

**Research Article****History**

Received: 26/03/2025

Accepted: 21/05/2025



This article is licensed under a Creative Commons Attribution-NonCommercial 4.0 International License (CC BY-NC 4.0)

**ABSTRACT**

While gastric cancer poses a significant problem in terms of global health with its high mortality rates, the limitations in current treatment methods necessitate the identification of new molecular targets and potential drug candidates. Benzenesulfonamide derivatives are among the compounds that have attracted attention in recent years due to their structural diversity and biological activity potential. In the study, the electronic properties, orbital distributions and thermodynamic stabilities of benzenesulfonamide derivative molecules were calculated using the Gaussian program; thus, the reactivity tendencies of the molecules and their interaction potential with target proteins were tried to be revealed. The calculations were made in the 6-31++g(d,p) basis set at the B3LYP, HF, M062X level. The theoretical data obtained were supported by molecular docking analyses; Docking studies have evaluated the binding affinities and interaction sites of benzenesulfonamide derivatives with the identified gastric cancer proteins, which are PDB ID: 3MAX and 4BKX proteins, in detail. Then, MM-GBSA values were calculated for the molecule with the highest activity among these molecules. Finally, ADME/T calculations were performed to examine the drug potential of the molecules.

**Keywords:** Benzenesulfonamide, DFT, Molecular docking, MM-GBSA, ADME/T.<sup>a</sup> [theburaktuzun@yahoo.com](mailto:theburaktuzun@yahoo.com) <https://orcid.org/0000-0002-0420-2043>**Introduction**

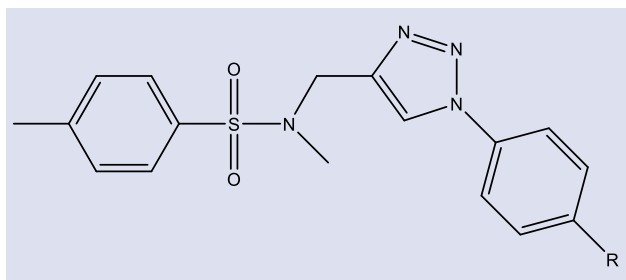
Gastric cancer is a serious health problem with high incidence rates worldwide, especially in regions such as Asia and Eastern Europe. This malignancy occurs as a result of uncontrolled growth of cells in the gastric mucosa and is usually triggered by a combination of *Helicobacter pylori* infection, genetic predisposition, irregular diet, high salt consumption, smoking and environmental factors. The absence of obvious symptoms in the early stage leads to late diagnosis and the detection of the disease in advanced stages, which negatively affects treatment options and prognosis. Although traditional treatment methods include surgical intervention, chemotherapy, radiotherapy and targeted therapies, multidisciplinary approaches are increasingly gaining importance in order to determine the most appropriate strategy for each patient [1].

Theoretical calculations play an important role in understanding the molecular complexity of gastric cancer and developing new disease-specific treatment strategies. In this context, quantum chemical calculations using the Gaussian program provide detailed analysis of the electron distribution, reactivity parameters and thermodynamic properties of target molecules [2]. Gaussian helps to deeply understand the molecular structure of proteins and other biological targets that affect gastric cancer with basic calculations such as the calculation of molecular orbitals, ionization potentials and electron affinities.

At the same time, the Maestro (Schrödinger) platform offers the opportunity to visualize in detail the interactions of potential drug candidates with target proteins through molecular modeling, docking studies and dynamic simulations. This program provides powerful tools to predict how drugs interact with active sites, their binding affinities and interaction mechanisms by integrating with structural biology data [3]. These approaches, supported by theoretical calculations, when combined with experimental data, allow for a better understanding of the molecular pathogenesis of gastric cancer and the development of personalized treatment strategies.

In conclusion, in the development of treatment and diagnostic methods for gastric cancer, the use of advanced theoretical computational tools such as Gaussian and Maestro Schrödinger, as well as experimental data obtained from clinical applications, plays a critical role in revealing the molecular basis of the disease. This integrated approach allows the development of promising, comprehensive and innovative strategies in terms of early diagnosis, increasing the effectiveness of treatment and identifying new drug candidates.





Scheme 1. Main skeleton of benzenesulfonamide derivative molecules

In this study, molecule 1 (N-((1-(4-methoxyphenyl)-1H-1,2,3-triazol-4-yl)methyl)-N,4-dimethylbenzenesulfonamide), molecule 2 (N,4-dimethyl-N-((1-(p-tolyl)-1H-1,2,3-triazol-4-yl)methyl)benzenesulfonamide), molecule 3 (N-((1-(4-isopropylphenyl)-1H-1,2,3-triazol-4-yl)methyl)-N,4-dimethylbenzenesulfonamide), molecule 4 (N-((1-(4-chlorophenyl)-1H-1,2,3-triazol-4-yl)methyl)-N,4-dimethylbenzenesulfonamide), molecule 5 (N-((1-(4-fluorophenyl)-1H-1,2,3-triazol-4-yl)methyl)-N,4-dimethylbenzenesulfonamide), molecule 6 (N,4-dimethyl-N-((1-(4-nitrophenyl)-1H-1,2,3-triazol-4-yl)methyl)benzenesulfonamide), molecule 7 (Ethyl-4-(((N,4-dimethylbenzenesulfonamido)methyl)-1H-1,2,3-triazol-1-yl)benzoate), and molecule 8 (N-((1-(4-acetylphenyl)-1H-1,2,3-triazol-4-yl)methyl)-N,4-dimethylbenzenesulfonamide) molecules were all synthesized by Şahin and co-worker [4] in Figure 1. Then, the quantum chemical parameters of these molecules were calculated with the Gaussian package program. Calculations using the 6-31++g(d,p) basis set in the B3LYP, HF, and M06-2x [5–7] techniques were performed using these programs. Then, the activities of the molecules against various proteins, which are PDB ID: 3MAX and 4BKX proteins [8,9], were compared. The interaction values of the molecule with the highest activity were examined by MM-GBSA calculation. Finally, the drug properties of the molecules were examined by ADME/T analysis of the molecules.

## Theoretical Methods

The chemical and biological characteristics of molecules may be greatly inferred from theoretical calculations. Theoretical simulations provide a great deal of information about quantum chemical parameters. The computed parameters are used to explain the chemical activity of the molecules. Molecules are calculated using a variety of applications. Gaussian09 RevD.01 and GaussView 6.0 are the names of these different applications [10,11]. Calculations using the 6-31++g(d,p) basis set in the B3LYP, HF, and M06-2x [5–7] techniques were performed using these programs. Several quantum chemical parameters have been discovered as a result of these quantum chemistry computations. The following displays the computed parameters, each of which denotes a distinct molecular chemical property [12,13]. The formulas for calculating these parameters are given in equations 1-3.

$$\chi = -\left(\frac{\partial E}{\partial N}\right)_{v(r)} = \frac{1}{2}(I + A) \cong \frac{1}{2}(E_{HOMO} + E_{LUMO}) \quad (1)$$

$$\eta = -\left(\frac{\partial^2 E}{\partial N^2}\right)_{v(r)} = \frac{1}{2}(I - A) \cong -\frac{1}{2}(E_{HOMO} - E_{LUMO}) \quad (2)$$

$$\sigma = 1/\eta \quad \omega = \chi^2/2\eta \quad \varepsilon = 1/\omega \quad (3)$$

The biological activities of molecules are compared to biological materials using molecular docking calculations. Molecular docking calculations were performed using Schrödinger's Maestro Molecular modeling platform (version 13.4) [14]. There are several stages involved in calculations. Every stage is carried out in a unique way. Proteins were prepared in the first phase using the protein preparation module [15]. The proteins' active sites were identified in this module. The next stage involves preparing the compounds under study. The LigPrep module [16] is ready for computations utilizing optimized structures once the molecules have first been optimized in the Gaussian software application. Following preparation, the interactions between the compounds and the cancer protein were investigated using the Glide ligand docking module [17,18]. All computations were performed using the OPLS4 technique. Finally, the pharmacological potential of the investigated compounds will be investigated using ADME/T analysis (absorption, distribution, metabolism, excretion, and toxicity). The effects and reactions of chemicals in human metabolism were predicted using the Schrödinger software's Qik-prop module [19].

## Result and Discussion

Knowledge of terms like the  $\Delta E$  energy gap,  $E_{HOMO}$ ,  $E_{LUMO}$ , chemical hardness, softness, electronegativity, and chemical potential is necessary to comprehend the electronic structure and chemical characteristics of molecules [20]. These are the fundamental standards used to evaluate the stability and reactivity of a chemical.

The difference in energy levels between a molecule's highest occupied molecular orbital (HOMO) and lowest unoccupied molecular orbital (LUMO) is measured by the energy gap, or  $\Delta E$  [21]. To fully comprehend the electrical stability and reactivity of a molecule, one must have a thorough comprehension of this value. While a larger  $\Delta E$  value suggests a more stable molecular structure, a smaller  $\Delta E$  value indicates stronger molecular reactivity [22].

In the context of molecular orbital energy,  $E_{HOMO}$  and  $E_{LUMO}$  stand for the energy of the highest occupied molecular orbital and the lowest unoccupied molecular orbital, respectively. While the LUMO determines a molecule's ability to take electrons, showing electrophilic behavior, the HOMO controls a molecule's tendency to give electrons, indicating nucleophilic activity [21]. To comprehend the mechanics of electron transport in chemical processes, one must have a thorough knowledge of the energy difference between the HOMO and LUMO states.

The ability of a molecule to withstand changes brought on by outside influences is known as chemical hardness.

Harder molecules are less reactive and have improved structural stability. Chemical softness is a measure of a molecule's reactivity; molecules that are softer are more vulnerable to changes in their chemical structure. The ideas of softness and hardness may help forecast the formation of chemical bonds and clarify the acid-base characteristics of molecules [23].

One important factor that determines the polarity of chemical bonds is electronegativity. It is a term used to describe the propensity of an atom or molecule to draw bonding electrons. Compounds with higher electronegativity are better at drawing electrons and displaying electrophilic properties during chemical reactions.

Chemical potential, as described in, quantifies the energy change inside a molecule and shows how the system reacts to variations in electron density [24]. This figure is an important indication in the measurement of molecule stability and reaction energy.

When combined, these ideas provide a thorough foundation for comprehending molecules' electrical structure, stability, and chemical reactivity. When combined with  $\Delta E$ , the evaluation of HOMO and LUMO energy levels provides a useful way to predict chemical reactivity. Characteristics like electronegativity, softness, and chemical hardness are essential for understanding how molecules react to outside stimuli. All of the factors are listed in detail in Table 1. and Figure 1..

Table 1. The calculated quantum chemical parameters of molecules.

	$E_{\text{HOMO}}$	$E_{\text{LUMO}}$	I	A	$\Delta E$	$\eta$	$\mu$	$\chi$	PA	$\omega$	$\epsilon$	dipol	Energy
<b>B3LYP/6-31g LEVEL</b>													
1	-6.2249	-1.3617	6.2249	1.3617	4.8633	2.4316	0.4112	3.7933	-3.7933	2.9587	0.3380	4.2117	-40849.7670
2	-6.3509	-1.4283	6.3509	1.4283	4.9226	2.4613	0.4063	3.8896	-3.8896	3.0734	0.3254	4.6627	-38803.3891
3	-6.3479	-1.4169	6.3479	1.4169	4.9310	2.4655	0.4056	3.8824	-3.8824	3.0568	0.3271	4.6850	-40941.6618
4	-6.5117	-1.7454	6.5117	1.7454	4.7664	2.3832	0.4196	4.1285	-4.1285	3.5761	0.2796	3.6492	-50240.6179
5	-6.4970	-1.5867	6.4970	1.5867	4.9103	2.4552	0.4073	4.0419	-4.0419	3.3270	0.3006	3.6481	-40434.7499
6	-6.7898	-3.2042	6.7898	3.2042	3.5857	1.7928	0.5578	4.9970	-4.9970	6.9638	0.1436	5.3898	-43299.0681
7	-6.5237	-2.1704	6.5237	2.1704	4.3533	2.1767	0.4594	4.3471	-4.3471	4.3408	0.2304	5.2673	-45003.6194
8	-6.5683	-2.3987	6.5683	2.3987	4.1696	2.0848	0.4797	4.4835	-4.4835	4.8210	0.2074	5.7166	-41887.1637
<b>HF/6-31g LEVEL</b>													
1	-8.9738	0.9568	8.9738	-0.9568	9.9306	4.9653	0.2014	4.0085	-4.0085	1.6181	0.6180	4.7966	-40647.3515
2	-8.9175	0.9608	8.9175	-0.9608	9.8784	4.9392	0.2025	3.9783	-3.9783	1.6022	0.6241	4.6128	-38610.8882
3	-8.9017	0.9391	8.9017	-0.9391	9.8408	4.9204	0.2032	3.9813	-3.9813	1.6107	0.6208	4.6529	-40733.8299
4	-9.1496	0.9426	9.1496	-0.9426	10.0922	5.0461	0.1982	4.1035	-4.1035	1.6685	0.5993	3.2312	-50036.8689
5	-9.1883	0.9407	9.1883	-0.9407	10.1290	5.0645	0.1975	4.1238	-4.1238	1.6789	0.5956	3.2566	-40239.4319
6	-9.4786	0.6803	9.4786	-0.6803	10.1589	5.0795	0.1969	4.3992	-4.3992	1.9050	0.5249	4.8067	-43086.1026
7	-9.1992	0.9568	9.1992	-0.9568	10.1559	5.0780	0.1969	4.1212	-4.1212	1.6724	0.5980	5.4619	-44777.4174
8	-9.2182	0.8811	9.2182	-0.8811	10.0993	5.0497	0.1980	4.1685	-4.1685	1.7206	0.5812	5.8118	-41678.4222
<b>M062X/6-31g LEVEL</b>													
1	-7.4024	-0.5448	7.4024	0.5448	6.8576	3.4288	0.2916	3.9736	-3.9736	2.3025	0.4343	4.7982	-40836.0737
2	-7.5618	-0.5606	7.5618	0.5606	7.0013	3.5006	0.2857	4.0612	-4.0612	2.3558	0.4245	4.7342	-38790.3383
3	-7.7221	-0.4816	7.7221	0.4816	7.2405	3.6202	0.2762	4.1019	-4.1019	2.3238	0.4303	5.1803	-40927.5710
4	-7.7382	-0.6566	7.7382	0.6566	7.0815	3.5408	0.2824	4.1974	-4.1974	2.4879	0.4019	5.7329	-50227.5167
5	-7.7270	-0.6093	7.7270	0.6093	7.1177	3.5589	0.2810	4.1681	-4.1681	2.4409	0.4097	5.5987	-40421.5428
6	-8.0274	-1.9552	8.0274	1.9552	6.0723	3.0361	0.3294	4.9913	-4.9913	4.1027	0.2437	8.5469	-43284.5808
7	-7.7624	-1.0621	7.7624	1.0621	6.7003	3.3502	0.2985	4.4122	-4.4122	2.9055	0.3442	4.9684	-44988.2096
8	-7.7967	-1.2640	7.7967	1.2640	6.5327	3.2663	0.3062	4.5303	-4.5303	3.1417	0.3183	5.9869	-41873.0026

Koopman's theorem [25,26], a fundamental concept in molecular orbital theory, connects a molecule's electron affinity and ionization energy to its HOMO and LUMO energy levels. The theory states that the energy of the HOMO is equivalent to the ionization energy of the molecule, whereas the energy of the LUMO indicates the electron affinity of the molecule. This method offers a strong tool for predicting the electrical properties and reactivity of molecules. The findings are only guesses that could need more complex calculations to support, despite the fact that the theory does not take electron-electron interactions into account.

The Hard and Soft Acid-Base (HSAB) paradigm [27] was created to understand acid-base chemistry. According to this view, hard acids interact strongly with hard bases, while soft acids create strong surfaces with soft bases

[28]. According to this theory, a system will often adopt a structure with increasing hardness since it is more stable and less reactive. This concept offers a helpful foundation for predicting the stability of molecules and chemical processes. The idea of maximum hardness is often used, particularly in the assessment of transition states and the creation of reactive intermediates.

These three core ideas provide a theoretical and practical basis for a comprehensive understanding of the characteristics of molecular bonding and reactivity. The HSAB principle explains the nature of acid-base interfaces [29], Koopman's theorem analyzes electron transport channels, and PMH largely predicts molecular stability [30]. Combining these methods might result in a thorough understanding of the behavior of chemical systems.

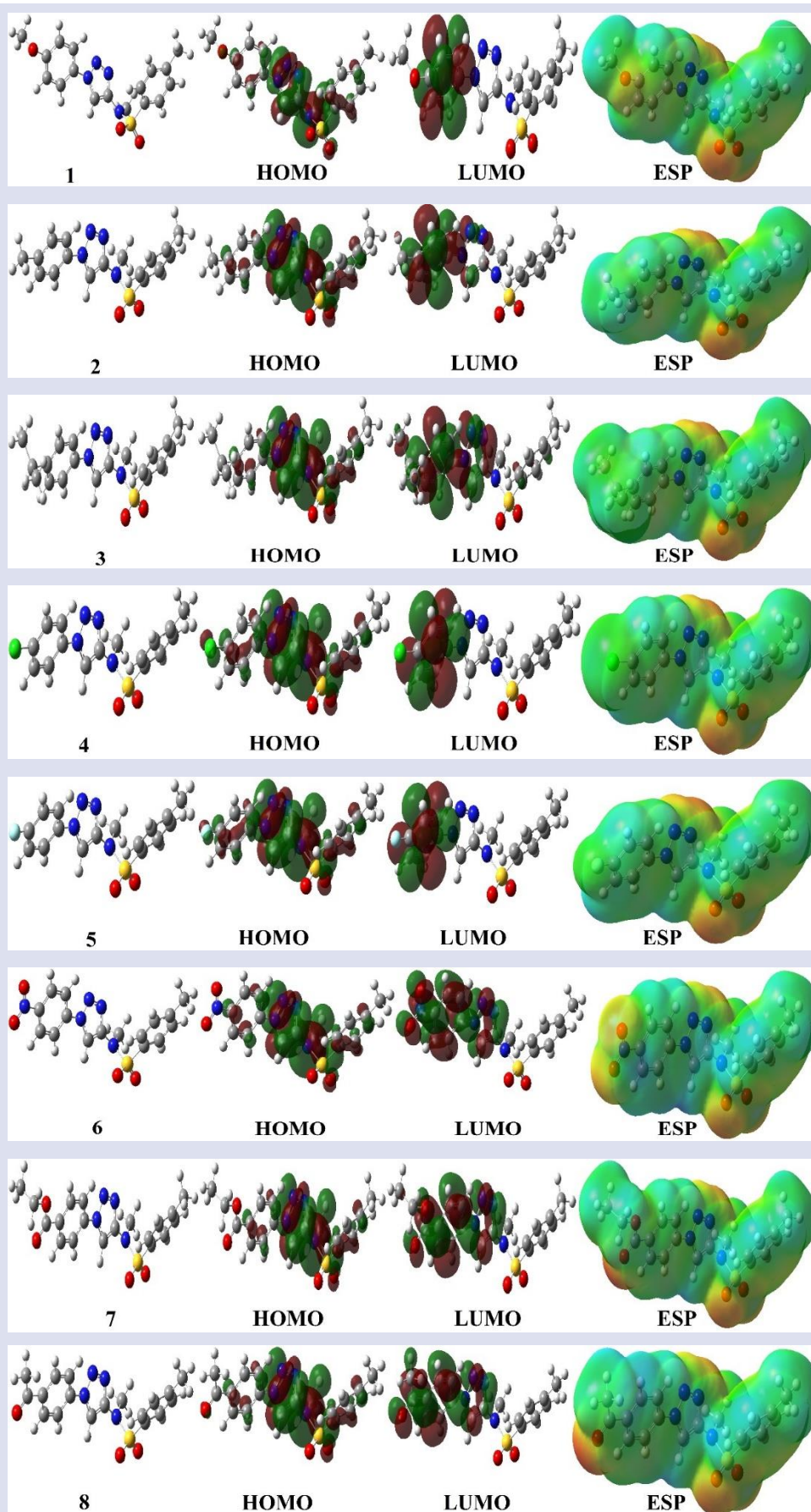


Figure 2. Representations of optimize structure, HOMO, LUMO, and ESP of molecules

As a result of the gaussian calculations, many quantum chemical parameters have been calculated. In these

calculations, one of the first important parameters is the HOMO energy value of the molecules, and when the



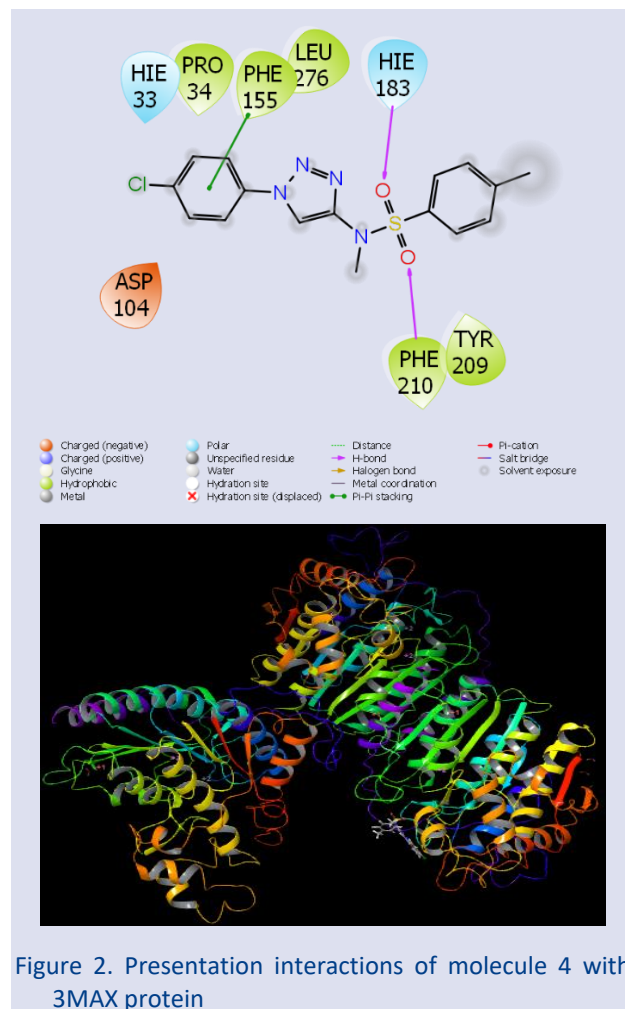
comparison is made according to the numerical values of these parameters, it is seen that molecule 1 has the highest activity at all three levels. On the other hand, when the comparison is made according to the numerical value of the LUMO parameter of the molecules, it is seen that molecule 6 has the highest activity at the B3LYP and M062X levels and molecule 8 has the highest activity at the HF level. When the comparison is made according to

the energy gap values of the molecules, it is seen that molecule 6 has the highest activity at the B3LYP and M062X levels and molecule 3 has the highest activity at the HF level. Finally, when the energy value of the electronegativity parameter of the molecules is examined, it is seen that molecule 1 has the highest activity at both the B3LYP and M062X levels and molecule 2 has the highest activity at the HF level.

Table 2. Numerical values of the docking parameters of molecule against enzymes

4BKX	Docking Score	Glide ligand efficiency	Glide hbond	Glide evdw	Glide ecoul	Glide emodel	Glide energy	Glide einternal	Glide posenum
1	-3.04	-0.12	0.00	-27.00	-3.74	-34.75	-30.74	4.50	234
2	-2.84	-0.12	0.00	-25.34	-3.45	-32.38	-28.79	3.60	352
3	-3.29	-0.13	0.00	-32.05	-2.92	-39.39	-34.97	3.14	126
4	-3.36	-0.14	0.00	-29.81	-0.34	-36.36	-30.15	0.34	378
5	-3.50	-0.15	0.00	-29.22	-0.38	-36.57	-29.60	0.69	244
6	-2.60	-0.10	0.00	-32.24	-2.06	-36.42	-34.30	3.94	238
7	-3.07	-0.11	0.00	-33.34	-2.54	-39.62	-35.87	6.20	322
8	-3.54	-0.14	0.00	-29.26	-3.06	-38.37	-32.32	4.06	278
3MAX	Docking Score	Glide ligand efficiency	Glide hbond	Glide evdw	Glide ecoul	Glide emodel	Glide energy	Glide einternal	Glide posenum
1	-1.76	-0.07	0.00	-20.44	-5.31	-24.26	-25.76	2.66	322
2	-2.41	-0.10	0.00	-27.33	-0.47	-29.53	-27.80	4.09	95
3	-3.03	-0.12	0.00	-29.99	-2.70	-36.56	-32.69	5.13	254
4	-3.55	-0.15	0.00	-27.60	-7.47	-40.74	-35.08	2.75	129
5	-3.44	-0.14	0.00	-26.31	-7.45	-38.98	-33.76	2.71	243
6	-1.66	-0.06	0.00	-26.75	-2.16	-26.50	-28.91	3.19	274
7	-3.42	-0.12	0.00	-33.15	-7.94	-47.46	-41.08	3.85	294
8	-3.22	-0.12	0.00	-31.44	-3.67	-40.80	-35.11	3.66	104

Recent studies indicate that the comparison of molecules' biological activities has been significantly expedited and made simpler by the extensive use of theoretical research and technological breakthroughs [31]. This is the outcome of widespread use of these two research methodologies. This assertion is supported by the findings of current research. Calculations have significantly sped up and simplified the process of identifying the most effective and successful medications before experimental testing [32]. The theoretical computations revealed a number of factors. This method is utilized to ascertain the relationship between the numerical values of these parameters and the biological activities of molecules. This is done in order to assess the biological parameters. The interactions between various proteins and chemicals are the most significant factor influencing the activities outlined [33]. The widespread nature of these interactions ultimately inhibits the proteins. This is the mechanism via which inhibition occurs. The way chemicals interact with proteins determines their energy levels. Molecules and proteins interact by  $\pi$ - $\pi$  interactions, halogen interactions, hydrogen bonds, and polar and hydrophobic contacts [31–33]. Molecular interaction is necessary for equilibrium to stay constant. Comprehensive studies of these chemical interactions have shown that there are many different ways in which chemicals and proteins interact. All of the characteristics are in Table 2, and all of the figures are in Figures 2-3.





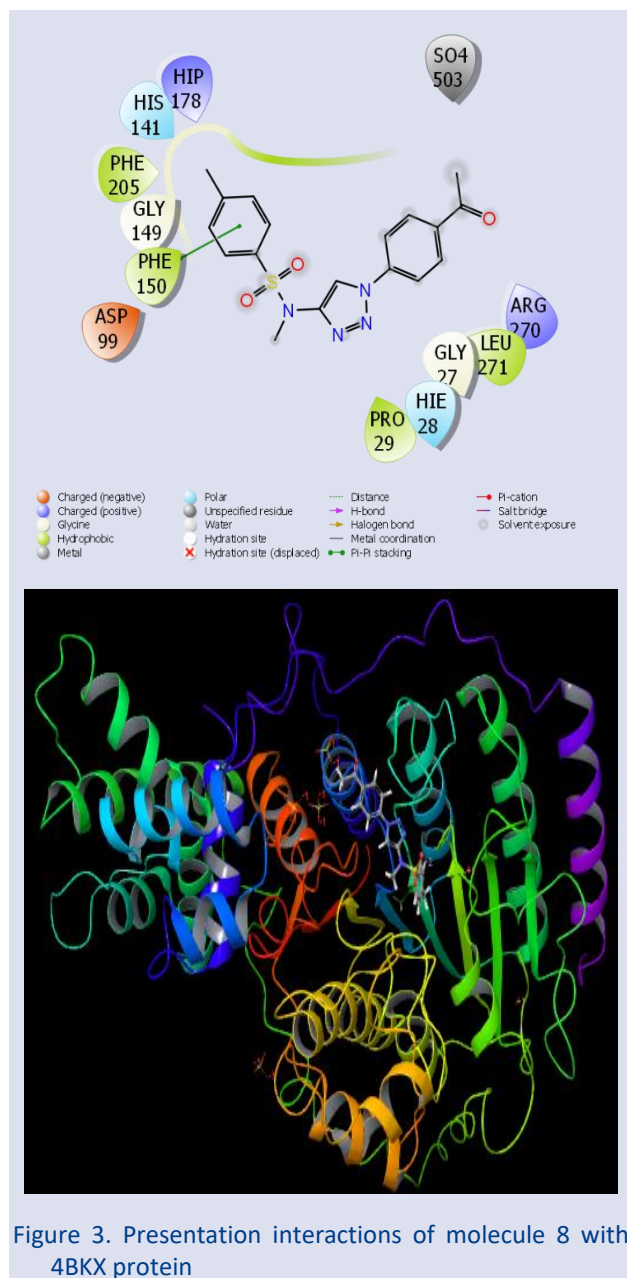


Figure 3. Presentation interactions of molecule 8 with 4BKX protein

The Glide ligand efficiency is the main parameter derived from molecular docking simulations. These are not the only complementary attributes. This numerical chart illustrates how well the ligand works against certain bacterial proteins. The Glide Hbond measures the quantity of hydrogen bonds formed during interactions between molecules and proteins [34]. The Van der Waals interaction number, often known as Glide Evdw [33], is another statistic that shows how chemicals and proteins interact. Additionally, a metric called Glide Ecoul is used to objectively evaluate the Coulomb interactions that occur between drugs and proteins. The Glide Einternal, a numerical value derived by integrating many components, is the last parameter derived from these computations [34].

Table 3. MM-GBSA parameter of molecule 4 with 4UYA protein

MMGBSA dG Bind	-31.79
MMGBSA dG Bind Coulomb	0.43
MMGBSA dG Bind Covalent	2.53
MMGBSA dG Bind Hbond	-0.95
MMGBSA dG Bind Lipo	-13.66
MMGBSA dG Bind Packing	-2.87
MMGBSA dG Bind Solv GB	0.00

MM-GBSA computations were used to ascertain the molecule's binding free energy values. The calculations revealed that the 4UYA protein and molecule 4 had the greatest negative docking score parameter. As a result, the energy values of molecule 4 against the 4UYA protein are shown in Table 3. According to the calculations, the binding free energy of molecule 4 among the 4UYA protein is -31.79. However, the obtained data showed that there were several interactions between the chemical and the protein. These interactions include the coulomb, covalent, Hbond, lipophilic, packing, SolvGB, and vdW interactions [35,36]. For example, the packing, lipophilic, and Hbond interactions seem to have a higher negative value.

Following an evaluation of the compounds' biological activity against various proteins, the ADME/T study was carried out to theoretically forecast the impacts and interactions of the most active molecules inside human metabolism [35]. Numerous factors were discovered throughout this theoretical investigation, as shown in Table 4.

ADME/T (Absorption, Distribution, Metabolism, Elimination/Toxicity) simulations utilizing Schrödinger Maestro software are crucial for evaluating the pharmacokinetic and toxicological properties of substances throughout the drug-development process. These simulations may be used to forecast how a potential chemical would behave in biological systems [36]. The Schrödinger program's QikProp module provides a comprehensive analysis of ADME/T parameters. Calculating and describing the following parameters is standard procedure. Molecular weight (MW) is a measure of a molecule's total atomic mass. A medication candidate is deemed successful according to Lipinski's "Rule of 5 [37]," if its molecular weight is fewer than 500 daltons. LogP (Hydrophobicity or Lipophilicity), which measures a molecule's lipophilicity, calculates the octanol/water partition coefficient. Potential toxicity or insufficient bioavailability may be indicated by both high and low LogP values. Generally speaking, a LogP number between 0 and 3 is optimal. Hydrogen Bond Donors and Acceptors (HBD/HBA) are the number of functional groups in a molecule that may create hydrogen bonds. The number of hydrogen bond donors (HBD) and hydrogen bond acceptors (HBA) affects a molecule's solubility and permeability across biological membranes.

Table 4. ADME properties of molecule

	1	2	3	4	5	6	7	8	Reference Range
mol_MW	358	342	370	363	346	373	400	370	130-725
dipole (D)	8.6	8.0	11.5	6.5	6.4	6.5	11.8	4.8	1.0-12.5
SASA	618	616	678	606	591	623	720	646	300-1000
FOSA	244	239	314	151	151	151	288	233	0-750
FISA	117	117	105	117	117	214	160	169	7-330
PISA	255	258	257	265	274	256	270	243	0-450
WPSA	2	2	2	73	49	2	2	2	0-175
volume (Å <sup>3</sup> )	1095	1080	1198	1064	1036	1094	1259	1141	500-2000
donorHB	0	0	0	0	0	0	0	0	0-6
accptHB	7.3	6.5	6.5	6.5	6.5	7.5	8.5	8.5	2.0-20.0
glob (Sphere =1)	0.8	0.8	0.8	0.8	0.8	0.8	0.8	0.8	0.75-0.95
QPpolrz (Å <sup>3</sup> )	37.5	37.6	41.7	37.0	36.0	37.5	43.6	39.3	13.0-70.0
QPlogPC16	11.0	10.9	11.9	11.3	10.3	11.7	13.0	11.7	4.0-18.0
QPlogPoct	17.1	16.7	18.6	16.6	16.1	17.3	20.6	18.0	8.0-35.0
QPlogPw	10.0	9.5	9.3	9.5	9.6	10.9	11.6	11.6	4.0-45.0
QPlogPo/w	2.4	2.7	3.5	2.9	2.6	1.6	2.6	1.7	-2.0-6.5
QPlogS	-3.6	-4.0	-5.0	-4.1	-3.7	-3.4	-4.6	-3.3	-6.5-0.5
CIQlogS	-4.3	-4.3	-4.9	-4.8	-4.4	-4.5	-4.7	-4.0	-6.5-0.5
QPlogHERG	-5.5	-5.6	-5.9	-5.5	-5.5	-5.6	-6.3	-5.6	*
QPPCaco (nm/sec)	772	772	1004	770	766	92	301	248	**
QPlogBB	-0.8	-0.8	-0.8	-0.6	-0.6	-1.8	-1.5	-1.4	-3.0-1.2
QPPMDCK (nm/sec)	383	382	508	939	684	38	138	112	**
QPlogKp	-2.4	-2.5	-2.2	-2.5	-2.4	-4.2	-3.0	-3.4	Kp in cm/hr
IP (ev)	9.0	9.0	9.0	9.1	9.1	9.4	9.2	9.2	7.9-10.5
EA (eV)	0.9	1.0	1.0	1.2	1.2	2.1	1.5	1.5	-0.9-1.7
#metab	2	2	2	1	1	2	1	1	1-8
QPlogKhsa	-0.3	-0.1	0.2	-0.2	-0.2	-0.4	-0.2	-0.5	-1.5-1.5
Human Oral Absorption	3	3	3	3	3	3	3	3	-
Percent Human Oral Absorp.	93	94	100	95	94	71	86	80	***
PSA	77	68	69	69	69	114	105	98	7-200
RuleOfFive	0	0	0	0	0	0	0	0	Maximum is 4
RuleOfThree	0	0	0	0	0	0	0	0	Maximum is 3
Jm	0.5	0.1	0.0	0.1	0.2	0.0	0.0	0.1	-

\* concern below -5, \*\*<25 is poor and >500 is great, \*\*\* <25% is poor and >80% is high.

In general, drug-like compounds should contain ten or less hydrogen bond acceptors (HBA) and five or fewer hydrogen bond donors (HBD) [1]. Total polar surface area, or TPSA, is the surface area of a molecule that is occupied by polar functional groups. TPSA is associated with the chemical's solubility and ability to cross biological membranes. Favorable bioavailability is indicated by a TPSA of less than 140 Å<sup>2</sup>. Aqueous Solubility (LogS) is a metric used to quantify a molecule's solubility in water. The LogS value affects the formulation processes and the bioavailability of the medication candidate [34-36].

Bioavailability is typically restricted for compounds with low solubility. Plasma protein binding, or PPB, is the proportion of a substance that binds to plasma proteins. The drug's efficacy and free concentration may be lowered by increased binding to plasma proteins. Blood-brain barrier permeability is the ability of a substance to permeate the blood-brain barrier. Increased BBB permeability is beneficial for drugs used to treat central nervous system problems, whereas lower BBB permeability may reduce toxicity in systemic treatment. Metabolic Stability: Predicts the rate at which a drug will be broken down by liver enzymes. The drug's half-life is extended and its therapeutic effectiveness is enhanced by increased metabolic stability [35]. Hepatotoxicity and

HERG Inhibition Toxicity Predictions: The possible cardiotoxicity of HERG channel inhibition is evaluated. The substance's potential for hepatotoxicity may be evaluated. The Caco-2 cell monolayer experiment replicates the translocation of a substance across the human intestinal epithelium. Increased Caco-2 permeability indicates better intestinal absorption. The absorption rate of a chemical predicts the proportion that will be absorbed when taken orally. A quick rate of absorption is an essential element of a successful pharmaceutical drug.

Lipinski's "Rule of Five" (RO5) is a guideline used to evaluate the pharmacological properties of a substance [38,39]. Determining the possibility that a chemical would have good oral bioavailability was the aim of these guidelines. The Rule of Five variables are Molecular Weight (MW), LogP, Hydrogen Bond Donors (HBD), and Hydrogen Bond Acceptors (HBA). The "Rule of Three" (RO3) is a criteria used in the pharmaceutical development process to identify lead molecules [40]. This rule, which is more stringent than RO5, focuses on the identification of low molecular weight, chemically simpler chemicals. For a molecule to be classified as a lead molecule under RO3, it must meet certain criteria. The Rule of Five includes the following criteria: Rotatable

Bonds, Hydrogen Bond Donors (HBD), Hydrogen Bond Acceptors (HBA), Molecular Weight (MW), and LogP. Since all parameters are expected to satisfy the criteria, the values of these two parameters are projected to be zero. Its calculations make it an essential tool for assessing toxicological risks at every stage of the drug development process. These simulations estimate the probability that a suggested chemical might negatively affect biological systems. Schrödinger, QikProp, and other modules are used to assess a range of toxicity parameters. The potassium ion channels known as HERG (Human Ether-à-go-go-Related Gene) channels regulate the electrical activity of cardiac myocytes. HERG Channel Inhibition (Cardiotoxicity) is the first parameter. Another criterion is blood-brain barrier (BBB) toxicity; drugs that can pass across the BBB may negatively impact the central nervous system [36]. Another measure is the substrate and inhibition of P-glycoprotein (P-gp). P-glycoprotein eliminates substances from cells, preventing dangerous accumulation.

## Conclusions

In the present study, a comprehensive in silico approach was employed to investigate the electronic structure, chemical reactivity, and biological interaction potential of a series of benzenesulfonamide derivatives against key protein targets associated with gastric cancer. Utilizing density functional theory (DFT)-based Gaussian calculations, critical quantum chemical descriptors—such as frontier molecular orbital energies, chemical potential, and electrophilicity index—were determined, providing insights into the electronic distribution and stability of the molecules. These parameters not only elucidate the molecules' potential sites for nucleophilic and electrophilic attack but also support their thermodynamic favorability and chemical robustness in biological systems. Complementing the theoretical evaluations, molecular docking simulations were conducted to explore the binding affinities and interaction patterns of the studied compounds with two relevant gastric cancer-related proteins (PDB IDs: 4BKX and 3MAX). The docking results revealed that several benzenesulfonamide derivatives formed energetically favorable and geometrically stable complexes within the active sites of the target proteins, primarily via hydrogen bonding, hydrophobic contacts, and  $\pi$ - $\pi$  stacking interactions. Notably, molecule 4 exhibited the most pronounced binding affinity toward the 4BKX protein with a docking score of -3.55, while molecule 8 demonstrated the highest affinity for the 3MAX protein, registering a docking score of -3.54. These results suggest that both molecules possess significant potential as lead structures for further optimization in gastric cancer drug discovery.

In addition to docking evaluations, ADME/T (Absorption, Distribution, Metabolism, Excretion, and Toxicity) predictions were performed using the QikProp module to assess the pharmacokinetic profiles and drug-likeness of the molecules. Although certain

pharmacokinetic parameters—specifically QPPCaco and QPPMDCK, which are indicators of intestinal and cellular permeability—were observed to exceed ideal threshold values, potentially indicating suboptimal membrane penetration or blood-brain barrier permeability, the compounds demonstrated compliance with Lipinski's Rule of Five and the Rule of Three. These findings suggest that despite certain limitations in absorption-related parameters, the overall physicochemical characteristics and drug-likeness profiles of the compounds support their viability as orally administrable therapeutic candidates.

In conclusion, this integrated computational study underscores the potential of benzenesulfonamide derivatives as structurally and electronically suitable agents for targeting gastric cancer-related proteins. The favorable binding profiles, chemical stability, and compliance with drug-likeness rules collectively support their advancement into further stages of preclinical evaluation. Moreover, the findings contribute to a broader understanding of the structural features that govern ligand-target interactions in gastric cancer and offer a valuable platform for the rational design of novel, targeted chemotherapeutic agents.

## Acknowledgments

The numerical calculations reported in this paper were fully/partially performed at TUBITAK ULAKBIM, High Performance and Grid Computing Center (TRUBA resources). This work was supported by the Scientific Research Project Fund of Sivas Cumhuriyet University (CUBAP) under the project number RGD-020.

## Conflicts of Interest

The author declare no competing financial interest or personal relationships.

## References

- [1] Acar Cevik U., Ünver H., Bostancı H. E., Tüzün B., Gedik N. İ., Kocyigit Ü. M., New hydrazone derivatives: synthesis, characterization, carbonic anhydrase I-II enzyme inhibition, anticancer activity and in silico studies. *Zeitschrift für Naturforschung C.*, (2025) (0) article in press.
- [2] Allah A. E. M. A., Mortada S., Tüzün B., Guerrab W., Qostal M., Mague J. T., Ramli Y., Novel Thiohydantoin Derivatives: Design, Synthesis, Spectroscopic Characterization, Crystal Structure, SAR, DFT, Molecular Docking, Pharmacological and Toxicological activities, *Journal of Molecular Structure*, (2025) 141995.
- [3] Karatas H., Kul İ. B., Aydın M., Tüzün B., Taslimi P., Kokbudak Z., Alzheimer's Disease Drug Design by Synthesis, Characterization, Enzyme Inhibition, In Silico, SAR Analysis and MM-GBSA Analysis of Schiff Bases Derivatives, *Korean Journal of Chemical Engineering*, (2025) 1-19.
- [4] Şahin İ., Çeşme M., Güngör Ö., Özgeriş F. B., Köse M., Tümer, New sulfonamide derivatives based on 1, 2, 3-triazoles: synthesis, in vitro biological activities and in silico

- studies, *Journal of Biomolecular Structure and Dynamics*, 42(9) (2024) 4782-4799.
- [5] Becke A.D., Density-functional thermochemistry. I. The effect of the exchange-only gradient correction, *The Journal of Chemical Physics*, 96(3) (1992) 2155-2160.
  - [6] Vautherin D., Brink D. T., Hartree-Fock calculations with Skyrme's interaction. I. Spherical nuclei, *Physical Review C*, 5(3) (1972) 626.
  - [7] Hohenstein E. G., Chill S. T., Sherrill C. D., Assessment of the performance of the M05- 2X and M06- 2X exchange-correlation functionals for noncovalent interactions in biomolecules, *Journal of Chemical Theory and Computation*, 4(12) (2008) 1996-2000.
  - [8] Bressi, J. C., Jennings, A. J., Skene, R., Wu, Y., Melkus, R., De Jong, R., ... & Gangloff, A. R. Exploration of the HDAC2 foot pocket: Synthesis and SAR of substituted N-(2-aminophenyl) benzamides, *Bioorganic & Medicinal Chemistry Letters*, 20(10) (2010) 3142-3145.
  - [9] Millard C. J., Watson P. J., Celardo I., Gordiyenko Y., Cowley S. M., Robinson C. V., Schwabe J. W., Class I HDACs share a common mechanism of regulation by inositol phosphates, *Molecular Cell*, 51(1) (2013) 57-67.
  - [10] Dennington R., Keith T. A., Millam J. M., GaussView 6.0. 16. Semichem Inc.: Shawnee Mission, KS, (2016) USA.
  - [11] Frisch M.J., Trucks G.W., Schlegel H.B., Scuseria G.E., Robb M.A., Cheeseman J.R., Scalmani G., Barone V., Mennucci B., Petersson G.A., Nakatsuji H., Caricato M., Li X., Hratchian H.P., Izmaylov A.F., Bloino J., Zheng G., Sonnenberg J.L., Hada M., Ehara M., Toyota K., Fukuda R., Hasegawa J., Ishida M., Nakajima T., Honda Y., Kitao O., Nakai H., Vreven T., Montgomery J.A., Peralta J.E., Ogliaro F., Bearpark M., Heyd J.J., Brothers E., Kudin K.N., Staroverov V.N., Kobayashi R., Normand J., Raghavachari K., Rendell A., Burant J.C., Iyengar S.S., Tomasi J., Cossi M., Rega N., Millam J.M., Klene M., Knox J.E., Cross J.B., Bakken V., Adamo C., Jaramillo J., Gomperts R., Stratmann R.E., Yazyev O., Austin A.J., Cammi R., Pomelli C., Ochterski J.W., Martin R.L., Morokuma K., Zakrzewski V.G., Voth G.A., Salvador P., Dannenberg J.J., Dapprich S., Daniels A.D., Farkas O., Foresman J.B., Ortiz J.V., Cioslowski J., Fox D.J. (2009) Gaussian 09, revision D.01. Gaussian Inc, Wallingford CT
  - [12] Medetalibeyoğlu H., Atalay A., Sağlamtaş R., Manap S., Ortaakarsu A. B., Ekinci E., Tüzün B., Synthesis, design, and cholinesterase inhibitory activity of novel 1, 2, 4-triazole Schiff bases: A combined experimental and computational approach, *International Journal of Biological Macromolecules*, 306 (2025) 141350.
  - [13] Akkus M., Kirici M., Poustforoosh A., Erdogan M. K., Gundogdu R., Tüzün B., Taslimi P., Phenolic Compounds: Investigating Their Anti-Carbonic Anhydrase, Anti-Cholinesterase, Anticancer, Anticholinergic, and Antiepileptic Properties Through Molecular Docking, MM-GBSA, and Dynamics Analyses, *Korean Journal of Chemical Engineering*, (2025) 1-20.
  - [14] Schrödinger Release 2022-4: Maestro, Schrödinger, LLC, New York, NY, 2022.
  - [15] Schrödinger Release 2022-4: Protein Preparation Wizard; Epik, Schrödinger, LLC, New York, NY, 2022; Impact, Schrödinger, LLC, New York, NY; Prime, Schrödinger, LLC, New York, NY, 2022
  - [16] Schrödinger Release 2022-4: LigPrep, Schrödinger, LLC, New York, NY, 2022.
  - [17] Shahzadi I., Zahoor A. F., Tüzün B., Mansha A., Anjum M. N., Rasul A., Mojzych M., Repositioning of acefylline as anti-cancer drug: Synthesis, anticancer and computational studies of azomethines derived from acefylline tethered 4-amino-3-mercapto-1, 2, 4-triazole, *Plos One*, 17(12) (2022) e0278027.
  - [18] El Faydy M., Lakhrissi L., Dahaieh N., Ounine K., Tüzün B., Chahboun N., Zarrouk A. Synthesis, Biological Properties, and Molecular Docking Study of Novel 1, 2, 3-Triazole-8-quinolinol Hybrids, *ACS omega*, 9(23) (2024) 25395–25409.
  - [19] Schrödinger Release 2022-4: QikProp, Schrödinger, LLC, New York, NY, 2022.
  - [20] Ullah N., Alam A., Tüzün B., Rehman N. U., Ayaz M., Elhenawy A. A., Ahmad M., Synthesis of novel thiazole derivatives containing 3-methylthiophene carbaldehyde as potent anti  $\alpha$ -glucosidase agents: In vitro evaluation, molecular docking, dynamics, MM-GBSA, and DFT studies. *Journal of Molecular Structure*, 1321 (2025) 140070.
  - [21] Yalazan H., Koç D., Aydın Kose F., Fandaklı S., Tüzün B., Akgül, M. İ, Kantekin H. Design, syntheses, theoretical calculations, MM-GBSA, potential anti-cancer and enzyme activities of novel Schiff base compounds, *Journal of Biomolecular Structure and Dynamics*, 42(23) (2024) 13100-13113.
  - [22] Manap S., Medetalibeyoğlu H., Kılıç A., Karataş O. F., Tüzün B., Alkan M., Yüksek H., Synthesis, molecular modeling investigation, molecular dynamic and ADME prediction of some novel Mannich bases derived from 1, 2, 4-triazole, and assessment of their anticancer activity, *Journal of Biomolecular Structure and Dynamics*, 42(21) (2024) 11916-11930.
  - [23] Rafik A., Tuzun B., Zouihri H., Poustforoosh A., Hssissou R., Elhenaey A. A., Guedira T., Morphology studies, optic proprieties, hirschfeld electrostatic potential mapping, docking molecular anti-inflammatory, and dynamic molecular approaches of hybrid phosphate, *Journal of the Indian Chemical Society*, 101(11) (2024) 101419.
  - [24] Barghady N., Assou S. A., Er-Rajy M., Boujdi K., Arzine A., Rhazi Y., El Yazidi M., Design, synthesis, characterization, and theoretical calculations, along with in silico and in vitro antimicrobial proprieties of new isoxazole-amide conjugates, *Open Chemistry*, 22(1) (2024) 20240109.
  - [25] Schrader T., Khanifaev J., Perl E., Koopmans' theorem for acidic protons, *Chemical Communications*, 59(93) (2023) 13839-13842.
  - [26] Phillips J. C., Generalized Koopmans' Theorem., *Physical Review*, 123(2) (1961) 420.
  - [27] Pearson R. G., Hard and soft acids and bases, *Journal of the American Chemical Society*, 85(22) (1963) 3533-3539.
  - [28] Pearson R. G., Hard and soft acids and bases, *Journal Of The American Chemical Society*, 85(22) (1963) 3533-3539.
  - [29] Ayers P. W., An elementary derivation of the hard/soft-acid/base principle, *The Journal of Chemical Physics*, 122(14) (2005).
  - [30] Parr R. G., Chattaraj P. K., Principle of Maximum Hardness, *Journal of the American Chemical Society*, 113(5) (1991) 1854-1855.
  - [31] Goswami A. K., Aboul-Soud M. A., Gogoi N., El-Shazly M., Giesy J. P., Tüzün B., Sharma H. K., Integrative in silico evaluation of the antiviral potential of terpenoids and its metal complexes derived from Homalomena aromatica based on main protease of SARS-CoV-2, *Open Chemistry*, 22(1) (2024) 20240085.
  - [32] Medetalibeyoğlu H., Manap S., Alkan M., Beytur M., Barlak N., Karatas O. F., Taslimi P., Novel Schiff Bases: Synthesis, characterization, bioactivity, cytotoxicity, and computational evaluations, *Polycyclic Aromatic Compounds*, (2024) 1-19.



- [33] Tapera M., Kekeçmuhammed H., Tüzün B., Daştan S. D., Çelik M. S., Taslimi P., Sarıpınar E., Novel 1, 2, 4-triazole-maleamic acid derivatives: Synthesis and evaluation as anticancer agents with carbonic anhydrase inhibitory activity, *Journal of Molecular Structure*, 1313 (2024) 138680.
- [34] Alishba Ali I., Hameed S., Khan K. M., Salar U., Taha M., Ulukaya E., Exploring Benzo [b][1, 4] Thiazine Derivatives: Multitarget Inhibition, Structure–Activity Relationship, Molecular Docking, and ADMET Analysis, *ChemistrySelect*, 9(38) (2024) e202404087.
- [35] Belkheiri A., Dahmani K., Mzioud K., Rbaa M., Galai M., Hmada A., Al-Maswar, B. M., Advanced evaluation of novel quinoline derivatives for corrosion inhibition of mild steel in acidic environments: A comprehensive electrochemical, computational, and surface study, *International Journal of Electrochemical Science*, 19(10) (2024) 100772.
- [36] Çelik M. S., Kütük N., Yenidünya A. F., Çetinkaya S., Tüzün B., Removal of safranin O from wastewater using *Streptomyces griseobrunneus* dead biomass and in silico calculations, *Biomass Conversion and Biorefinery*, 14(20) (2024) 25873-25884.
- [37] Zahirović A., Fočak M., Fetahović S., Tüzün B., Višnjevac A., Muzika V., Roca S., Hydrazone-flavonol based oxidovanadium (V) complexes: Synthesis, characterization and antihyperglycemic activity of chloro derivative in vivo, *Journal of Inorganic Biochemistry*, 258 (2024) 112637.
- [38] Lipinski C. A., Lead-and drug-like compounds: the rule-of-five revolution, *Drug Discovery Today: Technologies*, 1(4) (2004) 337-341.
- [39] Lipinski C. A., Lombardo F., Dominy B. W., Feeney P. J., Experimental and computational approaches to estimate solubility and permeability in drug discovery and development settings, *Advanced Drug Delivery Reviews*, 23 (1997) 3-25.
- [40] Jorgensen W.J., Duffy E.M., Prediction of drug solubility from structure, *Advanced Drug Delivery Reviews*, 54(3) (2002) 355-366.

## Network Pharmacology-Based Approach to Unveil the Therapeutic Mechanism of *Viburnum opulus* L. on Glomerulonephritis

Şeyda Kaya<sup>1,a,\*</sup>, Sevgi Durna Daştan<sup>2,b</sup>

<sup>1</sup> Department of Biology, Institute of Science, Sivas Cumhuriyet University, Sivas, Türkiye

<sup>2</sup> Department of Biology, Faculty of Science, Sivas Cumhuriyet University, Sivas, Türkiye

\*Corresponding author

### Research Article

#### History

Received: 04/04/2025

Accepted: 28/05/2025



This article is licensed under a Creative Commons Attribution-NonCommercial 4.0 International License (CC BY-NC 4.0)

### ABSTRACT

This study aimed to investigate the potential targets and pathways of the bioactive compounds of *Viburnum opulus* L. – a plant recognized in ethnopharmacology for its therapeutic applications in renal disorders - on glomerulonephritis (GN) disease. The phytochemical profile of *V. opulus* was obtained from review articles in the literature on plant contents. GN-associated target genes were retrieved from the GeneCards database, and interaction mapping was conducted using Cytoscape 3.10.0. The intersection of compound - target - disease was imported into the STRING database to create a PPI network. GO and KEGG enrichment analyses were applied to define the biological functions of the targets. A molecular docking study simulated the binding capabilities of key targets and active ingredients. A total of 9 bioactive constituents were identified from *V. opulus*, with rutin and quercetin demonstrating the highest binding affinities. The resulting compound–target interaction network consisted of 125 nodes and 358 edges. Central hub proteins within the PPI network included TP53, SRC, and EGFR indicating their potential role in the mechanism of action. GO and KEGG analyses suggested that the treatment of GN by *V. opulus* mainly involves the generation of cellular response to chemical and oxidative stress, protein tyrosine kinase activity, transcription regulatory complex, and other biological processes. The results of KEGG enrichment analysis indicate that *V. opulus* mainly involves some pathways, such as chemical carcinogenesis-receptor activation, EGFR tyrosine kinase inhibitor resistance in the treatment of GN. Molecular docking data presented that rutin and quercetin have the highest affinity score with TP53, SRC, and EGFR proteins. Overall, this study reveals the active compounds and potential molecular pathways of *V. opulus* in the treatment of GN and presents a source for further basic studies.

**Keywords:** *Viburnum opulus*, Glomerulonephritis, Network pharmacology, Molecular docking.

<sup>a</sup> [sydkaya58@gmail.com](mailto:sydkaya58@gmail.com)

<sup>b</sup> <https://orcid.org/0000-0001-8489-8687>

<sup>c</sup> [sdurna@cumhuriyet.edu.tr](mailto:sdurna@cumhuriyet.edu.tr)

<sup>d</sup> <https://orcid.org/0009-0003-8565-6841>

## Introduction

The kidneys play a crucial role in filtering metabolic waste from the body. The microscopic building blocks in its structure are called glomeruli [1]. Glomerulonephritis (GN) is a disease that causes impaired kidney function as a result of inflammation of the glomeruli [2]. It is important to produce an effective drug for the treatment of GN.

Ethnopharmacology is the science of using traditional medicines and practices derived from plants for healing purposes. Ethnobotanical studies have been utilised to develop a safe method for many diseases with the therapeutic properties of plants from ancient times to the present day [3].

*Viburnum opulus* L. is a plant in the Adoxaceae family, interesting for both its decorative and medicinal uses, known colloquially as gilaburu, guelder rose, European cranberrybush, and is widespread in Europe, Russia, North Africa, and North Asia. *V. opulus* is traditionally preferred in the treatment of many diseases such as colds, coughs,

tuberculosis, rheumatic pains, ulcers, stomach and kidney ailments [4].

Network pharmacology is a modern approach to understanding drug targets, mechanisms of action and side effect profiles by analysing the complex interactions of biological systems [5]. In contrast to the traditional single-target focus of pharmacology, network-based approaches recognise that a drug can interact with many biomolecules and cellular pathways. This method aims to systematically study drug-gene, drug-protein, and drug-disease relationships using bioinformatics, systems biology, computational modelling and data mining techniques [6]. In particular, multi-targeted drug design has great potential in the areas of better understanding of disease mechanisms and personalised medicine [5]. In recent years, herbal medicines have emerged as an important research area for polypharmacological strategies.

Molecular docking is a computational method used to imagine how a ligand (drug candidate molecule) binds to a target protein. This technique is of great importance, especially in drug discovery, analysis of protein-ligand interactions, and elucidation of biomolecular mechanisms. Molecular docking helps to determine the optimal conformation and affinity by assessing the binding site, interaction energy, and stability [7].

In this research, we aimed to determine the therapeutic qualities of *V. opulus* in the treatment of GN using network pharmacology and molecular docking approaches. By using in silico analysis to investigate the bioactive contents and molecular mechanisms of *V. opulus* in GN treatment, it was aimed to provide useful data for further research.

## Materials and Methods

### Network Analysis

The active compounds belonging to *V. opulus* plant are arranged and given in Table 1 from the articles in the literature in which the contents of the plant were determined by using various extraction methods and chromatographic techniques [4,8]. GN disease targets were obtained by searching associated genes in GeneCards (<https://www.genecards.org/>) with the keyword 'glomerulonephritis' [9]. Target genes of *V. opulus* were obtained from the SwissTargetPrediction (<http://www.swisstargetprediction.ch/>) database [10]. Potentially active components of *V. opulus* and their matching targets were loaded into Cytoscape 3.10.0, and a network model including GN components and targets was created [11] (Figure 1). The jvenn database was used to find the intersection of the active ingredients in the plant and the overlapping targets of GN (<http://www.bioinformatics.com.cn/static/others/jvenn/example.html>) [12]. In order to obtain information about the protein interaction network of genes intersecting *V. opulus* and GN, it was transferred to the STRING (<https://string-db.org/>) database and analysed by identifying the species as 'homo sapiens' [13]. Protein-protein interaction (PPI) data were analysed, then target nodes with BC and CC degree scores above the median values in the PPI network were identified and 10 potential

core targets were chosen for further analysis. Within the scope of gene ontology (GO) analysis, Metascape (<https://metascape.org/gp/index.html#/main/step1>) tool was used for the evaluation of Kyoto Encyclopedia of Genes and Genomes (KEGG) pathways together with cellular components (CC), molecular functions (MF) and biological processes (BP) and SRPLOT (<https://www.bioinformatics.com.cn/srplot>) was used for visualisation [14,15].

### Molecular Docking

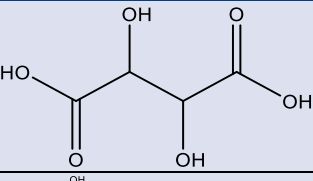
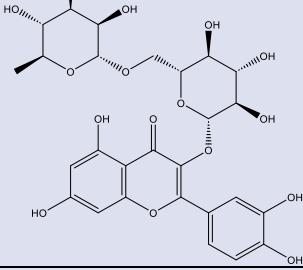
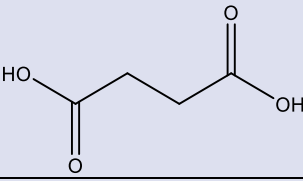
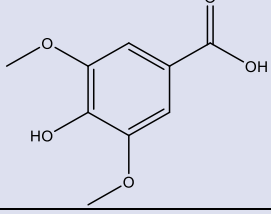
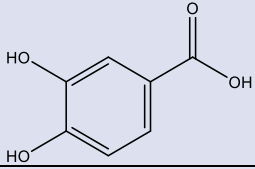
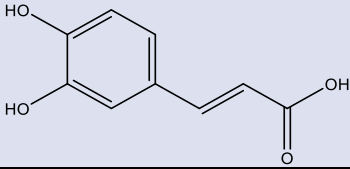
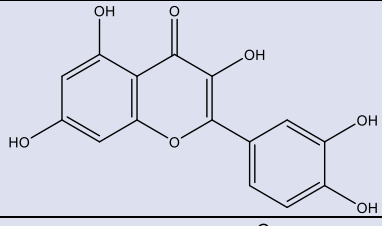
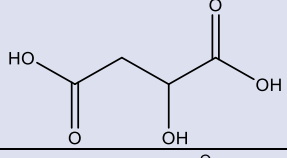
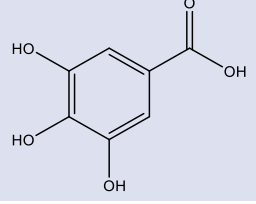
For the molecular docking study, which examines the binding of two molecules (receptor–ligand) and is frequently used in the fields of structural biology and drug design, the three-dimensional (3D) structure of the target protein was obtained from the RCSB PDB database (<http://www.rcsb.org/>) [16]. The three-dimensional (3D) molecular structures of the 9 ligands identified in the plant content were obtained from the PubChem database (<https://pubchem.ncbi.nlm.nih.gov/>) [17]. Ligand binding model and interaction analysis were performed using the Maestro Schrödinger package software. Since the receptors obtained from the PDB database were not suitable for direct docking calculations, they were subjected to a structural optimisation process. In this process, hydrogen atoms were added to the receptor, partial charges were assigned, and the missing loops in the chains were completed. Water molecules within 3 Å (Angstrom) of the binding site in the crystal structure were removed from the system. In order to model the receptor and ligand interaction in accordance with biological conditions, the system was minimised at pH 7.4, and ligands were prepared at the same pH conditions [18].

## Results

The molecular structures and IUPAC names of the 9 active components organised according to the literature are taken from Pubchem and given in Table 1 [4,8,17].

The network between the active compounds in *V. opulus* and GN is represented by a node. The relationship between the component and the target is represented by a connecting line. As shown in Figure 1, there are 125 nodes and 358 edges.

Table 1. Potential active compounds of *V. opulus* [4,8,17].

Compound	Molecular Structure	IUPAC Name
Tartaric acid		(2R,3R)-2,3-dihydroxybutanedioic acid
Rutin		2-(3,4-dihydroxyphenyl)-5,7-dihydroxy-3- [[2S,3R,4S,5S,6R]-3,4,5-trihydroxy-6- [[[(2R,3R,4R,5R,6S)-3,4,5-trihydroxy-6-methyloxan- 2-yl]oxymethyl]oxan-2-yl]oxychromen-4-one
Succinic acid		butanedioic acid
Syringic acid		4-hydroxy-3,5-dimethoxybenzoic acid
Protocatechuic acid		3,4-dihydroxybenzoic acid
Caffeic acid		(E)-3-(3,4-dihydroxyphenyl)prop-2-enoic acid
Quercetin		2-(3,4-dihydroxyphenyl)-3,5,7-trihydroxychromen- 4-one
Malic acid		2-hydroxybutanedioic acid
Gallic acid		3,4,5-trihydroxybenzoic acid



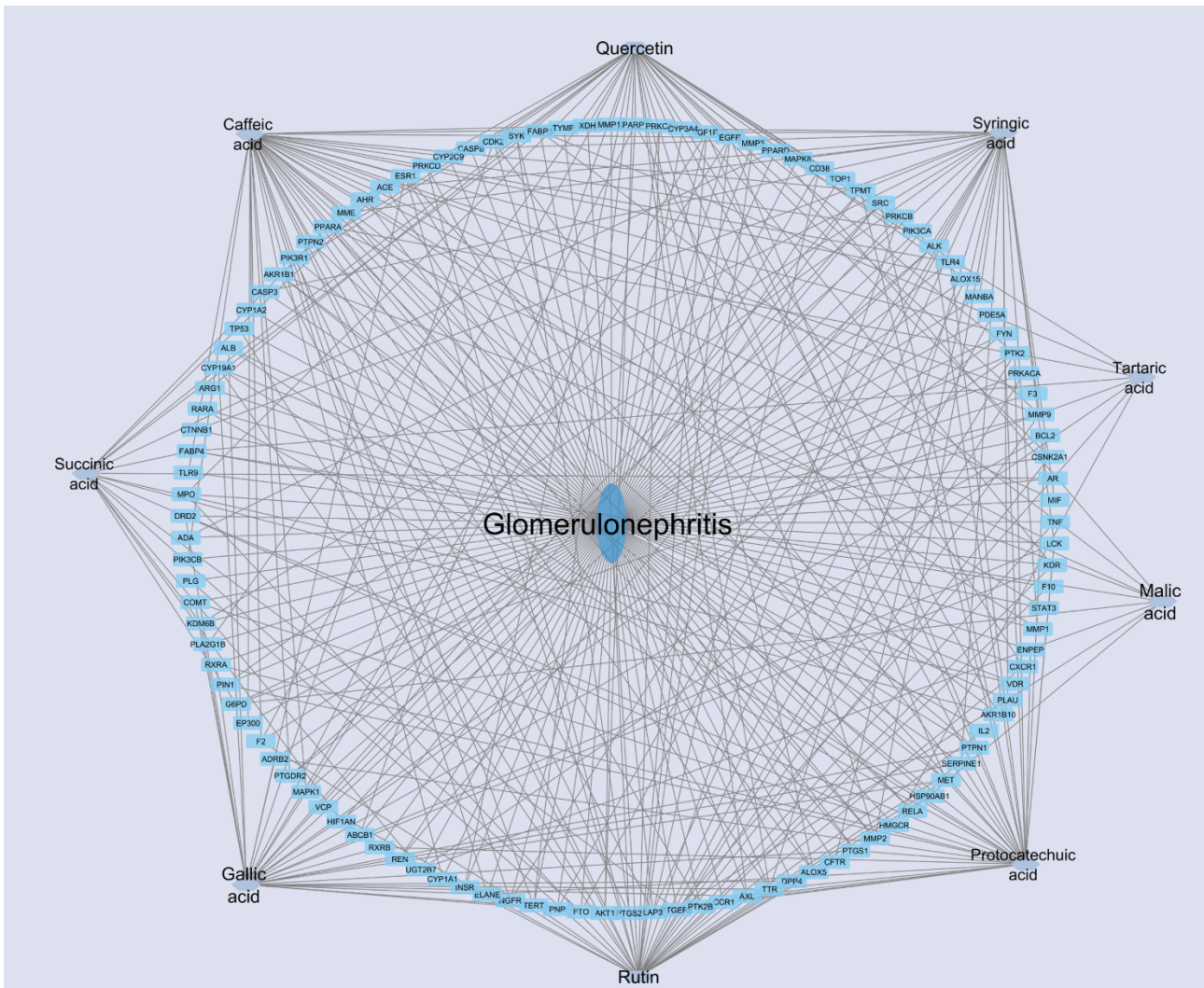


Figure 1. Bioactive compounds and corresponding targets network of *V. opulus* of GN. The ellipse in the centre represents the disease. Hexagons represent 9 phytochemical compounds. Blue rectangles represent 358 potential target genes of *V. opulus*.

When looking at the Venn diagram results, there are 114 common targets between *V. opulus* targets and GN disorder targets (Figure 2).

The protein-protein interaction (PPI) network was analysed by transferring the drug-disease intersection genes to the STRING database and as a result, an interaction network containing 106 nodes and 581 edges was created (Figure 3).

The degree values of the first ten targets were evaluated according to DC (Degree Centrality), BC (Betweenness Centrality) and CC (Closeness Centrality) criteria as shown in Table 2. As a result of this analysis, the top 10 proteins were TP53, SRC, EGFR, STAT3, CTNNB1, TNF, AKT1, BCL2, PTGS2 and ESR1 (Figure 3).

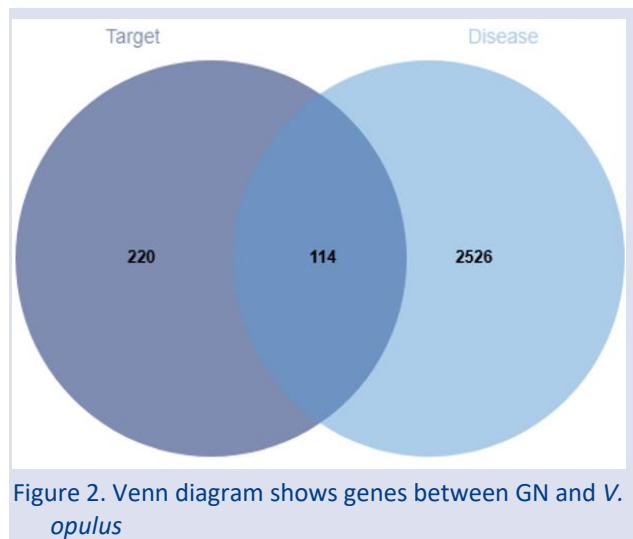


Figure 2. Venn diagram shows genes between GN and *V. opulus*

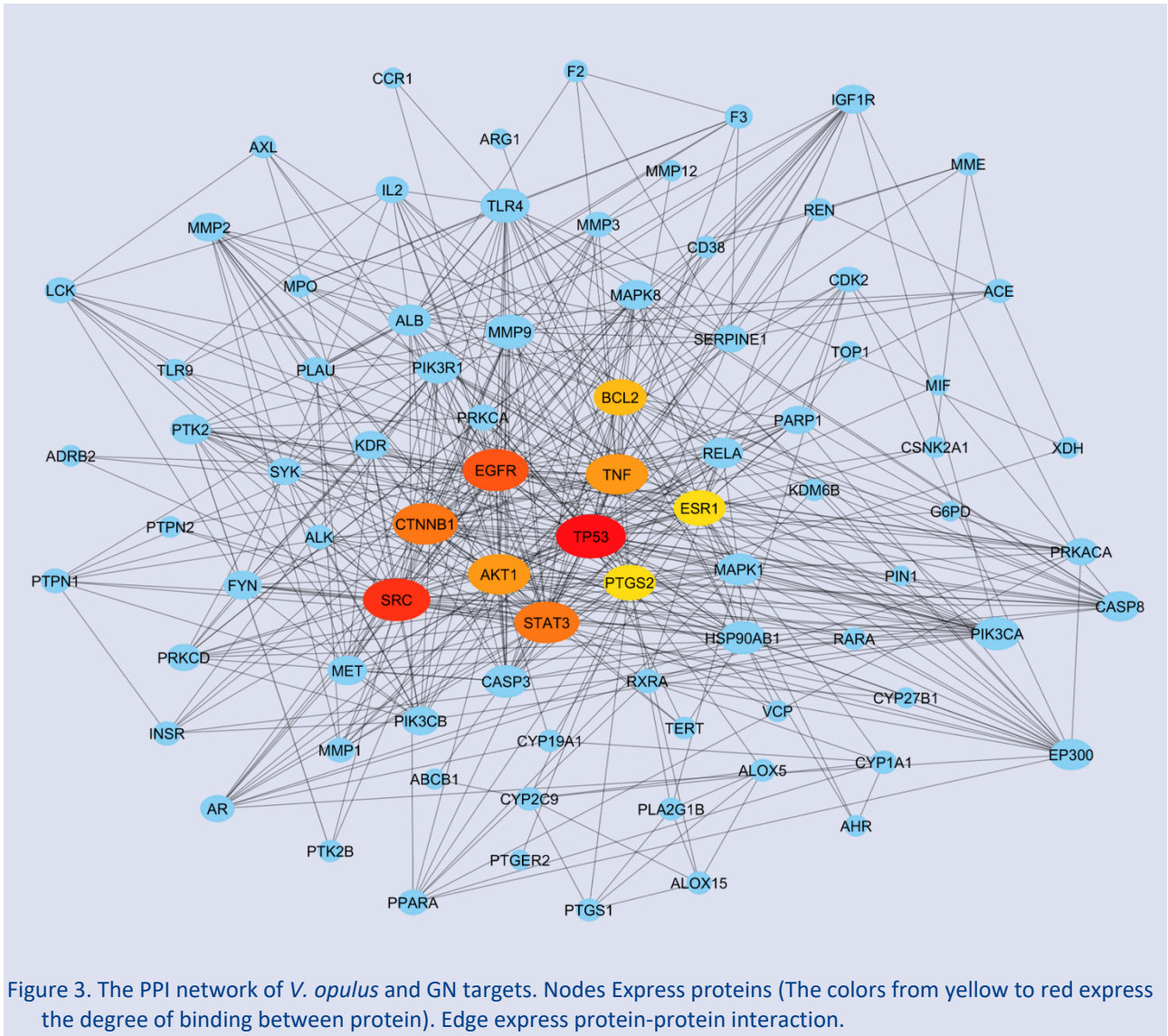


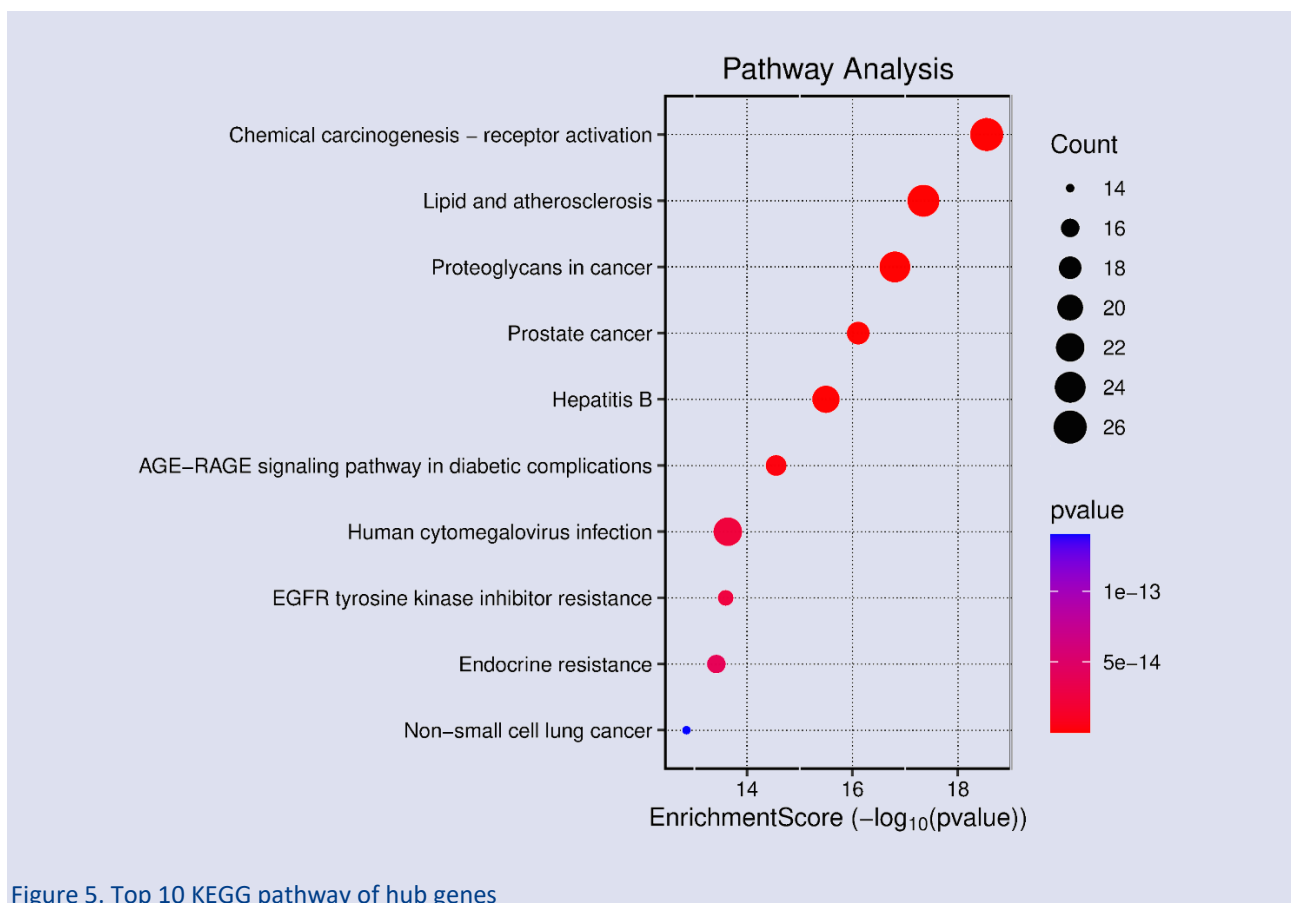
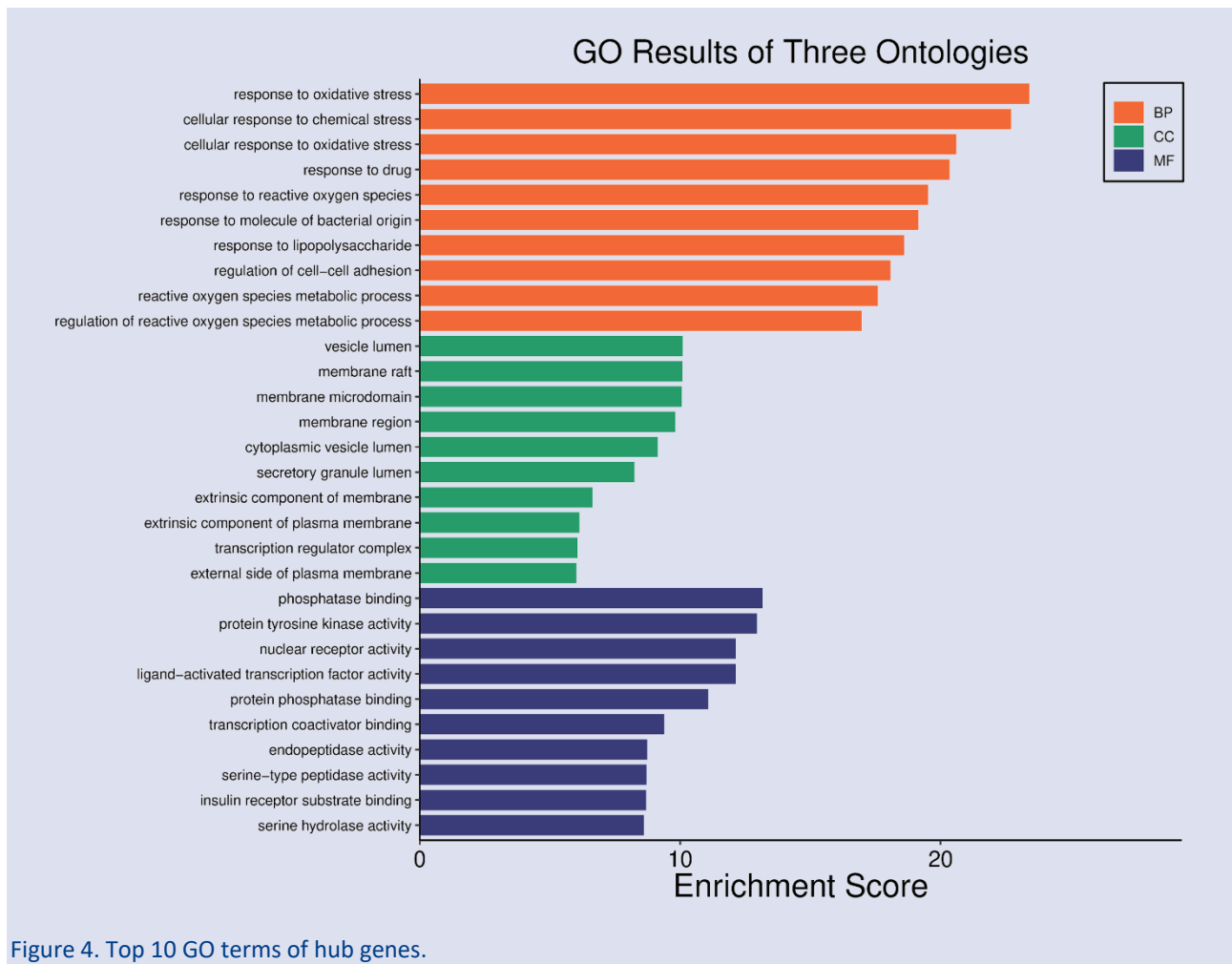
Figure 3. The PPI network of *V. opulus* and GN targets. Nodes Express proteins (The colors from yellow to red express the degree of binding between protein). Edge express protein-protein interaction.

Table 2. Some data on attributes of the top 10 target according to the degree value.

Name	Score	Betweenness Centrality	Closeness Centrality
TP53	40	0.12813816862591176	0.5706521739130435
SRC	38	0.06527801831039313	0.5440414507772021
EGFR	37	0.05731073423629428	0.5614973262032086
STAT3	36	0.07122806909889566	0.5497382198952879
CTNNB1	36	0.054655771432631	0.5614973262032086
TNF	34	0.10591636291065458	0.5585106382978723
AKT1	34	0.05521460279319312	0.5585106382978723
BCL2	27	0.02951844026402951	0.5329949238578681
PTGS2	26	0.03372253267195596	0.525
ESR1	26	0.05514466457790829	0.5147058823529412

The 114 intersection targets obtained were mapped to their biological processes (BP), GO molecular functions (MF) and cellular components (CC) through the Metascape database and SRPLOT was used for visualisation. The first 30 items were selected from the

terms obtained by GO analysis. As shown in Figure 4, GO (Gene Ontology) analysis shows the enrichment scores of genes under three different ontology categories (BP: Biological Process, CC: Cellular Component, MF: Molecular Function). In the BP category, oxidative stress response, chemical stress response, response to drugs and response to reactive oxygen species are the most enriched biological processes. In the CC category, vesicle lumen, membrane microdomains and extrinsic membrane components are the most prominent cellular components. In the MF category, protein tyrosine kinase activity, phosphatase binding, transcription coactivator binding and serine-type peptidase activity are the most enriched molecular functions. Figure 5 reveals that biological pathways associated with cancer, metabolic diseases and infections were enriched, with the most significant pathways being chemical carcinogenesis, lipid metabolism and cancer-related processes, with bubble size indicating the number of genes and colour scale indicating statistical significance.





According to the molecular docking informations presented in Table 3 and Table 4, among the 9 active compounds in the plant, rutin and quercetin are the compounds with the best docking score with genes. It is

seen that these compounds belonging to the flavonoid group have the lowest binding energy (highest binding affinity) compared to other compounds.

Table 3. Molecular docking results of rutin

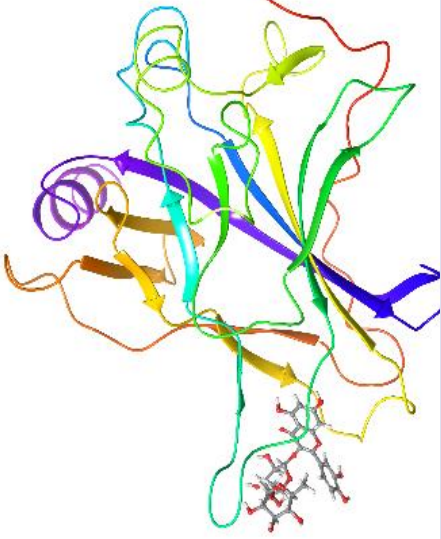
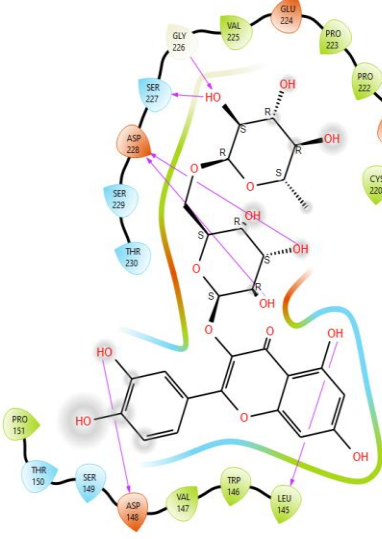
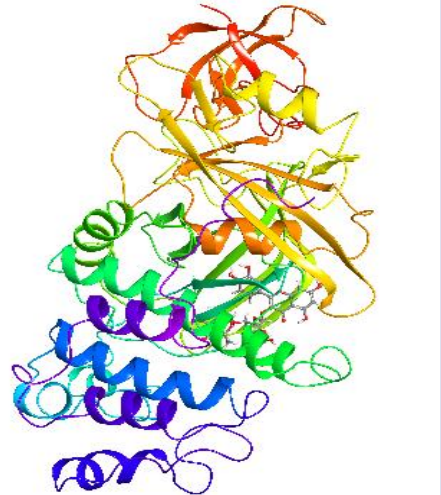
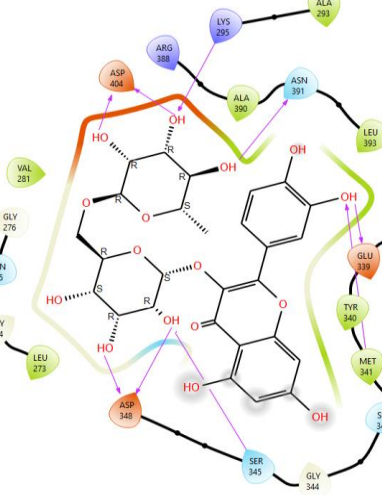

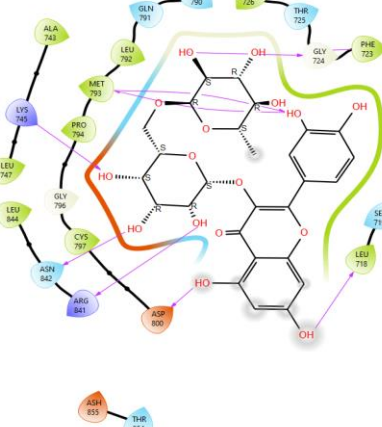
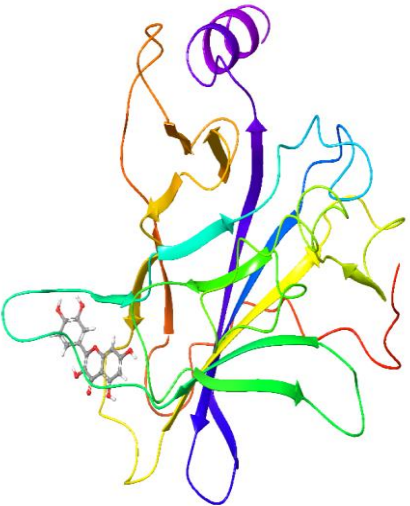
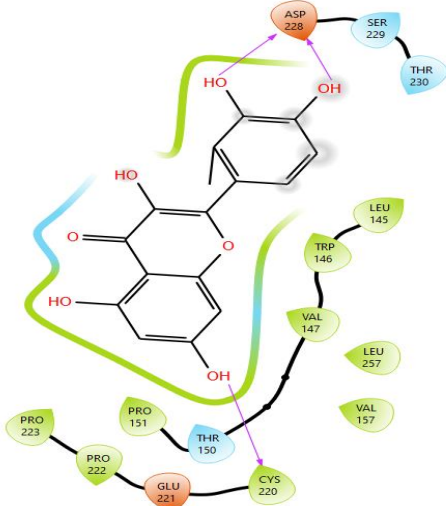

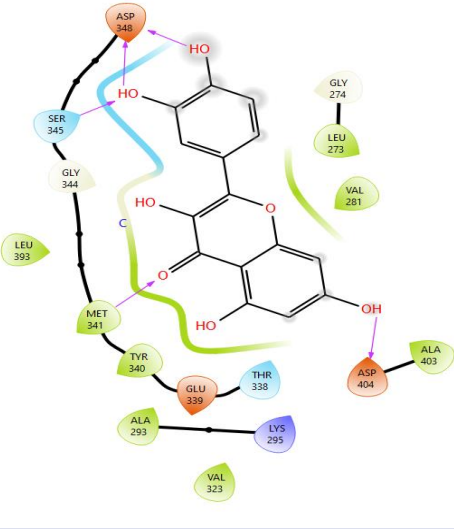

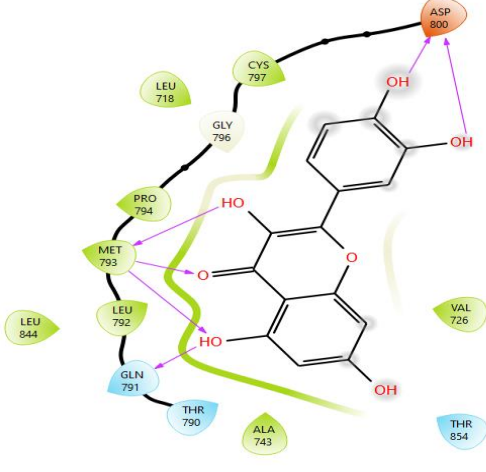
Target	3D Structure	2D Structure	Docking Score
TP53 (8DC7) - Rutin			-7.862
SRC (1A07) - Rutin			-9.939
EGFR - (2ITN) Rutin			-9.153



Table 4. Molecular docking results of quercetin

Target	3D Structure	2D Structure	Docking Score
TP53 (8DC7) - Quercetin			-6.021
SRC (1A07) - Quercetin			-7.719
EGFR (2ITN) - Quercetin			-8.625

Molecular docking consequences showed that rutin and quercetin can interact well with TP53, SRC and EGFR proteins. Rutin formed 2 hydrogen bonds with amino acid ASP228 and one hydrogen bond with amino acids ASP148, LEU145, GLY226, SER227 in TP53 protein. The molecular

docking score was determined as -7,862 kcal/mol. Rutin formed two hydrogen bonds at positions ASP348 and ASP404 and one hydrogen bond at positions LYS295, GLU339, MET341, SER345, ASN391 in SRC protein. The molecular docking score was determined as -9.939

kcal/mol. In EGFR protein, rutin formed a hydrogen bond with the amino acids MET793, GLY724, PHE723, LEU718, ASP800, ARG841, ASN842, LYS745. The molecular docking score was determined as -9.153 kcal/mol.

Quercetin created 2 hydrogen bonds with ASP228 amino acid and one hydrogen bond with CYS220 amino acid in its interaction with TP53 protein. The molecular docking score was determined as -6,021 kcal/mol. Quercetin created two hydrogen bonds with amino acid ASP348 and one hydrogen bond with amino acids SER345, MET341, ASP404 in its interaction with SRC protein. The molecular docking score was determined as -7,719 kcal/mol. Quercetin formed three hydrogen bonds with amino acid MET793, two hydrogen bonds with amino acid ASP800 and one hydrogen bond with amino acid GLN791 in its interaction with EGFR protein. The molecular docking score was determined as -8.625 kcal/mol.

In molecular docking studies, the affinity between receptor and ligand is stronger if the binding energy is lower than -5 kcal/mol [19]. Accordingly to the molecular docking results we obtained, the binding energies show that all of them are lower than -5 kcal/mol. The lowest binding energy is between SRC and rutin (-9.939 kcal/mol), while the docking of TP53 and quercetin has the highest binding energy (-6.021 kcal/mol).

Rutin and quercetin connect well to three key targets (TP53, SRC and EGFR) and based on this, we guess that these bioactive ingredients may act an important role in the treatment of GN.

## Discussion

The incidence of kidney diseases, one of the most common chronic diseases on a global scale, is gradually increasing, and this situation is considered an important issue in the field of health [20]. GN is a condition of damage to the glomeruli caused by acute or chronic inflammation, and this process can affect each of the basement membrane, mesenchyme, and capillary endothelium that make up the glomerular structure [2]. Studies have shown that *V. opulus*, which is popularly used to reduce kidney stones, can be used as an important non-invasive herbal treatment method that facilitates the passage of ureteral stones. In various experimental studies, it has been explained that *V. opulus* facilitates the passage of <10 mm ureteral stones and can be used as an alternative herbal treatment material [21]. In this research, the goal was to determine the potential molecular mechanism of *V. opulus* plant by network pharmacology and molecular docking applications to have information about its therapeutic properties in GN disease.

Using both papers by Polka et al. (2019) and Kajszyk et al. (2020), 9 chemical constituents with common intersections were compiled [4,8]. These 9 chemical components can be divided into groups as organic acids (tartaric acid, succinic acid, malic acid), phenolic acids (gallic acid, syringic protocatechuic acid, caffeic acid), and flavonoids (rutin-quercetin). The human immune system

secretes various pro-inflammatory mediators, contributing to the activation and recruitment of immune cells. However, excessive production of these components can lead to the development of different chronic diseases [22]. Phenolic compounds, which are known to have many protective properties for living organisms, can show their anti-inflammatory effects by inhibiting the production or activity of pro-inflammatory mediators that are overproduced in the organism [23]. Flavonoids, also commonly known as hydroxylated polyphenols, have many properties (analgesic, anti-proliferative, antioxidant, anticancer, anti-angiogenic, anti-microbial, anti-inflammatory, anti-viral, and anti-malarial) [24–26]. In a research on the protective effect of quercetin on sepsis-induced lung damage, it was observed that quercetin can reduce the amount of ROS in the lung tissue of rats with sepsis, increase SOD, APX and CAT activities, and reduce the expression of study-related (HMGB1) protein [27]. In addition, it was found that quercetin regulates the effect of reducing inflammation and oxidative stress by down-regulating the expression of Toll-like receptor protein [28]. According to these findings, it is promising that these 9 different bioactive components may have therapeutic effects in the treatment of GN, but further research is needed.

In this study, through the PPI network containing 114 common genes, the top 10 core genes with high ranking value were obtained, namely TP53, SRC, EGFR, STAT3, CTNNB1, TNF, AKT1, BCL2, PTGS2, and ESR1 genes. TP53 is a tumour suppressor gene and has an essential role in vital reactions such as controlling the cell cycle, responding to DNA disorders, and apoptosis (programmed cell death). TNF- $\alpha$  has an effect on inflammation in serum levels [29,30].

On the other hand, within the scope of this study, GO and KEGG enrichment applications were applied to investigate the mechanism of action of *V. opulus* in GN treatment. GO results expressed that the target genes were mainly took part in regulation of oxidative stress response, generation of cellular response to chemical and oxidative stress, regulation of drug response, regulation of secretory granule lumen, activation of transcription regulatory complex and external part of plasma membrane, tyrosine kinase activity, phosphatase binding, ligand-activation of transcription factors, transcription coactivator binding, serine-type peptidase and hydrolase activity.

The results of KEGG enrichment analysis indicate that *V. opulus* in GN treatment mainly involves some pathways, such as EGFR tyrosine kinase inhibitor resistance, chemical carcinogenesis-receptor activation. Dysregulation or abnormal activation of receptor tyrosine kinases (RTKs) has compensatory functions against EGFR inhibition. Currently, many clinical trials are underway intending to solve and prevent TKIs resistance in various inflammatory conditions and cancers. The EGFR-TKIs offer a promising first-line strategy for further clinical events in inflammatory diseases [31].

Rapidly progressive glomerulonephritis (RPGN) is a disease characterised by quick loss of renal function with the lesions in the glomeruli, accumulation of proliferation of intrinsic glomerular cells. Nowadays, a link between the HB-EGF-EGFR pathway and RPGN in a mouse model of nephritis has been described. However, HB-EGF-deficient mice were found to show EGFR phosphorylation and were resistant against RPGN. The inhibition pharmacologically of EGFR has been shown to effectively reduce glomerular damage and ameliorate acute renal failure in this animal model [32]. Future studies are needed to further investigate the role of HB-EGF and EGFR in the pathogenesis of GN. Recent studies have shown that EGFR activation also play a role in to the many renal diseases. like GN. In this case, the indication that *V. opulus* may be effective as an EGFR tyrosine kinase inhibitor in the treatment of GN suggests that the use of this plant in the treatment of GN may be promising for clinical applications [33].

Chen et al. (2012) reported that when SRC activation is induced, it mediates sustained EGFR phosphorylation and TGF- $\beta$  expression. [34]. These data suggest that SRC is a important factor of renal fibrosis. Another study presented that activation of c-Src is consistent with the mesangial proliferation in GN [35]. Jalal and Kone (2006) showed that SRC activates the NF- $\kappa$ B in GN and inflammatory host responses [36]. Since mesangial cell proliferation is the defining mechanism in GN, these results suggest that c-Src is critically involved in the pathogenesis of this disease. In addition, Gruden et al. (2003) suggested that SRC is involved in the insulin-like growth factor-induced production of VEGF (vascular endothelial cell growth factor), which is involved in the pathogenesis of early renal impairment in diabetes [37]. Wu et al. (2015) revealed in their study that inhibition of SRC by PP2 caused a decrease in Bax-Bcl-2 and caspase-3 levels in the kidneys of diabetic mice [38]. Some common pathological changes, such as activation of renal fibroblasts and inflammation, are regulated by SRC Family Kinases (SFKs). Therefore, knocking out one SFK may not be sufficient to prevent pathological effects. Therefore, with the combined use of highly selective inhibitors and gene silencing techniques, further studies are necessary to explain clearly the relative participation of SFK members in pathologies [39].

p53, an important part of defence mechanisms against DNA damage, is a critical protein that prevents tumour formation by regulating repair processes, limiting cellular growth, and inducing apoptosis when necessary [40]. Although the role of p53 in tumour formation is well established, recent studies suggest that p53 plays roll in the beginning and attending of various kidney disorders. The drug studies suggest that clinical targeting of p53 may make way as a novel therapeutic approach for acute and chronic kidney disease [41]. This demonstrates the potential benefits of targeting p53 to suppress progressive kidney injury and chronic kidney injury (CKD) [42]. In conclusion, in this study, while investigating the potential mechanism of *V. opulus* in the treatment of GN, based on

the results of network pharmacology, the screening results of the active components of the plant and the screening results of the targets in the PPI network, the bioactive components of rutin and quercetin as the most effective compound were screened in further analyses. As a result of molecular docking, it was determined that rutin and quercetin compounds showed the highest degree of molecular binding with TP53, SRC, and EGFR proteins. According to the molecular docking results, it was found that rutin and quercetin compounds can bind very well to these three proteins and have the lowest binding energy. This shows that the protein-bioactive compound combinations obtained are the most stable.

There are still some limitations in this study. Current network analysis techniques need to be improved and optimized. Also, the accuracy and sensitivity of database data need to be further increased, and the margin of error needs to be reduced. At the same time, according to the literature, compounds or targets that have not been validated or have never been recorded may not have been included in our study. Although the 9 active ingredients selected in this study were identified as the most important bioactive components of this plant, it should always be considered that they may not fully represent the plant content in reality. Therefore, pharmacodynamic experiments and molecular biology experiments should definitely be planned in the future to further confirm our research results. Since the effects of the potential active constituents herein on GN have not been proven by controlled experiments, we believe that the research area is of great interest, and the importance of this research is great.

## Conclusion

This study revealed the preliminary investigation of the main chemical contents and possible mechanism of *V. opulus* in the treatment of GN, based on network pharmacology and molecular docking techniques. Our research shows that rutin and quercetin may be the important basic active components of *V. opulus* with therapeutic nature, and the protein targets TP53, SRC, and EGFR may be potential therapeutic target of *V. opulus* in the treatment of GN. The effective components of *V. opulus* plant may provide therapeutic agents in GN disease through TP53, SRC, and EGFR pathways. In addition, this study will support a reference for further studies on the mechanism of *V. opulus* in the treatment of GN.

## Conflict of Interest

The authors declare that they have no conflicting interests.

## Acknowledgments

The authors would like to thank Sivas Cumhuriyet University for their support and permission to access the Maestro Schrödinger program under the project number RGD-020. This article is based on the PhD thesis conducted at Sivas Cumhuriyet University, Institute of Science.



## References

- [1] Madsen K.M., Nielsen C.S., Tisher C., Anatomy of the Kidney, *Brenner and Rector's The Kidney*, (2008).
- [2] Chadban S., Atkins R., Glomerulonephritis, *The Lancet*, 365 (2005) 1797–1806.
- [3] Houghton P.J., Traditional plant medicines as a source of new drugs, *Trease and Evans' Pharmacognosy*, Elsevier, (2009) 62–74.
- [4] Kajszyk D., Zakłós-Szyda M., Podśedek A., *Viburnum opulus* L.- A Review of Phytochemistry and Biological Effects, *Nutrients*, 12 (2020) 3398.
- [5] Li L., Yang L., Yang L., He C., He Y., Chen L., et al., Network pharmacology: a bright guiding light on the way to explore the personalized precise medication of traditional Chinese medicine, *Chin. Med.*, 18(1) (2023) 146.
- [6] Hopkins A.L., Network pharmacology: the next paradigm in drug discovery, *Nat. Chem. Biol.*, 4(11) (2008) 682–690.
- [7] Torres P.H.M., Sodero A.C.R., Jofily P., Silva-Jr F.P., Key Topics in Molecular Docking for Drug Design, *Int. J. Mol. Sci.*, 20(18) (2019) 4574.
- [8] Polka D., Podśedek A., Koziołkiewicz M., Comparison of Chemical Composition and Antioxidant Capacity of Fruit, Flower and Bark of *Viburnum opulus*, *Plant Foods Hum. Nutr.*, 74 (2019) 436–442.
- [9] Stelzer G., Rosen N., Plaschkes I., Zimmerman S., Twik M., Fishilevich S., et al., The GeneCards Suite: From Gene Data Mining to Disease Genome Sequence Analyses, *Curr. Protoc. Bioinform.*, 54 (2016).
- [10] Daina A., Michielin O., Zoete V., SwissTargetPrediction: updated data and new features for efficient prediction of protein targets of small molecules, *Nucleic Acids Res.*, 47 (2019) W357–W364.
- [11] Shannon P., Markiel A., Ozier O., Baliga N.S., Wang J.T., Ramage D., et al., Cytoscape: A Software Environment for Integrated Models of Biomolecular Interaction Networks, *Genome Res.*, 13 (2003) 2498–2504.
- [12] Bardou P., Mariette J., Escudié F., Djemiel C., Klopp C., jvenn: an interactive Venn diagram viewer, *BMC Bioinform.*, 15 (2014) 293.
- [13] Szklarczyk D., Kirsch R., Koutrouli M., Nastou K., Mehryary F., Hachilif R., et al., The STRING database in 2023: protein–protein association networks and functional enrichment analyses for any sequenced genome of interest, *Nucleic Acids Res.*, 51 (2023) D638–D646.
- [14] Zhou Y., Zhou B., Pache L., Chang M., Khodabakhshi A.H., Tanaseichuk O., et al., Metascape provides a biologist-oriented resource for the analysis of systems-level datasets, *Nat. Commun.*, 10 (2019) 1523.
- [15] Tang D., Chen M., Huang X., Zhang G., Zeng L., Zhang G., et al., SRplot: A free online platform for data visualization and graphing, *PLoS One*, 18 (2023) e0294236.
- [16] Burley S.K., Bhikadiya C., Bi C., Bittrich S., Chen L., Crichlow G.V., et al., RCSB Protein Data Bank: powerful new tools for exploring 3D structures of biological macromolecules for basic and applied research and education in fundamental biology, biomedicine, biotechnology, bioengineering and energy sciences, *Nucleic Acids Res.*, 49 (2021) D437–D451.
- [17] Kim S., Chen J., Cheng T., Gindulyte A., He J., He S., et al., PubChem 2019 update: improved access to chemical data, *Nucleic Acids Res.*, 47 (2019) D1102–D1109.
- [18] Schrödinger Release 2021-3: Maestro, LLC, New York, Schrödinger, (2021).
- [19] Liu T., Gao Y.C., Qin X.J., Gao J.R., Exploring the mechanism of Jianpi Qushi Huayu Formula in the treatment of chronic glomerulonephritis based on network pharmacology, *Naunyn Schmiedebergs Arch. Pharmacol.*, 394 (12) (2021) 2451–2470.
- [20] Venuthurupalli S.K., Hoy W.E., Healy H.G., Cameron A., Fassett R.G., CKD.QLD: establishment of a chronic kidney disease [CKD] registry in Queensland, Australia, *BMC Nephrol.*, 18 (2017) 189.
- [21] Kizilay F., Ulker V., Celik O., Ozdemir T., Cakmak O., Can E., et al., The evaluation of the effectiveness of Gilaburu (*Viburnum opulus* L.) extract in the medical expulsive treatment of distal ureteral stones, *Turk. J. Urol.*, 45 (Suppl. 1) (2019) 63–69.
- [22] Rock K.L., Kono H., The Inflammatory Response to Cell Death, *Annu. Rev. Pathol.*, 3 (2008) 99–126.
- [23] Ambriz-Perez D.L., Leyva-Lopez N., Gutierrez-Grijalva E.P., Heredia J.B., Phenolic compounds: Natural alternative in inflammation treatment. A Review, *Cogent Food Agric.*, 2 (2016) 1131412.
- [24] Ferraz C.R., Carvalho T.T., Manchope M.F., Artero N.A., Rasquel-Oliveira F.S., Fattori V., et al., Therapeutic Potential of Flavonoids in Pain and Inflammation: Mechanisms of Action, Pre-Clinical and Clinical Data, and Pharmaceutical Development, *Molecules*, 25 (2020) 762.
- [25] Ullah A., Munir S., Badshah S.L., Khan N., Ghani L., Poulson B.G., et al., Important Flavonoids and Their Role as a Therapeutic Agent, *Molecules*, 25 (2020) 5243.
- [26] Crozier A., Jaganath I.B., Clifford M.N., Dietary phenolics: chemistry, bioavailability and effects on health, *Nat. Prod. Rep.*, 26 (2009) 1001.
- [27] Cui W., Hu G., Peng J., Mu L., Liu J., Qiao L., Quercetin Exerted Protective Effects in a Rat Model of Sepsis via Inhibition of Reactive Oxygen Species (ROS) and Downregulation of High Mobility Group Box 1 (HMGB1) Protein Expression, *Med. Sci. Monit.*, 25 (2019) 5795–5800.
- [28] Karimi A., Naeini F., Asghari Azar V., Hasanzadeh M., Ostadrahimi A., Niazkar H.R., et al., A comprehensive systematic review of the therapeutic effects and mechanisms of action of quercetin in sepsis, *Phytomedicine*, 86 (2021) 153567.
- [29] de Pádua Lúcio K., Rabelo A.C.S., Araújo C.M., Brandão G.C., de Souza G.H.B., da Silva R.G., et al., Anti-Inflammatory and Antioxidant Properties of Black Mulberry (*Morus nigra* L.) in a Model of LPS-Induced Sepsis, *Oxid. Med. Cell. Longev.*, 2018 (2018) 5048031.
- [30] Li X., Wei S., Niu S., Ma X., Li H., Jing M., et al., Network pharmacology prediction and molecular docking-based strategy to explore the potential mechanism of Huanglian Jiedu Decoction against sepsis, *Comput. Biol. Med.*, 144 (2022) 105389.
- [31] Liu Q., Yu S., Zhao W., Qin S., Chu Q., Wu K., EGFR-TKIs resistance via EGFR-independent signaling pathways, *Mol. Cancer*, 17(1) (2018) 53.
- [32] Bollée G., Flamant M., Schordan S., Fligny C., Rumpel E., Milon M., et al., Epidermal growth factor receptor promotes glomerular injury and renal failure in rapidly progressive crescentic glomerulonephritis, *Nat. Med.*, 17(10) (2011) 1242–1250.
- [33] Tang J., Liu N., Zhuang S., Role of epidermal growth factor receptor in acute and chronic kidney injury, *Kidney Int.*, 83(5) (2013) 804–810.
- [34] Chen J., Chen J.-K., Nagai K., Plieth D., Tan M., Lee T.-C., et al., EGFR Signaling Promotes TGFβ-Dependent Renal Fibrosis, *J. Am. Soc. Nephrol.*, 23 (2) (2012) 215–224.



- [35] Striker L.J., Doi T., Elliot S., Striker G.E., The contribution of glomerular mesangial cells to progressive glomerulosclerosis, *Semin. Nephrol.*, 9 (4) (1989) 318–328.
- [36] alal D.I., Kone B.C., Src activation of NF-kappaB augments IL-1beta-induced nitric oxide production in mesangial cells, *J. Am. Soc. Nephrol.*, 17(1) (2006) 99–106.
- [37] Gruden G., Araf S., Zonca S., Burt D., Thomas S., Gnudi L., et al., IGF-I induces vascular endothelial growth factor in human mesangial cells via a Src-dependent mechanism, *Kidney Int.*, 63(4) (2003) 1249–1255.
- [38] Wu H., Shi Y., Deng X., Su Y., Du C., Wei J., et al., Inhibition of c-Src/p38 MAPK pathway ameliorates renal tubular epithelial cells apoptosis in db/db mice, *Mol. Cell. Endocrinol.*, 417 (2015) 27–35.
- [39] Wang J., Zhuang S., Src family kinases in chronic kidney disease, *Am. J. Physiol. Renal Physiol.*, 313 (3) (2017) F721–F728.
- [40] Vousden K.H., Prives C., Blinded by the Light: The Growing Complexity of p53, *Cell*, 137(3) (2009) 413–431.
- [41] Overstreet J.M., Gifford C.C., Tang J., Higgins P.J., Samarakoon R., Emerging role of tumor suppressor p53 in acute and chronic kidney diseases, *Cell. Mol. Life Sci.*, 79(9) (2022) 474.
- [42] Molitoris B.A., Dagher P.C., Sandoval R.M., Campos S.B., Ashush H., Fridman E., et al., siRNA Targeted to p53 Attenuates Ischemic and Cisplatin-Induced Acute Kidney Injury, *J. Am. Soc. Nephrol.*, 20(8) (2009) 1754–1764.

## Modeling The Physicochemical Characteristics of Benzene Compounds Through the Application of Zagreb Omicron Indices

İdris Çiftçi<sup>1,a,\*</sup><sup>1</sup> Department of Mathematics, Faculty of Education, Van Yüzüncü Yıl University, Van, Türkiye

\*Corresponding author

### Research Article

#### History

Received: 10/01/2025

Accepted: 26/05/2025



This article is licensed under a Creative Commons Attribution-NonCommercial 4.0 International License (CC BY-NC 4.0)

### ABSTRACT

Quantitative structure–property relationship (QSPR) studies commonly utilize topological indices to describe the chemical and physical characteristics of molecular structures. This study primarily focuses on the omicron degree of vertices and the corresponding Zagreb omicron indices for connected graphs, representing a notable contribution to the field of chemical graph theory. It has been demonstrated that the Zagreb omicron indices exhibit correlations greater than 0.995 with various physicochemical properties of benzene derivatives, including  $\pi$ -electron energy, molecular weight, polarization, and relative formula mass. The findings reveal that the first Zagreb omicron index correlates with degree-based topological indices of benzene derivatives with coefficients exceeding 0.96. Additionally, structural sensitivity and abruptness analyses of the proposed indices were conducted and compared with those of other established topological indices. The overall results provide compelling evidence that Zagreb omicron indices serve as valuable tools in QSPR research applications.

**Keywords:** QSPR studies, Benzenes, Topological indices, Omicron degree, Zagreb omicron indices.

<sup>a</sup> [idrisciftci@yyu.edu.tr](mailto:idrisciftci@yyu.edu.tr) <https://orcid.org/0000-0002-2698-0807>

## Introduction

Topological indices are essential tools used to derive real-valued descriptors closely linked to molecular structures, allowing for comprehensive analysis of their structural characteristics. These descriptors can be used to develop mathematical models that incorporate parameters obtained from experimental studies in chemistry and physics.

Recent research in chemical graph theory has introduced thousands of different topological indices. To propose a new index, it is essential to demonstrate its superiority over existing indices based on three key criteria:

- I. The new index should show a correlation coefficient greater than 0.99 with at least one physicochemical property of the studied molecules.
- II. It should have correlation coefficients above 0.9 with known topological indices.
- III. The index should demonstrate clear superiority in structural characteristics, such as smoothness and degeneracy, compared to existing indices [1].

This study introduces the concept of the omicron degree of a vertex, representing a new contribution to graph theory. We present the Zagreb omicron indices for the inaugural time, predicated upon this foundational concept. A thorough investigation of the newly formulated indices is conducted based on the designated criteria, concentrating on parameters such as boiling point,  $\pi$  electron energy, molecular weight, polarization,

molecular volume, and relative formula mass of benzene derivatives. The structure of this paper is as follows: The introductory section defines pivotal terms and elucidates the most frequently employed indices within the literature, including the omicron degrees and Zagreb omicron indices pertinent to this study. The subsequent section delineates the Zagreb omicron indices pertinent to benzene molecules. In this segment, we executed analyses of the correlations among several properties—specifically boiling point,  $\pi$  electron energy, molecular weight, polarization, molecular volume, and relative formula mass of benzene—and the values associated with the Zagreb omicron indices. These values were systematically juxtaposed with all relevant data documented in the extant academic literature. We identified the second highest correlation associated with the third Zagreb omicron index. Consequently, we formulated mathematical models for benzene's boiling point,  $\pi$  electron energy, molecular weight, polarization, molecular volume, and relative formula mass in conjunction with the Zagreb omicron indices. The fourth section elucidates the correlation coefficients that link benzene's Zagreb omicron indices with other topological indices. The fifth segment encompasses a diverse array of structural evaluations. These investigations collectively substantiate that the Zagreb omicron indices represent distinctive instruments particularly adept for quantitative structure-activity relationship (QSAR) analyses.

## Basic Definitions

The study of topological indices began in 1947, when Harold Wiener introduced an index to estimate the boiling points of alkanes [2]. The Wiener index is based on the sum of distances between all pairs of vertices in a graph. Contrary to common belief, the Zagreb index was not the first degree-based topological index. The first degree-based index is the Platt index, proposed in 1947 [3]. The third topological index, known as the Hosoya index, appeared in the literature in 1971. For a detailed discussion on the Hosoya index, refer to reference [4].

Subsequently, the Randić and Zagreb indices were introduced [5,6].

Let  $G$  be a graph and  $v$  a vertex in  $G$ . The degree of  $v$ , denoted as  $\deg v$ , is the number of edges incident to it. We denote the set of vertices of a graph as  $V(G)$ , and the set of edges as  $E(G)$ . Table 1 provides definitions of the degree-based topological indices referenced in the literature and applied in this study. We selected the indices in Table 1 due to the smoothness analysis results in [1]. These indices will later be compared with the Zagreb omicron indices defined in this study, particularly in Section 5.

Table 1. Indices and their definitions

Name of Index	Symbol	Formula	Reference
The first Zagreb	$M_1$	$M_1 = \sum_{v \in V(G)} \deg v^2$	[6]
The second Zagreb	$M_2$	$M_2 = \sum_{uv \in E(G)} \deg u \deg v$	[6]
Randić	$R$	$R = \sum_{uv \in E(G)} \frac{1}{\sqrt{\deg u \deg v}}$	[1]
Reciprocal Randić	$RR$	$RR = \sum_{uv \in E(G)} \sqrt{\deg u \deg v}$	[7]
Sum-connectivity	$SCI$	$SCI = \sum_{uv \in E(G)} \frac{1}{\sqrt{\deg u + \deg v}}$	[8]
Symmetric division deg	$SDD$	$SDD = \sum_{uv \in E(G)} \left( \frac{\deg u}{\deg v} + \frac{\deg v}{\deg u} \right)$	[9]
Inverse sum indeg	$ISI$	$ISI = \sum_{uv \in E(G)} \frac{\deg u \deg v}{\deg u + \deg v}$	[9]
Harmonic	$H$	$H = \sum_{uv \in E(G)} \frac{1}{\sqrt{\deg u + \deg v}}$	[10]
Atom-bond connectivity	$ABC$	$ABC = \sum_{uv \in E(G)} \sqrt{\frac{\deg u + \deg v - 2}{\deg u \deg v}}$	[11]
Augmented Zagreb index	$AZI$	$AZI = \sum_{uv \in E(G)} \left( \frac{\deg u \deg v}{\deg u + \deg v - 2} \right)^3$	[12]
The first hyper-Zagreb	$HM_1$	$HM_1 = \sum_{uv \in E(G)} (\deg u + \deg v)^2$	[13]
The second hyper-Zagreb	$HM_2$	$HM_2 = \sum_{uv \in E(G)} (\deg u \deg v)^2$	[14]
Geometric-arithmetic	$GA$	$GA = \sum_{uv \in E(G)} \frac{2\sqrt{\deg u \deg v}}{\deg u + \deg v}$	[15]
The fourth geometric-arithmetic	$GA_4$	$GA_4 = \sum_{uv \in E(G)} \frac{2\sqrt{\varepsilon_u \varepsilon_v}}{\varepsilon_u + \varepsilon_v}$	[16]
Arithmetic-geometric index	$AG$	$AG = \sum_{uv \in E(G)} \frac{\deg u + \deg v}{2\sqrt{\deg u \deg v}}$	[17]
Sombor	$SO$	$SO = \sum_{uv \in E(G)} \sqrt{\deg u^2 + \deg v^2}$	[18]

Modified Sombor	$SO^m$	$SO^m = \sum_{uv \in E(G)} \frac{1}{\sqrt{\deg u^2 + \deg v^2}}$	[19]
Nirmala	$N$	$N = \sum_{uv \in E(G)} \sqrt{\deg u + \deg v}$	[20]
The first inverse Nirmala	$IN_1$	$IN_1 = \sum_{uv \in E(G)} \sqrt{\frac{1}{\deg u} + \frac{1}{\deg v}}$	[21]
The second inverse Nirmala	$IN_2$	$IN_2 = \sum_{uv \in E(G)} \frac{1}{\sqrt{\frac{1}{\deg u} + \frac{1}{\deg v}}}$	[21]

The indices presented in Table 1 were selected based on their high structural smoothness scores and frequent application in recent QSPR studies, particularly those analyzed in [1]. While alternative indices such as F-index or Y-index are also effective, they were not included due to their limited coverage in recent smoothness-focused comparisons.

We are now ready to offer the formal definition of the omicron degree related to a vertex, together with the specification of three unique Zagreb omicron indices, which represent the essential basis of this research.

**Definition 2.1** Let  $G$  be an  $n$ -vertex connected graph and let  $v$  be a vertex of  $G$ . The omicron degree of the vertex  $v$  is defined as,

$$o(v) = \deg v^{1/\deg(v)} \quad (1)$$

Here,  $M_v$  is the multiplication of the degrees of all vertices neighbouring  $v$ .

**Definition 2.2** The first Zagreb omicron index of an  $n$ -vertex connected graph  $G$  is defined as;

$$M_1O(G) = \sum_{v \in V(G)} o(v)^2 \quad (2)$$

**Definition 2.3** The second Zagreb omicron index of an  $n$ -vertex connected graph  $G$  is defined as;

$$M_2O(G) = \sum_{uv \in E(G)} o(u)o(v) \quad (3)$$

**Definition 2.4** The third Zagreb omicron index of an  $n$ -vertex connected graph  $G$  is defined as;

$$M_3O(G) = \sum_{uv \in E(G)} (o(u) + o(v)) \quad (4)$$

### Zagreb Omicron Indices For Benzenes

This section presents correlations greater than 0.95 between the Zagreb omicron indices and the physicochemical properties of benzene derivatives, including boiling point (BP),  $\pi$ -electron energy ( $\pi$ -ele), molecular weight (MW), polarization (PO), molecular volume (MV), and relative formula mass (MR). Consequently, we introduce mathematical models that describe the chemical properties of benzene derivatives based on Zagreb omicron indices. The latest related findings can be found in studies [4], [21–29]. The concentrations of benzene derivatives used in this study were obtained from the current dataset.

Table 2. Zagreb omicron indices of benzenes.

Benzenes	The first Zagreb Omicron index	The second Zagreb Omicron index	The third Zagreb Omicron index
Benzene	12,000	12,000	16,970
Naphthalene	20,160	22,238	31,280
Phenanthrene	28,320	32,478	45,590
Anthracene	28,320	32,477	45,590
Chrysene	36,481	42,717	59,901
Benzo[a] anthracene	36,481	42,716	59,901
Triphenylene	36,481	42,719	59,901
Tetracene	36,481	42,715	59,901
Benzo[a]pyrene	40,641	48,957	68,554
Benzo[e]pyrene	40,641	48,958	68,554
Perylene	40,641	49,786	68,554
Anthanthrene	44,801	55,196	77,207



Benzo[ghi] perylene	44,801	55,197	77,207
Dibenz[a,c] nthalene	44,641	52,957	74,211
Dibenz[a,h]anthracene	44,641	52,956	74,211
Dibenz[a,j]anthracene	44,641	52,956	74,211
Picene	44,641	52,957	74,211
Coronene	48,961	61,436	85,860
Dibenzo[a,h] pyrene	48,801	59,196	82,864
Dibenzo[a,i] pyrene	48,801	59,196	82,864
Dibenzo[a,l] pyrene	48,801	59,197	82,864
Pyrene	32,481	38,717	54,244

Table 3 presents selected physicochemical properties of benzene derivatives.

Table 3. Some physical-chemical properties of benzenes.

Benzenes	BP	Pi-ele	MW	PO	MV	MR
Benzene	78,800	8,000	78,110	10,400	89,400	26,300
Naphthalene	221,500	13,683	128,170	17,500	123,500	44,100
Phenanthrene	337,400	19,448	178,230	24,600	157,700	61,900
Anthracene	337,400	19,314	178,230	24,600	157,700	61,900
Chrysene	448,000	25,192	228,300	31,600	191,800	79,800
Benzo[a] anthracene	436,700	25,101	228,300	31,600	191,800	79,800
Triphenylene	425,000	25,275	228,300	31,600	191,800	79,800
Tetracene	436,700	25,188	228,300	31,600	191,800	79,800
Benzo[a]pyrene	495,000	28,222	252,300	35,800	196,100	90,300
Benzo[e]pyrene	467,500	28,336	252,300	35,800	196,100	90,300
Perylene	467,500	28,245	252,300	35,800	196,100	90,300
Anthanthrene	497,100	31,253	276,300	40,000	200,400	100,800
Benzo[ghi] perylene	501,000	31,425	276,300	40,000	200,400	100,800
Dibenz[a,c] nthalene	518,000	30,942	278,300	38,700	225,900	97,600
Dibenz[a,h]anthracene	524,700	30,881	278,300	38,700	225,900	97,600
Dibenz[a,j]anthracene	524,700	30,880	278,300	38,700	225,900	97,600
Picene	519,000	30,943	278,300	38,700	225,900	97,600
Coronene	525,600	34,572	300,400	44,100	204,700	111,400
Dibenzo[a,h] pyrene	552,300	33,928	302,400	42,900	230,200	108,100
Dibenzo[a,i] pyrene	552,300	33,954	302,400	42,900	230,200	108,100
Dibenzo[a,l] pyrene	552,300	34,031	302,400	42,900	230,200	108,100
Pyrene	404,000	22,506	202,250	28,700	162,000	72,500

Table 4 summarizes the correlation coefficients between the physicochemical properties of benzene derivatives and the Zagreb omicron indices.

Table 4. The correlation coefficients between properties of benzenes and the Zagreb omicron indices.

	The first Zagreb Omicron index	The second Zagreb Omicron index	The third Zagreb Omicron index
BP	0,9835	0,9755	0,9761
Pi-ele	0,9998	0,9990	0,9993
MW	0,9998	0,9967	0,9971
PO	0,9988	0,9998	1,0000
MV	0,9639	0,9458	0,9472
MR	0,9988	0,9998	1,0000

As shown in Table 4, the correlation coefficients between the three newly defined indices and the physicochemical characteristics of benzene derivatives exceed 0.9458. The third Zagreb omicron index shows a perfect correlation ( $r = 1.000$ ) with both PO and MR. This result is the best found in the literature so far. These results satisfy the first criterion proposed in this study for validating a newly defined index. Now we provide the linear regression graphs of the physico-chemical properties using the index that provides the greatest correlation.

Figure 1 shows a linear regression model of benzene boiling points using the first Zagreb omicron index.

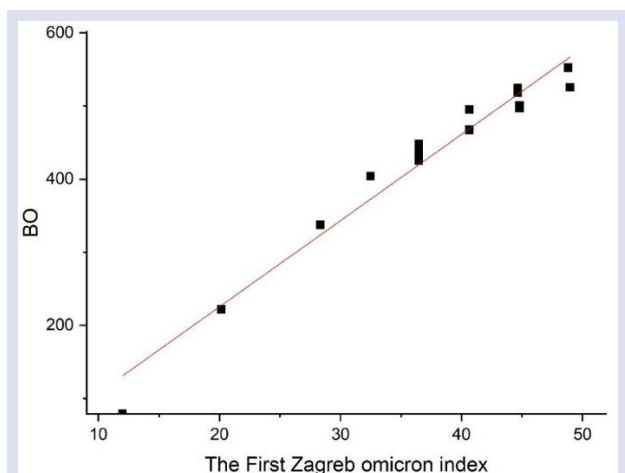


Figure 1. The linear fitting modelling of boiling points of benzenes via the first Zagreb omicron index

The technical details of the graph given in Figure 1 are given below in Table 5.

Table 5. Details of linear regression model of boiling points of benzenes via the first Zagreb omicron index

Linear regression model of boiling points of benzenes via the first Zagreb omicron index	
Equation	
Intercept	-10,75115 ± 19,39041
Slope	11,79726 ± 0,48604
Pearson's R	0,98345
R-Square (COD)	0,96717
Adj. R-Square	0,96553

Linear regression model of pi-electron energy levels of benzenes via the first Zagreb omicron index is shown in Figure 2.

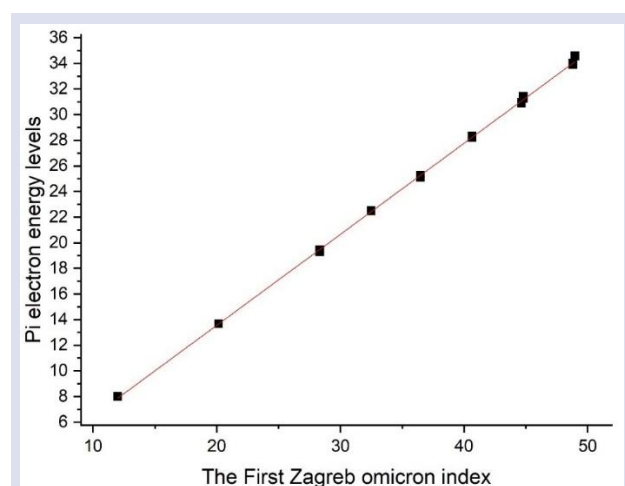


Figure 2. The linear fitting modelling of pi electron energy levels of benzenes via the first Zagreb omicron index

The technical details of the graph given in Figure 2 are given below in Table 6.

Table 6. Details of linear regression model of pi electron energy levels of benzenes via the third Zagreb omicron index

Linear regression model of pi electron energy levels of benzenes via the first Zagreb omicron index	
Equation	
Intercept	-0,65859 ± 0,13755
Slope	0,71049 ± 0,00345
Pearson's R	0,99976
R-Square (COD)	0,99953
Adj. R-Square	0,99951

Linear regression model of molecular weight of benzenes via the first Zagreb omicron index is shown in Figure 3.

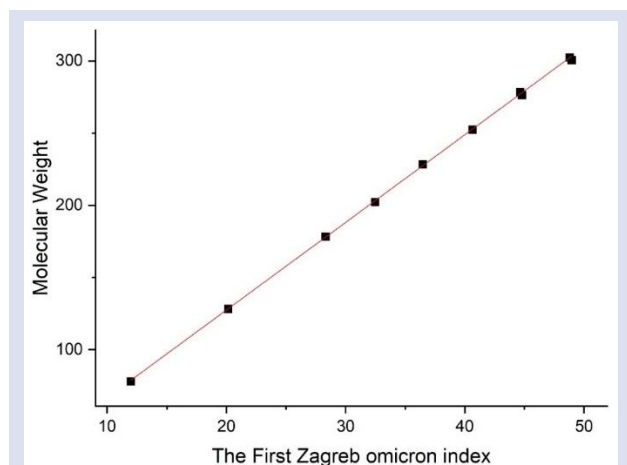


Figure 3. The linear fitting modelling of molecular weight of benzenes via the first Zagreb omicron index

The technical details of the graph given in Figure 3 are given below in Table 7.

Table 7. Details of linear regression model of molecular weight of benzenes via the first Zagreb omicron index

Equation	Linear regression model of molecular weight of benzenes via the first Zagreb omicron index
Intercept	$6,03113 \pm 1,01243$
Slope	$6,0702 \pm 0,02538$
Pearson's R	0,99983
R-Square (COD)	0,99965
Adj. R-Square	0,99963

Linear regression model of polarization of benzenes via the third Zagreb omicron index is shown in Figure 4.

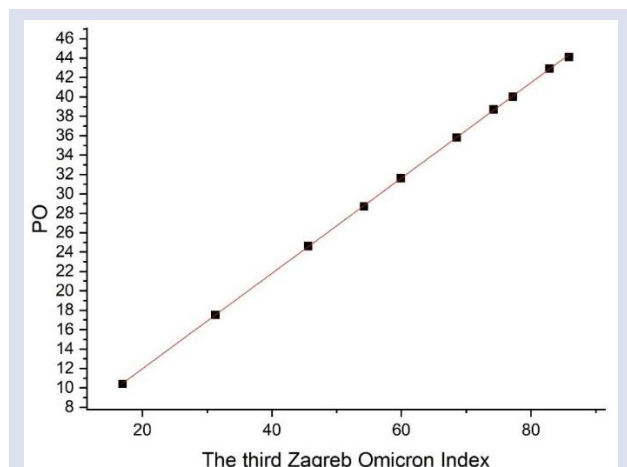


Figure 4. The linear fitting modelling of polarization of benzenes via the third Zagreb omicron index

The technical details of the graph given in Fig 4 are given below in Tab 8.

Table 8. Details of linear regression model of polarization of benzenes via the third Zagreb omicron index

Equation	Linear regression model of polarization of benzenes via the third Zagreb omicron index
Intercept	$2,13198 \pm 0,06761$
Slope	$0,49156 \pm 0,00101$
Pearson's R	0,99996
R-Square (COD)	0,99992
Adj. R-Square	0,99991

Linear regression model of molecular volume of benzenes via the first Zagreb omicron index is shown in Figure 5.

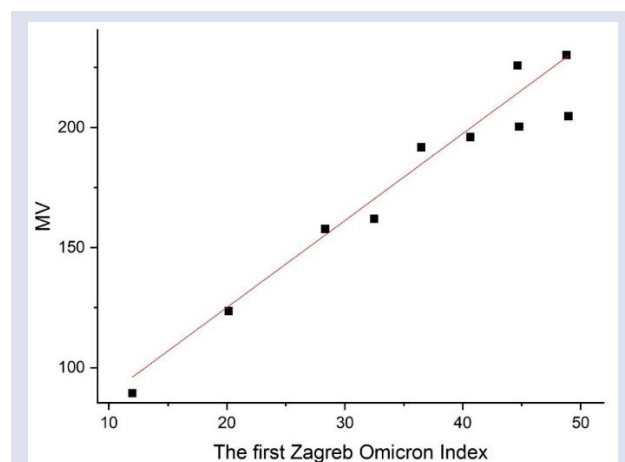


Figure 5. The linear fitting modelling of molecular volume of benzenes via the first Zagreb omicron index

The technical details of the graph given in Figure 5 are given below in Table 9.

Table 9. Details of linear regression model of molecular volume of benzenes via the first Zagreb omicron index

Equation	Linear regression model of molecular volume of benzenes via the first Zagreb omicron index
Intercept	$52,6429 \pm 8,91779$
Slope	$3,62086 \pm 0,22353$
Pearson's R	0,97479
R-Square (COD)	0,95022
Adj. R-Square	0,94773

Linear regression model of MR of benzenes via the third Zagreb omicron index is shown in Figure 6.

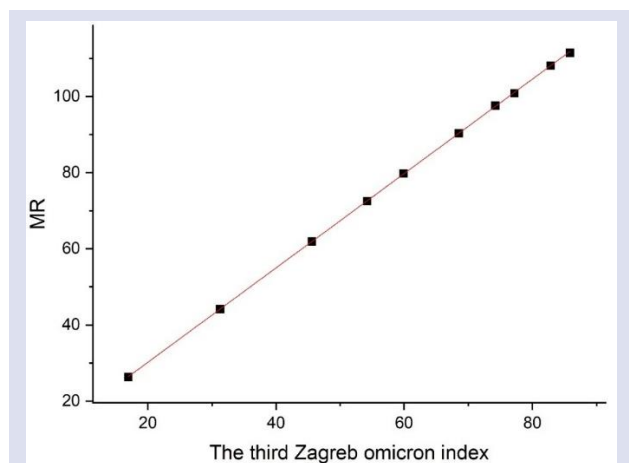


Figure 6. The linear fitting modelling of MR of benzenes via the third Zagreb omicron index

The technical details of the graph given in Fig 6 are given below in Tab 10.

Table 10. Details of linear regression model of MR of benzenes via the third Zagreb omicron index

Linear regression model of MR of benzenes via the third Zagreb omicron index	
Equation	
Intercept	$5,41268 \pm 0,15478$
Slope	$1,2392 \pm 0,00231$
Pearson's R	0,99997
R-Square (COD)	0,99993
Adj. R-Square	0,99993

## Relations With Other Indices

Section 4 presents correlation coefficients between the Zagreb omicron indices and established degree-based topological indices—Randić (R), atom–bond connectivity (ABC), augmented Zagreb index (AZI), geometric–

arithmetic index (GA), the first and second Zagreb indices ( $M_1$ ,  $M_2$ ), and the Sombor index (SO). The values derived from sources [22] and [26].

Table 11 shows the values of classical degree-based indices calculated for the same set of benzene derivatives. These data serve as the basis for correlation analysis with the newly proposed Zagreb omicron indices.

Table 11. Well-known degree-based topological indices of benzenes.

Benzenes	R	ABC	AZI	GA	$M_1$	$M_2$	SO
Benzene	3,000	4,2426	48	6	24	24	16,9706
Naphthalene	4,966	7,7377	91,3906	10,9192	50	57	35,6354
Phenanthrene	6,950	11,1924	138,1719	15,8788	76	91	54,1602
Anthracene	6,933	11,2328	134,7813	15,8384	76	90	54,3003
Chrysene	8,933	14,647	184,9531	20,8384	102	125	72,785
Benzo[a] anthracene	8,916	14,6875	181,5625	20,798	102	124	72,8251
Triphenylene	8,950	14,6066	188,3438	20,8788	102	126	72,545
Tetracene	8,899	14,7279	178,1719	20,7576	102	123	72,9651
Benzo[a]pyrene	9,916	16,647	219,125	23,8384	120	152	85,413
Benzo[e]pyrene	9,933	16,647	219,125	23,798	120	151	85,553
Perylene	9,933	16,647	219,125	23,8384	120	152	85,413
Anthanthrene	10,899	18,7279	246,5156	26,7576	138	177	98,4209
Benzo[ghi] perylene	10,916	18,6875	249,9063	26,798	138	178	98,2809
Dibenz[a,c] Anthracene	10,916	18,1017	231,7344	25,798	128	159	91,2098
Dibenz[a,h]anthracene	10,899	18,1421	228,3438	25,7576	128	158	91,3499
Dibenz[a,j]anthracene	10,899	18,1421	228,3438	25,7576	128	158	91,3499
Picene	10,915	18,1017	231,7344	25,798	128	159	91,2098
Coronene	11,899	20,7279	280,6875	29,7576	156	204	111,1489
Dibenzo[a,h] pyrene	11,582	20,1421	262,5156	28,7576	146	185	104,0778
Dibenzo[a,i] pyrene	11,566	20,1421	262,5156	28,7576	146	185	104,0778
Dibenzo[a,l] pyrene	11,491	20,1017	265,9063	28,798	146	186	103,9378
Pyrene	11,915	13,2328	168,9531	18,8384	94	117	67,0282

Table 12 summarizes the correlation coefficients between the classical indices—Randić (R), ABC, AZI, GA,  $M_1$ ,  $M_2$ , SO—and the newly defined Zagreb omicron indices.



Table 12. The correlation coefficients between the well-known topological indices and the Zagreb omicron indices.

Indices	R	ABC	AZI	GA	M <sub>1</sub>	M <sub>2</sub>	SO
The first Zagreb Omicron index	0,96274	0,96119	0,96033	0,96274	0,96119	0,96033	0,96274
The second Zagreb Omicron index	0,86228	0,86371	0,86214	0,86228	0,86371	0,86214	0,86228
The third Zagreb Omicron index	0,85	0,85311	0,85132	0,85	0,85311	0,85132	0,85

As shown in Table 12, the first Zagreb omicron index correlates with other classical indices with coefficients exceeding 0.96119, indicating a very strong relationship.

To further justify the relevance of the new indices, we also examine correlations between established indices and physicochemical properties. Table 13 displays the correlation coefficients between classical indices (R, ABC,

AZI, GA, M<sub>1</sub>, M<sub>2</sub>, SO) and the physicochemical properties of benzene derivatives. The results show that some established indices, such as M<sub>1</sub> and M<sub>2</sub>, yield correlation coefficients near unity, underscoring the need to demonstrate the structural and mathematical advantages of the Zagreb omicron indices.

Table 13. Pearson Correlation Coefficients Between Classical Degree-Based Topological Indices and Physicochemical Properties of Benzene Derivatives

Property	R	ABC	AZI	GA	M <sub>1</sub>	M <sub>2</sub>	SO
BP	0,9408	0,5111	0,6324	0,3456	0,9672	0,9555	0,5286
Pi-ele	0,932	0,565	0,661	0,33	0,996	0,991	0,587
MW	0,9299	0,5664	0,6631	0,3277	0,9922	0,9848	0,5861
PO	0,933	0,565	0,658	0,336	0,998	0,994	0,591
MV	0,8802	0,5522	0,6548	0,2822	0,9302	0,9112	0,547
MR	0,9336	0,564	0,6581	0,3365	0,9983	0,9943	0,5902

Legend: This table presents the correlation coefficients between several well-known degree-based topological indices (R, ABC, AZI, GA, M<sub>1</sub>, M<sub>2</sub>, SO) and key physicochemical properties of benzene derivatives, including boiling point (BP), pi-electron energy (Pi-ele), molecular weight (MW), polarization (PO), molecular volume (MV), and molar refractivity (MR). These results provide a comparative context for evaluating the predictive strength of the newly introduced Zagreb omicron indices.

### Smoothness Analysis

This section investigates the smoothness characteristics of the Zagreb omicron indices and compares them with previously established results for various well-known topological indices. Reference [27]

introduced two graph-based structural metrics—structure sensitivity (SS) and abruptness (Abr)—used to evaluate the smoothness of molecular descriptors. Recent studies have examined the structural sensitivity of eigenvalue-based topological indices and the continuity of graph energy in chemical structures, as reported in references [28] and [29], respectively. Reference [27] provides the algorithm used to compute SS and Abr values for topological indices applied to specific classes of connected graphs. Kumar and Das applied this algorithm to evaluate the smoothness of fifteen degree-based topological indices (listed in Table 1) on all tree graphs with 4 to 10 vertices.

Using the same algorithm, SS and Abr values of the Zagreb omicron indices were calculated for tree graphs with 4 to 9 vertices, and the results are presented in Table 13.

Table 14. Structure sensitivity (SS) and abruptness (Abr) analysis results of Zagreb omicron indices on tree graphs

Zagreb Omicron Indices	n=4		n=5		n=6		n=7		n=8		n=9	
	SS	Abr	SS	Abr	SS	Abr	SS	Abr	SS	Abr	SS	Abr
M <sub>1</sub> O	0.1672	0.1672	0,1453	0,1491	0,1000	0,1231	0,068	0,108	0,0590	0,0919	0,0513	0,0966
M <sub>2</sub> O	0.1098	0.1098	0,0949	0,0999	0,0652	0,0822	0,0561	0,1009	0,0394	0,0620	0,0339	0,0661
M <sub>3</sub> O	0.0441	0.0441	0,0411	0,0438	0,0293	0,0373	0,0286	0,0508	0,0181	0,0288	0,0805	0,2247

An effective topological index should exhibit a low *Abr* value and a relatively high *SS* value, indicating stable structural behavior. For tree graphs with 9 vertices, comparison of Table 13 with Table 1 in reference [5] and Table 3 in reference [27] reveals that the *SS* value of the Zagreb omicron indices exceeds those of the first Zagreb, Randić, ABC, and GA indices. However, it is also observed that the *Abr* values of the Zagreb omicron indices are higher than those of all other indices.

## Conclusion

This study introduced the concept of the omicron degree within the framework of chemical graph theory. Based on this new degree concept, three Zagreb omicron indices were defined. Their applicability was evaluated in QSAR studies modeling key physicochemical properties of benzene derivatives, including boiling point,  $\pi$ -electron energy, molecular weight, polarization, molecular volume, and relative formula mass. The results showed that Zagreb omicron indices correlated strongly ( $r > 0.995$ ) with properties such as  $\pi$ -electron energy, molecular weight, polarization, and molar refractivity. Additionally, structural sensitivity and abruptness analyses were carried out and compared with those of established topological indices. Overall, the findings demonstrate that the Zagreb omicron indices are highly suitable for use in QSPR research.

Although this study focused on degree-based indices, future research could investigate the inclusion of distance-based indices—such as the Wiener, Harary, and Balaban indices—to determine whether stronger correlations with physicochemical properties can be obtained.

## Conflicts of interest

There are no conflicts of interest in this work.

## References

- [1] Kumar V., Das S., On Structure Sensitivity and Chemical Applicability of Some Novel Degree-Based Topological Indices, *MATCH Commun. Math. Comput. Chem.*, 92 (2024) 165–203.
- [2] Wiener H., Structural determination of paraffin boiling points, *J. Am. Chem. Soc.*, 69 (1947) 17–20.
- [3] Platt J. R., Influence of neighbour bonds on additive bond properties in paraffins, *J. Chem. Phys.*, 15 (1947) 419–420.
- [4] Hosoya H., The most private features of the topological index, *MATL*, (1) (2019) 25–33.
- [5] Gutman I., Trinajstić N., Graph theory and molecular orbitals, Total  $\pi$  electron energy of alternant hydrocarbons, *Chem. Phys. Lett.*, 17 (1972) 535–538.
- [6] Randić M., Characterization of molecular branching, *J. Am. Chem. Soc.*, 97 (1975) 6609–6615.
- [7] Gutman I., Furtula B., Elphick C., Three new/old vertex-degree-based topological indices, *MATCH Commun. Math. Comput. Chem.*, 72 (2014) 617–632.
- [8] Zhou B., Trinajstić N., On a novel connectivity index, *J. Math. Chem.*, 46 (2009) 1252–1270.
- [9] Vukičević D., Gašperov M., Bond additive modeling 1. Adriatic indices, *Croat. Chem. Acta.*, 83 (2010) 243–260.
- [10] Favaron O., Mahéo M., Sacle J. F., Some eigenvalue properties in graphs (conjectures of graffiti-II), *Discrete Math.*, 111 (1993) 197–220.
- [11] Estrada E., Torres L., Rodriguez L., Gutman I., An atom-bond connectivity index: modelling the enthalpy of formation of alkanes, *Indian J. Chem.*, 37A (1998) 849–855.
- [12] Furtula B., Graovac A., Vukičević D., Augmented Zagreb index, *J. Math. Chem.*, 48 (2010) 370–380.
- [13] Shirdel G., Rezapour H., Sayadi A., The hyper-Zagreb index of graph operations, *Iran. J. Math. Chem.*, 4 (2013) 213–220.
- [14] Alameri A., Second hyper-Zagreb index of titania nanotubes and their applications, *IEEE Access.*, 9 (2021) 9567–9571.
- [15] Vukičević D., Furtula B., Topological index based on the ratios of geometrical and arithmetical means of end-vertex degrees of edges, *J. Math. Chem.*, 46 (2009) 1369–1376.
- [16] Ediz S., Computing GA4 index of an infinite class of nano star dendrimers, *Optoelectronics and Advanced Materials Rapid Communications.*, 4 (12) (2010) 2198–2199.
- [17] Shegehalli V., Kanabur R., Arithmetic-Geometric indices of path graph, *J. Comput. Math. Sci.*, 16 (2015) 19–24.
- [18] Gutman I., Geometric approach to degree-based topological indices: Sombor indices, *MATCH Commun. Math. Comput. Chem.*, 86 (2021) 11–16.
- [19] Kulli V., Gutman I., Computation of Sombor indices of certain networks, *SSRG Int. J. Appl. Chem.*, 8 (2021) 1–5.
- [20] Kulli V., Nirmala index, *Int. J. Math. Trends Technol.*, 67 (2021) 8–12.
- [21] Kulli V., Lokesh V., Nirupadi K., Computation of inverse Nirmala indices of certain nanostructures, *Int. J. Math. Comb.*, 2 (2021) 33–40.
- [22] Nikolić S., Trinajstić N., Comparison between the Vertex- and Edge-Connectivity Indices for Benzenoid Hydrocarbons, *J. Chem. Inf. Comput. Sci.*, 38 (1998) 42–46.
- [23] Hayat S., Khan S., Khan A., Imran M., Distance-based topological descriptors for measuring the  $\pi$ -electronic energy of benzenoid hydrocarbons with applications to carbon nanotubes, *Math. Meth. Appl. Sci.*, (2020) 1–20.
- [24] Hayat S., Khani S., Khan A., Imran M., A Computer-Based Method to Determine Predictive Potential of Distance-Spectral Descriptors for Measuring the  $\pi$ -Electronic Energy of Benzenoid Hydrocarbons with Applications, *IEEE Access.*, 9 (2021) 19238–19253.
- [25] Shanmukha M. C., Usha A., Kulli V. R., Shilpa K. C., Chemical applicability and curvilinear regression models of vertex-degree-based topological index: Elliptic Sombor index, *Int J Quantum Chem.*, (2024) 124: e27376.
- [26] Malik M. Y. H., Binyamin M. A., Hayat S., Correlation ability of degree-based topological indices for physicochemical properties of polycyclic aromatic hydrocarbons with applications, *Polycyclic Aromatic Compounds.*, 42 (2022) 6267–6281.
- [27] Furtula B., Gutman I., Dehmer M., On structure-sensitivity of degree-based topological indices, *Appl. Math. Comput.*, 219 (2013) 8973–8978.
- [28] Redžepović I., Furtula B., Comparative study on structural sensitivity of eigenvalue-based molecular descriptors, *J. Math. Chem.*, 59 (2021) 476–487.
- [29] Zemljić K., Žigert Pleteršek P., Smoothness of graph energy in chemical graphs, *Mathematics.*, 11 (2023) #552.

## Enhanced Breast Cancer Risk Classification Through Genetic Algorithm-Based Feature Selection and Machine Learning Techniques

Aynur Yonar<sup>1,a,\*</sup>, Harun Yonar<sup>2,b</sup>, Öznur Özaltın<sup>3,c</sup>

<sup>1</sup> Department of Statistics, Faculty of Science, Selcuk University, Konya, Türkiye

<sup>2</sup> Department of Biostatistics, Faculty of Veterinary, Selcuk University, Konya, Türkiye

<sup>3</sup> Department of Actuarial Science, Faculty of Science, Hacettepe University, Ankara, Türkiye

\*Corresponding author

### Research Article

#### History

Received: 27/02/2024

Accepted: 03/05/2025



This article is licensed under a Creative Commons Attribution-NonCommercial 4.0 International License (CC BY-NC 4.0)

### ABSTRACT

Breast cancer remains one of the leading causes of mortality among women worldwide and represents a major global health challenge. Accurate classification of breast tumors as benign or malignant is therefore of critical importance for timely diagnosis and effective treatment. This study aims to enhance breast cancer risk classification by integrating machine learning (ML) techniques with a genetic algorithm-based feature selection method. Initially, multiple ML algorithms are applied to features extracted from digitized images obtained through fine-needle aspiration (FNA) of breast masses. Subsequently, a genetic algorithm-based feature selection approach is employed to identify a subset of the most discriminative features. The results demonstrate that ML models utilizing the feature subsets selected by the genetic algorithm consistently achieve higher classification accuracy compared to their baseline counterparts. This highlights the effectiveness of the proposed feature selection strategy in improving the discriminative capacity of ML models. Beyond the observed improvements in accuracy, the refined ML models developed in this study show potential for more precise and reliable breast cancer diagnoses. By enhancing the performance of ML-based decision support systems, the genetic algorithm-based feature selection approach may contribute to the advancement of personalized treatment strategies in breast cancer care.

**Keywords:** Breast cancer, Machine learning, Risk classification, Genetic algorithm, Feature selection.

<sup>a</sup> [aynursahin@selcuk.edu.tr](mailto:aynursahin@selcuk.edu.tr)

<sup>b</sup> <https://orcid.org/0000-0003-1681-9398>

<sup>c</sup> [oznurozaltin@hacettepe.edu.tr](mailto:oznurozaltin@hacettepe.edu.tr)

<sup>b</sup> <https://orcid.org/0000-0001-9841-1702>

<sup>b</sup> [hyonar@selcuk.edu.tr](mailto:hyonar@selcuk.edu.tr)

<sup>c</sup> <https://orcid.org/0000-0003-1574-3993>

## Introduction

Breast cancer stands as one of the most common malignant tumors globally, constituting 10.4% of all cancers. Notably, it holds the unfortunate distinction of being the primary cause of mortality among women aged between 20 and 50 years [1,2]. According to the World Health Organization (WHO), there were 2.3 million cases of breast cancer and 685,000 deaths worldwide in 2020. By the end of 2020, the number of women currently living who have been diagnosed with breast cancer within the previous five years amounted to 7.8 million, establishing it as the most widespread form of cancer globally [3]. Timely detection, prompt diagnosis, and early treatment are imperative in preventing the advancement of the disease and mitigating its mortality rate. Hence, the accurate classification of breast cancers as either benign or malignant is of vital importance [4].

Machine Learning (ML), a subset of artificial intelligence, operates on the principle that machines should be provided with access to data and allowed to autonomously learn and explore. Its focus lies in extracting meaningful patterns from extensive datasets. This field harnesses the power of algorithms and statistical models to enable machines to learn from experience, adapt to changing scenarios, and make informed decisions without explicit programming. The essence of ML lies in its

capacity to uncover insights and patterns, enhancing its utility across various domains such as data analysis, pattern recognition, and predictive modeling [5].

Classification serves as a supervised learning approach where a computer program learns from provided data and subsequently generates new observations or classifications in both ML and statistics. The fundamental process entails training an algorithm on a labeled dataset, where the desired output is known, allowing the program to discern patterns and relationships within the data. Following this training phase, the classifier is equipped to predict class labels or categories for new, unseen data based on the patterns it has learned. Leveraging ML algorithms, this process empowers systems to identify intricate patterns within data, finding applications in diverse domains such as image recognition, natural language processing, and fraud detection. Classification plays a pivotal role in enhancing automated decision-making by enabling systems to categorize and interpret data effectively. The accuracy of classification is heavily contingent on the nature of features within a dataset, where the presence of irrelevant or redundant data can impact performance. To enhance classification accuracy, the utilization of feature selection becomes crucial [6]. This process aims to eliminate irrelevant or redundant

features, optimizing the dataset by retaining only the most significant attributes. Through feature selection, the model's efficiency is improved, contributing to more accurate and streamlined classification outcomes [7, 8].

In recent years, researchers have proposed a wide range of feature selection techniques based on optimization and metaheuristic algorithms. Ye, Xu [9] introduced a feature selection approach utilizing adaptive particle swarm optimization with leadership learning. Ghosh, Datta [10] focused on hyperspectral image data and employed Self-adaptive Differential Evolution (SADE) for feature subset generation. Zhang, Mistry [11] presented a modified version of the Firefly Algorithm (FA) specifically designed to select discriminative features in classification and regression models. Baig, Aslam [12] introduced hybrid approach that combines a Differential Evolution (DE) optimization algorithm to seek out the feature space and yield an optimal subset of features. Sindhu and Ngadiran [13] proposed a Sine-Cosine Algorithm (SCA) with an Elitism strategy and the best new solution update mechanism to select features and enhance classification accuracy. Mafarja and Mirjalili [14] employed a wrapper feature selection model to simultaneously decrease the quantity of features and improve classification accuracy. Abdel-Basset, El-Shahat [15] suggested a novel Grey Wolf Optimizer algorithm via a Two-phase Mutation to select optimal features.

Beyond these techniques, the use of Genetic Algorithm (GA) has garnered considerable attention due to its simplicity, adaptability, and ability to effectively explore complex, high-dimensional search spaces. Recent studies have applied GA in various medical diagnostic tasks, including breast cancer detection. For instance, Sehgal et al. [16] employed GA to optimize hyperparameters in deep learning models, achieving significant improvements in AUC scores for breast cancer classification. Similarly, Yaqoob et al. [17] developed a hybrid GA-deep learning model using RNA-Seq gene expression data, successfully handling high-dimensional biological data. Boumaraf et al. [18] used GA for selecting BI-RADS features from mammogram images and applied a backpropagation neural network for classification. These studies emphasize the importance of integrating metaheuristic-based feature selection with ML to enhance diagnostic accuracy and efficiency in real-world clinical scenarios.

Building on these developments, this study investigates the effect of GA-based feature selection on the performance of various ML classifiers in breast cancer diagnosis. Specifically, five ML algorithms—Decision Tree (DT), K-Nearest Neighbors (KNN), Logistic Regression (LR), Multi-Layer Perceptron (MLP), and Random Forest (RF)—are used to classify samples based on features extracted from digitized images of fine-needle aspiration Fine-Needle Aspiration (FNA) of breast masses. The classification is performed both before and after applying GA for feature selection. The effectiveness of each approach is evaluated using key performance metrics: accuracy, precision, recall, and F1-score.

The aim of this study is to systematically assess how GA-based feature selection influences the performance of different ML classifiers in breast cancer classification. The findings are expected to contribute to the growing body of knowledge on intelligent diagnostic systems and offer practical insights into the design of more accurate and reliable clinical decision support tools.

The remainder of this paper is organized as follows: Section 2 introduces the ML algorithms, GA-based feature selection strategy, and experimental setup. Section 3 presents the application of classifiers to the breast cancer dataset and summarizes the classification results. Section 4 discusses the findings of literature, and Section 5 concludes the study.

## Material And Methods

In this section, a concise overview of the dataset used, ML algorithms, feature selection strategy, and the GA employed in this study is presented.

### Dataset

This study utilizes the Breast Cancer Wisconsin (Diagnostic) Dataset obtained from the University of California, Irvine (UCI) Machine Learning Repository [19]. The dataset consists of 30 numerical features that were extracted from digitized images of FNA of breast masses. These features describe characteristics of the cell nuclei present in the images.

Specifically, for each cell nucleus, 10 real-valued attributes are computed:

Radius: Mean of distances from the center to points on the perimeter  
 Texture: Standard deviation of gray-scale values  
 Perimeter: Perimeter of the cell nucleus  
 Area: Area of the cell nucleus  
 Smoothness: Local variation in radius lengths  
 Compactness:  $(Perimeter^2 / Area) - 1$   
 Concavity: Severity of concave portions of the contour  
 Concave points: Number of concave portions of the contour  
 Symmetry: Degree of symmetry of the cell nucleus  
 Fractal dimension: "Coastline approximation" (fractal measure of complexity)

For each of the above attributes, the mean, standard error, and "worst" (mean of the three largest values) were calculated, resulting in a total of 30 features per instance. The dataset includes a total of 569 samples, comprising 357 benign and 212 malignant tumor instances.

Prior to model training and feature selection, a series of preprocessing steps were applied to the dataset to ensure data quality and improve model performance. First, the dataset was examined for missing values, and no missing observations were detected. All feature values were then normalized using min-max normalization to scale the data to the [0, 1] range, ensuring that features with different scales would not bias the learning algorithms. Since the dataset was relatively balanced, no



resampling methods such as the Synthetic Minority Oversampling Technique (SMOTE) or under sampling were required. Finally, the class labels (benign and malignant) were encoded as binary values (0 and 1) to allow compatibility with the classification algorithms.

Although only a single dataset is used in this study, the Breast Cancer Wisconsin (Diagnostic) dataset is widely accepted as a benchmark in the biomedical ML literature. It offers a balanced class distribution, clinically relevant morphological features derived from diagnostic imaging, and enough instances for classification tasks. These characteristics justify its use for evaluating the effectiveness of the proposed feature selection method. Future studies may expand upon this work by applying the same methodology to additional datasets to assess generalizability.

### **Machine Learning Algorithms**

ML algorithms, which are tasked with classification, are computational techniques designed to categorize data into distinct classes or groups. These algorithms learn patterns from labeled training data and apply these learned patterns to new, unseen data for classification purposes. A brief overview of the algorithms used in this study, including LR, DT, KNN, MLP, and RF, is provided below.

#### **Logistic Regression (LR)**

LR is a linear model specifically developed for classification tasks, rather than regression. This model involves using a logistic function to represent the probabilities linked to various outcomes in a single trial. Despite its linear nature, logistic regression is particularly powerful in binary and multiclass classification problems, making it a widely employed algorithm in various fields such as statistics, machine learning, and epidemiology [20].

#### **Decision Tree (DT)**

DT is a type of non-parametric supervised learning method used for classification and regression applications. A DT algorithm is organized in a hierarchical manner, where each node corresponds to a test of a certain feature, each branch represents the outcome of that test, and each leaf represents either a class label or a distribution of classes [21].

#### **K-Nearest Neighbors (KNN) Classifier**

The KNN method is the predominant Neighbors-based classification method. The ideal selection of the 'k' number relies significantly on the data: typically, a higher 'k' value reduces the impact of noise but can also blur the classification boundaries [22].

#### **Multi-Layer Perceptron (MLP) Classifier**

A supervised learning approach called the MLP classifier is utilized for learning a function. It makes use of stochastic gradient descent, or LBFGS, to optimize the log-loss function. This algorithm can be used for a variety of

classification tasks because it excels at identifying complex patterns and correlations in the data [23].

#### **Random Forest (RF)**

RF is one of the ensemble classification approaches that builds multiple DT classifiers on different subsets of the dataset and uses averaging to improve prediction accuracy and reduce overfitting. Each tree in a random forest ensemble is built using a bootstrap sample selected with replacement from the training data. This methodology, known as bagging, contributes to the robustness and generalization capabilities of the overall model [24].

#### **Feature Selection**

Feature selection involves eliminating unnecessary and unimportant features from a dataset to enhance the efficiency of a learning algorithm. However, this task poses significant challenges, primarily due to the vast search space involved. The dataset with  $n$  features has a total of  $2^n$  potential solutions. The complexity of this task is exacerbated as  $n$  increases, which is often the case with advancements in data collection techniques and the growing complexity of the problems being addressed.

Feature selection methods are widely employed in studies to enhance the accuracy of classification. Among the commonly used methods for dimensionality reduction are Principal Component Analysis (PCA) [25], Independent Component Analysis (ICA) [26], and Sequential Forward and Backward Searches [27]. However, these methods often encounter challenges such as local optimal traps or high computational costs.

To address these issues, researchers have turned to evolutionary algorithms like GA [28, 29], Particle Swarm Optimization (PSO) [9, 30], DE [12,31] and Artificial Bee Colony (ABC) [32, 33] optimization. These algorithms have demonstrated success in handling tasks with large feature search spaces. In this study, GA is employed for feature selection, showcasing its effectiveness in optimizing classification outcomes.

#### **Genetic Algorithm (GA)**

GA, conceptualized by Holland [34], is widely recognized as a highly effective search method for approximating solutions in optimization problems. The algorithm kicks off by generating an initial population at random and iterates through a series of steps to facilitate population evolution.

As a population-based method and a prominent class of evolutionary algorithms, GA eliminates concerns related to initial values. Typically, the GA commences with the creation of random initial population and proceeds through an iterative process known as a generation. Each generation encompasses stages such as selection, reproduction involving crossover and mutation operators, evolution, and replacement [35, 36]. The flowchart of GA is shown Figure 1.

The GA was implemented for feature selection using a population size of 30 individuals and a maximum of 50 generations. The algorithm utilized standard binary

tournament selection, single-point crossover with a probability of 0.8, and a mutation rate of 0.02.

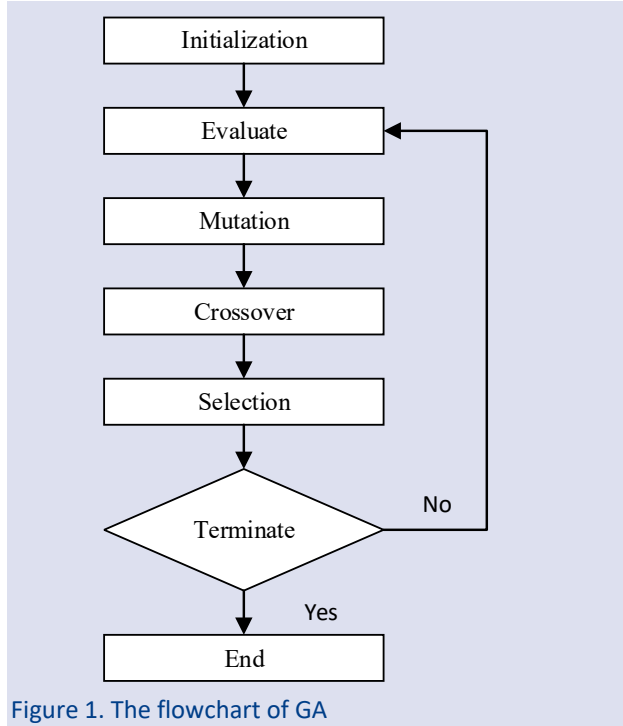


Figure 1. The flowchart of GA

A fitness function based on classification accuracy obtained from a 3-Nearest Neighbor classifier was employed to evaluate feature subsets.

### Application and Experimental Results

In the era of precision medicine, developing accurate and robust models for breast cancer plays a pivotal role in facilitating early diagnosis and improving patient outcomes. To contribute to this goal, the present study examines the impact of GA-based feature selection on the performance of several ML algorithms for classifying breast tumors as benign or malignant.

The Breast Cancer Wisconsin (Diagnostic) dataset from the UCI ML Repository was utilized. A stratified 80:20 train-test split was employed, with 80% of the samples allocated for training and the remaining 20% reserved for testing. Classification models were developed using several well-established ML algorithms, including LR, DT, KNN, MLP, and RF. These models were first evaluated using the full feature set, after which the same classifiers were re-trained on a subset of features selected via a GA-based feature selection method. All implementations were carried out in Python, utilizing the scikit-learn and matplotlib libraries for training, evaluation, and visualization.

All ML models were evaluated using 5-fold cross-validation to ensure robustness and minimize overfitting. The dataset was partitioned into 5 equal subsets, with 4 folds used for training and 1-fold for testing in each iteration. The average performance across all folds was recorded for each metric.

Hyperparameter tuning for classifiers such as DT, KNN, and RF was conducted using grid search within a 5-fold cross-validation framework to determine optimal parameter configurations. For the DT classifier, the maximum tree depth (max\_depth) was searched over the range of [3, 5, 10, 15, 20], and the optimal depth was found to be 10. For K-Nearest Neighbors, the number of neighbors (n\_neighbors) varied between [1, 3, 5, 7, 9], with 3 neighbors yielding the best performance. In the case of RF, the number of trees (n\_estimators) was explored within [50, 100, 200], and the maximum depth was selected from [None, 10, 20, 30]. The best results were obtained using 100 estimators and maximum depth = 20. The final hyperparameter configurations were selected based on the highest average accuracy achieved across five folds.

To assess and compare the classification performance of the baseline and GA-enhanced models, four evaluation metrics were calculated: accuracy, precision, recall, and F1-score. In addition, confusion matrices were generated to provide a visual breakdown of correctly and incorrectly classified instances. The formulas used for these metrics are presented below:

$$Accuracy = \frac{TP + TN}{TP + FP + TN + FN} \quad (1)$$

$$Precision = \frac{TP}{TP + FP} \quad (2)$$

$$Recall = \frac{TP}{TP + FN} \quad (3)$$

$$F1 - score = 2 \times \frac{Precision \times Recall}{Precision + Recall} \quad (4)$$

Here, TP denotes true positives, TN true negatives, FP false positives, and FN false negatives.

Figure 2 presents the confusion matrices of all classifiers, both with and without GA-based feature selection. These matrices reveal the distribution of TP, TN, FP, and FN predictions, allowing for a visual assessment of classification improvements. In most cases, GA leads to a reduction in FP and FN values, indicating enhanced precision and recall.

For example, KNN and MLP show visible improvements after GA, with fewer misclassified instances. DT also benefits from GA by reducing misclassification rates. In contrast, RF displays minimal change in its confusion matrix, consistent with its inherent feature selection capability.

These matrix-based observations align with the metric values in Table 1, confirming that GA contributes to more accurate and reliable classification by eliminating less relevant features and focusing on the most informative ones.

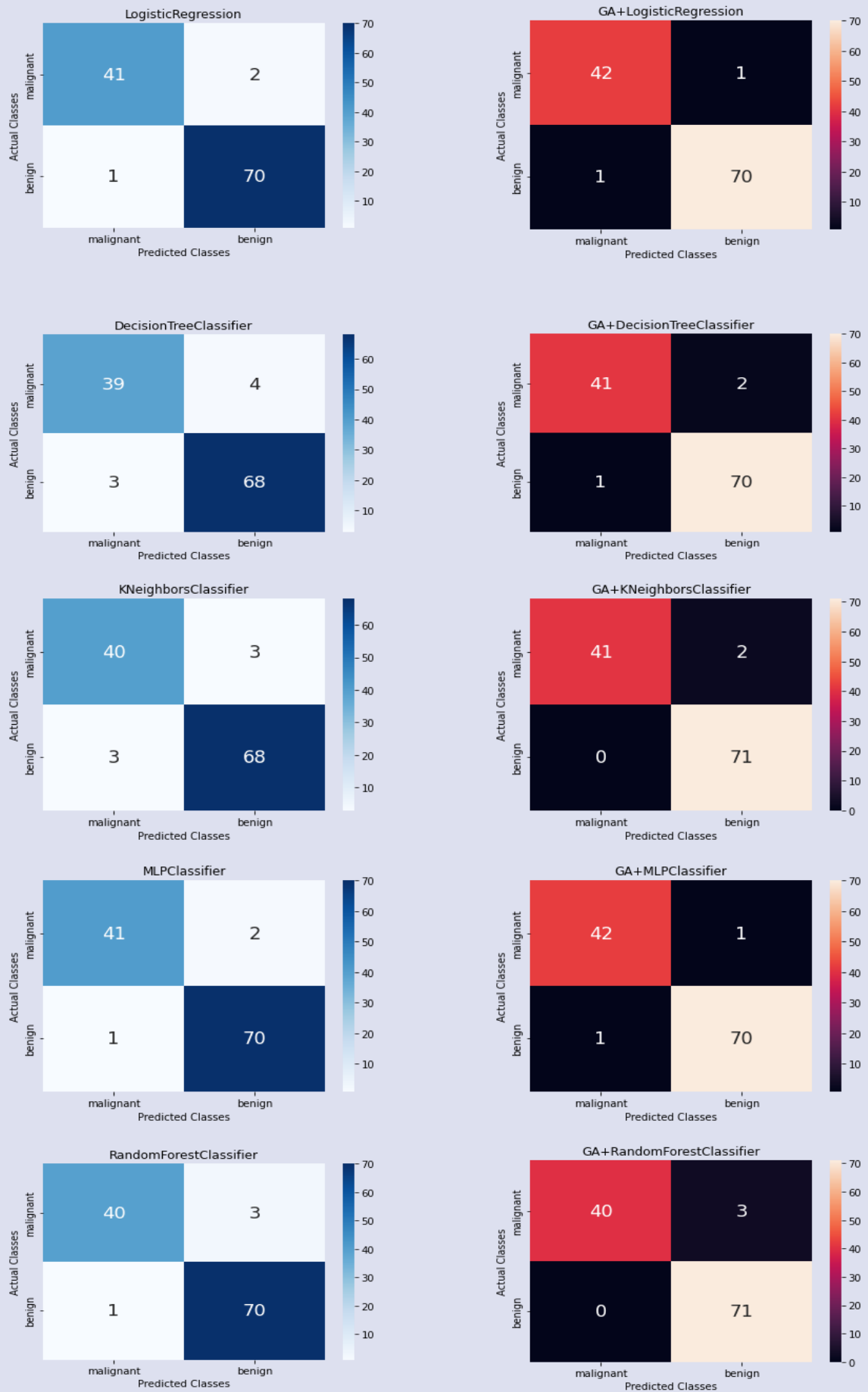


Figure 2. Confusion matrices of the classifiers before and after Genetic Algorithm-based feature selection, showing differences in TP, TN, FP, and FN rates.

The corresponding performance metrics for each model are summarized in Table 1, offering a clear comparison between the baseline ML models and those optimized through GA-based feature selection.

Table 1. Performance comparison of ML algorithms

Model	Accuracy	Precision	Recall	F1-score
LR	0.9736	0.9824	0.9859	0.9790
GA-LR	0.9754	0.9816	0.9830	0.9803
DT	0.9350	0.9485	0.9492	0.9479
GA_DT	0.9456	0.9555	0.9549	0.9562
KNN	0.9473	0.9577	0.9577	0.9577
GA_KNN	0.9561	0.9713	0.9774	0.9652
MLP	0.9701	0.9781	0.9802	0.9761
GA-MLP	0.9719	0.9803	0.9830	0.9776
RF	0.9631	0.9768	0.9830	0.9707
GA_RF	0.9631	0.9754	0.9802	0.9707

The numerical results indicate that most classifiers benefit from GA in terms of improved predictive accuracy, recall, and F1-score. Among the classifiers, DT, KNN, and MLP demonstrated the most substantial improvements following feature selection. The accuracy of DT increased from 0.9350 to 0.9456, and its F1-score rose from 0.9479 to 0.9562, indicating a more reliable and generalizable model. KNN also exhibited a consistent enhancement across all metrics, particularly in recall (from 0.9577 to 0.9774), which is essential in medical contexts where false negatives must be minimized. MLP showed increased precision, recall, and F1-score, achieving a final F1-score of 0.9776, reflecting its improved balance between sensitivity and specificity after GA was applied.

LR, which already exhibited strong baseline performance, experienced marginal gains in accuracy (from 0.9736 to 0.9754) and F1-score (from 0.9790 to 0.9803). However, a slight decline in recall was observed, suggesting that GA may have limited impact on classifiers with inherently stable decision boundaries.

In the case of RF, performance metrics remained unchanged after applying GA. This is consistent with its ensemble nature and built-in feature selection mechanism, where redundant or less informative features are implicitly down weighted during training. As a result, external feature selection techniques like GA may offer minimal added value for RF.

These results suggest that GA can effectively enhance the performance of various ML classifiers, especially those more sensitive to feature dimensionality. By eliminating irrelevant or redundant features, GA helps improve classification robustness and focus on the most discriminative patterns in the data. This is particularly important in medical diagnostics, where high recall and precision are critical to ensuring accurate and safe decision-making.

Therefore, integrating GA as a preprocessing step can be a valuable strategy in the development of more efficient and interpretable ML-based clinical decision support systems. Future research should consider testing the proposed methodology on larger and more diverse datasets, as well as comparing GA with other

metaheuristic algorithms to further evaluate its adaptability and generalization capability in complex medical applications.

## Discussion

The results of this study demonstrate that applying GA-based feature selection prior to ML classification significantly enhances diagnostic performance for breast cancer detection. Specifically, classifiers such as DT, KNN, and MLP exhibited notable gains in accuracy, recall, and F1-score after feature reduction. These findings confirm the critical role of eliminating redundant or non-informative attributes in improving classification reliability.

Recent literature also supports the integration of metaheuristic feature selection methods with ML models in cancer classification. For example, Tan et al. [37] applied genetic programming to oral cancer prognosis, reporting an average accuracy of 83.87%, while Sharma et al. [38] achieved 96.66% and 93.06% accuracy using Support Vector Machine (SVM) and Artificial Neural Network (ANN), respectively, on the WBCD dataset. Sidey-Gibbons and Sidey-Gibbons [39] reached up to 96% accuracy using ensemble models. In comparison, our study reported 97.5% accuracy with LR and 97.1% with MLP after GA optimization, demonstrating the competitive performance of our proposed approach.

A key strength of this study lies in its flexibility across multiple classifiers. Unlike many existing studies that evaluate feature selection within a single model, we assessed five classifiers, both linear (LR) and nonlinear (MLP, RF), and observed consistent performance improvements. This adaptability makes the framework broadly applicable in clinical diagnostic modeling. Additionally, reducing the feature set improves interpretability, an essential aspect in medical decision-making.

From a clinical perspective, enhancing classification performance directly supports more reliable decision support systems. Improving recall reduces the risk of false negatives, which is critical for detecting malignant cases early. Simultaneously, improved precision minimizes false positives, preventing unnecessary interventions and patient distress.

Nonetheless, certain limitations must be acknowledged. The current study was conducted using a single, albeit well-established and clinically relevant, dataset (WBCD). While its quality and balance make it ideal for benchmarking, broader validation is required. Future studies should evaluate the proposed framework on additional datasets, including those from real-world clinical environments or public repositories.

Moreover, while GA demonstrated strong performance, it also carries known limitations such as sensitivity to hyperparameters, risk of convergence to local optima, and higher computational cost. Future research may consider comparing GA with alternative metaheuristic or hybrid approaches—such as PSO, ABC,



Grey Wolf Optimizer (GWO) or filter-wrapper ensembles—to enhance both robustness and efficiency.

In summary, the integration of GA with ML classifiers proves to be an effective strategy for breast cancer classification. The proposed method achieves high predictive accuracy, promotes model interpretability, and holds promise for clinical application. However, continued evaluation on diverse data sources and comparative studies with alternative optimization strategies will be essential for building more generalizable and scalable diagnostic systems.

## Conclusions

This study evaluated the effectiveness of GA-based feature selection in enhancing the performance of ML classifiers for breast cancer diagnosis. Using a dataset comprising 30 features derived from fine-needle aspirate images, GA was employed to identify the most informative subset before classification.

The experimental findings confirmed that applying GA led to improvements in classification accuracy, recall, and F1-score, particularly for DT, KNN, and MLP. These results underscore the importance of dimensionality reduction and the role of relevant feature selection in improving diagnostic accuracy.

While GA offers valuable advantages—such as adaptability and effective search capability—it also presents certain limitations. These include sensitivity to parameter tuning, potential convergence to local optima, and high computational cost. To overcome these challenges, future work should explore and compare alternative metaheuristic approaches in similar classification tasks.

Additionally, validating the proposed approach on more diverse and larger datasets, beyond the WBCD, such as those publicly available, will be crucial in assessing generalizability and scalability. Overall, this study supports GA as a promising preprocessing technique for improving ML-based breast cancer diagnostic systems, while also highlighting the importance of comparative evaluations and broader dataset applications in future research.

## Conflicts of interest

There are no conflicts of interest in this work.

## References

- [1] Lacoviello, L., Bonaccio, M., de Gaetano, G., and Donati, M. B. Epidemiology Of Breast Cancer, A Paradigm Of The “Common Soil” Hypothesis, *Seminars In Cancer Biology*, (2021) 4-10.
- [2] Siegel, R. L., Miller, K. D., and Jemal, A., Cancer Statistics, *CA: A Cancer Journal For Clinicians*, 69 (1) (2019), 7-34.
- [3] WHO. Available at <https://www.who.int/news-room/fact-sheets/detail/breast-cancer>. Retrieved March 10, 2023.
- [4] Mridha, M. F., Hamid, M. A., Monowar, M. M., Keya, A. J., Ohi, A. Q., Islam, M. R., and Kim, J.-M., A Comprehensive Survey On Deep-Learning-Based Breast Cancer Diagnosis, *Cancers*, 13 (23) (2021) 6116.
- [5] Mehrotra, D., Basics Of Artificial Intelligence & Machine Learning, *Notion Press*, (2019).
- [6] Segal, M. R., Machine Learning Benchmarks And Random Forest Regression, (2004).
- [7] Blum, A. L. and Langley, P., Selection Of Relevant Features And Examples In Machine Learning, *Artificial Intelligence*, 97 (1-2) (1997) 245-271.
- [8] Chen, R.-C., Dewi, C., Huang, S.-W., and Caraka, R. E., Selecting Critical Features For Data Classification Based On Machine Learning Methods, *Journal of Big Data*, 7 (1) (2020) 52.
- [9] Ye, Z., Xu, Y., He, Q., Wang, M., Bai, W., and Xiao, H., Feature Selection Based on Adaptive Particle Swarm Optimization With Leadership Learning, *Computational Intelligence Neuroscience*, (2022).
- [10] Ghosh, A., Datta, A., and Ghosh, S., Self-Adaptive Differential Evolution For Feature Selection In Hyperspectral Image Data, *Applied Soft Computing*, 13 (4) (2013) 1969-1977.
- [11] Zhang, L., Mistry, K., Lim, C. P., and Neoh, S. C., Feature Selection Using Firefly Optimization For Classification And Regression Models, *Decision Support Systems*, 106 (2018) 64-85.
- [12] Baig, M. Z., Aslam, N., Shum, H. P., and Zhang, L., Differential Evolution Algorithm As A Tool For Optimal Feature Subset Selection In Motor Imagery EEG, *Expert Systems With Applications*, 90 (2017) 184-195.
- [13] Sindhu, R., Ngadiran, R., Yacob, Y. M., Zahri, N. A. H., and Hariharan, M., Sine-Cosine Algorithm For Feature Selection With Elitism Strategy And New Updating Mechanism, *Neural Computing Applications*, 28 (2017) 2947-2958.
- [14] Mafarja, M. and Mirjalili, S., Whale Optimization Approaches for Wrapper Feature Selection, *Applied Soft Computing*, 62 (2018) 441-453.
- [15] Abdel-Basset, M., El-Shahat, D., El-Henawy, I., De Albuquerque, V. H. C., and Mirjalili, S., A New Fusion Of Grey Wolf Optimizer Algorithm With A Two-Phase Mutation For Feature Selection, *Expert Systems with Applications*, 139 (2020) 112824.
- [16] Sehgal, A., Sehgal, M., La, H. M., and Bebis, G., Deep Learning Hyperparameter Optimization for Breast Mass Detection in Mammograms, *International Symposium on Visual Computing*, Cham: Springer Nature Switzerland, (2022) 270–283.
- [17] Yaqoob, A., Verma, N. K., Aziz, R. M., and Shah, M. A., RNA-Seq Analysis for Breast Cancer Detection: A Study on Paired Tissue Samples Using Hybrid Optimization and Deep Learning Techniques, *Journal of Cancer Research and Clinical Oncology*, 150(10) (2024) 455.
- [18] Boumaraf, S., Liu, X., Ferkous, C., and Ma, X., A New Computer-Aided Diagnosis System with Modified Genetic Feature Selection for BI-RADS Classification of Breast Masses in Mammograms, *BioMed Research International*, 2020(1) (2020) 7695207.
- [19] UCI, Available at <https://archive.ics.uci.edu/dataset/17/breast+cancer+wisconsin+diagnostic> Retrieved January 28, 2024.
- [20] Maalouf, M. and Strategies, Logistic Regression in Data Analysis: An Overview, *International Journal of Data Analysis Techniques*, 3 (3) (2011) 281-299.
- [21] ZhuParris, A., de Goede, A. A., Yocarini, I. E., Kraaij, W., Groeneveld, G. J., and Doll, R. J., Machine Learning Techniques for Developing Remotely Monitored Central Nervous System Biomarkers Using Wearable Sensors: A Narrative Literature Review, *Sensors*, 23 (11) (2023) 5243.

- [22] Dillen, A., Lathouwers, E., Miladinović, A., Marusic, U., Ghaffari, F., Romain, O., Meeusen, R., and De Pauw, K., A Data-Driven Machine Learning Approach For Brain-Computer Interfaces Targeting Lower Limb Neuroprosthetics, *Frontiers In Human Neuroscience*, 16 (2022) 949224.
- [23] Awadallah, M. A., Abu-Doush, I., Al-Betar, M. A., and Braik, M. S. Metaheuristics For Optimizing Weights, *Neural Networks In Comprehensive Metaheuristics*, Elsevier, (2023) 359-377.
- [24] Fawagreh, K., Gaber, M. M., and Elyan, E., Random Forests: From Early Developments To Recent Advancements, *Systems Science Control Engineering: An Open Access Journal*, 2 (1) (2014) 602-609.
- [25] Yu, X., Chum, P., and Sim, K.-B., Analysis The Effect Of PCA For Feature Reduction In Non-Stationary EEG Based Motor Imagery Of BCI System, *Optik* 125 (3) (2014) 1498-1502.
- [26] Guo, X., Wu, X., Gong, X., and Zhang, L. (Year) Envelope Detection Based On Online ICA Algorithm And Its Application To Motor Imagery Classification. in: *2013 6th International IEEE/EMBS Conference on Neural Engineering (NER)*, (2013) 1058-1061 IEEE.
- [27] Chandrashekar, G. and Sahin, F., A Survey On Feature Selection Methods. *Computers Electrical Engineering*, 40 (1) (2014) 16-28.
- [28] Aalaei, S., Shahraki, H., Rowhanimanesh, A., and Eslami, S., Feature Selection Using Genetic Algorithm For Breast Cancer Diagnosis: Experiment On Three Different Datasets, *Iranian journal of basic medical sciences*, 19 (5) (2016) 476.
- [29] Leardi, R., Boggia, R., and Terrile, M., Genetic Algorithms As A Strategy For Feature Selection, *Journal of chemometrics*, 6 (5) (1992) 267-281.
- [30] Sakri, S. B., Rashid, N. B. A., and Zain, Z. M., Particle Swarm Optimization Feature Selection For Breast Cancer Recurrence Prediction, *IEEE Access*, 6 (2018) 29637-29647.
- [31] Wang, P., Xue, B., Liang, J., and Zhang, M., Multiobjective Differential Evolution For Feature Selection In Classification, *IEEE Transactions on Cybernetics*, (2021)
- [32] Hancer, E., Xue, B., Karaboga, D., and Zhang, M., A Binary ABC Algorithm Based On Advanced Similarity Scheme For Feature Selection, *Applied Soft Computing*, 36 (2015) 334-348.
- [33] Rostami, O. and Kaveh, M., Optimal Feature Selection For SAR Image Classification Using Biogeography-Based Optimization (BBO), Artificial Bee Colony (ABC) And Support Vector Machine (SVM): A Combined Approach Of Optimization And Machine Learning. *Computational Geosciences*, 25 (2021) 911-930.
- [34] Holland, J. H. (1975) *Adaptation In Natural And Artificial Systems* The University of Michigan Press.
- [35] Talbi, E.-G., *Metaheuristics: From Design To Implementation*, John Wiley & Sons, 2009.
- [36] Yang, X.-S., *Engineering Optimization: An Introduction with Metaheuristic Applications*, John Wiley & Sons, (2010).
- [37] Tan, M. S., Tan, J. W., Chang, S.-W., Yap, H. J., Kareem, S. A., and Zain, R. B., A Genetic Programming Approach to Oral Cancer Prognosis, *PeerJ*, 4 (2016).
- [38] Sharma, A., Kulshrestha, S., and Daniel, S. B., Machine Learning Approaches for Cancer Detection, *International Journal of Engineering and Manufacturing (IJEM)*, 8(2) (2018) 45–55.
- [39] Sidey-Gibbons, J. A. M., and Sidey-Gibbons, C. J., Machine Learning in Medicine: A Practical Introduction, *BMC Medical Research Methodology*, 19(1) (2019) 64.

## Genetic and Morphological Diversity of *Tenthredopsis* (Tenthredinidae: Symphyta: Hymenoptera) Species: A Case Study in Anatolia

Sevda Hastaoğlu Örgen <sup>1,a,\*</sup>, Hasan Hüseyin Başbüyük <sup>2,b</sup>

<sup>1</sup> Department of Medical Services and Techniques, Vocational School of Healthcare Services, Sivas Cumhuriyet University, Türkiye

<sup>2</sup> Department of Gerontology, Faculty of Health Sciences, Akdeniz University, Antalya, Türkiye

\*Corresponding author

### Research Article

#### History

Received: 27/12/2024

Accepted: 07/05/2025




This article is licensed under a Creative Commons Attribution-NonCommercial 4.0 International License (CC BY-NC 4.0)

### ABSTRACT


The genus *Tenthredopsis* (Tenthredinidae: Hymenoptera), characterized by a Palearctic distribution, is widely recognized as a taxonomic challenge due to its limited morphological variation. This study aims to evaluate the phylogenetic and biogeographical characteristics of *Tenthredopsis* species in Anatolia by analyzing their morphological and molecular traits. Initially, morphotypes were defined based on morphological characters, and the taxonomic validity of each morphotype was assessed through phylogenetic analyses using three mitochondrial gene regions. The findings revealed congruence between morphological and molecular data. The study identified the distribution of 27 taxa within Anatolia, comprising 17 confirmed and 10 potential taxa, represented by 250 individuals belonging to the genus *Tenthredopsis*. The results underscore Anatolia's significance as a hotspot for genetic and morphological diversity within the genus *Tenthredopsis* and highlight its critical role in the evolutionary adaptations of these species. Additionally, the observed distribution patterns further support the importance of Anatolia as a refugium during the last glacial periods.

**Keywords:** *Tenthredopsis*, COI, COII, Cytochrome b, Biogeography.

 [hastaoглу@cumhuriyet.edu.tr](mailto:hastaoглу@cumhuriyet.edu.tr)

 <https://orcid.org/0000-0001-8313-2946>

 [hbasibuyuk@akdeniz.edu.tr](mailto:hbasibuyuk@akdeniz.edu.tr)

 <https://orcid.org/0000-0001-6504-6139>

## Introduction

The understanding and classification of biological diversity are of paramount importance for elucidating the fundamental mechanisms underlying natural systems [1]. The field of systematics provides a framework for comprehending the evolutionary relationships of organisms, thereby offering essential insights into the foundations of biodiversity. Taxonomic studies not only facilitate the identification of existing species but also contribute to understanding their ecological roles and devising effective conservation strategies [2]. Within this context, an in-depth understanding of biodiversity dynamics enables the formulation of more robust policies to address environmental changes.

Anatolia occupies a unique position globally due to its exceptional biodiversity. Its geographic location at the intersection of Asia, Europe, and Africa has resulted in a mosaic of habitats that are both in floristic and faunistic rich. This distinctive geographic structure has accelerated species adaptation processes in the region, leading to a high degree of genetic diversity [3]. The exceptional biodiversity of Anatolia renders it an ideal model for investigating evolutionary processes in species adapted to diverse ecological conditions. This unique status of Anatolia is critical not only for the survival of endemic species but also for their adaptation to environmental stressors. Geographic barriers have shaped species distributions and genetic divergence, thereby enhancing regional biodiversity. For instance, Anatolia's mountainous terrain and varied microclimatic zones are

significant factors supporting the genetic variation observed in resident species. This phenomenon offers a pertinent example of adaptive evolution and biogeographical distribution within the genus *Tenthredopsis*.

The *Tenthredopsis* species, which exhibit broad distribution across the Palearctic region, demonstrate considerable variation in response to the unique environmental conditions of Anatolia. During past glacial periods, Anatolia functioned as a refugium for numerous species. Following the retreat of glaciers, these species expanded to different regions, thereby increasing genetic diversity. The geological history of Anatolia offers critical insights into the current genetic structure and distribution of species in the region [1]. Within this framework, *Tenthredopsis* species represent an ideal model group for understanding the biogeographical and evolutionary processes of Anatolia. Their adaptation processes integrate both morphological and genetic characteristics.

Systematic studies of *Tenthredopsis* species necessitate the integrated application of genetic and morphological methods. These species are notable for their high adaptive capacity to environmental factors. Limitations encountered in morphological analyses are effectively addressed through molecular biology techniques, leading to more precise results. For instance, species exhibiting similar morphological traits can be distinctly identified using DNA sequencing methods. In particular, mitochondrial DNA markers play a crucial role

in elucidating phylogenetic relationships taxonomic units. Gene regions such as COI, COII, and cytochrome b serve as effective tools for assessing genetic distances among species.

Anatolia is considered a transition zone for both plant and animal species in terms of biogeography. This perspective not only facilitates an understanding of current species distributions but also provides critical insights into their origins and evolutionary trajectories. In this regard, *Tenthredopsis* species serve as pivotal examples for investigating the nexus between biogeography and evolutionary biology. The findings of this study are anticipated to contribute not only to the understanding of *Tenthredopsis* species but also to the development of broader biodiversity strategies for Anatolia.

This study comprehensively examines *Tenthredopsis* species to elucidate the role of Anatolia in fostering biological diversity. The primary objective is to analyze the genetic and morphological characteristics of these species, thereby providing a clearer understanding of their evolutionary processes and biogeographical distributions. Future research should focus on the population dynamics and habitat requirements of these species in greater depth.

Given the ecological significance of Anatolia, developing conservation strategies for these species constitutes a critical step toward ensuring the sustainability of biodiversity at both local and global scales. *Tenthredopsis* species, in this context, emerge as a model group for advancing studies in conservation biology and evolutionary biology.

## Materials and Methods

The specimens belonging to the genus *Tenthredopsis* examined in this study were collected from Anatolia during April - July between 1995 and 2006. DNA isolation was performed on a total of 250 individuals belonging to 27 putative taxa, including one outgroup. COI, COII, and Cyb fragments were amplified using the PCR method. The fragments were sequenced, aligned, and data sets were prepared for analysis. Datasets were analyzed using different contemporary approaches to determine species boundaries.

### Preparation of Specimens for Morphological Data

A total of 250 specimens belonging to 27 putative taxa, including one outgroup, were examined in this study. As a result of studies conducted in Anatolia, 18 taxa were recorded by researchers; however, not all of these taxa could be collected during field study. Therefore, some localities of the specimens belong to different countries. For morphological data analysis, one of the 250 selected specimens belonged to the genus *Aglaostigma*, which was selected as the outgroup. Each specimen analyzed in the study was assigned a unique number. Nikon SMZ-645 and Comecta-SQF-E stereomicroscopes were used to describe

the characters. Based on the morphological character examination, the specimens were categorized into 27 morphotypes (putative taxa).

### Preparation of Specimens for Molecular Data: DNA Isolation, Amplification, and Sequencing

Total genomic DNA was isolated from specimens preserved in 85% ethanol following the DNA isolation protocol of Moritz (1990) [4]. Primer pairs for the gene regions —COI s1859/a2590, C2J3400/C2N3600, and CB1/CB2—were based on studies conducted on the Hymenoptera order [3]. For the PCR reactions, the prepared 50 µl reaction mixture contained 10 µl [100 µM/µl each of dATP, dGTP, dCTP, and dTTP (MBI Fermentas)], 5 µl of 1x Taq DNA polymerase buffer (75 mM Tris-HCl pH 8.8 at 25°C, 20 mM (NH<sub>4</sub>)<sub>2</sub>SO<sub>4</sub>, 0.01% Tween 20), 4 µl (1.5 mM/µl MgCl<sub>2</sub>, 1 pmol forward primer, and 1 pmol reverse primer), 0.3 U (5 U/µl) Taq DNA Polymerase (MBI Fermentas), and 1 µl (200 ng/µl) template DNA. The final volume was adjusted to 50 µl with distilled water. Sequencing reactions were performed by MacroGen.

### Morphological Data Analysis

In the morphological study, characters were coded as "0, 1, 2, 3, 4, ?" depending on their character states. In the coding, "0" indicates the character state observed in the outgroup, while "1, 2, 3, 4" denote states differing from the outgroup. When multiple character states were observed within the same morphotype, the state was coded as polymorphic (e.g., 0 and 1). A total of 28 characters were examined for each morphotype. The morphological data set was analyzed using the PAUP\* 4.0b10 software [5]. The data set was analyzed under the Parsimony approach, considering the recommended steps and options [6].

### Molecular Data Analysis

The DNA sequence data obtained from the three gene regions consisted of a total of 1278 nucleotides in length. DNA sequence analyses were conducted using the PAUP\* 4.0b10 software under Parsimony and Maximum Likelihood approaches.

### Findings and Discussion

Morphological and molecular data analyses of Anatolian *Tenthredopsis* species were performed in this study. COI, COII, and cytochrome b gene regions from mitochondrial DNA were used to the molecular analysis of individuals belonging to the genus of *Tenthredopsis*. The generated sequence lengths of the COI, COII and cytochrome b gene regions were 652 bp, 221 bp and 406 bp; respectively.

### Morphological Data Analyses

Prior to the analysis, *Aglaostigma* was designated as the outgroup. The "uncertainty" option was selected for multiple character states. The character polarization option was set to "unordered." In the first step of the



heuristic method, the "stepwise addition" phase employed the "simple" algorithm. the "branch-swapping" phase and the "Tree Bisection and Reconnection" algorithm was utilized in the second research step. As a result of the analysis, 4485 most parsimonious trees with a length of 108 steps were obtained. The index values for the dataset were calculated as CI: 0.4630, HI: 0.5370, RI: 0.6027, and RC: 0.2790. Subsequently, character weighting was performed 1000 times under the RC and "best-fit" options. The number of trees was fixed at 260.

In cases where a large number of alternative parsimonious trees existed, a "Consensus Tree" summarizing the common information of these trees was constructed using the "majority" option. The Maximum Likelihood tree obtained is illustrated in Figure 1a. The majority-rule consensus tree of the 4485 parsimonious trees is shown in Figure 1b.

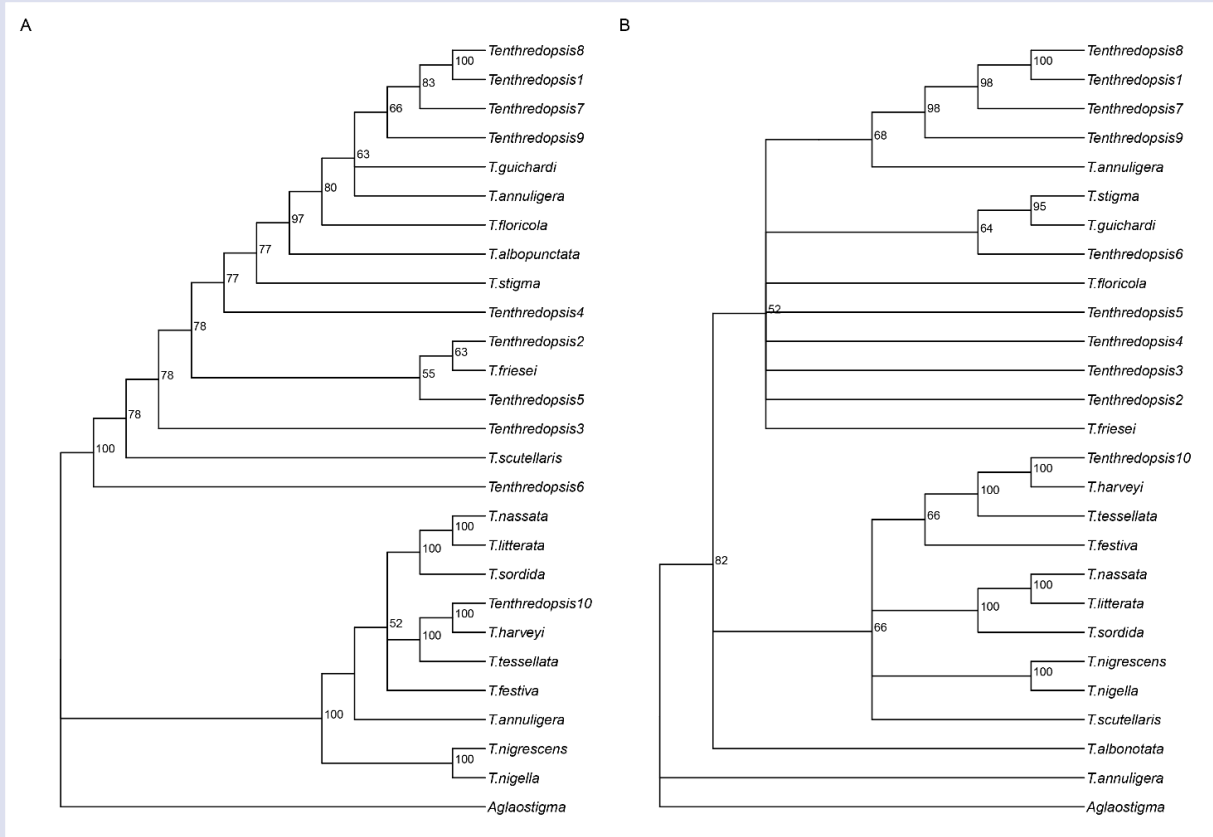


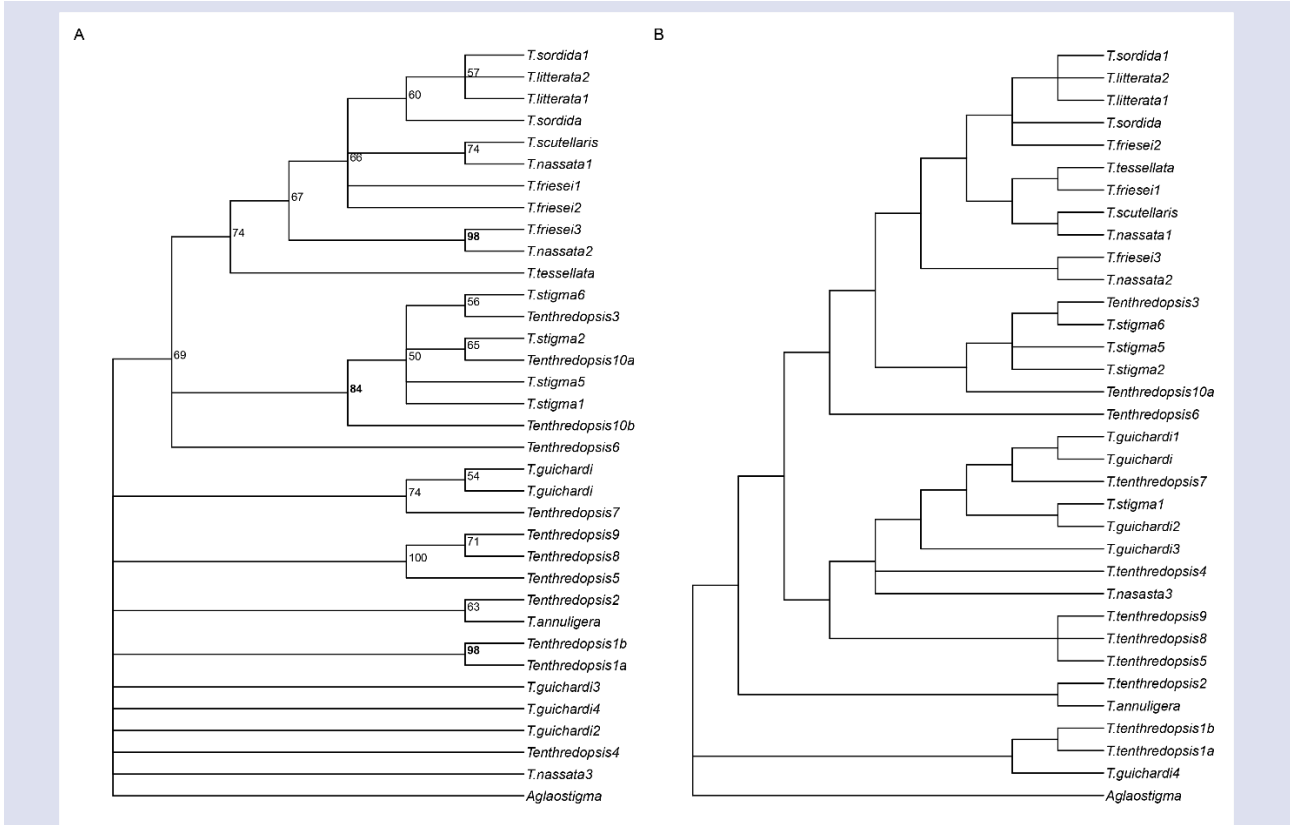
Figure 1. The majority-rule consensus tree obtained from 4485 parsimony trees (A) and the Maximum Likelihood analysis of morphological data based on 260 trees (B).

### Molecular Data Analysis

The analysis was conducted on the total molecular data set, which was created by combining data obtained from all three gene regions. **Parsimony Analysis:** For the COII region, the analysis options were applied as in the morphological data analysis. For the COI and Cyb regions, the analysis was performed using the branch-and-bound algorithm. As a result, 40,900 parsimonious trees with a step length of 684 were obtained. Character weighting did not reduce the number of trees. Consensus trees derived from the high number of parsimonious trees were found to be unresolved. Therefore, the analysis was repeated using 1000 parsimonious trees. Post-analysis character

weighting did not alter the number of parsimonious trees. To evaluate the reliability of the parsimonious trees obtained from the analysis, the bootstrapping method was applied [6]. The majority-rule consensus trees resulting from the parsimony and Maximum Likelihood approaches are presented in Figure 2.

Lineweaver-Burk plot was drawn according to the data obtained in vitro by using 4 different concentrations of XO enzyme substrate (2, 1, 0.5, 0.3 mM). Vmax and Km values were calculated with the help of Lineweaver-Burk plot (Figures 2) (Table 2).



represent separate taxa, both morphological and molecular datasets were analyzed using phylogenetic methods. The character states of 28 morphological characters belonging to 27 taxa are presented in the upper part of this section. Majority-rule consensus trees based on the parsimony method of morphological data were evaluated (Figures 1 and 2). Two main clades were observed in the majority-rule consensus tree of 260 parsimonious trees, while four main clades were revealed in the tree derived from 4485 parsimonious trees. However, when *T. albonotata* was included in the first clade and *T. annuligera* in the second clade, three distinct taxon groups were identified in both trees.

In parsimony and maximum likelihood analyses of the COII gene region, three main groups were observed. The only difference between the parsimony tree and the maximum likelihood tree is that *T. friesei*1, *T. nassata*2, and *T. tessellata* are not included in any of the three groups in the parsimony tree. The emergence of *Tenthredopsis*2 as a separate lineage in both trees supports the hypothesis that it may represent a new taxon. Similarly, *Tenthredopsis*4, *Tenthredopsis*5, *Tenthredopsis*6, *Tenthredopsis*8, and *Tenthredopsis*9 may either represent separate taxa or species groups, or alternatively, they may belong to a single species. *Tenthredopsis*10a and *Tenthredopsis*10b appear to belong within or closely related to *T. stigma*. Similarly, *Tenthredopsis*1a, *Tenthredopsis*1b, and *Tenthredopsis*7 are observed within or near *T. guichardi*.

The parsimony and maximum likelihood analyses for the COI gene region resulted in fundamentally similar trees. In the parsimony tree, *T. annuligera* was excluded. Compared to trees from other gene regions, the longer sequence of the COI gene resulted in more resolved trees. Specimens belonging to *T. guichardi* grouped together, as did specimens of *T. stigma*. These findings provide strong support for the distinction of both species as separate taxa. In the maximum likelihood trees, *T. litterata* and *T. friesei* were observed as closely related species. *Tenthredopsis*4 and *Tenthredopsis*10b, *Tenthredopsis*2 and *Tenthredopsis*1b, and *Tenthredopsis*9 and *Tenthredopsis*5 were identified as closely related taxa in both trees.

The parsimony and maximum likelihood trees constructed for the cytochrome b gene region were largely consistent with those for the COI and COII regions. While *T. nassata*2 and *T. nassata*3 were found in different groups, three main groups were observed in the tree. Parsimony-absolute consensus trees, maximum likelihood trees, and bootstrap trees constructed for the combined dataset of COI, COII, and cytochrome b gene regions also revealed three main groups. *T. nassata*, *T. scutellaris*, *T. friesei*, *T. tessellata*, *T. litterata*, and *T. sordida* consistently grouped together in all analyses. Except for *T. guichardi*4, other specimens of *T. guichardi* were also grouped on the same branch.

Among the studied specimens, *T. guichardi* had the longest available sequence. Morphological analysis revealed significant color variations within this species.

While *T. guichardi*4 emerged as a separate clade in the genetic analyses, the available data are insufficient to confirm its status as a distinct taxon. In the maximum likelihood and bootstrap analyses, *T. stigma*, *Tenthredopsis*10a, *Tenthredopsis*10b, *Tenthredopsis*6, and *Tenthredopsis*3 were grouped together. Across all total analyses, *Tenthredopsis*5, *Tenthredopsis*8, and *Tenthredopsis*9 consistently grouped together, suggesting the possibility that they represent a single species. Similarly, in all total analyses, *Tenthredopsis*7 was placed on the same branch as *T. guichardi*, indicating that they are either two closely related species or a single species.

In Benson's (1968) key for *Tenthredopsis* species, the genus was divided into six species groups based on the shape of the clypeus. The groups observed in our analyses, based on both morphological and molecular data, support Benson's (1968) species groups. During the identification of specimens in this study, *Tenthredopsis*10a and *Tenthredopsis*10b were observed to be morphologically similar to *T. stigma*. However, due to certain structural differences, they were not classified as the same species. Phylogenetic analyses also placed these taxa in the same groups, suggesting that they may represent either two closely related species or a single species.

*T. nassata*, *T. scutellaris*, *T. friesei*, *T. tessellata*, *T. litterata*, *T. stigma*, and *T. sordida* are species with a broad Palearctic distribution and are grouped together in phylogenetic analyses based on both morphological and molecular data. The distributions of *T. harveyi* and *T. stramineata*, on the other hand, are restricted to Turkey. *T. guichardi* is the most commonly encountered *Tenthredopsis* species in Anatolia. Similarly, *T. festiva*, *T. nigella*, and *T. nigrescens* are species with a limited distribution across Anatolia and its neighboring countries (Russia and Armenia). When considering regional distribution data, species distributed within the Iran-Turan subregion (*T. nassata*, *T. scutellaris*, *T. friesei*, *T. tessellata*, *T. litterata*, *T. stigma*, *T. sordida*, *T. nigella*, and *T. albonotata*) are found on the same lineage in almost all phylogenetic analyses, except for *T. guichardi*. Similarly, species distributed in the European and Mediterranean subregions, such as *T. annuligera* and *T. floricola*, are grouped together in our morphology-based trees (Figures 1 and 2). Considering the distribution patterns and phylogenetic analyses of these species, as well as evidence from other taxonomic groups with broad Palearctic distributions [22-23-24], it is supported that Anatolia served as a primary refugium during the last glacial period. Additionally, the distribution of certain *Tenthredopsis* species lies along the Balkan-Anatolian corridor. For instance, *T. albonotata* and *T. annuligera* are examples of species distributed across Anatolia, Greece, Macedonia, Croatia, Hungary, Romania, and Ukraine. Three potential routes for their dispersal during interglacial periods are proposed. The first route is the Anatolia-Caucasus corridor, but due to the presence of significant geographical barriers between Anatolia and the Caucasus, this route seems less viable for species with low ecological tolerance and dispersal capability. The second route

involves dispersal from eastern Anatolia through Iran, south of the Caspian Sea, and into Russia, eventually reaching Northern Europe. The third potential route suggests dispersal through the straits into the Balkans and subsequently through the Balkans into Europe.

## Conclusions

This study comprehensively evaluated both the genetic and morphological characteristics of *Tenthredopsis* species distributed in Anatolia, once again emphasizing the region's importance in terms of the symphytan diversity. The findings of the study demonstrated that species that are difficult to identify morphologically can be classified more precisely using molecular markers, revealing significant genetic diversity among them. The data obtained clearly show that Anatolia has historically served as a biological refuge. During glacial periods, the region functioned as a sanctuary for many species, which also explains its high current biodiversity. Particularly, *Tenthredopsis* species can be considered a model group for understanding Anatolia's biodiversity strategies due to their ecological adaptations and genetic diversity. Phylogenetic analyses have contributed to understanding the evolutionary relationships among *Tenthredopsis* species and have revealed that some species exhibit genetic variations unique to Anatolia. For instance, the phylogenetic trees constructed from COI and COII gene regions have elucidated the historical distributions and adaptation processes of the species. Additionally, analyses based on the cytochrome b region have provided insights into the geographical distribution patterns and potential evolutionary origins of these species. In conclusion, *Tenthredopsis* species distributed in Anatolia present a unique model for biodiversity conservation and evolutionary biology studies. The region's biodiversity is of paramount importance, not only for preserving existing species but also for ensuring the sustainability of future ecosystem services. In this context, increasing genetic and ecological research will significantly contribute to biodiversity conservation at both local and global scales.

## Conflicts of interest

There are no conflicts of interest in this work.

## Acknowledgement

This study was supported by CUBAB F-170, Sivas Cumhuriyet University.

## References

- [1] Avise J.C., Molecular Markers, Natural History, and Evolution. New York : Chapman and Hall, (1994) 511.
- [2] Benson R.B., Hymenoptera from Turkey, Symphyta, *Bulletion of the British Museum (Natural History) Entomology*, 22 (4) (1968) 109–207.
- [3] Simon C., Frati F., Beckenbach A., Crespi B., Liu H., Flook P., Evolution, weighting, and phylogenetic utility of mitochondrial gene sequences and a compilation of conserved polymerase chain reaction primers, *Annals of the Entomological Society of America*, 87 (6) (1994) 651–701.
- [4] Moritz C., *Molecular Systematics* (p. 3). D. M. Hillis, & B. K. Mable (Eds.). Sunderland, MA: Sinauer Associates. (1990)
- [5] Swofford D.L., PAUP. Phylogenetic Analysis Using Parsimony (And Other Methods 4.ed. Massachusetts: Sinauer Assoc, Sunderland, (2002) 294–307.
- [6] Başbüyük H.H., Bardakçı F., Belshaw R., and Quicke D.L.J., Phylogenetic Systematics: A concise practical guide, Sivas: Önder Matbaa, (2000) 134.
- [7] Felsenstein J., Maximum likelihood estimation of evolutionary trees, *Systematic Biology*, 22 (3) (1973) 240–249.
- [8] Königsman E., Das Phylogenetische System der Hymenoptera. Teil 3: Terebrantes (Unterordnung Apocrita), *Deutsche Entomologische Zeitschrift*, 25 (1978a) 1–55.
- [9] Königsman E., Das Phylogenetische System der Hymenoptera. Teil 4: Aculeta (Unterordnung Apocrita), *Deutsche Entomologische Zeitschrift*, 25 (1978b) 365–465.
- [10] Rasnitsyn A.P., An outline of evolution of the hymenopterous insects, *Oriental Insects*, 22 (1988) 115–145.
- [11] Ronquist F., Rasnitsyn AP., Roy A., Eriksson K., Lindgren M., Phylogeny of the Hymenoptera: A cladistic reanalysis of Rasnitsyn's (1988) data. *Zoologica Scripta*. 28 (1999) 13–50.
- [12] Başbüyük H.H., Quicke D.L.J., Morphology of the antenna cleaner in the Hymenoptera with particular reference to non-aculeata families (Insecta), *Zoologica Scripta*, 24(2) (1995) 157–177.
- [13] Başbüyük H.H., Quicke D.L.J., Hamuli in the Hymenoptera (Insecta) with their phylogenetic implications, *Journal of Natural History*, 31 (1997) 1563–1585.
- [14] Başbüyük H.H., Quicke D.L.J., Grooming behaviours in the Hymenoptera (Insecta): potential phylogenetic significance, *Zoological Journal of the Linnean Society*, 125 (1999) 349–382.
- [15] Gauld I.D, Bolton B., *The Hymenoptera*, British Museum (Natural History). New York: Oxford University Press, (1998) 322.
- [16] Wolf F., Hyménoptères Symphytes de Turquie, *Bulletin des Recherches agronomiques de Gembloux*, 3 (1968) 562–565.
- [17] Chevin H., Chenon R., Contribution à la des Hyménoptères Symphytes de Turquie, *Bulletin de la Société entomologique de France*, 87 (1982) 43–45.
- [18] Zhelochovtsev A.N., Zinovjev A.G., A list of horntails (Hymenoptera, Symphyta) of the fauna of Russian and adjacent territories, II. *Entomologicheskoe Obozrenie*, 74 (2) (1995) 395–415.
- [19] Lacourt J., Répertoire des Tenthredinidae ouest-paléarctiques (Hymenoptera, Symphyta), *Mém. Soc. ent. France*, 3 (1999) 1–432.
- [20] Çalmaşur Ö., Özbek H., A contribution to the knowledge of the Tenthredinidae (Symphyta, Hymenoptera) fauna of Turkey. Part I: The Subfamily Tenthredininae, *Turkish Journal of Zoology*, 28 (2004) 37–54.
- [21] Blank S.M., and Ritzau C., Die Tenthredopsini Deutschlands (Hymenoptera: Tenthredinidae). In: Taeger, A. & Blank, S. M. 1998 (Hrsg.), *Pflanzenwespen Deutschlands (Hymenoptera, Symphyta)*. Kommentierte Bestandsaufnahme. Goecke & Evers, (1998) 227–246.



- [22] Tarkhnishvili D., Thorpe R.S., Arntzen J.W, Pre-pleistocene refugia and differentiation between populations of the Caucasian salamender (*Mertensiella caucasica*), *Molecular Phylogenetics and Evolution*, 14 (2000) 414-422.
- [23] Rokas A., Atkinson R.J., Webster L.M.I., Csokas G., Stone G.N., Out of Anatolia: longitudinal gradients in genetic diversity support an eastern origin for a circum-Mediterranean oak gallwasp *Andricus quercustozae*, *Molecular Ecology*, 12 (2003) 2153-2174.
- [24] Çıplak B., Systematics, phylogeny and biogeography of *Anterastes* (Orthoptera, Tettigoniidae, Tettigoniinae): evolution within a refugium, *Zoologica Scripta*, 33 (2004) 19-44.

## Superlattice Structure of Quantum Cascade Lasers: Structural and Morphological Effects of AsH<sub>3</sub> Flow

Merve Nur Koçak<sup>1,3,a</sup>, İlkey Demir<sup>2,3,b,\*</sup>

<sup>1</sup> Department of Metallurgical and Materials Engineering, Sivas Cumhuriyet University, 58140 Sivas, Türkiye

<sup>2</sup> Department of Nanotechnology Engineering, Sivas Cumhuriyet University, 58140 Sivas, Türkiye

<sup>3</sup> Sivas Cumhuriyet University Nanophotonics Application and Research Center-CÜNAM, 58140 Sivas, Türkiye

\*Corresponding author

### Research Article

#### History

Received: 09/04/2025

Accepted: 14/06/2025




This article is licensed under a Creative Commons Attribution-NonCommercial 4.0 International License (CC BY-NC 4.0)


### ABSTRACT

Quantum cascade lasers (QCLs) have been widely used in mid-infrared applications due to their high power, efficiency, and design flexibility. The InP-based quantum cascade lasers, particularly those utilizing In  $In_{0.53}Ga_{0.47}As/In_{0.52}Al_{0.48}As$  superlattices, have been preferred for their lattice compatibility and well-established fabrication processes. However, the superlattice growth has required optimization, as relaxation mechanisms have affected structural quality beyond the critical thickness. In this study, InP-based quantum cascade lasers structures have been grown and characterized using Metal-Organic Vapor Phase Epitaxy (MOVPE). The impact of AsH<sub>3</sub> (arsine) flow rate on superlattice quality has been investigated by growing samples with flow rates of 47 sccm, 60 sccm, and 75 sccm. Structural analysis has been conducted using high-resolution X-ray diffraction (HRXRD), while atomic force microscopy (AFM) has been used to examine surface morphology. The results obtained revealed the critical role of superlattice growth parameters on the performance of quantum cascade laser devices and provided important findings for determining the optimal AsH<sub>3</sub> flow rate. This study contributes to the improvement of growth processes of InP-based quantum cascade laser structures, leading to improved semiconductor laser performance.

**Keywords:** MOVPE, epitaxy, InGaAs/InAlAs superlattice, AsH<sub>3</sub> effect, QCL

<sup>a</sup> [mervenurkocak@cumhuriyet.edu.tr](mailto:mervenurkocak@cumhuriyet.edu.tr)  <https://orcid.org/0000-0002-4913-5614>

<sup>b</sup> [idemir@cumhuriyet.edu.tr](mailto:idemir@cumhuriyet.edu.tr) 

 <https://orcid.org/0000-0002-2224-989X>

## Introduction

Even though semiconductor laser technology has been around for a while, it wasn't until the introduction of Quantum Cascade Laser (QCL) technology that compact semiconductor lasers with comparatively high power density in the mid-wave infrared (MWIR), long-wave infrared (LWIR), and far-infrared (FIR) spectral regions could be developed [1-3]. In 1994, QCL was invented, and in 1997, it was first shown to function as a single mode [4, 5]. QCLs have garnered considerable interest in recent years for mid-wave infrared (MWIR) and long-wave infrared (LWIR) applications due to their wavelength tunability, compact dimensions, continuous-wave functionality at ambient temperature, elevated optical power output, and minimal cooling demands [6, 7]. QCLs are utilized in several applications including explosive detection, infrared countermeasures, food safety, greenhouse gas monitoring, breath analysis, blood urea measurement, and free-space optical communication [8-10]. Given these remarkable applications, QCLs are important both for the present and the future.

The architecture of a QCL has numerous repeated quantum wells and barriers, enabling intersubband emission. The key advantage of this feature is that the emitted radiation wavelength of QCL is not limited to the bandgap of the material. In superlattice (SL) material systems, energy levels and sub-band transitions can be controlled depending on the material composition and

thickness of the layers, and thus light emission at the targeted wavelength can be achieved by adjusting only the quantum well and barrier thicknesses [3, 11]. QCLs have a relatively thick active core obtained by growing hundreds of layers on top of each other. The most important requirement is very precise control of the growth process. Small variations in both alloy ratios and the thickness of the wells and barriers can degrade laser performance. For this reason, Molecular Beam Epitaxy (MBE) and Metalorganic Vapor Phase Epitaxy (MOVPE) growth methods are commonly employed for QCL fabrication. Samples grown with MOVPE have lower background doping levels due to the use of high-purity precursors and highly controlled flows, and are preferred because they are suitable for mass production [12]. InP based QCL active cores are generally designed using InGaAs wells and InAlAs barrier layers in the literature due to their lattice compatible growth capabilities [13, 14]. Optimization of quantum wells and barriers is of great importance to provide precise control. There are many parameters affecting wells and barriers. These are growth temperature, growth pressure, growth ratio, flow rates of group V and group III gases are important parameters for QCL optimization. The conditions required for high quality growth of InGaAs and InAlAs are different from each other, making optimization of SL structured active core even more difficult [15-18]. In order to obtain these layers

with desired concentrations and thicknesses, initially, single-layer growth is performed. However, since layers much thicker than SL structures are grown during single layer optimization, critical thickness is exceeded and relaxation mechanism comes into play. Therefore, optimization of devices with SL structures should be verified with SL optimizations. In this study, AsH<sub>3</sub> flow investigations were conducted on SL structures intended for use in QCL structure. SL structures were grown using MOVPE. Alloy concentration and thickness of the structure were obtained by high resolution X-ray diffraction method. Also, the change in surface morphology was investigated by atomic force microscopy.

## Materials and Methods

The samples to be examined in this paper were grown in an Aixtron 200-4 RF/S horizontal reactor using the Metalorganic Chemical Vapor Deposition Method (MOCVD). The InGaAs/InAlAs SL structure was grown on InP substrate with (100) orientation. The SL was grown for 30 periods with the InGaAs layer of 5 nm and InAlAs layer of 5 nm in a lattice matched manner. TMIn, TMGa and TMAI metalorganic sources were used to grow the samples. A PH<sub>3</sub> hybrid source was used to prevent the P atoms escaping from the surface while heating the substrate and an AsH<sub>3</sub> hybrid source was used to grow the SL layers. During the growth of the three samples, TMIn, TMGa and TMAI flows were kept constant and the AsH<sub>3</sub> flow was varied. Table 1 shows the AsH<sub>3</sub> flows of the

samples. To analyze the effect of AsH<sub>3</sub> flow on the properties of the lattice-matched SL, its structural properties were characterized using Rigaku High Resolution XRD at room temperature. The surface morphology was analyzed using Atomic Force Microscopy.

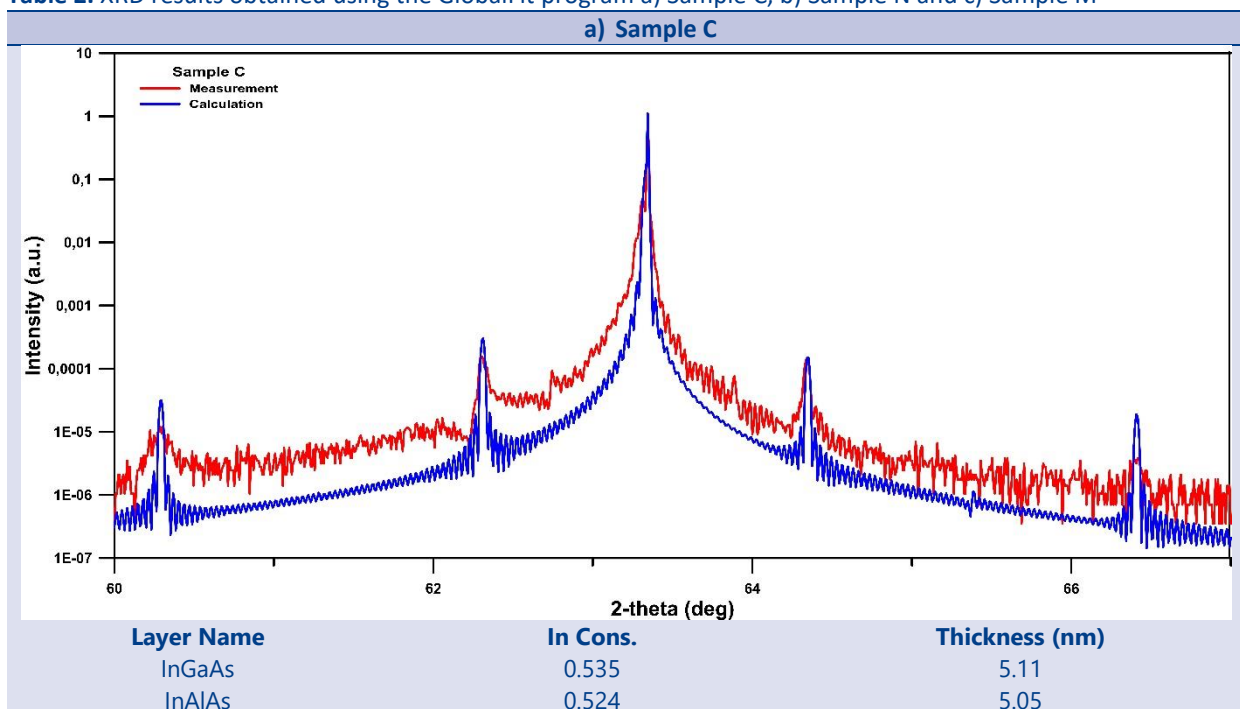
## Results and Discussion

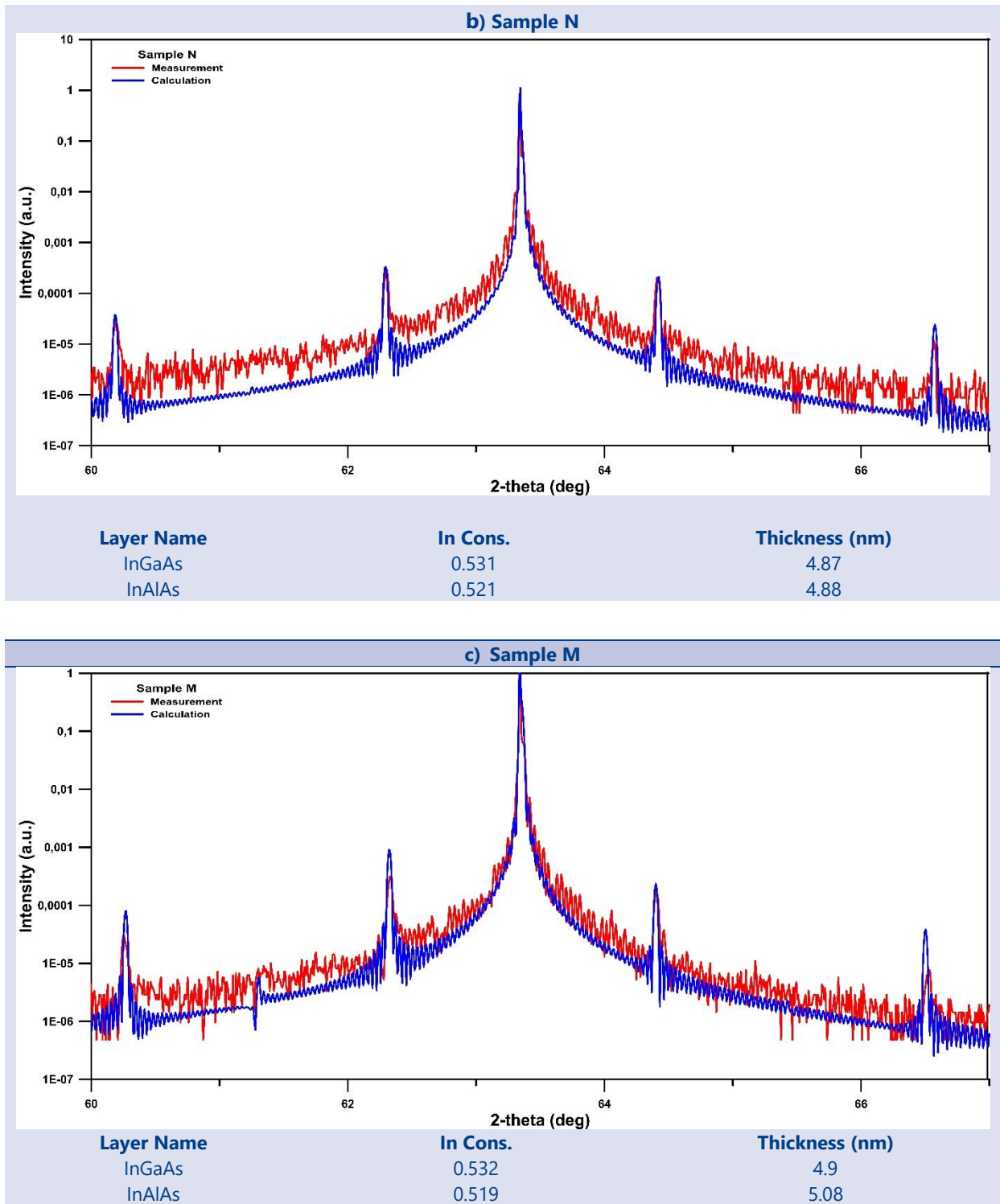
XRD is an important method for structural characterization of SL. In semiconductor devices such as QCL, where thin and multi-repeat structures such as SL structure are used, the thickness and concentration are determined by XRD method with SL optimization. The out-of-plane  $\theta$ -2 $\theta$  scans obtained by HR-XRD were modeled using GlobalFit software [19] and the thicknesses of the SL layers and In concentrations were determined. Table 2 shows the results of the SL structures of Sample C, Sample N and Sample M. The As atom on the surface during growth affects the In and Ga placement. This effect is more effective in strain-balanced structures and less effective in lattice-compatible structures [20]. When the results are analyzed, no serious effect on the In concentration is observed for this reason. It is seen that sample C slightly increases the In concentration, but it is not a significant increase. Even if As did not significantly affect the In concentration in lattice-matched structures, it is thought to cause alloy disordering. Alloy disorder increases the interface roughness and decreases the device performance [21].

**Table 1.** Growth parameters of the samples

Sample Name	AsH <sub>3</sub> Flow (sccm)
C	47
N	60
M	75

**Table 2.** XRD results obtained using the GlobalFit program a) Sample C, b) Sample N and c) Sample M





In Figure 1, the XRD patterns are plotted on top of each other to facilitate comparison between the samples. When the graph is examined, slight shifts in the positions of the SL peaks are observed between the samples. As can be seen from the layer thicknesses presented in Table 2, differences in the amount of As flow affected the layer thicknesses to a certain extent. Firstly, when the -1st SL peaks marked in red are examined, slight distortions are observed in the peak shapes of Sample C and Sample M, although there is no significant difference. When the  $\pm 2$ nd SL peaks, marked in pink and green, were analyzed, it was found that the peaks of Sample C were significantly

broadened. In addition, the 2nd SL peak of Sample M (green marking) has a lower intensity and a relatively more irregular peak shape compared to Sample N. In Sample C, the relatively low  $\text{AsH}_3$  flow likely caused incomplete group-V coverage during layer transitions, promoting interface grading and compositional fluctuations. It is considered that the  $\text{AsH}_3$  flow rate may have been insufficient to prevent the desorption of As atoms from the growing surface [22]. As a result, the lack of  $\text{AsH}_3$  leads to a group-III-rich surface environment, which in turn deteriorates the crystal quality. These effects result in broader and asymmetric satellite peaks in



HRXRD. Conversely, in Sample M, excessive  $\text{AsH}_3$  flow is thought to suppress atomic mobility, thereby limiting the formation of sharp transitions between quantum wells and barriers. This leads to weaker and irregular higher-order satellite peaks. The symmetric and well-resolved SL peaks observed in Sample N indicate sharp interfaces and

a well-preserved superlattice periodicity, reflecting optimal  $\text{AsH}_3$  flow conditions during growth. Based on the structural analysis, Sample N is considered to have optimal growth conditions.

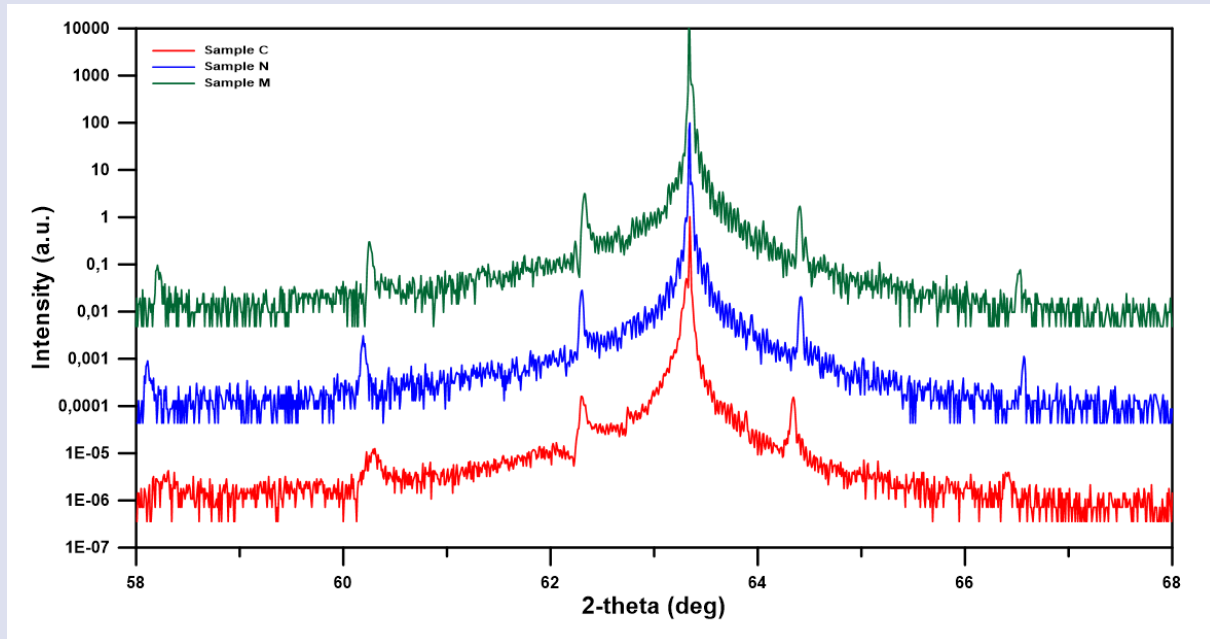


Figure 1. Comparative representation of XRD graphs of Sample C, Sample N and Sample M. The XRD data was shifted up for clarity.

Figure 2 shows the AFM images and Figure 3 shows the RMS plot obtained from these images. The AFM images show distinct linear step-flow-like structures in Sample N where optimal surface mobility is achieved. In cases where atoms are bound in the right place and have sufficient time and kinetic energy, efficient surface migration of group III atoms allows growth to occur in a step-flow mode [23]. When optimal epitaxial growth conditions are met, the step-flow mode dominates. The surface morphology of Sample C and Sample M shows a less ordered appearance. The low flow of  $\text{AsH}_3$  in Sample C caused a lack of As atoms on the surface, resulting in an

inhomogeneous distribution. Unsuitable conditions lead to surface defects and problems in the proper bonding of elements to the surface [19]. As the  $\text{AsH}_3$  flow increases, the movement of group III atoms on the surface decreases, reducing surface migration. Atoms that cannot move sufficiently on the surface cause disordered structures and increase the RMS. The  $\text{AsH}_3$  flow should be high enough to find a place on the surface to hold In, Ga and Al atoms and low enough for group III atoms to move on the surface [21]. Sample N has both a low RMS value and a step-flow mode surface morphology.

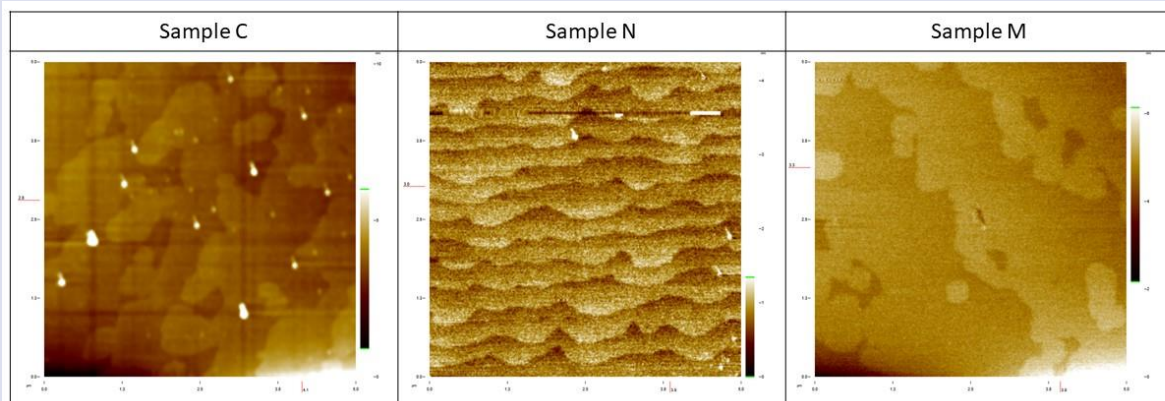


Figure 2. AFM images of samples (5um x 5um)

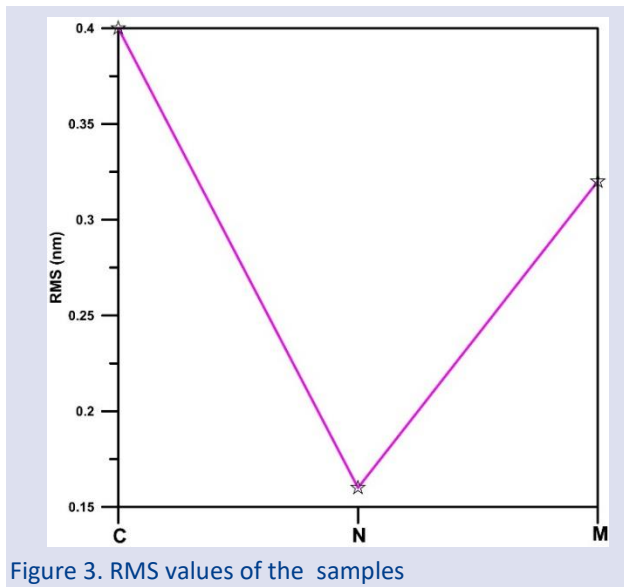


Figure 3. RMS values of the samples

### Conclusion

In this study, the effects of  $\text{AsH}_3$  flow amount on the structural and surface morphology within the scope of SL optimization of QCL structures were investigated. As a result of characterization studies using HR-XRD measurements and AFM analyses, it was observed that the  $\text{AsH}_3$  flow amount had a significant effect on the crystal quality and surface smoothness of SL structures.

HRXRD measurements showed that  $\text{AsH}_3$  flow directly affects the SL peak shapes. In addition, AFM analysis confirmed the changes in surface morphology and showed that the step-flow growth mechanism becomes dominant under optimal  $\text{AsH}_3$  flow conditions. The results show that the  $\text{AsH}_3$  flow rate must be carefully controlled to achieve optimal crystal quality and surface smoothness in SL structures. In the absence of optimal growth conditions, insufficient or excessive  $\text{AsH}_3$  flow rates can lead to surface and alloy disordered and consequent structural distortions that can adversely affect laser performance. In conclusion, the  $\text{AsH}_3$  flow parameter plays a critical role in SL optimization in InP-based QCL growth, and determining the appropriate growth conditions is an important step in improving the performance of SL structures

### Conflicts of interest

There are no conflicts of interest in this work.

### Acknowledgement

This work is based on results obtained during the ongoing Ph.D. thesis of the first author, titled "Development of Short- and Mid-Wavelength Quantum Cascade Lasers". Merve Nur Koçak is supported by the YÖK (Council of Higher Education) 100/2000 Ph.D. Scholarship Program and The Scientific and Technological Research Council of Turkey (TÜBİTAK) 2211/A Program. This study is supported by the Scientific Research Project Fund of Sivas Cumhuriyet University, Turkey, under Project No. MRK-2024-004, and TÜBİTAK under Project No. 22AG074.

### References

- [1] Demir I., Elagoz S., Interruption time effects on InGaAs/InAlAs superlattices of quantum cascade laser structures grown by MOCVD, *Superlattices Microstruct.*, 100 (2016) 723-729.
- [2] Perkitel I., Demir I., Effect of Si-doped and undoped inter-layer transition time on the strain-compensated InGaAs/InAlAs QCL active region grown with MOVPE, *J. Mol. Struct.*, 1272 (2023) 134203.
- [3] Lee W.J., Sohn W.B., Shin J.C., Han I.K., Kim T.G., Kang J., Growth of InGaAs/InAlAs superlattices for strain balanced quantum cascade lasers by molecular beam epitaxy, *J. Cryst. Growth*, 614 (2023) 127233.
- [4] Faist J., Capasso F., Sivco D.L., Sirtori C., Hutchinson A.L., Cho A.Y., Quantum cascade laser, *Science*, 264 (5158) (1994) 553-556.
- [5] Tian W., Zhang D.L., Zheng X.T., Yang R.K., Liu Y., Lu L.D., Zhu L.Q., MBE growth and optimization of the InGaAs/InAlAs materials system for quantum cascade laser, *Front. Mater.*, 9 (2022) 1050205.
- [6] Wysocki G., Curl R.F., Tittel F.K., Maulini R., Bulliard J.M., Faist J., Widely tunable mode-hop free external cavity quantum cascade laser for high resolution spectroscopic applications, *Appl. Phys. B*, 81 (2005) 769-777.
- [7] Yoshinaga H., Mori H., Hashimoto J.I., Tsuji Y., Murata M., Katsuyama T., Low Power Consumption (<1 W) Mid-Infrared Quantum Cascade Laser for Gas Sensing, *SEI Tech. Rev.*, 79 (2014) 112-115.
- [8] Li J., Parchatka U., Fischer H., Development of field-deployable QCL sensor for simultaneous detection of ambient  $\text{N}_2\text{O}$  and CO, *Sens. Actuators B Chem.*, 182 (2013) 659-667.
- [9] Zhang M., Yeow J.T., Nanotechnology-Based Terahertz Biological Sensing: A review of its current state and things to come, *IEEE Nanotechnol. Mag.*, 10 (3) (2016) 30-38.
- [10] Kosterev A., Wysocki G., Bakhirkin Y., So S., Lewicki R., Fraser M., Curl R.F., Mid-infrared quantum cascade lasers, *Proc. SPIE*, 10974 (2018) 59-70.
- [11] Lee W.J., Seo J., Shin J.C., Han I.K., Kim T.G., Kang J., Interfacial characteristics dependence on interruption times in InGaAs/InAlAs superlattice grown by molecular beam epitaxy, *J. Alloys Compd.*, 1006 (2024) 176297.
- [12] Koçak M.N., Pürü K.M., Perkitel I., Altuntaş İ., Demir İ., In-situ and ex-situ face-to-face annealing of epitaxial AlN, *Vacuum*, 203 (2022) 111284.
- [13] Bugajski M., Pierścińska D., Gutowski P., Pierściński K., Sobczak G., Janus K., Kuźmich A., Mid-infrared quantum cascade lasers, *Laser Technol, Progress Appl. Lasers, Proc. SPIE*, 10974 (2018) 59-70.
- [14] Wang C.A., Goyal A.K., Menzel S., Calawa D.R., Spencer M., Connors M.K., Capasso F., High power (>5 W)  $\lambda \sim 9.6 \mu\text{m}$  tapered quantum cascade lasers grown by OMVPE, *J. Cryst. Growth*, 370 (2013) 212-216.
- [15] Demir I., Altuntas I., Elagoz S., Arsine flow rate effect on the low growth rate epitaxial InGaAs layers, *Semiconductors*, 55 (10) (2021) 816-822.
- [16] Welch D.F., Wicks G.W., Eastman L.F., Parayanthal P., Pollak F.H., Improvement of optical characteristics of  $\text{Al}_{0.48}\text{In}_{0.52}\text{As}$  grown by molecular beam epitaxy, *Appl. Phys. Lett.*, 46 (2) (1985) 169-171.
- [17] Kurihara K., Takashima M., Sakata K., Ueda R., Takahara M., Ikeda H., Shimoyama K., Phase separation in InAlAs grown by MOVPE with a low growth temperature, *J. Cryst. Growth*, 271 (3-4) (2004) 341-347.

- [18] Bass S.J., Barnett S.J., Brown G.T., Chew N.G., Cullis A.G., Pitt A.D., Skolnick M.S., Effect of growth temperature on the optical, electrical and crystallographic properties of epitaxial indium gallium arsenide grown by MOCVD in an atmospheric pressure reactor, *J. Cryst. Growth*, 79 (1-3) (1986) 378-385.
- [19] Konya T., X-ray thin-film measurement techniques. X-ray reflectivity measurement, *The Rigaku Journal*, 25 (2) (2009) 1-8.
- [20] Zhang S., Zhu L., Lu L., Cui J., Jia H., Du S., Li M., Effect of the V/III Ratio on the Quality of Strain-Balanced GaInAs/AlInAs Superlattices in Quantum Cascade Lasers, *Opt. Mater.*, (2025) 116882.
- [21] Franckié M., Winge D.O., Wolf J., Liverini V., Dupont E., Trinité V., Wacker A., Impact of interface roughness distributions on the operation of quantum cascade lasers, *Opt. Express*, 23 (4) (2015) 5201-5212.

## MOVPE Growth and Doping Optimization of n- $\text{Al}_x\text{Ga}_{1-x}\text{As}$ Layers for Laser Diode Applications

Gamze Yolcu <sup>1, 2, a</sup>, İlkyay Demir <sup>2, 3, b, \*</sup><sup>1</sup> Department of Metallurgical and Materials Engineering, Sivas Cumhuriyet University, 58140 Sivas, Türkiye<sup>2</sup> Sivas Cumhuriyet University Nanophotonics Application and Research Center-CÜNAM, 58140 Sivas, Türkiye<sup>3</sup> Department of Nanotechnology Engineering, Sivas Cumhuriyet University, 58140 Sivas, Türkiye

\*Corresponding author

### Research Article

#### History

Received: 09/04/2025



Accepted: 16/06/2025



This article is licensed under a Creative Commons Attribution-NonCommercial 4.0 International License (CC BY-NC 4.0)

### ABSTRACT

Epitaxially grown n- $\text{Al}_x\text{Ga}_{1-x}\text{As}$  layers, which form the basis of the modern semiconductor laser structures, play a critical role in both optical and electrical performance of the device. These layers provide electron injection into the active region and at the same time act as optical waveguides, allowing efficient steering of the laser light. Since Al concentration and doping levels have a direct effect on fundamental properties such as band gap, carrier density and resistive losses, it is of great importance to meticulously optimize these parameters. In this study, n- $\text{Al}_x\text{Ga}_{1-x}\text{As}$  layers were epitaxially grown on GaAs substrate by MOVPE (Metal Organic Vapor Phase Epitaxy) method, with n-type doping using  $\text{SiH}_4$  (silane) precursor. Here we focused on the effects of increasing Al concentration on doping density in the  $\text{Al}_x\text{Ga}_{1-x}\text{As}$  layers. The obtained results showed that when Al concentration is above 30%, no significant increase in doping density was observed despite the maximization of  $\text{SiH}_4$  flow. This phenomenon is thought to be associated with the formation of DX centers (deep donor levels), which become more prominent at high Al concentrations and can trap free electrons, thereby reducing the effective doping efficiency. Furthermore, the data obtained from Hall and ECV (Electrochemical Capacitance Voltage) measurements exhibited good agreement at low Al concentrations, while significant differences were observed for Al fractions above 0.2. This comprehensive analysis reveals the current limitations of epitaxially grown n- $\text{Al}_x\text{Ga}_{1-x}\text{As}$  layers and emphasizes the need for precise control of Al concentration, while providing a more in-depth interpretation by systematically comparing the obtained results with the data reported in the literature.

**Keywords:** MOVPE method, epitaxial growth, carrier density, n  $\text{Al}_x\text{Ga}_{1-x}\text{As}$  layers, DX center.<sup>a</sup>  [gamzeyolcu@cumhuriyet.edu.tr](mailto:gamzeyolcu@cumhuriyet.edu.tr) <sup>ib</sup>  <https://orcid.org/0000-0003-0201-8266><sup>b</sup>  [idemir@cumhuriyet.edu.tr](mailto:idemir@cumhuriyet.edu.tr)<sup>ib</sup>  <https://orcid.org/0000-0002-2224-989X>

## Introduction

$\text{Al}_x\text{Ga}_{1-x}\text{As}$ -based semiconductor laser diodes have become prominent in various fields such as scientific research, industrial production, medical devices, and imaging technologies, thanks to their high efficiency, compact size, configurable design possibilities, and capability to operate under harsh environmental conditions [1,2]. These diodes are notable for their low operating current requirement and high electrical-to-optical power conversion efficiency. For instance, in communication systems, where high data transmission speeds and stable signal transmission are required, these low-operating-current  $\text{Al}_x\text{Ga}_{1-x}\text{As}$ -based semiconductor laser stand out as a key components and plays a critical role in both communication application and data transfer. Furthermore, since long-term and stable operation of lasers depends directly on the applied electric current, using devices that provide high performance at low pump currents significantly enhances system efficiency. On the other hand, since applications like optical recording (e.g., rewritable CDs), which rely on high light output for fast writing and erasing speeds and high recording density, require high-power laser diodes [3]. This broad spectrum of performance demands underscores the need for

precise optimization of structural parameters in laser diode design.

The performance of high-power semiconductor lasers depend directly on the quality of the epitaxially grown semiconductor material [4]. In this context, the n-type  $\text{Al}_x\text{Ga}_{1-x}\text{As}$  layers in  $\text{Al}_x\text{Ga}_{1-x}\text{As}/\text{GaAs}$  laser diode structures represent one of the fundamental components governing the device's electrical and optical characteristics [5]. The n-type  $\text{Al}_x\text{Ga}_{1-x}\text{As}$  layers enables the efficient operation of the  $\text{Al}_x\text{Ga}_{1-x}\text{As}$  based-laser diode by providing the transport of negatively charged electrons and plays a critical role in the formation of optical gain at the p-n junction. [6]. Moreover, accurate control of the doping concentration is essential for maintaining the optimal balance between electronic conductivity and optical losses in the n-  $\text{Al}_x\text{Ga}_{1-x}\text{As}$  based-laser diode structures.

However, the aluminum (Al) concentration in the  $\text{Al}_x\text{Ga}_{1-x}\text{As}$  layers has a major impact on the laser's optical and electronic properties, which in turn determines the band gap and refractive index profile of the material [7,8]. Careful optimization of the Al content contributes to the improvement of the waveguide mechanism and the increase of laser efficiency. For high-power laser diodes to operate effectively, precise control over doping levels,



accurate definition of layer composition, and minimization of impurity concentrations are essential. Additionally, both composition and doping conditions must be dynamically adjusted during the growth process. In this context, optimization of n-type doping and Al concentration is critical for the development of highly efficient and reliable  $\text{Al}_x\text{Ga}_{1-x}\text{As}$ -based laser diodes. Studies in the literature show that adjusting the carrier density above 30% Al concentration poses a significant challenge for researchers.

For instance, Watanabe et al reported that Silicon (Si) donor levels in  $\text{Al}_x\text{Ga}_{1-x}\text{As}$  layers showed significant changes depending on the material composition and growth conditions. It was determined that the energy levels of DX centers were related to the Fermi level and that these levels changed with the increase in Al concentration. In particular a rapid decrease in the concentration of DX centers was observed in the  $X_{\text{Al}} < 0.3$  range, while it was revealed that the shallow donor density increased with the decrease of DX centers in the  $X_{\text{Al}} > 0.5$  region [9].

In another study conducted by Pfeffer et al.,  $\text{Al}_x\text{Ga}_{1-x}\text{As}$  samples with different aluminum contents ( $x = 0.10, 0.25$  and  $0.35$ ) were grown and it was revealed that the Hall carrier concentration decreased rapidly as the Al content increased. These observed changes in carrier density were further supported by Secondary Ion Mass Spectrometry (SIMS) and ECV measurements. Although the Hall mobility measurement ranged from  $300$  to  $900 \text{ cm}^2/\text{V}\cdot\text{s}$ , this variation can't serve as an indication of the presence of DX centers as suggested by the author. Additionally, it was determined that SIMS, ECV and Hall data were consistent for the  $X_{\text{Al}} = 0.1$  sample; however, significant discrepancies between the measurements emerged for the sample that exhibit Al concentration of  $X_{\text{Al}} \geq 0.2$ .

Although the presence of DX centers could not be definitively confirmed, the observed decrease in carrier density is suggested to be associated with DX centers, consistent with the band structure model proposed by Kuech et al. The findings reveal that n-type doping levels and Al concentration in  $\text{Al}_x\text{Ga}_{1-x}\text{As}$  systems require more accurate optimization process for the efficiency and stability of high-power semiconductor lasers [10, 11].

To make it clear, the donor ionization energy increases significantly in  $\text{Al}_x\text{Ga}_{1-x}\text{As}$  compounds when the Al content exceeds 25% [12]. This causes the ionized carrier density to decrease, reducing the doping efficiency. In addition, high Al concentrations, especially at high flow rates of

source gases such as TMAI, lead to increased carbon contamination. Since carbon acts as a acceptor, its incorporation further suppresses the free electron concentration in the material. However, high Al content can cause dopant atoms such as Si to change position in the crystal lattice and become passive DX centers. DX centers emerge as a result of the dopant atom forming a complex with a donor-cation vacancy and are not electrically active [13]. Moreover, the tendency of Al atoms to attract impurities such as oxygen into the crystal promotes the formation of DX centers. Oxygen creates deep-level, nonradiative trap centers, causing donor compensation and a reduction in the material's radiative efficiency [14]. Collectively, these factors contribute to an increase in the density and activity of DX centers, which ultimately reduces the free carrier concentration and degrades electrical conductivity.

## Materials and Methods

Epitaxial n-  $\text{Al}_x\text{Ga}_{1-x}\text{As}$  layers were grown on undoped GaAs substrate by AIXTRON 200/4 RF-S horizontal flow, MOVPE. Trimethylaluminum (TMAI), trimethylgallium (TMGa) and arsine ( $\text{AsH}_3$ ) gases were used as Al, Ga and As sources, respectively, while  $\text{SiH}_4$  gas was used for n-type doping. In situ optical reflection was measured with a monitoring wavelength of 880 nm to control important parameters such as growth rate and surface quality during growth. In order to determine the crystal quality and Al concentrations of the grown films, Rigaku High Resolution X-Ray Diffraction (HRXRD) system was employed. Carrier concentrations were determined using both Hall effect and ECV measurement systems. All the necessary characterizations were performed in detail.

## Findings and Discussion

Extensive growth optimizations have been carried out to obtain the desired doping levels in the n- $\text{Al}_x\text{Ga}_{1-x}\text{As}$  layer. During these experiments, it was noticed that the doping level decreased with the increase of the Al concentration ratio. Notably, when the Al concentration exceeded 30%, the carrier concentration plateaued around  $5 \times 10^{17} \text{ cm}^{-3}$  even when the  $\text{SiH}_4$  flow was adjusted to the maximum value. Representative results from these optimization experiments are presented in Table 1.

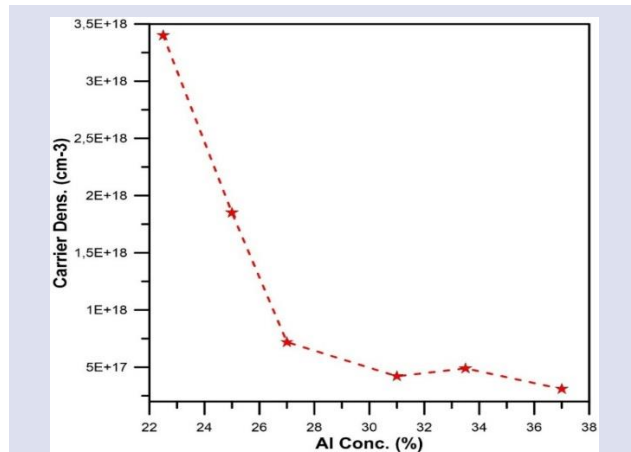
Table 1. Growth parameters and results obtained for the growth of  $n\text{-Al}_x\text{Ga}_{1-x}\text{As}$  layers for the optimization of Al concentration and doping level.

Sample Name	Growth Temp. (°C)	TMGa (sccm)	TMAI (sccm)	AsH <sub>3</sub> (sccm)	SiH <sub>4</sub> (sccm)	Al Conc. (%)	Carrier Conc. (cm <sup>-3</sup> )
Sample A	650	16	23	20	15	0.25	$1.85 \times 10^{18}$
Sample B	650	16	41	20	20	0.37	$3.1 \times 10^{17}$
Sample C	650	16	38	20	31	0.335	$4.9 \times 10^{17}$
Sample D	650	16	23	50	15	0.225	$3.4 \times 10^{18}$
Sample E	700	8	23	20	31	0.27	$7.2 \times 10^{17}$
Sample F	650	10	23	20	15	0.31	$4.21 \times 10^{17}$
Sample G	650	10	23	20	15	0.35	$5 \times 10^{17}$
Sample H	650	16	36	20	10 - 30	0.35	$4.1 \times 10^{17}$

For the Samples A, B, and C, in which only the TMAI and SiH<sub>4</sub> flows were changed, it was noticed that as the Al concentration increased, carrier density decreased even though the SiH<sub>4</sub> flow was increased. In order to investigate the effect of increasing the As flow, another experiment was preformed taking Sample A as reference in this experiment, indicated by sampled D, the AsH<sub>3</sub> flow was increased from 20 sccm to 50 sccm. The results showed that although the carrier density increased in Sample D, the Al concentration decreased from 0.25 to 0.22.

Another experiment, referred to as Sample E, was conducted to gain clearer insight into the doping mechanism at high aluminum concentrations. The objective was to increase the Al content by reducing the TMGa and AsH<sub>3</sub> flow, while simultaneously enhancing the carrier density by raising the growth temperature and increasing the SiH<sub>4</sub> flow rate. However, carrier density could not be increased up to  $1 \times 10^{18}$  cm<sup>-3</sup> levels.

In Sample F growth, unlike Sample A, TMGa flow was decreased, and reactor pressure was increased from 100 mbar to 250 mbar. In this growth, carrier density could not be increased even though Al concentration was increased. It is clearly seen from the Figure 1 that the dopant density decreases rapidly with increasing Al concentration and after 30% Al concentration the carrier density was always around  $5 \times 10^{17}$  cm<sup>-3</sup>. When literature studies are examined, it is observed that researchers encounter the same problem. In Al<sub>x</sub>Ga<sub>1-x</sub>As layers when  $x > 0.25$ , it is thought that the increase in donor ionization energy, carbon contamination, deep trap levels originating from oxygen and the formation of DX centers cause a significant decrease in the electron carrier concentration. The increase in donor ionization energy leads to a decrease in the free electron density, while the high TMAI flow rate suppresses electron carriers by increasing carbon contamination. In addition, the interaction of oxygen and aluminum creates deep trap levels, increasing the electrical resistance of the material and decreasing its conductivity. DX centers that occur at  $x > 0.2$  levels restrict electron mobility due to their high activation energies and further reduce the conductivity [14].

Figure 1. Variation of carrier density in  $n\text{-Al}_x\text{Ga}_{1-x}\text{As}$  layer versus Al concentration

In order to obtain more comprehensive information about the crystal structure and material quality for these samples, XRD measurements were performed conducted using  $\theta$ - $2\theta$  scans. The Al composition, FWHM (full width-half maximum) values and lattice parameters of each sample were determined using the Global Fit simulation program [15]. Based on the obtained lattice constants, the reference lattice constants  $a_0$  values were calculated with the help of Vegard's law [16]. In this way, the strain in the samples were also calculated and all obtained values are presented in Table II.

Based on the obtained data, the crystal quality and lattice mismatch of the samples were comparatively evaluated depending on FWHM and strain values [17, 18]. Although the FWHM and strain values of the samples are relatively close to each other, Sample B exhibits the highest crystal quality with the lowest FWHM value (113.6 arcsec), while also having the highest strain ( $4.50 \times 10^{-4}$ ), indicating the greatest lattice mismatch. In contrast, Sample D shows the highest FWHM value (231.7 arcsec) and the lowest strain ( $1.35 \times 10^{-4}$ ), suggesting better lattice compatibility despite the presence of more structural defects. These findings suggest that the relationship between FWHM and strain may not be strictly linear or directly correlated.

Table 2. Measured FWHM and Calculated Strain Values of the  $\text{Al}_x\text{Ga}_{1-x}\text{As}$  Layers

Sample Name	Al Conc. (%)	FWHM (arscec)	$a_0$ (Å)	$a_{\text{measurement}}$ (Å)	Strain (%)
Sample A	0.25	181.1	5.65532	5.65648	$2.05 \times 10^{-4}$
Sample B	0.37	113.6	5.65629	5.65884	$4.50 \times 10^{-4}$
Sample C	0.335	158.6	5.65601	5.65808	$3.66 \times 10^{-4}$
Sample D	0.225	231.7	5.65512	5.65588	$1.35 \times 10^{-4}$
Sample E	0.27	149.8	5.65548	5.65696	$2.62 \times 10^{-4}$
Sample F	0.31	154.4	5.65581	5.65716	$2.39 \times 10^{-4}$

As a last experiment Sample F was taken as reference, and a new experiment was conducted and the reactor pressure was set to 100 mbar again resulting in Sample G. Al concentration increased from 31% to 35% and carrier density increased from  $4.20 \times 10^{17}$  to  $5 \times 10^{17} \text{ cm}^{-3}$  (Hall measurement). ECV measurement of Sample G was contacted and it was noticed that the carrier density was in the range of  $2 \times 10^{18} \text{ cm}^{-3}$  (Figure 2). In the studies conducted in the literature, when the Al ratio was around 0.1, a good agreement was observed between ECV and Hall data, but when the Al ratio was greater than 0.2, a serious inconsistency was noticed between the measurements [19].

In the studies conducted on Si-doped  $\text{Al}_x\text{Ga}_{1-x}\text{As}$ , it was reported that there were two types of donor centers: deep and shallow [10]. In general, when measuring n-type materials with ECV, unlike p-type materials, the UV light source used allows the detection of deep donor levels that cannot be detected by Hall measurement. Since all Si atoms are electrically active, ECV measurement was taken into account for n-type layers.

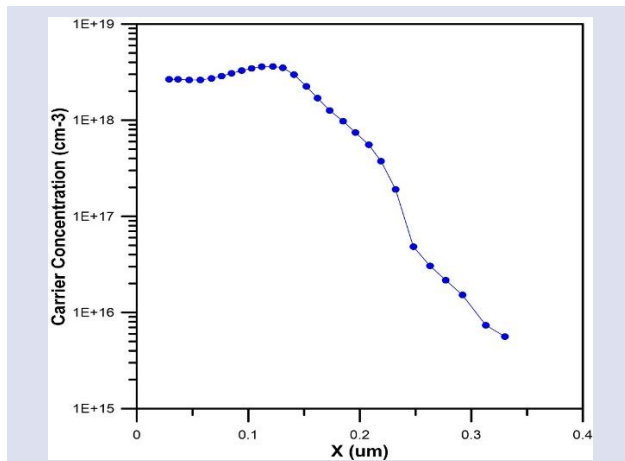


Figure 2. Sample G is the ECV measurement result of the sample

Although an inconsistency was noticed in ECV and Hall measurements in n- $\text{Al}_x\text{Ga}_{1-x}\text{As}$  samples, it was also proven by ECV measurements that when the Al concentration exceeded 30%, the carrier density remained constant and could not be increased. The structure of Sample H and ECV measurement are given below (Figure 3). In Sample H,  $\text{Al}_x\text{Ga}_{1-x}\text{As}$  with 35% Al concentration was grown and the  $\text{SiH}_4$  flow was changed as 10, 15, 20, 25, 30, and 35 sccm. The change in carrier density with increasing the  $\text{SiH}_4$  flow was investigated. ECV measurement of Sample H is given in Figure 4. Although the  $\text{SiH}_4$  flow was increased, the carrier density of the  $\text{Al}_x\text{Ga}_{1-x}\text{As}$  layer with 35% Al concentration remained constant at  $1 \times 10^{18} \text{ cm}^{-3}$  levels.

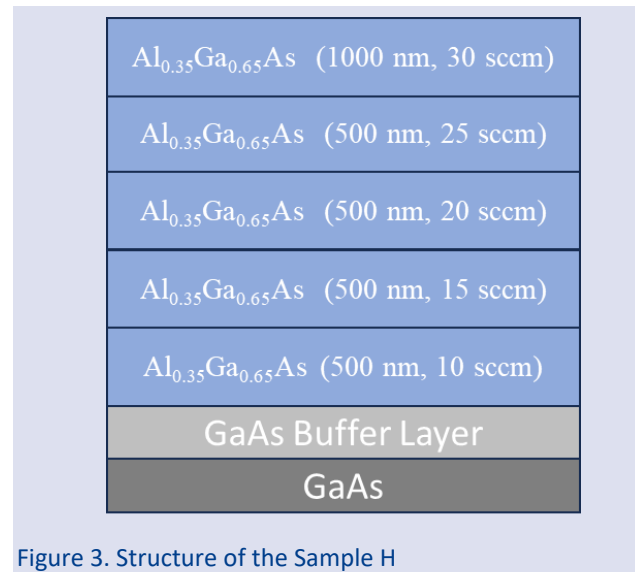


Figure 3. Structure of the Sample H

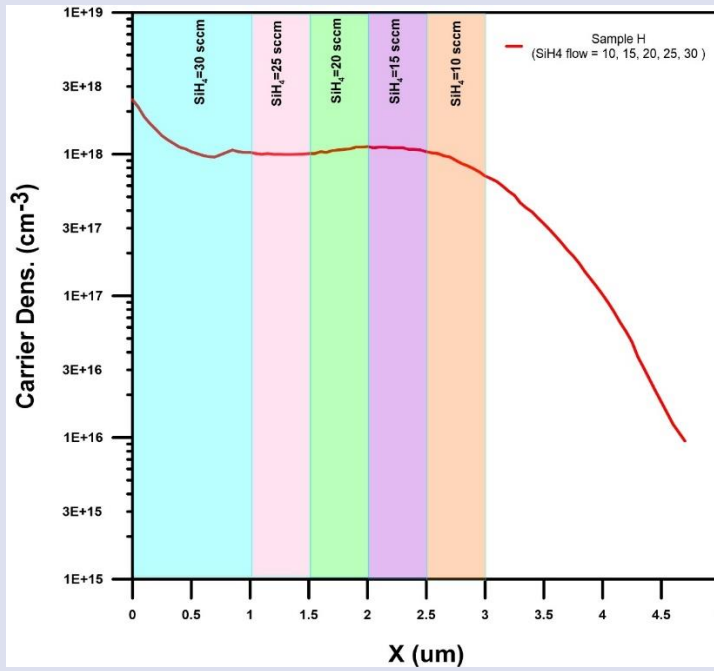


Figure 4. ECV measurement result of Sample G

## Conclusions

In conclusion, the optimization of doping density and Al concentration on epitaxially grown  $n\text{-Al}_x\text{Ga}_{1-x}\text{As}$  layers in this study clearly revealed the main challenges encountered in the production of high-power semiconductor laser diodes. Experimental data showed that when the Al concentration exceeds 30%, the expected increase in doping density could not be achieved despite the adjustment of the  $\text{SiH}_4$  flux to the maximum level. While the agreement between Hall and ECV measurements was achieved at low Al ratios, significant differences occurred above 0.2 Al ratio. This situation indicates that the current limitations in n-type doping processes and precise control of Al concentration should be reviewed. The obtained results indicate that the process parameters should be re-evaluated for the development of high efficiency and reliable laser diodes and provide a solid basis for further research by providing data consistent with similar studies reported in the literature.

## Conflicts of interest

There are no conflicts of interest in this work.

## Acknowledgement

This work is based on results obtained during the ongoing Ph.D. thesis of the first author, titled "Development of a GaAs-based pump laser diode structure ( $\lambda = 88\text{ nm}$ )". Gamze YOLCU is supported by the YÖK (Council of Higher Education) 100/2000 Ph.D. Scholarship Program and The Scientific and Technological Research Council of Turkey (TUBITAK) 2211/A Program. The authors acknowledge the usage of the Sivas Cumhuriyet University Nanophotonics Application and

Research Center-CUNAM facilities. This study supported by The Scientific Research Project Fund of Sivas Cumhuriyet University, Turkey under the Project number M-2023-857.

## References

- [1] Ladugin M.A.E., Marmalyuk A.A.E., Effect of (Al)GaAs/AlGaAs quantum confinement region parameters on the threshold current density of laser diodes, *Quantum Electron.*, 49 (6) (2019) 529.
- [2] Saeed S., Usman M., Ali S., Ali H., Mustafa L., High performance near-infrared III-Arsenide laser diodes with p-AlGaAs barriers, *Opt. Mater.*, 139 (2023) 113809.
- [3] Kim K.C., Kim T.G., Sung Y.M., Choi Y.C., Park Y.J., Han I.K., Park J.I., Performance improvement of high-power AlGaAs lasers, *J. Korean Phys. Soc.*, 47 (2005) S572.
- [4] Zappe H., *Laser Diode Microsystems*, Springer Science & Business Media, (2004).
- [5] Knauer A., Wenzel H., Erbert G., Sumpf B., Weyers M., Influence of oxygen in AlGaAs-based laser structures with Al-free active region on device properties, *J. Electron. Mater.*, 30 (2001) 1421–1424.
- [6] Ito M., Kimura T., Carrier density dependence of refractive index in AlGaAs semiconductor lasers, *IEEE J. Quantum Electron.*, 16 (9) (1980) 910–911.
- [7] Perkitel I., Kekül R., Altuntas I., Gür E., Demir I., Influence of Highly Efficient Carbon Doping on  $\text{Al}_x\text{Ga}_{1-x}\text{As}$  Layers with Different Al Compositions (x) Grown by MOVPE, *J. Electron. Mater.*, 52 (9) (2023) 6042–6051.
- [8] Gullu H.H., Yıldız D.E., Yıldırım M., Demir I., Altuntas I., Electrical characteristics of Al/AlGaAs/GaAs diode with high-Al concentration at the interface, *J. Mater. Sci.: Mater. Electron.*, 35 (2) (2024) 189.
- [9] Watanabe M.O., Morizuka K., Mashita M., Ashizawa Y., Zohta Y., Donor levels in Si-doped AlGaAs grown by MBE, *Jpn. J. Appl. Phys.*, 23 (2A) (1984) L103.



- [10] Pfeffer T.L., et al., The use of diethylsulphide for the doping of  $\text{Al}_x\text{Ga}_{1-x}\text{As}$  grown by chemical beam epitaxy, *J. Cryst. Growth*, 146 (1–4) (1995) 399–403.
- [11] Kuech T.F., Tischler M.A., Potemski R., Cardone F., Scilla G., Doping and dopant behavior in (Al, Ga)As grown by metalorganic vapor phase epitaxy, *J. Cryst. Growth*, 98 (1–2) (1989) 174–187.
- [12] Ishikawa T., Saito J., Sasa S., Hiyamizu S., Electrical properties of Si-doped  $\text{Al}_x\text{Ga}_{1-x}\text{As}$  layers grown by MBE, *Jpn. J. Appl. Phys.*, 21 (11A) (1982) L675.
- [13] Oh-hori T., Itoh H., Tanaka H., Kasai K., Takikawa M., Komeno J., Donor–cation vacancy complex in Si-doped AlGaAs grown by metalorganic chemical vapor deposition, *J. Appl. Phys.*, 61 (9) (1987) 4603–4605.
- [14] Shieh H.M., Wu T.S., Hsu W.C.,  $\text{SiH}_4$ -doped AlGaAs epilayers formed by MOCVD, *J. Cryst. Growth*, 121 (4) (1992) 665–670.
- [15] Kalyon G., Mutlu S., Kuruoğlu F., Perkitel İ., Demir İ., Erol A., InGaAs-based Gunn light emitting diode, *Mater. Sci. Semicond. Process.*, 159 (2023) 107389.
- [16] Kaynar E., Sayrac M., Altuntaş İ., Demir İ., Determination of optical properties of MOVPE-grown  $\text{In}_x\text{Ga}_{1-x}\text{As}/\text{InP}$  epitaxial structures by spectroscopic ellipsometry, *Braz. J. Phys.*, 52 (5) (2022) 184.
- [17] Perkitel İ., Altuntaş İ., Demir İ., The effect of Si (111) substrate surface cleaning on growth rate and crystal quality of MOVPE grown AlN, *Gazi Univ. J. Sci.*, 35 (1) (2022) 281–291.
- [18] Pürlü K.M., Koçak M.N., Yolcu G., Perkitel İ., Altuntaş İ., Demir İ., Growth and characterization of PALE Si-doped AlN on sapphire substrate by MOVPE, *Mater. Sci. Semicond. Process.*, 142 (2022) 106464.
- [19] Nanometrics, ECVPro: Electrochemical C-V Profiler User Manual, P/N: 9PROF-UM01 Rev. B.

## Optical Polarization Response of Hybrid Gratings Made of Metals and Polymers Based on Bruggeman Theory

Emirhan Taze<sup>1,a</sup>, Talha Erdem<sup>1,b,\*</sup><sup>1</sup> Department of Electrical-Electronics Engineering, Abdullah Gül University, Kayseri 38080, Türkiye

\*Corresponding author

### Research Article

#### History

Received: 24/01/2025


Accepted: 20/06/2025



This article is licensed under a Creative Commons Attribution-NonCommercial 4.0 International License (CC BY-NC 4.0)

### ABSTRACT

The current state of the art in grating designs has not adequately addressed compositions involving different metals and polymers. Our study aims to fill this gap by investigating how varying material compositions influence polarization properties. To explore this, we computed the refractive indices of hybrid mixtures containing gold, silver, and poly(dimethyl siloxane) (PDMS) using the Bruggeman effective medium theory. We then conducted simulations of optical transmission and reflection for gratings composed of these hybrid materials. Our analysis revealed distinct extinction coefficient peaks at specific wavelengths depending on the material ratios. Notably, our simulations indicate the possibility of fine-tuning the extinction coefficient within the spectral range of 450–1000 nm by modifying material composition. We also observed the ability to achieve polarization ratios of 0 and 1, demonstrating the potential for precise polarization control in optical applications. These findings suggest that carefully engineered metal-polymer hybrid gratings can serve as tunable optical filters and polarizers tailored to specific wavelength ranges. Customizing extinction properties and polarization response by varying the constituent materials provides new opportunities. Our results highlight the importance of material selection in grating design, paving the way for developing next-generation optical components with enhanced functionality.

**Keywords:** Hybrid nanomaterials, Optical polarization, Gratings, Effective medium approximation, FDTD. [emirhan.taze@agu.edu.tr](mailto:emirhan.taze@agu.edu.tr) <https://orcid.org/0009-0007-4183-6954> [erdem.talha@agu.edu.tr](mailto:erdem.talha@agu.edu.tr) <https://orcid.org/0000-0003-3905-376X>

## Introduction

A grating is a periodically varying structural or compositional system [1,2]. There are different types of gratings, depending on the periodicity direction and types. Such structures are employed in various applications including spectroscopy, optical polarizers, optical filtering, communication, ellipsometry, and lasers [1–7]. Their polarization-dependent reflection and transmission spectra [1,3,5,7–12] can be fine-tuned by controlling the period and duty cycle of the grating as well as by tailoring the material composition.

One of the promising class of structures utilizing gratings is metamaterials or metasurfaces [13,14]. Metasurfaces are periodic dielectric or optical structure which has unconventional optical properties such as linear [15] and circular [16] dichroism, negative refractive index, and total absorption characteristics [13]. These structures have periodicity in the sub-wavelength regime; in this regime, metallic nanoparticles have plasmonic characteristics causing strong wavelength-dependent responses [5,11]. Schnabel et al. showed a periodic thin metallic line on top of a dielectric surface where polarization-dependent transmission was observed [11]. Furthermore, Zhang et al. introduced plasmonic gratings made of gold nanowires with a tunable output band using solution-processed methods [5]. In recent years, soft materials have been employed together with these metallic plasmonic nanoparticles [13,14]. PDMS

(Polydimethylsiloxane) is one of the widely used materials because of its stiffness, non-toxicity, inertness, and easy integration into the structures while SU-8 (Poly[(phenyl glycidyl ether)-co-formaldehyde]) and PEN (Polyethylene naphthalate) are among other alternatives [13]. Owing to their high elasticity [13,17], they find applications in transparent displays [17], tunable meta holograms [14], wearable biosensors in-vivo bioimaging with meta lens designs [14], deformation measurements [14,18], chiral spectroscopy and optomechanical MEMS devices [16]. In these works, soft materials were employed together with metals such as gold, silver, and aluminum [12,16–20] and achieved linear [19] and circular dichroism [16].

Thanks to the compatibility and scalable processing, plasmonic gratings made of gold or silver embedded in elastomers like PDMS have been widely studied in the literature [12–14,18–20]. In these works, polarization-dependent and/or independent wavelength-selective extinction characteristics have been demonstrated [12–14,16–20]. Nevertheless, a comprehensive analysis is missing to understand how the deformation or structural characteristics and material compositions affect linear dichroism.

To fill this gap in the literature, here, we want to reveal the potential optical performance of an exemplary hybrid system made of gold, silver, and poly (dimethyl siloxane) (PDMS). In our design, we first employed the Bruggeman

Theory [21–23] to calculate the effective refractive index of the composites. We then validated our results with the ellipsometry measurement data of gold and silver alloys in the literature [24]. Next, we modeled the gratings of composite materials having the calculated effective refractive indices as flat, thin stripes with varying periods and grating widths, and calculated polarization-dependent optical transmission and reflection using the Lumerical FDTD tool. Although the whole grating structure could have been modeled using an effective medium approximation, such an approach would lead to inaccurate results and remove polarization dependency because effective refractive index approximations perform better in randomly distributed systems [15]. Therefore, here we preferred to model the composite material using Bruggeman theory and calculate the effect of grating structure using FDTD [15,19,21–23]. Our simulation results revealed that employing metal and polymer compositions in gratings offers excellent wavelength selectivity in the polarization ratio of transmission and reflection. By adjusting material fractions and structural parameters, peak wavelength of polarization ratios could be adjusted between the wavelengths of 450 and 1000 nm. Furthermore, reaching 95% polarization ratios turn out to be possible.

After this brief introduction, in this article, we continue with the “Material and Method” section, where we explain the details of our calculations and the simulation parameters. These include the effective refractive index calculations and the geometrical design of the gratings and simulation structure. This section is followed by a “Results and Discussion” section which starts with the analysis of effective refractive index calculations followed by the electromagnetic simulation results on the polarization-dependent transmission and reflection characteristics of the gratings made of composite material system. Finally, we conclude by summarizing our key findings and presenting with a future outlook focusing on possible applications of our results.

## Material and Method

### Effective Refractive Index Calculations

We selected three materials, gold, silver, and poly (dimethyl siloxane) (PDMS), which will act as the building blocks of the hybrid stripes. Next, we calculated the effective refractive indices of these hybrids before running the electromagnetic simulations involving the stripes of these hybrids. Different methods for determining the effective refractive indices of hybrid materials have been developed in the literature. Each method is appropriate for a particular composition or type of material [21–23]. In this work, we preferred using the Bruggeman effective medium approximation since it is appropriate for modeling metal-based composites and widely employed in optical modeling [19,24] thanks to accurate optical response prediction in subwavelength-scale composite regions [21–23]. This model offers a useful and computationally efficient method to depict the

average optical behavior of the composite regions before simulating their structured arrangement, even though it assumes an isotropic and random distribution of materials in bulk mixtures.

The entire grating structure was not directly simulated in our study using the Bruggeman model. Rather, it was used to calculate the local effective refractive indices of hybrid regions made of gold, silver, and PDMS. The periodic geometry was then explicitly considered in full-wave electromagnetic simulations using these estimates as input parameters. The validation of Bruggeman’s theory approximation is carried out by comparing it with measurements obtained through ellipsometry, using the results of experimental results of Ref. [24].

In Eq. 1, the governing relation according to Bruggeman’s theory is presented where  $f$  stands for the fraction of the first material,  $1 - f$  indicates the fraction of the second material,  $\varepsilon_{mix}$ ,  $\varepsilon$ ,  $\varepsilon_1$  are the electric permittivity’s of the mixture, the permittivity of the first material, and the permittivity of the second material, respectively.

$$f \frac{\varepsilon(\omega) - \varepsilon_{mix}(\omega)}{\varepsilon(\omega) + 2\varepsilon_{mix}(\omega)} + (1 - f) \frac{\varepsilon_1(\omega) - \varepsilon_{mix}(\omega)}{\varepsilon_1(\omega) + 2\varepsilon_{mix}(\omega)} = 0 \quad (1)$$

Rearranging the terms in Eq. 1 to find  $\varepsilon_{mix}$  results in a quadratic equation (Eq. 2) that has two solutions. We numerically calculated the roots of this equation using the NumPy library of Python and then employed the  $n^2 = \varepsilon$  relation to determine the effective refractive index  $n$ . To validate which solution is the effective refractive index, we used the Arago–Biot equation (Eq. 3) having a single solution [25,26] where  $n$  is the effective refractive index of the mixture,  $\phi_i$  is the fraction of the  $i^{th}$  material, and  $n_i$  is the refractive index of the  $i^{th}$  material. We calculated the absolute difference between the roots of the Bruggeman theory and the Arago–Biot equation. We selected the root that minimizes the obtained result as the correct root.

$$\frac{2}{f-1} \times \varepsilon_{mix}(\omega)^2 + \frac{3f-1}{f-1} \times \varepsilon_{mix}(\omega) \times (\varepsilon(\omega) - \varepsilon_1(\omega)) + \frac{1}{f-1} \times \varepsilon(\omega) \times \varepsilon_1(\omega) = 0 \quad (2)$$

$$n = \sum_i \phi_i n_i \quad (3)$$

Since these equations can only design a mixture of two materials, we used them twice to calculate the refractive indices of the mixture made of different fractions of gold, silver, and PDMS. First, we designed different fractions of gold and silver according to the ratios. Then, we calculated the effective refractive index of the hybrid made of PDMS and the gold-silver mixture. PDMS fractions are varied from 0% to 40% with an increment of 2% while the remaining material was the gold-silver hybrid calculated in the previous step. In total, we calculated the effective refractive indices of 105 different material compositions.

### Geometrical Design of the Gratings

Geometrical design of the gratings is illustrated in Figure 1. There are four distinct parameters that define these gratings. These are the effective refractive index of the hybrid material, the period of the gratings ( $G$ ), the

width of the stripes ( $W$ ), and the height of the stripes ( $H$ ). We kept the height parameter constant in our simulations at  $20\text{ nm}$  and set the distance between gratings the same as the width of the stripes. This parameter changed between  $150\text{ nm}$  to  $250\text{ nm}$  in  $10\text{ nm}$  intervals, as Table 1 shows.

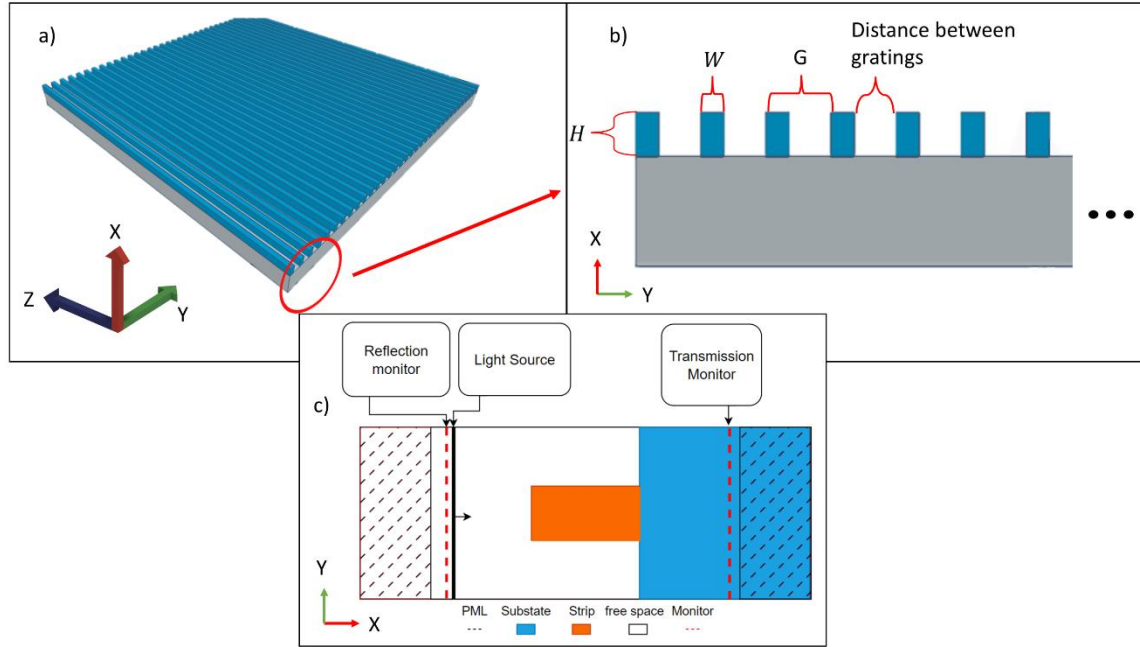


Figure 1. Representative image of the structure: (a) Isometric view and (b) side view of the structure.  $H$ ,  $G$ , and  $W$  represent the height, period, and width of the gratings, respectively. (c) Illustration of the electromagnetic simulation setup in 2D.

Table 1. Geometrical parameters employed in simulations. Width ( $W$ ), and period ( $G$ ).

$W$	$G$
$150\text{ nm}$	$300\text{ nm}$
$160\text{ nm}$	$320\text{ nm}$
$170\text{ nm}$	$340\text{ nm}$
$180\text{ nm}$	$360\text{ nm}$
$190\text{ nm}$	$380\text{ nm}$
$200\text{ nm}$	$400\text{ nm}$
$210\text{ nm}$	$420\text{ nm}$
$220\text{ nm}$	$440\text{ nm}$
$230\text{ nm}$	$460\text{ nm}$
$240\text{ nm}$	$480\text{ nm}$
$250\text{ nm}$	$500\text{ nm}$

The electromagnetic simulations were carried out using Lumerical FDTD. Since we assumed infinitely long gratings, we ran the simulations in two dimensions, whereas y-axis and x-axis boundaries were set periodic and as perfectly matched layers (PML), respectively (Figure 1c). Further details of the simulation dimensions were presented in Supporting Information (SI). We recorded the reflected and transmitted power using a power monitor and the source was set as a plane wave whose polarization was set as  $0^\circ$  and  $90^\circ$ . The polarization ratio of the reflected and transmitted light was calculated using Eq. 4, where  $I_1$  and  $I_2$  stand for the recorded optical powers by the monitors at  $0^\circ$  and  $90^\circ$ , respectively.

$$\text{Polarization ratio} = \frac{|I_1 - I_2|}{I_1 + I_2} \quad (4)$$

Multiple convergence tests were conducted to optimize the computational cost (details are presented in the SI). The conventional uniform meshing was employed with the differential size being  $1\text{ nm}$  (see the Supplementary File).

## Results and Discussion

### Refractive Indices of Hybrid Media

We calculated the refractive index values as explained in the methodology section. Figure 2 shows the real and imaginary parts of the calculated refractive indices for different fractions of gold and silver. Results reveal a gradual change of the refractive index as the fraction of the metals varies. We observe that by controlling the concentration of the metals involved, we can tailor the real and imaginary parts of the refractive index over a very broad spectral range, starting from the ultraviolet regime and extending to the infrared wavelengths. To confirm that Bruggeman's theory leads to similar results with experiments, we compared the calculated effective refractive indices with measurements obtained through ellipsometry for gold and silver mixtures presented in Ref.

[24]. Figure S1 shows a comparison of the calculated and measured refractive index of a gold-silver mixture. The calculated and measured refractive indices strongly resemble each other such that a mean squared error of

only 0.032 and 0.015 are calculated for the real and imaginary parts of the refractive index, respectively. This rigorous validation process ensures the accuracy and reliability of our theoretical calculations.

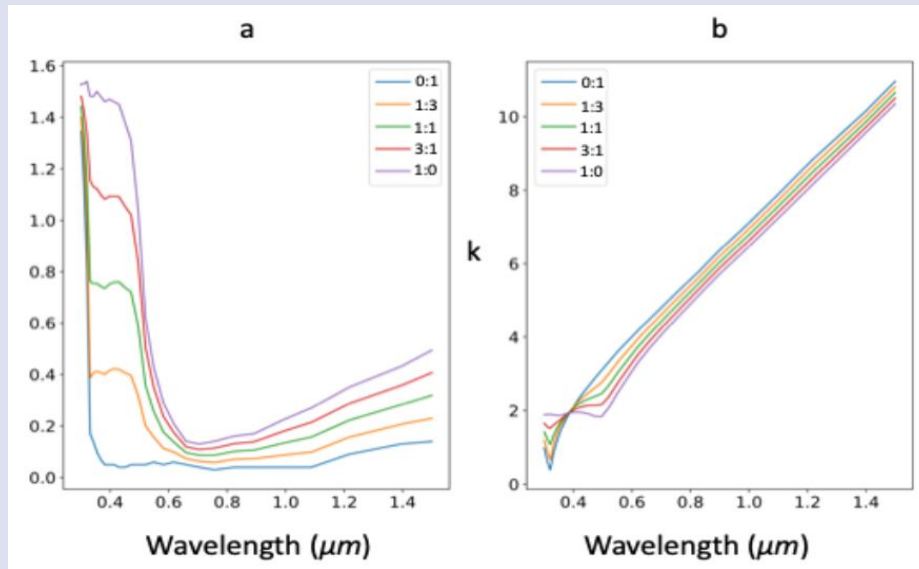


Figure 2. (a) Real and (b) imaginary parts of the refractive index belonging to the gold-silver mixture for different volume fractions. Legends are showing different concentrations of gold and silver. First number is gold fraction, second number is silver fraction.

After calculating the refractive index of hybrid material composed of gold and silver, we introduce PDMS as the third material. We calculated the refractive index of the final material systems by following the Bruggeman theory as described in the methods section. Results show that addition of PDMS decreases the extinction coefficient (k)

and increase the real part of the refractive indices in the green-red regions of the spectrum (Figure 3). Furthermore, we observe that these variations are more prominent when silver is more dominant than gold in the mixtures.

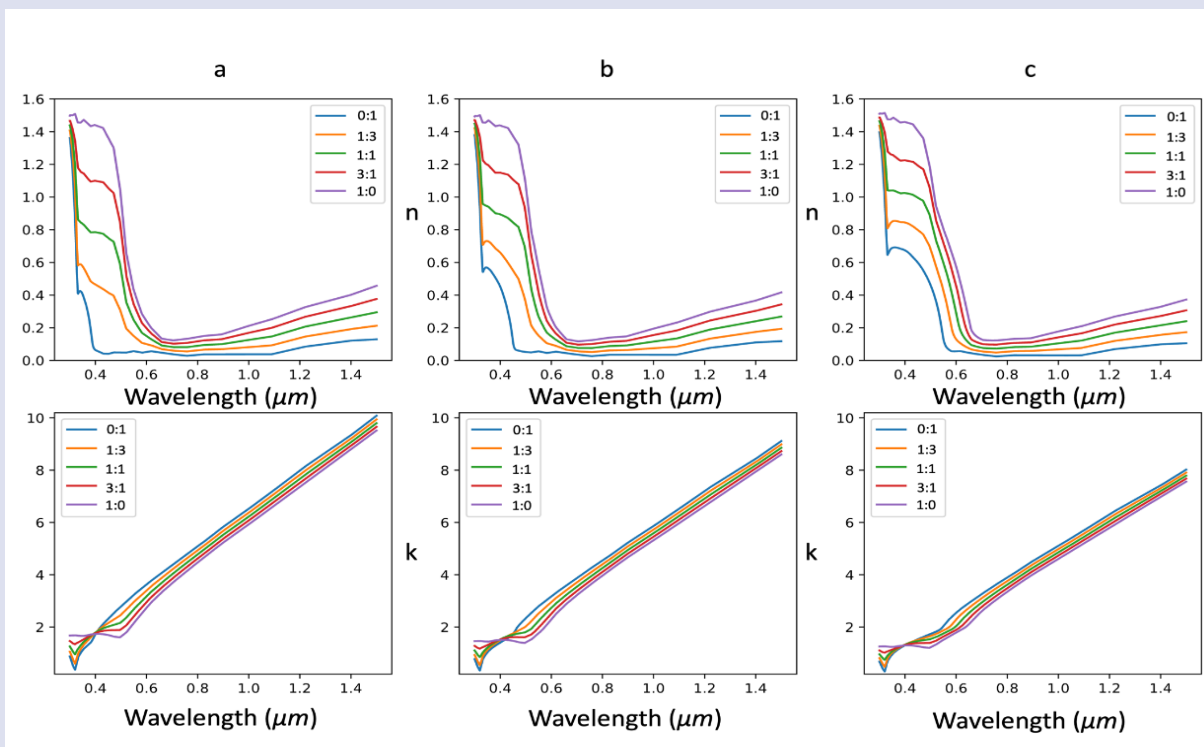


Figure 3. Real (n) and imaginary parts (k) of the refractive index belonging to hybrid materials composed of gold (G), silver (S), and PDMS (P) for different volume fractions. a) 10% PDMS used, b) 20% PDMS used, c) 30% PDMS used. Legends in the graphs show the ratio of Au - Ag concentration for the remaining part of the composition.



### Analyses of polarization ratio in transmission spectra of the gratings

Composite materials are studied for use in tailoring the optical polarization of transmitted and reflected light in the gratings. In Figure 4, we present the polarization ratio of the light transmitted through gratings for different material compositions. Figure 4a shows polarization-dependent transmission spectra and Figure 4b shows polarization ratios of the transmitted light for a grating period of 300 nm and grating width of 150 nm without PDMS addition. Polarization-dependent transmission spectra belonging to the other structural parameters are given in Figure S2, and Figures S4-S24 present polarization ratios of the transmitted light both for remaining structural parameters and for all different material combinations. Results presented in Figure 4b and Figures S4-S24, which show the polarization ratio of the transmission results, indicate that there is always a single peak in the spectrum of the polarization ratio of the transmitted light. This peak appears because the transmission of the parallel polarized light takes its minimum value while the transmission of the vertically polarized light remains relatively high (Figure 4a). The characteristics of parallel polarized light are influenced by the material composition and structural parameters. Figures 4c and 4d show the effect of PDMS concentration in the material composition on the peak polarization ratio and its wavelength. Each point in Figure 4c corresponds to the wavelength at which the polarization ratio makes a peak for a single simulation, and Figure 4d indicates the corresponding peak polarization ratios. Results in Figure 4c indicate that by tailoring silver to gold ratio, the peak polarization wavelengths can be changed within an interval of ~200 nm for any PDMS ratio. Furthermore, increasing the PDMS ratio red shifts the polarization ratio peak wavelengths without changing the span of the wavelengths when the metal composition changes.

To quantify the effects of structural and material parameters on the peak polarization ratio and its wavelengths, we calculated their average and standard deviations for all the simulation parameters and analyzed how they change with respect to changes of a certain simulation parameter (Table 2). We observe that the peak polarization ratios of the transmission spectra take values close to unity. For most of the different material compositions, the peak point in the polarization ratio remains above 0.90.

On the other hand, the average wavelength where the peaks of polarization ratios appear is ~716 nm accompanied by a broad standard deviation of ~102 nm. Supporting our observation based on Figure 4, this indicates that gratings that have high polarization ratio response can be obtained over a broad spectral range by arranging the material and structural parameters. In Figure 4, we also observe that when the same material is used, minima of polarization ratios occur at slightly longer wavelengths than the peak polarization wavelengths.

Table 1. Average and standard deviations of peak polarization ratios and corresponding wavelengths for the transmitted light for all the material and structural parameters in addition to the polarization peak ratio wavelength shifts as gold concentration, PDMS concentration, and grating constant change. Detailed explanations how these analyses were made are presented in the SF.

Result Type	Average	Standard deviation
Polarization ratio's peak wavelengths for all the material and structural parameter combinations	716.2 nm	101.6 nm
Polarization ratio's peak values for all the material and structural parameter combinations	0.98	0.02
Silver-Gold concentration effect: The polarization peak wavelength shift per 1% Gold concentration increase for all the other material and structural parameters	1.03 nm	0.21 nm
PDMS concentration effect: The shift of the polarization peak wavelength per 2 %PDMS concentration increase for all the other material and structural parameters	15.2 nm	8.6 nm
Grating constant effect: The shift of the polarization peak wavelength per 20 nm increase in grating constant for all the other material and structural parameters	25.7 nm	4.5 nm

These minima typically take polarization ratio values below 0.10. This shows that such gratings can act as strong, polarization-dependent band-pass filters for light.

Analyses of the effect of the material composition also provides valuable insights (Table 2). Higher concentrations of gold in the gold-silver mixture result in a redshift in the polarization ratio of the transmission spectrum, per 1% increase in the gold concentration creates an average shift of 1.03 nm and a standard deviation of 0.21 nm. Gold, silver, and PDMS all contribute to this shift. The addition of PDMS to the composite extends the spectral coverage of the polarization ratio peaks into the red portion of the visible spectrum. Each 2% change in PDMS concentration causes the peak wavelength of the transmission spectrum to redshift by an average of 15.2 nm, with a standard deviation of 8.6 nm. A summary of how the polarization ratio of transmitted light varies as a function of PDMS concentration is presented in Figure 4d.

For the structural parameters, grating constant has an effect of 25.7 nm red shift of the peak location for each 20 nm change in the grating constant with 4.5 nm standard deviation. This shows that not only the material properties, but also the structural parameters are important to tailor the polarization ratio.

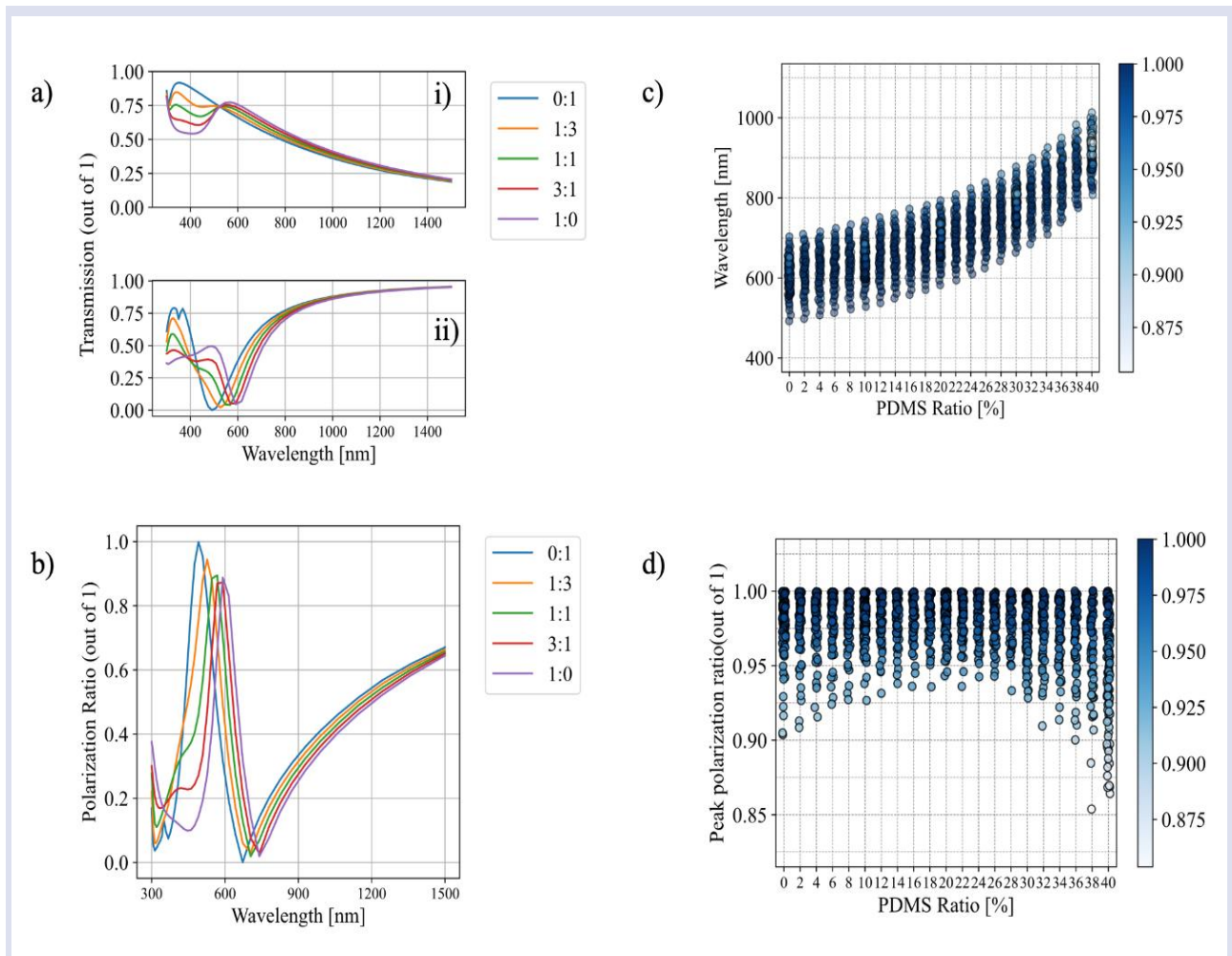


Figure 4. Polarization-dependent transmission response of the hybrid gratings made of silver, gold, and PDMS for a grating period of 300 nm and grating width of 150 nm. a) Transmission spectra belonging to the composites made of gold and silver at varying ratios without the addition of PDMS. i) parallel polarized light ii) perpendicular polarized light, legend shows gold: silver ratios. b) Polarization ratio of the transmission spectra belonging to the composites made of gold and silver at varying ratios without the addition of PDMS, legend shows gold: silver ratios. c) Peak wavelengths of the polarization ratio of transmission spectra for different PDMS fractions with respect to the gold and silver mixtures. d) Peak polarization ratio of transmission spectra for various PDMS fractions in gold and silver mixtures. The x-axis shows PDMS fractions, and the y-axis displays the corresponding peak values. Color heatmaps in c) and d) parts show the value of the peak polarization.

### Analysis of Polarization Ratio in Reflection Spectra of the Gratings

In addition to the transmission, we analyzed the polarization-dependent reflection response of the gratings made of the hybrid materials. In Figure 5 and Table 3 we present results of polarization ratio of the reflected light for various material compositions and structural parameters. Figure 5a shows polarization-dependent reflection spectra and Figure 5b shows polarization ratios of the reflected light for a grating period of 300 nm and grating width of 150 nm without PDMS addition. Polarization-dependent reflection spectra belonging to the other structural parameters are given in Figure S3, and Figures S25-S45 present polarization ratios of the reflected light both for remaining structural parameters and for all different material combinations.

The calculated reflection spectra possess some general trends. Reflection of the s-polarized light exhibit

minima, whereas the p-polarized light shows relatively higher reflection, resulting in sharp peaks in the polarization ratio calculations. As shown in Figure 5a, this mainly occurs due to strongly polarization-dependent reflection characteristics of silver and gold. As a result of these characteristics, polarization ratios make a valley in the ultraviolet regime. As the wavelength of interest gets longer, the polarization ratios first make a peak followed by a sharp valley in the red spectral region. In the infrared region, the polarization ratio increases further.

Figures 5c and 5d show the effect of PDMS concentration in the material composition on the peak polarization ratio and its wavelength. Each point in Figure 5c corresponds to the wavelength at which the polarization ratio makes a peak for a single simulation, and Figure 5d indicates the corresponding peak polarization ratios. In Table 3, we present our statistical analysis about the effects of structural and material

parameters on the polarization ratio and its wavelengths. Results indicate that the peak polarization ratios can be obtained over a broad spectral range by tailoring the material compositions. On the other hand, the peak polarization ratios are around 0.67 with a low standard

deviation, indicating that the peaks of the polarization ratios rarely can get larger values. Compared to the available polarization ratio peaks of the transmitted light, the potential values that can be obtained in the reflected light remain much lower.

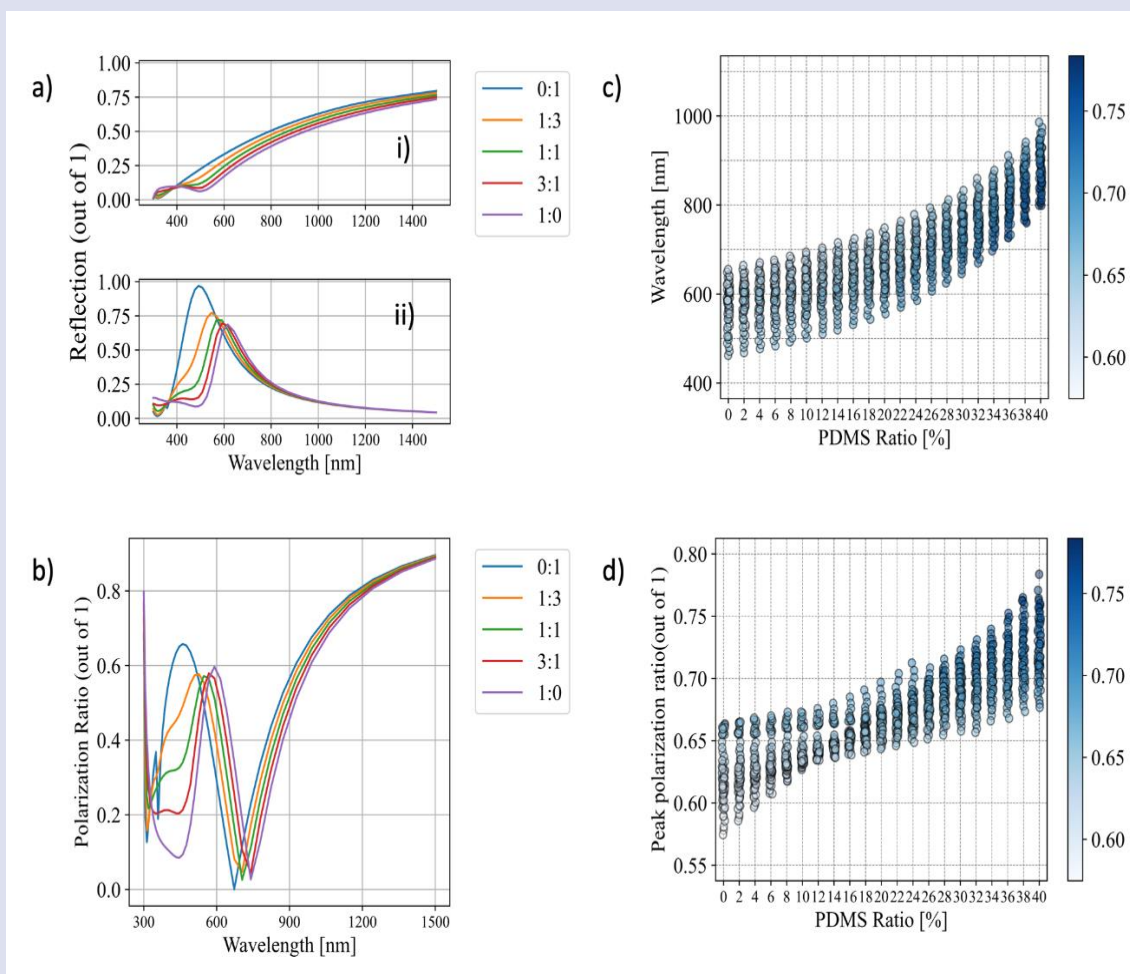


Figure 5. Polarization-dependent reflection spectra of the hybrid gratings made of silver, gold, and PDMS for a grating period of 300 nm and grating width of 150 nm. a) Reflection spectra of to the composites made of gold and silver at varying ratios without the addition of PDMS. i) parallel polarized light ii) perpendicular polarized light. Legend shows gold: silver ratios b) Polarization ratio spectra of the composites made of gold and silver at varying ratios without the addition of PDMS. Legend shows gold: silver ratios c) Peak wavelengths of the polarization ratio spectra of reflection for different PDMS fractions with respect to the gold and silver mixtures. d) Peak polarization ratios of reflection for various PDMS fractions in gold and silver mixtures. The x-axis shows PDMS fractions, and the y-axis displays the corresponding peak values. Color heatmaps in c) and d) parts show the value of the peak polarization.

We also analyzed how the change in the material and structural parameters affect the peak polarization ratios and their wavelengths. We calculated that for 1% change in the gold concentration, the wavelength of the peak polarization ratios red-shifts on average by  $1.14 \text{ nm}$  ( $\pm 0.38 \text{ nm}$ ). The inclusion of PDMS in the material leads to a red shift in the polarization ratio peaks across the results. On average, each 2% change of PDMS concentration results in a shift of  $15.3 \text{ nm}$  ( $\pm 9.31 \text{ nm}$ ).

Effect of structural parameters for the incident light reflection from the structure differs from the transmission results. For a grating constant change of 20 nm, the average wavelength of the peak polarization ratios red-shifts by 19.2 nm, with a standard deviation of 5.46 nm,

which indicates a strong effect of grating constant on the wavelength at which the polarization ratio makes a peak

Given these findings, by carefully adjusting the amount of the materials and structural parameters, it becomes possible to tailor the peak wavelength of the polarization ratio for the reflected light over a broad spectral range. Simulations show different peak values for each of the polarization ratio peaks, and while the position can be adjusted, the highest amount of polarization peak ratio can be selected by meticulously choosing the ratios. Across all simulation results, the peak polarization ratios of the reflected light reach up to 0.78 while the minimum polarization ratio becomes 0.57 (Figure 5d).



Table 2. Statistical analysis of reflection spectra: Polarization ratio's peak values and the wavelengths where these peaks occur.

Result Type	Average Value	Standard deviation
Reflection polarization ratio's peak locations	684.75 nm	100.6 nm
Reflection polarization ratio's peak values (out of 1)	0.67	0.03
Silver-Gold concentration effect on the peak location shift for per 1% Gold concentration increase.	1.14 nm	0.38 nm
PDMS concentration effect on redshift of the peak location per 2 %PDMS concentration increase.	15.3 nm	9.3 nm
Grating constant effect on shift of the peak location per 20 nm increase in grating constant.	19.2 nm	5.5 nm

## Conclusions

Unidirectional periodic structures exhibit distinct polarization-dependent characteristics. To expand the library of potential materials for polarizers, in this study, we analyzed the potential of gratings acting as linear polarizers made of hybrid materials containing gold, silver, and PDMS. We first calculated the refractive indices of these hybrids using Bruggeman and Arago-Biot theories followed by the electromagnetic simulations. In these simulations, gratings were formed with these hybrid materials, and the transmission and the reflection of the light was analyzed as a function of polarization.

The analyses of the polarization-dependent transmission spectra reveals that the polarization ratios can have maxima close to unity and minima close to zero for the same material and geometric configuration. This shows us that the gratings of these hybrid materials can act as strongly polarization-dependent optical band-pass filters. We also found out that increasing the gold content red-shifts the wavelength of the polarization ratio peak by ~1nm per 1% increase in the gold concentration. Addition of PDMS was found to have a more profound effect as it red-shifts the polarization peak by ~15 nm for an increase of 2% in the PDMS concentration. Furthermore, increasing the grating constant by 1 nm was found to red-shift the polarization ratio peak by ~1.3 nm.

The analyses of the reflection spectra show us that for all the composition combinations, the polarization ratio spectra have valleys in the ultraviolet regime. At longer wavelengths, a strong peak occurs followed by another valley, both of which fall in the visible regime. In the infrared regime the polarization ratio was found to take larger values. Compared to the polarization ratio of the transmitted light, that of the reflected light takes significantly lower values, which means that polarization-dependent absorption of the light plays a crucial role in obtaining high polarization ratios of the transmitted light.

The material-dependent polarization ratios of the reflected light have similar trends with the transmitted light, i.e., higher gold concentration red-shift the polarization ratio peaks and introducing PDMS results in more profound shifts of the polarization response. Furthermore, we found out that increasing grating-constant redshifts the wavelength at which the polarization ratio peak occurs.

Overall, our results show that with the hybrids of gold, silver, and PDMS, we can achieve strong polarization-dependent transmission and reflection characteristics. These effects turn out to be strongly wavelength-dependent, enabling polarization-dependent optical band-pass filters. Furthermore, we found out that selecting the correct material and geometrical properties for a desired polarization response is critical. We believe that these results can guide the design of hybrid polarizers and optical band-pass filters.

## Acknowledgements

TE acknowledges the support from Tübitak 2247-A program Grant No. 120C124, from Science Academy (Bilim Akademisi) for BAGEP 2023 Award, and from the Turkish Academy of Sciences for the GEBİP Award. ET thanks YÖK 100/2000 program and Tübitak BİDEB 2211-A program.

## Conflicts of interest

There are no conflicts of interest in this work.

## References

- [1] Palmer C., Loewen E., Diffraction grating handbook, 6th ed. New York (2005) 12-155.
- [2] Loewen E., Popov E., Diffraction gratings and applications, 1st ed. New York (2018)
- [3] Arkhipkin V. G., Myslivets S. A., One- and two-dimensional Raman-induced diffraction gratings in atomic media, *Phys Rev A (Coll Park)*, 98 (1) (2018) 013838.
- [4] Knop K., Rigorous diffraction theory for transmission phase gratings with deep rectangular grooves, *JOSA* 68 (9) (1978) 1206-1210.
- [5] Zhang X., Liu H., Tian J., Song Y., Wang L., Band-selective optical polarizer based on gold-nanowire plasmonic diffraction gratings, *Nano Lett*, 8 (9) (2008) 2653-2658
- [6] Zhao L., Electromagnetically induced polarization grating, *Scientific Reports*, 8 (1) (2018) 1-10.
- [7] Cincotti G., Polarization Gratings: Design and Applications, *IEEE J Quantum Electron*, 39 (12) (2003) 1645-1652.
- [8] Wu J., Zhou C., Cao H., Hu A., Polarization-dependent and -independent spectrum selective absorption based on a metallic grating structure, *Opt Commun*, 309 (2013) 57-63.
- [9] Ouyang M., Cao Y., Gao H., Shi J., Zhou J., Liu D., Analysis on polarization dependence of Fraunhofer diffraction by metallic grating with short period, *Opt Laser Technol*, 40 (1) (2008) 201-207.
- [10] Sadv S. Yu., McGreer K. A., Polarization dependence of diffraction gratings that have total internal reflection facets, *JOSA A* 17 (9) (2000) 1590-1593.

- [11] Schnabel B., Kley E.-B., and F. Wyrowski, "Study on polarizing visible light by subwavelength-period metal-stripe gratings," *Opt. Eng.*, 38, (2) (1999) 220-226.
- [12] Xu Y., Xu Y., Wang Y., Yang Y., Yang S., Li L., Xiang R., Xiang R., Liu J., Liu J, Stretchable structural colors with polarization dependence using lithium niobate metasurfaces, *Optics Express*, 32(4)(2024) 6776-6790.
- [13] Chen Y., Ai B., Wong Z. J., Soft optical metamaterials, *Nano Convergence*, 7(1)(2020) 18.
- [14] Effah E., Nettey-Oppong E. E., Ali A., Byun K. M., Choi S. H., Tunable Metasurfaces Based on Mechanically Deformable Polymeric Substrates, *Photonics*, 10(2)(2023) 119.
- [15] Dolan J. A., Saba M., Dehmel R., Gunkel I., Gu Y., Wiesner U., Hess O., Wilkinson T. D., Baumberg J., Steiner U., Wilts B. D., Gyroid Optical Metamaterials: Calculating the Effective Permittivity of Multidomain Samples, *ACS Photonics*, 3(10)(2016) 1888-1896.
- [16] Liu Z., Xu Y., Ji C., Chen S., Li X., Zhang X., Yao Y., Li J., Fano-Enhanced Circular Dichroism in Deformable Stereo Metasurfaces, *Advanced Materials*, 32(8)(2020) 1907077.
- [17] Kumagai H., Fujie T., Sawada K., Takahashi K, Stretchable and High-Adhesive Plasmonic Metasheet Using Al Subwavelength Grating Embedded in an Elastomer Nanosheet, *Adv. Optical Mater.* 8 (15)(2020) 1902074.
- [18] Li P., Gao K., Ma R., Pan K., Li D., Liu F., Li P., Gan X., Zhao J., Wen D., Stretchable plasmonic metasurfaces for deformation monitoring, *Nanophotonics*, 13(24)(2024) 4483-4490.
- [19] Kim J., Kim H., Kim B., Chang T., Lim J., Jin H., Mun J., Choi Y., Chung K., Shin J., Fan S., Kim S., Highly tunable refractive index visible-light metasurface from block copolymer self-assembly, *Nature Communications*, 7(1)(2016) 1-9.
- [20] Yoo D., Johnson T. W., Cherukulappurath S., Norris D. J., Oh S., Template-Stripped Tunable Plasmonic Devices on Stretchable and Rollable Substrates, *ACS Nano*, 9(11)(2015) 10647-10654.
- [21] Bruggeman D. A. G, Berechnung verschiedener physikalischer Konstanten von heterogenen Substanzen. I. Dielektrizitätskonstanten und Leitfähigkeiten der Mischkörper aus isotropen Substanzen, *AnP*, 416 (7) (1935) 636-664.
- [22] Gaponenko S. V., Nanoplasmonics I: metal nanoparticles. In: Gaponenko S. V., Introduction to Nanophotonics. 1st ed. New York: Cambridge University Press (2010) 166-198.
- [23] Koledintseva M. Y., DuBroff R. E., Schwartz R. W., A Maxwell Garnett model for dielectric mixtures containing conducting particles at optical frequencies, *Progress in Electromagnetics Research*, 63 (2006) 223-242.
- [24] Peña-Rodríguez O., Caro M., Olivares J., Perlado J. M., Rivera A., Caro A., Optical properties of Au-Ag alloys: An ellipsometric study, *Optical Materials Express*, 4(2)(2014) 403-410.
- [25] An N., Zhuang B., Li M., Lu Y., Wang Z. G., Combined Theoretical and Experimental Study of Refractive Indices of Water-Acetonitrile-Salt Systems, *J Phys Chem B*, 119 (33) (2015) 10701-10709.
- [26] Reis J. C. R., Lampreia I. M. S., Santos Â. F. S., Moita M. L. C. J., Douhéret G., Refractive Index of Liquid Mixtures: Theory and Experiment, *ChemPhysChem*, 11 (17) (2010) 3722-3733.



## Recursive Polynomial Sets and Their Some Algebraic Applications

Hacı Aktaş<sup>1, a, \*</sup><sup>1</sup> Department of Mathematics, Erciyes University, Kayseri, Türkiye.

\*Corresponding author

### Research Article

#### History

Received: 30/07/2024


Accepted: 12/03/2025



This article is licensed under a Creative Commons Attribution-NonCommercial 4.0 International License (CC BY-NC 4.0)

### ABSTRACT

This paper primarily defines the framework for a new class of polynomial sets over a finite field  $GF(2)$ , providing a recursive definition and delving into pertinent algebraic properties. We also studied some applications of the obtained polynomial classes on coding theory, such as obtaining new code classes. Our focus lies on polynomial sets with degrees equal to or less than  $n$ , for which we present a methodology for encoding and decoding utilizing an irreducible polynomial  $p(x) = x^m + xs + 1$ , ( $m = 2n - 1$ ). Furthermore, as an application of this method in coding theory, we created new code classes and studied some features of these codes.

**Keywords:** Polynomial sets, Polynomial codes, Generator matrix.. [haciaktas@erciyes.edu.tr](mailto:haciaktas@erciyes.edu.tr) <https://orcid.org/0009-0001-6977-5133>

### Introduction

Polynomials appear in a wide range of scientific and mathematical fields. In more advanced mathematical settings, they are basic building blocks for formulating algebraic varieties and polynomial rings, which are essential concepts in algebra and algebraic geometry. Polynomial systems defined over finite fields hold particular significance owing to their wide-ranging applications in fields such as cryptography, coding theory, and various domains within information science and technology. Recursive polynomials have been studied in many fields for different purposes. For example, Cadilhac et al. [1] studied the expressive power of polynomial recursive sequences, a nonlinear extension of the well-known class of linear recursive sequences. Fu et al. [2] construct two classes of permutation polynomials over  $F_{q^2}$  with odd characteristic from rational R edei functions. With the help of a computer, they find that the number of permutation polynomials of these types is quite big. Sidki et al.[3] gave three recursive algorithms for computing the orthogonal polynomials. Unlike the models mentioned above, we obtained polynomial sets using recurrence relations. We studied the algebraic structure of these polynomial sets and presented some examples of how these sets can be used in coding theory in our study.

In 1948, Claude Shannon's paper [4] gave rise to information theory and coding theory, which aim to improve communication regarding convenience, reliability, and efficiency. In recent studies on polynomial codes, Ding and Ling [5] constructed a new family of cyclic codes using  $q$ -polynomials. Abdullaev and Efanov [6] presented the revealed patterns of constructing polynomial codes with different detecting characteristics. Chiu [7] proposed an alternative expression of polar codes using polynomial representations. Wang, Hao, and Qiao [8] used a method to construct new  $q$ -ary linear codes and applied it to the

construction of generalized  $R - S$  codes over  $F_q$  in order to extend the length of the codes. Nalli and Haukkane [9] introduced  $h(x)$ -Fibonacci polynomials that generalize both Catalan's Fibonacci polynomials and Byrd's Fibonacci polynomials, and also the  $k$ -Fibonacci numbers, and they provide properties for these  $h(x)$ -Fibonacci polynomials. Prasad [10] defined  $(h(x), g(y))$ -extension of Fibonacci  $p$ -numbers and golden  $(p, h(x), g(y))$ -proportion. He also established a relation among Golden  $(p, h(x), g(y))$ -proportion, Golden  $(p, h(x))$ -proportion, and Golden  $p$ -proportion. Stakhov [11] considered a new approach to coding theory, which is based on the  $Q_p$ -matrices. Kaymak [12] introduced  $h(x)$ -Fibonacci coding/decoding method for  $h(x)$ -Fibonacci polynomials.

This article aims to define a new polynomial set and study its algebraic properties and then study some applications in coding theory using these polynomial sets. For this, we first define a set of polynomials. We then survey on algebraic properties of polynomials. Besides, we obtained code sets with the created polynomial classes. We studied some algebraic properties of these codes. We expressed tools such as the generator matrix, the parity check matrix, length, and weight. Finally, we conclude the study with suggestions for future research.

### Preliminaries

This section provides some basic notions needed for the following sections. Let's give some well-known basic concepts in coding theory [13-16], as follows:

1. A linear  $[n, k]$  code  $C$  of length  $n$  over  $GF(q)$  is a  $k$ -dimensional vector subspace of  $GF(q)^n$ .

2. The number of non-zero coordinates in a code word, which is an element of  $C$ , is its (Hamming) weight.  $wt(x)$  is the (Hamming) weight of a codeword  $x$ . A linear code  $C$  with a minimum weight is represented as follows:  $w(C) := \min\{wt(x) : x \in C, x \neq 0\}$ .

3. The (Hamming) distance between two vectors  $x = (x_1, \dots, x_n)$  and  $y = (y_1, \dots, y_n)$  is the number of places where they differ and is denoted by  $d(x, y)$ . A minimum distance of a linear code  $C$  is denoted by  $d(C) = \min\{d(x, y) : x, y \in C\}$ .

4. An alternative notation for a linear code  $C$  over  $GF(q)$  is a  $[n, k, d]$  linear code, where  $d$  is the minimum distance of  $C$ .

5.  $x \cdot y = \sum_{i=1}^n x_i y_i$  is the Euclidean inner product of the two vectors  $x = (x_1, \dots, x_n)$  and  $y = (y_1, \dots, y_n)$ .

6.  $C^\perp = \{x \in GF(q)^n : x \cdot y = 0, \forall y \in C\}$  is the definition of the dual code  $C^\perp$  of  $C$ .  $C$  is referred to as self-orthogonal if  $C \subset C^\perp$  and self-dual if  $C = C^\perp$ . Binary code is a linear code over  $GF(2)$ .

**Definition 2.1.** [13] A  $k \times n$  matrix whose rows form a basis of a linear  $[n, k]$  –code is called a generator matrix of the code.  $G = [I_k : A]$  is called the standard form generator matrix.

**Definition 2.2.** [13] A parity-check matrix  $H$  for an  $[n, k]$  –code  $C$  is a generator matrix of  $C^\perp$ . If  $G = [I_k : A]$  is the standard form generator matrix of an  $[n, k]$  –code  $C$ , then a parity-check matrix for  $C$  is  $H = [-A^T : I_{n-k}]$ .

## Polynomial Sets and Algebraic Properties

In this section, we will define a new polynomial set and study some of its algebraic properties. Firstly, we construct some polynomial sets. Throughout this paper,

$$GF(2)[x] = \{a_0 + a_1x + a_2x^2 + \dots + a_nx^n : a_i \in GF(2) = \{0, 1\}\}$$

is the set of polynomials with coefficients in the field  $GF(2)$  and indeterminate  $x$ .

**Definition 3.1.**  $f_{rn} = \{a_0 + a_1x + a_2x^2 + \dots + a_nx^n : a_i \in GF(2)\}$  is a polynomial set with degree equal to or less than  $n$ , and the recursive definition of these polynomials is as follows.

$$f_{0n} = \{0, x^n + x^{n-1} + \dots + x + 1\}$$

$$f_{rn} = (x^n + f_{(r-1)(n-1)}) \cup f_{(r-1)(n-1)}$$

**Example 3.2.** A polynomial set  $f_{rn}$  is a set involving sets of polynomials.

$$f_{00} = \{0, 1\}$$

$$f_{01} = \{0, x + 1\}$$

$$f_{02} = \{0, x^2 + x + 1\}$$

$$f_{11} = (x + f_{00}) \cup f_{00} = \{0, 1, x, 1 + x\} = GF(2)^1[x]$$

$$f_{22} = (x^2 + f_{11}) \cup f_{11} = \{0, 1, x, 1 + x, x^2, x^2 + 1, x^2 + x, x^2 + x + 1\} = GF(2)^2[x]$$

$$f_{nn} = (x^n + f_{(n-1)(n-1)}) \cup f_{(n-1)(n-1)} = GF(2)^n[x]$$

$$f_{12} = (x^2 + f_{01}) \cup f_{01} = \{0, 1 + x, x^2, x^2 + x + 1\}$$

$$f_{rn} = (x^n + f_{(r-1)(n-1)}) \cup f_{(r-1)(n-1)}$$

Here,  $f_{22}$  is a polynomial set with degree equal to or less than 2. Moreover, logical representations of the polynomial sets are provided in Table 1.

Table 1. Logical representations of the polynomial sets

	$f_{00}$	$f_{01}$	$f_{02}$	$f_{11}$	$f_{12}$	$f_{22}$
0	1	1	1	1	1	1
1	1	0	0	1	0	1
$x$	0	0	0	1	0	1
$1 + x$	0	1	0	1	1	1
$x^2$	0	0	0	0	1	1
$1 + x^2$	0	0	0	0	0	1
$x + x^2$	0	0	0	0	0	1
$1 + x + x^2$	0	0	1	0	1	1

**Proposition 3.3.**  $f_{rn} = (x^n + f_{(r-1)(n-1)}) \cup f_{(r-1)(n-1)}$  is a  $r + 1$  dimensional vector space over field  $GF(2)$  and has  $2r + 1$  elements.

**Proof.** We use induction on  $r$  for the proof of the proposition. Since  $f_{1n}$  is a set

$$f_{1n} = (x^n + f_{0(n-1)}) \cup f_{0(n-1)} = \{0, x^{n-1} + \dots + x + 1, x^n, x^n + x^{n-1} + \dots + x + 1\}$$

and  $\{x^n, x^{n-1} + \dots + x + 1\}$  is a bases for  $f_{1n}$ , it is a two dimensional vector space over  $GF(2)$ . Suppose that  $f_{(r-1)(n-1)}$  is a vector space over  $GF(2)$ . Since  $f_{rn} = (x^n + f_{(r-1)(n-1)}) \cup f_{(r-1)(n-1)}$  is a  $r + 1$  dimensional and  $(x^n + f_{(r-1)(n-1)}) \cap f_{(r-1)(n-1)} = \emptyset$ , it is easy to show that  $u + v \in f_{rn}$  for all  $u, v \in f_{rn}$  and  $ru \in f_{rn}$  for all  $u \in f_{rn}, r \in GF(2)$ . Thus  $f_{rn}$  is a vector space on  $GF(2)$ . The set  $\{x^n, x^{n-1}, x^{n-2}, \dots, x^{n-(r-1)}, x^{n-r} + x^{n-(r+1)} + \dots + x + 1\}$  is a base for  $f_{rn}$ . The number of elements of  $f_{(r-1)(n-1)}$  is  $2r$ , so the number of elements of  $f_{rn}$  is  $2r + 1$  and of dimension is  $r$ .

**Example 3.4.** Using Definition 3.1 and Example 3.2, we obtain

$$f_{3n} = \{0, x^{n-3} + x^{n-4} + \dots + x + 1, x^{n-2}, x^{n-2} + x^{n-3} + \dots + x + 1, x^{n-1}, x^{n-1} + x^{n-3} + \dots + x + 1, x^{n-1} + x^{n-2}, x^{n-1} + x^{n-2} + \dots + x + 1, x^n, x^n + x^{n-3} + \dots + x + 1, x^n + x^{n-2}, x^n + x^{n-2} + \dots + x + 1, x^n + x^{n-1}, x^n + x^{n-1} + x^{n-3} + \dots + x + 1, x^n + x^{n-1} + x^{n-2}, x^n + x^{n-1} + \dots + x + 1\}.$$

$f_{3n}$  is a vector space over  $GF(2)$ . The set  $\{x^n, x^{n-1}, x^{n-2}, x^{n-3} + x^{n-4} + \dots + x + 1\}$  is a base for  $f_{3n}$ . Therefore,  $f_{3n}$  is a vector space of 4 dimensional and 24 elements.

**Proposition 3.5.** For  $r + 1 \leq n$ ,  $f_{rn}$  is a subspace of  $f_{(r+1)n}$ .

**Proof.** From Proposition 3.3, we know that  $f_{rn}$  is a vector space. The set

$$\{x^n, x^{n-1}, x^{n-2}, \dots, x^{n-(r-1)}, x^{n-r} + x^{n-(r+1)} + \dots + x + 1\}$$

is a base for the vector space  $f_{rn}$  and  $\{x^n, x^{n-1}, x^{n-2}, \dots, x^{n-(r-1)}, x^{n-r}, x^{n-(r+1)} + x^{n-(r+2)} + \dots + x + 1\}$

is a base for vector space  $f_{(r+1)n}$ . The base of  $f_{rn}$  is a subset of the base of  $f_{(r+1)n}$ . Thus,  $f_{rn}$  subspace of  $f_{(r+1)n}$

### Polynomial Sets and Codes

In coding theory, a polynomial code is a type of linear code whose set of valid code words consists of polynomials divisible by a given fixed polynomial. In this section, we construct a new kind of polynomial code. We use polynomial sets  $f_{rn}$  for this.

**Definition 4.1.** Let  $f_{rn}$  be a polynomial set and  $p(x)$  be a prime polynomial in  $GF(2)[x]$  such that  $p(x)$  has degree  $m = 2n - 1$  and format  $p(x) = xm + xs + 1$ . Then, recursive definitions of these polynomials, such as;

$$F_{0n} = p(x)f_{0n}$$

$$F_{rn} = p(x)f_{rn}$$

$F_{0n}$  and  $F_{rn}$  are called generated polynomial sets (GPS) from  $f_{0n}$  and  $f_{rn}$  respectively. Corresponding to this definition, we formulate a polynomial set

$$F_{rn} = ((x^{n+m} + x^{n+s} + x^n) + f_{(r-1)(n-1)}) \cup f_{(r-1)(n-1)}.$$

GPS  $F_{rn}$  has polynomials of degree equal to or less than  $n + m$ .

**Example 4.2.** Let  $f_{03} = \{0, x^3 + x^2 + x + 1\}$ . Then,  $p(x) = x^7 + x + 1$  is a prime polynomial of degree 23 - 1. Thus,  $F_{03} = \{0, x^{10} + x^9 + x^8 + x^7 + x^4 + 1\}$ . Moreover, let  $f_{23} = \{0, x + 1, x^2, x^2 + x + 1, x^3, x^3 + x + 1, x^3 + x^2, x^3 + x^2 + x + 1\}$ . Then,  $F_{23} = p(x)\{0, x + 1, x^2, x^2 + x + 1, x^3, x^3 + x + 1, x^3 + x^2, x^3 + x^2 + x + 1\} = \{0, x^8 + x^7 + x^2 + 1, x^9 + x^3 + x^2, x^9 + x^8 + x^7 + x^3 + 1, x^{10} + x^4 + x^2, x^{10} + x^9 + x^8 + x^7 + x^4 + 1\}$  be GPS. Then, the codes GPC obtained from  $F_{03}$  and  $F_{23}$  are  $C_{03} = \{0000000000, 11110010001\}$  and  $C_{23} = \{0000000000, 00110000101, 01000001100, 01110001001, 10000011000, 10110011101, 11000010100, 11110010001\}$  respectively.

**Theorem 4.3.** For  $r \leq n$ ,  $F_{rn}$  is a linear space of dimension  $r + 1$  over  $GF(2)$ .

**Proof.** Let  $p(x) = x^m + x^s + 1$  be an irreducible polynomial of degree  $2n - 1$ . Then  $F_{0n} = p(x)f_{0n}$  is a linear space over  $GF(2)$  and  $\{p(x)(x^n + x^{n-1} + \dots + 1)\}$  is a base of  $F_{0n}$ . The polynomial set  $F_{rn} = p(x)f_{rn} = (x^{n+m} + x^{n+s} + x^n) + f_{(r-1)(n-1)} \cup f_{(r-1)(n-1)}$  generated with the set  $\{x^{2^n+n-1} + (x^s + 1)x^n, x^{2^n+n-2} + (x^s + 1)x^{n-1}, \dots, x^{2^n+n-r} + (x^s + 1)x^{n-(r-1)}, x^{2^n+n-(r+1)} + p(x)(x^{n-(r+1)} + \dots + 1)x^{n-r}(x^s + 1)\}$ . It is obviously that the set  $\{x^{2^n+n-1} + (x^s + 1)x^n, x^{2^n+n-2} + (x^s + 1)x^{n-1}, \dots, x^{2^n+n-r} + (x^s + 1)x^{n-(r-1)}, x^{2^n+n-(r+1)} + p(x)(x^{n-(r+1)} + \dots + 1)x^{n-r}(x^s + 1)\}$  is linear independent and it generate  $F_{rn}$ . Thus, for  $u(x), v(x) \in F_{rn}$ ,  $u(x) + v(x) \in F_{rn}$ . In that case,  $F_{rn}$  is a linear space.

A string of length  $n + 1$  can be represented by a polynomial, with the bits representing the coefficients of a polynomial over a field. The basic similarity between codes and polynomials is that codes are an ordered sequence of numbers strung together to mean a single

expression. In the case of polynomials, the digits represent the coefficients of each term. The order instead represents the bit's position in the code. We could take the first bit to represent the highest power of  $x$  down to the last, meaning the constant term. Or we could consider the first bit to be the constant term and proceed up through the increasing powers of  $x$ .

Let  $GF(2)^n[x]$  denote the set of all polynomials in  $GF(2)[x]$  having a degree equal or less to  $n$ . The polynomial  $q(x) = a_0 + a_1x + \dots + a_{n-1}x^{n-1} + a_nx^n$  of degree at most  $n$  over  $GF(2)$  may be regarded in general as the word  $a_0a_1 \dots a_{n-1}a_n$  of length  $n + 1$  in  $GF(2)^n$ . Of course, each word in  $GF(2)^n$  corresponds to a polynomial in  $GF(2)^n[x]$  so we define a one-to-one mapping between  $GF(2)^n$  and  $GF(2)^n[x]$ . It is easy to check that this mapping is an isomorphism  $GF^n(2) \cong GF^n(2)[x]$  as linear spaces. Now we define codes corresponding to polynomial set  $F_{rn}$ .

**Definition 4.4.** Let  $F_{rn}$  be a GPS and  $C_{rn}$  be a code set corresponding to the polynomial set  $F_{rn}$ . Then  $C_{rn}$  is the generated polynomial code (GPC).

**Example 4.5.** Let  $F_{03} = \{0, x^{10} + x^9 + x^8 + x^7 + x^4 + 1\}$  and  $F_{23} = p(x)\{0, x + 1, x^2, x^2 + x + 1, x^3, x^3 + x + 1, x^3 + x^2, x^3 + x^2 + x + 1\} = \{0, x^8 + x^7 + x^2 + 1, x^9 + x^3 + x^2, x^9 + x^8 + x^7 + x^3 + 1, x^{10} + x^4 + x^2, x^{10} + x^9 + x^8 + x^7 + x^4 + 1\}$  be GPS. Then, the codes GPC obtained from  $F_{03}$  and  $F_{23}$  are  $C_{03} = \{0000000000, 11110010001\}$  and  $C_{23} = \{0000000000, 00110000101, 01000001100, 01110001001, 10000011000, 10110011101, 11000010100, 11110010001\}$  respectively.

Provide a recursive construction for the  $C_{rn}$  generator matrix, denoted by  $G_{rn}$ .

**Definition 4.6.** Let  $p(x) = x^m + x^s + 1$  ( $m = 2n - 1$ ) be an irreducible polynomial over  $GF(2)[x]$ . Then for  $0 < r < n$ ,

$$G_{rn} = \begin{pmatrix} x^{2^n+n-1} + (x^s + 1)x^n \\ x^{2^n+n-2} + (x^s + 1)x^{n-1} \\ x^{2^n+n-2} + (x^s + 1)x^{n-1} \\ \vdots \\ x^{2^n+n-r} + (x^s + 1)x^{n-(r-1)} \\ x^{2^n+n-(r+1)} + p(x)(x^{n-(r+1)} + \dots + 1) \\ + (x^s + 1)x^{n-r} \end{pmatrix} \quad (1)$$

is generator matrix of  $C_{rn}$ . From 1, we obtain for  $r = 0$ ,  $G_{0n} = (x^{2^n+n-1} + p(x)(x^{n-1} + \dots + 1) + x^n(x^s + 1))$  and for  $r = n$

$$G_{nn} = \begin{pmatrix} x^{2^n+n-1} + (x^s + 1)x^n \\ x^{2^n+n-2} + (x^s + 1)x^{n-1} \\ \vdots \\ x^{2^n-1} + x^s + 1 \end{pmatrix}$$

**Example 4.7.** The generator matrix for  $C_{02}$ ,  $C_{22}$ , and  $C_{12}$  are  $G_{02} = (110001)$ ,  $G_{22} = \begin{pmatrix} 1 & 0 & 0 & 1 & 1 & 1 \\ 0 & 1 & 0 & 1 & 1 & 1 \\ 0 & 0 & 1 & 0 & 1 & 1 \end{pmatrix}$  and  $G_{12} = \begin{pmatrix} 1 & 0 & 1 & 1 & 0 & 0 \\ 0 & 1 & 1 & 1 & 0 & 1 \end{pmatrix}$ .

If  $G_{rn}$  is form in 4.1, then  $G_{rn}$  is in standard form. If  $G_{rn}$  is not in standard form, then  $G_{rn}$  can be reduced to standard form with elementary operations of rows or columns.

**Theorem 4.8.** The binary  $C_{rn}$  code has a length of  $2^n + n$  and a dimension of  $r + 1$ .

**Proof.** From the definition of  $F_{rn}$ , the largest degree polynomial in  $F_{rn}$  is  $2^n - 1 + n$ . The length of the code words corresponding to this polynomial is  $2^n + n$ . From the definition of generator matrix,  $G_{rn}$  has  $r + 1$  rows and  $2^n + n$  columns. Rows of  $G_{rn}$  are a base for code  $C_{rn}$ . So, the dimension of  $C_{rn}$  is  $r + 1$ .

**Theorem 4.9.**  $C_{(r-1)n}$  is contained in  $C_{rn}$ .

**Proof.** For  $r = 1$  and  $r = 2$ , the generator matrix are

$$G_{1n} = \begin{pmatrix} x^{2^n+n-1} + (x^s + 1)x^n \\ x^{2^n+n-2} + p(x)(x^{n-2} + \dots + 1)x^{n-1}(x^s + 1) \end{pmatrix}$$

and

$$G_{2n} = \begin{pmatrix} x^{2^n+n-1} + (x^s + 1)x^n \\ x^{2^n+n-2} + (x^s + 1)x^{n-1} \\ x^{2^n+n-3} + (x^s + 1)x^{n-2} \\ x^{2^n+n-4} + p(x)(x^{n-3} + \dots + 1)x^{n-2}(x^s + 1) \end{pmatrix}$$

Since  $G_{1n}$  is a submatrix of  $G_{2n}$ , we obviously have  $C_{1n}$  is contained in  $C_{2n}$ . In general, since  $G_{(r-1)n}$  is a submatrix of  $G_{rn}$ , it follows that  $C_{rn}$  is a subcode of  $C_{2n}$ . In Table 2, we obtain some results for  $r$  and  $n$ .

Table 2.  $C_{rn}$  codes for  $r \in \{1, 2, 3, 4, 5, 6\}$  and  $n \in \{2, 3, 4, 5, 6\}$

Cod e	$2^n + n = \text{Length}$	$d = \text{distance}$	$r + 1 = \text{dimension}$	$p(x) = \text{irreducible polynomial}$
$C_{12}$	6	3	2	$x^3 + x + 1$
$C_{22}$	6	3	3	$x^3 + x + 1$
$C_{13}$	11	6	2	$x^7 + x + 1$
$C_{23}$	11	4	4	$x^7 + x + 1$
$C_{33}$	11	4	4	$x^7 + x + 1$
$C_{14}$	20	7	2	$x^{15} + x + 1$
$C_{24}$	20	4	3	$x^{15} + x + 1$
$C_{34}$	20	4	4	$x^{15} + x + 1$
$C_{44}$	20	4	5	$x^{15} + x + 1$
$C_{15}$	37	12	2	$x^{31} + x^3 + 1$
$C_{25}$	37	6	3	$x^{31} + x^3 + 1$
$C_{35}$	37	6	4	$x^{31} + x^3 + 1$
$C_{45}$	37	4	5	$x^{31} + x^3 + 1$
$C_{55}$	37	4	6	$x^{31} + x^3 + 1$
$C_{16}$	70	9	2	$x^{63} + x + 1$
$C_{26}$	70	4	3	$x^{63} + x + 1$
$C_{36}$	70	4	4	$x^{63} + x + 1$
$C_{46}$	70	4	5	$x^{63} + x + 1$
$C_{56}$	70	4	6	$x^{63} + x + 1$
$C_{66}$	70	4	7	$x^{63} + x + 1$

We construct a parity-check matrix using the generator matrix  $G_{rn}$  for code  $C_{rn}$ . The generator matrix given in (4.1) is in a standard form. From Definition 2.2 parity-check matrix is

$$H_{rn} = \begin{pmatrix} 0 & (x^s + 1)x^n \\ 0 & (x^s + 1)x^{n-1} \\ \vdots & \vdots \\ 0 & (x^s + 1)x^{n-(r-1)} \\ p(x)(x^{n-(r+1)} + \dots + 1) + x^{n-r}(x^s + 1) \\ I_{2^n+n-(r+1)} \end{pmatrix}$$

If a parity-check matrix in standard form specifies a code  $H_{rn} = \begin{pmatrix} B \\ I_{2^n+n-(r+1)} \end{pmatrix}$  or  $H_{rn} = (B: I_{2^n+n-(r+1)})$ , then a generator matrix for the code is  $G_{rn} = [I_{r+1}: -B^T]$ . Many codes are most easily defined by specifying a party-check matrix or a set of parity-check equations equivalently. If a code is given by a party-check matrix  $H_{rn}$ , which is not in standard form, then  $H_{rn}$  can be reduced to standard form, like for a generator matrix.

**Example 4.10.** Generator matrix in the standard form of the code  $C_{23}$  is

$$G_{23} = \begin{pmatrix} 1 & 0 & 0 & 0 & 1 & 1 & 0 & 1 & 1 & 0 & 0 & 0 \\ 0 & 1 & 0 & 0 & 0 & 1 & 1 & 0 & 1 & 1 & 0 & 0 \\ 0 & 0 & 1 & 1 & 0 & 0 & 1 & 0 & 1 & 1 & 0 & 1 \end{pmatrix}$$

We obtain a parity-check matrix of  $C_{23}$  from the generator matrix  $G_{23}$ . Thus,

$$H_{23} = \begin{pmatrix} 0 & 1 & 1 & 0 & 1 & 1 & 0 & 0 & 0 \\ 0 & 0 & 1 & 1 & 0 & 1 & 1 & 0 & 0 \\ 1 & 0 & 0 & 1 & 0 & 1 & 1 & 0 & 1 \\ 1 & 0 & 0 & 0 & 0 & 0 & 0 & 0 & 0 \\ 0 & 1 & 0 & 0 & 0 & 0 & 0 & 0 & 0 \\ 0 & 0 & 1 & 0 & 0 & 0 & 0 & 0 & 0 \\ 0 & 0 & 0 & 1 & 0 & 0 & 0 & 0 & 0 \\ 0 & 0 & 0 & 1 & 0 & 0 & 0 & 0 & 0 \\ 0 & 0 & 0 & 0 & 1 & 0 & 0 & 0 & 0 \\ 0 & 0 & 0 & 0 & 0 & 1 & 0 & 0 & 0 \\ 0 & 0 & 0 & 0 & 0 & 0 & 1 & 0 & 0 \\ 0 & 0 & 0 & 0 & 0 & 0 & 0 & 1 & 0 \\ 0 & 0 & 0 & 0 & 0 & 0 & 0 & 0 & 1 \end{pmatrix}$$

Moreover,  $H_{23}$  is a generator matrix of the dual code  $C_{23}^\perp$ .

## Conclusion and Suggestions

In this paper, we defined a polynomial set  $f_{rn}$  with recursive formulae over  $GF(2)$ .  $f_{rn}$  has polynomials with degree equal to or less than  $n$ . We encode elements of  $f_{rn}$  using a  $p(x)$  irreducible polynomial with the format  $x^{2^n-1} + x^s + 1$ . We obtained a new polynomial set  $F_{rn} = p(x)f_{rn}$ .  $C_{rn}$  is a code corresponding to  $F_{rn}$ . We give coding and decoding algorithms for the code  $C_{rn}$ . This study focused on a polynomial set, polynomial code, a generator matrix, and a parity-check matrix of  $C_{rn}$ . To extend this study, one could study the same topic on finite fields  $GF(q)$ .

## Conflict of interest

There are no conflicts of interest in this work.

## Acknowledgments

We would like to thank the referees for their helpful comments and valuable suggestions.

## References

- [1] Cadilhac M., Mazowiecki F., Paperman C., Pilipczuk M., S'enizergues G., On Polynomial Recursive Sequences, Theory of Computing Systems, (68) (2024) 593–614.
- [2] Fu S., Feng X., Linc D., Wangd Q., A Recursive Construction of Permutation Polynomials over  $F_{(q^2)}$  with OddCharacteristic from R edei Functions, Designs, Codes and Cryptography, 87 (2019) 1481–1498.
- [3] Sidki S., Sadaka R., Benazzouz A., Computing recursive orthogonal polynomial with Schur complements, Journal of Computational and Applied Mathematics, 373 (2020) 112406.
- [4] Shannon C., A Mathematical Theory of Communication, The Bell System Technical Journal, 27 (1948) 379–423, 623–656.
- [5] Dinga C., Ling S., Aq-polynomial approach to cyclic codes, Finite Fields and Their Applications, 20 (2013) 1–14.
- [6] R. Abdullaev, D. Efanov, Polynomial Codes Properties Application in Concurrent Error-Detection Systems of Combinational Logic Devices, IEEE East-West Design & Test Symposium (EWDTS), Batumi, Georgia, 2021.
- [7] Mao-Ching Chiu, Polynomial Representations of Polar Codes and Decoding under Overcomplete Representations, IEEE Communications Letters, 17 (12) (2013) 2340-2343.
- [8] Wang X., Hao Y., Qiao D., Constructions of Polynomial Codes Based on Circular Permutation Over Finite Fields, IEEE, 8 (2020) 134219 - 134223.
- [9] Nalli A. and Haukkanen P., On generalized Fibonacci and Lucas polynomials, Chaos Solitons And Fractals, 42 (2009) 3179-3186.
- [10] Prasad B., Coding theory on  $(h(x), g(y))$ -extension of Fibonacci p-numbers polynomials, Universal Journal of Computational Mathematics, 2 (1) (2014) 6-10.
- [11] Stakhov A. P., Fibonacci matrices, a generalization of the Cassini formula and a new coding theory, Chaos Solitons and Fractals, 30 (1) (2006) 56-66.
- [12] Kaymak O. O., Coding theory for  $h(x)$ -Fibonacci polynomials, J. BAUN Inst. Sci. Technol., 26 (1) (2024) 226-236
- [13] Hill R., A First Course in Coding Theory. Oxford: Clarendon Press, (1986) 1-67.
- [14] F.J. MacWilliams, N.J.A. Sloane, The Theory of Error-Correcting Codes. New York: North-holland Publishing company, (1977) 1-37, 188-215.
- [15] Ling S., Xing C., Coding Theory A First Course. Cambridge University Press, (2004) 39-57.
- [16] Hoffman D. G., Leonard D. A., Lindner C. C., Phelps K. T., Rodger C. A., Wall J. R., Coding Theory, Marcel Dekker Inc., New York, (1991)29-117.Alam M. N., Bonyah E., Fayz-Al-Asad M., Reliable analysis for the Drinfeld-Sokolov-Wilson equation in mathematical physics, *Palest. J. Math.*, 11 (1) (2022) 397-407.



## Digraph Groups Without Leaves Whose Arc Count Exceeds Their Vertex Count by One

Mehmet Sefa Cihan<sup>1,a,\*</sup>

<sup>1</sup> Department of Mathematics, Science Faculty, Sivas Cumhuriyet University, Sivas, Türkiye

\*Corresponding author

### Research Article

#### History

Received: 12/03/2025

Accepted: 11/06/2025



This article is licensed under a Creative Commons Attribution-NonCommercial 4.0 International License (CC BY-NC 4.0)

### ABSTRACT

This paper investigates a particular class of digraph groups that are defined by non-empty presentations. Each relation is expressed in the form  $R(x,y)$ , where  $x$  and  $y$  are distinct generators, and  $R(\cdot,\cdot)$  is based on a fixed cyclically reduced word  $R(a,b)$  involving both  $a$  and  $b$ . A directed graph is constructed for each such presentation, where vertices correspond to generators and edges represent the relations. In previous research, Cihan identified 35 families of digraphs satisfying  $|V(\Gamma)|=|A(\Gamma)|-1$ , of which 11 do not contain leaves. This paper demonstrates that, with two exception families, the rank of the associated groups is either 1 or 2.

**Keywords:** Digraph group, Pride group, Finite cyclic, Rank, Presentations.

<sup>a</sup>  [msefacihan@cumhuriyet.edu.tr](mailto:msefacihan@cumhuriyet.edu.tr)  <https://orcid.org/0000-0002-4303-9023>

## Introduction

This paper focuses on a distinct category of finite connected digraphs and their corresponding group presentations, in which each relator is structured as  $R(x,y)$ , where  $x$  and  $y$  are distinct generators and  $R(\cdot,\cdot)$  is determined by some fixed cyclically reduced word  $R(a,b)$  in the free group generated by  $a$  and  $b$  that involves both  $a$  and  $b$ . Such groups have previously been analyzed in the paper by Cuno and Williams [1].

A fundamental aspect of this study is the construction of a group presentation from a digraph. Let  $\Lambda$  be a finite digraph with a set of vertices  $V(\Lambda)$  and a set of directed arcs  $A(\Lambda)$ . Each vertex  $v \in V(\Lambda)$  correspond to the generators  $x_v$  while each arc  $(u,v) \in A(\Lambda)$  correspond to the relators  $R(x_u, x_v)$ . Consequently, the group  $G_\Lambda(R)$  is defined by the presentation.

$$P_\Lambda(R) = \langle x_v \mid R(x_u, x_v) \mid (u,v) \in A(\Lambda) \rangle.$$

A digraph group is defined as a group that is isomorphic to  $G_\Lambda(R)$  for some  $\Lambda$  and  $R$  [1]. In 2020, the terminology of digraph groups was first introduced by Cuno and Williams [1]. However, the study of such groups predates this terminology, as several previously explored group classes fall into the category of digraph groups, even though they were not explicitly classified as such. In particular, Cihan and Williams also examined the Johnson and Mennicke digraph groups in [2].

Consider the free group with basis  $x_0, \dots, x_{n-1}$  and let  $w$  be a word in the free group, where  $n > 0$ . The shift, denoted by  $\theta$ , is the free group automorphism mapping  $x_i \mapsto x_{i+1}$ , with subscripts mod  $n$ . Then is called a *cyclic presentation*, and we write  $G_n(w)$  for the corresponding cyclically presented group [3].

If  $w$  involves exactly two generators then  $G_n(w)$  is a digraph group by setting  $\Lambda$  to be a directed  $n$ -cycle, i.e.  $V(\Lambda) = \{1, 2, \dots, n\}$  and  $A(\Lambda) = \{(1,2), (2,3), \dots, (n,1)\}$ .

Our focus will be on determining when digraph groups are finite. It is well known that if a group is defined by a presentation with more generators than relators, it must be infinite, which can be verified by abelianizing the groups [3-4]. Therefore, we will concentrate on cases where the number of relators is greater than or equal to the number of generators ( $|V| \leq |A|$ ). The first case we consider is balanced presentations, where the number of generators and relators is equal. Cuno and Williams [1] studied digraph groups  $G_\Gamma(R)$  under the condition  $|V(\Gamma)| = |A(\Gamma)|$ , with the additional assumption that the undirected graph is triangle-free (i.e.,  $\text{girth}(\Gamma) \geq 4$ ). In most cases, they showed that the corresponding group  $G_\Gamma(R)$  is either a finite cyclic group or infinite. Building on this, Cihan [5] identified 35 digraph families satisfying  $|V(\Gamma)| = |A(\Gamma)| - 1$ , of which 11 of them do not contain a leaf. In this paper, we aim to characterize finite cyclic digraph groups within the case  $|V(\Gamma)| = |A(\Gamma)| - 1$ , specifically for digraphs without leaves. Before formally defining these digraph classes, we first construct graphs that meet the conditions outlined in [5].

Under these circumstances (i), (ii), (iv), (v) in [5], there are possible 11 digraph families without leaf as indicated in Figure 1 [5].

We will begin by presenting the classes of digraphs in Figure 1 and stating the main theorem. Following this, we will provide some remarks and lemmas that will be referenced throughout the paper. Next, we will focus on proving whether the corresponding groups are finite cyclic groups. For five of these digraph families, we demonstrate that  $G_\Lambda(R)$  is a finite and cyclic group (i.e.,  $\text{rank}(G_\Lambda(R)) = 1$ ), and in these cases, we will determine the group's order. In four of the families, we establish that the rank of  $G_\Lambda(R)$  is either 1 or 2.

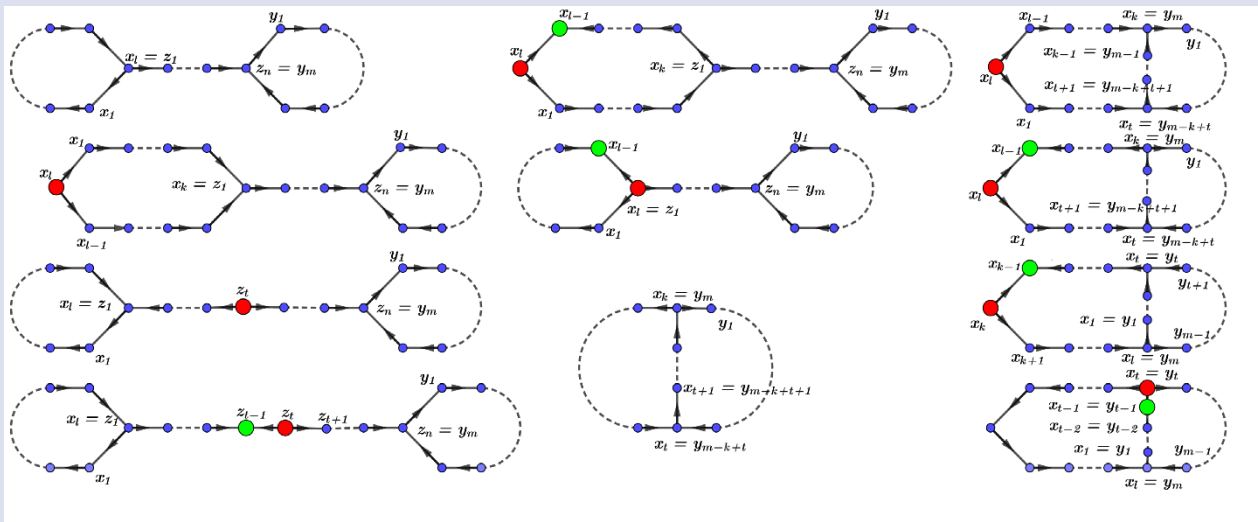


Figure 1. Classes of digraphs without leaf referred to in the statement of Main Theorem

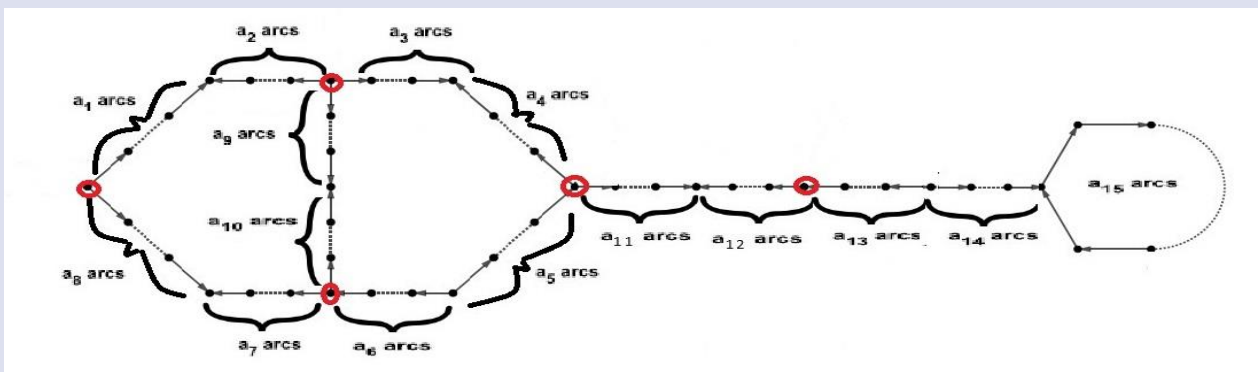


Figure 2. The digraph family that covers all possible digraphs of Main Theorem

**Main Theorem .** Let  $\Lambda$  be a non-empty finite digraph without leaf that the number of generators is equal to the number of relators minus one ( $|V| = |A| - 1$ ) whose underlying undirected graph has girth  $n$  ( $n \geq 4$ ) and let  $R(a, b)$  be a cyclically reduced word that involves both  $a$  and  $b$  with exponent sums  $\alpha$  and  $-\beta$  in  $a$  and  $b$ , respectively where  $|\alpha| \geq 2$ ,  $|\beta| \geq 2$ . If  $G_\Lambda(R)$  is finite, then  $\alpha \neq 0$ ,  $\beta \neq 0$ ,  $(\alpha, \beta) = 1$ ,  $\alpha^n - \beta^n \neq 0$ ,  $a^\alpha = b^\beta$  in  $K = \langle a, b \mid R(a, b) \rangle$ ,  $G_\Lambda(R)$  is non-trivial, and  $\Lambda$  is the digraph in Figure 1.

It is important to note that these digraph families can also be constructed using alternative notations. For instance, the digraph (i) can be represented by the sequence  $a_1, a_3, a_6, a_7, a_{11}, a_{14}, a_{15}$ , but it is equally valid to construct it as  $a_1, a_7, a_9, a_{11}, a_{15}$ . The primary objective in constructing these digraph families is to systematically integrate the designated circle with an appropriate arc, when applicable, as illustrated in Figure 2.

	The possible arcs $a_i$ in Figure 2	in which case
(i)	$a_1, a_3, a_6, a_7, a_{11}, a_{14}, a_{15}$	$G_\Lambda(R) \cong  \alpha^{(l,m)} - \beta^{(l,m)} $
(ii)	$a_1, a_3, a_5, a_8, a_{11}, a_{14}, a_{15}$ ( $l < 2k$ ) ( $l > 2k$ ) ( $l = 2k$ )	$G_\Lambda(R) \cong  \alpha^{\min\{l-k,  n+l-k-1 \}}(\alpha(m, 2k-l) - \beta(m, 2k-l)) $ $G_\Lambda(R) \cong  \alpha^{\min\{k,  n+l-k-1 \}}(\alpha(m, l-2k) - \beta(m, l-2k)) $ $G_\Lambda(R) \cong  \alpha^{n+l-k-1}(\alpha^m - \beta^m) $
(iii)	$a_1, a_3, a_6, a_7, a_{12}, a_{14}, a_{15}$	$G_\Lambda(R) \cong  \alpha^{\min\{ n-1 ,  l-1 \}}(\alpha(l, m) - \beta(l, m)) $
(iv)	$a_1, a_3, a_6, a_7, a_{11}, a_{14}, a_{15}, (a_{12} = 1)$	$\text{rank}(G_\Lambda(R)) \in \{1, 2\}$
(v)	$a_4, a_5, a_6, a_{11}, a_{14}, a_{15}, (a_1 = 1)$	$\text{rank}(G_\Lambda(R)) \in \{1, 2\}$
(vi)	$a_1, a_6, a_7, a_{11}, a_{14}, a_{15}, (a_4 = 1)$	$\text{rank}(G_\Lambda(R)) \in \{1, 2\}$
(vii)	$a_2, a_3, a_6, a_8, a_{10}$	$G_\Lambda(R) \cong  \alpha^{(l,m)} - \beta^{(l,m)} $

(viii)	$a_1, a_3, a_6, a_8, a_{10}$	$G_\Lambda(R)   \alpha^{\min\{k,  l-k \}} (\alpha(m, l-2k) - \beta(m, l-2k))  $
(ix)	$a_2, a_3, a_6, a_8, a_{10}, (a_1 = 1)$	$\text{rank}(G_\Lambda(R)) \in \{1, 2\},$
(x)	$a_2, a_4, a_5, a_8, a_{10}, (a_1 = 1)$	?
(xi)	$a_2, a_3, a_6, a_8, a_{10}, (a_9 = 1)$	?

### A Brief Overview Before Proving The Main Theorem

We now state a reflection principle, a convention, partially introduced by Pride in [6], Lemma 2.4 is a specialisation of a result due to Pride, which was stated without proof in [6] and the proof was stated in [1] and the Lemma 2.5 proved by Cuno & Williams in [1] as we use them frequently throughout the paper. It is also important to understand why we have these conditions in our theorem by the readers.

**Remark 2.1** [1]. We will occasionally make use of a reflection principle: if  $\Lambda$  is any digraph and  $R(a, b)$  is any word, then we may consider the digraph  $\Lambda'$  that is obtained from  $\Lambda$  by reversing the direction of each arc and the word  $R'(a, b)$  that is obtained from  $R(a, b)$  by interchanging  $a$  and  $b$  and further replacing every letter by its inverse so that also  $\alpha$  and  $\beta$  are interchanged (without any change of sign). Then, by definition,  $G_\Lambda(R) \cong G_{\Lambda'}(R')$ .

**Convention 1** [1] We use  $\alpha$  and  $-\beta$  to represent the exponent sums of  $a$  and  $b$  in a cyclically reduced word  $R(a, b)$ , respectively, and  $K$  is used to indicate a group defined by the presentation  $\langle a, b \mid R(a, b) \rangle$ . As far as cyclic permutation is considered, the word  $R$  has the form  $a^{\alpha_1} b^{\beta_1} \dots a^{\alpha_t} b^{\beta_t}$  with  $t \geq 1$  and  $\alpha_i, \beta_i \in \mathbb{Z} \setminus \{0\}$  ( $1 \leq i \leq t$ ).

The following property is defined by Pride in [6]: If no non-empty word of the form  $a^k b^{-\ell}$  ( $k, \ell \in \mathbb{Z}$ ) is equal to the identity in that group, then a two-generator group with generators  $a$  and  $b$  is said to have *Property  $W_1$*  (with respect to  $a$  and  $b$ ). Under the hypothesis that the girth of the underlying undirected graph of  $\Lambda$  is at least 4.

**Corollary 2.2.** [6] Let  $\Lambda$  be a non-empty finite digraph whose underlying undirected graph has  $\text{girth}(G) \geq 4$  and let  $R(a, b)$  be as in convention 1. If  $K$  has Property  $W_1$ , then  $G_\Lambda(R)$  is infinite.

It is therefore important to study groups that do not have Property  $W_1$ .

**Proposition 2.3.** [6] If there exist  $k, \ell \in \mathbb{Z} \setminus \{0\}$  with  $a^k = b^\ell$  in  $K$ , then  $\alpha \neq 0, \beta \neq 0$ , and  $a^\alpha = b^\beta$  in  $K$ .

Therefore,  $K$  does not have Property  $W_1$  if and only if  $\alpha \neq 0, \beta \neq 0$ , and  $a^\alpha = b^\beta$  in  $K$ .

**Lemma 2.4.** [1, 6] Let  $\Lambda$  be a non-empty finite digraph whose underlying undirected graph has girth at least 4 and let  $R(a, b)$  be a cyclically reduced word that involves both  $a$  and  $b$ . Let  $R(a, b)$  be as in convention 1 and  $|\alpha| \geq 2$  and  $|\beta| \geq 2$ . If  $G_\Lambda(R)$  is finite, then  $(\alpha, \beta) = 1$  and  $\Lambda$  has at most one source and at most one sink.

We will now state Lemma 2.5 (a),(b) proved by Cuno and Williams [1] and we add (c), (d). It enables us to simplify the presentations that arise. Therefore, it is stated here for later use without further explanation throughout the paper.

**Lemma 2.5.** [1] Let  $R(a, b)$  be a word such that  $a^\alpha = b^\beta$  in  $K$  and let  $G$  be a group defined by a presentation  $\langle \mathcal{X} \mid \mathcal{R} \rangle$ . Further suppose that there are distinct generators  $x_i, x_j \in \mathcal{X}$  such that  $R(x_i, x_j) \in \mathcal{R}$ . Then the following hold:

- If  $x_i^\gamma \in \mathcal{R}$  for some  $\gamma \in \mathbb{Z}$  with  $(\alpha, \gamma) = 1$ , then every  $p \in \mathbb{Z}$  with  $p\alpha \equiv 1 \pmod{\gamma}$  yields a new presentation  $\langle \mathcal{X} \setminus \{x_i\} \mid \mathcal{S} \rangle$  of  $G$ . The relators  $\mathcal{S}$  are obtained from  $\mathcal{R}$  by removing  $R(x_i, x_j)$  and  $x_i^\gamma$ , replacing all remaining occurrences of  $x_i$  by  $x_j^{p\beta}$ , and adjoining  $x_j^{\beta\gamma}$ .
- If  $x_j^\gamma \in \mathcal{R}$  for some  $\gamma \in \mathbb{Z}$  with  $(\beta, \gamma) = 1$ , then every  $p \in \mathbb{Z}$  with  $p\beta \equiv 1 \pmod{\gamma}$  yields a new presentation  $\langle \mathcal{X} \setminus \{x_j\} \mid \mathcal{S} \rangle$  of  $G$ . The relators  $\mathcal{S}$  are obtained from  $\mathcal{R}$  by removing  $R(x_i, x_j)$  and  $x_j^\gamma$ , replacing all remaining occurrences of  $x_j$  by  $x_i^{p\alpha}$ , and adjoining  $x_i^{\alpha\gamma}$ .
- If  $x_i^\gamma \in \mathcal{R}$  for some  $\gamma \in \mathbb{Z}$  with  $(\alpha, \gamma) = 1$  then every  $p \in \mathbb{Z}$  with  $p\alpha \equiv 1 \pmod{\gamma}$  yields a new presentation  $\langle \mathcal{X} \mid \mathcal{S} \rangle$  of  $G$  where  $\mathcal{S} = \mathcal{R} \cup \{x_i x_j^{-p\beta}, x_j^{\beta\gamma}\}$ .
- If  $x_j^\gamma \in \mathcal{R}$  for some  $\gamma \in \mathbb{Z}$  with  $(\beta, \gamma) = 1$  then every  $p \in \mathbb{Z}$  with  $p\beta \equiv 1 \pmod{\gamma}$  yields a new presentation  $\langle \mathcal{X} \mid \mathcal{S} \rangle$  of  $G$  where  $\mathcal{S} = \mathcal{R} \cup \{x_j x_i^{-p\alpha}, x_i^{\alpha\gamma}\}$ .

If  $\Lambda$  is a directed  $n$ -cycle ( $n \geq 4$ ) and  $R(a, b)$  is a cyclically reduced word that involves both  $a$  and  $b$ , then  $G_\Lambda(R)$  can never be finite of rank 3 or trivial [1]. We now give precise statement of Theorem 2.6 that forms the cornerstone of this paper. The following Theorem 2.6 was stated without proof in [6], a proof was given in [7] and a different proof was given in [4].

**Theorem 2.6.** [1, 6, 7] Let  $R(a, b)$  be as in Convention 1. Further suppose that  $(\alpha, \beta) = 1$  and  $a^\alpha = b^\beta$  in  $K$ . If  $\Lambda = \Lambda(n)$ , where  $\Lambda(n)$  is directed  $n$ -cycle ( $n \geq 2$ ), then  $G_\Lambda(R) \cong \mathbb{Z}_{|\alpha^n - \beta^n|}$ .

The Theorem 2.6 is generalized from cyclic presentations to balanced presentations (i.e.  $|V| = |A|$ ) in [4]. We extend the theorem from balanced presentations to  $|V| = |A| - 1$  without leaf in this paper.

**Lemma 2.7.** [1] Let  $R(a, b)$  be as in Theorem 1. Further suppose that  $(\alpha, \beta) = 1$  and  $a^\alpha = b^\beta$  in  $K$ . Then the following hold:

- If  $\Lambda = \Lambda(n; \xrightarrow{m})$  ( $n \geq 2, m \geq 1$ ), then  $G_\Lambda(R) \cong \mathbb{Z}_{|\beta^m(\alpha^n - \beta^n)|}$ .
- If  $\Lambda = \Lambda(n; \xleftarrow{m})$  ( $n \geq 2, m \geq 1$ ), then  $G_\Lambda(R) \cong \mathbb{Z}_{|\alpha^m(\alpha^n - \beta^n)|}$ .

In many of our digraphs  $\Gamma$  there will be a configuration of the form  $\Lambda(n; \xrightarrow{m})$  or  $\Lambda(n; \xleftarrow{m})$ ; Lemma 2.7 allows us to replace this sub-digraph with a vertex  $x_v$  and adding a corresponding relator  $x_v^P$  to the presentation. To assist the reader in (i) we will explain this reduction in detail, then in later we will use this technique without further explanation.

We now show that if  $l, k$  are vertices of a directed circuit (see Figure 3) then the generator  $x_k$  can be written in terms of generator  $x_l$ . Then we will use this relation in our presentations. We set  $\gamma = \alpha^l - \beta^l$  and  $\zeta = \beta(p\alpha - 1)$ , where  $p\alpha \equiv 1 \pmod{\gamma}$ .

**Lemma 2.8.** Suppose that  $\Lambda_1$  is the circuit in Figure 3 and  $k, l$  are vertices of  $\Lambda_1$  and suppose  $(\alpha, \beta) = 1$ . Let  $p, q$  be integers such that  $p\alpha + q\beta = 1$ . Then  $x_k = x_l^{p^{l-k}\beta^{l-k}}$ .

$$\begin{aligned}
 G_{\Lambda_1}(R) &= \langle x_2, \dots, x_k, \dots, x_l \mid x_2^{\beta\gamma}, R(x_2, x_3), \dots, R(x_{k-1}, x_k), R(x_k, x_{k+1}), \dots, R(x_{l-1}, x_l), R(x_l, x_2^{\beta\gamma}) \rangle \\
 &= \langle x_3, \dots, x_k, \dots, x_l \mid x_3^{\beta^2\gamma}, R(x_3, x_4), \dots, R(x_{k-1}, x_k), R(x_k, x_{k+1}), \dots, R(x_{l-1}, x_l), R(x_l, x_3^{\beta^2\gamma}) \rangle \\
 &= \dots \\
 &= \langle x_k, x_{k+1}, \dots, x_l \mid x_k^{\beta^{k-1}\gamma}, R(x_k, x_{k+1}), R(x_{k+1}, x_{k+2}), \dots, R(x_{l-1}, x_l), R(x_l, x_k^{\beta^{k-1}\gamma}) \rangle \\
 &= \langle x_k, x_{k+1}, \dots, x_l \mid x_k^{\beta^{k-1}\gamma}, x_k = x_{k+1}^{p\beta}, R(x_k, x_{k+1}), R(x_{k+1}, x_{k+2}), \dots, R(x_{l-1}, x_l), R(x_l, x_k^{\beta^{k-1}\gamma}) \rangle \\
 &= \langle x_k, x_{k+1}, \dots, x_l \mid x_k^{\beta^{k-1}\gamma}, x_k = x_{k+1}^{p\beta}, R(x_{k+1}^{p\beta}, x_{k+1}), R(x_{k+1}, x_{k+2}), \dots, R(x_{l-1}, x_l), R(x_l, x_{k+1}^{p\beta}) \rangle \\
 &= \langle x_k, x_{k+1}, \dots, x_l \mid x_k^{\beta^{k-1}\gamma}, x_k = x_{k+1}^{p\beta}, x_{k+1}^{\beta(p\alpha-1)}, R(x_{k+1}, x_{k+2}), \dots, R(x_{l-1}, x_l), R(x_l, x_{k+1}^{p\beta}) \rangle \\
 &= \langle x_k, x_{k+2}, \dots, x_l \mid x_k^{\beta^{k-1}\gamma}, x_k = x_{k+2}^{p^2\beta^2}, x_{k+2}^{\beta\zeta}, R(x_{k+2}, x_{k+3}), \dots, R(x_{l-1}, x_l), R(x_l, x_{k+2}^{p^{k+1}\beta^{k+1}}) \rangle \\
 &= \langle x_k, x_{k+3}, \dots, x_l \mid x_k^{\beta^{k-1}\gamma}, x_k = x_{k+3}^{p^3\beta^3}, x_{k+3}^{\beta^2\zeta}, R(x_{k+3}, x_{k+4}), \dots, R(x_{l-1}, x_l), R(x_l, x_{k+3}^{p^{k+2}\beta^{k+2}}) \rangle \\
 &= \dots \\
 &= \langle x_k, x_l \mid x_k^{\beta^{k-1}\gamma}, x_k = x_l^{p^{l-k}\beta^{l-k}}, x_l^{\beta^{l-k-1}\zeta}, R(x_l, x_l^{p^{l-1}\beta^{l-1}}) \rangle \\
 &= \langle x_k, x_l \mid x_k^{\beta^{k-1}\gamma}, x_k = x_l^{p^{l-k}\beta^{l-k}}, x_l^{\beta^{l-k-1}\zeta}, x_l^{p^{l-1}\beta^{l-1}-\alpha} \rangle \\
 &= \langle x_k, x_l \mid x_k^{\beta^{k-1}\gamma}, x_k = x_l^{p^{l-k}\beta^{l-k}}, x_l^\gamma \rangle. \text{ Hence } x_k = x_l^{p^{l-k}\beta^{l-k}}
 \end{aligned}$$

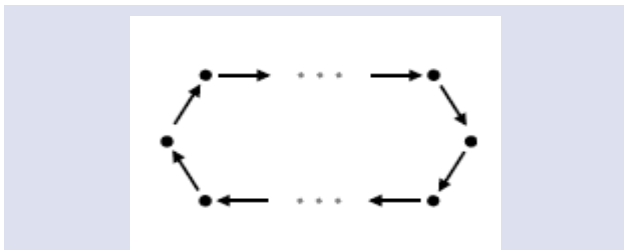


Figure 1.  $\Lambda_1$ : set up a relation between  $x_k$  and  $x_l$ .

**Remark 2.9.** Suppose  $(\alpha, \beta) = 1$ ,  $l, m \geq 1$  and let  $\gamma = \alpha^l - \beta^l$ ,  $\eta = \alpha^m - \beta^m$ . Then  $(\alpha, \gamma) = (\beta, \eta) = 1$ .

$$G_\Gamma(R) = \left\langle \begin{matrix} x_1, \dots, x_l, \\ y_1, \dots, y_m, \\ z_1, \dots, z_n \end{matrix} \mid \begin{matrix} R(x_1, x_2), R(x_2, x_3), \dots, R(x_l, x_1), \\ R(y_1, y_2), R(y_2, y_3), \dots, R(y_m, y_1), \\ R(z_1, z_2), R(z_2, z_3), \dots, R(z_{n-1}, z_n), \\ x_l = z_1, z_n = y_m \end{matrix} \right\rangle$$

$a^\alpha = b^\beta$  in  $K = \langle a, b \mid R(a, b) \rangle$  by Proposition 2.3, thus we get

**Proof.** In this case, we have the presentation of  $G_{\Lambda_1}(R)$  for Figure 3,

$$\langle x_1, x_2, \dots, x_k, \dots, x_l \mid \begin{matrix} x_1^\gamma, R(x_1, x_2), R(x_2, x_3), \dots, R(x_{k-1}, x_k), \\ R(x_k, x_{k+1}), \dots, R(x_{l-1}, x_l), R(x_l, x_1) \end{matrix} \rangle.$$

Note that  $p\alpha \equiv 1 \pmod{\gamma}$ . We continue simplifying this presentation by Lemma 2.5 (a),

### Proving The Main theorem

Recall that we can always suppose that  $\alpha \neq 0$ ,  $\beta \neq 0$ ,  $|\alpha| \geq 2$ ,  $|\beta| \geq 2$ ,  $(\alpha, \beta) = 1$ , and  $a^\alpha = b^\beta$  in  $K$ . Otherwise, the group  $K$  has Property  $W_1$  and thus  $G_\Lambda(R)$  is infinite by Corollary 2.2 and Proposition 2.3.

(i)  $a_1, a_3, a_6, a_7, a_{11}, a_{14}, a_{15}$

The group  $G_\Gamma(R)$  is defined by the presentation

$$\begin{aligned} x_1^{\alpha^l} &= x_2^{\alpha^{l-1}\beta} = x_3^{\alpha^{l-2}\beta^2} = \dots = x_l^{\alpha\beta^{l-1}} = x_1^{\beta^l}. \\ y_1^{\alpha^m} &= y_2^{\alpha^{m-1}\beta} = y_3^{\alpha^{m-2}\beta^2} = \dots = y_m^{\alpha\beta^{m-1}} = y_1^{\beta^m}. \end{aligned}$$

We set  $\gamma = \alpha^l - \beta^l$  and  $\eta = \alpha^m - \beta^m$  obtain that  $x_1^\gamma = 1$ , and  $y_1^\eta = 1$  in  $G_\Gamma(R)$ . Adjoining the relator  $x_1^\gamma$  and  $y_1^\eta$  yield

$$G_\Gamma(R) = \left\langle \begin{array}{l} x_1, \dots, x_l, \\ y_1, \dots, y_m, \\ z_1, \dots, z_n \end{array} \left| \begin{array}{l} x_1^\gamma, R(x_1, x_2), R(x_2, x_3), \dots, R(x_l, x_1), \\ y_1^\eta, R(y_1, y_2), R(y_2, y_3), \dots, R(y_m, y_1), \\ R(z_1, z_2), R(z_2, z_3), \dots, R(z_{n-1}, z_n), \\ x_l = z_1, z_n = y_m \end{array} \right. \right\rangle$$

Applying precisely the same transformations as in the proof of Theorem 2.6, we get

$$G_\Gamma(R) = \left\langle \begin{array}{l} x_1, \dots, x_l, \\ y_1, \dots, y_m, \\ z_1, \dots, z_n \end{array} \left| \begin{array}{l} x_2^{\beta\gamma}, R(x_2, x_3), \dots, R(x_l, x_2^{p\beta}), \\ y_2^{\beta\eta}, R(y_2, y_3), \dots, R(y_m, y_2^{p\beta}), \\ R(z_1, z_2), R(z_2, z_3), \dots, R(z_{n-1}, z_n), \\ x_l = z_1, z_n = y_m \end{array} \right. \right\rangle$$

Simplifying this presentation in that way, what remains is

$$\begin{aligned} G_\Gamma(R) &= \left\langle \begin{array}{l} x_l, y_m, \\ z_1, \dots, z_n \end{array} \left| \begin{array}{l} x_l^\gamma \\ y_m^\eta \\ R(z_1, z_2), R(z_2, z_3), \dots, R(z_{n-1}, z_n), \\ x_l = z_1, z_n = y_m \end{array} \right. \right\rangle \\ &= \left\langle \begin{array}{l} x_l, y_m, \\ z_1, \dots, z_n \end{array} \left| \begin{array}{l} x_l^\gamma \\ z_n^\eta, R(z_1, z_2), R(z_2, z_3), \dots, R(z_{n-1}, z_n), \\ x_l = z_1 \end{array} \right. \right\rangle. \end{aligned}$$

Since  $(\beta, \eta) = 1$  by Remark 2.9 and an iterated application of Lemma 2.5 (b) for the relation inside the box yields

$$\begin{aligned} G_\Gamma(R) &= \langle x_l, z_1 \mid x_l^\gamma, z_1^{\alpha^{n-1}\eta}, x_l = z_1 \rangle \\ &= \langle x_l \mid x_l^\gamma, x_l^{\alpha^{n-1}\eta} \rangle \\ &= \langle x_l \mid x_l^{((\alpha^l - \beta^l), \alpha^{n-1}(\alpha^m - \beta^m))} \rangle \\ &= \langle x_l \mid x_l^{((\alpha^l - \beta^l), (\alpha^m - \beta^m))} \rangle \\ &= \langle x_l \mid x_l^{\alpha^{(l,m)} - \beta^{(l,m)}} \rangle. \end{aligned}$$

So  $G_\Gamma(R)$  is finite cyclic of order  $\alpha^{(l,m)} - \beta^{(l,m)}$ .

(ii)  $\mathbf{a}_1, \mathbf{a}_3, \mathbf{a}_5, \mathbf{a}_8, \mathbf{a}_{11}, \mathbf{a}_{14}, \mathbf{a}_{15}$

The group  $G_\Gamma(R)$  is defined by the presentation

$$G_\Gamma(R) = \left\langle \begin{array}{l} x_1, \dots, x_l, \\ y_1, \dots, y_m, \\ z_1, \dots, z_n \end{array} \left| \begin{array}{l} R(x_l, x_1), R(x_1, x_2), R(x_2, x_3), \dots, R(x_{k-1}, x_k), \\ R(x_l, x_{l-1}), R(x_{l-1}, x_{l-2}), \dots, R(x_{k+1}, x_k), \\ R(y_1, y_2), R(y_2, y_3), \dots, R(y_m, y_1), \\ R(z_1, z_2), R(z_2, z_3), \dots, R(z_{n-1}, z_n), \\ x_k = z_1, z_n = y_m \end{array} \right. \right\rangle.$$

We set as  $\gamma = \alpha^m - \beta^m$  and after applying precisely the same transformations as in the proof of Lemma 2.5 (b) for the relation inside the box yields

$$G_\Gamma(R) = \left\langle \begin{array}{l} x_1, \dots, x_l, \\ y_m, \\ z_1, \dots, z_n \end{array} \left| \begin{array}{l} R(x_l, x_1), R(x_1, x_2), R(x_2, x_3), \dots, R(x_{k-1}, x_k), \\ R(x_l, x_{l-1}), R(x_{l-1}, x_{l-2}), \dots, R(x_{k+1}, x_k), \\ y_m^\gamma, \\ R(z_1, z_2), R(z_2, z_3), \dots, R(z_{n-1}, z_n), \\ x_k = z_1, z_n = y_m \end{array} \right. \right\rangle$$



$$= \left\langle x_1, \dots, x_l, \begin{array}{l} R(x_l, x_1), R(x_1, x_2), R(x_2, x_3), \dots, R(x_{k-1}, x_k), \\ R(x_l, x_{l-1}), R(x_{l-1}, x_{l-2}), \dots, R(x_{k+1}, x_k), \\ z_n^\gamma, R(z_1, z_2), R(z_2, z_3), \dots, R(z_{n-1}, z_n), \\ x_k = z_1 \end{array} \right\rangle.$$

Since  $(\beta, \gamma) = 1$  and (see Remark 2.9), an iterated application of Lemma 2.5 (b) yields

$$\begin{aligned} G_\Gamma(R) &= \left\langle x_1, \dots, x_l, \begin{array}{l} R(x_l, x_1), R(x_1, x_2), R(x_2, x_3), \dots, R(x_{k-1}, x_k), \\ R(x_l, x_{l-1}), R(x_{l-1}, x_{l-2}), \dots, R(x_{k+1}, x_k), \\ z_1^{\alpha^{n-1}\gamma}, x_k = z_1 \end{array} \right\rangle \\ &= \left\langle x_1, \dots, x_k, \dots, x_l \begin{array}{l} R(x_l, x_1), R(x_1, x_2), R(x_2, x_3), \dots, \\ R(x_{k-1}, x_k), \\ x_k^{\alpha^{n-1}\gamma}, \\ R(x_l, x_{l-1}), R(x_{l-1}, x_{l-2}), \dots, R(x_{k+1}, x_k) \end{array} \right\rangle. \end{aligned}$$

Since  $(\beta, \alpha^{n-1}\gamma) = (\beta, \gamma) = 1$  (see Remark 2.9) there exists integers  $p, q$  such that  $p\beta + q\gamma = 1$  and hence  $p\beta = 1 \pmod{\gamma}$ , an iterated application of Lemma 2.5 (b) yields

$$\begin{aligned} G_\Gamma(R) &= \left\langle x_1, \dots, x_{k-1}, \begin{array}{l} R(x_l, x_1), R(x_1, x_2), R(x_2, x_3), \dots, R(x_{k-1}, x_k^{p\alpha}), \\ x_{k+1}^{\alpha^n\gamma}, R(x_l, x_{l-1}), R(x_{l-1}, x_{l-2}), \dots, R(x_{k+2}, x_{k+1}) \end{array} \right\rangle \\ &= \left\langle x_1, \dots, x_{k-1}, \begin{array}{l} R(x_l, x_1), R(x_1, x_2), R(x_2, x_3), \dots, R(x_{k-1}, x_k^{p\alpha^2}), \\ x_{k+2}^{\alpha^{n+1}\gamma}, R(x_l, x_{l-1}), R(x_{l-1}, x_{l-2}), \dots, R(x_{k+3}, x_{k+2}) \end{array} \right\rangle \\ &= \left\langle x_1, \dots, x_{k-1}, \begin{array}{l} x_l^{\alpha^{n+l-k-1}\gamma}, \\ R(x_l, x_1), R(x_1, x_2), R(x_2, x_3), \dots, R(x_{k-1}, x_l^{(p\alpha)^{l-k}}) \end{array} \right\rangle \\ &= \left\langle x_1, \dots, x_{k-1}, \begin{array}{l} x_l^{\alpha^{n+l-k-1}\gamma}, \\ R(x_l, x_1), R(x_1, x_2), R(x_2, x_3), \dots, R(x_{k-1}, x_l^{(p\alpha)^{l-k}}), \\ x_i = x_l^{(p\alpha)^i} \ (1 \leq i \leq k-1) \text{ by Lemma 2.5 (b)} \end{array} \right\rangle \\ &= \left\langle x_l \begin{array}{l} x_l^{\alpha^{n+l-k-1}\gamma}, R(x_l, x_l^{p\alpha}), R(x_l^{p\alpha}, x_l^{(p\alpha)^2}), R(x_l^{(p\alpha)^2}, x_l^{(p\alpha)^3}), \dots, \\ R(x_l^{(p\alpha)^{k-1}}, x_l^{(p\alpha)^{l-k}}) \end{array} \right\rangle \\ &= \left\langle x_l \begin{array}{l} x_l^{\alpha^{n+l-k-1}\gamma}, x_l^{\alpha-\beta p\alpha}, x_l^{p\alpha^2-\beta(p\alpha)^2}, \dots, x_l^{\alpha(p\alpha)^{k-2}-\beta(p\alpha)^{k-1}}, \\ x_l^{\alpha(p\alpha)^{k-1}-\beta(p\alpha)^{l-k}} \end{array} \right\rangle. \end{aligned}$$

We can remove redundant relators  $x_l^{\alpha-\beta p\alpha}, x_l^{p\alpha^2-\beta(p\alpha)^2}, \dots, x_l^{\alpha(p\alpha)^{k-2}-\beta(p\alpha)^{k-1}}$  since  $p\beta \equiv 1 \pmod{\gamma}$ . Thus, we get

$$\begin{aligned} G_\Gamma(R) &= \langle x_l \mid x_l^{\alpha^{n+l-k-1}\gamma}, x_l^{p^{k-1}\alpha^k - p^{l-k}\alpha^{l-k}\beta} \rangle \\ &= \langle x_l \mid x_l^{(\alpha^{n+l-k-1}\gamma, p^{k-1}\alpha^k - p^{l-k}\alpha^{l-k}\beta)} \rangle \\ &= \langle x_l \mid x_l^d \rangle, \text{ where } d = (\alpha^{n+l-k-1}\gamma, p^{k-1}\alpha^k - p^{l-k}\alpha^{l-k}\beta). \end{aligned}$$

$$\begin{aligned} d &= (\alpha^{n+l-k-1}\gamma, p^{k-1}\alpha^k - p^{l-k}\alpha^{l-k}\beta) \\ &= (\alpha^{n+l-k-1}\gamma, (p\beta)p^{k-1}\alpha^k - p^{l-k}\alpha^{l-k}\beta) \text{ since } p\beta \equiv 1 \pmod{\gamma} \\ &= (\alpha^{n+l-k-1}\gamma, \beta(p^k\alpha^k - p^{l-k}\alpha^{l-k})) \\ &= (\alpha^{n+l-k-1}\gamma, p^k\alpha^k - p^{l-k}\alpha^{l-k}) \text{ since } (\beta, \alpha\gamma) = 1 \\ &= (\alpha^{n+l-k-1}\gamma, (p\alpha)^k - (p\alpha)^{l-k}). \end{aligned}$$

After that supposing  $k < l - k$  and continue to simplify the equation above, we get

$$\begin{aligned}
d &= (\alpha^{n+l-k-1}\gamma, (p\alpha)^k(1 - (p\alpha)^{l-2k})) \text{ since } p\beta \equiv 1 \pmod{\gamma} \\
&= (\alpha^{n+l-k-1}\gamma, (p\alpha)^k((p\beta)^{l-2k} - (p\alpha)^{l-2k})) \text{ since } p\beta \equiv 1 \pmod{\gamma} \\
&= (\alpha^{n+l-k-1}\gamma, (p\alpha)^k(p^{l-2k}(\beta^{l-2k} - \alpha^{l-2k}))) \\
&= (\alpha^{n+l-k-1}\gamma, p^{l-k}\alpha^k(\beta^{l-2k} - \alpha^{l-2k})) \\
&= (\alpha^{\min\{k, n+l-k-1\}}(\alpha^{(m, l-2k)} - \beta^{(m, l-2k)})).
\end{aligned}$$

Hence,  $G_\Gamma(R)$  is finite cyclic of order  $\alpha^{\min\{k, |n+l-k-1|\}}(\alpha^{(m, l-2k)} - \beta^{(m, l-2k)})$ .

Now supposing  $k > l - k$  and simplifying the equation, we get

$$\begin{aligned}
d &= (\alpha^{n+l-k-1}\gamma, (p\alpha)^{l-k}((p\alpha)^{2k-l} - 1)) \text{ since } p\beta \equiv 1 \pmod{\gamma} \\
&= (\alpha^{n+l-k-1}\gamma, (p\alpha)^{l-k}((p\alpha)^{2k-l} - (p\beta)^{2k-l})) \text{ since } p\beta \equiv 1 \pmod{\gamma} \\
&= (\alpha^{n+l-k-1}\gamma, (p\alpha)^{l-k}(p^{2k-l}(\beta^{2k-l} - \alpha^{2k-l}))) \\
&= (\alpha^{n+l-k-1}\gamma, p^k\alpha^{l-k}(\beta^{2k-l} - \alpha^{2k-l})) \\
&= (\alpha^{\min\{l-k, n+l-k-1\}}(\alpha^{(m, 2k-l)} - \beta^{(m, 2k-l)})).
\end{aligned}$$

Hence,  $G_\Gamma(R)$  is finite cyclic of order  $\alpha^{\min\{l-k, |n+l-k-1|\}}(\alpha^{(m, 2k-l)} - \beta^{(m, 2k-l)})$ .

Now, supposing  $k = l - k$ , we get

$$x_l^{p^{k-1}\alpha^k - p^{l-k}\alpha^{l-k}\beta} = x_l^{(p\alpha)^k - (p\alpha)^{l-k}} = x_l^{(p\alpha)^k - (p\alpha)^k} = x^0 = 1.$$

Thus, we can remove redundant relators from the presentation. Hence, we get  $G_\Gamma(R) = \langle x_l \mid x_l^{\alpha^{n+l-k-1}\gamma} \rangle$ . Therefore,  $G_\Gamma(R)$  is finite cyclic of order  $\alpha^{n+l-k-1}(\alpha^m - \beta^m)$ .

(iii)  $a_1, a_3, a_6, a_7, a_{12}, a_{14}, a_{15}$

The group  $G_\Gamma(R)$  is defined by the presentation

$$G_\Gamma(R) = \left\langle x_1, \dots, x_l, y_1, \dots, y_m, z_1, \dots, z_n \left| \begin{array}{l} x_1^\gamma, R(x_1, x_2), R(x_2, x_3), \dots, R(x_l, x_1), \\ y_1^\eta, R(y_1, y_2), R(y_2, y_3), \dots, R(y_m, y_1), \\ R(z_t, z_{t-1}), R(z_{t-1}, z_{t-2}), \dots, R(z_2, z_1), \\ R(z_t, z_{t+1}), R(z_{t+1}, z_{t+2}), \dots, R(z_{n-1}, z_n), \\ x_l = z_1, y_m = z_n \end{array} \right. \right\rangle.$$

We set  $\gamma = \alpha^l - \beta^l$  and  $\eta = \alpha^m - \beta^m$ , and apply precisely the same transformations as in the proof of Theorem 2.6. Then, what remains is

$$\begin{aligned}
G_\Gamma(R) &= \left\langle x_l, y_m, z_1, \dots, z_n \left| \begin{array}{l} x_l^\gamma, y_m^\eta, \\ R(z_t, z_{t-1}), R(z_{t-1}, z_{t-2}), \dots, R(z_2, z_1), \\ R(z_t, z_{t+1}), R(z_{t+1}, z_{t+2}), \dots, R(z_{n-1}, z_n), \\ x_l = z_1, y_m = z_n \end{array} \right. \right\rangle \\
&= \left\langle z_1, \dots, z_n \left| \begin{array}{l} z_1^\gamma, R(z_t, z_{t-1}), R(z_{t-1}, z_{t-2}), \dots, R(z_2, z_1), \\ z_n^\eta, R(z_t, z_{t+1}), R(z_{t+1}, z_{t+2}), \dots, R(z_{n-1}, z_n) \end{array} \right. \right\rangle.
\end{aligned}$$

Since  $(\beta, \gamma) = 1$  and  $(\beta, \eta) = 1$  (see Remark 2.9) and an iterated application of Lemma 2.5 (b) yields

$$\begin{aligned}
G_\Gamma(R) &= \left\langle z_2, \dots, z_{n-1} \left| \begin{array}{l} z_2^{\alpha\gamma}, R(z_t, z_{t-1}), R(z_{t-1}, z_{t-2}), \dots, R(z_3, z_2), \\ z_{n-1}^{\alpha\eta}, R(z_t, z_{t+1}), R(z_{t+1}, z_{t+2}), \dots, R(z_{n-2}, z_{n-1}) \end{array} \right. \right\rangle \\
&= \langle z_t \mid z_t^{\alpha^{t-1}\gamma}, z_t^{\alpha^{n-t}\eta} \rangle \\
&= \langle z_t \mid z_t^{\alpha^{\min\{n-t, t-1\}}(\alpha^{(l, m)} - \beta^{(l, m)})} \rangle.
\end{aligned}$$

Hence,  $G_\Gamma(R)$  is finite cyclic of order  $\alpha^{\min\{n-t, t-1\}}(\alpha^{(l, m)} - \beta^{(l, m)})$ .

(iv)  $a_1, a_3, a_6, a_7, a_{11}, a_{14}, a_{15}, (a_{12} = 1)$

The group  $G_\Gamma(R)$  is defined by the presentation

$$G_{\Gamma}(R) = \left\langle \begin{matrix} x_1, \dots, x_l, \\ y_1, \dots, y_m, \\ z_1, \dots, z_n \end{matrix} \left| \begin{matrix} R(x_1, x_2), R(x_2, x_3), \dots, R(x_l, x_1), \\ R(z_1, z_2), R(z_2, z_3), \dots, R(z_{t-2}, z_{t-1}), \\ x_l = z_1, \\ R(y_1, y_2), R(y_2, y_3), \dots, R(y_m, y_1), \\ R(z_t, z_{t+1}), R(z_{t+1}, z_{t+2}), \dots, R(z_{n-1}, z_n), \\ y_m = z_n, \\ R(z_t, z_{t-1}) \end{matrix} \right. \right\rangle$$

We set  $\gamma = \alpha^l - \beta^l$  and  $\eta = \alpha^m - \beta^m$ , and apply precisely the same transformations as we have in the form  $\Gamma(n; \xrightarrow{m})$  for the first box and  $\Gamma(n; \xleftarrow{m})$  for the second box, by Lemma 2.7, we get

$$G_{\Gamma}(R) = \langle z_{t-1}, z_t \mid z_{t-1}^{\beta^{t-2}\gamma}, z_t^{\alpha^{n-t}\eta}, R(z_t, z_{t-1}) \rangle.$$

After we get this presentation, we cannot eliminate  $z_{t-1}$  or  $z_t$  from the presentation. It is because we are not able to apply Lemma 2.5 further since  $(\alpha^{n-t}\eta, \alpha) \neq 1$  and  $(\beta^{t-2}\gamma, \beta) \neq 1$ . Therefore, we cannot go further. Thus, the group  $G_{\Gamma}(R)$  has a 2-generator presentation.

(v)  $a_4, a_5, a_6, a_{11}, a_{14}, a_{15}, (a_1 = 1)$

The group  $G_{\Gamma}(R)$  is defined by the presentation

$$G_{\Gamma}(R) = \left\langle \begin{matrix} x_1, \dots, x_l, \\ y_1, \dots, y_m, \\ z_1, \dots, z_n \end{matrix} \left| \begin{matrix} R(x_l, x_{l-1}), \\ R(x_k, x_{k+1}), \dots, R(x_{l-2}, x_{l-1}), \\ R(x_l, x_1), R(x_1, x_2), \dots, R(x_{k-1}, x_k), \\ R(y_1, y_2), R(y_2, y_3), \dots, R(y_m, y_1), \\ R(z_1, z_2), R(z_2, z_3), \dots, R(z_{n-1}, z_n), \\ x_k = z_1, z_n = y_m \end{matrix} \right. \right\rangle.$$

We set  $\gamma = \alpha^m - \beta^m$  and apply precisely the same transformations as in the proof of (ii) to obtain that

$$G_{\Gamma}(R) = \left\langle \begin{matrix} x_1, \dots, x_l \end{matrix} \left| \begin{matrix} R(x_l, x_{l-1}), \\ R(x_k, x_{k+1}), \dots, R(x_{l-2}, x_{l-1}), \\ x_k^{\alpha^{n-1}\gamma}, R(x_l, x_1), R(x_1, x_2), \dots, R(x_{k-1}, x_k) \end{matrix} \right. \right\rangle.$$

Since  $(\beta, \alpha^{n-1}\gamma) = 1$  (see Remark 2.9) and an iterated application of Lemma 2.5 (b) yields

$$G_{\Gamma}(R) = \left\langle \begin{matrix} x_k, x_{k+1}, \dots, x_l \end{matrix} \left| \begin{matrix} R(x_l, x_{l-1}), \\ R(x_k, x_{k+1}), \dots, R(x_{l-2}, x_{l-1}), \\ x_l^{\alpha^{n+k-1}\gamma} \end{matrix} \right. \right\rangle.$$

Adjoin the relations  $x_i = x_{l-1}^{(p\beta)^{l-1-i}}$  for  $k+1 \leq i \leq l-1$ , where  $p \in \mathbb{Z}$ , to the presentation so we get

$$\begin{aligned} G_{\Gamma}(R) &= \left\langle \begin{matrix} x_k, \dots, x_{l-1}, x_l \end{matrix} \left| \begin{matrix} R(x_l, x_{l-1}), \\ R(x_k, x_{k+1}), \dots, R(x_{l-2}, x_{l-1}), \\ x_l^{\alpha^{n+k-1}\gamma}, x_i = x_{l-1}^{(p\beta)^{l-1-i}} \text{ for } k+1 \leq i \leq l-1 \end{matrix} \right. \right\rangle \\ &= \left\langle \begin{matrix} x_{l-1}, x_l \end{matrix} \left| \begin{matrix} R(x_l, x_{l-1}), \\ R(x_{l-1}^{(p\beta)^{l-k-1}}, x_{l-1}^{(p\beta)^{l-k-2}}), \dots, R(x_{l-1}^{p\beta}, x_{l-1}), \\ x_l^{\alpha^{n+k-1}\gamma} \end{matrix} \right. \right\rangle \\ &= \left\langle \begin{matrix} x_{l-1}, x_l \end{matrix} \left| \begin{matrix} x_l^{\alpha^{n+k-1}\gamma}, R(x_l, x_{l-1}) \end{matrix} \right. \right\rangle. \end{aligned}$$

After we get this presentation, we cannot eliminate  $x_{l-1}$  or  $x_l$  from the presentation. It is because we are not able to apply Lemma 2.5 further since  $(\alpha^{n+k-1}\gamma, \alpha) \neq 1$ . Therefore, we cannot go further. Thus, the group  $G_{\Gamma}(R)$  has a 2-generator presentation.

(vi)  $a_1, a_6, a_7, a_{11}, a_{14}, a_{15}, (a_4 = 1)$

The group  $G_\Gamma(R)$  is defined by the presentation

$$G_\Gamma(R) = \left\langle x_1, \dots, x_l, \begin{array}{l} R(x_l, x_{l-1}), \\ R(x_l, x_1), R(x_1, x_2), \dots, R(x_{k-1}, x_k), \\ y_1^\eta, R(y_1, y_2), R(y_2, y_3), \dots, R(y_m, y_1), \\ z_1, \dots, z_n \\ R(z_1, z_2), R(z_2, z_3), \dots, R(z_{n-1}, z_n), \\ x_l = z_1, y_m = z_n \end{array} \right\rangle.$$

We set  $\gamma = \alpha^m - \beta^m$  and apply precisely the same transformations as in the proof (v) for the relation inside the box to obtain that

$$G_\Gamma(R) = \left\langle x_1, \dots, x_l \mid \begin{array}{l} R(x_l, x_{l-1}), \\ R(x_l, x_1), R(x_1, x_2), \dots, R(x_{l-2}, x_{l-1}), \\ x_l^{\alpha^{n-1}\gamma} \end{array} \right\rangle.$$

Now, adjoin these relations  $x_l = x_1^{p\beta}, x_i = x_{l-1}^{(p\beta)^{l-1-i}}$  for  $1 \leq i \leq l-1$ , where  $p \in \mathbb{Z}$ , to the presentation and we get

$$\begin{aligned} G_\Gamma(R) &= \left\langle x_1, \dots, x_l \mid \begin{array}{l} R(x_l, x_{l-1}), \\ R(x_l, x_1), R(x_1, x_2), \dots, R(x_{l-2}, x_{l-1}), \\ x_l^{\alpha^{n-1}\gamma}, \\ x_l = x_1^{p\beta}, x_i = x_{l-1}^{(p\beta)^{l-1-i}} \text{ for } 1 \leq i \leq l-1 \end{array} \right\rangle \\ &= \left\langle x_1, x_{l-1}, x_l \mid \begin{array}{l} R(x_l, x_{l-1}), \\ R(x_l^{(p\beta)^{l-1}}, x_l^{(p\beta)^{l-2}}), R(x_{l-1}^{(p\beta)^{l-2}}, x_{l-1}^{(p\beta)^{l-3}}), \dots, \\ R(x_{l-1}^{(p\beta)^2}, x_{l-1}^{p\beta}), R(x_{l-1}^{p\beta}, x_{l-1}), \\ x_l^{\alpha^{n-1}\gamma} \end{array} \right\rangle. \end{aligned}$$

Since  $R(x_l^{(p\beta)^i}, x_l^{(p\beta)^{i-1}}) = x_l^{\alpha(p\beta)^i - \beta(p\beta)^{i-1}} = x_l^{(p\beta)^{i-1}(\alpha p\beta - \beta)}$  for  $1 \leq i \leq l-1$ , and  $\alpha p\beta - \beta = 0 \pmod{\gamma}$  since  $p\alpha \equiv 1 \pmod{\gamma}$ . Thus, these relations are redundant so can be removed

$$G_\Gamma(R) = \langle x_{l-1}, x_l \mid x_l^{\alpha^{n-1}\gamma}, R(x_l, x_{l-1}) \rangle.$$

After we get this presentation, we cannot eliminate  $x_{l-1}$  or  $x_l$  from the presentation. It is because we are not able to apply Lemma 2.5 further since  $(\alpha^{n-1}\gamma, \alpha) \neq 1$ . Therefore, we cannot go further. Thus, the group  $G_\Gamma(R)$  has a 2-generator presentation.

(vii)  $a_2, a_3, a_6, a_8, a_{10}$

The group  $G_\Gamma(R)$  is defined by the presentation

$$G_\Gamma(R) = \left\langle x_1, \dots, x_l, \begin{array}{l} x_1^\gamma, R(x_1, x_2), R(x_2, x_3), \dots, R(x_l, x_1) \\ y_1^\eta, R(y_1, y_2), R(y_2, y_3), \dots, R(y_m, y_1), \\ x_t = y_{m-k+t}, x_{t+1} = y_{m-k+t+1}, \dots, x_k = y_m \end{array} \right\rangle.$$

We set  $\gamma = \alpha^l - \beta^l$ ,  $\eta = \alpha^m - \beta^m$ . Since  $p_1\alpha \equiv 1 \pmod{\gamma}$ , there is an integer  $q_1 \in \mathbb{Z}$  such that  $p_1\alpha + q_1\gamma = 1$ . Moreover,  $p_1\alpha \equiv 1 \pmod{\gamma}$  implies that  $y_i = y_i^{p_1\alpha} = y_j^{p_1\beta}$  in  $G$ . This allows us to adjoin the relation  $y_i = y_j^{p_1\beta}$  and to eliminate the generator  $y_i$ , and since  $p_2\alpha \equiv 1 \pmod{\eta}$ , there is an integer  $q_2 \in \mathbb{Z}$  such that  $p_2\alpha + q_2\eta = 1$ . Moreover,  $p_2\alpha \equiv 1 \pmod{\eta}$  implies that  $x_i = x_i^{p_2\alpha} = x_j^{p_2\beta}$  in  $G$ . This allows us to adjoin the relation  $x_i = x_j^{p_2\beta}$  and to eliminate the generator  $x_i$  as follows:

$$\begin{aligned} y_1 &= y_2^{(p_1\beta)} = y_3^{(p_1\beta)^2} = \dots = y_t^{(p_1\beta)^{t-1}} = \dots = y_m^{(p_1\beta)^{m-1}} \\ x_1 &= x_2^{(p_2\beta)} = x_3^{(p_2\beta)^2} = \dots = x_t^{(p_2\beta)^{t-1}} = \dots = x_l^{(p_2\beta)^{l-1}} \end{aligned}$$

$$G_{\Gamma}(R) = \left\langle x_2, \dots, x_l, \begin{array}{l} x_2^{\beta\gamma}, R(x_2, x_3), \dots, R(x_l, x_2^{p_2\beta}) \\ y_2^{\beta\eta}, R(y_2, y_3), \dots, R(y_m, y_2^{p_1\beta}), \\ x_t = y_{m-k+t}, x_{t+1} = y_{m-k+t+1}, \dots, x_k = y_m \end{array} \right\rangle$$

$$= \left\langle x_3, \dots, x_l, \begin{array}{l} x_3^{\beta^2\gamma}, R(x_3, x_4), \dots, R(x_l, x_3^{(p_2\beta)^2}), \\ y_3^{\beta^2\eta}, R(y_3, y_4), \dots, R(y_m, y_3^{(p_1\beta)^2}), \\ x_t = y_{m-k+t}, x_{t+1} = y_{m-k+t+1}, \dots, x_k = y_m \end{array} \right\rangle.$$

Simplifying in that way, what remains is

$$G_{\Gamma}(R) = \left\langle x_k, \begin{array}{l} x_k^{\gamma}, y_m^{\eta} \\ x_k^{(p_2\beta)^{k-t}} = x_k^{(p_1\beta)^{k-t}}, x_k^{(p_2\beta)^{k-t-1}} = x_k^{(p_1\beta)^{k-t-1}}, \dots, x_k = y_m \end{array} \right\rangle$$

$$= \left\langle x_k \begin{array}{l} x_k^{\gamma}, x_k^{\eta} \\ x_k^{(p_2\beta)^{k-t} - (p_1\beta)^{k-t}}, x_k^{(p_2\beta)^{k-t-1} - (p_1\beta)^{k-t-1}}, \dots, x_k^{p_2\beta - p_1\beta} \end{array} \right\rangle$$

$$= \left\langle x_k \begin{array}{l} x_k^{\gamma}, x_k^{\eta} \\ x_k^{\beta^{k-t}(p_2^{k-t} - p_1^{k-t})}, x_k^{\beta^{k-t-1}(p_2^{k-t-1} - p_1^{k-t-1})}, \dots, x_k^{\beta(p_2 - p_1)} \end{array} \right\rangle$$

$$= \left\langle x_k \begin{array}{l} x_k^{\gamma}, x_k^{\eta} \\ x_k^{(\beta^{k-t}, \beta^{k-t-1}, \dots, \beta)(p_2^{k-t} - p_1^{k-t}, p_2^{k-t-1} - p_1^{k-t-1}, \dots, p_2 - p_1)} \end{array} \right\rangle$$

$$= \left\langle x_k \begin{array}{l} x_k^{\gamma}, x_k^{\eta}, x_k^{\beta(p_2 - p_1)} \end{array} \right\rangle$$

$$= \left\langle x_k \begin{array}{l} x_k^{(\gamma, \eta, \beta(p_2 - p_1))} \end{array} \right\rangle$$

$$= \left\langle x_k \mid x_k^{(\gamma, \eta, p_2 - p_1)} \right\rangle.$$

Now,  $p_1\alpha \equiv 1 \pmod{\gamma}$ , and we can say  $p_1\alpha \equiv 1 \pmod{(\gamma, \eta)}$ ,

$p_2\alpha \equiv 1 \pmod{\eta}$ , and we can say  $p_2\alpha \equiv 1 \pmod{(\gamma, \eta)}$ . So,  $p_1\alpha - p_2\alpha \equiv 0 \pmod{(\gamma, \eta)}$ .

Since  $(\alpha, \gamma) = 1$  and  $(\alpha, \eta) = 1$ ,  $\Delta = (\gamma, \eta, (p_1 - p_2)) = (\gamma, \eta, (p_1 - p_2)\alpha) = (\gamma, \eta)$ . Then the presentation is

$$G_{\Gamma}(R) = \langle x_k \mid x_k^{(\gamma, \eta)} \rangle$$

$$= \langle x_k \mid x_k^{\alpha^{(l, m)} - \beta^{(l, m)}} \rangle.$$

So  $G_{\Gamma}(R)$  is finite cyclic of order  $\alpha^{(l, m)} - \beta^{(l, m)}$ .

**(viii)  $a_1, a_3, a_6, a_8, a_{10}$**

The group  $G_{\Gamma}(R)$  is defined by the presentation

$$G_{\Gamma}(R) = \left\langle x_1, \dots, x_l, \begin{array}{l} R(x_l, x_{l-1}), R(x_{l-1}, x_{l-2}), \dots, R(x_{k+1}, x_k), \\ R(x_l, x_1), R(x_1, x_2), \dots, R(x_{k-1}, x_k), \\ y_1^{\eta}, R(y_1, y_2), R(y_2, y_3), \dots, R(y_m, y_1), \\ x_t = y_{m-k+t}, x_{t+1} = y_{m-k+t+1}, \dots, x_k = y_m \end{array} \right\rangle.$$

We set  $\eta = \alpha^m - \beta^m$  and since  $p_1\alpha \equiv 1 \pmod{\eta}$ , there is an integer  $q_1 \in \mathbb{Z}$  such that  $p_1\alpha + q_1\eta = 1$ . Moreover,  $p_1\alpha \equiv 1 \pmod{\eta}$  implies that  $y_i = y_i^{p_1\alpha} = y_j^{p_1\beta}$  in  $G$  and after applying precisely the same transformations as in the proof of Lemma 2.5 (a), we get



$$\begin{aligned}
G_{\Gamma}(R) &= \left\langle x_1, \dots, x_l, \begin{array}{l} R(x_l, x_{l-1}), R(x_{l-1}, x_{l-2}), \dots, R(x_{k+1}, x_k), \\ R(x_l, x_1), R(x_1, x_2), \dots, R(x_{k-1}, x_k), \\ y_m^{\eta}, \\ x_t = y_m^{(p_1\beta)^{k-t}}, x_{t+1} = y_m^{(p_1\beta)^{k-t-1}}, \dots, x_{k-1} = y_m^{p_1\beta}, \\ x_k = y_m \end{array} \right\rangle \\
&= \left\langle x_1, \dots, x_l \begin{array}{l} R(x_l, x_{l-1}), R(x_{l-1}, x_{l-2}), \dots, R(x_{k+1}, x_k), \\ x_k^{\eta}, R(x_l, x_1), R(x_1, x_2), \dots, R(x_{k-1}, x_k), \\ x_t = x_k^{(p_1\beta)^{k-t}}, x_{t+1} = x_k^{(p_1\beta)^{k-t-1}}, \dots, x_{k-1} = x_k^{p_1\beta} \end{array} \right\rangle.
\end{aligned}$$

Since  $(\beta, \eta) = 1$ , there are integers  $p_2, q_2 \in \mathbb{Z}$  such that  $p_2\beta + q_2\eta = 1$  so  $p_2\beta \equiv 1 \pmod{\eta}$ . We can thus apply Lemma 2.5 (b),

$$\begin{aligned}
G_{\Gamma}(R) &= \left\langle x_1, x_2, \dots, x_{k-1}, \begin{array}{l} R(x_l, x_{l-1}), R(x_{l-1}, x_{l-2}), \dots, R(x_{k+1}, x_{k-1}^{p_2\alpha}) \\ x_{k-1}^{\alpha\eta}, R(x_l, x_1), R(x_1, x_2), \dots, R(x_{k-2}, x_{k-1}) \\ x_t = x_k^{(p_1\beta)^{k-t}}, x_{t+1} = x_k^{(p_1\beta)^{k-t-1}}, \dots, \\ x_{k-1} = x_{k-1}^{p_2\alpha p_1\beta} \end{array} \right\rangle \\
&= \left\langle x_1, x_2, \dots, x_{k-2}, \begin{array}{l} R(x_l, x_{l-1}), R(x_{l-1}, x_{l-2}), \dots, R(x_{k+1}, x_{k-2}^{(p_2\alpha)^2}), \\ x_{k-2}^{\alpha^2\eta}, R(x_l, x_1), R(x_1, x_2), \dots, R(x_{k-3}, x_{k-2}), \\ x_t = x_k^{(p_1\beta)^{k-t}}, x_{t+1} = x_k^{(p_1\beta)^{k-t-1}}, \dots, \\ x_{k-2} = x_{k-2}^{(p_2\alpha)^2(p_1\beta)^2} \end{array} \right\rangle.
\end{aligned}$$

Simplifying in that way, what remains is

$$G_{\Gamma}(R) = \left\langle x_1, x_2, \dots, x_t, \begin{array}{l} R(x_l, x_{l-1}), R(x_{l-1}, x_{l-2}), \dots, R(x_{k+1}, x_t^{(p_2\alpha)^{k-t}}), \\ x_t^{\alpha^{k-t}\eta}, R(x_l, x_1), R(x_1, x_2), \dots, R(x_{t-1}, x_t), \\ x_t = x_t^{(p_2\alpha)^{k-t}(p_1\beta)^{k-t}} \end{array} \right\rangle.$$

Since  $(\beta, \alpha^{k-t}\eta) = 1$ , we can thus apply Lemma 2.5 (b),

$$\begin{aligned}
G_{\Gamma}(R) &= \left\langle x_1, \begin{array}{l} x_1^{\alpha^{k-1}\eta}, R(x_l, x_1), \\ R(x_l, x_{l-1}), R(x_{l-1}, x_{l-2}), \dots, \\ R(x_{k+1}, x_1^{(p_2\alpha)^{k-1}}) \end{array} \right\rangle \\
&= \left\langle x_{k+1}, x_{k+2}, \dots, x_l \begin{array}{l} x_l^{\alpha^k\eta}, R(x_l, x_{l-1}), R(x_{l-1}, x_{l-2}), \dots, \\ R(x_{k+1}, x_l^{(p_2\alpha)^k}), \\ x_i = x_l^{(p_2\alpha)^{l-i}} \text{ for } k+1 \leq i \leq l-1 \end{array} \right\rangle \\
&= \left\langle x_l \begin{array}{l} x_l^{\alpha^k\eta}, R(x_l, x_l^{p_2\alpha}), R(x_l^{p_2\alpha}, x_l^{(p_2\alpha)^2}), \dots, R(x_l^{(p_2\alpha)^{l-k-2}}, \\ x_l^{(p_2\alpha)^{l-k-1}}), R(x_l^{(p_2\alpha)^{l-k-1}}, x_l^{(p_2\alpha)^k}) \end{array} \right\rangle \\
&= \left\langle x_l \begin{array}{l} x_l^{\alpha^k\eta}, x_l^{\alpha-\beta p_2\alpha}, x_l^{p_2\alpha^2-\beta(p_2\alpha)^2}, \dots, \\ x_l^{\alpha(p_2\alpha)^{l-k-2}-\beta(p_2\alpha)^{l-k-1}}, x_l^{\alpha(p_2\alpha)^{l-k-1}-\beta(p_2\alpha)^k} \end{array} \right\rangle \\
&= \left\langle x_l \begin{array}{l} x_l^{\alpha^k\eta}, x_l^{\alpha-\beta p_2\alpha}, x_l^{p_2\alpha(\alpha-\beta p_2\alpha)}, \dots, \\ x_l^{(p_2\alpha)^{l-k-2}(\alpha-\beta p_2\alpha)}, x_l^{\alpha(p_2\alpha)^{l-k-1}-\beta(p_2\alpha)^k} \end{array} \right\rangle.
\end{aligned}$$

Since  $x_l^{\alpha-\beta p_2\alpha} = x_l^{\alpha-\alpha} = 1 \pmod{\eta}$ , we get

$$G_{\Gamma}(R) = \langle x_l \mid x_l^{\alpha^k\eta}, x_l^{\alpha(p_2\alpha)^{l-k-1}-\beta(p_2\alpha)^k} \rangle.$$

Supposing  $l - k < k$ , then

$$\begin{aligned}
\alpha(p_2\alpha)^{l-k-1} - \beta(p_2\alpha)^k &= p_2^{l-k-1}\alpha^{l-k} - \beta p_2^k\alpha^k \\
&= p_2^{l-k-1}\alpha^{l-k} - p_2^{k-1}\alpha^k \\
&= p_2^{l-k-1}\alpha^{l-k}(1 - p_2^{2k-l}\alpha^{2k-l}) \\
&= p_2^{l-k-1}\alpha^{l-k}(p_2^{2k-l}\beta^{2k-l} - p_2^{2k-l}\alpha^{2k-l}) \text{ since } p_2\beta \equiv 1 \pmod{\eta} \\
&= p_2^{l-k-1}\alpha^{l-k}p_2^{2k-l}(\beta^{2k-l} - \alpha^{2k-l}) \\
&= p_2^{k-1}\alpha^{l-k}(\beta^{2k-l} - \alpha^{2k-l}).
\end{aligned}$$

Thus, we get

$$\begin{aligned}
G_\Gamma(R) &= \langle x_l \mid x_l^{\alpha^k\eta}, x_l^{p_2^{k-1}\alpha^{l-k}(\beta^{2k-l} - \alpha^{2k-l})} \rangle \\
&= \langle x_l \mid x_l^{\alpha^{\min\{k, l-k\}}(\beta^{(m, 2k-l)} - \alpha^{(m, 2k-l)})} \rangle.
\end{aligned}$$

Hence,  $G_\Gamma(R)$  is finite cyclic of order  $\alpha^{\min\{k, l-k\}}(\alpha^{(m, 2k-l)} - \beta^{(m, 2k-l)})$ .  
Supposing  $l - k > k$ , then

$$\begin{aligned}
\alpha(p_2\alpha)^{l-k-1} - \beta(p_2\alpha)^k &= p_2^{l-k-1}\alpha^{l-k} - \beta p_2^k\alpha^k \\
&= p_2^{l-k-1}\alpha^{l-k} - p_2^{k-1}\alpha^k \\
&= p_2^{k-1}\alpha^k(p_2^{l-2k}\alpha^{l-2k} - 1) \\
&= p_2^{k-1}\alpha^k(p_2^{l-2k}\alpha^{l-2k} - p_2^{l-2k}\beta^{l-2k}) \text{ since } p_2\beta \equiv 1 \pmod{\eta} \\
&= p_2^{l-k-1}\alpha^k(\alpha^{l-2k} - \beta^{l-2k}).
\end{aligned}$$

Therefore, we get

$$\begin{aligned}
G_\Gamma(R) &= \langle x_l \mid x_l^{\alpha^k\eta}, x_l^{p_2^{l-k-1}\alpha^k(\alpha^{l-2k} - \beta^{l-2k})} \rangle \\
&= \langle x_l \mid x_l^{\alpha^k(\alpha^{(m, l-2k)} - \beta^{(m, l-2k)})} \rangle.
\end{aligned}$$

Hence,  $G_\Gamma(R)$  is finite cyclic of order  $\alpha^k(\alpha^{(m, l-2k)} - \beta^{(m, l-2k)})$ .

Supposing  $k = l - k$ , then  $x_l^{p_2^{k-1}\alpha^{l-k}(\beta^{2k-l} - \alpha^{2k-l})} = x_l^{p_2^{k-1}\alpha^k(p_2^{l-2k}\alpha^{l-2k-1})} = x_l^0 = 1$ .

Therefore, it can be removed from the presentation. Thus, we get  $G_\Gamma(R) = \langle x_l \mid x_l^{\alpha^k\eta} \rangle$ . Hence,  $G_\Gamma(R)$  is finite cyclic of order  $|\alpha^k(\alpha^m - \beta^m)|$ .

(ix)  $a_2, a_3, a_6, a_8, a_{10}, (a_1 = 1)$

The group  $G_\Gamma(R)$  is defined by the presentation

$$G_\Gamma(R) = \left\langle x_1, \dots, x_l, y_1, \dots, y_m \mid \begin{array}{l} R(x_l, x_{l-1}), \\ R(x_k, x_{k+1}), \dots, R(x_{l-2}, x_{l-1}), \\ R(x_l, x_1), R(x_1, x_2), \dots, R(x_{k-1}, x_k), \\ y_1^\eta, R(y_1, y_2), R(y_2, y_3), \dots, R(y_m, y_1), \\ x_t = y_{m-k+t}, x_{t+1} = y_{m-k+t+1}, \dots, x_k = y_m \end{array} \right\rangle.$$

We set  $\eta = \alpha^m - \beta^m$ ,  $p_1\alpha \equiv 1 \pmod{\eta}$  and  $p_2\beta \equiv 1 \pmod{\eta}$  as in (viii) then we apply precisely the same transformations as in the proof of (viii) for the relations inside the box to obtain that

$$\begin{aligned}
G_\Gamma(R) &= \left\langle x_{k+1}, x_{k+2}, \dots, x_l \mid \begin{array}{l} R(x_l, x_{l-1}), \\ x_l^{\alpha^k\eta}, R(x_l^{(p_2\alpha)^k}, x_{k+1}), R(x_{k+1}, x_{k+2}), \dots, \\ R(x_{l-2}, x_{l-1}) \end{array} \right\rangle \\
&= \left\langle x_{k+1}, x_{k+2}, \dots, x_l \mid \begin{array}{l} R(x_l, x_{l-1}), \\ x_l^{\alpha^k\eta}, R(x_l^{(p_2\alpha)^k}, x_{k+1}), R(x_{k+1}, x_{k+2}), \dots, \\ R(x_{l-2}, x_{l-1}), \\ x_i = x_{l-1}^{(p_2\beta)^{l-1-i}} \text{ for } k+1 \leq i \leq l-1 \end{array} \right\rangle \\
&= \left\langle x_{l-1}, x_l \mid \begin{array}{l} R(x_l, x_{l-1}), \\ x_l^{\alpha^k\eta}, R(x_l^{(p_2\alpha)^k}, x_{k+1}), R(x_{k+1}, x_{k+2}), \dots, R(x_{l-2}, x_{l-1}), \\ x_i = x_{l-1}^{(p_2\beta)^{l-1-i}} \text{ for } k+1 \leq i \leq l-1 \end{array} \right\rangle
\end{aligned}$$

$$\begin{aligned}
 &= \left\langle x_{l-1}, x_l \left| \begin{array}{l} R(x_l, x_{l-1}), \\ x_l^{\alpha k \eta}, R(x_l^{(p_2 \alpha)^k}, x_{l-1}^{(p_2 \beta)^{l-k-2}}), R(x_{l-1}^{(p_2 \beta)^{l-k-2}}, x_{l-1}^{(p_2 \beta)^{l-k-3}}), \\ \dots, R(x_{l-1}^{p_2 \beta}, x_{l-1}) \end{array} \right. \right\rangle \\
 &= \left\langle x_{l-1}, x_l \left| x_{l-1}, x_l \mid R(x_l, x_{l-1}), x_l^{\alpha k \eta}, R(x_l^{(p_2 \alpha)^k}, x_{l-1}^{(p_2 \beta)^{l-k-2}}) \right. \right\rangle \\
 &= \left\langle x_{l-1}, x_l \left| x_l^{\alpha k \eta}, x_l^\alpha = x_{l-1}^\beta, x_l^{\alpha(p_2 \alpha)^k} = x_{l-1}^{\beta(p_2 \beta)^{l-k-2}} \right. \right\rangle \\
 &= \left\langle x_{l-1}, x_l \left| x_l^{\alpha k \eta}, x_l^\alpha = x_{l-1}^\beta, x_l^{\alpha(p_2 \alpha)^k} = x_l^{\alpha(p_2 \beta)^{l-k-2}} \right. \right\rangle \\
 &= \left\langle x_{l-1}, x_l \left| x_l^{(\alpha k \eta, \alpha(p_2 \alpha)^k - \alpha(p_2 \beta)^{l-k-2})}, x_l^\alpha = x_{l-1}^\beta \right. \right\rangle.
 \end{aligned}$$

After we get this presentation, we cannot eliminate  $x_{l-1}$  or  $x_l$  from the presentation by our limited knowledge now (it is because we cannot apply Lemma 2.5 further). Thus, the group  $G_\Gamma(R)$  has a 2-generator presentation.

(x)  $a_2, a_4, a_5, a_8, a_{10}, (a_1 = 1)$

The group  $G_\Gamma(R)$  is defined by the presentation

$$G_\Gamma(R) = \left\langle x_1, \dots, x_l, y_1, \dots, y_m \left| \begin{array}{l} R(x_k, x_{k+1}), R(x_{k+1}, x_{k+2}), \dots, R(x_{l-1}, x_l), \\ R(x_k, x_{k-1}), \\ R(x_t, x_{t+1}), R(x_{t+1}, x_{t+2}), \dots, R(x_{k-2}, x_{k-1}), \\ R(y_m, y_1), R(y_1, y_2), \dots, R(y_{t-1}, y_t), \\ R(y_m, y_{m-1}), R(y_{m-1}, y_{m-2}), \dots, R(y_{t+1}, y_t), \\ x_l = y_m, x_1 = y_1, x_2 = y_2, \dots, x_t = y_t \end{array} \right. \right\rangle.$$

There are no directed cycles in that graph. Therefore, we cannot apply Theorem 2.6 and thus it is still an open problem.

(xi)  $a_2, a_3, a_6, a_8, a_{10}, (a_9 = 1)$

The group  $G_\Gamma(R)$  is defined by the presentation

$$G_\Gamma(R) = \left\langle x_1, \dots, x_{l-1}, \dots, y_m \left| \begin{array}{l} R(x_t, x_{t+1}), R(x_{t+1}, x_{t+2}), \dots, R(x_{l-1}, x_l), \\ R(x_l, x_1), R(x_1, x_2), \dots, R(x_{t-2}, x_{t-1}), \\ R(x_t, x_{t-1}), \\ R(y_t, y_{t+1}), R(y_{t+1}, y_{t+2}), \dots, \\ R(y_{m-1}, y_m), \\ x_l = y_m, x_1 = y_1, x_2 = y_2, \dots, x_t = y_t \end{array} \right. \right\rangle.$$

There are no directed cycles in that graph. Therefore, we cannot apply Theorem 2.6 and thus it is still an open problem.

## Conflicts of interest

There are no conflicts of interest in this work.

## Acknowledgement

The author thanks Gerald Williams for their careful readings and insightful comments on a draft of this article. This paper is derived from the author's doctoral dissertation.

## References

- [1] Cuno J., Williams G., A class of digraph groups defined by balanced presentations, *Journal of Pure and Applied Algebra*, 224(8) (2020) 106342.
- [2] Cihan M.S., Williams G., Finite groups defined by presentations in which each defining relator involves exactly two generators, *Journal of Pure and Applied Algebra* 228 (4) (2024) 107499.
- [3] Johnson D.L., Topics in the theory of group presentations, *London Mathematical Society Lecture Note Series*, 42. Cambridge University Press, (1980).

- [4] Johnson D.L., Robertson E.F., Finite groups of deficiency zero, In Homological group theory (Proc. Sympos., Durham, 1977), *London Math. Soc. Lecture Note Ser.*, Cambridge Univ. Press, Cambridge-New York, (36) 1979 275-289.
- [5] Cihan M.S., Digraph groups corresponding to digraphs with one more vertex than arcs, *European Journal of Science and Technology.*, (41) (2022) 31–35.
- [6] Pride S.J., Groups with presentations in which each defining relator involves exactly two generators, *J. Lond. Math. Soc.*, II. Ser. 36 (1-2) (1987) 245–256.
- [7] Bogley W.A., Williams G., Efficient finite groups arising in the study of relative asphericity, *Math. Z.* 284(1) (2016) 507–535.
- [8] Cihan M.S., Digraph Groups and Related Groups, Doctoral dissertation, University of Essex, 2022.

# AUTHOR GUIDELINES

Thank you for choosing to submit your paper to Cumhuriyet Science Journal. The following instructions will ensure we have everything required so your paper can move through pre-evaluating, peer review, production and publication smoothly. Please take the time to read and follow them as closely as possible, as doing so will ensure your paper matches the journal's requirements.

## Submission

*Cumhuriyet Science Journal* is an international, peer-reviewed, free of charge journal covering the full scope of both natural and engineering sciences. Manuscripts should be submitted by one of the authors of the manuscript as online submission after registration to the Cumhuriyet Sciences Journal. Microsoft Word (.doc, .docx, .rtf), files can be submitted. There is no page limit. If there is a problem while uploading the files of manuscript, please try to reduce their file size, especially manuscripts including embedded figures. Submissions by anyone other than one of the authors will not be accepted. The submitting author takes responsibility for the paper during submission and peer review. If for some technical reason submission through the online submission system is not possible, the author can contact [csj@cumhuriyet.edu.tr](mailto:csj@cumhuriyet.edu.tr) for support.

## Submission or processing charges

*Cumhuriyet Science Journal* does not charge any article submission, processing charges, and printing charge from the authors.

## Terms of Submission

Papers must be submitted on the understanding that they have not been published elsewhere (except in the form of an abstract or as part of a published lecture, review, or thesis) and are not currently under consideration by another journal. The submitting author is responsible for ensuring that the article's publication has been approved by all the other coauthors. It is also the authors' responsibility to ensure that the articles emanating from a particular institution are submitted with the approval of the necessary institution. Only an acknowledgment from the editorial office officially establishes the date of receipt. Further correspondence and proofs will be sent to the author(s) before publication unless otherwise indicated. It is a condition of submission of a paper that the corresponding author permit editing of the paper for readability. All enquiries concerning the publication of accepted papers should be addressed to [csj@cumhuriyet.edu.tr](mailto:csj@cumhuriyet.edu.tr). Please note that Cumhuriyet Science Journal uses iThenticate software to screen papers for unoriginal material. By submitting your paper to Cumhuriyet Science Journal are agreeing to any necessary originality checks your paper may have to undergo during the peer review and production processes. Upon receiving a new manuscript, the Editorial office conducts initial pre-refereeing checks to ensure the article is legible, complete, correctly formatted, original, within the scope of the journal in question, in the style of a scientific article and written in clear English. Any article that has problems with any of the journal criteria may be rejected at this stage.

## Peer Review

This journal operates a single blind review process. All contributions will be initially assessed by the editor for suitability for the journal. Papers deemed suitable are then typically sent to a minimum of two independent expert reviewer to assess the scientific quality of the paper. The author is required to upload the revised article to the system within 15 days by making the corrections suggested by the referee. The article will be rejected if there are no fixes in it. The Editor is responsible for the final decision regarding acceptance or rejection of articles. The Editor's decision is final

## Title and Authorship Information

The following information should be included

Paper title

Full author names

Full institutional mailing addresses



Corresponding address

Email address

### **Abstract**

The manuscript should contain an abstract. The researchers who are native speakers of Turkish have to add Turkish title and abstract as well. The abstract should be self-contained and citation-free and should be 250-300 words.

### **Keywords**

Keywords of the scientific articles should be selected from the web address of [www.bilimadresleri.com](http://www.bilimadresleri.com)

### **Introduction**

This section should be succinct, with no subheadings.

### **Materials and Methods**

This part should contain sufficient detail so that all procedures can be repeated. It can be divided into subsections if required.

### **Conflicts of interest**

Sample sentence if there is no conflict of interest: The authors stated that did not have conflict of interests.

### **Acknowledgements**

Sample sentences for acknowledgements: The work was supported by grants from CUBAP (T-11111). We would like to acknowledge Prof. Mehmet Sözer, MD, for his precious technical and editorial assistance. We would like to thank

### **References**

References to cited literature should be identified by number in the text in square brackets and grouped at the end of the paper in numerical order of appearance. Each reference must be cited in the text. Always give inclusive page numbers for references to journal articles and a page range or chapter number for books. References should be styled and punctuated according to the following examples

- [1] Karaca E., Ulusoy S., Morgül Ü., Ulusoy H.I., Development of Analytical Method for Sensitive Determination of Streptozotocin based on Solid Phase Extraction, Cumhuriyet Sci. J., 41 (4) (2020) 826-831. (sample reference for journals)
- [2] Keskin B., Ozkan A.S., Inverse Spectral Problems for Dirac Operator with Eigenvalue Dependent Boundary and Jump Conditions, Acta Math. Hungar., 130 (2011) 150-159(sample reference for journals)
- [3] Mazur M.T., Kurman R.J., Dysfunctional Uterine Bleeding. In: Mazur M.T., Kurman R.J., (Eds). Diagnosis of endometrial biopsies and curettings, A practical approach. 2nd ed. Berlin: Springer, (2005) 100-120. (sample reference for book chapters)
- [4] Mazur M.T., Kurman R.J.,Diagnosis of endometrial biopsies and curettings, A practical approach. 2nd ed. Berlin, (2005) 100-120. (sample reference for book)
- [5] National Cancer Institute, Surveillance Epidemiology and End Results. Cancer of the Corpus and Uterus, NOS. Available at: [http://seer.cancer.gov/statfacts/html/corp.html?statfacts\\_page=corp](http://seer.cancer.gov/statfacts/html/corp.html?statfacts_page=corp). Retrieved March 2, 2008. (sample reference for websites)
- [6] Surname N., Title of thesis, PD or master thesis, Name of university, name of institue, year. (sample reference for thesis)
- [7] Surname N., Title of fulltext conference paper, name of conference, city, year, pages. (sample reference for Abstratcs in conferences are not accepted as a valid reference except full text )

### **Preparation of Figures**

Each figure can be integrated in the paper body or separately uploaded and should be cited in a consecutive order. Figure widths can be 4-6 inch as 300 dpi. The labels of the figures should be clear and informative. The name and the subtitles of the figures must be 9-point font.

## **Preparation of Tables**

Tables should be cited consecutively in the text. Every table must have a descriptive title and if numerical measurements are given, the units should be included in the column heading. Tables should be simple with simple borders and text written as left text. The name and the subtitle of the tables must be 9-point font

## **Proofs**

Corrected proofs must be returned to the publisher within 2 weeks of receipt. The publisher will do everything possible to ensure prompt publication. It will therefore be appreciated if the manuscripts and figures conform from the outset to the style of the journal.

## **Copyright**

Open Access authors retain the copyrights of their papers, and all open access articles are distributed under the terms of the Creative Commons Attribution license, which permits unrestricted use, distribution and reproduction in any medium, provided that the original work is properly cited.

The use of general descriptive names, trade names, trademarks, and so forth in this publication, even if not specifically identified, does not imply that these names are not protected by the relevant laws and regulations.

While the advice and information in this journal are believed to be true and accurate on the date of its going to press, neither the authors, the editors, nor the publisher can accept any legal responsibility for any errors or omissions that may be made. The publisher makes no warranty, express or implied, with respect to the material contained herein.

## **Ethical Guidelines**

New methods and ethically relevant aspects must be described in detail, bearing in mind the following:

**Human Experiments.** All work must be conducted in accordance with the Declaration of Helsinki (1964). Papers describing experimental work on human subjects who carry a risk of harm must include:

A statement that the experiment was conducted with the understanding and the consent of the human subject.

A statement that the responsible Ethical Committee has approved the experiments.

**Animal Experiments.** Papers describing experiments on living animals should provide:

A full description of any anaesthetic and surgical procedure used.

Evidence that all possible steps were taken to avoid animal suffering at each stage of the experiment. Papers describing experiments on isolated tissues must indicate precisely how the donor tissues were obtained.

## **Submission Preparation Checklist**

As part of the submission process, authors are required to check off their submission's compliance with all of the following items, and submissions may be rejected that do not adhere to these guidelines.

The submission has not been previously published, nor is it before another journal for consideration (or an explanation has been provided in Comments to the Editor).

The submission file is in Microsoft Word document file (Times New Roman) format.

Where available, URLs for the references have been provided.

The text is single-spaced; uses a 11-point font; employs italics, rather than underlining (except with URL addresses); and all illustrations, figures, and tables are placed within the text at the appropriate points, rather than at the end.

The text adheres to the stylistic and bibliographic requirements outlined in the Author Guidelines, which is found in About the Journal.

If submitting to a peer-reviewed section of the journal, the instructions in Ensuring a Double-Blind Review have been followed.